Universitat Autònoma de Barcelona

Environmental Applications of Engineered Nanomaterials: Synthesis and Characterization

Ahmad Mohamed Ahmad Abo Markeb

Universitat Autònoma de Barcelona

PhD thesis

Environmental Applications of Engineered Nanomaterials: Synthesis and Characterization

Ahmad Mohamed Ahmad Abo Markeb

September 2017

Title: Environmental Applications of Engineered Nanomaterials: Synthesis and Characterization

Realized by: Ahmad Mohamed Ahmad Abo Markeb

Supervised by: Dr. Xavier Font & Dr. Amanda Alonso

PhD program in Environmental Science and Technology

Departament d'Enginyeria Química Biològica i Ambiental.

Escola d'Enginyeria

Universitat Autònoma de Barcelona (UAB)

Part of the work presented here was developed in the framework of the following project:

Desarrollo de una nueva generación de nanoestructuras para la eliminación de gases de efecto invernadero (NANO-GEI). Founded by: Fundación Areces.

Universitat Autònoma de Barcelona

Xavier Font Segura i Amanda Alonso González, professors del Departament d'Enginyeria Química Biològica i Ambiental de la Universitat Autònoma de Barcelona,

CERTIFIQUEM:

Que el Llicenciat en Químiques, Ahmad Mohamed Ahmad Abo Markeb, ha realitzat sota la nostra direcció el treball que, amb títol *Environmental Applications of Engineered Nanomaterials: Synthesis and Characterization*, es presenta en aquesta memòria, la qual constitueix la seva Tesi per optar al Grau de Doctor per la Universitat Autònoma de Barcelona.

I perquè en prengueu coneixement i consti als efectes oportuns, presentem a l'Escola d'Enginyeria de la Universitat Autònoma de Barcelona l'esmentada Tesi, signant el present certificat.

Bellaterra, 15 de juny de 2017

Prof. Xavier Font Segura **Dr. Amanda Alonso**

To my parents, brother, and sister

To my lovely wife and son

To Faculty of Science, Assiut University, Egypt

Acknowledgments

Acknowledgments

First and foremost, I thank ALLAH the most Beneficent and Merciful for this thesis. Then I would like to divide my grateful thanks into two parts;

I- In Spain

Thank you very much Prof. Toni Sánchez, leader of GICOM group, for helping me to obtain the scholarship from Egypt to get my PhD thesis from Universitat Autònoma de Barcelona (UAB), and to his continuously encouragement and supports.

Very special gratitude to Prof. Xavier Font, and Dr. Amanda Alonso for being such as wonderful and helpful supervisors to me. Thank you very much for your guidance and I am highly indebted to both of you for your encouragement, the patience for my imperfections and open up the opportunity for me to work in such an interesting research.

I would like to express my appreciations to all members of GICOM group and especially Prof. Teresa Gea, Prof. Adriana, Dr. Raquel, Dr. Javier Moral for their supports and encouragements. I am very grateful being a member of this extremely supportive research group.

Very special thanks to all my colleagues in GICOM group and especially to Pedro, Oscar, Alejandra, Cindy, and Maria for their helps and supports.

Also, a special mention to Lucia Delgado, I would like to express my thanks for her help in Toxicity measurements and other technical staff in the lab.

Thanks to the director and to all members of the secretary of Departament d'Enginyeria Química Biològica i Ambiental.

I would like to acknowledge Manuel, Pili, and Rosi for their technical assistance.

Acknowledgment

Besides, I would like to express all my appreciations to people who work in Servei d'Anàlisi Química, Servei de Microscopia, Institut Català de Nanociència i Nanotecnologia (ICN2), and Institut Català de Materials Avançats de Barcelona (ICMAB) for their helps to characterize the nanomaterials.

Special thanks to Montserrat, coordinator of Institut de Ciencia i Tecnología Ambiental (ICTA), and to Cristina Duran for their helps.

My Sincere thanks are extended to the examination committee for reviewing the thesis.

II- In Egypt

First, I would like to thank the cultural affairs sector and missions (Ministry of higher education and scientific research) for the grant to study my PhD at Universitat Autònoma de Barcelona (UAB), Spain.

I would like to express my great thanks and deep appreciation to my previous supervisor Prof. Nagwa Abo EL-Maali**,** Vice-Dean of the Faculty of Science for Post Graduate and Research, Assiut University and Professor of Analytical Chemistry, Faculty of Science, Assiut University for her continuous encouragement and helpful advices.

I am indebted to Prof. Hassan El Hawary, Dean of the Faculty of Science, and Prof. Kamal Ibrahim, Head of Chemistry Department, Faculty of Science, Assiut University, for their help and moral supports.

I am also grateful to all members of the Chemistry Department, Faculty of Science, Assiut University, who presented their aids in different directions.

Acknowledgments

Last but not least, sincere thanks and appreciation are presented to my parents, brother, sister, lovely wife, son and all my good friends who provide me their helps, patience, assistance and encouragement during this work.

Ahmad Abo Markeb
2017

Table of Contents

Index		i
Summary		xi
Resum		xiii
Resumen		xv
Abbreviations		xvii
Chapter 1	**General introduction**	1
1.1	World challenges for environmental pollution	3
1.2	Water pollution and remediation	4
1.2.1	Contaminants of emerging concerns	5
1.2.2	Remediation techniques	11
1.2.3	Adsorption method	12
1.3	Air pollution and treatments	16
1.3.1	Air pollution	16
1.3.2	Air pollution treatment	18
1.4	Nanotechnology	20
1.4.1	Introduction	20
1.4.2	Classification of nanomaterials	21
1.4.3	Synthetic methods of nanomaterials	25
1.4.4	Environmental applications of nanomaterials	28
1.4.5	Nanomaterials as adsorbents for water and gases remediation	29
1.4.6	Toxicity of nanomaterials	33
1.5	References	35
Chapter 2	**Research objectives and thesis outline**	53
2.1	Research objectives	55
2.2	Thesis outline	56
Chapter 3	**General methods and materials**	59
3.1	Characterization of the nanomaterials	61
3.1.1	Inductive Coupled Plasma - optical emission spectroscopy	61
3.1.2	Inductive coupled plasma –mass spectrometry	62
3.1.3	X-Ray Diffraction	63
3.1.4	Scanning Electron Microscopy	64
3.1.5	Transmission Electron Microscopy	65
3.1.6	Energy-Dispersive X-Ray Spectroscopy	66
3.1.7	Scanning Transmission Electron Microscopy coupled with Electron Energy Loss Spectra	67
3.1.8	Surface area measurements by Brunauer-Emmett-Teller method	68
3.1.9	Luminescence spectrometer	68
3.1.10	Zeta potential measurements	69

3.1.11	Toxicity tests	70
3.2	Analytical methods	70
3.2.1	Ionic Chromatography	70
3.2.2	Biosystems Analyzer	71
3.2.3	Ultraviolet visible spectrophotometer	72
3.2.4	Gas Chromatography	73
3.2.5	Turbidimeter	74
3.3	Experimental set-up	75
3.3.1	Batch experiments	75
3.3.2	Fixed-bed column studies	76
3.4	Isotherm models	78
3.5	Central composite design, CCD, and Response Surface methodology, RSM	81
3.6	Statistical analysis	82
3.7	References	82
Part A	**Water remediation**	87
Chapter 4	**Engineered nanomaterials: synthesis, characterization, and its potential efficiencies on water remediation**	89
4.1	Introduction	91
4.2	Materials and methods	92
4.2.1	Materials	92
4.2.2	Synthesis of the nanomaterials	93
4.2.2.1	Metal oxides NPs synthesis	93
4.2.2.1.1	Magnetite NPs	93
4.2.2.1.2	Cerium oxide NPs	94
4.2.2.1.3	Titanium oxide NPs	94
4.2.2.2	Preparation of functionalized magnetite NPs	95
4.2.2.2.1	Fe_3O_4 NPs functionalized with NH_2 groups	95
4.2.2.2.1.1	Polyethyleneimine-modified Fe_3O_4 NPs	95
4.2.2.2.1.2	Cetyltrimethylammonium bromide coated Fe_3O_4 NPs	95
4.2.2.3	Preparation of graphene based nanomaterials	96
4.2.2.3.1	Synthesis of graphene oxide	96
4.2.2.3.2	Synthesis of reduced graphene oxide	96
4.2.2.4	Synthesis of metal oxide/reduced graphene oxide nanocomposites	96
4.2.3	Synthesis of chitosan and description of the supplied supports	97
4.2.3.1	Synthesis of Chitosan beads (wet and dried)	97
4.2.3.2	Supplied supports	98
4.2.4	Characterization of the nanomaterials	98

4.2.5	Adsorption studies	98
4.2.6	Analytical methods	99
4.2.6.1	Anions analysis (fluoride, nitrate, and phosphate)	99
4.2.6.2	Heavy metals determination	100
4.2.6.3	Persistent organic pollutants determination	100
4.2.7	Toxicity measurements	101
4.3	Results and discussion	101
4.3.1	Characterization of the synthesized nanomaterials	101
4.3.1.1	Metal oxides NPs	101
4.3.1.2	Metal oxides/ reduced graphene oxide NCs	104
4.3.1.3	XRD pattern of the metal oxide nanoparticles	105
4.3.2	Applications of the nanoparticles	107
4.3.2.1	Anions removal	107
4.3.2.2	Heavy metals removal	112
4.3.2.3	Persistent organic pollutants removal	114
4.3.3	Toxicity of the nanoparticles	117
4.4	Conclusions	118
4.5	References	119
Chapter 5	**Novel magnetic core-shell Ce-Ti@Fe_3O_4 nanoparticles as adsorbent for water contaminants removal**	127
5.1	Introduction	129
5.2	Materials and methods	130
5.2.1	Materials	130
5.2.2	Synthesis of the core shell nanoparticles	130
5.2.2.1	Preparation of magnetite nanoparticles	130
5.2.2.2	Preparation of Ce-Ti@Fe_3O_4nanoparticles	131
5.2.3	Characterization of the Ce-Ti@Fe_3O_4 NPs	131
5.2.4	Analytical methods used in the Adsorption Experiments	132
5.2.4.1	Ionic chromatography for fluoride, nitrate and phosphate analysis	132
5.2.4.2	UV-Vis for Cadmium analysis	132
5.2.5	Adsorption experiments procedure	133
5.3	Results and discussion	134
5.3.1	Characterization of the synthesized Ce-Ti@Fe_3O_4 nanoparticles	134
5.3.1.1	Metal composition	134
5.3.1.2	Size, structure and crystallinity	134
5.3.1.3	Absorption and Luminescence spectra of the Ce-Ti@Fe_3O_4	140
5.3.2	Adsorption tests by using Ce-Ti@Fe_3O_4NPs as adsorbent for	142

	fluoride, nitrate, phosphates and cadmium contaminants	
5.4	Conclusions	144
5.5	References	145
Chapter 6	**Adsorption process of fluoride from drinking water with magnetic core-shell Ce-Ti@Fe_3O_4 and Ce-Ti oxide nanoparticles**	151
6.1	Introduction	153
6.2	Materials and methods	154
6.2.1	Materials	154
6.2.2	Synthesis of the bimetal oxide and core-shell NPs	154
6.2.2.1	Preparation of Ce-Ti bimetal oxide NPs	154
6.2.2.2	Preparation of Ce-Ti oxide nanoparticles and Ce-Ti@Fe_3O_4 nanoparticles	155
6.2.3	Characterization of the nanomaterials	155
6.2.4	Adsorption and desorption experiments procedure	156
6.2.4.1	Adsorption isotherm	156
6.2.4.2	Fluoride desorption procedure	156
6.2.5	Reusability of the Ce-Ti@Fe_3O_4 NPs as adsorbent and characterization	157
6.2.6	pH effect on the adsorption capacity	157
6.2.7	Effect of temperature on the fluoride adsorption and estimation of the thermodynamic parameters	158
6.2.8	Fluoride removal from spiked drinking water by using Ce-Ti@Fe_3O_4 NPs	158
6.2.9	Statistical data analysis	159
6.3	Results and discussion	159
6.3.1	Characterization of the synthesized nanomaterials	159
6.3.2	Fluoride adsorption on Ce-Ti@Fe_3O_4 adsorbents	161
6.3.3	Adsorption isotherms and modeling for the adsorption mechanism	162
6.3.4	Evaluation of the fluoride recovery and the reusability of the Ce-Ti@Fe_3O_4 NPs	169
6.3.5	Characterization of the Ce-Ti@Fe_3O_4 NPs as adsorbent after reuse	171
6.3.6	Effect of the pH value for the fluoride adsorption	175
6.3.7	Temperature effect and thermodynamic parameters	176
6.3.8	Application of Ce-Ti@Fe_3O_4nano adsorbent for fluoride removal from real water sample	178
6.4	Conclusions	179

6.5	References	180
Chapter 7	**Phosphate removal and recovery from water using nanocomposite of immobilized magnetite nanoparticles on cationic polymer**	187
7.1	Introduction	189
7.2	Material and methods	192
7.2.1	Materials	192
7.2.2	Synthesis of the nanocomposite based on magnetite NPs	192
7.2.3	Characterization of the nanocomposites	193
7.2.4	Ionic chromatography for phosphate analysis	193
7.2.5	Adsorption-desorption tests	193
7.2.5.1	Phosphate solutions	193
7.2.5.2	Adsorption studies in a fixed bed column	194
7.2.5.3	Phosphate adsorption isotherm and modeling	194
7.2.6	Desorption of phosphate and reusability of the nanocomposite	195
7.3	Results and discussion	196
7.3.1	Synthesis and characterization of the nanocomposites	196
7.3.1.1	Metal ions content in the nanocomposites	196
7.3.1.2	SEM-EDS, XRD and TEM analysis of the nanocomposites	196
7.3.1.3	Magnetic characterization and surface area measurements of the nanocomposites	199
7.3.2	Adsorption studies in fixed-bed column	199
7.3.2.1	Determination of the adsorption capacities for the NCs with different Fe_3O_4NPs content (Protocol A, B, C and D)	199
7.3.2.2	Effect of the pH on the adsorption capacities and on the nanocomposite stability	200
7.3.3	Adsorption Isotherms and modeling	201
7.3.4	Evaluation of the phosphate recovery procedure and the reusability of the magnetite nanocomposite for several adsorption-desorption cycles	206
7.4	Conclusions	208
7.5	References	209
Chapter 8	**Optimization of high efficiency Scenedesmus sp. microalgae harvesting using low-cost magnetic iron oxide based nanoparticles**	219
8.1	Introduction	221
8.2	Materials and Methods	223
8.2.1	Materials	223

8.2.2	Microalgae production	223
8.2.3	Synthesis of magnetite based NPs	223
8.2.3.1	Magnetite (Fe_3O_4) NPs	223
8.2.3.2	CTAB coated Fe_3O_4 NPs	224
8.2.3.3	PEI-modified Fe_3O_4 NPs	224
8.2.3.4	Amine functionalized Fe_3O_4 NPs	224
8.2.4	Characterization of nanoparticles and microalgae	224
8.2.4.1	Inductively coupled plasma optical emission spectrometry	224
8.2.4.2	Scanning Electron Microscopy and Transmission Electron Microscopy	224
8.2.5	Microalgae analysis	225
8.2.6	Zeta potential measurements	225
8.2.7	Algae separation experiments	226
8.2.7.1	Procedure of the algae harvesting using the nanoparticles	226
8.2.7.2	Screening of the algae separation using magnetite-based nanoparticles	226
8.2.7.3	Effect of the shaking type for the algae removal using the Fe_3O_4 NPs	226
8.2.8	Optimization of the microalgae harvesting efficiency using the response surface method	227
8.2.9	Adsorption isotherms and zeta potential measurements	227
8.2.10	Reusability of the nanoparticles	227
8.3	Results and Discussion	228
8.3.1	Microalgal biomass characterization	228
8.3.2	Characterization of the nanoparticles	229
8.3.2.1	Metals ion concentration in the nanoparticles	229
8.3.2.2	TEM-EDS analysis of the nanoparticles	230
8.3.3	Optimization procedure of the microalgae harvesting efficiency	231
8.3.3.1	Screening of the nanoparticles for the removal of microalgae	231
8.3.4	Characterization of algae with nanoparticles using TEM and SEM	233
8.3.5	Effect of shaking type	235
8.3.6	Central composite design with a response surface method to optimize the harvesting efficiency	236
8.3.7	Statistical analysis	240
8.3.8	Adsorption isotherms and possible mechanism of interactions	241
8.3.9	Regeneration and reusability studies of the Fe_3O_4 NPs	243
8.4	Conclusions	245

8.5	References	245
Part B	**Gases treatment**	251
Chapter 9	**Catalytic oxidation of CO using Au/CeO_2core-shell nanoparticles supported in UiO-66 beads**	253
9.1	Introduction	255
9.2	Materials and methods	256
9.2.1	Materials	256
9.2.2	Synthesis of PVP-Stabilized Au/CeO_2 Nanoparticles	256
9.2.3	Synthesis of UiO-66@Au/CeO_2	256
9.2.4	Synthesis of PVP-Stabilized Pd Nanoparticles	257
9.2.5	Synthesis of UiO-66@Pd	257
9.2.6	Catalytic CO Oxidation Study	258
9.2.7	Characterization	258
9.3	Results and discussion	259
9.3.1	Characterization of the nanomaterials	259
9.3.2	Catalytic oxidation of CO	265
9.4	Conclusions	272
9.5	References	273
Chapter 10	**Methane adsorption with modified polyurethane sponges with magnetite nanoparticles synthesized by chemical co-precipitation method**	279
10.1	Introduction	281
10.2	Materials and methods	282
10.2.1	Materials	282
10.2.2	Synthesis of the Fe_3O_4 NPs stabilized in the PUF matrix	283
10.2.3	Characterization of the NC	284
10.2.4	CH_4 analysis	284
10.2.5	Adsorption-desorption tests	284
10.2.5.1	Adsorption studies in a fixed bed column	284
10.2.5.2	Methane adsorption Isotherm	286
10.2.5.3	Isotherm models for CH_4 adsorption	286
10.2.5.4	Desorption of methane and reusability of the nanocomposite	286
10.3	Results and discussion	287
10.3.1	Synthesis and characterization of the NCs	287
10.3.1.1	Metal ions content in the NCs	287
10.3.1.2	TEM/EDX/EDS analysis of the NCs	288
10.3.2	Adsorption studies in fixed-bed column	289
10.3.2.1	Effect of flow effect on the adsorption capacity of CH_4	289
10.3.2.2	Determination of the adsorption capacities for the Fe_3O_4-PUF	290

	(A) and (B) NC	
10.3.2.3	Adsorption isotherms and modellings	291
10.3.2.4	Reusability of the magnetite NC for several adsorption-desorption cycles for methane	296
10.4	Conclusion	297
10.5	References	298
Chapter 11	**General conclusions and future work**	303
11.1	General conclusions	305
11.2	Future work	309
Annexes/ Accepted articles		
A-1	Novel magnetic core–shell Ce–Ti@Fe_3O_4nanoparticles as an adsorbent for water contaminants removal	313
A-2	Adsorption process of fluoride from drinking water with magnetic core-shell Ce-Ti@Fe_3O_4 and Ce-Ti oxide nanoparticles	321
A-3	Phosphate removal and recovery from water using nanocomposite of immobilized magnetite nanoparticles on cationic polymer	335
A-4	Critical review of existing nanomaterial adsorbents to capture carbon dioxide and methane	353
A-5	Core-shell Au/CeO2 nanoparticles supported in UiO-66 beads exhibiting full CO conversion at 100 ˚C	369

Summary

This thesis is based on the development (synthesis) of different nanomaterials for their application as adsorbent materials for the removal of pollutants from water (inorganic anions, heavy metals and pesticides) and for the adsorption of methane gas. The development of the different materials has been based on an extensive bibliographical search of the state of the art of the materials currently used for this application, and it has been tried to improve the efficiency of the process by using nanomaterials. Thus, magnetic (magnetite) nanoparticles are synthesized by different methods. These are functionalized with organic groups to adapt and/or improve their adsorption function or stabilize in supports (polymers, zeolites, sponges, etc.) to improve their application on a real scale. In addition, a new method for the formation of core-shell nanoparticles with a magnetite core is developed. All the synthesized nanomaterials have been characterized in depth, using the most advanced techniques for the characterization of nanomaterials. Techniques such as electron microscopy, X-ray diffraction, among others, allow to know the characteristics and properties of the materials (size, dispersion, crystallinity, structure, etc.) and thus conclude their contribution to the efficiency of their application with adsorbent material.

As for the contaminants in water, the work focuses on fluoride, phosphates, nitrates, cadmium, nickel and pesticides, obtaining outstanding results for the nanoparticles of Ce-Ti @Fe_3O_4.

In the case of gas treatment, on the one hand has developed a new nanomaterial based on magnetic nanoparticles stabilized in polyurethane sponges which present interesting results for the adsorption of methane and great applicability on a real scale. In addition, we have collaborated with the Institut Català de Nanotecnologia for the applicability of Metal Organic Frameworks in the oxidation of CO.

Another application that has been given to magnetic nanoparticles has been its use to separate algae from wastewater treatment processes, in order to substitute the current sedimentation processes.

With all this, the thesis offers a range of nanomaterials for different uses in environmental engineering, with the possibility of investigating and developing on its applicability on a large scale. To this end, different solutions are provided for the improvement of the environment.

Resum

Aquesta tesi es basa en el desenvolupament (síntesi) de diferents nanomaterials per a la seva aplicació com a materials adsorbents per a l'eliminació de contaminants en aigua (anions inorgànics, metalls pesats i pesticides) i per l'adsorció de gas metà. El desenvolupament dels diferents materials s'ha basat en una extensa recerca bibliogràfica de l'estat de l'art dels materials utilitzats actualment per a aquesta aplicació, i s'ha tractat de millorar l'eficiència del procés mitjançant l'ús de nanomaterials. Amb aquest objectiu s'han sintetitzat materials magnètics per diferents mètodes. En alguns casos, aquests han estat funcionalitzats amb grups orgànics per adaptar i/o millorar la seva funció d'adsorció o estabilitzar-los en suports (polímers, zeolites, esponges, etc.) per millorar la seva aplicació a una escala real en un futur. A més, es va desenvolupar un nou mètode per a la formació de nanopartícules core-shell amb un nucli de magnetita. Tots els nanomaterials sintetitzats s'han caracteritzat en profunditat, utilitzant les tècniques més avançades per a la caracterització dels nanomaterials. Tècniques com ara la microscòpia electrònica, difracció de raigs X, entre d'altres, permeten conèixer les característiques i propietats dels materials (mida, dispersió, estructura cristal·lina, etc.) i per tant concloure la seva contribució a l'eficàcia de cada un dels materials adsorbents.

Pel que fa als contaminants en aigua, el treball se centra en el fluorur, el fosfat, el nitrat, els metalls cadmi i níquel i pesticides, destacant l'obtenció de resultats excepcionals per a les nanopartícules de Ce-Ti@Fe_3O_4.

En el cas de tractament de gas, per una banda s'ha desenvolupat un nou nanomaterial basat en nanopartícules magnètiques estabilitzades en esponges de poliuretà que ha presentat resultats interessants per a l'adsorció de metà. A més, s'ha col·laborat amb la Institut Català de Nanotecnologia per a l'aplicabilitat dels Metal Organic Frameworks en l'oxidació de CO.

Una altra aplicació que s'ha donat a les nanopartícules magnètiques ha estat la seva utilització en la separació de algues procedents de processos de tractament d'aigües, per tal de substituir el procés actual de decantació.

Amb tot això, la tesi ofereix una gamma de nanomaterials per a diferents usos en enginyeria ambiental, amb la possibilitat d'investigar i desenvolupar en la seva aplicabilitat a gran escala. Amb aquesta finalitat, es proporcionen diferents solucions per a la millora del medi ambient.

Resumen

Esta tesis se basa en el desarrollo (síntesis) de diferentes nanomateriales para su aplicación como materiales adsorbentes para la eliminación de contaminantes en aguas (aniones inorgánicos, metales pesados y pesticidas) y para la adsorción de gas metano. El desarrollo de los diferentes materiales se ha basado en una extensa búsqueda bibliográfica del estado del arte de los materiales actualmente usados para dicha aplicación y, se ha intentado mejorar la eficiencia del proceso mediante el uso de nanomateriales. Así, se sintetizan nanopartículas magnéticas (de magnetita) mediante diferentes métodos. Éstas, se funcionalizan con grupos orgánicos para adaptar y/o mejorar su función de adsorción o bien, se estabilizan en soportes (polímeros, zeolitas, esponjas, etc) para mejorar su aplicación a escala real. Además, se desarrolla un nuevo método para la formación de nanopartículas core-shell con un núcleo de magnetita. Todos los nanomateriales sintetizados han sido caracterizados en profundidad, utilizando las técnicas más avanzadas para su caracterización. Técnicas como microscopia electrónica, difracción de rayos X, entre otras, permiten conocer las características y propiedades de los materiales (tamaño, dispersión, cristalinidad, estructura, etc.) y así concluir su aportación a la eficiencia de su aplicación como material adsorbente.

En cuanto a los contaminantes en agua, el trabajo se centra en fluoruros, fosfatos, nitratos, los metales cadmio y níquel y pesticidas, obteniéndose resultados destacado para las nanopartículas de Ce-Ti@Fe_3O_4.

En el caso de tratamiento de gases, por un lado, se ha desarrollado un nuevo nanomaterial basado en nanopartículas magnéticas estabilizadas en esponjas de poliuretano las cuales presentan resultados interesantes para la adsorción de metano. Además, se ha colaborado con el Institut Català de Nanotecnologia para la aplicabilidad de Metal Organic Framework en la oxidación del CO.

Otra de las aplicaciones que se ha dado a las nanopartículas magnéticas ha sido su utilización en la separación de algas procedentes de procesos de tratamiento de aguas residuales, con el objetivo de sustituir el actual proceso de decantación.

Con todo esto, la tesis ofrece un abanico de nanomateriales para diferentes usos en ingeniería medioambiental, con la posibilidad de investigar y desarrollar sobre su futura aplicabilidad a escala real. Con este fin, se aportan distintas soluciones para la mejora del medio ambiente.

Abbreviations

Aminopropyltriethoxysilane	*APTES*
Analysis of the variance	*ANOVA*
Brunauer-Emmett-Teller	*BET*
Carbon Capture and Storage	*CCS*
Central composite design	*CCD*
Cetyltrimethylammonium bromide	*CTAB*
Chitosan	*CS*
Contaminants of Emerging Concerns	*CECs*
Dry Cell Weight	*DCW*
Electron Diffraction	*ED*
Electron Energy Loss Spectra	*EELS*
Energy dispersive spectroscopy	*EDS/ EDX*
Environmental Protection Agency	*EPA*
Field-Emission	*FE*
Flame Ionization Detector	*FID*
Gas Chromatography	*GC*
Graphene oxide	*G.O*
Greenhouse Gases	*GHGs*
Haloacetic Acids	*HAAs*
Hexamethylenetetramine	*HMT*
High Rate Algal Ponds	*HRAP*
High angle annular dark field	*HAADF*
Hydraulic RetentionTime	*HRT*
Hydrofluorocarbons	*HFCs*
Hydroxyapatite	*HAP*
Inductive coupled plasma – mass spectrometry	*ICP-MS*
Inductive coupled plasma - optical emission spectroscopy	*ICP-OES*
Intergovernmental Panel on Climate Change	*IPCC*
Intermatrix Synthesis	*IMS*
Ionic chromatography	*IC*
Ion-exchange capacity	*IEC*
Ionic liquids	*IL*
Layer doubled hydroxides	*LDH*
Mass Spectrometry	*MS*
Maximum Contaminated Level	*MCL*
Metal organic frameworks	*MOFs*

Nanocomposites	*NCs*
Nanoparticles	*NPs*
Organochlorines	*Ocs*
Organophosphates	*OPs*
Osmotic adjusting solution	*OAS*
Part per billion	*ppb*
Part per trillion	*ppt*
Perfluorocarbons	*PFC*
Persistent Organic Pollutants	*POPs*
Polyethyleneimine	*PEI*
Polyurethane foam	*PUF*
Reduced graphene oxide	*r-G.O*
Relative standard deviation	*RSD*
Response surface methodology	*RSM*
Scanning Electron Microscope	*SEM*
Scanning transmission electron microscopy	*STEM*
Selected Area Electron Diffraction	*SAED*
Selected ion monitoring	*SIM*
Soluble Chemical Oxygen Demand	*SCOD*
Tetramethylammonium hydroxide	*TMOAH*
Thermal conductivity detector	*TCD*
Total Suspended Solids	*TSS*
Transmission electron microscope	*TEM*
Trihalomethanes	*THM*
Volatile Suspended Solids	*VSS*
World Health Organization	*WHO*
X-Ray Diffraction	*XRD*

Chapter 1

General Introduction

1.1. World challenges for environmental pollution

The use and cost of energy affects each of us every day of our lives. Many issues arise from the use of energy: greenhouse gas emissions, acid rain, climate change, dependency on depleting supplies of fossil fuels, especially from politically unstable regions of the world. Today, 80% of the world's electrical production comes from fossil and nuclear fuels, and virtually all transportation is fueled by liquid petroleum (gasoline) [1]. The World Energy Council projects primary energy demand will triple by 2050, as population grows to 8-9 billion and developing nations elevate living standards. The fossil fuels are nonrenewable and are destined to run out, so economies will be forced to change as these fuels are depleted. Rich nations will be insulated a bit longer, yet scarcity will surely create geopolitical tensions. The emissions from the burning of fossil and nuclear fuels create atmospheric, water, and land pollution and toxic waste. The United Nations Intergovernmental Panel on Climate Change (IPCC) says this combustion is causing a discernible change of the global weather and climate patterns that will affect all humanity in decades to come [2].

Then, one of the issues that the planet is facing recently is the environmental pollution, increasing with each passing year and inflicting grave and irreparable injury to the world. Air, water, and soil are the basic kinds of the environmental pollution [3]. Hence, environmental pollution is a subject of increasing worldwide public health concern. For instance, all living organisms need water to survive. And, a direct impact on humans has been observed when the polluted water poisons the plants and animals. The main causes of water pollution are sewage, industrial wastes, oil spills and the use of pesticides in agriculture [4].

Air, like other components of the environment such as water, and soil, was created clean. However, decline of the air quality has been observed by the human activities. Terrible consequences to health and safety of humans, animals and plants occur when there is a release of substances or pollutants to air due to those activities. Air pollution is responsible for adverse environmental effects such as acid rain, smog and greenhouse gases. Exhaust gases from engines of vehicles and planes are one of the major causes of air

pollution. They are operated by burning fossil fuels such as gasoline, diesel, natural gas, and jet fuels. Therefore, the exhausted gases are generated and discharged to the environment through the exhaust pipes of the vehicles/ planes. Several substances come from those exhausts such as; water vapor; nitrogen; carbon dioxide; some hydrocarbons from un-burnt fossil fuels; carbon monoxide from incomplete fuel combustion; nitrous oxide; ozone; and some tiny solid particles (atmospheric particulate matter, PM) [5].

Moreover, soil contamination as part of land degradation is caused by the presence of chemicals (human-made) or other alteration in the nature soil environment. The most common chemicals involved are petroleum hydrocarbons, polynuclear aromatic hydrocarbons (such as naphthalene and benzo(a)pyrene), solvents, pesticides, lead, and other heavy metals. Contamination is correlated with the degree of industrialization and intensity of chemical usage [6]. The concern over soil contamination stems primarily from health risks, from direct contact with the contaminated soil, vapors from the contaminants, and from secondary contamination of water supplies within and underlying the soil.

Herein, this work focus, mainly, on water and air remediation by the development of novel technologies. In addition, due to the need of alternative source of energy, this work also includes a starting research on the harvesting of microalgae from wastewater treatment as source of biogas production.

1.2. Water pollution and remediation

Water is one of the four essential elements of life [7, 8]. As a result of the tremendous increase in the population, industrialization, and other environmental impacts, the contamination of water became a serious problem overall the world [9, 10]. In addition, large amount of wastewater had been generated due to the enormous demand of fresh water in the field of agriculture, domestic, and industrial sectors. Hence, 70 %, 8 %, and 22 % decrease of the fresh water occurred by supplying the previous sectors, respectively, and increase of the pollutants in the wastewater produced [11]. Various pollutants have been registered as water hazardous such as organic, inorganic, and biological contaminants [12].

For this reason, the water will not be safe for drinking due to the harmful effects on the human beings [13, 14]. To that end, water decontamination is a critical issue to decrease and eliminate the side effects of those pollutants as well as to compensate the clean water demand due to the growth of populations.

1.2.1. Contaminants of emerging concerns

The contaminants of emerging concerns (CECs) are chemical compounds which have been in the environment for a while, but for which concerns are recently recognized as significant water pollutants [15]. The CECs are natural or synthetically occurring substances not commonly monitored in the environment and having known or suspected undesirable effects on humans and the ecosystem [16]. Various contaminants are emergent, well known and need to eliminate from water. Encompassed by nutrients, fluoride, heavy metals, pharmaceutical, personal care products, pesticides, and microbial pollutants that have diverse effects on the human health [17]. This section describes the occurrence and adverse effects of fluoride, nutrients, heavy metals, persistent organic pollutants, and microalgae in water.

Fluoride

Fluoride is an essential element for human beings and ranks 13th in the abundance of the element sand that constitutes about 0.1% of the Earth's crust [18]. A beneficial effect to the human body is produced when the fluoride was ingested with the permissible limit for the maintenance of the healthy bone, in addition to the calcification of dental enamel [19]. Because fluoride can enter the human body through drinking water, food, industrial exposure, cosmetics, drugs, etc. [20], is one of the major inorganic contaminants in the world. Adverse effects due to the excessive of fluoride can lead to various diseases [21, 22] as such as dental and skeletal fluorosis [23]. Moreover, fluorosis is endemic in several parts of the world, particularly India, and China are the worst affected [24].

The fluoride contaminant could be found in groundwater, surface water, and industrial wastewater discharges. High concentration level of fluoride in ground water

could be attributed to the deposition of natural minerals, such as fluorite in the earth, and discharges from the industrial facilities [25-30]. Hence, World Health Organization (WHO) sets the maximum contaminated level (MCL) of fluoride in drinking water to be 1.5 mg/L [31]. Accordingly, great challenge and various technologies have been used to maintain the fluoride level below the MCL (as it is described in Section 1.2.2).

Nutrients

Nutrients, such as nitrogen and phosphorus, are essential for plant and animal growth and nourishment, but the overabundance of certain nutrients in water can cause several adverse health and ecological effects [32]. Harmful effects of eutrophication, a reduction in dissolved oxygen in water bodies caused by an increase of mineral and organic nutrients, to many lakes and surface waters could occur due to the excessive release of nitrate and phosphate [33]. Thus, these contaminants are among the most problematic pollutants which highly affect the water all around the world.

Phosphorus is found as phosphate (PO_4^{3-}) in nature and present as orthophosphate, polyphosphate and organic phosphate in water. Orthophosphates are usually applied to agricultural or residential land as fertilizer which will then be carried into surface waters with storm runoff and melting snow. In addition, phosphates can also be found in various consumer products such as baking powders, toothpastes, cured meats, evaporated milk, soft drinks, processed cheeses, pharmaceuticals and water softeners. Besides, phosphates are also found abundant in the wastewater from laundering agents for examples shampoo and detergents [34]. Additionally, phosphorus is also a constituent of extremely toxic compounds, such as orthophosphate insecticides and military poison nerve gases [35]. Also, phosphorus is essential for food production that the human needs where it is a common constituent of manure, and organic wastes in sewage and industrial effluent [32, 36]. Phosphorus tends to attach to soil particles and, thus, moves into surface-water bodies from runoff. Besides, the phosphine compound which is a toxic gas can be formed from the interaction of the white phosphorus with water, and then moved into air. Additionally, the white phosphorus in the contaminated water could built up in the fishes bodies, which will be harmful to the human body [37]. Adverse effects to the human body could be liver, heart

or kidney damage, stomach cramps, vomiting, drowsiness, and even death due to the consumption of high concentration of phosphorus by drinking or eating [38]. Owing to these adverse effects of phosphate, the Environmental Protection Agency (EPA) set a MCL of phosphate in drinking water as 0.15 mg PO_4^{-3}-P/L [39]. Various technologies have been reported for phosphate removal from water such precipitation, reverse osmosis, adsorption, and biological methods (further information in Section 1.2.2).

Besides to phosphorus, nitrogen, in the forms of nitrate, nitrite or ammonium/ ammonia, is also a nutrient needed for plant growth. In general, about 78 % of the air that we breathe is composed of the nitrogen (N_2) gas molecule which is very stable and readily being broken down into nitrates and nitrites in the atmosphere. Therefore, increasing of nutrients level in water could occurred due to the high concentrations of phosphates and nitrates in wastewater effluents and from agricultural runoff. Subsequently, the algal blooms disrupt the normal aquatic ecosystem functioning. The huge population of algae will use up all the dissolved oxygen in the water, unable any flora and fauna to live. Besides, the massive lumps of algae also block sunlight from penetrate through the water for the photosynthesis of aquatic plants. This is called the eutrophication phenomenon. In terms of high turbidity, low dissolved oxygen concentration, unpleasant odor and bad flavor, the eutrophication will deteriorate the water quality [40]. Besides decreasing the water quality, the eutrophication will significantly increase the cost of surface water treatment. The worst thing of all is that the excess weed and algae growth will contaminate our drinking water which affect human's health. In addition to the adverse effects to the aquatic plants, growth of algae, fish and animals due to the high concentration of nitrate in water resources, hazardous effects could be happened to human such as infant methemoglobinemia, blue baby syndrome due to the reduction of nitrate into nitrite inside the stomach of the pregnant woman, higher affinity to hemoglobin will bind to it and form methemoglobinemia which is unable to combine with oxygen, and also teratogenic effects [41-43]. Also, gastric cancer was proved when nitrate compounds are reduced inside the stomach to nitrosamines [44, 45]. Thus, the Environmental Protection Agency (EPA) set a MCL of nitrate as 44 mg NO_3^-/L [46], while the World health organization, WHO, put a regulate in drinking water as 50 mg NO_3^-/L [31]. Since nitrate is a stable and highly soluble

ion which makes it difficult to remove using conventional water treatment methods such as precipitation [47].

Heavy metals

Heavy metal pollution has become a greatly worldwide environmental problem [48]. Due to the amount of heavy metal ions used in different industrial activities are keeping pace with the rapid spreading chemical manufacturing [49]. Discharge of heavy metals from industrial, municipal, agricultural and domestic wastewater has become a serious threat for the ecosystem. The heavy metals such as lead, cadmium, nickel, mercury, zinc, chromium, cobalt, arsenic, and selenium, are the major contaminants to concern for removal from water due to its toxicity, persistency and are easily enriched at organisms through the food chain [50]. Contamination of water by heavy metals could occur through refineries, sludge disposal, mining operations, manufacturing industries such as paints, electronic and electrical devices, batteries, fertilizers, and pesticides. Their presence in water may pose serious threats to all forms of life, because they may be mutagenic and carcinogenic. Their presence above prescribed limits in body can cause severe damages to vital organs of the body, such as kidney, liver and brain, reproductive and nervous system [51]. Upon of the previously mentioned heavy metals, cadmium pollutant in water may arise from mining wastes and industrial discharges, especially from metal plating [35]. Adverse effects of cadmium to human body could be high blood pressure, kidney damage, damage to testicular tissue, and destruction of red blood cells [52]. Therefore, the WHO set a MCL of cadmium in water to be 0.005 mg/L [53]. Furthermore, groundwater and surface water sometimes contain substances that do not occur frequently in such water such as nickel, iron, and manganese. For example, nickel can be found in minerals usually with sulfur and antimony. Anthropogenic sources of nickel include mainly wastewater from metal surface treatment and wastewater from color metallurgy. Also, it is used in ceramic and glass making industries, some chemical syntheses as a catalyst, and nickel-plated parts of equipment that can in touch with water. Adverse effects of nickel to human body was reported as carcinogenic [54]. Pollution of nickel is considered when the concentration exceeds 0.04 mg/L, 0.10 mg/L, 0.5 mg/L, 0.80 mg/L, and 0.02 mg/L for surface water,

industrial wastewater discharged into municipal sewerage systems, electro-technical operations, water discharged from metal surface treatment, and drinking water [55, 56].
Variety of methods have been explored for the removal of heavy metals such as ion exchange, lime coagulation, evaporation, reverse osmosis, electrochemical treatment, solvent extraction, chemical precipitation and filtration, and redox reactions. However, these methods were reported as expensive, high operational costs and inadequate due to the low removal efficiency. Besides of these removal techniques, the adsorption method is the most convenient due to its ease of operations and high adsorption capacity for heavy metals [57] (Section 1.2.2).

Persistent organic pollutants

The persistent organic pollutants (POPs), are organic compounds that are resistant to environmental degradation through chemical, biological and photolytic processes. They are used as pesticides, pharmaceuticals, solvents, and industrial chemicals. POPs accumulate in the environment due to their persistence [58, 59]. There are four main classes of pesticides as organochlorines (OCs), organophosphates (OPs), carbamates, and substituted urea. The OC pesticides, insecticides, are hydrocarbons functionalized with chloride groups, used in agriculture and mosquito control [60] whilethe OPs are the basis of many insecticides, herbicides, and nerve agents. Among the diverse types of pesticides, such as fungicides, acaricides, nematicides, and rodenticides, the insecticides and herbicides are the most widely used. Moreover, insecticides and fungicides are the most important pesticides with respect to human exposure in food because they are applied shortly before or even after harvesting. Herbicide production has increased as chemicals have increasingly replaced cultivation of land in the control of weeds and now accounts for most agricultural pesticides. The potential exists for large quantities of pesticides to enter water either directly, in applications such as mosquito control or indirectly, primarily from drainage of agricultural lands [35].

Microalgae

In recent years, algae pollution has become a global issue [61]. The occurrence of harmful algal bloom in water source has posed a serious water safety problem to local water supply systems (Figure 1.1). Several problems could occur using the conventional water treatment such as bad taste and odors, formation of disinfection by-products such as trihalomethanes (THMs) and chloroacetic acids, and clogging of filter beds due to the algal bloom in water reservoir [62]. Therefore, the algal bloom is directly endangering human and biological health [63]. In addition, the blue–green algae contain toxins and secrete mucus, resulting in the emergence of flocculation in the distribution pipeline network. THM parent could be formed by conversion those secretions. Unfortunately, this THM could make the removal process of algae from water very difficult, also it causes the growth of algae in the eutrophic water. So, the blue-green algae, and other freshwater algae are among diverse types microbiological contaminants in drinking water [64]. Besides, a lot of researches in the recent years are performed to remove the algae and the algae toxins due to the quick propagation of algae and the great damage that cause to water quality [65]. The most common methods used for algae removal from water are physical process such as filtration and barriers, biological process such as slow sand filters or activated sludge, chemical process such as coagulation, flocculation and chlorination, and the electromagnetic radiation such as ultraviolet light [66-68]. However, the chemical algae removal methods are considered as cost-effective and user-friendly. The addition of oxidants, such as chlorine, ozone, permanganate in the pretreatment step of the chemical coagulation process, enhances the algae removal. The major disadvantages of chlorine pre-oxidants are the harmful by-products produced as THMs and haloacetic acids (HAAs). Moreover, disadvantages of the peroxidation with permanganate are the promotion of the aggregation of algae cells, and the adsorption of the reducing products of MnO_2 into algae flocs [69].

Figure 1.1. Microlage from sewage wastewater treatment plant [70].

1.2.2. Remediation techniques

Various techniques have been developed and applied in the last decades for water and wastewater treatments including the mentioned contaminants. The most common physic-chemical methods for remediation are precipitation, electrodialysis, flotation, biological process, electrolysis, sedimentation and gravity separation, electrocoagulation, reverse osmosis, adsorption, ion exchange, etc. Among them, the chemical precipitation is the most widely used method to remove the pollutants such as metals, phosphate, fluoride, etc. by adding precipitating agent of metal salts into water [71]. During the wastewater treatment using the chemical precipitation method, the pollutants of inorganic anions are interacted with the added divalent or trivalent metal salt (such as calcium, aluminum, or iron) at several stages to form an insoluble metal anion precipitate at fixed pH, for example metal phosphate that is settled out by sedimentation [72]. Disadvantages of the water treatments by using the chemical precipitation method are the high production of sludge which is environmentally unfriendly, as well as the complexity of the process. Electrocoagulation is another common method used for water, and wastewater treatments. This technique involves the application of electric current to the sacrificial electrodes, mostly iron and aluminum, resulting in coagulation of colloidal contaminants and

production of gas bubbles [73, 74]. There are three main stages in this process; (1) coagulants formation which is due to the anode electrical oxidation, (2) destabilization of pollutants and suspended substances in addition to emulsion breaking and (3) flocculation of unstable particles [75, 76]. Although there are advantages by using this method such as low sludge production, low concentration of the secondary pollution, disadvantages of this method are the highest cost due to usage of great amount of electricity, anode passivation, and lacking system for the electrocoagulation reactor design and operation [77, 78]. Furthermore, the biological treatment is an integral part of any wastewater treatment plant that treats wastewater from either municipality or industry [79]. The biological treatment could be aerobic or anaerobic. Aerobic activated sludge process has been in practice over a century. Both are directly related to the type of bacteria or microorganisms that are involved in the degradation of organic impurities in a given wastewater and the operating conditions of the bioreactor. However, drawbacks of this process are the production of excess amount of sludge, high cost, and requires technically skilled manpower for operation and maintenance [80]. A comparison of the adsorption method was carried out with other water treatment technologies.

The order of cost effectiveness is adsorption > evaporation > aerobic > anaerobic > ion exchange > electrodialysis > micro- and ultra-filtration > reverse osmosis > precipitation > distillation > oxidation > solvent extraction [11]. The detail about the adsorption technique will be discussed in the following section.

1.2.3. Adsorption method

Adsorption is a phase transfer process that is widely used in practice to remove substances from fluid phases (gases or liquids) [81]. As shown in Figure 1.2, in adsorption theory, the adsorbent refers to the solid material that provides the surface for adsorption, while adsorbate points out to the pollutants that will be adsorbed.

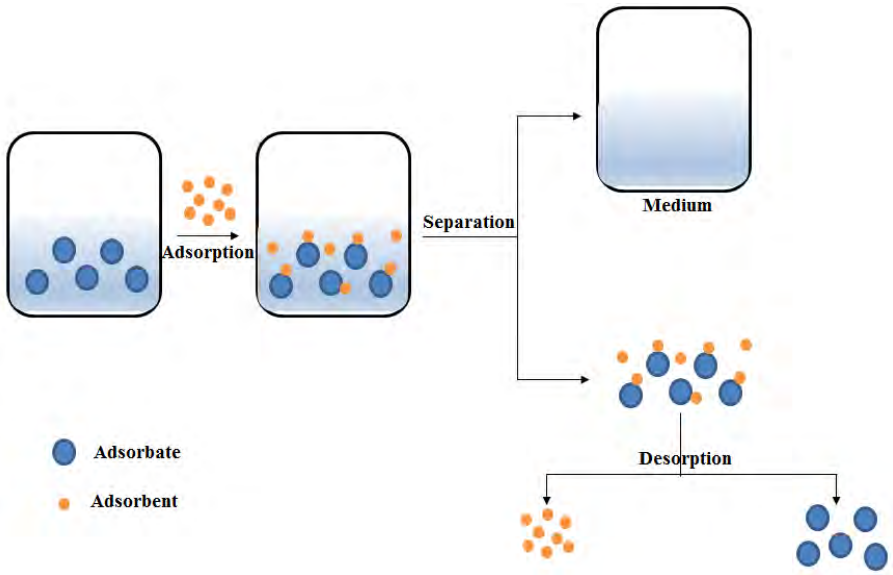

Figure 1.2. Basic terms of adsorption theory.

The chemisorption and physical adsorption are the two main types of adsorption. In the physical adsorption process, there is a physical attraction of the dissolved species to the surface of the adsorbent. Physical adsorption is non-site-specific, reversible, and occurred closed to the room temperature. On the contrary, in the chemisorption process, the dissolved pollutants are concentrated on the surface of the adsorbent by chemical reaction. This reaction could be occurred by the formation of ionic or covalent bonds. In the contrary of the physical adsorption, the chemisorption is irreversible and site specific.

The adsorption process, in general, could be divided into three steps:

(i) External mass transfer of solute molecules from bulk solution to the sorbent particle surface by diffusion or turbulent movement,

(ii) diffusion within particle internal structure to transport adsorbate molecules to the available adsorption sites of adsorbents surface, and

(iii) rapid uptake

At the end of the adsorption process, the seesaw behavior phenomenon appears which is important for the equilibrium system. This phenomenon bases on the fact that some of the solutes adsorb to the adsorbent and at the same time others will be desorbed until the

achievement of the equilibrium state. In case of physical adsorption process in aqueous solution, there are three types of interactions; (1) adsorbate-water interactions, (2) adsorbate –surface interactions and (3) water-surface interactions. The adsorbate-water, and water-surface interactions are related to the solubility of the adsorbate, while the adsorbate-surface interactions are determined by the surface chemistry.

The adsorption process could be explained by one of the following mechanisms to understand the type of interaction between the adsorbate and adsorbent:

(i) Van der Waals forces (outer-sphere surface complexation),

(ii) ion exchange (outer-sphere surface complexation),

(iii) hydrogen bonding (inner-sphere surface complexation),

(iv) ligand exchange (inner-sphere surface complexation),

(v) surface precipitation,

(vi) diffusion and

(vii) chemical modification of the adsorbent surface.

The van der Waals and ion exchange mechanisms are most relevant for adsorption of inorganic anions, and heavy metals, for instance, for nitrate adsorption by weak physical adsorption. While, the ligand exchange, precipitation, diffusion and the hydrogen bonding mechanisms are more specific to phosphate and fluoride. Also, the formation of surface metal complex could be proposed to the heavy metals removal mechanism [82]. The chemical modification of the adsorbent surface mechanism could occur for any anion which it is conducted to both specific and non-specific adsorption [83-85].

For instance, the adsorption process is the most effective and cheapest method for fluoride removal from water due to its ease of operation, convenience, simplicity of design [86-90]. In general, one of the three mechanisms could be used to explain the adsorption of fluoride [91]:

(i) External mass transfer, where a diffusion or transport of fluoride ions to the external surface of the adsorbent from bulk solution takes place across the boundary layer surrounding,

(ii) adsorption of fluoride ions on to particle surfaces, and

(iii) intra particle diffusion, where the adsorbed fluoride ions exchanged with the structural elements inside adsorbent particles.

In the case of phosphates, the adsorption method is the cost-effective method for the treatment of water and wastewaters that contain high level of phosphates [92-94]. Useful information on the adsorption optimization process could be provided by understanding the mechanism of interaction (1-7).

The type of the adsorption mechanism depends on the physical and chemical characteristics of the sorbent and the environmental/operational conditions [84].

Various parameters could affect the adsorption process:

(i) The characteristics of the adsorbent: surface charge, surface area, particle size, pore structure,

(ii) the characteristics of the adsorbate: solubility, molecular structure, ionic or neutral nature,

(iii) the characteristics of the solution: pH, ionic strength, temperature, presence of other anions, and

(iv) duration of adsorption.

The maximum amount of adsorption is proportional to the amount of surface area on the surface and within the pores of the adsorbents that is accessible to the adsorbate. Where, the two crucial factors that determine the approachability of the sites for adsorbates and the number of adsorption sites are the surface area and the pore size. When the pores of the adsorbent are smaller, larger surface area available for adsorption. Therefore, inverse relationship is between the surface area and pore size.

Also, the adsorption equilibrium is one of the main elements for the adsorption theory because it describes the dependence of the adsorbed amount on the adsorbate concentration and the temperature. At constant temperature during the adsorption process, the equilibrium relationship is expressed in the form of the adsorption isotherm.

Various adsorption parameters could be estimated by applying different isotherm models. Among of them, Langmuir, Freundlich, Dubinin–Radushkevich, Redlich–Peterson, Radke–Prausnitz, and Brunauer–Emmett–Teller are the well-known isotherm models used to explain the adsorption studies [95]. Moreover, adsorption is considered as one of the

suitable techniques for water treatments, due to its ease of operation, low cost and the availability of a wide range of adsorbents. Besides, various contaminants could be removed by using adsorption method. In addition, reclamation for potable, and industrial waters could be performed using adsorption technique. However, the lack of suitable adsorbents with high adsorption capacity that can be used on large scale columns, and the inapplicability of single adsorbent to remove all kinds of pollutants act as drawbacks of this method and need a great challenge to overcome [11].

Because of a lot of studied work in recent year for water decontamination using adsorption method to eliminate pollutants in a batch mode process, adsorption method will be a great water treatment technology in the near future [96]. Various adsorbents (including nanomaterials) have been used and evaluated for contaminants removal from water (as described in Section 1.5.5).

1.3. Air pollution and treatments

1.3.1. Air pollution

Greenhouse gases (GHGs) emissions play an important role in regulating the Earth surface temperature. Humans are increasingly influencing the climate and the earth's temperature by burning fossil fuels, cutting down rainforests and farming livestock. This adds enormous amounts of greenhouse gases to those naturally occurring in the atmosphere, increasing the greenhouse effect and global warming. Therefore, nowadays overall the world suffers a big problem due to the high concentration of the GHGs. The GHGs are methane, CH_4, carbon dioxide, CO_2, nitrous oxide, N_2O, hydrofluorocarbons HFCs, perfluorocarbons, PFCs, and sulfur hexafluorocarbon (F_6C). The GHGs that are most abundantly emitted today are CO_2 and CH_4 by human activities. According to the European commission, the CO_2 is responsible for 64 % of man-made global warming, and its concentration in the atmosphere is currently 40% higher than it was when industrialization began. Followed by the CH_4, which is responsible for 17 % of man-made global warming. Besides, other GHG that is emitted in a small quantity is N_2O, and its responsible for 6 % of man-made global warming. Causes for rising emission are;

- Carbon dioxide and nitrous oxide produced from burning coal, oil and gas.
- Cutting down forests where trees help to regulate the climate by absorbing CO_2 from the atmosphere. So instead of storing the carbon in the trees, it is released to the atmosphere, adding to the greenhouse effect.
- Increasing livestock farming. Cows and sheep produce large amounts of methane when they digest their food.
- Nitrous oxide emissions are produced from the fertilizers containing nitrogen.
- Fluorinated gases produce a very strong warming effect, up to 23 000 times greater than CO_2. Fortunately, small quantities of those gases are released.

CO_2 is produced in many industrial processes (i.e. fossil fuel power plants) including new prospective areas, such as the purification of hydrogen from biomass. Fossil fuel power plants are the largest point sources of CO_2 emissions (40% of total CO_2 emissions) [97]; thus, they are the main targets for imminent CO_2 reduction [98, 99]. The most convenient path towards lower CO_2 concentrations in the atmosphere would be to strongly reduce CO_2 emissions through cleaner and more environmentally friendly industrial processes. However, it is not expected that this can be achieved in the imminent future [100]. Several options exist to reduce CO_2 emissions, such as demand-side conservation, supply-side efficiency improvement, increasing dependence on nuclear and renewable energy, and implementation of Carbon Capture and Storage (CCS) systems [97, 100-102].

The CO_2 capture is preferred to be applied directly on-site, since the capture materials and technologies have demonstrated better performances at high CO_2 concentrations rather than at atmospheric levels (400 ppm in 2014, Mauna Loa Observatory) [103]. Hence, as CO_2 is the most important gas in terms of amounts emitted, it has been widely studied.

Moreover, atmospheric concentrations of CH_4 (~1,800 ppb) are currently much higher than those in preindustrial levels (~680–715 ppb) [104]. Anthropogenic CH_4 emissions account for 50–65% of the global CH_4 budget of ~395–427 $TgC \cdot y^{-1}$ (526–569 Tg CH_4) [105]. It is estimated that the principal CH_4 anthropogenic sources are [106];

(i) Livestock (enteric fermentation and manure management),

(ii) natural gas production and distribution,

(iii) landfills, and

(iv) coal mining.

Also, it is reported that a rise in natural wetland emissions and fossil fuel emissions probably accounts for the renewed increase in global methane levels after 2006, although the relative contribution of these two sources remains uncertain [105].

Furthermore, carbon monoxide (CO) is a toxic gas, but, being colorless, odorless, tasteless, and initially non-irritating, it is difficult for people to detect. CO is a product of incomplete combustion of organic matter [107]. It is often produced by motor vehicles that run on gasoline, diesel, methane or other carbon-based fuels and from tools, gas heaters, and cooking equipment that are powered by carbon-based fuels such as propane, butane and charcoal. Exposure at 100 ppm or greater can be dangerous to human health [108]. CO mainly causes adverse effects by combining with hemoglobin to form carboxyhemoglobin (HbCO) in the blood. This prevents hemoglobin from carrying oxygen to the tissues. In addition, CO could be easily absorbed by the lungs, and its inhalation led hypoxic injury, nervous system damage, and even death [109]. The CO gas can originate from different sources such as cigarette smoke, house fires, faulty furnaces, heaters, wood-burning stoves, internal combustion vehicle exhaust, electrical generators, propane-fueled equipment such as portable stoves, and gasoline-powered tools such as leaf blowers, lawn mowers, high-pressure washers, concrete cutting saws, power trowels, and welders [110, 111]. Thus, many countries are facing a fatal poisoning due to the contamination of CO [112].

1.3.2. Air pollution treatment

Carbon capture and storage (CCS) are playing a significant role to attain the required GHG emissions reduction [113]. The separation and capture of CO_2 produced at stationary sources, followed by transport and storage in geological reservoirs or the ocean are called CCS [114, 115]. There are three major approaches for CCS: Post-combustion capture, and are the three major approaches for CCS.

(i) Pre-combustion process

The syngas (mixture of CO and H_2) are formed in the pre-combustion process when the fossil fuel is partially oxidized by the reaction with air. Then, a mixture of CO_2, and more H_2 are produced when the syngas produced are reacted with a steam in a gasification reactor. Then, a hydrogen-rich fuel could be used in several applications after separation of CO_2.

(ii) Oxyfuel process

A flue gas that consists of pure CO_2 could be obtained by using oxy-combustion process which depends on the use of oxygen instead of air. This pure gas is potentially suitable for storage.

(iii) Post-combustion

In this process, the CO_2 could be separated or captured from the flue gas by passing the flue gas through the equipment instead of discharging into the atmosphere [116].

Hence, the post-combustion approach is the first widely technology due to it makes the capture is easier to implement as a retrofit option (to existing power plants) compared to the other two approaches.

There are several post combustion gas separation and capture technologies being investigated, namely;

(i) Absorption,

(ii) cryogenic separation,

(iii) membrane separation,

(iv) micro algal biofixation, and

(v) adsorption.

It has been demonstrated that the adsorption technique is the most suitable due to its ease of operations, and because the adsorbent could be regenerated by the effect of thermal or pressure modulations [117]. In addition to the high separation efficiency, and high adsorption capacity by using the adsorption method, reduction of the cost and energy of the post-combustion capture was reported in comparison to the other technologies [118]. Since CH_4 often co-exists with CO_2 in gaseous mixtures, such as natural gas, biogas and landfill

gas, selective removal of CO_2 is an important process to upgrade the energy content of those mixtures [119].

The technologies based on adsorption processes, such as activated carbon, zeolites and mesoporous silica, present limitations on the CO_2 retention capabilities per adsorbent mass [120-122].

In addition, the storage of CH_4 on adsorbents has been pursued actively as an alternative to high pressure compressed gas storage. Thus, the use of adsorbent materials, such as activated carbons and zeolites for the storage of natural gas at low pressures, has also been reported [123]. However, it was concluded that none of those conventional adsorbents showed sufficient CH_4 storage capacity to meet that required for commercial viability [124]. In this sense, there is a widespread interest in the development of advanced adsorbent materials with better characteristics and with a specialized functionality for each pollutant. Advanced materials have been investigated as potential CH_4 adsorbents including modified activated carbons, metal-organic frameworks (MOFs) and other porous polymers [125] (Section 1.5.5).

1.4. Nanotechnology

1.4.1. Introduction

The most commonly accepted definition for a nanomaterial refers to any material which has at least one dimension less than 100 nanometers (nm) in size, whereas NPs are defined as objects with their three dimensions of less than 100 nm [126]. So nanotechnology could be defined as is the science of material at the scale spans between 10^{-9} and 10^{-7} of a meter [127]. Or in another word, it is the science of materials and devices whose structures and constituents demonstrate novel and considerably altered physical, chemical and biological phenomenon due to their nanoscale size. Thus, nanotechnology is defined as the manipulation of matter on an atomic, molecular, and supramolecular scale involving the design, production, characterization and application of different nanoscale materials in different potential areas [128]. As indicated by a search on the ISI web of knowledge database [129], the number of publications on nanomaterials have been

increasing, in almost linear rate, since the year 2010 as shown in Figure 1.3. Therefore, nanotechnology and nanoscience comprise wide range of applications, such as optoelectronics, chemistry, device storage, physics, medicine, biology, and environmental restoration. Consequently, there has been a very rapid spread of nanotechnologies in many fields of daily life including fillers, cosmetics, catalysts, pharmaceuticals, lubricants, electronic devices, advanced materials, biomedical applications, environmental remediation and imaging tools [130-134].

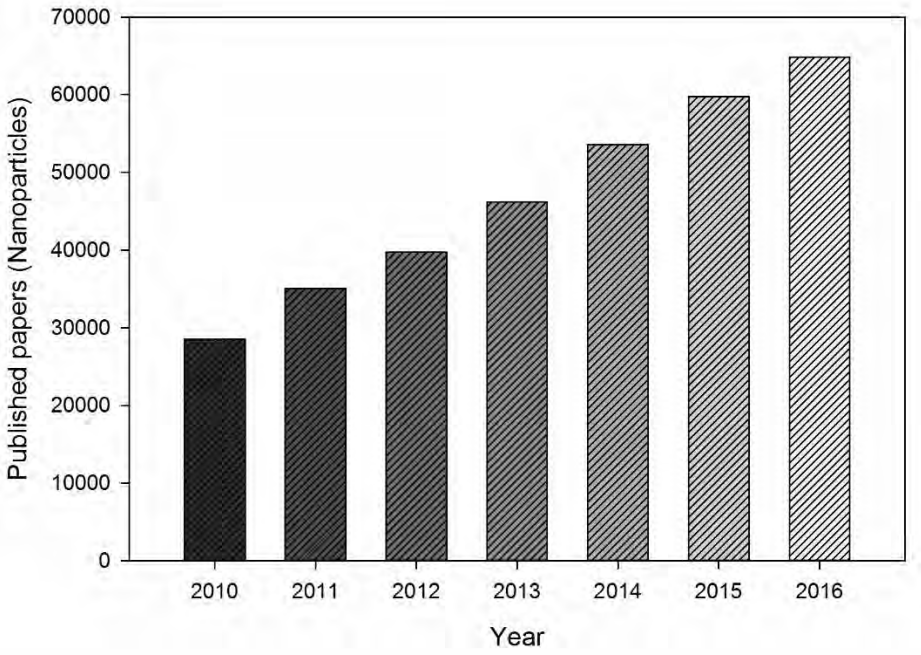

Figure 1.3. Statistics of the published paper on the nanoparticles since 2010, according to ISI web of knowledge database search.

1.4.2. Classification of nanomaterials

In general, the nanomaterials can be classified into two ways; the first one is based on if they are natural or synthetic [135], and the second one is based on their dimensionality, morphology, composition, uniformity, and agglomeration. Figure 1.4 shows the differences in sizes of the materials, in terms of nano, and micro, also the size comparison between the nanomaterials and the biological substances.

In the first classification, the natural nanomaterials exist in the biological system such as viruses (Capsid), substance in our bone matrix, natural colloid such milk and blood, and horny materials such hair, paper, and cotton [136].

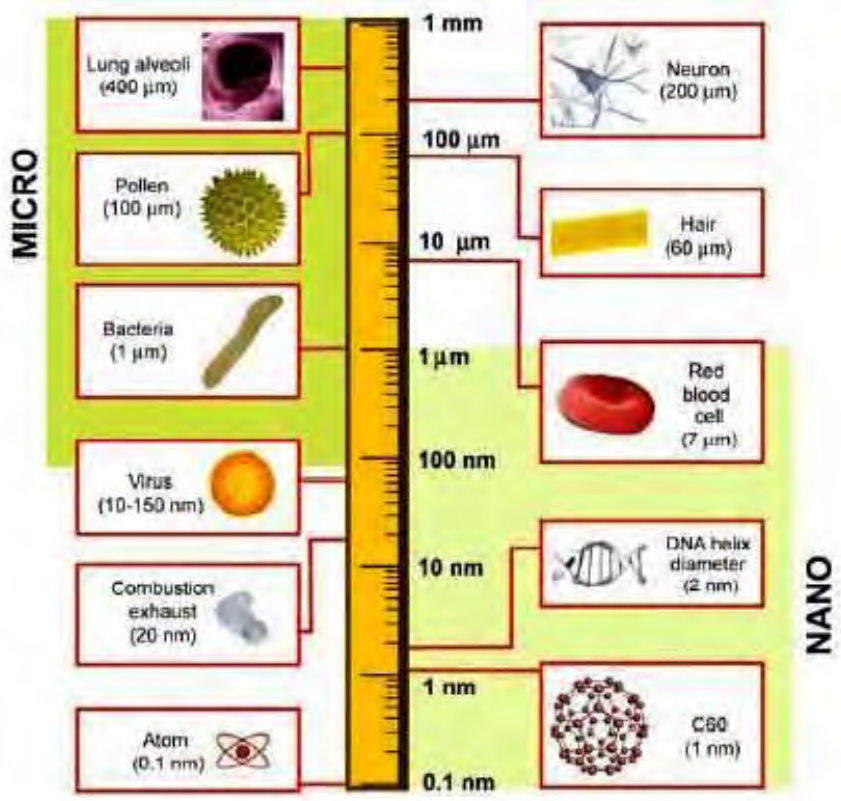

Figure 1.4. Comparison of the size of the nanomaterials to the biological components [137].

While the the synthetic nanomaterials are fabricated by different experiments. These artificial nanomaterials are divided into four classes [138]:

(1) Carbonaceous

These nanomaterials are composed mostly of carbon, commonly taking the form of hollow spheres, ellipsoids, or tubes. Spherical and ellipsoidal carbon nanomaterials are referred to as fullerenes, while cylindrical ones are called nanotubes. These nanomaterials have many potential applications, including improved films and coatings, stronger and lighter materials, and applications in electronics.

(2) Metal based

This type of nanomaterials includes quantum dots, nanogold, nanosilver and metal oxides such as iron oxide, titanium oxide, etc. They have many potential applications such as removal of inorganic anions, heavy metals, and organic pollutants.

(3) Dendrimers

These nanomaterials are nanosized polymers built from branched units. The surface of a dendrimer has numerous chain ends, which can be tailored to perform specific chemical functions. This property could also be useful for catalysis. Also, because three-dimensional dendrimers contain interior cavities into which other molecules could be placed, they may be useful for drug delivery.

(4) Composites

Composites combine nanoparticles, i.e, NPs are type of nanomaterials and have the same size (1-100 nm), with other nanoparticles or with larger, bulk-type materials. NPs such as nano sized clays, are already being added to products ranging from auto parts to packaging materials, to enhance mechanical, thermal, barrier, and flame-retardant properties. The NCs also could be formed by impregating NPs into supports such as zeolite or activated carbon, among others. Also, the NCs could be a core/shell type which composed of two or more nanomaterials. The core/shell nanomaterials could be defined as comprising a core (inner material) and a shell (outer layer material). A wide range of different combinations in close interaction including inorganic/ inorganic, inorganic/organic, organic/inorganic and organic/organic materials. The choice of the shell material of the core/shell nanomaterial is strongly depends on the end application and use [139]. Also, the core/shell nanomaterial has the properties of both materials (core and shell). Thus, the NCs could be useful for the desired application such as the environmental remediation. In this work, we developed inorganic/inorganic (metal oxide/metal oxide NPs, detailed information is explained in Chapter 5) and organic/inorganic type to produce the core/shell NCs. Among the organic materials, it has been used the cationic exchange polymer (C100), and the polyurethane foam (PUF). Chapters 7 and 10 describe in detail their synthesis and composition as well as their application. Examples of the different shapes of the core/shell nanomaterials are shown in Figure 1.5.

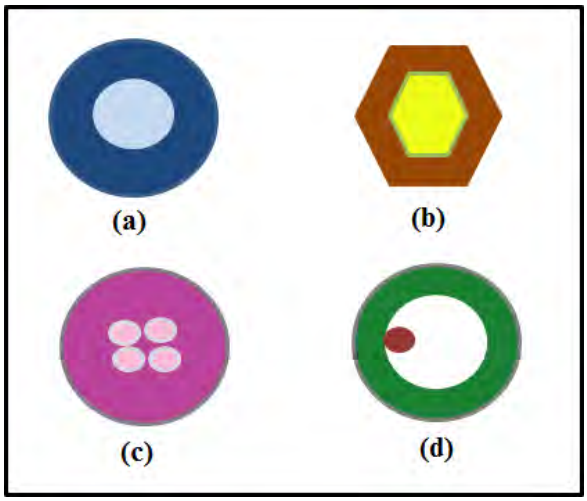

Figure 1.5. Shapes of the core/shell nanomaterials; (a) spherical, (b) hexagonal, (c) multiple small core materials coated by single shell material, (d) movable core within hollow shell materials (adapted from [139]).

Regarding dimensionality, Figure 1.6 shows the second way of classification form the point of view of dimensionality, morphology, composition, uniformity, and agglomeration.

(i) Dimensionality, in this term the nanomaterials could be divided into three parts; (a) *One dimensional* (1D) nanomaterials, where the materials are thin films or surface coatings, and include the circuitry of computer chips and the antireflection and hard coatings on eyeglasses.

(b) *Two dimensional* (2D) nanomaterials, which include 2D nanostructured films, with nanostructures firmly attached to a substrate, or nanopore filters.

(c) *Three dimensional* (3D) nanomaterials, which include the thin films that generate atomic-scale porosity, colloids, and free nanoparticles with various morphologies.

(ii) Morphology, the nanomaterials could be nanotubes and nanowires, with various shapes, such as helices, zigzags as high aspect ratio NPs or spherical, oval, cubic, prism, helical, or pillar as low aspect ratio NPs.

(iii) Composition, where the nanomaterials could be single NPs or composite of several NPs.

(iv) Uniformity, and agglomeration, where the NPs could exist as dispersed, suspension/ colloids, or in agglomerated form.

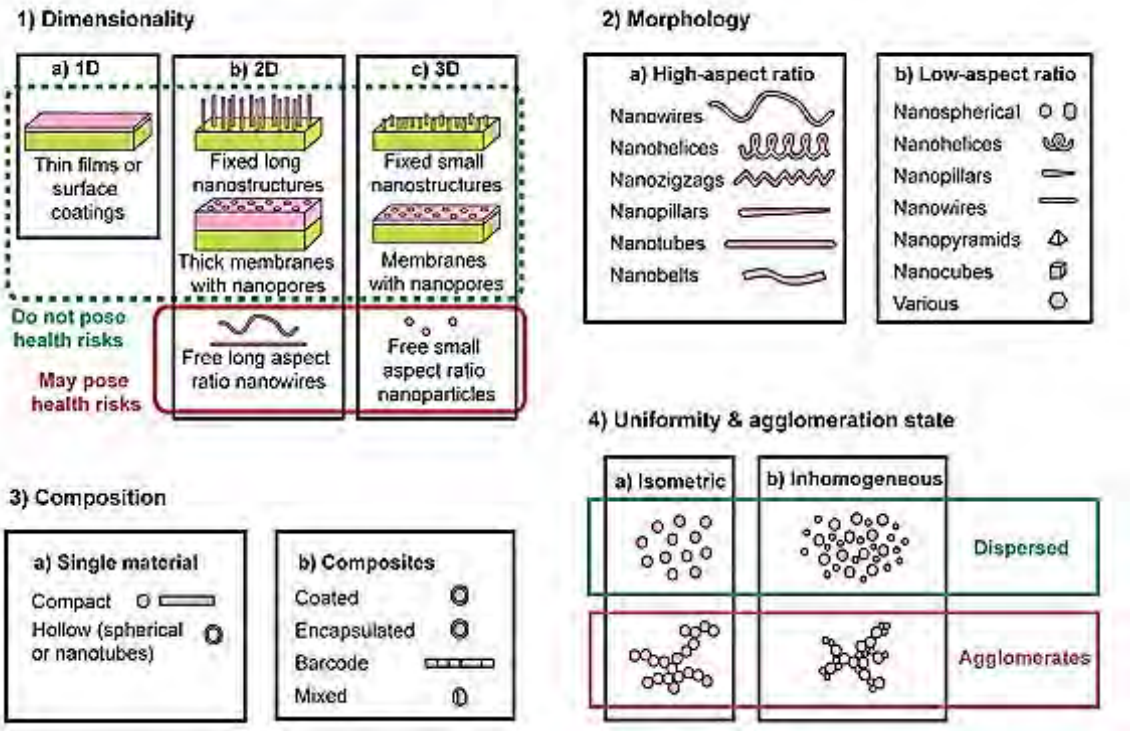

Figure 1.6. Classification of nanomaterials based on dimensionality, morphology, composition, uniformity, and agglomeration [137].

1.4.3. Synthetic methods of nanomaterials

Since the nanomaterials have large surface area and high reactivity, which led to form agglomerates into large secondary particles when reacted together, the trouble to overcome is the synthesis of highly stable nanomaterials with the required properties [140]. Hence, to meet the requirements for the desired applications using the nanomaterials, the synthetic methods played an important tool for the design of the NPs with the required properties as mentioned below [141-143]:

- Control of particle size, size distribution, shape, crystal structure and composition distribution,

- improvement of the purity of NPs,
- control of aggregation,
- stabilization of physical properties, structures and reactants,
- higher reproducibility, and
- higher mass production, scale-up and lower costs.

Generally, the NPs are synthesized via two main approaches named as top-down, and bottom-up methods as shown in Figure 1.7 [144]. The first method depends on the breakdown of the solid particles by the application of an external force. While the second method depends on the atomic transformations or molecular condensations of atoms, from gas or liquid phases, to produce the NPs as built-up method.

Regarding the top-down approach, an advantage of the wet drying method, is that highly dispersible NPs could be obtained in comparison to the dry grinding method due to that the condensation of the NPs is prevented in the first case.

The bottom-up approach, in general, is divided into gaseous phase and liquid phase methods. Excessive costs and low productivity are involved in the case of using the gaseous phase method due to the use of complicated vacuum equipment. Furthermore, liquid phase methods had been used for many years to produce the NPs. This method is divided into chemical methods, and physical methods as illustrated in Figure 1.7. Among the variety of processes had been used in the liquid/ liquid methods, various shapes of NPs such as nanorods, nanowires, nanoplates, and hollow NPs could be produced by using the chemical reduction method. Besides the liquid/ liquid methods which used to produce the NPs, various wet chemical techniques such as sol-gel, hydrothermal, co-precipitation, combustion, etc., had been used to synthesize a wide range of the NPs [145-149]. For instance, hydrolysis, polymerization, gelation, and drying among other steps [150, 151] are involved in the sol gel process to obtain pure NPs. However, disadvantages of this process are coming from the use of expensive starting materials, possibility of high carbon contents when organic reagents are used, and monitoring the process is required during the multi-steps. Metal oxides can be produced through bottom-up approach. For example, fine powders of NPs, such as metal oxide NPs, could be prepared by using hydrothermal

process where this technique based on the use of high pressure and temperature. Therefore, disadvantages of this process are an accidental explosion of the high-pressure reactor could have happened, and the hydrothermal slurries are corrosive. However, the most commonly used to synthesize the metal oxide NPs is the coprecipitation method which depends on the formation of insoluble NPs that can be easily separated from the medium. Also, the crystal growth and their aggregations depend on the concentration of the precursor, the pH, and the temperature. Consequently, advantages of this method are the relatively low reaction temperature, the fine and uniform particle size with weakly agglomerated particles, the homogeneity of component distribution, and the low cost. However, no universal experimental conditions could be used to synthesize various metal oxide NPs. Furthermore, another simple cost effective and versatile low temperature method is known as the polymeric precursor process [152]. The benefit of this process is the distribution of the metal ions throughout the polymeric structure, thus led to the inhibition of the aggregations and precipitations, and yields ultra-fine NPs [153]. Consequently, the co-precipitation, and polymeric precursor methods will be used in this work.

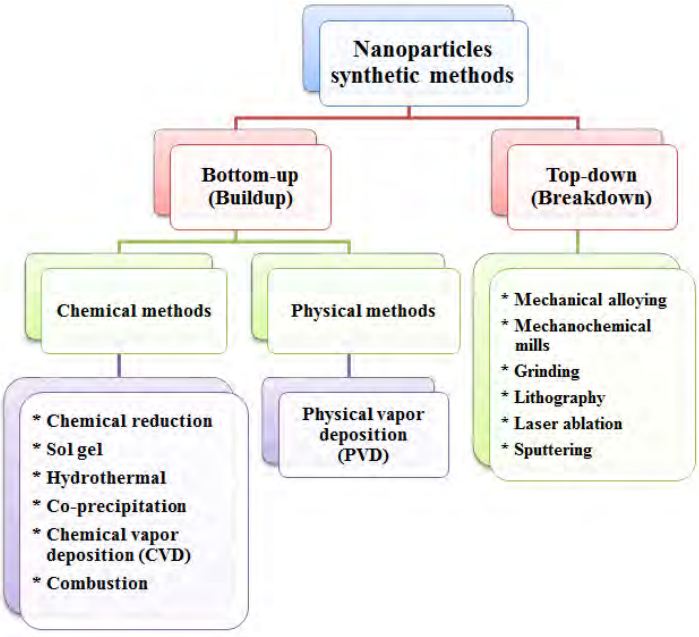

Figure 1.7. Synthetic methods for building-up NPs (adapted from [144]).

1.4.4. Environmental applications of nanomaterials

The quality of water, soil, and air was maintained and restored by the removal of contaminants from the environment to prevent problems of the human health. The environmental remediation using nanotechnology is divided into two main groups; ex-situ and in-situ adsorptive or reactive methods [154]. For instance, the pollutants are removed from the media in case of in-situ, while, for the ex-situ, the media contained the contaminants were pumped to the surface and followed by purifications. Among the wide group of nanotechnology, the use of nanoparticles for environmental remediation can be considered a novel application of nanotechnology [155]. So, a great challenge to remove the contaminants from water, and soil as well as to clean air is the environmental remediation using a cheap method by the potential efficiencies of the engineered nanomaterials and NPs. The benefits of the nanomaterials, i.e the sizes were less than 100 nm, in comparison with those of the same materials in the bulk form for the environmental applications arise from the high surface area to volume ratio due to their small size. In addition, both in-situ, and ex-situ methods can solve the environmental problem by using low dose of NPs [156].

The most widely used adsorbents for environmental applications are the carbon-based nanomaterials, metal and metal oxide NPs, and nanocomposites (NCs) (as described in Section 1.5.4. Recently, increasing attention of the use of metal and metal oxide NPs in environmental remediation such as water and gases treatment due to their high performance and low cost for contaminants removal [157]. These type of NPs include nanosized ferric oxides, aluminum oxides, zero-valent iron, titanium oxides, cerium oxides and manganese oxide [158]. Also, enormous applications have been reported using the magnetic adsorbents due to the strong adsorption capability, operational simplicity and resourcefulness [159]. In addition, the nanosized magnetite NPs could be produced in a large quantity, as well as its widely applications towards a wide range of contaminants due to the low cost, simple manipulation, large surface area, fast adsorption process, highly active surface sites and environment friendly properties [160, 161]. Titanium oxide NPs are the most widely studied photocatalyst. Also, they are applied in the removal of micropollutants such as

endocrine disrupting compounds, as well as the decomposition and mineralization of various organic pollutants and for general water purification [162]. Furthermore, some studies indicate that, by doping Ce, N or Zr into metal oxide NPs, the potential efficiency and stability of the metal oxide NPs could be enhanced [163]. As well, graphene based nanomaterials has aroused interests of many applications including environmental remediation due to they have large surface area [164]. For example, reduced graphene oxide is relatively easy to be modified by other functional groups, then it could be applied for various contaminants removal from water [165]. Besides, when concerning the large-scale application of NPs in water treatment, they have to face some inherent technical bottlenecks, such as aggregation, difficult separation, leakage into the contact water, potential adverse effect imposed on ecosystem and human health. One promising approach to forward the application of nano-particulate materials is to develop NC materials that take advantages of both the hosts and impregnated NPs. For instance, the NC materials of organic, such as polymers, and inorganic supports, include carbon based nanomaterials and natural minerals such as zeolite, have been used for several applications comprising water and gases treatment [166, 167]. Therefore, in this work, focuses on the environmental remediation using the metal oxides NPs, carbon based nanomaterials, and the NCs.

1.4.5. Nanomaterials as adsorbents for water and gases remediation

As mentioned before, the inorganic anions such as fluoride and nutrients have adverse effects to the human health when the water contain elevated levels of them. Among of several adsorbents, oxides and hydroxides of trivalent and tetravalent metals such as Fe, Al, Mn, Ti and Zr are the most commonly used to remove both anionic and cationic contaminants from water and wastewaters because of their strong tendencies to adsorb these ions [84].

For instance, a wide variety of adsorbents have been reported for fluoride removal from water such as activated carbons, activated alumina, bauxite, hematite, polymeric resins chitin, chitosan and alginate, modified ferric oxide/hydroxide, hydroxyapatite (HAP), zirconium and cerium modified materials, and titanium-derived adsorbents [91]. For

example, *Liang et al*. studied the removal efficiency of fluoride by using the TiO_2 based nanocomposites (NCs) [168]. Although, the SiO_2-TiO_2 NCs were demonstrating the highest adsorption capacity (152.20 mg/g) comparing to the others NCs of TiO_2, its efficiency being decreased when the Fe_3O_4 NPs were impregnated (Fe_3O_4-SiO_2-TiO_2 NCs). In addition to the lack of the regeneration, and reusability study of this NCs. Also, *Pepper et al.* compared the efficiency of the iron oxide NPs synthesized from the red mud (Bauxite residue) with the akageneite (β-FeOOH) iron oxide NPs [169]. Although, the synthesized NPs from the red mud showed high adsorption capacity of fluoride (11.4 mg/g) comparing to the β-FeOOH NPs (9.23 mg/g), optimization of the fluoride removal process were not studied. Therefore, lack of the critical parameters of the adsorption process of fluoride such as; pH, temperature effect, co-existent ions, reusability, and the real application into real water were observed.

Additionally, potential efficiency of nanomaterials for nutrients removal have been reported. Of the oxides and hydroxides of metals used to remove phosphate, Fe and Al oxides and hydroxides have been studied the most. Iron oxides occur as goethite (α-FeOOH), akaganeite (β-FeOOH), lepidocrocite (γ-FeOOH), haematite (α-Fe_2O_3) and magnetite (Fe_3O_4) [84]. For example, *Zach-Maor et al.* used granular activated carbon (GAC) as a support for Fe_3O_4) NPs to produce (nFeGAC) NCs, and evaluate its the efficiency for phosphate removal [170]. Although the authors estimate the maximum adsorption capacity of phosphate to be 4.9 mgP/gNCs, but lack of more details about the effect of co-ions, and the reusability studies were observed. *Gu et al.* found the maximum adsorption capcity of phosphate using zinc ferrite ($ZnFe_2O_4$) NPs is 5.23 mg/g [171]. However, the maximum adsorption capcity was found at low pH medium, hence it is difficult for application into real water due to the low adsorption capcity at the neutral pH value. Moreover, *Recillas et al.* studied the efficiency of CeO_2 NPs for phosphate removal. However, they found a low adsorption capacity of phosphate (0.4 mg/g), and also only 27 % of phosphate could be desorbed using 0.5 NaOH. Hence, the NPs failed in terms of regeneration and reusability [172]. Additionally, several adsorbents have been reported for nitrate removal such as carbon based adsorbents, clay adsorbents, layer doubled hydroxides (LDHs), zeolites, chitosan based adsorbents, etc. [173].

The heavy metals are also emerging contaminants and needed to be removed. Therefore, wide variety of materials were used for heavy metals removal such metal oxides, and hydroxides, cationic exchange resins, carbon based adsorbents, chitosan based adsorbent, and silica NPs [51]. For instance, metal oxide NPs as TiO_2, Fe_3O_4, and CeO_2 NPs were applied for cadmium removal by *Contreras et al.* [174]. The authors found the adsorption capacity of cadmium was found to be 12.20, 101.10, and 49.10 mg/g by using TiO_2, Fe_3O_4, and CeO_2 NPs, respectively. However, lack of reusability study was observed. Another study was reported by *Contreras et al.* for cadmium removal using CeO_2 NPs [175]. Enhancement of the maximum adsorption capacity (93.4 mg/g) was proved by decreasing the dose of the NPs. Although, the NPs showed that adsorption capacity is not affected by multi-component system, the regeneration and reusability of the NPs are still needed for further investigation.

Regarding to the separation of microalgae from water, magnetic NPs have been reported for the harvesting due to its high specific surface area, biocompatibility and that they could adhere to the algae cells and then easily be separated from the medium by applying an external magnetic field [176, 177]. Moreover, by surface coating or modification of the magnetic nanoparticles (NPs), with diverse materials such as polymers and surfactants, the stability of the NPs suspension can be enhanced, jointly with the harvesting efficiency [178-180]. Different types of magnetic NPs (Fe_3O_4 NPs), with or without surface coating, have been used for the harvesting of different microalgae such as the oleaginous Chlorella sp. [179], Scenedesmus Dimorphus [178] and Chlorella Vulgaris [181]. However, optimization of the harvesting efficiency of the microalgae is still under investigation by using the iron oxide based NCs.

Besides, in the applications of nanotechnology for gas treatment, there is a huge interest in the development of advanced adsorbent materials that present better features than the conventional materials and have specialized functionalities for CO_2 and CH_4 capture and their separation [119]. These novel sorbents are i) ionic liquids, and ii) modified porous supports. Ionic liquids (IL) are solvent sorbents that are based on a stable liquid composed by a combination of inorganic or organic anions and large organic bulky asymmetric cations [182]. Due to their thermal stability, negligible vapour pressure, tuneable physico-

chemical characteristics and high CO_2 solubility, IL are utilized in CO_2 removal applications [183]. Furthermore, modification of IL with functional groups [184] to better adsorb and solubilize CO_2 has been developed. The high CO_2 solubility in ionic liquids, when compared to CH_4, gives them the potential to be utilized in the separation of CO_2 from natural gas [185]. Some other studies have demonstrated the potential of different IL to remove CO_2 from natural gas based on the CO_2 / CH_4 solubility and selectivity. Moreover, the modified porous supports showed a potential application for CO_2 and / or CH_4 capture. For example, zeolite-templated N-doped carbons exhibit a high CO_2 uptake capacity in comparison to carbonaceous or inorganic and organic porous materials [186]. Furthermore, nanomaterials have a number of physicochemical properties that make them particularly attractive as separation supports for gas purification and gas capture. Novel nanomaterials, like advanced nanoporous materials, MOFs and porous organic polymers, have received considerable attention in adsorption storage applications due to their exceptionally high surface areas and their chemically-tunable structures [187]. Some of these materials have been tested for CH_4 and CO_2 adsorption and have gained increased interest recently. In fact, several research papers have reported improved CO_2 sorption and, more interestingly, improved CH_4 adsorption capacity compared to conventional sorbents. Hence, among all the nanomaterials used for CO_2 or CH_4 capture, the most significant ones are, namely: 1) Nanosized Zeolites; 2) Mesoporous Silica NPs; 3) MOFs and derived MOFs with embedded NPs; 4) Metal and Metal Oxide NPs (MNPs and MONPs), and 5) Carbonaceous nanoadsorbents. In addition, various types of NPs encapsulated into MOFs were studied as catalyst for CO oxidation. However, the T100, i.e the temperature required for 100 % conversion, is higher than 200 °C, hence the challenge is to find nanomaterials that can catalyze the CO at low temperature. So, finding a promising material to remove pollutants is a matter that admits of no delay. Also, evaluation of this materials should be in terms of low cost, reusability, and low toxicity (as well be discussed in the next section) to the environment.

1.4.6. Toxicity of nanomaterials

Nanotoxicology deals with the study and application of toxicity of nanomaterials [137]. The toxic effect of the nanomaterials in the biological environment depends on the type of interaction in the surroundings as well as their initial morphology, size, composition, and the synthetic method utilized [188]. There are five possible routes where the human could be exposed to the NPs. The skin is the effective fence to foreign matters, the lungs and digestive system are the most defenseless, in addition to the injections and implants. The NPs can enter the circulatory and lymphatic systems, and ultimately to body tissues and organs due to their small sizes. In fact, it is known that NPs can be easily ingested, inhaled or permeated through the skin of the human body and taken up by animal cells [189]. Thus, the adverse health effects are illustrated in Figure 1.6. The most principal factors that influence the toxicity of NPs include size, aggregation, composition, crystallinity, and surface functionalization. The toxicity of the NPs could arise from various sources such:

(1) From natural process such as photochemical reactions, volcanic eruptions, forest fires, and simple erosion, and by plants and animals due to part of the NPs are abundant in nature [190].

(2) Anthropogenic nanoparticles such as the by-products of simple combustion, chemical manufacturing, welding, ore refining and smelting, combustion in vehicle and airplane engines, combustion of treated pulverized sewage sludge, and combustion of coal and fuel oil for power generation. In addition to the NPs used in cosmetics, sporting goods, tires, stain resistant clothing, sunscreens, toothpaste, food additives [191].

(3) Environmental exposure to toxic substance leads to several diseases such as the lead, cadmium, aluminum, nickel and chromium metals NPs when they released into the environment [192].

(4) Aerosol pollution which is a combination of particulate matter and gaseous and liquid phases from natural and anthropogenic sources [193].

However, not all NPs produce adverse effects to human. Also, the toxicity of nanoparticles in our earth's ecosystem is not easy to determine due to the presence of some obstacles that need to overcome: the characterization of nanoscale pollutant is difficult to assess and, the biological systems at the nanoscale are not known [194]. In addition, there is lack of complete information about human toxicity and environmental waste of nanomaterials [195].

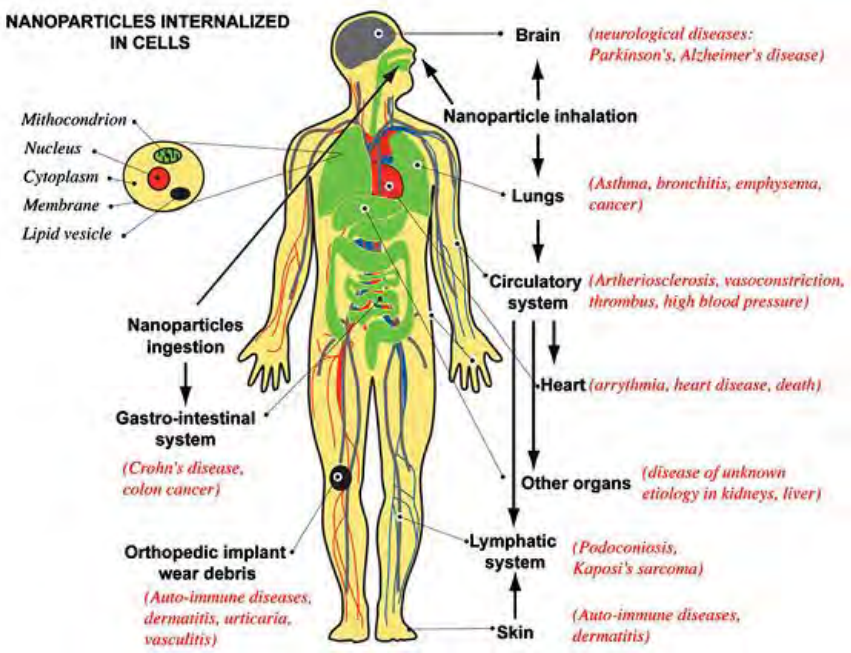

Figure 1.6. In vivo, and in vitro epidemiological studies for the affect organs and the corresponding diseases when the human body espouse to NPs [137].

1.5. References

1. Escobar, J.C., et al., *Biofuels: environment, technology and food security.* Renewable and sustainable energy reviews, 2009. **13**(6): p. 1275-1287.
2. GENI. *Concerns about global energy problems*. Available from: Global network energy institute, http://www.geni.org/globalenergy/faq/general/faq_I-am-concerned-about-global-energy-problems.shtml, (Access date 21/05/2017).
3. OMICS. *Environmental Pollution*. 2017 20/05/2017]; Available from: https://www.omicsonline.org/environmental/environmental-pollution-review-articles.php.
4. Owa, F.D., *Water Pollution: Sources, Effects, Control and Management.* Mediterranean Journal of Social Sciences, 2013. **4**(8): p. 65-68.
5. *Air Pollution*. 2017; Available from: http://www.environbusiness.com/pollute/air (Access date 19/05/2017).
6. Wikipedia and contributors, *Soil contamination*. May 2017, Wikipedia, The Free Encyclopedia.
7. Ball, P., *The Elements: A Very Short Introduction*. 2004: OUP Oxford.
8. Boyd, T.J.M. and J.J. Sanderson, *The Physics of Plasmas*. 2003, Cambridge: Cambridge University Press.
9. Busch, M.A., *Chiral Pollutants: Distribution, Toxicity and Analysis by Chromatography and Capillary Electrophoresis By Imran Ali (National Institute of Hydrology, Roorkee, India) and Hassan Y. Aboul-Enein (King Faisal Specialist Hospital, Riyadh, Saudi Arabia). John Wiley & Sons: Chichester, U.K. 2004. xx + 344 pp. $175.00. ISBN 0-470-86780-9.* Journal of the American Chemical Society, 2004. **126**(44): p. 14680-14680.
10. Ali, I. and H.Y. Aboul-Enein, *Introduction*, in *Chiral Pollutants: Distribution, Toxicity and Analysis by Chromatography and Capillary Electrophoresis*. 2004, John Wiley & Sons, Ltd. p. 1-35.
11. Santhosh, C., et al., *Role of nanomaterials in water treatment applications: A review.* Chemical Engineering Journal, 2016. **306**: p. 1116-1137.

12. Laws, E.A., *Aquatic Pollution: An Introductory Text*. 2017: Wiley.
13. Forgacs, E., T. Cserháti, and G. Oros, *Removal of synthetic dyes from wastewaters: a review.* Environment International, 2004. **30**(7): p. 953-971.
14. Rai, H.S., et al., *Removal of Dyes from the Effluent of Textile and Dyestuff Manufacturing Industry: A Review of Emerging Techniques With Reference to Biological Treatment.* Critical Reviews in Environmental Science and Technology, 2005. **35**(3): p. 219-238.
15. Sauvé, S. and M. Desrosiers, *A review of what is an emerging contaminant.* Chemistry Central Journal, 2014. **8**(1): p. 15.
16. Rodriguez, O., et al., *Treatment Technologies for Emerging Contaminants in water: A review.* Chemical Engineering Journal, 2017.
17. Ali, I., *New Generation Adsorbents for Water Treatment.* Chemical Reviews, 2012. **112**(10): p. 5073-5091.
18. Zhou, J., et al., *Hierarchically porous calcined lithium/aluminum layered double hydroxides: Facile synthesis and enhanced adsorption towards fluoride in water.* Journal of Materials Chemistry, 2011. **21**(48): p. 19353-19361.
19. Marinho, V., *Fluoride gel inhibits caries in children who have low caries-risk but this may not be clinically relevant.* Evid-based Dent, 2004. **5**(4): p. 95-95.
20. WHO, *Environmental health criteria for fluorides, 27*. 2002, World Health Organization: Geneva.
21. Vinati, A., B. Mahanty, and S.K. Behera, *Clay and clay minerals for fluoride removal from water: A state-of-the-art review.* Applied Clay Science, 2015. **114**: p. 340-348.
22. Bhatnagar, A., E. Kumar, and M. Sillanpää, *Fluoride removal from water by adsorption—A review.* Chemical Engineering Journal, 2011. **171**(3): p. 811-840.
23. Daifullah, A.A.M., S.M. Yakout, and S.A. Elreefy, *Adsorption of fluoride in aqueous solutions using KMnO4-modified activated carbon derived from steam pyrolysis of rice straw.* Journal of Hazardous Materials, 2007. **147**(1–2): p. 633-643.
24. Ayoob, S. and A.K. Gupta, *Fluoride in Drinking Water: A Review on the Status and Stress Effects.* Critical Reviews in Environmental Science and Technology, 2006. **36**(6): p. 433-487.

25. Goswami, A. and M.K. Purkait, *Kinetic and Equilibrium Study for the Fluoride Adsorption using Pyrophyllite.* Separation Science and Technology, 2011. **46**(11): p. 1797-1807.
26. Reardon, E.J. and Y. Wang, *A Limestone Reactor for Fluoride Removal from Wastewaters.* Environmental Science & Technology, 2000. **34**(15): p. 3247-3253.
27. Shen, F., et al., *Electrochemical removal of fluoride ions from industrial wastewater.* Chemical Engineering Science, 2003. **58**(3–6): p. 987-993.
28. Fan, C.-S. and K.-C. Li, *Production of insulating glass ceramics from thin film transistor-liquid crystal display (TFT-LCD) waste glass and calcium fluoride sludge.* Journal of Cleaner Production, 2013. **57**: p. 335-341.
29. Drouiche, N., et al., *Photovoltaic solar cells industry wastewater treatment.* Desalination and Water Treatment, 2013. **51**(31-33): p. 5965-5973.
30. Paudyal, H., et al., *Removal of Fluoride from Aqueous Solution by Using Porous Resins Containing Hydrated Oxide of Cerium(IV) and Zirconium(IV).* JOURNAL OF CHEMICAL ENGINEERING OF JAPAN, 2012. **45**(5): p. 331-336.
31. WHO, *Guidelines for Drinking-water Quality, 4th ed.* 2011, World Health Organization: Geneva, Switzerland. p. 1-564.
32. Nolan, B. and J. Stoner, *Nutrients in groundwaters of the conterminous United States, 1992-1995.* USGS Staff--Published Research, 2000: p. 59.
33. Khalil, A.M.E., et al., *Optimized nano-scale zero-valent iron supported on treated activated carbon for enhanced nitrate and phosphate removal from water.* Chemical Engineering Journal, 2017. **309**: p. 349-365.
34. Köhler, *Detergent phosphates and detergent ecotaxes: a policy assessment*. 2001, University of Cambridge, UK: Centre Européen d'Etudes des Polyphosphates-a European Chemical Industry Council (CEFIC) sector group.
35. Manahan, S.E., *Environmental Chemistry*. 9th Edition ed. 2010, U.S.: CRC Press, Taylor & Francis Group.
36. Wang, Z., et al., *A bench-scale study on the removal and recovery of phosphate by hydrous zirconia-coated magnetite nanoparticles.* Journal of Magnetism and Magnetic Materials, 2017. **424**: p. 213-220.

37. Garry, V., et al., *Human genotoxicity: pesticide applicators and phosphine.* Science, 1989. **246**(4927): p. 251-255.
38. Eldad, A. and G.A. Simon, *The phosphorous burn - a preliminary comparative experimental study of various forms of treatment.* Burns, 1991. **17**(3): p. 198-200.
39. Acelas, N.Y., et al., *Selective removal of phosphate from wastewater using hydrated metal oxides dispersed within anionic exchange media.* Chemosphere, 2015. **119**: p. 1353-1360.
40. Sharpley, A.N., et al., *Sources of phosphorus exported from an agricultural watershed in Pennsylvania.* Agricultural Water Management, 1999. **41**(2): p. 77-89.
41. Hu, Q., et al., *Kinetic and isotherm studies of nitrate adsorption on granular Fe-Zr-chitosan complex and electrochemical reduction of nitrate from the spent regenerant solution.* RSC Advances, 2016. **6**(66): p. 61944-61954.
42. Rezaei Kalantary, R., et al., *Nitrate adsorption by synthetic activated carbon magnetic nanoparticles: kinetics, isotherms and thermodynamic studies.* Desalination and Water Treatment, 2016. **57**(35): p. 16445-16455.
43. Fewtrell, L., *Drinking-Water Nitrate, Methemoglobinemia, and Global Burden of Disease: A Discussion.* Environmental Health Perspectives, 2004. **112**(14): p. 1371-1374.
44. Chiu, H.-F., S.-S. Tsai, and C.-Y. Yang, *Nitrate in Drinking Water and Risk of Death from Bladder Cancer: An Ecological Case-Control Study in Taiwan.* Journal of Toxicology and Environmental Health, Part A, 2007. **70**(12): p. 1000-1004.
45. Gálvez, J.M., et al., *Influence of hydraulic loading and air flowrate on urban wastewater nitrogen removal with a submerged fixed-film reactor.* Journal of Hazardous Materials, 2003. **101**(2): p. 219-229.
46. USEPA, *Risk based Concentration Table*. 2000, United States Environmental Protection Agency: Philadelphia, PA; Washington DC.
47. Nur, T., et al., *Nitrate removal using Purolite A520E ion exchange resin: batch and fixed-bed column adsorption modelling.* International Journal of Environmental Science and Technology, 2015. **12**(4): p. 1311-1320.

48. Chen, K., et al., *Removal of cadmium and lead ions from water by sulfonated magnetic nanoparticle adsorbents.* Journal of Colloid and Interface Science, 2017. **494**: p. 307-316.
49. Fu, F. and Q. Wang, *Removal of heavy metal ions from wastewaters: A review.* Journal of Environmental Management, 2011. **92**(3): p. 407-418.
50. Tête, N., et al., *Histopathology related to cadmium and lead bioaccumulation in chronically exposed wood mice, Apodemus sylvaticus, around a former smelter.* Science of The Total Environment, 2014. **481**: p. 167-177.
51. Achla Kaushal and S.K. Singh, *Removal of heavy metals by nanoadsorbents: A review*. Journal of Environment and Biotechnology Research, 2017. **6**(1): p. 96-104.
52. Chabicovsky, M., W. Klepal, and R. Dallinger, *Mechanisms of cadmium toxicity in terrestrial pulmonates: Programmed cell death and metallothionein overload.* Environmental Toxicology and Chemistry, 2004. **23**(3): p. 648-655.
53. Xi, Y., et al., *Removal of Cadmium(II) from Wastewater Using Novel Cadmium Ion-Imprinted Polymers.* Journal of Chemical & Engineering Data, 2015. **60**(11): p. 3253-3261.
54. Ferrante, M., et al., *Health Effects of Metals and Related Substances in Drinking Water*. 2013: IWA Publishing.
55. Biela, R. and T. Kučera, *Efficacy of Sorption Materials for Nickel, Iron and Manganese Removal from Water*. Procedia Engineering, 2016. **162**: p. 56-63.
56. Gray, N.F., *Drinking Water Quality: Problems and Solutions*. 2008, Cambridge, UK: Cambridge University Press.
57. Ilavský, J., D. Barloková, and K. Munka, *Antimony Removal from Water by Adsorption to Iron-Based Sorption Materials.* Water, Air, & Soil Pollution, 2014. **226**(1): p. 2238.
58. Verhaert, V., et al., *Persistent organic pollutants in the Olifants River Basin, South Africa: Bioaccumulation and trophic transfer through a subtropical aquatic food web.* Science of The Total Environment, 2017. **586**: p. 792-806.
59. Wikipedia, *Persistent organic pollutant*. 2017, Wikipedia, The Free Encyclopedia.

60. Rani, M., U. Shanker, and V. Jassal, *Recent strategies for removal and degradation of persistent & toxic organochlorine pesticides using nanoparticles: A review.* Journal of Environmental Management, 2017. **190**: p. 208-222.
61. Shen, Q., et al., *Enhanced algae removal by drinking water treatment of chlorination coupled with coagulation.* Desalination, 2011. **271**(1–3): p. 236-240.
62. Hung, M.T. and J.C. Liu, *Microfiltration for separation of green algae from water.* Colloids and Surfaces B: Biointerfaces, 2006. **51**(2): p. 157-164.
63. Henriksen, P., *Estimating nodularin content of cyanobacterial blooms from abundance of Nodularia spumigena and its characteristic pigments—a case study from the Baltic entrance area.* Harmful Algae, 2005. **4**(1): p. 167-178.
64. EPA, *Drinking water standards and health advisories table*. 2007, United states environmental protection agency. p. 1-30.
65. Gao, S., et al., *Electro-coagulation–flotation process for algae removal.* Journal of Hazardous Materials, 2010. **177**(1–3): p. 336-343.
66. Ma, J. and W. Liu, *Effectiveness of ferrate (VI) preoxidation in enhancing the coagulation of surface waters.* Water Research, 2002. **36**(20): p. 4959-4962.
67. Sakai, H., et al., *Effects of low- or medium-pressure ultraviolet lamp irradiation on Microcystis aeruginosa and Anabaena variabilis.* Water Research, 2007. **41**(1): p. 11-18.
68. Heng, L., et al., *Algae removal by ultrasonic irradiation–coagulation.* Desalination, 2009. **239**(1): p. 191-197.
69. Chen, J.-J. and H.-H. Yeh, *The mechanisms of potassium permanganate on algae removal.* Water Research, 2005. **39**(18): p. 4420-4428.
70. Overney, J. *A Fast Track From Algae Biomass to Biogas*. Available from: https://actu.epfl.ch/news/a-fast-track-from-algae-biomass-to-biogas/ (Access date 01/06/2017).
71. Tchobanoglous, G., et al., *Wastewater Engineering: Treatment and Reuse*. 2003: McGraw-Hill Education.
72. Szabó, A., et al., *Significance of Design and Operational Variables in Chemical Phosphorus Removal.* Water Environment Research, 2008. **80**(5): p. 407-416.

73. Xiong, Y., et al., *Treatment of dye wastewater containing acid orange II using a cell with three-phase three-dimensional electrode.* Water Research, 2001. **35**(17): p. 4226-4230.
74. Kim, T.-H., et al., *Decolorization of disperse and reactive dyes by continuous electrocoagulation process.* Desalination, 2002. **150**(2): p. 165-175.
75. Babu, R.R., et al., *Treatment of tannery wastewater by electrocoagulation.* J. Univ. Chem. Technol. Metal, 2007. **42**(2): p. 201-206.
76. Ghernaout, D., et al., *Application of electrocoagulation in Escherichia coli culture and two surface waters.* Desalination, 2008. **219**(1): p. 118-125.
77. Kumar, N.S. and S. Goel, *Factors influencing arsenic and nitrate removal from drinking water in a continuous flow electrocoagulation (EC) process.* Journal of Hazardous Materials, 2010. **173**(1–3): p. 528-533.
78. Zaroual, Z., et al., *Optimizing the removal of trivalent chromium by electrocoagulation using experimental design.* Chemical Engineering Journal, 2009. **148**(2–3): p. 488-495.
79. Wei, Y., et al., *Minimization of excess sludge production for biological wastewater treatment.* Water Research, 2003. **37**(18): p. 4453-4467.
80. *Advantage-disadvantage-biological-treatment* Available from: http://www.thewatertreatments.com/wastewater-sewage-treatment/biological-treatment/attachment/advantage-disadvantage-biological-treatment/, (Access date 21/05/2017).
81. Worch, E., *Adsorption Technology in Water Treatment: Fundamentals, Processes, and Modeling*. 2012: De Gruyter.
82. Barakat, M.A., *New trends in removing heavy metals from industrial wastewater.* Arabian Journal of Chemistry, 2011. **4**(4): p. 361-377.
83. Loganathan, P., et al., *Defluoridation of drinking water using adsorption processes.* Journal of Hazardous Materials, 2013. **248–249**: p. 1-19.
84. Loganathan, P., et al., *Removal and Recovery of Phosphate From Water Using Sorption.* Critical Reviews in Environmental Science and Technology, 2014. **44**(8): p. 847-907.

85. Loganathan, P., S. Vigneswaran, and J. Kandasamy, *Enhanced removal of nitrate from water using surface modification of adsorbents – A review.* Journal of Environmental Management, 2013. **131**: p. 363-374.
86. Ghosh, D., M.K. Sinha, and M.K. Purkait, *A comparative analysis of low-cost ceramic membrane preparation for effective fluoride removal using hybrid technique.* Desalination, 2013. **327**: p. 2-13.
87. Guo, Q. and J. Tian, *Removal of fluoride and arsenate from aqueous solution by hydrocalumite via precipitation and anion exchange.* Chemical Engineering Journal, 2013. **231**: p. 121-131.
88. Tezcan Un, U., A.S. Koparal, and U. Bakir Ogutveren, *Fluoride removal from water and wastewater with a bach cylindrical electrode using electrocoagulation.* Chemical Engineering Journal, 2013. **223**: p. 110-115.
89. Sarkar, M., et al., *Use of laterite for the removal of fluoride from contaminated drinking water.* Journal of Colloid and Interface Science, 2006. **302**(2): p. 432-441.
90. Turner, B.D., P. Binning, and S.L.S. Stipp, *Fluoride Removal by Calcite: Evidence for Fluorite Precipitation and Surface Adsorption.* Environmental Science & Technology, 2005. **39**(24): p. 9561-9568.
91. Habuda-Stanić, M., M. Ravančić, and A. Flanagan, *A Review on Adsorption of Fluoride from Aqueous Solution.* Materials, 2014. **7**(9): p. 6317.
92. Mezenner, N.Y. and A. Bensmaili, *Kinetics and thermodynamic study of phosphate adsorption on iron hydroxide-eggshell waste.* Chemical Engineering Journal, 2009. **147**(2–3): p. 87-96.
93. Li, M., et al., *Phosphate adsorption on metal oxides and metal hydroxides: A comparative review.* Environmental Reviews, 2016. **24**(3): p. 319-332.
94. Reijnders, L., *Phosphorus resources, their depletion and conservation, a review.* Resources, Conservation and Recycling, 2014. **93**(0): p. 32-49.
95. Lewinsky, A.A., *Hazardous Materials and Wastewater: Treatment, Removal and Analysis*. 2007: Nova Science Publishers.
96. Matschullat, J., *Arsenic in the geosphere — a review.* Science of The Total Environment, 2000. **249**(1–3): p. 297-312.

97. D'Alessandro, D.M., B. Smit, and J.R. Long, *Carbon Dioxide Capture: Prospects for New Materials.* Angewandte Chemie International Edition, 2010. **49**(35): p. 6058-6082.
98. Doman, L.E., et al., *Energy-Related Carbon Dioxide Emissions*. 2010: International Energy Outlook International Energy Outlook, US Energy Information Administration, Washington, DC.
99. Metz, B., et al., *IPCC, 2005: IPCC Special Report on Carbon Dioxide Capture and Storage. Prepared by Working Group III of the Intergovernmental Panel on Climate Change* Vol. 442. 2005, Cambridge, United Kingdom and New York, NY, USA: Cambridge University Press.
100. Ciferno, J.P., et al., *Capturing Carbon Existing Coal-Fired Power Plants.* Chemical Engineering Progress 2009. **105**(4): p. 33-41.
101. Yang, H., et al., *Progress in carbon dioxide separation and capture: A review*. Journal of Environmental Sciences, 2008. **20**(1): p. 14-27.
102. Spigarelli, B.P. and S.K. Kawatra, *Opportunities and challenges in carbon dioxide capture*. Journal of CO2 Utilization, 2013. **1**: p. 69-87.
103. Baltrėnaitė, E., P. Baltrėnas, and A. Lietuvninkas, *The Sustainable Role of the Tree in Environmental Protection Technologies*. 2016, Switzerland: Springer International Publishing. 344.
104. Butler, J.H. and S.A. Montzka. *THE NOAA ANNUAL GREENHOUSE GAS INDEX (AGGI)*. 2012; Available from: http://esrl.noaa.gov/gmd/aggi/aggi.html.
105. Kirschke, S., et al., *Three decades of global methane sources and sinks.* Nature Geosci, 2013. **6**(10): p. 813-823.
106. EPA, *Inventory of U.S. Greenhouse Gas Emissions and Sinks: 1990-2014*. U.S. Environmental Protection Agency, 2016. **EPA 430-R-16-002**.
107. Wikipedia and contributors, *Carbon monoxide poisoning*, in *Wikipedia, The Free Encyclopedia*. 2017.
108. Prockop, L.D. and R.I. Chichkova, *Carbon monoxide intoxication: An updated review*. Journal of the Neurological Sciences. **262**(1): p. 122-130.

109. Ernst , A. and J.D. Zibrak *Carbon Monoxide Poisoning.* New England Journal of Medicine, 1998. **339**(22): p. 1603-1608.
110. Fife, C.E., et al., *Dying to Play Video Games: Carbon Monoxide Poisoning From Electrical Generators Used After Hurricane Ike.* Pediatrics, 2009. **123**(6): p. e1035-e1038.
111. Steven J. Emmerich and L. Wang, *Measured CO Concentrations at NIST IAQ Test House from Operation of Portable Electric Generators in Attached Garage – Interim Report*. 2011, United States National Institute of Standards and Technology.
112. Omaye, S.T., *Metabolic modulation of carbon monoxide toxicity.* Toxicology, 2002. **180**(2): p. 139-150.
113. Plaza, M.G., et al., *Post-combustion CO2 capture with a commercial activated carbon: Comparison of different regeneration strategies.* Chemical Engineering Journal, 2010. **163**(1–2): p. 41-47.
114. Damen, K., et al., *A comparison of electricity and hydrogen production systems with CO2 capture and storage. Part A: Review and selection of promising conversion and capture technologies.* Progress in Energy and Combustion Science, 2006. **32**(2): p. 215-246.
115. Grande, C.A., et al., *Electric swing adsorption as emerging CO2 capture technique.* Energy Procedia, 2009. **1**(1): p. 1219-1225.
116. Thiruvenkatachari, R., et al., *Post combustion CO2 capture by carbon fibre monolithic adsorbents.* Progress in Energy and Combustion Science, 2009. **35**(5): p. 438-455.
117. Pellerano, M., et al., *CO2 capture by adsorption on activated carbons using pressure modulation.* Energy Procedia, 2009. **1**(1): p. 647-653.
118. Clausse, M., J. Merel, and F. Meunier, *Numerical parametric study on CO2 capture by indirect thermal swing adsorption.* International Journal of Greenhouse Gas Control, 2011. **5**(5): p. 1206-1213.
119. Li, Y., et al., *Adsorption separation of CO2/CH4 gas mixture on the commercial zeolites at atmospheric pressure.* Chemical Engineering Journal, 2013. **229**: p. 50-56.

120. Smart, S.K., et al., *The biocompatibility of carbon nanotubes.* Carbon, 2006. **44**(6): p. 1034-1047.
121. Cinke, M., et al., *CO2 adsorption in single-walled carbon nanotubes.* Chemical Physics Letters, 2003. **376**(5–6): p. 761-766.
122. Lu, C., et al., *Comparative Study of CO2 Capture by Carbon Nanotubes, Activated Carbons, and Zeolites.* Energy & Fuels, 2008. **22**(5): p. 3050-3056.
123. Cecilia, S., et al., *Adsorption of methane in porous materials as the basis for the storage of natural gas*. 2010, Intechopen: Science, Technology, and Medicine.
124. Saha, D., et al., *Adsorption of CO2, CH4, N2O, and N2 on MOF-5, MOF-177, and Zeolite 5A.* Environmental Science & Technology, 2010. **44**(5): p. 1820-1826.
125. Austin, C.K., et al., *Enhanced Methane Sorption in Densified Forms of a Porous Polymer Network.* Materials Sciences and Applications, 2014. **5**: p. 387-394.
126. Alonso, A., *Development of polymeric nanocomposites with enhanced distribution of catalytically active or bactericide nanoparticles*, in *Departament d'Enginyeria Química, Escola d'Enginyeria* 2012, Universitat Autònoma de Barcelona (UAB).
127. ISO, *ISO/TS 80004-2:2015; Nanotechnologies — Vocabulary — Part 2: Nano-objects*. 2015.
128. Bhatia, S., *Nanoparticles Types, Classification, Characterization, Fabrication Methods and Drug Delivery Applications*, in *Natural Polymer Drug Delivery Systems: Nanoparticles, Plants, and Algae*. 2016, Springer International Publishing: Cham. p. 33-93.
129. ISI. *Web of science*. (16-05-2017)]; Available from: https://apps.webofknowledge.com.
130. Nel, A., et al., *Toxic Potential of Materials at the Nanolevel.* Science, 2006. **311**(5761): p. 622-627.
131. Hafner, J.H., et al., *Structural and functional imaging with carbon nanotube AFM probes.* Progress in Biophysics and Molecular Biology, 2001. **77**(1): p. 73-110.
132. Thompson, S.E. and S. Parthasarathy, *Moore's law: the future of Si microelectronics.* Materials Today, 2006. **9**(6): p. 20-25.

133. Martin, C.R. and P. Kohli, *The emerging field of nanotube biotechnology*. Nat Rev Drug Discov, 2003. **2**(1): p. 29-37.
134. He, F. and D. Zhao, *Preparation and Characterization of a New Class of Starch-Stabilized Bimetallic Nanoparticles for Degradation of Chlorinated Hydrocarbons in Water*. Environmental Science & Technology, 2005. **39**(9): p. 3314-3320.
135. Azonano. *Classification of Nanomaterials, The Four Main Types of Intentionally Produced Nanomaterials*. 2007 [cited 2017 15/05/2017]; Available from: http://www.azonano.com/article.aspx?ArticleID=1872.
136. Wikipedia, *Nanomaterials*. 2017, Wikipedia, The Free Encyclopedia.
137. Buzea, C., I.I. Pacheco, and K. Robbie, *Nanomaterials and nanoparticles: Sources and toxicity*. Biointerphases, 2007. **2**(4): p. MR17-MR71.
138. Savage, N. and M. Diallo, *Nanomaterials and Water Purification: Opportunities and Challenges*. Journal of Nanoparticle Research, 2005. **7**(4-5): p. 331-342.
139. Ghosh Chaudhuri, R. and S. Paria, *Core/Shell Nanoparticles: Classes, Properties, Synthesis Mechanisms, Characterization, and Applications.* Chemical Reviews, 2012. **112**(4): p. 2373-2433.
140. X. Feng and M.Z. Hu, *Ceramic Nanoparticle Synthesis* in *Encyclopedia of Nanoscience and Nanotechnology*, H.S. Nalwa, Editor. 2004, Amencan Scientific Publishers: USA. p. 687-726.
141. Sediri, F., F. Touati, and N. Gharbi, *A one-step hydrothermal way for the synthesis of vanadium oxide nanotubes containing the phenylpropylamine as template obtained via non-alkoxide route*. Materials Letters, 2007. **61**(8–9): p. 1946-1950.
142. Jiang, X., et al., *Ethylene glycol-mediated synthesis of metal oxide nanowires.* Journal of Materials Chemistry, 2004. **14**(4): p. 695-703.
143. Hyeon, T., *Chemical synthesis of magnetic nanoparticles.* Chemical Communications, 2003(8): p. 927-934.
144. Horikoshi, S. and N. Serpone, *Introduction to Nanoparticles*, in *Microwaves in Nanoparticle Synthesis*. 2013, Wiley-VCH Verlag GmbH & Co. KGaA. p. 1-24.

145. Lu, C.-Z. and G.T.-K. Fey, *Nanocrystalline and long cycling LiMn2O4 cathode material derived by a solution combustion method for lithium ion batteries.* Journal of Physics and Chemistry of Solids, 2006. **67**(4): p. 756-761.
146. Ng, S.H., et al., *Polyol-mediated synthesis of ultrafine tin oxide nanoparticles for reversible Li-ion storage.* Electrochemistry Communications, 2007. **9**(5): p. 915-919.
147. Subramanian, V., H. Zhu, and B. Wei, *Nanostructured MnO2: Hydrothermal synthesis and electrochemical properties as a supercapacitor electrode material.* Journal of Power Sources, 2006. **159**(1): p. 361-364.
148. Lee, D.K., et al., *High capacity Li[Li0.2Ni0.2Mn0.6]O2 cathode materials via a carbonate co-precipitation method.* Journal of Power Sources, 2006. **162**(2): p. 1346-1350.
149. Dziembaj, R. and M. Molenda, *Stabilization of the spinel structure in Li1+δMn2−δO4 obtained by sol–gel method.* Journal of Power Sources, 2003. **119–121**: p. 121-124.
150. Brinker, C.J. and G.W. Scherer, *CHAPTER 1 - Introduction*, in *Sol-Gel Science*. 1990, Academic Press: San Diego. p. xvi-18.
151. Kozuka, H., *Handbook of Sol-Gel Science and Technology 1*, ed. S. Sakka. Vol. 1. 2005, US: Springer
152. de Lucena, P.R., et al., *Synthesis by the polymeric precursor method and characterization of undoped and Sn, Cr and V-doped ZrTiO.* Journal of Alloys and Compounds, 2005. **397**(1–2): p. 255-259.
153. Marinšek, M., K. Zupan, and J. Maček, *Citrate-nitrate gel transformation behavior during the synthesis of combustion-derived NiO-yttria-stabilized zirconia composite.* Journal of Materials Research, 2011. **18**(7): p. 1551-1560.
154. Tratnyek, P.G. and R.L. Johnson, *Nanotechnologies for environmental cleanup*. Nano Today, 2006. **1**(2): p. 44-48.
155. Gautam, R.K. and M.C. Chattopadhyaya, *Chapter 1 - Nanotechnology for Water Cleanup*, in *Nanomaterials for Wastewater Remediation*. 2016, Butterworth-Heinemann: Boston. p. 1-18.

156. Mueller, N.C. and B. Nowack, *Nanoparticles for Remediation: Solving Big Problems with Little Particles.* Elements, 2010. **6**(6): p. 395-400.
157. Zhang, Y., et al., *Nanomaterials-enabled water and wastewater treatment.* NanoImpact, 2016. **3–4**: p. 22-39.
158. Hua, M., et al., *Heavy metal removal from water/wastewater by nanosized metal oxides: A review.* Journal of Hazardous Materials, 2012. **211–212**: p. 317-331.
159. Mahdavian, A.R. and M.A.-S. Mirrahimi, *Efficient separation of heavy metal cations by anchoring polyacrylic acid on superparamagnetic magnetite nanoparticles through surface modification.* Chemical Engineering Journal, 2010. **159**(1–3): p. 264-271.
160. Hu, J., G. Chen, and I.M.C. Lo, *Removal and recovery of Cr(VI) from wastewater by maghemite nanoparticles.* Water Research, 2005. **39**(18): p. 4528-4536.
161. Hu, J., G. Chen, and I.M.C. Lo, *Selective Removal of Heavy Metals from Industrial Wastewater Using Maghemite Nanoparticle: Performance and Mechanisms.* Journal of Environmental Engineering, 2006. **132**(7): p. 709-715.
162. Gelover, S., P. Mondragón, and A. Jiménez, *Titanium dioxide sol–gel deposited over glass and its application as a photocatalyst for water decontamination.* Journal of Photochemistry and Photobiology A: Chemistry, 2004. **165**(1–3): p. 241-246.
163. Forouzani, M., et al., *Comparative study of oxidation of benzyl alcohol: Influence of Cu-doped metal cation on nano ZnO catalytic activity.* Chemical Engineering Journal, 2015. **275**: p. 220-226.
164. Wang, H., et al., *Graphene-based materials: Fabrication, characterization and application for the decontamination of wastewater and wastegas and hydrogen storage/generation.* Advances in Colloid and Interface Science, 2013. **195–196**: p. 19-40.
165. Wang, H., et al., *Adsorption characteristics and behaviors of graphene oxide for Zn(II) removal from aqueous solution.* Applied Surface Science, 2013. **279**: p. 432-440.

166. Foo, K.Y. and B.H. Hameed, *Decontamination of textile wastewater via TiO2/activated carbon composite materials.* Advances in Colloid and Interface Science, 2010. **159**(2): p. 130-143.
167. Arcibar-Orozco, J.A., M. Avalos-Borja, and J.R. Rangel-Mendez, *Effect of Phosphate on the Particle Size of Ferric Oxyhydroxides Anchored onto Activated Carbon: As(V) Removal from Water.* Environmental Science & Technology, 2012. **46**(17): p. 9577-9583.
168. Liang, S., et al., *Removal of fluoride from aqueous solution by TiO2-based composites.* Journal of the Taiwan Institute of Chemical Engineers, 2017. **74**: p. 205-210.
169. Pepper, R.A., S.J. Couperthwaite, and G.J. Millar, *Value Adding Red Mud Waste: High Performance Iron Oxide Adsorbent for Removal of Fluoride.* Journal of Environmental Chemical Engineering, 2017.
170. Zach-Maor, A., R. Semiat, and H. Shemer, *Synthesis, performance, and modeling of immobilized nano-sized magnetite layer for phosphate removal.* Journal of Colloid and Interface Science, 2011. **357**(2): p. 440-446.
171. Gu, W., et al., *Phosphate removal using zinc ferrite synthesized through a facile solvothermal technique.* Powder Technology, 2016. **301**: p. 723-729.
172. Recillas, S., et al., *Preliminary study of phosphate adsorption onto cerium oxide nanoparticles for use in water purification; nanoparticles synthesis and characterization.* Water Science and Technology, 2012. **66**(3): p. 503.
173. Bhatnagar, A. and M. Sillanpää, *A review of emerging adsorbents for nitrate removal from water.* Chemical Engineering Journal, 2011. **168**(2): p. 493-504.
174. Contreras, A.R., et al., *Potential use of CeO2, TiO2 and Fe3O4 nanoparticles for the removal of cadmium from water.* Desalination and Water Treatment, 2012. **41**(1-3): p. 296-300.
175. Contreras A.R., et al., *Use of cerium oxide (CeO2) nanoparticles for the adsorption of dissolved cadmium (II), lead (II) and chromium (VI) at two different pHs in single and multi-component systems,.* Global Nest Journal, 2015. **17**(3): p. 536-543.

176. Schwertmann, U. and R.M. Cornell, *Magnetite*, in *Iron Oxides in the Laboratory*. 2007, Wiley-VCH Verlag GmbH. p. 135-140.
177. Procházková, G., I. Šafařík, and T. Brányik, *Surface Modification of Chlorella Vulgaris Cells Using Magnetite Particles.* Procedia Engineering, 2012. **42**: p. 1778-1787.
178. Ge, S., et al., *Influences of Surface Coating, UV Irradiation and Magnetic Field on the Algae Removal Using Magnetite Nanoparticles.* Environmental Science & Technology, 2015. **49**(2): p. 1190-1196.
179. Wang, T., et al., *Magnetic nanoparticles grafted with amino-riched dendrimer as magnetic flocculant for efficient harvesting of oleaginous microalgae.* Chemical Engineering Journal, 2016. **297**: p. 304-314.
180. Lin, Z., et al., *Application and reactivation of magnetic nanoparticles in Microcystis aeruginosa harvesting.* Bioresource Technology, 2015. **190**: p. 82-88.
181. Prochazkova, G., I. Safarik, and T. Branyik, *Harvesting microalgae with microwave synthesized magnetic microparticles.* Bioresource Technology, 2013. **130**: p. 472-477.
182. Han, D., et al., *Application of ionic liquid in liquid phase microextraction technology.* Journal of Separation Science, 2012. **35**(21): p. 2949-2961.
183. Park, Y., et al., *Recent Advances in Anhydrous Solvents for CO2 Capture: Ionic Liquids, Switchable Solvents, and Nanoparticle Organic Hybrid Materials.* Frontiers in Energy Research, 2015. **3**.
184. Bates, E.D., et al., *CO2 Capture by a Task-Specific Ionic Liquid.* Journal of the American Chemical Society, 2002. **124**(6): p. 926-927.
185. Ramdin, M., et al., *Solubility of Natural Gas Species in Ionic Liquids and Commercial Solvents: Experiments and Monte Carlo Simulations.* Journal of Chemical & Engineering Data, 2015. **60**(10): p. 3039-3045.
186. Xia, Y., et al., *Superior CO2 Adsorption Capacity on N-doped, High-Surface-Area, Microporous Carbons Templated from Zeolite.* Advanced Energy Materials, 2011. **1**(4): p. 678-683.

187. Gadipelli, S. and Z.X. Guo, *Graphene-based materials: Synthesis and gas sorption, storage and separation.* Progress in Materials Science, 2015. **69**: p. 1-60.
188. García, A., et al., *Acute toxicity of cerium oxide, titanium oxide and iron oxide nanoparticles using standardized tests.* Desalination, 2011. **269**(1–3): p. 136-141.
189. Oberdörster, G., V. Stone, and K. Donaldson, *Toxicology of nanoparticles: A historical perspective.* Nanotoxicology, 2007. **1**(1): p. 2-25.
190. Taylor, D.A., *Dust in the wind.* Environmental Health Perspectives, 2002. **110**(2): p. A80-A87.
191. Rogers, F., et al., *Real-Time Measurements of Jet Aircraft Engine Exhaust.* Journal of the Air & Waste Management Association, 2005. **55**(5): p. 583-593.
192. Shah, C.P., *Public Health and Preventive Medicine in Canada*. 2003: Elsevier Saunders.
193. Fubini, B. and A. Hubbard, *Reactive oxygen species (ROS) and reactive nitrogen species (RNS) generation by silica in inflammation and fibrosis.* Free Radical Biology and Medicine, 2003. **34**(12): p. 1507-1516.
194. Fauré, J., et al., *Exosomes are released by cultured cortical neurones.* Molecular and Cellular Neuroscience, 2006. **31**(4): p. 642-648.
195. Mogharabi, M., M. Abdollahi, and M.A. Faramarzi, *Toxicity of nanomaterials; an undermined issue.* DARU Journal of Pharmaceutical Sciences, 2014. **22**(1): p. 59.

Chapter 2

Research objectives and thesis outline

2.1. Research objectives

In a perspective of the above realities, the aim of the present work is the synthesis and characterization of engineered nanomaterials to be used in different applications for environmental remediation. In order to achieve the general objective, this work has been divided into three main parts with the following specific objectives:

- Synthesis and characterization of different types of nanomaterials, such as magnetic nanoparticles and polymeric based nanocomposites.
- Applications to water remediation
    - Screening of the synthesized nanomaterials for contaminants removal: fluoride, nitrate, phosphate, cadmium, nickel, atrazine, carbaryl, 4-bromo-3,5-dimethylphenyl-N-methylcarbamate, and alachlor.
    - Application of the nanomaterials with high potential efficiencies to the removal of fluoride and phosphate.
    - Harvesting of microalgae from wastewater treatment using iron oxide NPs.
- Applications to gases streams
    - Application of the magnetite nanoparticles onto polyurethane foams to methane adsorption.
    - Application of gold and cerium oxide nanoparticles encapsulated into metal organic frameworks to the catalytic oxidation of carbon monoxide.

2.2. Thesis outline

The thesis is divided into eleven chapters;

Chapter 1 describes a general introduction to explain the current environmental pollutions' concerns and the challenges of using nanotechnology for its treatment.

Chapter 2 indicates the aim, and the specific objectives of the work.

Chapter 3 includes the general methods implemented to carry out the characterization of the synthesized nanoparticles and nanocomposites, the analytical methods used to determine the concentration of the adsorbates, and the experimental studies for the adsorption tests as well as the models used for experimental data fittings.

Chapter 4 describes the different types of nanomaterials that have been synthesized by using the co-precipitation methodology and its characterization. Also, comparison of the removal efficiencies for anions, heavy metals, and pesticides were evaluated using the different nanomaterials. Besides, toxicity of some of the nanomaterials was determined by using the Microtox bioassay.

Chapter 5 explains the synthetic method of a novel magnetic core-shell Ce-Ti@Fe_3O_4 nanoparticles under mild experimental conditions. Additionally, its efficiency for inorganic anions and heavy metals removal were evaluated.

Chapter 6 presents the optimization of the fluoride removal and the adsorption studies using the synthesized magnetic core-shell Ce-Ti@Fe_3O_4 nanoparticles.

Chapter 7 shows the synthetic method of a nanocomposite based on magnetite nanoparticles (Fe_3O_4-NPs) immobilized on the surface of the cationic exchange polymer (C100), and its potential application for phosphate removal and recovery from water.

Chapter 8 offers a novel approach for the harvesting of the *Scenedesmus sp.* microalgae from real wastewater treatment by using cost-effective adsorbents of magnetite-based nanoparticles.

Chapter 9 exhibits the catalytic activity of the metal organic framework (MOF), i.e hybrid core-shell Au/CeO_2 NPs into the support of porous UiO-66 beads, for CO oxidation and recyclability.

Chapter 10 displays the development of a novel adsorbent, by immobilization iron oxide NPs onto polyurethane foam support, for methane adsorption.

Chapter 11 summaries the general conclusions of the main findings through the whole investigation, and the recommendations for the future work.

Finally, the annex presents the accepted publications.

Chapter 3

General methods and materials

3.1. Characterization of the nanomaterials

Characterization of the nanomaterials is essential to determine its properties, which can be divided into chemical, physicochemical, surface, and thermodynamic properties [1]. In this study, the following equipment for characterization are used.

3.1.1. Inductive Coupled Plasma - optical emission spectroscopy

Inductive coupled plasma - optical emission spectroscopy (ICP-OES) is a metal analysis technique that uses the emission spectra of a sample to identify and quantify the metals present. This technique depends on desolvation of the sample introduced into the plasma, followed by ionization, and finally excitation of the constituent elements. Then, each metal could be identified and quantified by its characteristic emission lines. Pre-treatment of the samples was performed by an acid digestion process, followed by filtration using 0.22 µm Nylon filter. For instance, for the determination of Ce, Ti, and Fe, in the nanocomposites samples, they were treated with 1% of HNO_3 for Fe and Ce determination, while with 1% of HNO_3, and 1% of HF for titanium determination. The metal amount was reported in terms of mg_M/g_{NPs}, where M refers to the metal ion and NPs refers to the nanoparticles (NPs). The metal content of the samples was analyzed by using a Perkin Elmer ICP-OES Optima 4300DV (Figure 3.1). The instrument percent relative standard deviation (% RSD) was less than 2 %. Analyses were performed at Servei d'Anàlisi Química, Universitat Autònoma de Barcelona (UAB), Spain.

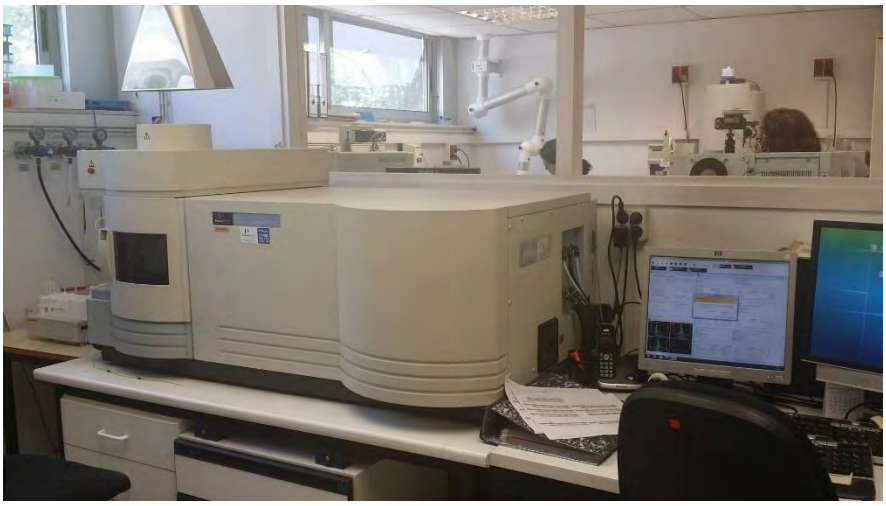

Figure 3.1. ICP-OES instrument from Servei d'Anàlisi Química, Universitat Autònoma de Barcelona.

3.1.2. Inductive coupled plasma – mass spectrometry

Trace element analysis could be conducted by using a high sensitivity detector as mass spectrometry where the analysis depends on ionization of the species, followed by quadrupole mass spectrometry analysis. Therefore, each element could be identified and quantified in a lower level as part per billion (ppb) or part per trillion (ppt) by its individual mass fragments. Determination of the metal contents in the samples was performed by using the same previous treatments described in section 3.1.1 (ICP-OES). The analysis of samples by Inductive coupled plasma – mass spectrometry (ICP-MS) was carried out by using Agilent ICP-MS 7500CE (Figure 3.2). The instrument percent relative standard deviation (% RSD) was less than 2 %. Analyses were performed at Servei d'Anàlisi Química, Universitat Autònoma de Barcelona (UAB), Spain.

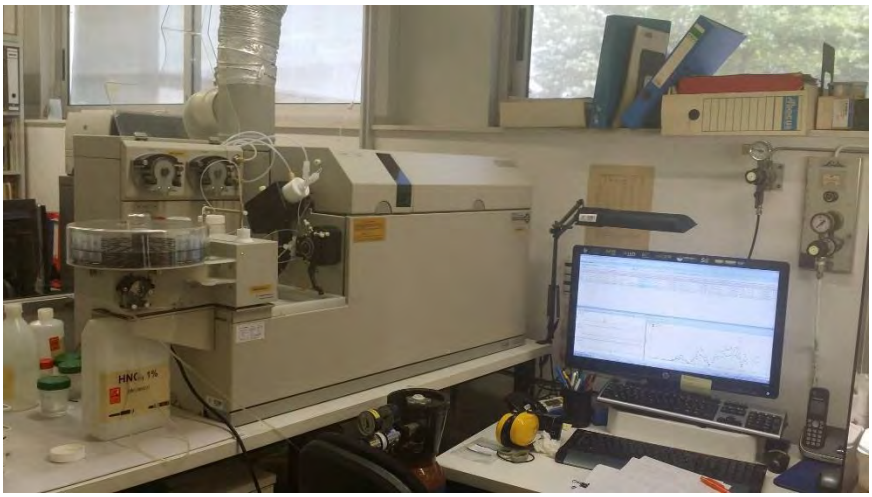

Figure 3.2. ICP-MS instrument from Servei d'Anàlisi Química, Universitat Autònoma de Barcelona.

3.1.3. X-Ray Diffraction

X-Ray Diffraction (XRD) technique was used to obtain the crystalline structure of the particles. The sample is irradiated with a beam of monochromatic X-Rays over a variable incident angle range. Interaction with atoms in the sample results in diffracted X-Rays when the Bragg equation is satisfied [2]. Resulting spectra are characteristics of chemical composition and phase. Moreover, in a diffraction pattern, the location of the peaks on the 2θ scale can be compared to reference peaks. The observed diffraction peaks are associated with planes of atomes to assist in analyzing the atomic structure and microstructure of sample. Miller indices (hkl) define the reciprocal of the axial intercepts and are used to identify different planes of atoms [3]. Diffraction patterns were collected on a Panalytical X´Pert PRO MPD (Multipurpose Diffractometer) as shown in Figure 3.3. Analyses were performed at Institut Català de Nanociència i Nanotecnologia (ICN2), Spain.

Figure 3.3. X-Ray Powder diffractometer (XRD) instrument from Institut Català de Nanociència i Nanotecnologia.

3.1.4. Scanning Electron Microscopy

Crystal shape, surface morphology, dispersed and agglomerated nanomaterials, and surface functionalization could be observed by using Scanning Electron Microscope (SEM). Field Emission microscope, Zeiss Merlin (Figure 3.4a), from Servei de Microscopia at UAB, was used to study the cross-sectioned or the surface morphology of the nanomaterial samples. Cross sections were obtained by embedding the nanomaterial in epoxy resin and cross- sectioning with a Leica UC7 ultramicrotome shown in Figure 3.4b (using a 35° diamond knife from Diatome). Cross-sectioning was used to obtain both the NPs dispersion and the metal concentration profiles into a support material. Moreover, the surface morphology of the sample was obtained by adding little drops of the sample on a silicon grid [4].

Figure 3.4. (a) Scanning electron microscopy, Zeiss Merlin, and (b) Leica UC7 ultramicrotome instruments from Servei de Microscopia at UAB.

3.1.5. Transmission Electron Microscopy

Transmission electron microscope (TEM) coupled with energy dispersive spectroscopy (EDS) was used to determine the size distribution of the nanomaterials and to confirm the elements by scanning line profile in a specific area. A JEM-2011/JEOL microscope (Figure 3.5) from Servei de Microscopia at UAB was used to characterize either the NPs and the NCs or its cross-sectioned. The samples were embedded in epoxy resin for cross-sectioned analysis as described in SEM section (section 3.1.4). Electron diffraction pattern allows studying the crystal structure of the NPs. The periodic structure of a crystalline solid acts as a diffraction grating, scattering the electrons in a predictable manner. From the observed diffraction pattern, it may be possible to deduce the structure of the crystal producing the diffraction pattern [5]. Electron diffraction is also a useful technique to study the short-range order of amorphous solids.

Figure 3.5. Transmission electron microscope (JEM-2011/JEOL) instruments from Servei de Microscopia at UAB.

3.1.6. Energy-Dispersive X-Ray Spectroscopy

Energy-Dispersive X-Ray Spectroscopy (EDS/EDX) coupled to SEM or TEM microscopes from Servei de Microscopia at UAB, provides the metal chemical composition of the samples based on the X-Rays emitted by an atom which has been interacting with an electron beam. Each atom has a unique X-ray spectrum and so the elemental composition can be obtained by the detected radiation. These microscopes are also equipped for X-ray diffraction techniques that allow knowing the crystalline structure of the particles by diffraction patterns. EDS measurements were acquired with an Oxford INCA X-MAX detector [6].

3.1.7. Scanning Transmission Electron Microscopy coupled with Electron Energy Loss Spectra

The chemical composition and the morphology of the core-shell NPs were estimated by using the high-angle annular dark field scanning transmission electron microscopy (HAADF-STEM) coupled with Electron Energy Loss Spectra (EELS) (illustrated in Figure 3.6) [7]. Images were acquired using an FEI Tecnai G2 F20 microscope operated at 200 kV and equipped with a GIF Quantum energy filter. All spectra were recorded using a convergence semiangle of about 12 mrad and a collection semiangle of about 40 mrad. EDX spectra were obtained using an EDAX super ultra-thin window (SUTW) X-ray detector. The sample was first dispersed in ethanol and sonicated, then deposited onto the copper microscopy grid coated with an amorphous carbon film. By imaging with the electrons that have an energy loss corresponding to core losses of particular elements using STEM, one can obtain elemental information with high spatial resolution. A full energy loss spectrum from a series of points across the particle in a STEM configuration, which allows the extraction of linear compositional variation, was used to obtain chemical information about the nanostructure. Analyses were performed at Institut Català de Nanociència i Nanotecnologia (ICN2), Spain.

Figure 3.6. Scanning transmission electron microscopy (STEM- HAADF) coupled with Electron Energy Loss Spectra (EELS) instruments from Institut Català de Nanociència i Nanotecnologia (ICN2).

3.1.8. Surface area measurements by Brunauer-Emmett-Teller method

The Brunauer-Emmett-Teller method (BET) method determines the specific surface area and porosity of the materials by physical adsorption of gas on the material's surface [8]. The surface area of dry resin, NCs and the metal organic frameworks (MOFs) were determined from conventional nitrogen sorption isotherms at Institut Català de Materials Avançats de Barcelona (ICMAB), Spain, utilizing the BET theory [9]. The instrument employed was a Micromeritics ASAP2000 with dedicated software.

3.1.9. Luminescence spectrometer

The measurement of fluorescence, phosphorescence, chemiluminescence or bioluminescence of a liquid, solid, powder, or thin film samples were carried out by using the luminescence spectrometry. For instance, the valence of the cerium cation in the core-shell NPs and its speciation were estimated by using the luminescence spectra. Samples were prepared by suspension of 1 g of the Ce-Ti@Fe_3O_4 core-shell nanomaterial in 1 L Milli-Q water adjusted to pH 7.0 using 0.1M NaOH. Luminescence spectra was analyzed using Perkin Elmer LS 55 luminescence spectrometer (Figure 3.7a). pH was adjusted using Crison pH meter 2001 (Figure 3.7b).

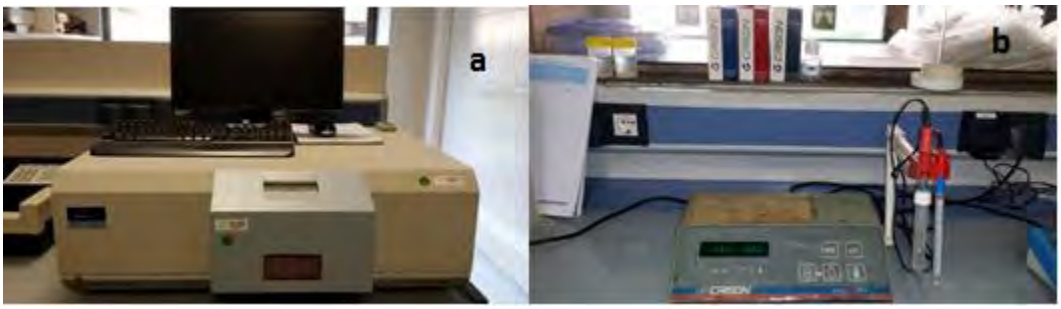

Figure 3.7. (a) Perkin Elmer LS 55 luminescence spectrometer, and (b) Crison pH meter 2001.

3.1.10. Zeta potential measurements

The magnitude of the electrostatic or charge repulsion or attraction between particles, and the stability of the suspension could be determined by measuring the zeta potential value. The zeta potential is a key indicator of the stability of colloidal dispersions. The measurement of zeta potential has important applications in a wide range of industries including; ceramics, pharmaceuticals, medicine, mineral processing, electronics and water treatment. Samples were prepared by dispersing a fixed amount of the nanomaterial in a definite volume of water or medium at the desired pH value by ultrasonication treatments. The zeta potential of the samples was measured using the Zetasizer Nano-ZS (Malvern, UK) as shown in Figure 3.8 and calculated according to Henry's equation at 25 °C. Analyses were performed at Institut Català de Nanociència i Nanotecnologia (ICN2), Spain.

Figure 3.8 Malvern Zetasizer Nano-ZS instrument from Institut Català de Nanociència i Nanotecnologia.

3.1.11. Toxicity tests

To access the toxicity of the nanomaterials, A Microtox® system (Figure 3.9) from Microbics Corporation was used. This method based on the percentage of decrease in the amount of light emitted by the bioluminescent marine bacterium *Vibrio fischeri* upon contact with a filtered sample at pH 7. Toxicity is, then, inversely proportional to the intensity of light emitted after the contact with the toxic substances. The effective concentration, EC50, is defined as the concentration that produces a 50% light reduction. EC50 was measured after 5 and 15 min of contact time. Bioluminescent tests were carried out using 2 % of sodium chloride. Stability of the nanomaterials was confirmed during the test or the adjustment of the pH value of the medium, where no precipitate was observed [10, 11].

Figure 3.9. Microtox® system.

3.2. Analytical methods

3.2.1. Ionic Chromatography

The determination of the concentration of anions, as fluoride (F^-), phosphorous (PO_4^{3-}-P), and nitrate (NO_3^--N) was performed utilizing ICS-2000 (Dionex) ion chromatographic system (IC), with ultimate 3000 autosampler as shown in Figure 3.10. An ion exchange column specifically designed for rapid analysis of inorganic anion (Dionex

IonPac AS18, 4 x 250 mm) equipped with an IonPac guard column (Dionex IonPac AG18, 4 x 50 mm) was used. Chromeleon® software was used to acquire data and control the instrumentation. Calibration standards and samples were filtered using 0.45 µm Nylon membrane filter before injection.

Figure 3.10. Ion chromatographic system (ICS-2000, Dionex).

3.2.2. Biosystems Analyzer

The determination of phosphate (PO_4^{3-}-P) was carried out using Biosystems Y15 analyzer as illustrated in Figure 3.11. Briefly, the analysis depends on the use of two solutions; reagent A which consists of sulfuric acid and sodium chloride, and reagent B consisting of ammonium molybdate dissolved in sulfuric acid. Then, the determination of the inorganic phosphorus (PO_4^{-3}-P) in the sample reacts with molybdate in acid medium forming a phosphomolybdate complex that can be measured by the biosystems analyzer [12].

Figure 3.11. Biosystems Y15 analyzer.

3.2.3. Ultraviolet visible spectrophotometer

The analysis of heavy metals was performed by using UV-VIS spectrophotometer model Cary 50 Bio (Figure 3.12) consisting in the measurements of the attenuation of a beam of light after it passes through a sample, or after reflection from a sample surface, thus the absorbance measurements could be performed at a single wavelength or over spectral range [13]. The calibration curve was obtained from a series of dilutions of calibration standards and measured at the specific wavelength.

Figure 3.12. UV-VIS (Cary 50 Bio) spectrophotometer.

3.2.4. Gas Chromatography

The Gas Chromatography (GC) techniques was used for several determinations. The analysis of the organic pollutants (i.e. pesticides) such as atrazine, carbaryl, alachlor and BDMC, among others, before and after the adsorption process, were performed by using Agilent Gas Chromatograph 7820A coupled to Mass Spectrometry 5975B (GC/MS) equipped with DB-5 (30 m x 0.25 mm x 0.25 µm) column as shown in Figure 3.13a. The mentioned pesticides analysis was performed using selected ion monitoring (SIM) acquisition mode.

The catalytic conversion of the carbon monoxide (CO) into carbon dioxide (CO_2), by the use of a synthesized MOF, was studied by using the Hewlett-Packard gas chromatograph 5890 coupled to the thermal conductivity detector (GC/TCD) equipped with Agilent J&W HP-plot Q (30 m x 0.32 mm x 20 µm) column as shown in Figure 3.13b.

The adsorption of methane (CH_4) using different nanomaterials as adsorbents was carried out by using Agilent gas chromatograph 6890 coupled to flame ionization detector (GC/FID) as shown in Figure 3.13c.

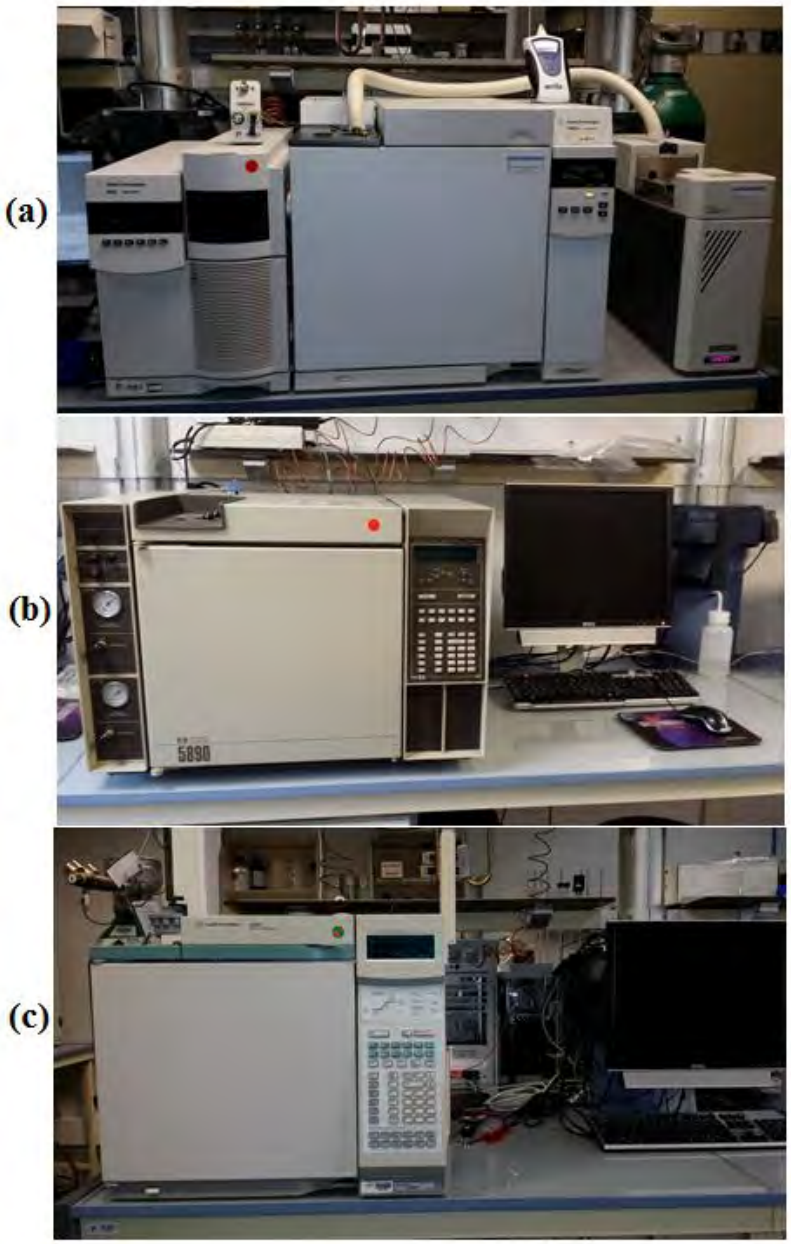

Figure 3.13. Gas chromatograph; (a) GC/MS, (b) GC/TCD, and (c) GC/FID.

3.2.5. Turbidimeter

The harvesting efficiency of the microalgae using different magnetic iron oxide NPs based-adsorbents was studied by using a Hanna Microprocessor Turbidity Meter HI93703

(Figure 3.15) supplied from the Department of Civil and Environmental Engineering, Universitat Politècnica de Catalunya.

Figure 3.14. Hanna Microprocessor Turbidity Meter equipment from Universitat Politècnica de Catalunya.

3.3. Experimental set-up

Applications of the nanomaterials were performed in a laboratory scale. The adsorption studies were conducted either by using batch or continuous flow experiments.

3.3.1. Batch experiments

Equilibrium adsorption data for the potential adsorbent used in this work for water remediation was obtained by using the batch system as shown in Figure 3.15. In general, the adsorption tests were carried out by adding a definite amount of adsorbents to a series of 250 mL Erlenmeyer flasks containing 100 mL of different pollutants as adsorbate. Then, the flasks were shaken at a constant rate, fixed temperature and intervals of time until reaching the equilibrium. Next, each solution was separated from the adsorbent by magnetic separation or centrifugation depending on the nanomaterial used. Finally, the residual concentration of each pollutant was determined by the suitable technique as described in section 2.2. Various parameters were studied such as the effect of contact time, amount of adsorbents, temperature, pH, and initial concentration of pollutants. More details

are given in the experimental part of the following chapters relative to each adsorbate. The adsorption capacity under equilibrium, Q_e, was calculated by using Equation 3.1:

$$Q_e = \frac{(C_o - C_e) * V}{m} \qquad \text{(Equation 3.1)}$$

Where Q_e (g/g) is the adsorption at equilibrium, C_o, and C_e are the initial and the equilibrium concentrations (mg/L) of adsorbate, respectively, m is the adsorbent amount (g), and V is the volume of the solution.

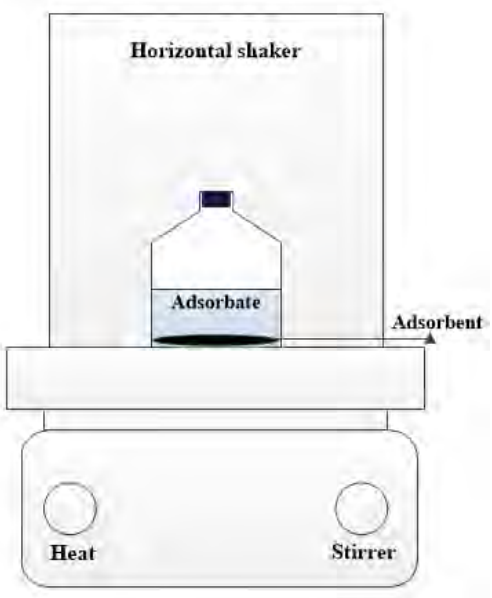

Figure 3.15. Batch mode experimental set-up.

3.3.2. Fixed-bed column studies

In the continuously flow method (fixed-bed column), a solution containing the pollutant, with a known initial concentration, flows continuously through a column of adsorbent or a packed bed where dynamic adsorption of the solute occurs as shown in Figure 3.16. Herein in this work, the continuous flow experiments were performed for both treatment of water and gases, and conducted in a fixed-bed column with a definite dimension of inner diameter and length (depending on the material used in each application). Briefly, a glass wool plug was placed at the bottom of the column to avoid the

adsorbent washing out. Next, the column was packed with a known amount of adsorbent in order to receive the desired bed height. Then, an initial concentration of adsorbate was pumped upward through the column at a desired flow rate by using a peristaltic pump (Watson Marlow, 403U). After that, samples were collected from the outlet of the column and analyzed for residual concentration of pollutant. Prior to starting the experiment, the adsorbent was pre-conditioned. More details of the experimental part will be discussed later in the corresponding chapters 7 and 10.

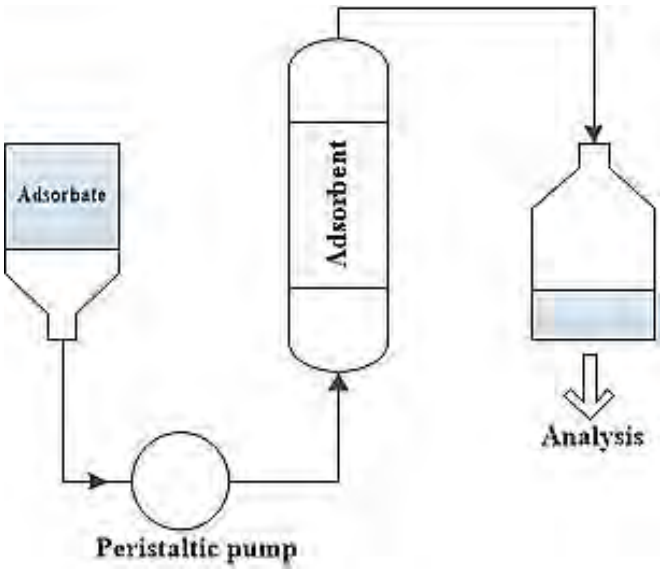

Figure 3.16. Fixed-bed column mode experimental set-up.

The continuous adsorption process is usually characterized by the so-called breakthrough curves, i.e., a representation of the adsorbate effluent concentration versus time profile. In addition, breakthrough curve prediction through mathematical models is a useful tool for scale-up and design purposes. The breakthrough curves show the loading behavior of adsorbate to be removed in a fixed-bed column and are usually expressed in terms of adsorbate concentration (C_{ad}) as a function of time. Equilibrium uptake, q_{eq} (mg/g), is defined as the adsorption capacity of adsorbate per mass of adsorbent at a certain initial concentration and can be calculated using Equation 3.2.

$$Q_e = \frac{F}{m} \int_0^t (C_{in} - C_t) * dt \qquad \text{(Equation 3.2)}$$

Where Q_e (g/g) is the adsorption capacity at equilibrium, C_{in} is the initial adsorbate concentration (g/m^3), C_t is the concentration of adsorbate at time t at the outlet of the column (g/m^3), m is the adsorbent amount (g), and F is the flow rate (m^3/min) [14].

3.4. Isotherm models

The most useful way of expressing the feasibility of an adsorbent for an adsorbate is the adsorption isotherms. In general, the adsorption isotherms were obtained by adding a fixed amount of the adsorbent into a series of Erlenmeyer flasks containing different concentrations of adsorbate solutions. Then, the flasks were shaken under the optimum conditions of adsorption such as the time required achieving the equilibrium, pH, temperature, followed by calculating the adsorption capacity at equilibrium. Fitting of the experimental data were conducted by using different isotherm models including three of two parameters, namely; Freundlich, Langmuir, and Dubinin–Radushkevich, three of three parameters, namely; Redlich–Peterson, Radke–Prausnitz, Brunauer–Emmett–Teller (BET), and a combination isotherm model.

Regarding the two parameter isotherm models; the Langmuir isotherm model is assuming a monolayer adsorption on a homogeneous surface. The basic assumptions of this models are the followings [15]:

- The molecules are adsorbed on definite sites on the surface of the adsorbent.
- Each site can accommodate only one molecule (monolayer).
- The area of each site is a fixed quantity determined solely by the geometry of the surface.
- The adsorption energy is the same at all sites.
- The adsorbed molecules cannot migrate across the surface or interact with neighboring molecules.

The non-linear expression of the Langmuir isotherm model can be illustrated as Equation 3.3.

$$Q_e = \frac{Q_m . K_L . C_e}{1 + K_L . Ce} \qquad \text{(Equation 3.3)}$$

where C_e is the concentration of adsorbate at equilibrium (mg/L or g/m^3); Q_e is the corresponding adsorption capacity at equilibrium (mg/g); Q_m is the maximum adsorption capacity (mg/g) and K_L (L/mg or mg/m^3) is the Langmuir constant which are related to energy of adsorption.

Also, the Langmuir equation can be expressed in term of the dimensionless separation factor, R_L, which could be calculated as presented in Equation 3.4:

$$R_L = \frac{1}{1 + K_L C_o} \qquad \text{(Equation 3.4)}$$

Where C_o is the initial concentration of adsorbate (mg/L or g/m^3), K_L is the Langmuir constant (L/mg or mg/m^3). If the R_L is lying between 0 and 1, it means favorable adsorption. On the other hand, unfavorable adsorption will be if R_L is higher than 1.

The Freundlich isotherm model is the earliest known relationship describing the non-ideal and reversible adsorption. It can be applied to multilayer adsorption, on the basis of an assumption concerning the energetic surface heterogeneity where the energy of interaction between pollutant and adsorbent material is distributed on the surface, grouping into one patch those having the same adsorption energy. On each patch, a pollutant molecule only adsorbs onto one adsorption site of the material [16].

The non-linear expression of Freundlich isotherm model can be illustrated as Equation 3.5.

$$Q_e = K_F . C_e^{\,1/n} \qquad \text{(Equation 3.5)}$$

where Q_e is the adsorption capacity at equilibrium (mg/g), K_F is the first Freundlich parameter constant (L/mg)$^{1/n}$, C_e is the equilibrium concentration of adsorbate in mg/L or g/m, n is the second Freundlich parameter constant (dimensionless).

The Dubinin-Radushkevich isotherm model is another empirical model which describes the adsorption process following a pore filling mechanism, and to distinguish between the physical and chemical adsorption [17]. It is generally applied to express the adsorption process occurred onto both homogeneous and heterogeneous surfaces. The non-linear expression of Dubinin-Radushkevich isotherm model can be illustrated as Equation 3.6.

$$Q_e = Q_m \, exp^{(-\beta . \varepsilon^2)} \qquad \text{(Equation 3.6)}$$

Where, Q_e is the adsorption capacity of adsorbate at equilibrium (mg/g) and C_e is the adsorbate concentration at equilibrium (mg/L or mg/m^3), β is a constant related to the mean of the adsorption energy (E), and ε is the potential energy of the surface and it can be calculated as shown in Equation 3.7:

$$\varepsilon = RTLn[1 + {}^{1}/_{C_e}] \qquad \text{(Equation 3.7)}$$

where R (J/mol.K) is the gas constant, T (K) is the absolute temperature, and C_e is the equilibrium concentration of adsorbate. The mean adsorption energy (E) can be calculated as presented in Equation 3.8:

$$E = \frac{1}{\sqrt{2.B}} \qquad \text{(Equation 3.8)}$$

The adsorption process is supposed to proceed via chemisorption, if the magnitude of E is between 90 and 180 kJ/g, while for values of E less than 90 kJ/g, the adsorption process tends to be of physical nature [18, 19].

Regarding the three parameter isotherms, the Redlich-Peterson has been combining the properties of the Langmuir and Freundlich isotherms into one equation as presented in Equation 3.9.

$$\mathrm{Q_e} = \frac{\mathrm{A.C_e}}{1+\mathrm{B.C_e}^{\mathrm{g}}} \qquad \text{(Equation 3.9)}$$

where A, B, and n are Redlich–Peterson isotherm constants, and Q_e, and C_e are the adsorption capacity and the concentration of adorbate at equilibrium respectively.

The Radke-Prausnitz isotherm model expresses the adsorption capacity as an explicit function of the equilibrium concentration and it is based on thermodynamic considerations. This model is illustrated in Equation 3.10.

$$\mathrm{Q_e} = \frac{\mathrm{K_{RP}\alpha_{RP}C_e}}{(1+\mathrm{K_{RP}C_e})^{\mathrm{m_{RP}}}} \qquad \text{(Equation 3.10)}$$

where K_{RP} and α_{RP} are Radke–Prausnitz constants and m_{RP} is an exponent. For m_{RP} = 0, Equation 3.10 reduces to the Langmuir Equation 3.3.

The Brunauer Emmett Teller (BET) isotherm model is an extension of the Langmuir theory to multilayer adsorption, where the Langmuir theory can be applied in each layer and it is used as an analysis technique for the specific surface area of materials. The theory

has limited accuracy at very low pressures where adsorbents tend to be strongly heterogeneous and at high pressures where capillary condensation can occur [20]. This model is illustrated in Equation 3.11.

$$Q_e = \frac{B\,Q_m C_e}{(C_s - C_e)[1+(B-1)\left(\frac{C_e}{C_s}\right)]} \qquad \text{(Equation 3.11)}$$

where *Qe* is the amount of adsorbate adsorbed at equilibrium by packing adsorbents (mg/g) and C_e is the adsorbate concentration at equilibrium (g/m^3), *B* is a constant relating to the energy of interaction with the surface, Q_m is the maximum adsorption capacity and C_s is the saturation constant of the solute.

Finally, a combination of the above proposed isotherm models may be described as Equation 3.12.

$$Q_e = \frac{b\,Q_m\,C_e^{1/n}}{1+b\,C_e^{1/n}} \qquad \text{(Equation 3.12)}$$

where Q_e is the amount of adsorbate adsorbed by packing adsorbents (mg/g) and C_e is the adsorbate concentration at equilibrium (mg/m^3), *b* and *n* are the constant parameters of the isotherm, and Q_m is the maximum adsorption capacity of adsorbate.

3.5. Central composite design, CCD, and Response Surface methodology, RSM

The central composite design (CCD) and response surface methodology (RSM) were used to determine the optimum conditions for the pollutant removal by using a combination of mathematical and statistical techniques to evaluate the relative significant factors for the removal efficiency, respectively. Two of three-levels full factorial design, 3^k, were used. The experimental design was set up based on a central level, 0, in the middle point between the lowest (-1) and the highest levels (+1). Therefore, twelve experiments were performed for the experimental design, including triplicate at the central point. All the possible combinations of the factors and their levels were included.

The behavior of the removal was fitted to a quadratic modeling and the quality of the fitted model was quantitatively assessed by the analysis of the variance (ANOVA) to characterize the interaction between the independent parameters and the removal. The obtained results were refined by the Design Expert v6.0 software to fit a quadratic model, with a general expression as shown in Equation 3.13.

$$Y = \beta_0 + \sum_{i=1}^{k} \beta_i X_i + \sum_{i=1}^{k} \beta_{ii} X_i^2 + \sum_{i=1}^{k-1} \sum_{j=2}^{k} \beta_{ij} X_i X_j \qquad \text{(Equation 3.13)}$$

Where Y is the response, x_i, x_j, …., and x_k are the input variables, β_0 is the intercept term, β_i (i=1, 2, …, k) is the linear effect, β_{ii} (i=1, 2, …, k) is the squared effect, and β_{ij} (i=1, 2, …, k, j= 1, 2, …, k) is the interaction effect. The validity of the equation to fit the second order model was verified by the correlation coefficients R^2.

3.6. Statistical analysis

Statistical analysis of the data was performed by using Sigmaplot v12.5 and Design Expert v6.0 software.

3.7. References

1. Singh, A.K., *Chapter 4 - Experimental Methodologies for the Characterization of Nanoparticles,* in *Engineered Nanoparticles*. 2016, Academic Press: Boston. p. 125-170.
2. Pradeep Sharma, et al., *Synthesis and X-ray diffraction study of new copper (II) complexes of a-aminonitrile derived from P- methoxybenzaldehyde with aromatic amine.* Journal of Physics: Conference Series, 2014. **534**: p. 1-4.
3. Speakman, S.A. *Basics of X-Ray Powder Diffraction*. Available from: http://prism.mit.edu/xray (Access date 2/6/2017).

4. Alonso, A., *Development of polymeric nanocomposites with enhanced distribution of catalytically active or bactericide nanoparticles*, in *Departament d'Enginyeria Química, Escola d'Enginyeria* 2012, Universitat Autònoma de Barcelona (UAB).
5. Berry, L.G. and R.M. Thompson, *X-ray diffraction data for minerals.* Waverly Press: New York, 1962: p. 194.
6. Singh, A.K., *Engineered Nanoparticles: Structure, Properties and Mechanisms of Toxicity*. 2015: Elsevier Science.
7. Epicier, T., et al., *Chemical composition dispersion in bi-metallic nanoparticles: semi-automated analysis using HAADF-STEM.* Journal of Nanoparticle Research, 2012. **14**(9): p. 1106.
8. Brunauer, S., P.H. Emmett, and E. Teller, *Adsorption of Gases in Multimolecular Layers.* Journal of the American Chemical Society, 1938. **60**(2): p. 309-319.
9. Zahedi, E., et al., *Kinetic and mechanistic study on the pyrolysis of 1,3-dihydroisothianaphthene-2,2-dioxide toward benzocyclobutene using RRKM and BET theories.* Chemical Physics, 2017. **483–484**: p. 12-25.
10. Sánchez, A., et al., *Ecotoxicity of, and remediation with, engineered inorganic nanoparticles in the environment.* TrAC Trends in Analytical Chemistry, 2011. **30**(3): p. 507-516.
11. Recillas, S., et al., *Use of CeO2, TiO2 and Fe3O4 nanoparticles for the removal of lead from water: Toxicity of nanoparticles and derived compounds.* Desalination, 2011. **277**(1–3): p. 213-220.
12. Muñoz, M.A., M. Balón, and C. Fernandez, *Direct determination of inorganic phosphorus in serum with a single reagent.* Clinical Chemistry, 1983. **29**(2): p. 372-374.
13. Akhter, M. *Ultraviolet spectroscopy*. 2014; Available from: https://www.slideshare.net/mariomS7/uvvis-spectroscopy.
14. Modak, J.B., A. Bhowal, and S. Datta, *Experimental study and mathematical modeling of breakthrough curve in rotating packed bed.* Chemical Engineering and Processing: Process Intensification, 2016. **99**: p. 19-24.

15. Ruthven, D.M., et al., *Adsorptive separation of Kr from N2 — Part I Adsorbent screening studies.* The Canadian Journal of Chemical Engineering, 1984. **62**(4): p. 526-534.
16. Do, D.D. and K. Wang, *A new model for the description of adsorption kinetics in heterogeneous activated carbon.* Carbon, 1998. **36**(10): p. 1539-1554.
17. Chen, X., *Modeling of Experimental Adsorption Isotherm Data.* Information, 2015. **6**(1): p. 14-22.
18. Dorado, A.D., et al., *The role of water in the performance of biofilters: Parameterization of pressure drop and sorption capacities for common packing materials.* Journal of Hazardous Materials, 2010. **180**(1–3): p. 693-702.
19. Mohan, D., C.U. Pittman Jr, and P.H. Steele, *Single, binary and multi-component adsorption of copper and cadmium from aqueous solutions on Kraft lignin—a biosorbent.* Journal of Colloid and Interface Science, 2006. **297**(2): p. 489-504.
20. Livingston, H.K., *The Relationship between the Brunauer-Emmett-Teller Adsorption Isotherm and the New Isotherm of Jura and Harkins.* The Journal of Chemical Physics, 1947. **15**(9): p. 617-624.

Part A:

Water remediation

Chapter 4

Engineered nanomaterials: synthesis, characterization, and its potential efficiencies on water remediation

4.1. Introduction

Nanomaterials have found immeasurable applications due to its unique properties such as high surface area, catalytic properties, etc. [1]. Nowadays, environmental applications of nanotechnology have been one of the most auspicious techniques in water remediation and treatment. Water remediation process involves the transformation of pollutants from toxic form to less toxic in water [2]. The most promising interest in the last decade is the advancements in nanotechnology for water remediation, especially after the most stringent health regulations. Several pollutants such as nutrients, fluoride, heavy metals, and pesticides have been registered as hazardous substance in water [3-6] when they exceed the maximum contaminants levels (MCLs) according to World Health Organization (WHO), and Environmental Protection Agency (EPA) [7-9]. Engineered nanomaterials act as novel tools in snatching pathogenic bacteria, environmental biomonitoring, treatment of water and wastewater, and so on [10, 11]. Adsorption is the most promising and suitable method for water treatment due to its ease of operation, simplicity, and low cost [4, 12-14]. Thus, taking into account the state-of-the art of the nanomaterials used for water remediation (Chapter 1), the main goal of this chapter is to develop different types of nanomaterials based on metal oxide nanoparticles (NPs) and nanocomposites (NCs) to apply them for a screening in the adsorption of a variety of contaminants. These types of nanomaterials are selected due to its high performance, fast adsorption process, and large surface area [15-17]. The synthetic procedure in all the cases is based on in-situ co-precipitation technique. The co-precipitation in-situ method of the NCs preparation is a method for a bottom-up approach where the metal oxide NPs can be produced inside the supports [18]. Also, a comparison of their effectiveness with common used materials such as activated carbon, chitosan and zeolite is shown. With the results obtained we design an improvement of new nanomaterials for the adsorption of specific contaminants in water. Herein, the specific objectives of this part of the work are: (1) to synthesize different engineered nanomaterials including: metal oxide NPs (Fe_3O_4, TiO_2, and CeO_2); metal oxide NPs (Fe_3O_4 and CeO_2) anchored on graphene based nanomaterials (r-G.O) and; functionalized core/shell magnetite based NPs (Fe_3O_4@$SiONH_2$, Fe_3O_4@PEI

and Fe_3O_4@CTAB) using a co-precipitation method; (2) to characterize the particle size, morphology, and properties of the synthesized nanomaterials; (3) screening of the potential efficiencies of the nanomaterials for the removal of contaminants such as inorganic anions: fluoride, phosphate and nitrate; heavy metals: cadmium and nickel and; POPs from water (5) to determine the toxicity of the synthesized nanomaterials.

4.2. Materials and methods

4.2.1. Materials

Iron (II) chloride ($FeCl_2$), iron (III) chloride hexahydrate ($FeCl_3 \cdot 6H_2O$), sodium fluoride (NaF), titanium chloride ($TiCl_4$), cerium nitrate hexahydrate ($Ce(NO_3)_3 \cdot 6H_2O$), polyethyleneimine (PEI), tetramethylammonium hydroxide (TMAOH), ammonia (NH_3) solution, cetyltrimethylammonium bromide (CTAB), 3-aminopropyl triethoxysilane (APTES), sodium phosphate monobasic (NaH_2PO_4), cadmium chloride ($CdCl_2$), dithizone, chloroform ($CHCl_3$), potassium cyanide (KCN), sodium chloride (NaCl), potassium permanganate (KMnO4), hydrogen peroxide (H_2O_2), atrazine, alachlor, carbaryl, 4-bromo-3,5-dimethylphenyl-N-methylcarbamate (BDMC), sodium nitrate ($NaNO_3$), ascorbic acid, hydroxylamine hydrochloride ($NH_2Cl \cdot H_2O$), zeolite, activated carbon, chitosan powder, and graphite powder, were purchased from Sigma-Aldrich, Spain. Sodium hydroxide pellet (NaOH) was purchased from Merck. Hydrochloric acid (HCl), nitric acid (HNO_3) was purchased from Panreac, SA. All the chemicals were of analytical grade or higher.

Microtox ® acute reagent, osmotic adjusting solution (OAS), Reconstitution solution, and microtox ® diluent were produced from Modern Water Inc., and purchased from Fisher Scientific, SA.

Catechol based nanomaterial with diameters ranging from 100 to 350 nm was supplied by Institut Català de Nanociència i Nanotecnologia (ICN2), and Departamento de Química at UAB, Spain.

The cationic exchange polymer (C100) was kindly supplied by Purolite S.A, Spain.

4.2.2. Synthesis of the nanomaterials

4.2.2.1. Metal oxides NPs synthesis

Among different methods had been reported to synthesis metal oxide NPs, co-precipitation method is the most common due to it is a facile and convenient way to produce it [19, 20]. The co-precipitation method used in this work involves the formation of precipitate of oxo-hydroxide by the addition of a base; such as TMAOH, NaOH or HMT, among others, into a solution of a precursor metal salt; such as iron, titanium and cerium, dissolved in water [21-23].

4.2.2.1.1. Magnetite NPs

Magnetite, Fe_3O_4, NPs were synthesized in aqueous phase using ultrapure water, and the method of synthesis was based on the reported in the literature using tetramethylammonium hydroxide (TMAOH) [23, 24] as showed in Equation 4.1. The addition of TMAOH increases the colloidal stability of the NPs and enhances the degree of crystallinity [25]. Briefly, 20 mmol of iron (II) chloride ($FeCl_2$), and 40 mmol of iron (III) chloride hexahydrate ($FeCl_3.6H_2O$) were dissolved in 200 mL of deoxygenated water for 20 min. Followed by the addition dropwise into 200 mL of 1 M deoxygenated TMAOH where the color changed into black at room temperature. Then, the mixture suspension was vigorously stirred at 600 rpm for 30 min under inert conditions of N_2 stream. Finally, the Fe_3O_4 NPs were washed three times by using ultrapure water using permanent magnet (magnetic decantation), and then redissolved into 1 mM of TMAOH to obtain the final suspension of Fe_3O_4 NPs.

$$Fe^{2+} + 2Fe^{3+} + 8OH^- \rightarrow Fe_3O_4 + 4H_2O \qquad \text{(Equation 4.1)}$$

4.2.2.1.2. Cerium oxide NPs

The cerium oxide, CeO_2, NPs was synthesized based on the reported method in the literature [26, 27], and the synthesis was performed in aqueous medium. Typically, 40 mM of cerium nitrate hexahydrate ($Ce(NO_3)_3.6H_2O$) was dissolved in 250 mL of ultrapure water (milli-Q) for 30 min at room temperature. Next, 250 mL of hexamethylenetetramine (HMT) was added dropwise into the cerium salt (Ce^{3+}) solution for oxidation into Ce^{4+}. Then, the suspension was continuously stirred at low rate of agitation, 200 rpm, for 24 h at room temperature to obtain CeO_2 NPs by converting all the Ce^{3+} into Ce^{4+}. After, the NPs were separated from the medium by centrifugation at 6000 rpm for 30 min and washed with ultrapure water three times, the CeO_2 NPs were suspended in 1 L of 10 mM HMT solution which forms the electrical double layer to prevent the NPs agglomeration [22, 23].

4.2.2.1.3. Titanium oxide NPs

The titanium oxide, TiO_2, NPs were synthesized in aqueous medium and based on the reported method in the literature [23, 28]. Briefly, 0.7 M of titanium ion (Ti^{4+}) stock solution was prepared in 100 mL of 3 M of HCl. Then, 5 mL of the stock solution was added dropwise into 30 mL of ultrapure water. Next, the pH of the solution of Ti^{4+} was adjusted to 5.0 by using 3 M of NaOH solution, followed by adjusting the total volume to 50 mL in order to obtain 0.07 M of Ti^{4+} ion concentration. After, the suspension was aged at 60 °C for one h and the produced TiO_2 NPs were separated by centrifugation at 10000 rpm for 30 min and followed by washing twice with adjusted ultrapure water to pH 5.0 as the same pH of the synthesis. Finally, the TiO_2 NPs were suspended into 50 mL of 1 mM of TMAOH.

4.2.2.2. Preparation of functionalized magnetite NPs

4.2.2.2.1. Fe_3O_4 NPs functionalized with NH_2 groups

Functionalization of the Fe_3O_4 NPs with 3-aminopropyl triethoxysilane (APTES), as a source of amine group, to obtain Fe_3O_4@$SiONH_2$ NPs was performed by modifying the reported method [29, 30]. Briefly, 1.0 g of Fe_3O_4 NPs were dispersed in 100 mL ultrapure water (Milli-Q) for 20 minutes by sonication. Then, 1 mL of APTES was added dropwise to the suspension of the NPs and the mixture was continuously stirred at 600 rpm for 12 h at room temperature. Later, the magnetic Fe_3O_4@$SiONH_2$ NPs were washed three times using ultrapure water and separated using the magnetic decantation and finally dried overnight at 60°C.

4.2.2.2.2. Polyethyleneimine-modified Fe_3O_4 NPs

Coating of Fe_3O_4 NPs with polyethyleneimine (PEI) was performed with a slight modifications in the reported method in the literature [31]. Briefly, 1 g of Fe_3O_4 NPs were dispersed in 100 mL ultrapure water (Milli-Q) by sonication for 20 min. Then, 2.5 g of PEI was titrated into Fe_3O_4 NPs suspension. After that, the mixture was continuously stirred for 30 min at room temperature. Later, the Fe_3O_4@PEI NPs were dried at 60°C for 12 h after washing the NPs with water and ethanol respectively using magnetic decantation.

4.2.2.2.3. Cetyltrimethylammonium bromide coated Fe_3O_4 NPs

Cetyltrimethylammonium bromide (CTAB) coated Fe_3O_4 NPs were prepared with a slight modification of the reported method [32]. The obtained black Fe_3O_4 NPs were sonicated for 20 min in 100 mL of the ultrapure water (Milli-Q), followed by the addition of the CTAB drop by drop to obtain a weight ratio of 1:1 between the CTAB and Fe_3O_4 NPs. Then, the mixture was continuously stirred for 30 min at room temperature. Subsequently, Fe_3O_4@CTAB NPs were separated using a NdFeB permanent magnet and washed using ultrapure water, followed by ethanol washing and then dried at 60°C for 12 h.

4.2.2.3. Preparation of graphene based nanomaterials

4.2.2.3.1. Synthesis of graphene oxide

Graphene oxide (G.O) was synthesized by using a modified Hummer's method [33]. Briefly, 2 g of graphite powder was mixed with 1.0 of sodium nitrate ($NaNO_3$) in 46 mL of H_2SO_4 on ice bath. Next, the mixture was stirred for 30 min. Followed by the dropwise addition of 6 g potassium permanganate ($KMnO_4$), and the resulting mixture was continuously stirred at 400 rpm for 30 min at 35 °C. Then, the mixture was diluted by 92 mL of ultrapure H_2O, and continuously stirred at 400 rpm for 4 h, at temperature lower than 10 °C. Afterwards, 7 mL of H_2O_2, and 280 mL of ultrapure H_2O were added to terminate the reaction. Lastly, the graphene oxide (G.O) produced, when bright yellow color of the solution was observed, was separated and washed with hydrochloric acid (HCl) by centrifugation at 6000 rpm for 30 min. Then, the G.O was dried at 60 °C for 24 h.

4.2.2.3.2. Synthesis of reduced graphene oxide

Reduced graphene oxide (r-G.O) was prepared as following: 0.13 g of the as-prepared graphene oxide as described in section 4.2.2.3.1 was first dispersed in 200 mL of ultrapure water by the effect of the ultrasonication treatment for 2 hours. Next, 2 mL of ascorbic acid solution (2.2 mM) was added dropwise into the G.O suspension, followed by vigorously stirring for 1 h to obtain the reduced form of r-G.O. Then, the r-G.O was dried at 60 °C for 24 h.

4.2.2.4. Synthesis of metal oxide/reduced graphene oxide nanocomposites

NCs of metal oxide NPs anchored onto r-G.O were prepared according to the protocols reported in the literature with a slight modification [34, 35]. r-G.O NCs were prepared using the in-situ co-precipitation method. Typically, Fe_3O_4/r-G.O NCs were prepared as follows; 25 mM of $FeCl_2$ and 50 mM $FeCl_3.6H_2O$ were dispersed, in 100 mL of deoxygenated ultrapure water containing 0.13 g of G.O, by the effect of ultrasonication

treatment for 2 h,followed by adjusting the pH to 9.0 by titration with 0.6 M of ammonium hydroxide (NH_4OH). Next, the colloidal solution was stirred for 1 h under N_2 stream and 40 °C after the addition of 2 mL of ascorbic acid solution (2 mM) as mentioned in section 4.2.2.2.2 to reduce the G.O. After washing three times with ultrapure water to remove the excess of alkali, the obtained Fe_3O_4/r-G.O NCs were dried overnight at 60 °C.

The following procedure was used to synthesis the CeO_2/r-G.O NCs. Briefly, 0.35 g of $Ce(NO_3)_3.6H_2O$ was dissolved in 200 mL of ultrapure water and continuously stirred for 30 minutes. Next, 0.13 g of G.O was dispersed in 200 mL of HMT (0.5 M) by the effect of ultrasonication treatment for 2 h. Then, the later suspended solution was added dropwise into the cerium salt solution and the formed colloidal solution was continuously stirred for one hour. After the addition of 2 mL of ascorbic acid solution (2.2 mM), the colloidal solution was moderately stirred at 300 rpm for 24 h at room temperature. Finally, the CeO_2/r-G.O NCs formed were washed with ultrapure water and ethanol and, then dried at 60 °C for 24 hours.

4.2.3. Synthesis of chitosan and description of the supplied supports

4.2.3.1. Synthesis of Chitosan beads (wet and dried)

Chitosan (CS) beads were synthesized using a modified cross linked method as reported [36]. Briefly, 2 g of CS were dissolved in 100 mL of 2 % (v/v) acetic acid solution. followed by agitation for 2 h until the dissolution of the formed gel. Next, 250 mL of a 0.5 M NaOH solution containing 12.5 % glutaraldehyde was dripped into CS solution using a peristaltic pump (Watson Marlow, 403U) connected to a needle of 3 mm forming beads upon contact of the gel drops with the alkaline solution. The beads remained in contact with the NaOH solution for 12 h. After this time, the beads were washed with ultrapure water until the rinse water presented a pH 7.0. The polymer in the form of beads was kept in the refrigerator at 4 °C and denotated as wet CS beads. Moreover, the dried beads of CS were obtained by drying the wet beads at low temperature of 60 °C for 3 h.

4.2.3.2. Supplied supports

Different supplied materials (supports) have been used for water remediation and for comparing with the developed nanomaterials, including cationic exchange polymer (C100), zeolite, activated carbon and catechol.

C100 polymer consists of polystyrene cross-linked with divenyl benzene functionalized with sulfonated group gel type. Pre-treatment of the C100 was carried out by following the reported procedure [18, 37]. First, the raw material was treated with 1.0 M NaCl for 2 h and washed with deionized water (3 times) so as to convert all the functional groups into Na^+ form. Afterwards, the polymer was dried at 80 ºC for 24 h for further reuse. The ion-exchange capacity (IEC) of the polymer was 2.0 mequiv/g. However, the other supplied supports were used without treatments.

The average diameter of the supplied catechol is 301 nm. The activated carbon has a particle diameter of < 100 µm. These supports are used as it is without pre-treatment.

4.2.4. Characterization of the nanomaterials

The properties and characteristics of the NPs such as morphology, size, metal contents, NPs distribution and the structures were obtained by using various techniques such as ICP-OES, HR-TEM, and XRD as previously explained in Chapter 3 (Section 3.1).

4.2.5. Adsorption studies

Adsorption properties, of the nanomaterials synthesized for specific contaminants in water, were determined in batch adsorption experiments. A solution of contaminant concentration of C_0 (mg/L) was prepared by dissolving the corresponding precursor standard into the suitable solvent of deionized water or organic solvent. Then, an adsorbent amount of W (g) was added into a conical flask containing a definite volume of the contaminant solution. After the adjustment the pH, depending on the experiment, of the suspension by using 0.1 M of NaOH or HCl, the flasks were shaken on a thermostat shaker

at 200 rpm and 25 ˚C. To ensure the adsorption equilibrium, the adsorption time was set for 24 hours. The concentration of residual contaminant in the solution, C_e, was measured with the specific equipment as will be discussed in Section 4.2.6. The adsorption capacity at the equilibrium was calculated according to the mentioned equation in Chapter 3 (Section 3.3.1).

4.2.6. Analytical methods

4.2.6.1. Anions analysis (fluoride, nitrate, and phosphate)

The determination of the inorganic anions (F^-, PO_4^{-3}-P, NO_3^--N) was determined using ICS-2000 (Dionex) ion chromatographic system, with ultimate 3000 autosampler. A stock solution of each contaminant was prepared by dissolving the appropriate amount of its precursor in ultrapure water. For instance, 100 mg/L of fluoride, nitrate, and 1000 mg/L of phosphate solutions were prepared by dissolving the appropriate amount of NaF, $NaNO_3$, and NaH_2PO_4 in 100 mL of ultrapure water. Next, series of calibration standards of each anions were prepared by diluting the stock solution into 50 mL of ultrapure water. Validation of the calibration curve of each anion was performed by the estimations of correlation coefficients (R^2) to be ≥ 0.99.

Thus, contaminant solutions for adsorption studies were prepared by diluting the stock solution of F^-, PO_4^{-3}-P, and NO_3^--N into 50 mL of ultrapure water to obtain 4 mg/L of F, 44 mg/L of nitrate which are the maximum contaminant levels in drinking water, and 100 mg/L of PO_4-P which is higher than could be found in the real water matrix. Furthermore, all the calibration standards and samples were filtered using 0.45 µm Nylon membrane filter before injection. In addition, the determination of PO_4^{-3}-P was confirmed by using the biosystem analyzer. Analysis conditions were performed using IC or biosystem analyzer are mentioned in Chapter 3 (Sections 3.2.1, and 3.2.2).

4.2.6.2. Heavy metals determination

The determination of the heavy metals such cadmium and nickel was based on the spectroscopic method. For instance, the colorimetric method was used for the determination of cadmium which it depends on the formation of red colored complex by the interaction of cadmium with the dithizone reagent that could be extracted with chloroform ($CHCl_3$), as reported in the literature with a slight modification [21]. Single extraction was performed for the determination of cadmium due to the non-interference of other metal ions in the analytical technique used [38]. Typically, a stock solution of 100 mg/L of cadmium was prepared by dissolving the appropriate amount of $CdCl_2$ salt into 100 mL of ultrapure water which contains 0.5 % of HNO_3. Then, a working standard solution of 10 mg/L of cadmium was prepared by diluting the stock solution into 250 mL of acidified ultrapure water with 1 % of HNO_3. Next, series of calibration standards were prepared from the working solution by dilution in 25 mL of ultrapure water. The determination of the cadmium was carried out by extracting the $CHCl_3$ and measured photometrically at 518 nm. The red complex of cadmium was formed by using the following procedure: 12.5 mL of cadmium solution was mixed with 125 µL of $NH_2OH.HCl$ (20 % in ultrapure water), 15 mL of dithizone reagent (0.004 % in $CHCl_3$), and 2.5 mL NaOH-KCN solution (3 % NaOH, and 0.5 % KCN in ultrapure water) in a separating funnel. Next, the mixture was shacked for 1 minute and then allowed to phase separation. Thus, a chloroform layer was separated and measured at 518 nm for cadmium determination using UV-VIS spectrophotometer as described in chapter 3 (section 3.2.3).

Nickel determination was performed using ICP-OES as described in chapter 3 (section 3.1.1).

4.2.6.3. Persistent organic pollutants determination

Determination of the persistent organic pollutants (POPs) was based on the using of liquid-liquid extraction technique due to its ease, strength, and broad approval by international standard methods [39, 40]. So, the determination of atrazine, alachlor,

carbaryl, and BDMC was based on the reported method in the literature [41]. Firstly, 100 mg/L stock solutions of each pesticide were prepared by dissolving an appropriate amount of each analytical standard into 10 mL of methanol, and keep it in amber flasks. Next, calibration standards were prepared by diluting the stock solution in 50 mL of ultrapure water. Then, 35 mL of each solution was exposed to 2 mL of n-hexane in a separating funnel, and followed by shaking for 2 min. After the phases are separated, the hexane layer was separated. 1 µL of each solution was injected into GC/MC (7820A/5975B), and analyzed as described in chapter 3 (section 3.2.4).

4.2.7. Toxicity measurements

The toxicity of the suspensions of the NPs was performed using the bioluminescence test [23, 27, 42]. Briefly, 0.05 g of each NPs of Fe_3O_4, Fe_3O_4@PEI, Fe_3O_4@CTAB, G.O, Fe_3O_4/r-G.O, and CeO_2/r-G.O were dispersed in 50 mL of ultrapure water by the effect of ultrasonication for 30 minutes. Next, the pH of the NPs suspensions was adjusted by using 0.1 M of HCl or NaOH. After that, the toxicity of the suspended solutions was performed by Mictrox® as described in chapter 3 (section 3.1.12).

4.3. Results and discussion

4.3.1. Characterization of the synthesized nanomaterials

4.3.1.1. Metal oxides NPs

The morphology and size of the Fe_3O_4, CeO_2 and TiO_2 NPs were determined by using HR-TEM as shown in Figure 4.1. The average particles size was determined using imageJ software. A cubic structure of Fe_3O_4 NPs was obtained as shown in Figure 4.1a with average size of 13.00 ± 1.77 nm. Also, the morphology of TiO_2 was found to be tetrahedral structure with particles size of 3.75 ± 0.65 nm as shown in Figure 4.1b. In addition, the average size of CeO_2 NPs was estimated to be 9.86 ± 1.40 nm, and its morphology was cubic structure as shown in Figure 4.1c. Moreover, a slight aggregation of the metal oxide NPs was found as shown in Figures 4.1a-c. Figures 4.1d-f indicate that

crystalline structure of the metal oxide NPs was obtained by the analysis of the ED patterns due to the presence of multiple rings consisting of discrete spots [18].

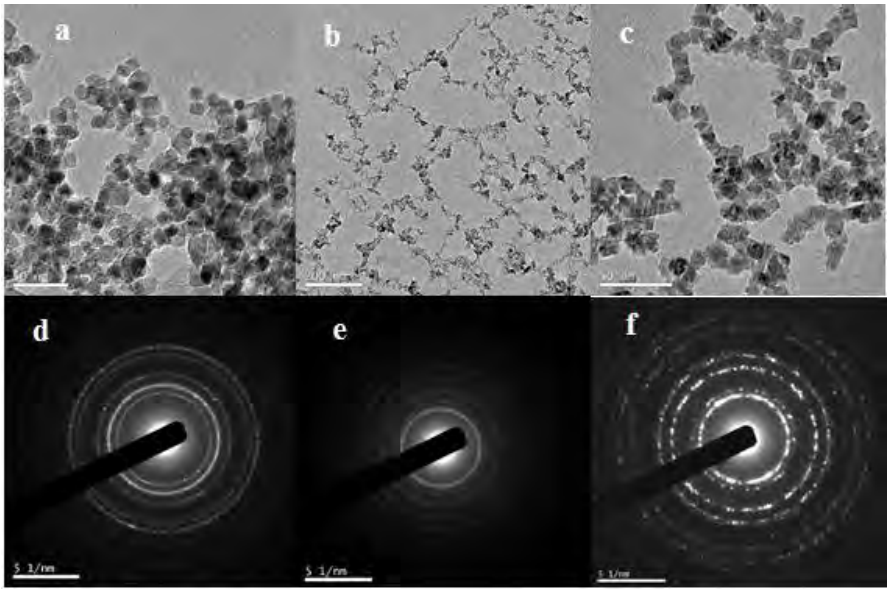

Figure 4.1. TEM images of: (a) Fe_3O_4, (b) TiO_2, and (c) CeO_2 NPs; and ED patterns of: (d) Fe_3O_4, (e) TiO_2, and (f) CeO_2 NPs.

Also, confirmation of the elemental analysis was proved by using the EDS spectra as shown in Figures 4.2 a-c. For instance, magnetite NPs was confirmed by the presence of iron (Fe) and oxygen (O) elements as illustrated in Figure 4.2a. Also, the existence of titanium (Ti) and O elements proved the titanium oxide NPs (Figure 4.2b). The same was proved in case of cerium oxide NPs due to presence of cerium (Ce) and O as shown in Figure 4.2c. Furthermore, the stability of the Fe_3O_4 and TiO_2 NPs was estimated by measuring the zeta potential values. It was found that highly stable NPs (zeta potential higher than ± 30 mV) are obtained due to the values were found to be - 55.6 mV, and – 43.8 mV for Fe_3O_4 and TiO_2 NPs, respectively, which is in agreement with the literature [23, 27]. Therefore, TMAOH is a good stabilizer for the Fe_3O_4 and TiO_2 NPs. In addition, the Fe, Ti, and Ce metal contents of the synthesized NPs were analyzed by ICP-OES. The mean of the duplicates of Fe, Ti, and Ce metal contents being 684.26 ± 10.43 mg_{Fe}/g_{NPs}, 103.31 ± 4.67 mg_{Ti}/g_{NPs}, and 41.62 ± 2.17 mg_{Ce}/g_{NPs} for Fe_3O_4, TiO_2, and CeO_2 NPs,

respectively. Characterization of magnetite functionalized NPs will be discussed in Chapter 8.

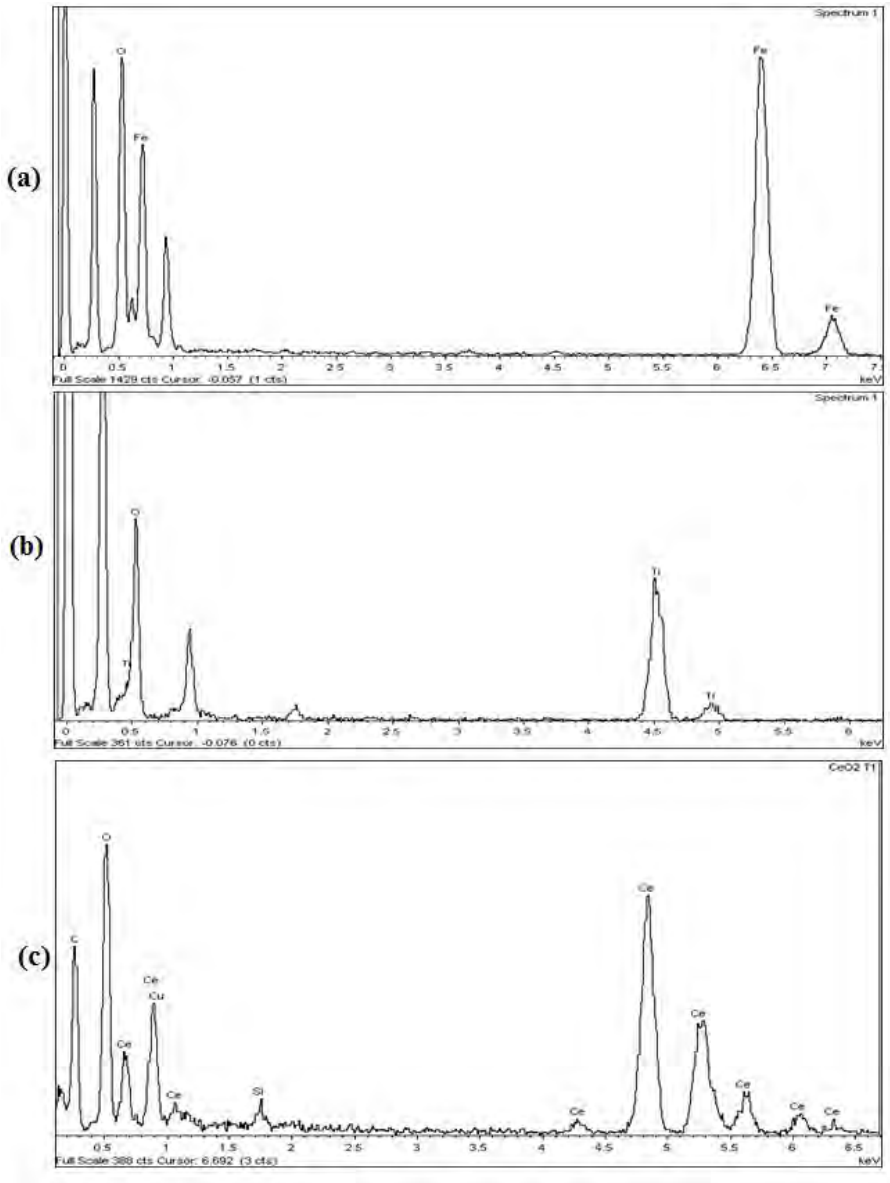

Figure 4.2. EDS spectra of: (a) Fe_3O_4, (b) TiO_2, and (c) CeO_2 NPs.

4.3.1.2. Metal oxides/ reduced graphene oxide NCs

Multilayer image of graphene oxide was shown in Figure 4.3a by TEM. Additionally, the impregnation of the metal oxide NPs as Fe_3O_4 and CeO_2 NPs into graphene oxide (G.O) layer was demonstrated as illustrated in Figures 4.3 b-c. For instance, a mixture of spherical and cubic structures of Fe_3O_4 NPs was obtained on the layer of the r-G.O as shown in Figure 4.3b with an average size of 6.82 ± 1.24 nm. In the case of the CeO_2 NPs impregnated into the reduced graphene oxide layer (r-G.O), an irregular shape of the NPs was obtained as illustrated in Figure 4.3c. In addition, the average size of the CeO_2 NPs was found to be 6.15 ± 1.30 nm. Therefore, approximately an equal size of the Fe_3O_4 and CeO_2 NPs was obtained. Moreover, the synthesized NCs were analyzed by ICP-OES. The mean of the duplicates of the iron (Fe), and cerium (Ce) metal contents being 493.27 ± 8.54 mg_{Fe}/g_{NCs}, 21.95 ± 1.37 mg_{Ce}/g_{NCs} for Fe_3O_4/r-G.O and CeO_2/r-G.O NCs, respectively.

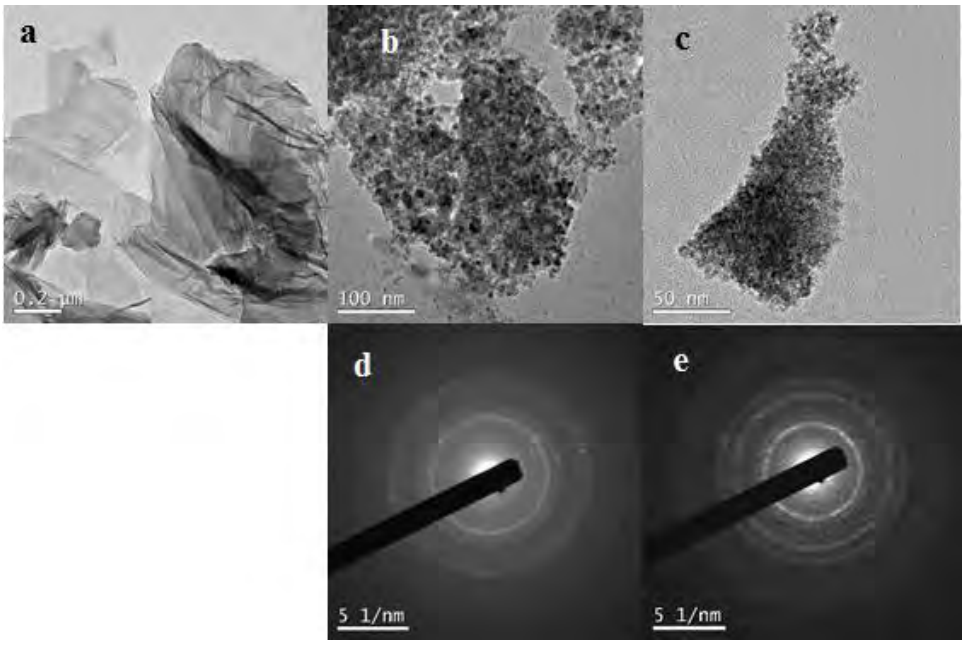

Figure 4.3 TEM images of: (a) G.O, (b) Fe_3O_4/r-G.O NCs, and (c) CeO_2/r-G.O NCs; and ED pattern of: (d) Fe_3O_4/r-G.O NCs, and (e) CeO_2/r-G.O NCs.

4.3.1.3. XRD pattern of the metal oxide nanoparticles

The phases and Miller indices (previously described in Chapter 3) of the metal oxides NPs were determined from the XRD patterns. Figure 4.4a-c shows the XRD patterns of Fe_3O_4, TiO_2, and CeO_2 NPs. For instance, the cubic structure of the Fe_3O_4 NPs was confirmed by matching the XRD pattern with the reference data base (JCPDS 1-1111) as shown in Figure 4.4a. The same was carried out for TiO_2, and CeO_2 NPs in comparison with the reference data bases (JCPDS 1-0562, and JCPDS 1-0800) to prove the tetrahedral, and cubic structures, respectively as illustrated in Figures 4.4b and 4.4c. Moreover, the XRD patterns present the diffraction peaks corresponding to the (220), (311), (222), (400), (422), (511), (440), (533), and (731) for the Fe_3O_4 NPs (Figure 4.4a). Also, the diffraction peaks of (101), (103), (200), (105), (213), (116), (107), and (303) planes are corresponding to anatase structure of TiO_2 NPs (Figure 4.4b). In addition, the cubic structure of CeO_2 NPs was obtained from the diffraction peaks of (111), (200), (311), (400), (331), (422), and (511) planes as shown in Figure 4.4c. The obtained crystalline phases are in agreement with the reported one in literature [43, 44].

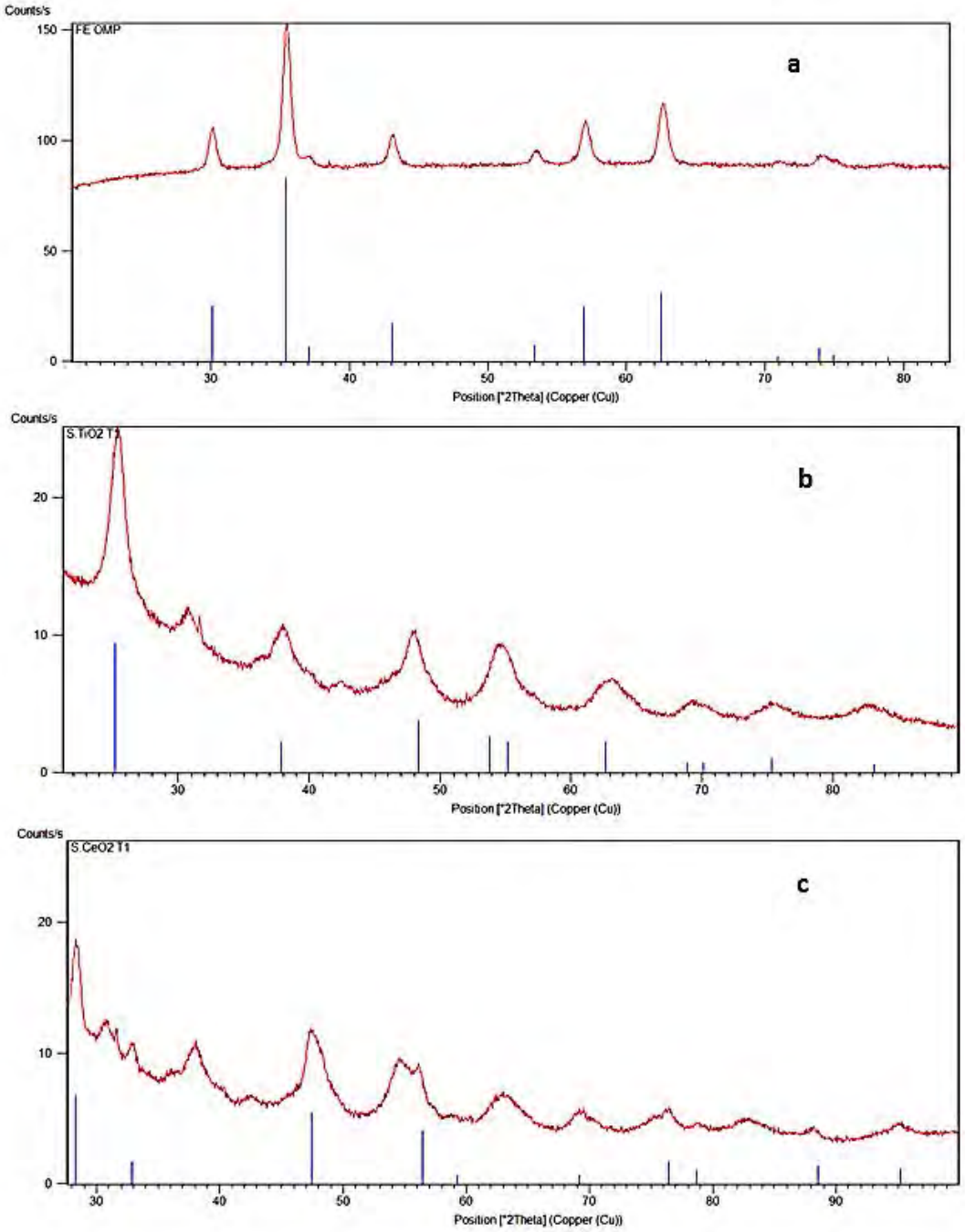

Figure 4.4 XRD patterns of: (a) Fe_3O_4, (b) TiO_2, and (c) CeO_2 NPs.

4.3.2. Applications of the nanoparticles

A screening of the potential efficiencies for the removal of inorganic contaminants: fluoride, phosphate, and nitrate, and heavy metals such as; cadmium and nickel, and persistent organic pollutants such as; atrazine was performed using different nanomaterials described, as adsorbents.

4.3.2.1. Anions removal

The efficiency of the metal oxides NPs on the removal of inorganic anions; fluoride, phosphate, and nitrate, is presented in Table 4.1. The initial concentrations of F^-, PO_4^{-3}, and NO_3^- were selected to be equal to their corresponding MCL or based on the real concentration in water. The anions removal was affected by the type of the metal oxide NPs. For instance, for the removal of fluoride the order, in terms of higher fluoride removal, was: CeO_2 NPs (51.51 %) > Fe_3O_4 (2.91 %) > TiO_2 (2.44 %) at pH 7.0. For phosphate: CeO_2 NPs (20.81 %), TiO_2 NPs (11.34 %) > Fe_3O_4 NPs (5.70 %) at pH 7.0. TiO_2 NPs showed the highest removal percentage of nitrate to be (16.44 %), followed by CeO_2 NPs (11.60 %), and Fe_3O_4 (11.31 %) at pH 7.0.

Table 4.1. Effect of metal oxides, and mixed oxide nanoparticles on the removal of inorganic pollutants.

Adsorbents	**Pollutants**	**Initial concentration, mg/L**	**Adsorbent dose, g/L**	**pH**	**Removal, %**
Fe_3O_4	F^-	4	1.0	5	7.94
		4	1.0	7	2.91
	PO_4^{-3}-P	100	1.0	5	7.56
		100	1.0	7	5.70
	NO_3^--N	44	1.0	5	12.33
		44	1.0	7	11.31
CeO_2	F^-	4	0.64	5	81.87
		4	0.64	7	51.51
	PO_4^{-3}-P	100	0.64	5	33.71
		100	0.64	7	20.81
	NO_3^--N	44	0.64	5	16.76
		44	0.64	7	11.60

Table 4.1. Continued

Adsorbents	Pollutants	Initial concentration, mg/L	Adsorbent dose, g/L	pH	Removal, %
TiO_2	F^-	4	1.0	5	12.90
		4	1.0	7	2.44
	PO_4^{-3}-P	100	1.0	5	19.54
		100	1.0	7	11.34
	NO_3^--N	44	1.0	5	21.00
		44	1.0	7	16.44
CeO_2, TiO_2 (Mixed oxide)	F^-	4	1.64	5	94.90
	PO_4^{-3}-P	100	1.64	5	45.38
	NO_3^--N	44	1.64	5	9.83

An enhancement of the removal efficiency for the inorganic anions was observed by decreasing the pH values as shown in Table 4.1. Same trends were observed in the case of the removal of fluoride at pH 5.0, where the removal followed the order of CeO_2 (81.87 %) > Fe_3O_4 (12.90 %) > and TiO_2 (7.94 %) NPs. Also, for the phosphate removal, the efficiency was found to be CeO_2 (33.71 %) > TiO_2 (19.54 %) > Fe_3O_4 (7.56 %). In addition, the order was TiO_2 (21.00 %) > CeO_2 (16.76 %) > Fe_3O_4 (12.33 %) for the removal of nitrate. The increase of the removal percentage values in all cases for the inorganic anions at lower pH value could be attributed to the increase of the surface' charge of the NPs in the acidic medium which enhance the interaction with the anions [45]. Moreover, regarding to the highest removal percentage of the inorganic anions found by using CeO_2, and TiO_2 NPs as presented in Table 4.1, improvement of the removal was proved by mixing CeO_2, and TiO_2 NPs to obtain removal efficiency of 94.90 %, 45.38 %, and 39.83 % for fluoride, phosphate, and nitrate, respectively at pH 5.0.

The removal of fluoride, phosphate, and nitrate anions was also assayed by using a commercial zeolite adsorbent, and the supplied catechol NPs as presented in Table 4.2. For commercial zeolite, an increase of the removal percentage values was observed by

decreasing the pH value from 7.0 to 5.0 for all cases. The removal efficiencies were found to be 44.81 %, 5.66 %, and 4.36 % for fluoride, phosphate, and nitrate, respectively at pH 5.0. However, in the case of using catechol, a decrease of the removal efficiencies was observed in all cases by decreasing the pH value from 7.0 to 5.0 which could be attributed to the degradation of the catechol in the acidic medium [46]. A removal percentage of 11.38 %, 4.14 %, and 14.19 % for fluoride, phosphate, and nitrate anions, respectively were obtained at pH 7.0. Adsorption capacities at equilibrium at pH 5.0 under the assayed conditions for all inorganic anions are illustrated in Figure 4.5. The adsorption capacities of fluoride, phosphate, and nitrate have the highest values by using the CeO_2 NPs being 5.12 mg/g, 52.67 mg/g, and 11.52 mg/g for fluoride, phosphate, and nitrate, respectively. On the contrary, the lowest values of the adsorption capacities under equilibrium were found 0.15 mg/g, and 1.82 mg/g using catechol, and 1.11 mg/g using mixed oxides of CeO_2 and TiO_2 NPs for fluoride, nitrate, and phosphate, respectively. Although, an enhancement of the removal percentage of fluoride was shown using mixed oxide of CeO_2 and TiO_2 NPs, however, a decrease of its adsorption capacity was observed. The decrease of the adsorption capacity could be attributed to the usage of high amount of the mixed oxides adsorbents. Also, negative effect for the removal efficiency of phosphate and nitrate using the mixed oxides of CeO_2 and TiO_2 NPs. Therefore, the method of mixing the oxides of CeO_2 and TiO_2 NPs was not selective to enhance the adsorption capacity of all the anions.

The adsorption mechanism of anions could be attributed to electrostatic attraction as chemisorption or as surface ion exchange process as physisorption [47-49]. Detailed information on the adsorption mechanisms will be discussed in the following chapters.

Table 4.2. Effect of zeolite, and catechol adsorbents on the removal of inorganic pollutants.

Adsorbents	Pollutants	Initial concentration, mg/L	Adsorbent dose, g/L	pH	Removal, %
Zeolite	F^-	4	1.0	5	44.81
		4	1.0	7	17.16
	PO_4^{-3}-P	100	1.0	5	5.66
		100	1.0	7	0.70
	NO_3^--N	44	1.0	5	4.36
		44	1.0	7	2.29
Catechol	F^-	4	1.0	5	3.66
		4	1.0	7	11.38
	PO_4^{-3}-P	100	1.0	5	4.08
		100	1.0	7	4.14
	NO_3^--N	44	1.0	5	4.13
		44	1.0	7	14.19

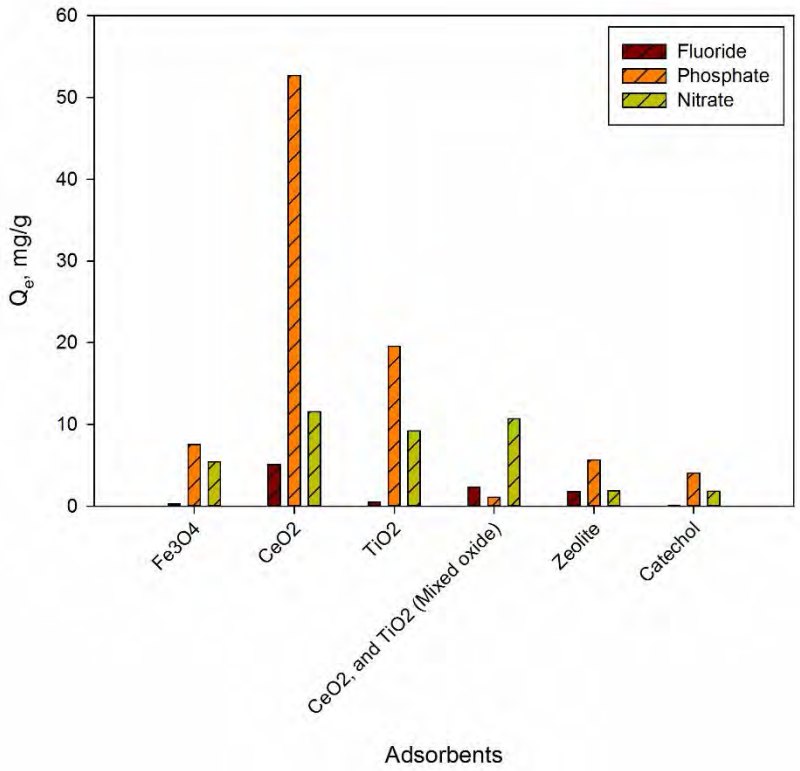

Figure 4.5 Adsorption capacity, Q_e, for fluoride, phosphate, and nitrate at equilibrium under the best conditions from tables 4.1 and 4.2.

4.3.2.2. Heavy metals removal

Screening of the potential efficiency of different adsorbents developed, the metal oxide NPs and graphene based nanomaterials were applied for the removal of cadmium and nickel compared with C100 polymer and activated carbon. As shown in Table 4.3, the highest removal of cadmium (70.16 %) was observed by using the cationic exchange polymer, C100. This could be attributed to ion exchange process. Followed by Fe_3O_4 NPs (25 %) and a low removal percentage was observed when activated carbon was used (21.60 %). Regarding nickel, C100 polymer exhibits the higher removal (100 %). While, Fe_3O_4 NPs shows removal percentage (47.83 %), but no efficiency was observed in case of using CeO_2 NPs. Moreover, drying of the chitosan beads enhanced the removal ten times, from 1.71 % to 17.1 %. In addition, the reduction of graphene oxide provides also a higher removal percentage. Indeed, reduced graphene oxide (r-G.O) could remove 34.86 % of

nickel, while G.O showed only 18.29 % of removal percentage. It is interesting to observe the increase of the removal percentage of nickel when Fe_3O_4 NPs anchored into the reduced G.O to obtain 96.23 % of nickel removal.

Table 4.3. Screening of heavy metals removal using different adsorbents.

Pollutants	Adsorbents	Initial concentration, mg/L	Adsorbent dose, g/L	pH	Removal, %
Nickel	G.O	14	1.00	7	18.29
	r-G.O	14	1.00	7	34.86
	CeO_2/r-G.O	14	1.00	7	2.29
	Fe_3O_4/r-G.O	14	1.00	7	96.23
	CeO_2	14	1.00	7	0.00
	Fe_3O_4	14	1.00	7	47.83
	Functionalized Fe_3O_4	14	1.00	7	54.80
	CS wet beads	14	1.00	7	1.71
	CS dry beads	14	1.00	7	17.71
	C100	14	1.00	7	100
Cadmium	Fe_3O_4	10	1.00	7	25.00
	C100	10	1.00	7	70.16
	Activated carbon	10	1.00	7	21.60

The adsorption capacity of nickel and cadmium for the different adsorbents is illustrated in Figure 4.5. The amount of nickel adsorbed (8.37 mg/g) onto Fe_3O_4 NPs was higher than of cadmium (2.50 mg/g). Therefore, higher affinity to nickel over cadmium was demonstrated by using Fe_3O_4 NPs. Same trend was observed when using the cationic exchange polymer, C100, where 17.50 mg of nickel could be adsorbed onto 1.00 g of

C100. While, only 7.02 mg of cadmium could be adsorbed by using the same cationic polymer.

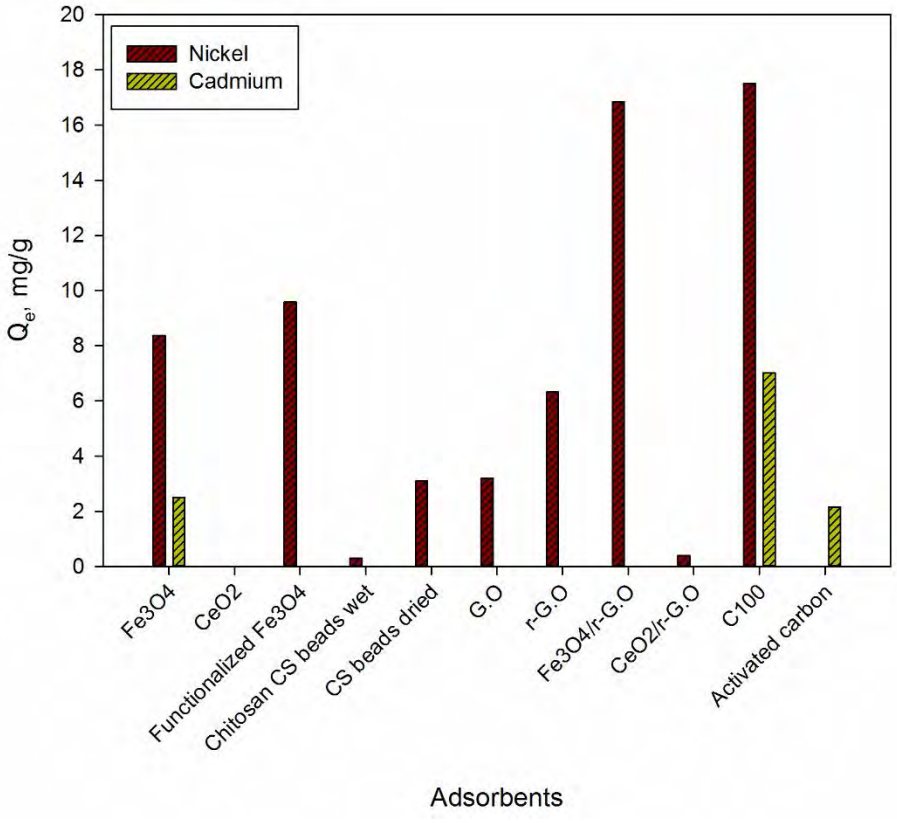

Figure 4.6. Adsorption capacities, *Qe*, of nickel and cadmium at pH 7.0, and 25 °C.

4.3.2.3. Persistent organic pollutants removal

A comparative study between the activated carbon and catechol was performed for the removal of the persistent organic pollutants such as atrazine, alachlor, carbaryl, and BDMC. A significant effect of the adsorbents used was observed as shown Figure 4.7 by using the same amount of adsorbent (1.0 g/L) and initial adsorbates' concentration (10 µg/L). By using catechol adsorbent, the highest removal efficiency was observed in case of the BDMC pesticide being removal 81.81 %, followed by alachlor, carbaryl, and atrazine to have removal of 39.38 %, 16.27 %, and 15.15 %, respectively. While, in the case of using

the activated carbon, 100 % of carbaryl could be removed. Also, the potential efficiency was found to be 94.40 %, 84.84 %, and 64.96 % for the removal of BDMC, alachlor, and atrazine, respectively.

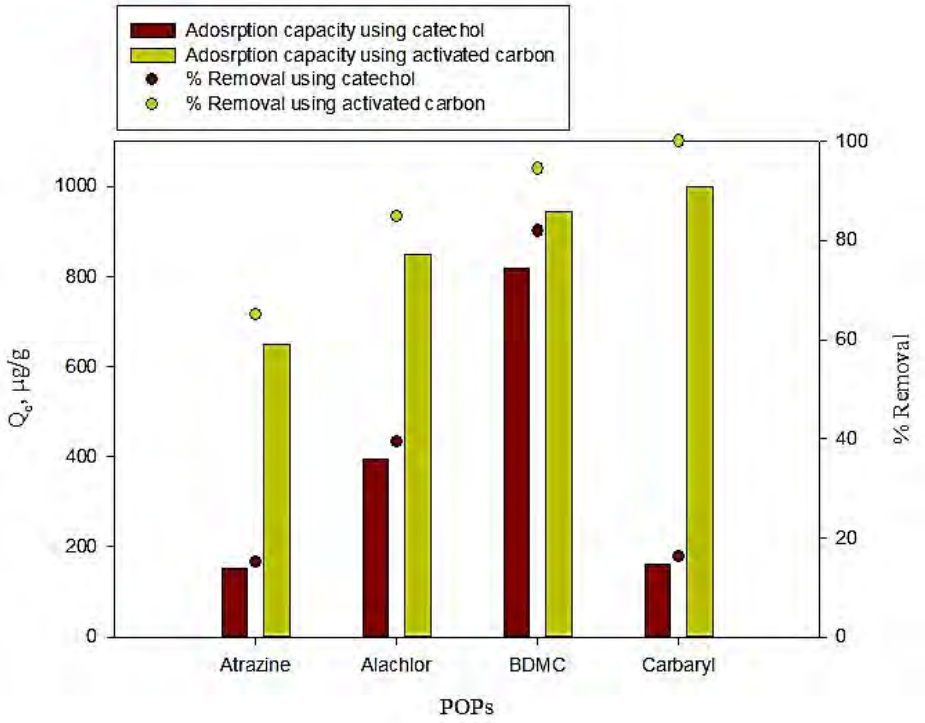

Figure 4.7. Adsorption capacities, *Qe*, and removal percentage of POPs at pH 7.0, and 25 °C.

Screening of its removal was tested by using metal oxides NPs, carbonaceous materials, and NCs of the carbonaceous adsorbents as presented in Table 4.4. For instance, 46.43 % of atrazine could be removed by using Fe_3O_4 NPs, but insignificant effect of the removal was observed by using CeO_2 NPs. Moreover, carbonaceous adsorbents exhibit higher efficiency compared to the metal oxide NPs. In addition, enhancement of the removal efficiency was observed by transforming the graphene oxide into the reduced form (r-G.O) to show an increase of the removal percentage from 82.85 % into 88.60 %. However, improvement of the removal efficiency was observed by impregnating Fe_3O_4 NPs onto reduced graphene oxide adsorbent, where 96.60 % of atrazine could be removed by using Fe_3O_4/r-G.O NCs compared to r-G.O (88.60 %), a decrease of the removal

percentage was observed when CeO_2 NPs was anchored onto r-G.O where 65.45 % of atrazine could be removed compared to r-G.O (88.60 %). Even the use of NCs, activated carbon demonstrated the highest removal percentage (100 %).

Table 4.4. Comparative study for the removal of persistent organic pollutants (POPs) using different adsorbents.

Adsorbents	Pollutants	Initial concentration, µg/L	Adsorbent dose, g/L	pH	Removal, %
Fe_3O_4	Atrazine	10	0.01	7	7.70
		10	0.10	7	23.88
		10	1.00	7	46.43
CeO_2		10	1.0	7	0.00
Catechol		10	0.01	7	15.15
		10	0.10	7	20.67
		10	1.00	7	36.65
Activated carbon		10	0.01	7	64.96
		10	0.10	7	100.00
		10	1.00	7	100.00
G.O		10	1.0	7	82.85
r-G.O		10	1.0	7	88.60
Fe_3O_4/ r-G.O		10	1.0	7	96.60
CeO_2/ r-G.O		10	1.0	7	65.45

Comparing of the adsorption capacities at equilibrium by using 1 g/L of adsorbent and 10 µg/L atrazine at pH 7.0 is illustrated in Figure 4.8. Adsorption capacity of atrazine follows the order of; activated carbon > Fe_3O_4/r-G.O > r-G.O > G.O > CeO_2/r-G.O > Fe_3O_4 > catechol. Therefore, Fe_3O_4/r-G.O NCs could be a promising adsorbent for atrazine removal for further work in terms of regeneration and reusability due to the presence of

magnetite NPs, which have magnetic properties that could be easily separated from the medium by magnetic field.

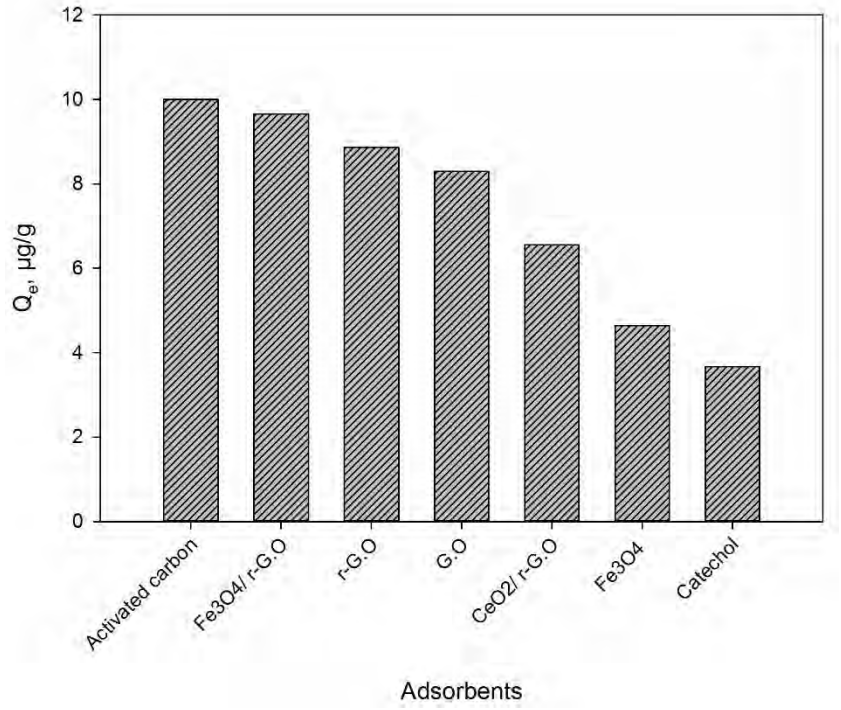

Figure 4.8. Adsorbents capacities of atrazine at pH 7.0, 25 °C, and 1.0 g/L of adsorbent amount, and 10 µg/L initial concentration of atrazine.

4.3.3. Toxicity of the nanoparticles

The possible toxicity effect of the NPs was firstly conducted by using the Microtox system [50]. Also, the potential harmful effects of effluent discharged into surface water was evaluated by using the bioluminescent test [51]. This test is based on the percentage of decrease in the amount of light emitted by the bioluminescence marine bacterium *vibrio fisheri* upon contact with the sample. The EC_{50}, and Toxicity unit (T.U.), equitox/m^3, values (for 5 and 15 min) obtained for the Fe_3O_4, Fe_3O_4@PEI, Fe_3O_4@CTAB, Fe_3O_4@$SiONH_2$, G.O, Fe_3O_4/r-G.O, and CeO_2/r-G.O nanomaterials are presented in Table 4.5. The highest values of the EC_{50} after 15 min were found to be in the following order; Fe_3O_4 > Fe_3O_4@PEI > Fe_3O_4@$SiONH_2$ > Fe_3O_4/r-G.O > G.O > Fe_3O_4@CTAB > CeO_2/r-

G.O nanomaterials. Therefore, the NCs with high toxicity are the CeO_2/r-G.O due to the presence of CeO_2 NPs which is in agreement with the literature regarding toxicity of CeO_2 NPs [42]. Moreover, a slight decrease of the EC_{50} values from 5 to 15 min, as presented in Table 4.5 were observed in all cases of nanomaterials except Fe_3O_4/r-G.O NCs. An increase of the EC_{50} value was observed from 5 to 15 min using Fe_3O_4/r-G.O NCs. Toxicity unit (T.U.) values were calculated and compared to the regulation limits of the bioluminescent toxicity test (25 equitox/m^3) at 15 min [52]. As the assayed concentrations, only CeO_2/r-G.O, and Fe_3O_4@CTAB NPs presented T.U higher than 25 equitox/m^3. Subsequently, the highly toxic nanomaterials used in this work are CeO_2/r-G.O, and Fe_3O_4@CTAB, while no toxicity for the other tested nanomaterials.

Table 4.5. EC_{50} values of some of the nanomaterials used in this study.

Nanomaterials	**EC_{50} (%)**		**T.U (equitox/m^3)**	
	5 min	**15 min**	**5 min**	**15 min**
Fe_3O_4	82.0	76.0	1.22	1.32
Fe_3O_4@PEI	72.0	70.0	1.39	1.43
Fe_3O_4@CTAB	4.0	3.0	25.00	33.33
Fe_3O_4@$SiONH_2$	32.0	33.0	3.11	3.03
G.O	4.0	5.0	25.00	20.00
Fe_3O_4/r-G.O	6.0	11.0	16.67	9.09
CeO_2/r-G.O	5.0	2.0	20.00	50.00

4.4. Conclusions

In this part of the study different nanomaterials have been synthesized using wet chemical method and its ability to remove pollutants from water was evaluated (and compared with other common and commercial materials). Therefore, the synthesis and the applications of the nanomaterials provided the following conclusions:

- The synthesized Fe_3O_4, TiO_2, and CeO_2 NPs present cubic, tetrahedral, and cubic structure, estimated from the HR-TEM images, with averages sizes of 13.00 ± 1.77 nm, 3.75 ± 0.65 nm, and 9.86 ± 1.40 nm, respectively.
- Crystalline structure and confirmation of the elemental analysis were demonstrated from the ED patterns, and EDS spectra, respectively.
- Impregnation of an approximately the same particles sizes of Fe_3O_4 and CeO_2 NPs have been successfully synthesized in the layers of reduced graphene oxide.
- Highest removal of fluoride and phosphate were obtained by using the CeO_2 NPs, followed by TiO_2 NPs whereas, the TiO_2 NPs showed the highest removal of nitrate. Combination of the three previously explained metal oxides (Fe_3O_4, CeO_2, and TiO_2) NPs to produce a core/shell nanomaterial for contaminants removal from water will be discussed in detail in Chapter 5. Application of the synthesized core-shell NPs will be evaluated for the fluoride removal from water (Chapter 6).
- Fe_3O_4/r-G.O NCs showed higher removal percentage of nickel compared to CeO_2/r-G.O NCs.
- The C100 exchange polymer and the Fe_3O_4 NPs showed a potential efficiency for the removal of cadmium as well as nickel. Therefore, NCs of C100@Fe_3O_4 NCs will be synthesized and tested for the removal of anions such as phosphate (Chapter 7).
- The activated carbon showed the highest removal of POPs, followed by the magnetite based graphene oxide NCs. Therefore, Fe_3O_4/r-G.O NCs had advantage in terms of easily separation by the effect of magnetic decantation for further study of the removal of POPs from water.

4.5. References

1. Vollath, D., *Nanomaterials: An Introduction to Synthesis, Properties and Applications*. 2013: Wiley.
2. Araújo, R., A.C.M. Castro, and A. Fiúza, *The Use of Nanoparticles in Soil and Water Remediation Processes.* Materials Today: Proceedings, 2015. **2**(1): p. 315-320.

3. Nolan, B. and J. Stoner, *Nutrients in groundwaters of the conterminous United States, 1992-1995.* USGS Staff--Published Research, 2000: p. 59.
4. Achla Kaushal and S.K. Singh, *Removal of heavy metals by nanoadsorbents: A review.* Journal of Environment and Biotechnology Research, 2017. **6**(1): p. 96-104.
5. Verhaert, V., et al., *Persistent organic pollutants in the Olifants River Basin, South Africa: Bioaccumulation and trophic transfer through a subtropical aquatic food web.* Science of The Total Environment, 2017. **586**: p. 792-806.
6. Habuda-Stanić, M., M. Ravančić, and A. Flanagan, *A Review on Adsorption of Fluoride from Aqueous Solution.* Materials, 2014. **7**(9): p. 6317.
7. Tangsir, S., et al., *Water defluoridation using Al2O3 nanoparticles synthesized by flame spray pyrolysis (FSP) method.* Chemical Engineering Journal, 2016. **288**: p. 198-206.
8. Acelas, N.Y., et al., *Selective removal of phosphate from wastewater using hydrated metal oxides dispersed within anionic exchange media.* Chemosphere, 2015. **119**: p. 1353-1360.
9. USEPA, *Risk based Concentration Table*. 2000, United States Environmental Protection Agency: Philadelphia, PA; Washington DC.
10. Ghasemzadeh, G., et al., *Applications of nanomaterials in water treatment and environmental remediation.* Frontiers of Environmental Science & Engineering, 2014. **8**(4): p. 471-482.
11. Qu, X., P.J.J. Alvarez, and Q. Li, *Applications of nanotechnology in water and wastewater treatment.* Water Research, 2013. **47**(12): p. 3931-3946.
12. Rodriguez, O., et al., *Treatment Technologies for Emerging Contaminants in water: A review.* Chemical Engineering Journal, 2017.
13. Li, M., et al., *Phosphate adsorption on metal oxides and metal hydroxides: A comparative review.* Environmental Reviews, 2016. **24**(3): p. 319-332.
14. Rajasulochana, P. and V. Preethy, *Comparison on efficiency of various techniques in treatment of waste and sewage water – A comprehensive review.* Resource-Efficient Technologies, 2016. **2**(4): p. 175-184.

15. Mahdavian, A.R. and M.A.-S. Mirrahimi, *Efficient separation of heavy metal cations by anchoring polyacrylic acid on superparamagnetic magnetite nanoparticles through surface modification.* Chemical Engineering Journal, 2010. **159**(1–3): p. 264-271.
16. Hu, J., G. Chen, and I.M.C. Lo, *Selective Removal of Heavy Metals from Industrial Wastewater Using Maghemite Nanoparticle: Performance and Mechanisms.* Journal of Environmental Engineering, 2006. **132**(7): p. 709-715.
17. Hu, J., G. Chen, and I.M.C. Lo, *Removal and recovery of Cr(VI) from wastewater by maghemite nanoparticles.* Water Research, 2005. **39**(18): p. 4528-4536.
18. Alonso, A., *Development of polymeric nanocomposites with enhanced distribution of catalytically active or bactericide nanoparticles*, in *Departament d'Enginyeria Química, Escola d'Enginyeria* 2012, Universitat Autònoma de Barcelona (UAB).
19. Tu, W. and H. Liu, *Continuous Synthesis of Colloidal Metal Nanoclusters by Microwave Irradiation.* Chemistry of Materials, 2000. **12**(2): p. 564-567.
20. Kim, D.K., et al., *Synthesis and characterization of surfactant-coated superparamagnetic monodispersed iron oxide nanoparticles.* Journal of Magnetism and Magnetic Materials, 2001. **225**(1–2): p. 30-36.
21. Contreras, A.R., et al., *Potential use of CeO2, TiO2 and Fe3O4 nanoparticles for the removal of cadmium from water.* Desalination and Water Treatment, 2012. **41**(1-3): p. 296-300.
22. Contreras A.R., et al., *Use of cerium oxide (CeO2) nanoparticles for the adsorption of dissolved cadmium (II), lead (II) and chromium (VI) at two different pHs in single and multi-component systems,*. Global Nest Journal, 2015. **17**(3): p. 536-543.
23. Recillas, S., et al., *Use of CeO2, TiO2 and Fe3O4 nanoparticles for the removal of lead from water: Toxicity of nanoparticles and derived compounds.* Desalination, 2011. **277**(1–3): p. 213-220.
24. Massart, R., *Preparation of aqueous magnetic liquids in alkaline and acidic media.* IEEE Transactions on Magnetics, 1981. **17**(2): p. 1247-1248.
25. A. L. Andrade, et al., *Effect of Tetramethylammonium Hydroxide on Nucleation, Surface Modification and Growth of Magnetic Nanoparticles.* Journal of Nanomaterials, 2012. **2012**: p. 10.

26. Zhang, F., Q. Jin, and S.-W. Chan, *Ceria nanoparticles: Size, size distribution, and shape.* Journal of Applied Physics, 2004. **95**(8): p. 4319-4326.
27. García, A., et al., *Acute toxicity of cerium oxide, titanium oxide and iron oxide nanoparticles using standardized tests.* Desalination, 2011. **269**(1–3): p. 136-141.
28. Pottier, A., et al., *Size tailoring of TiO2 anatase nanoparticles in aqueous medium and synthesis of nanocomposites. Characterization by Raman spectroscopy.* Journal of Materials Chemistry, 2003. **13**(4): p. 877-882.
29. Hasanzadeh, R., et al., *Effective removal of toxic metal ions from aqueous solutions: 2-Bifunctional magnetic nanocomposite base on novel reactive PGMA-MAn copolymer@Fe3O4 nanoparticles.* Journal of Colloid and Interface Science, 2017. **490**: p. 727-746.
30. Yazid, N.A., R. Barrena, and A. Sánchez, *The immobilisation of proteases produced by SSF onto functionalized magnetic nanoparticles: Application in the hydrolysis of different protein sources.* Journal of Molecular Catalysis B: Enzymatic, 2017.
31. Ge, S., et al., *Influences of Surface Coating, UV Irradiation and Magnetic Field on the Algae Removal Using Magnetite Nanoparticles.* Environmental Science & Technology, 2015. **49**(2): p. 1190-1196.
32. Khoshnevisan, K., et al., *Preparation and Characterization of CTAB-Coated Fe3O4 Nanoparticles.* Synthesis and Reactivity in Inorganic, Metal-Organic, and Nano-Metal Chemistry, 2012. **42**(5): p. 644-648.
33. Hummers, W.S. and R.E. Offeman, *Preparation of Graphitic Oxide.* Journal of the American Chemical Society, 1958. **80**(6): p. 1339-1339.
34. Ji, Z., et al., *Facile synthesis of reduced graphene oxide/CeO2 nanocomposites and their application in supercapacitors.* Ceramics International, 2015. **41**(7): p. 8710-8716.
35. Chandra, V., et al., *Water-Dispersible Magnetite-Reduced Graphene Oxide Composites for Arsenic Removal.* ACS Nano, 2010. **4**(7): p. 3979-3986.
36. Barreiro-Iglesias, R., et al., *Preparation of chitosan beads by simultaneous cross-linking/insolubilisation in basic pH: Rheological optimisation and drug*

loading/release behaviour. European Journal of Pharmaceutical Sciences, 2005. **24**(1): p. 77-84.

37. Alonso, A., et al., *Environmentally-safe bimetallic Ag@Co magnetic nanocomposites with antimicrobial activity.* Chemical Communications, 2011. **47**(37): p. 10464-10466.
38. APHA, AWWA, and WPCF, *Standard Methods for examination of water and wastewater*. 1999, Washington: American Public Health Association. 1325.
39. El-Gawad, H.A., *Validation method of organochlorine pesticides residues in water using gas chromatography–quadruple mass.* Water Science, 2016. **30**(2): p. 96-107.
40. Zuloaga, O., et al., *Overview of extraction, clean-up and detection techniques for the determination of organic pollutants in sewage sludge: A review.* Analytica Chimica Acta, 2012. **736**: p. 7-29.
41. Nagwa ABO EL-Maali and A.Y. Wahman, *Gas Chromatography-Mass Spectrometric Method for Simultaneous Separation and Determination of Several Pops with Health Hazards Effects.* Modern Chemistry & Applications, 2015.
42. Sánchez, A., et al., *Ecotoxicity of, and remediation with, engineered inorganic nanoparticles in the environment.* TrAC Trends in Analytical Chemistry, 2011. **30**(3): p. 507-516.
43. Berry, L.G. and R.M. Thompson, *X-ray diffraction data for minerals.* Waverly Press: New York, 1962: p. 194.
44. Zhang, J.L., R.S. Srivastava, and R.D.K. Misra, *Core−Shell Magnetite Nanoparticles Surface Encapsulated with Smart Stimuli-Responsive Polymer: Synthesis, Characterization, and LCST of Viable Drug-Targeting Delivery System.* Langmuir, 2007. **23**(11): p. 6342-6351.
45. Di, Z.-C., et al., *Chromium adsorption by aligned carbon nanotubes supported ceria nanoparticles.* Chemosphere, 2006. **62**(5): p. 861-865.
46. Araña, J., et al., *The effect of acetic acid on the photocatalytic degradation of catechol and resorcinol.* Applied Catalysis A: General, 2006. **299**: p. 274-284.
47. Pattanaik, M. and S.K. Bhaumik, *Adsorption behaviour of polyvinyl pyrrolidone on oxide surfaces.* Materials Letters, 2000. **44**(6): p. 352-360.

48. Zhang, K., et al., *Wide pH range for fluoride removal from water by MHS-MgO/MgCO3 adsorbent: Kinetic, thermodynamic and mechanism studies.* Journal of Colloid and Interface Science, 2015. **446**: p. 194-202.
49. Ko, Y.G., et al., *CeO2-covered nanofiber for highly efficient removal of phosphorus from aqueous solution.* Journal of Hazardous Materials, 2016. **307**: p. 91-98.
50. Barrena, R., et al., *Evaluation of the ecotoxicity of model nanoparticles.* Chemosphere, 2009. **75**(7): p. 850-857.
51. Griffitt, R.J., et al., *Effects of particle composition and species on toxicity of metallic nanomaterials in aquatic organisms.* Environmental Toxicology and Chemistry, 2008. **27**(9): p. 1972-1978.
52. Catalunya, G.d. *Diari Oficial de la Generalitat de Cataluña*. DOGC num. 4993 23/10/2007; Available from: http://dogc.gencat.cat/ca/pdogc_canals_interns/pdogc_resultats_fitxa/?documentId=411648&language=es_ES&action=fitxa (Accessed April 2017).

Chapter 5

Novel magnetic core-shell Ce-Ti@Fe_3O_4 nanoparticles as adsorbent for water contaminants removal

The results presented in this chapter have been published in RSC Advances journal:

"Ahmad Abo Markeb, Laura A. Ordosgoitia, Amanda Alonso, Antoni Sánchez, Xavier Font. Novel magnetic core-shell Ce-Ti@Fe_3O_4 nanoparticles as an adsorbent for water contaminants removal. RSC Advances, 2016. 6(62): p. 56913-56917".

5.1. Introduction

Contamination of water is a widespread problem throughout the world as a result of pollution and a wide range of pollutants can be considered for remediation [1]. Thus, the development of new technologies is fundamental. Among all the current decontamination methods, adsorption is considered the most effective, environmental friendly, and economically method for contaminants removal [2]. In addition, nanotechnology can offer new products and process alternatives for water purification [3]. Some examples are based on nanoparticles (NPs), nanocomposites, carbon based nanomaterials and nanofibers, among others [4]. Thus, the use of adsorbents nanomaterials has become an interesting way for the removal of various contaminants from drinking water [5] such as of heavy metals [6] and nutrients [7].

It has been previously shown the use of cerium oxide (CeO_2), magnetite (Fe_3O_4) and titanium oxide (TiO_2) NPs and magnetite based nanocomposites (NCs) for the adsorption of inorganic anions such fluoride, nitrate, and phosphate, and heavy metals such as cadmium (Chapter 4). The results showed a high efficiency of fluoride and phosphate contaminants using CeO_2 NPs, and of nitrate using TiO_2. In addition, other metal oxides and metal hydroxides had also been reported [8-11] for fluoride removal from water as well as bimetallic or mixed oxides such as Fe-Zr oxide, Fe_3O_4/Al_2O_3 mixed oxide NPs [12-15]. Further, it is worthy to consider the reusability and the regeneration of the adsorbents as well as the trapping of the NPs to prevent its environmental and health safety risks [16]. Thus, the use of magnetic NPs for pollutants removal provides efficiency, easy separation, and reusability. The magnetic NPs can be either used directly or as the core material in a core-shell NPs structure [17, 18]. In addition, it has been reported that cerium titanate nanomaterials ($Ce_{2/3}TiO_3$) have many applications as photocatalytic and ferroelectric materials [19], among others. However, its properties exhibit canted-antiferromagnetic order [20] and few studies for improving its properties have been reported [21]. So, a great challenge if this material has magnetic properties as well as potential efficiency for water remediation. Thus, the objectives of this work are: (1) to synthesize cerium titanate NPs with magnetic properties by coating it on magnetite, Fe_3O_4, NPs using a simple and easy

method as one step synthesis under room temperature to obtain magnetic core-shell Ce-Ti@Fe_3O_4 NPs (shell@core), and (2) to evaluate its efficiency for water remediation as a versatile adsorbent nanomaterial for typical inorganic contaminants.

5.2. Materials and methods

5.2.1. Materials

Iron (II) chloride ($FeCl_2$), iron (III) chloride hexahydrate ($FeCl_3 \cdot 6H_2O$), sodium fluoride (NaF), titanium chloride ($TiCl_4$), cerium nitrate hexahydrate ($Ce(NO_3)_3 \cdot 6H_2O$), ammonia (NH_3) solution, and cetyltrimethylammonium bromide (CTAB), sodium phosphate monobasic; NaH_2PO_4, cadmium chloride ($CdCl_2$), dithizone, chloroform ($CHCl_3$), potassium cyanide (KCN), hydroxylamine hydrochloride ($NH_2Cl \cdot H_2O$) were purchased from Sigma-Aldrich, Spain. Sodium hydroxide pellets (NaOH) was purchased from Merck. Hydrochloric acid (HCl), nitric acid (HNO_3) was purchased from Panreac, SA. All the chemicals were of analytical grade or higher, and all solutions were prepared with Milli-Q water and filtered using 0.45 µm Nylon membrane filter.

5.2.2. Synthesis of the core shell nanoparticles

5.2.2.1. Preparation of magnetite nanoparticles

Previously to the synthesis of the core-shell, Ce-Ti@Fe_3O_4 NPs, magnetite NPs (Fe_3O_4 NPs) were prepared by the co-precipitation method using cetyltrimethylammonium bromide, CTAB, as dispersant and reported elsewhere [22]. First, $FeCl_2$ and $FeCl_3 \cdot 6H_2O$, with Fe^{2+}/Fe^{3+} molar ratio of 1:2, were dissolved in 100 mL of deoxygenated ultrapure water (Milli-Q) containing 0.1% of CTAB as dispersant. Then, the suspension was incubated for 1 h at 40 °C and under N_2 atmosphere. Secondly, 0.6 M NH_3 solution was titrated into the iron salts solution under agitation until the pH 9.0 achieved. During titration process, the mixture's color turned from light yellow to red brown and then eventually to black which confirmed the formation of Fe_3O_4 NPs. Then, the suspension

containing Fe_3O_4 NPs incubated for 1 h under N_2 and at 40 °C. Afterwards, the NPs were washed three times using ultrapure water and magnetic decantation.

5.2.2.2. Preparation of Ce-Ti@Fe_3O_4 nanoparticles

Once the Fe_3O_4 NPs were washed and dried, Ce-Ti@Fe_3O_4 NPs were synthesized. $TiCl_4$ and $Ce(NO_3)_3 \cdot 6H_2O$ were mixed with 100 mL of Milli-Q water containing the previous formed Fe_3O_4-NPs, with a Ti^{4+}:Ce^{3+} molar ratio of 1:1 and to reach a total molar concentration of 50 mM. Mixing was under agitation at room temperature for 30 min. Next, a slowly dropwise titration with 12.5 %v/v NH_3 solution until pH 7.0 was reached. Then, the Ce-Ti@Fe_3O_4 NPs produced were washed with ultrapure water and magnetic decantation and finally dried at 80 °C for 24h. The synthetic procedure was adapted from similar works about core-shell magnetic Ti-NPs synthesis [23]. Besides, the cerium titanate ($Ce_{2/3}TiO_3$) NPs were prepared using the same protocol of Ce-Ti@Fe_3O_4 NPs in absence of Fe_3O_4 NPs.

5.2.3. Characterization of the Ce-Ti@Fe_3O_4 NPs

The Ce-Ti@Fe_3O_4 nanomaterial obtained was fully characterized for a deep understanding of its structure and properties. Fe, Ce and Ti metals from the nanoparticles were analyzed by using Inductively coupled plasma coupled with optical emission spectrometry (ICP-OES).

High Resolution Transmission Electron Microscope (HR-TEM) was used to characterize the morphology and sizes of the NPs. Electron Diffraction (ED) pattern was used to distinguish between amorphous and crystalline structure and to estimate the Miller indices. Energy Dispersive Spectroscopy (EDS) provided the metal chemical composition of the samples.

X-Ray Diffraction (XRD) technique was used to obtain the crystalline structure of the Ce-Ti@Fe_3O_4 NPs.

Also, the core/shell structure of the NPs was proved using the high-angle annular

dark field scanning transmission electron microscopy (HAADF-STEM) coupled with Electron Energy Loss Spectra (EELS).

Absorption and luminescence spectra of Ce-Ti@Fe_3O_4 NPs were carried out using UV-VIS spectrophotometer, and Luminescence spectrometer. Sample preparations for each technique was described in Chapter 3.

5.2.4. Analytical methods used in the Adsorption Experiments

5.2.4.1. Ionic chromatography for fluoride, nitrate and phosphate analysis

The determination of phosphate (PO_4^{-3}-P), fluoride anion (F^-) and nitrate (NO_3^--N) were determined using ion chromatographic system (ICS). Typically, 1000 mg/L stock solutions of each anion were prepared by dissolving the appropriate amount of each precursor salt into 100 mL measuring flasks contain ultrapure water. Next, calibration curves of each anion were obtained by preparation series of calibration standards in ultrapure water by diluting the stock solutions. Also, the working solution of each anion was prepared by diluting the stock solution to the desired concentration in ultrapure water. Then, the analysis of anions was performed as described in Chapter 3.

5.2.4.2. UV-Vis for Cadmium analysis

Calibration curves for cadmium (Cd) were constructed using 99.995% cadmium(II) chloride by using a colorimetric method, based on the reaction of cadmium with dithizone to form a complex that is extracted with chloroform. Then the absorbance is measured at 518 nm [24, 25]. Cadmium stock solution was prepared by dissolving the appropriate amount in 5 % nitric acid. The cadmium solutions for calibration curve and adsorption studies were prepared by diluting the stock solution. Analysis of Cd using UV/VIS spectrophotometer was performed as described in Chapter 3.

5.2.5. Adsorption experiments procedure

Batch adsorption tests were used to determine the adsorption efficiency by the synthesized NPs. A contaminant solution with an initial concentration (C_0) (mg/L) was prepared as mentioned before (Section 5.2.4.1). A concentration of adsorbent (W) (g/L) was added into a conical flask containing 25 mL of the aqueous contaminated solution. pH of the solution was adjusted when necessary using 0.1 M NaOH and/or HCl until pH 7. The flask was shaken (200 rpm) at 25 °C using a thermostat shaker. Residual contaminant concentration in the solution after 24 h of adsorption, C_e, was determined by the corresponding analytical method detailed in Section 2.4. Equilibrium adsorption capacity, Q_e, of the adsorbent was calculated using the previously explained Equation 3.1 (Chapter 3).

Adsorption experiments were preformed using different initial concentrations for each contaminant where based on the reported typical concentration in water or on the maximum contaminated level (MCL). For instance, phosphate initial concentration tested was 10 mg/L due to municipal wastewater may contain 4-15 mg/L, and domestic wastewater may contains 10-30 mg/L [7]. Furthermore, 10 mg/L initial fluoride concentration was selected due the maximum contaminated level in water is 1.5 mg/L [26, 27] but, it has been reported that the fluoride concentrations in groundwater range from well under 1.0 mg/L to more than 35.0 mg/L in several regions of India [28]. In addition, the initial nitrate concentration tested is 50 mg/L due to according WHO guideline the MCL is 50 mg/L [27]. Also, 10 mg/L initial cadmium concentration was selected due to wastewater contains 10 – 100 mg/L of cadmium contaminant [29]. All the experiments were performed at pH 7 as a typical value in real media.

5.3. Results and discussion

5.3.1. Characterization of the synthesized Ce-Ti@Fe_3O_4 nanoparticles

5.3.1.1. Metal composition

The metal content of the Ce-Ti@Fe_3O_4 NPs (determined by ICP–OES) is detailed in terms of mg_M/g and $mmol_M/g$ of the nanomaterial, where M corresponds to Ti, Ce and Fe, respectively. The results showed a metal content of 121.01 ± 7.70 mgTi/g, 199.29 ± 10.47 mgCe/g and 81.07 ± 4.49 mgFe/g, meaning 2.50 ± 0.16 mmolTi/g, 1.40 ± 0.07 mmolCe/g and 1.50 ± 0.08 mmolFe/g. Thus, the synthesized nanoadsorbent contents the molar ratio of Ce:Ti:Fe of 1:2:1, which is in accordance with the experimental synthetic protocol.

5.3.1.2. Size, structure and crystallinity

Figure 5.1 illustrates the TEM images coupled with EDS and ED pattern for Ce-Ti@Fe_3O_4 NPs. As shown in Figure 5.1a, Ce-Ti@Fe_3O_4 NPs present a particle size within the range of 10 – 15 nm. ED pattern allows studying the crystal structure of the NPs. Thus, the ED pattern for Ce-Ti@Fe_3O_4 NPs (Figure 5.1b), taken from randomly selected area of the nanomaterial (SAED), exhibits multiple rings consisting of discrete spots, which suggested that the core-shell NP is based on nanocrystals.

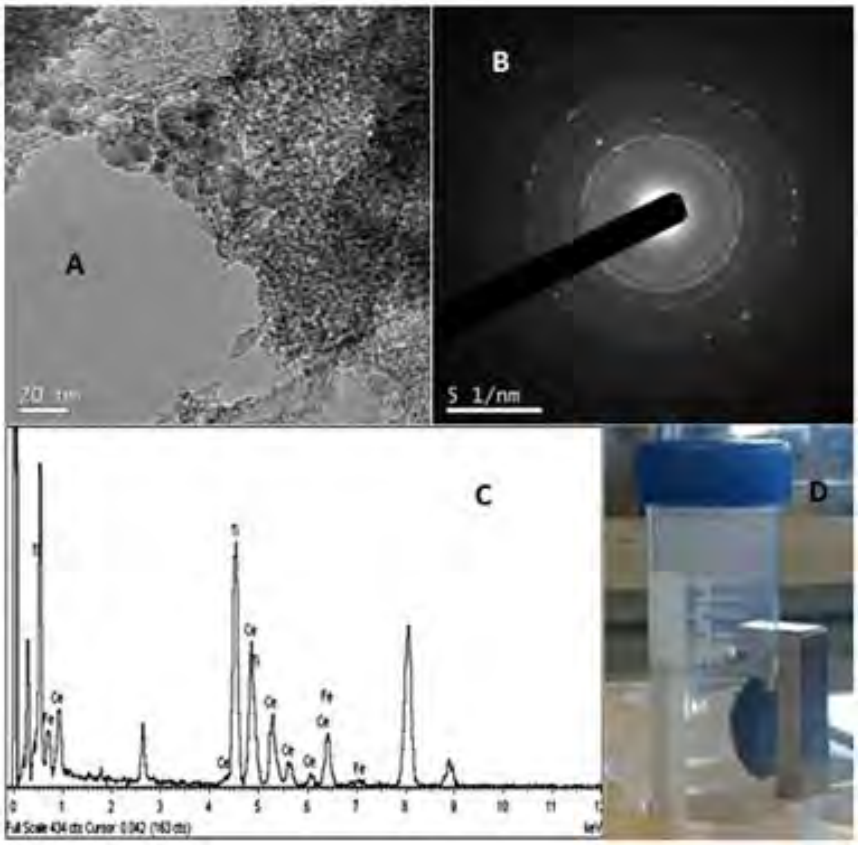

Figure 5.1. (a) HRTEM image, (b) SAED pattern; (c) EDS spectra and; (d) qualitative magnetic properties test for Ce-Ti@Fe3O4 NPs.

In addition, EDS provided the metal composition of the samples and Figure 5.1c proved the presence of the three components Ce, Ti, and Fe in the material. Moreover, magnetic properties of the Ce-Ti@Fe_3O_4 nanomaterial were qualitatively tested using a square magnet, showing the strong magnetism of the material (Figure 5.1d). This result demonstrates an enhancement on its properties comparing to the literature where $Ce_{2/3}TiO_3$ exhibits antiferromagnetic properties [20]. This also demonstrates that the NPs could be easily recovered from the reaction mixture for further reuse in its application.

Further, as shown in Table 5.1, the calculated interplanar distance (d) from the SAED pattern of the Ce-Ti@Fe_3O_4 NPs and the corresponding Miller indices (hkl diffraction plan) were compared to the standard values [30, 31]. The values concluded that the crystal pattern presented similarity to both cerium titanate and Fe_3O_4 patterns, which was in agreement with the XRD data further reported.

Table 5.1. Comparison of experimental and standard Interplanar Spacing (d) values with their respective Diffracting Plan Index (hkl) in Fe_3O_4 and Ce-Ti oxide NPs using ED pattern.

d, °A experimental	**Fe_3O_4 NPs**		**Ce-Ti oxide NPs**	
	d, °A standard	**hkl**	**d, °A standard**	**hkl**
3.01	2.97	220	---	---
2.74	---	---	2.73	110
2.47	2.53	311	---	---
2.20	---	---	2.23	112
2.06	2.10	400	---	---
2.04	---	---	1.94	004
1.86	---	---	1.87	201
1.77	---	---	1.73	210
1.68	---	---	1.69	211
1.56	---	---	1.58	212
1.42	1.48	440	---	---

XRD technique was used to obtain the crystalline structure of the Ce-Ti@Fe_3O_4 NPs. In a diffraction pattern, the location of the peaks on the bragg angles (2θ scale) can be compared to the reference peaks. Figure 5.2 shows the XRD pattern of the original Ce-Ti@Fe_3O_4 nanomaterial, which consists of two phases: magnetite and cerium titanate reference patterns that were proved by matching from database. The identification of magnetite and cerium titanate were based on the characteristic peaks in the diffractograms (Table 5.2) and comparing with the database [30, 31].

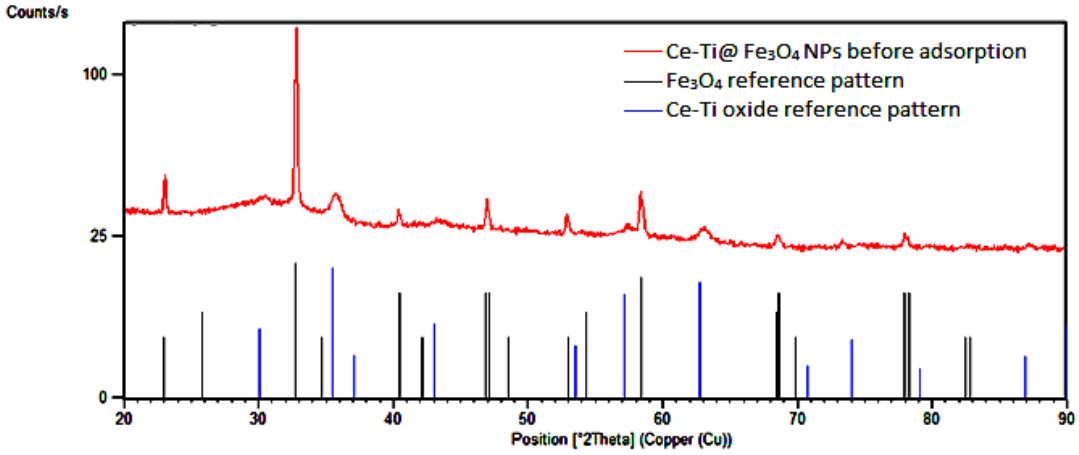

Figure 5.2. XRD pattern of the Ce-Ti@Fe_3O_4 material and matching comparison with both Fe_3O_4 and Ce-Ti oxide reference pattern from database.

Table 5.2. XRD Database reference patterns

Reference code:	00-033-0342	**Reference code:**	00-001-1111
PDF index name:	Cerium Titanium Oxide	**Mineral name:**	Magnetite
Empirical formula:	Ce0.66O2.98Ti	**Empirical formula:**	Fe3O4
Chemical formula:	Ce0.66TiO2.975	**Chemical formula:**	Fe3O4
		PDF index name:	Iron Oxide

Additionally, Table 5.3 shows the experimental 2θ positions from the XRD pattern and its comparison with the standard 2θ values [30, 31] and their respective Diffracting Plan Index (h k l) in Fe_3O_4 and Ce-Ti oxide NPs. These results could suggest that the diffracted peaks can be indexed to be face centered cubic structure of the Fe_3O_4 NPs according to the JCPDS 00-001-111118b. From the XRD patterns shown in Figure 5.2, one can notice the characteristic diffraction peaks belonging to cubic Fe_3O_4. They correspond to (220), (311), (400), (511) and (440) family planes (PDF 89–4319). After cerium titanium oxide coating, the characteristic peaks of cerium titanate were appeared and its bragg angles were found to be close to that of $Ce_{2/3}TiO_{2.98}$. Two peaks were observed corresponding to rutile/anatase in the

magnetic cerium titanate NPs: (110) peak of anatase and (101) peak of rutile closely positioned at each other, namely at around $2\theta = 25.3$ and $2\theta = 27.4$, respectively.

Table 5.3. Comparison of experimental and standard (2θ) values with their respective Diffracting Plan Index (h k l) in Fe_3O_4 and Ce-Ti oxide NPs using XRD pattern

2θ experimental	**Fe_3O_4 NPs**		**Ce-Ti oxide NPs**	
	2θ standard	**hkl Diffraction plan**	**2θ standard**	**hkl Diffraction plan**
23.13	---	---	25.82	101
31.42	30.06	220	---	---
32.85	---	---	32.74	110
35.77	35.45	311	---	---
40.44	---	---	40.45	112
43.64	43.04	400	---	---
47.14	---	---	46.82	004
52.98	---	---	52.98	210
57.45	57.17	511	---	---
58.42	---	---	58.44	212
63.18	62.73	440	---	---
68.63	---	---	68.40	024
78.05	---	---	77.90	106
87.29	86.91	642	---	---
90.20	89.93	731	---	---

The morphology of the core-shell structure of the Ce-Ti@Fe_3O_4 nanomaterial was demonstrated by STEM coupled with EELS. Thus, the images obtained from a HAADF detector provide density-based contrast, the core appeared bright due to their higher scattering probability [32]. As illustrated in Figure 5.3, the HAADF image of Ce-Ti@Fe_3O_4 shows that the Fe_3O_4 NPs was coated with Ce-Ti oxide layer (Figure 5.3a) as it can be seen a brightest core covered by a shell. STEM based EDS was used to confirm the elemental distribution of the Ti, Fe and Ce, respectively, as

shown in Figure 5.3b. In addition, the scanning line profile appears as a strong peak corresponding to the position of the bright Fe particle core, whilst the spectra on each side of the core are dominated by Ce and Ti edges (in the shell) as illustrated in Figure 5.3c.

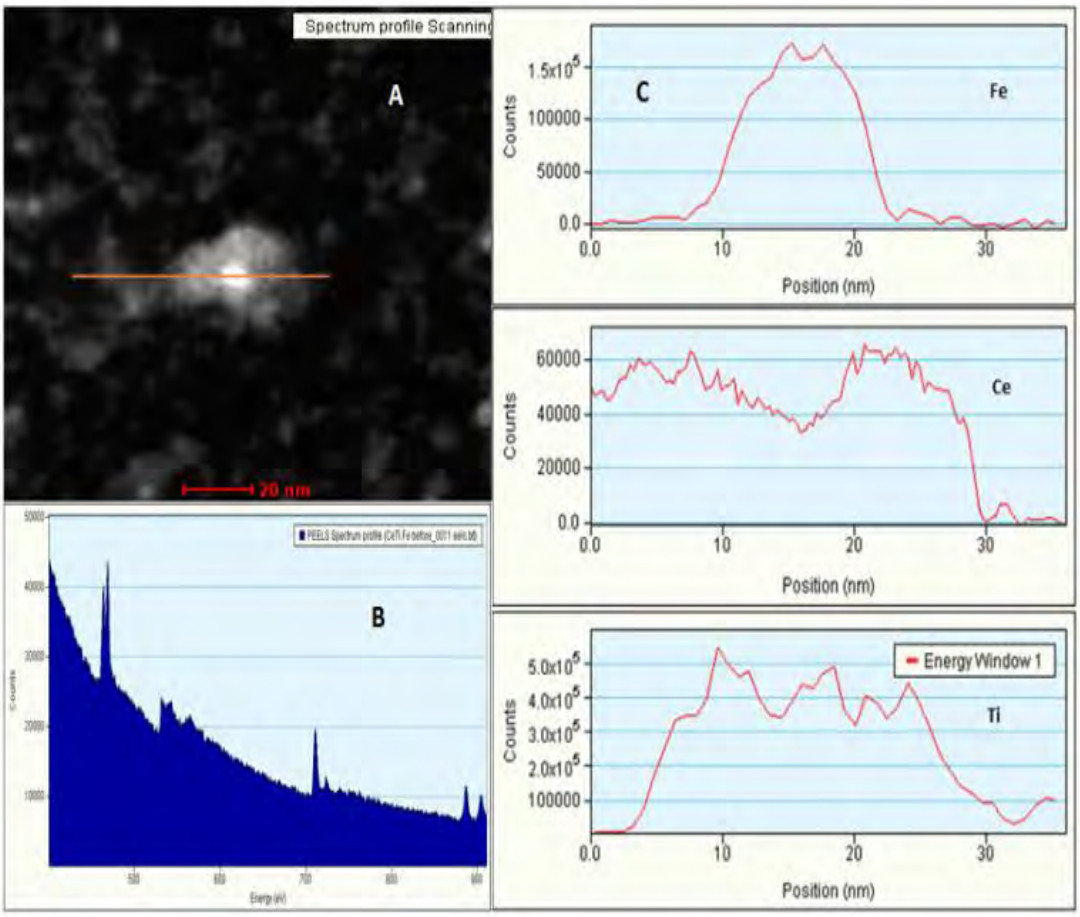

Figure 5.3. EELS line scan of the core-shell Ce-Ti@Fe_3O_4 nanocomposite. (A) STEM HAADF image of the Ce-Ti@Fe_3O_4 and position of line scan; (B) PEELS spectrum of the nanocomposite; and (C) Ions profile spectra along the line scanning.

5.3.1.3. Absorption and Luminescence spectra of the Ce-Ti@Fe_3O_4

UV/Vis Absorption and luminescence spectra of Ce-Ti@Fe_3O_4 NPs were performed to estimate the valence of the cerium in the NP and confirm its speciation. As reported, the cerium ion in the cerium titanate, $Ce_{2/3}TiO_3$, is mainly Ce(III) [21]. Figure 5.4 shows the absorption UV-Vis spectra of the Ce-Ti@Fe_3O_4 nanomaterial. As shown, two peaks were observed at 250 and 310 nm respectively, which could be attributed to the presence of either Ce(III) or both Ce(III) and Ce(IV) in the nanomaterial [33].

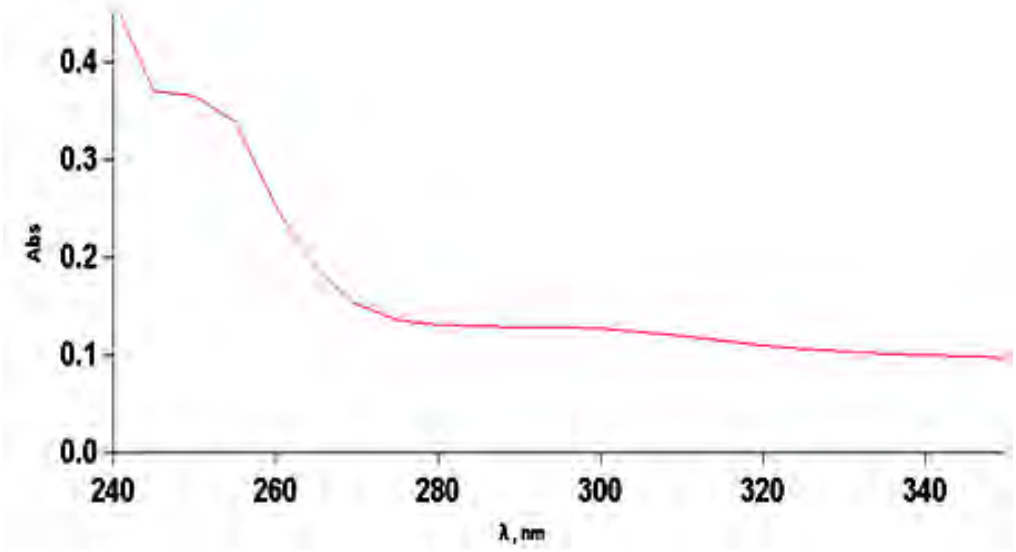

Figure 5.4. UV/Vis spectra for Ce-Ti@Fe_3O_4 nanomaterial.

Although the main absorption band is around 310 nm for Ce(III), characteristic broad bands in the UV region between 330 and 200 nm could be observed due to the coexistence of Ce(III) and Ce(IV) species because of its particular electronic configuration [34].

Therefore, because of the overlapping of both bands, it is difficult to determine the species responsible of colour with the colorimetric technique. Thus, luminescence spectroscopy is necessary to obtain information about the valence of

the cerium. Ce(III) ions presents a characteristic intense blue emission upon UV excitation [35]. Therefore, Figure 5.5 represents the excitation and emission spectra of the Ce-Ti@Fe_3O_4 nanomaterial. The excitation spectrum for λ_{em}=363 nm shows a band at 258 nm and the emission spectrum recorded upon λ_{exc}=266 nm shows the characteristic emission band at 325 nm, which corresponds to the transition to ground state to excited state as compared to literature [33, 36, 37]. The slightly shift of the wavelength comparing to the literature could be attributed to the lower temperature of the synthesis of the materials and to the presence of magnetite NPs in the core.

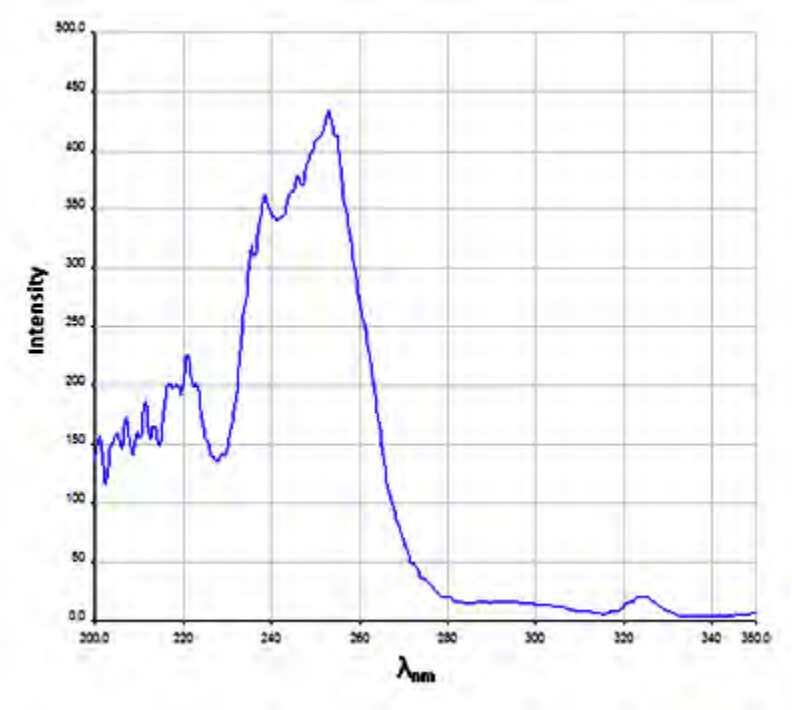

Figure 5.5. Luminescence spectra of the Ce-Ti@Fe_3O_4 nanomaterial at the excitation spectrum for λ_{em}=363 nm and the emission spectrum recorded upon λ_{exc}=266 nm.

5.3.2. Adsorption tests by using Ce-Ti@Fe_3O_4 NPs as adsorbent for fluoride, nitrate, phosphates and cadmium contaminants.

Table 5.4 shows the equilibrium adsorption capacities after 24 h, the percentage of removal of each contaminant using a concentration of 1g/L of the adsorbent for all the cases.

Table 5.4. Adsorption capacities and removal efficiencies values for contaminants removal

Pollutant	Initial concentration, mg/L	Dose, g/L	Q_e, mg/g	Removal, %
PO_4^{-3}-P	10	0.90	11.10	99.90
F^-	10	0.97	10.31	100.0
NO_3^--N	50	1.0	42.50	85.00
Cd^{2+}	10	1.0	4.53	45.28

It is shown that the Ce-Ti@Fe_3O_4 NPs have a potential effect for removal anionic contaminants (*i.e.* fluoride, nitrate and phosphates) from 85% removal for nitrate to 100% for phosphates and fluoride. However, it presents low removal for cationic contaminants such as cadmium (45% removal). The differences obtained on the adsorption process for the different contaminants tested may be discussed in terms of the physicochemical properties of the material and thus, the adsorption mechanism of the Ce-Ti@Fe_3O_4 material could be hypothesized. On the one hand, the metal oxides NPs present a relatively negative charge (hydroxyl groups, OH-) on the oxide surface due to its hydrolysis in aqueous media. On the other hand, as discussed in this study, Ce-Ti@Fe_3O_4 NPs consist of Ce(III) ions and also it has a potential of +165 mV at pH 7. Thus, different sorption processes could take place for these contaminants tested. The adsorption mechanism for the anions could be attributed to two explanations: i) electrostatic attraction (i.e. chemisorption) [38] and ii) surface ion-exchange process (i.e. physisorption) [39]. Phosphate removal could be explained in

terms of the formation of cerium phosphate, as reported [40]. In this sense, we may consider that the presence of Ce(III) should be the driven force and thus, the adsorption takes place throughout electrostatic attraction. On the contrary, the OH^- groups on the adsorbent surface played a dominant role. Therefore, fluoride or nitrate removal may suffer a surface ion-exchange process based on the exchange of the OH^- group with the contaminant anion as already reported [39]. The OH^- on the surface of the NPs are present due to the nature of the media (e.g. pH, which is further evaluated). Thus, the physical mechanism could be expressed by Equations 5.1 and 5.2 [39]:

$$M^{n+} + nH_2O \rightarrow M(OH)_n \qquad \text{(Equation 5.1)}$$

$$M(OH)_n + xA^- \rightarrow M(OH)_{n-x}A_x + xOH^- \qquad \text{(Equation 5.2)}$$

Where M, n, x are the adsorbent's metal ion, valence of the metal ion and, number of mole of anion (A), respectively. Further studies are under investigation by our group.

On the other hand, it has been reported that heavy metal adsorption onto NPs is an emerging technique for the removal of these pollutants due to its suitable electric charge given by an adequate Z-potential [41]. However, Ce-Ti@Fe_3O_4 material shows a low removal for cadmium due to the positive charge of the NPs surface (positive potential) that contributes to a weak electrostatic interaction between cadmium and the OH- from the oxide surface of the NPs. Further, the efficiency of this material was demonstrated by comparing the equilibrium adsorption capacities with those reported in literature (Table 5.5). As indicated, Ce-Ti@Fe_3O_4 NPs show high efficiency for anions comparing to cations. Thus, further studies on the promising properties of this new material in terms of adsorption capacity should be focused on anionic pollutants dissolved in water.

Table 5.5. Adsorption capacities and removal efficiencies, values for contaminants removal from the literature.

Pollutant	Nanoadsorbents	Initial concentration, mg/L	Dose, g/L	Q_e, mg/g	Removal, %	Ref.
PO_4-P	Ce-Ti@Fe_3O_4	10	0.90	**11.10**	**99.90**	This work
	C100@Fe_3O_4	10	1.0	3.60	36.00	[7]
	$Al(OH)_3$	10	2.32	2.46	57.07	[42]
	Fe_3O_4	10	10.0	0.88	88.00	[43]
F	Ce-Ti@Fe_3O_4	10	0.97	**10.31**	**100.0**	This work
	$Al(OH)_3$	10	1.60	5.74	91.84	[44]
NO_3-N	Ce-Ti@Fe_3O_4	50	1.0	**42.50**	**85.00**	This work
	Rice straw activated carbon	50	1.0	9.00	18.00	[45]
Cd^{2+}	Ce-Ti@Fe_3O_4	10	1.0	4.53	45.28	This work
	Cork biomass powder	10	1.0	6.40	64.48	[46]

5.4. Conclusions

Magnetic core-shell Ce-Ti@Fe_3O_4 nanoparticles were designed and synthesized by incorporating magnetite into Ce-Ti oxide nanoparticles by mild experimental conditions. The resulting magnetic and core-shell nanomaterial exhibited a suitable composition, crystallinity and magnetic properties to be functional as adsorbent for the removal of inorganic pollutants from aqueous media. Remarkably, the adsorption capacity and removal efficiency at pH 7 for anionic contaminants such as nitrates, phosphates and fluoride was from 85 to 100 % under the experimental conditions. In comparison with other materials reported in literature, this nanomaterial as adsorbent is highly competitive, as it has high adsorption capacity and promising features and magnetic properties for recovering.

Further studies regarding to adsorption mechanism and effect of other parameters will be focusing in our future work

5.5. References

1. Tchounwou, P.B., et al., *Heavy Metal Toxicity and the Environment*, in *Molecular, Clinical and Environmental Toxicology: Volume 3: Environmental Toxicology*, A. Luch, Editor. 2012, Springer Basel: Basel. p. 133-164.
2. Bhatnagar, A., E. Kumar, and M. Sillanpää, *Fluoride removal from water by adsorption—A review.* Chemical Engineering Journal, 2011. **171**(3): p. 811-840.
3. Gehrke, I., A. Geiser, and A. Somborn-Schulz, *Innovations in nanotechnology for water treatment.* Nanotechnology, Science and Applications, 2015. **8**: p. 1-17.
4. Recillas, S., et al., *Chromium VI adsorption on cerium oxide nanoparticles and morphology changes during the process.* Journal of Hazardous Materials, 2010. **184**(1–3): p. 425-431.
5. Qu, X., P.J.J. Alvarez, and Q. Li, *Applications of nanotechnology in water and wastewater treatment.* Water Research, 2013. **47**(12): p. 3931-3946.
6. Sánchez, A., et al., *Ecotoxicity of, and remediation with, engineered inorganic nanoparticles in the environment.* TrAC Trends in Analytical Chemistry, 2011. **30**(3): p. 507-516.
7. Abo Markeb, A., et al., *Phosphate removal and recovery from water using nanocomposite of immobilized magnetite nanoparticles on cationic polymer.* Environmental Technology, 2016. **37**(16): p. 2099-2112.
8. Kumar, E., et al., *Defluoridation from aqueous solutions by nano-alumina: Characterization and sorption studies.* Journal of Hazardous Materials, 2011. **186**(2–3): p. 1042-1049.
9. Lee, G., et al., *Enhanced adsorptive removal of fluoride using mesoporous alumina.* Microporous and Mesoporous Materials, 2010. **127**(1–2): p. 152-156.

10. Teng, S.-X., et al., *Removal of fluoride by hydrous manganese oxide-coated alumina: Performance and mechanism.* Journal of Hazardous Materials, 2009. **168**(2–3): p. 1004-1011.
11. Maliyekkal, S.M., A.K. Sharma, and L. Philip, *Manganese-oxide-coated alumina: A promising sorbent for defluoridation of water.* Water Research, 2006. **40**(19): p. 3497-3506.
12. Tripathy, S.S., J.-L. Bersillon, and K. Gopal, *Removal of fluoride from drinking water by adsorption onto alum-impregnated activated alumina.* Separation and Purification Technology, 2006. **50**(3): p. 310-317.
13. Ghorai, S. and K.K. Pant, *Equilibrium, kinetics and breakthrough studies for adsorption of fluoride on activated alumina.* Separation and Purification Technology, 2005. **42**(3): p. 265-271.
14. Biswas, K., D. Bandhoyapadhyay, and U.C. Ghosh, *Adsorption kinetics of fluoride on iron(III)-zirconium(IV) hybrid oxide.* Adsorption, 2007. **13**(1): p. 83-94.
15. Chai, L., et al., *Sulfate-doped Fe3O4/Al2O3 nanoparticles as a novel adsorbent for fluoride removal from drinking water.* Water Research, 2013. **47**(12): p. 4040-4049.
16. Alonso, A., *Development of polymeric nanocomposites with enhanced distribution of catalytically active or bactericide nanoparticles*, in *Departament d'Enginyeria Química, Escola d'Enginyeria* 2012, Universitat Autònoma de Barcelona (UAB).
17. Zhang, C., et al., *Synthesis and properties of a magnetic core–shell composite nano-adsorbent for fluoride removal from drinking water.* Applied Surface Science, 2014. **317**: p. 552-559.
18. Chen, L., et al., *Fe—Ti oxide nano-adsorbent synthesized by co-precipitation for fluoride removal from drinking water and its adsorption mechanism.* Powder Technology, 2012. **227**: p. 3-8.
19. Kong, L., et al., *Novel Chemical Synthesis and Characterization of CeTi2O6 Brannerite.* Inorganic Chemistry, 2014. **53**(13): p. 6761-6768.
20. Yoshii, K. and H. Abe, *Magnetic behavior of CeTi1−xVxO3.* Journal of Alloys and Compounds, 2002. **343**(1–2): p. 199-203.

21. Jung, W.H., *Magnetic and transport properties of Ce2/3TiO2.981*. J. Phys.: Condens. Matter, 1998. **10**: p. 8553.
22. Laurent, S., et al., *Magnetic Iron Oxide Nanoparticles: Synthesis, Stabilization, Vectorization, Physicochemical Characterizations, and Biological Applications.* Chemical Reviews, 2008. **108**(6): p. 2064-2110.
23. Zhang, C., et al., *Synthesis and properties of a magnetic core–shell composite nano-adsorbent for fluoride removal from drinking water.* Applied Surface Science, 2014. **317**(0): p. 552-559.
24. Contreras, A.R., et al., *Potential use of CeO2, TiO2 and Fe3O4 nanoparticles for the removal of cadmium from water.* Desalination and Water Treatment, 2012. **41**(1-3): p. 296-300.
25. A, G., C. J, and J. D, *Standard Methods for the Examination of Water and Wastewater book.* American Public Health, Association, American Water Works, Association, Water Environment Federation, 2005. **21st edition**.
26. WHO, *Chemical fact sheets: fluoride. In: Guidelines for drinking-water quality (electronic resource): incorporation first addendum.* 2006. **1 third edition, Geneva**: p. 375-377.
27. Drinking-water, p.i., *Background document for development of WHO Guidelines for Drinking-water Quality.* WHO, 2004.
28. Meenakshi and R.C. Maheshwari, *Fluoride in drinking water and its removal.* Journal of Hazardous Materials, 2006. **137**(1): p. 456-463.
29. Yurekli, Y., *Removal of heavy metals in wastewater by using zeolite nano-particles impregnated polysulfone membranes.* Journal of Hazardous Materials, 2016. **309**: p. 53-64.
30. Zhang, J.L., R.S. Srivastava, and R.D.K. Misra, *Core−Shell Magnetite Nanoparticles Surface Encapsulated with Smart Stimuli-Responsive Polymer: Synthesis, Characterization, and LCST of Viable Drug-Targeting Delivery System.* Langmuir, 2007. **23**(11): p. 6342-6351.
31. Berry, L.G. and R.M. Thompson, *X-ray diffraction data for minerals.* Waverly Press: New York, 1962: p. 194.

32. Knappett, B.R., et al., *Characterisation of Co@Fe3O4 core@shell nanoparticles using advanced electron microscopy.* Nanoscale, 2013. **5**(13): p. 5765-5772.
33. Martos, M., et al., *Sol–Gel Synthesis of Tunable Cerium Titanate Materials.* European Journal of Inorganic Chemistry, 2008. **2008**(20): p. 3163-3171.
34. Annapurna, K., et al., *Blue emission spectrum of Ce3+:ZnO-B2O3-SiO2 optical glass.* Materials Letters, 2004. **58**(5): p. 787-789.
35. Huang, L., et al., *Luminescence properties of Ce3+ and Tb3+ doped rare earth borate glasses.* Journal of Alloys and Compounds, 2001. **316**(1–2): p. 256-259.
36. Xu, G.Q., et al., *Spectroscopic properties of Ce3+ doped silica annealed at different temperatures.* Journal of Luminescence, 2007. **124**(1): p. 151-156.
37. Cordoncillo, E., et al., *Blue emitting hybrid organic–inorganic materials.* Optical Materials, 2001. **18**(3): p. 309-320.
38. Pattanaik, M. and S.K. Bhaumik, *Adsorption behaviour of polyvinyl pyrrolidone on oxide surfaces.* Materials Letters, 2000. **44**(6): p. 352-360.
39. Zhang, K., et al., *Wide pH range for fluoride removal from water by MHS-MgO/MgCO3 adsorbent: Kinetic, thermodynamic and mechanism studies.* Journal of Colloid and Interface Science, 2015. **446**: p. 194-202.
40. Ko, Y.G., et al., *CeO2-covered nanofiber for highly efficient removal of phosphorus from aqueous solution.* Journal of Hazardous Materials, 2016. **307**: p. 91-98.
41. Achla Kaushal and S.K. Singh, *Removal of heavy metals by nanoadsorbents: A review*. Journal of Environment and Biotechnology Research, 2017. **6**(1): p. 96-104.
42. Hsu, P.H. and D.A. Rennie, *REACTIONS OF PHOSPHATE IN ALUMINUM SYSTEMS.: I. ADSORPTION OF PHOSPHATE BY X-RAY AMORPHOUS "ALUMINUM HYDROXIDE"*. Canadian Journal of Soil Science, 1962. **42**(1): p. 197-209.
43. Le, G.T.T. and P. Sreearunothai, *Magnetic Particles for Phosphorus Adsorption in Simulated Phosphate Solution.* 4th International Conference on Informatics, Environment, Energy and Applications (IPCBEE), 2015. **82**.

44. Shimelis, B., F. Zewge, and B.S. Chandravanshi, *REMOVAL OF EXCESS FLUORIDE FROM WATER BY ALUMINUM HYDROXIDE.* Bull. Chem. Soc. Ethiop., 2006. **20**(1): p. 17-34.
45. Yakout, S.M. and A.A. Mostafa, *Equilibrium Isotherm Studies for Removal Nitrate from Aqueous Solution as Hazardous Anion in Animal System.* Journal of Animal and Veterinary Advances, 2014. **13**: p. 728-731.
46. Krika, F., N. Azzouz, and M.C. Ncibi, *Adsorptive removal of cadmium from aqueous solution by cork biomass: Equilibrium, dynamic and thermodynamic studies.* Arabian Journal of Chemistry.

Chapter 6

Adsorption process of fluoride from drinking water with magnetic core-shell Ce-Ti@Fe_3O_4 and Ce-Ti oxide nanoparticles

The results presented in this chapter have been published in Science of the Total Environment journal:

"Ahmad Abo Markeb, Amanda Alonso, Antoni Sánchez, Xavier Font. Adsorption process of fluoride from drinking water with magnetic core-shell Ce-Ti@Fe_3O_4 and Ce-Ti oxide nanoparticles. Science of the Total Environment, 2017, 598: p. 949-958".

6.1. Introduction

Fluoride contamination could be found in ground and surface water [1, 2] as well as in wastewater from fluoride chemical industries [3, 4]. Fluoride presents hazardous effects if it exceeds 1.5 mg/L in water [5-7] leading to various diseases [8-10]. The main source of these effects is from fluoride contaminated drinking water, which leads to 65% of endemic fluorosis diseases over the world [11, 12]. For example, contents in drinking water of 4.8 and 1.7 mg/L in Greece and India, respectively, have been reported [13-15]. Therefore, drinking water defluoridation is necessary to prevent human illness [16].

Various metal oxides and hydroxides of aluminium, iron, zirconium, magnesium, chromium and manganese ions based nanoparticles (NPs) had been reported [17-20] for fluoride removal from water [21]. Although bimetallic or mixed oxides such as Mn-Ce, Al-Ce, Zr-Mn and ceramic adsorbents were also studied for fluoride removal, some of these materials present disadvantages in terms of pH range, high cost and low adsorption capacity. [22-26]. Thus, Zhang et al. [27], used magnesium oxide nanomaterial for fluoride removal and it showed high adsorption capacity (about 300 mg/g) but regeneration was reported not to be favoured. V. Sivasankar et al. [20], reported low adsorption capacity (9.02 mg/g) for fluoride removal from drinking water utilizing manganese dioxide based nanomaterial compared to previously reported results. Using an Al-Ce hybrid nanomaterial, Liu et al. [26] found high adsorption capacity of fluoride (91.4 mg/g), but slow kinetics to reach the equilibrium. However, to our knowledge, no studies about the reusability of the adsorbents have been reported for the reported materials [23, 26]. In this sense, the use of magnetic NPs for pollutants removal may provide efficient, rapid and easy separation, and especially reusability. On the other hand, the hydrous Ce oxide, as rare earth metal, is reported to be more effective material for fluoride removal (46.84 mg/g) compared to other metals, although it is not useful for drinking water treatment due to its toxicity [28]. Furthermore, titanium based nanomaterials have also a great interest for fluoride removal with adsorption capacities that ranged from 15 to 47 mg/g [29, 30]. Therefore, mixing rare earth metals (i.e. Ce) with low-cost metals (i.e. Fe) could be advantageous for high adsorption capacities at neutral pH medium, improving the separation of the adsorbent by

magnetism as well as avoiding Ce-toxicity.

All in all, Chapter 5 showed in the synthesis of a new adsorbent based on magnetic core-shell Ce-Ti@Fe_3O_4 NPswhich presented promising properties in terms of magnetism, crystalline structure and adsorption for some inorganic water contaminants [31]. The core-shell, Ce-Ti@Fe_3O_4, NPs exhibit 100 % removal of fluoride, and phosphate as well as 85 % removal of nitrate. So, in the present Chapter, Ce-Ti oxide and Ce-Ti@Fe_3O_4 NPs were synthesized and compared as adsorbents for fluoride ion removal from aqueous solution. Adsorption kinetics, isotherms and the effect of different parameters (i.e. pH and temperature) in the adsorption capacity of the materials were studied. Also, the use of the Ce-Ti@Fe_3O_4 NPs for the treatment of real drinking water was performed. Further, the reuse of the Ce-Ti@Fe_3O_4 adsorbent was evaluated.

6.2. Materials and methods

6.2.1. Materials

Iron (II) chloride ($FeCl_2$, 98 %), iron (III) chloride hexahydrate ($FeCl_3 \cdot 6H_2O$, ≥ 99 %), sodium fluoride (NaF, ≥ 99 %), titanium chloride ($TiCl_4$, ≥ 99.98 %), cerium nitrate hexahydrate ($Ce(NO_3)_3.6H_2O$, ≥ 99 %), and ammonia solution were purchased from Sigma-Aldrich, Spain. Sodium hydroxide pellets (NaOH), was purchased from Merck. Hydrochloric acid (HCl), and cetyltrimethylammonium bromide (CTAB) were purchased from Panreac, SA. All the chemicals were of analytical grade or higher, and all solutions were prepared with Milli-Q water and filtered using 0.45 µm Nylon membrane filter.

6.2.2. Synthesis of the bimetal oxide and core-shell NPs

6.2.2.1. Preparation of Ce-Ti bimetal oxide NPs

This synthetic procedure for Ce-Ti oxide NPs was adapted from similar works about core-shell magnetic Ti-NPs synthesis [32]. Briefly, in this work, $TiCl_4$ and $Ce(NO_3)_3.6H_2O$ were dissolved in 100 mL of Milli-Q water to reach Ti^{4+} and Ce^{3+}

concentrations of 25 mM each and mixed for 30 min at room temperature. Then 12.5 % NH_3 solution was slowly added dropwise till pH 7.0 was reached. Then, the Ce-Ti NPs produced were washed with ultrapure water, centrifuged at 6000 rpm for 15 min and dried at 80 °C for 24 h.

6.2.2.2. Preparation of Ce-Ti oxide nanoparticles and Ce-Ti@Fe_3O_4 nanoparticles

The Ce-Ti@Fe_3O_4 NPs were prepared by the in-situ co-precipitation method reported by our research group [31]. Details of the magnetic core/shell NPs synthesis are explained in Chapter 5 (Sections 5.2.2.1 and 5.2.2.2).

6.2.3. Characterization of the nanomaterials

Inductively Coupled Plasma Optical Emission Spectrometry (ICP-OES) was used for the metal concentration analysis of both synthesized nanomaterials. The detailed sample preparation for ICP-OES analysis is in Chapter 3 (Section 3.1.1). In addition, treated water sample after the five cycles of adsorption-desorption process was analyzed by ICP-MS to determine the cerium release into the effluent of water. Also, High-Resolution Transmission Electron Microscopy (HRTEM) coupled with Energy-Dispersive Spectroscopy (EDS), and Electron Diffraction (ED) Pattern were acquired using a JEM-2011/ JEOL microscope operated at 200 kV and equipped with an INCA X-MAX detector. HRTEM was used to characterize the morphology and sizes of both Ce-Ti@Fe_3O_4 and Ce-Ti oxide NPs and, EDS and ED were used to analyze the composition and the crystalline structure. The detailed sample preparation is explained in Chapter 3 (Section 3.1.5). The morphology of the NPs was determined by Scanning Transmission Electron Microscopy (STEM) coupled with high-angle annular dark field (HAADF) detector and Electron Energy Loss Spectra (EELS). Detailed of the sample preparation is in Chapter 3 (Section 3.1.7).

6.2.4. Adsorption and desorption experiments procedure

For all the experiments, batch adsorption tests were used to determine the fluoride adsorption efficiency of both synthesized NPs. A dose of adsorbent (W) (g/L) was added into a conical flask containing fluoride solution with an initial fluoride concentration (C_0). Typically, 25 mg of the adsorbent was added into the conical flask, which contains 25 mL of the fluoride ion solution, C_0. Depending on the experiment, pH of the solution was adjusted using NaOH or HCl, both at 0.1 M. The flask was shaken (200 rpm) at 25 °C using a thermostatic shaker. Residual fluoride concentration in the solution, C_e, was determined by ionic chromatography by using ICS-2000 (Dionex) system. The detailed analysis using IC was explained in Chapter 3 (Section 3.2.1). Equilibrium adsorption capacity, Q_e, of the adsorbent was calculated according to Equation 3.1 (Chapter 3).

6.2.4.1. Adsorption isotherm

Adsorption isotherm experiments of both synthesized Ce-Ti oxides and Ce-Ti@Fe_3O_4 NPs were performed at different concentrations of fluoride from 1 to 500 mg/L at pH 7 with an adsorbent amount of 1 g/L and treated, as described in Section 6.2.4, for 60 min, to assure to reach the equilibrium. Then, residual fluoride concentrations were measured after filtration using 0.45 µm Nylon membrane filter. All experiments were performed in triplicate. Detailed information of the adsorption isotherm models is provided in Chapter 3 (Section 3.4).

6.2.4.2. Fluoride desorption procedure

Different studies proved that the most effective desorbing reagent for regeneration of the adsorbent is the NaOH solution [33, 34]. The desorption experiments were performed after adsorption of 10 mg/L of fluoride using 1.0 g/L of Ce-Ti@Fe_3O_4 NPs for 60 min at pH 7.0, by shaking the adsorbent at 200 rpm using two different concentrations

and volumes of NaOH desorbing solution: 25 mL of 0.5 M NaOH, and 5 mL of 0.1 M NaOH, at intervals of time of 2, 4, 6, 8, and 12 h. Then, the fluoride concentrations of the desorbing solutions were analyzed as previously mentioned.

6.2.5. Reusability of the Ce-Ti@Fe_3O_4 NPs as adsorbent and characterization

Under the optimized conditions for desorption, five cycles of the adsorption-desorption processes were performed for evaluating the reusability of the synthesized NPs for fluoride removal and its recovery. The composition, morphology, and size of the Ce-Ti@Fe_3O_4 NPs were analyzed after its use for five adsorption-desorption cycles and compared to the original material (sample preparation as explained in Chapter 3, Section 3.1). TEM images were obtained to analyze the size and NPs distribution and EELS spectra were obtained after the use of Ce-Ti@Fe_3O_4 NPs for 5 cycles of adsorption-desorption of fluoride. Moreover, the possibility of Ce releases from the Ce-Ti@Fe_3O_4 NPs after its use was determined by Inductively Coupled Plasma Mass Spectrometry (ICP-MS) either in the treated water or in the regenerating solution, after each adsorption-desorption cycle. The detailed sample preparation and analysis for ICP-MS analysis is explained in Chapter 3 (Section 3.1.2).

6.2.6. pH effect on the adsorption capacity

The effect of the pH value in the media for fluoride adsorption was conducted using 10 mg/L initial fluoride concentration with 1 g/L of Ce-Ti@Fe_3O_4 adsorbent. Then, each conical flask at fixed pH of 5, 7, 9 and 11 was shaken and the adsorption capacity was calculated. All experiments were performed in triplicates.

6.2.7. Effect of temperature on the fluoride adsorption and estimation of the thermodynamic parameters

The effect of the temperature on the fluoride adsorption onto Ce-Ti@Fe_3O_4 adsorbent was studied at 20, 25, 30, 35, and 40 °C using 30 mg/L of fluoride initial concentration at pH 7 with 1 g/L adsorbent dose, 60 min contact time, and 200 rpm shaking. The adsorption capacity was calculated in all the cases. To estimate the effect of temperature on the adsorption of fluoride onto Ce-Ti@Fe_3O_4 NPs, the free energy Gibbs change ($\Delta G°$), enthalpy change ($\Delta H°$), and entropy change ($\Delta S°$) were determined as previously reported [35]. In this method, the thermodynamic parameters were obtained directly from the plot of $\log(Q_e/C_e)$ versus 1/T as presented in Equations 6.1 and 6.2.

$$\ln\left(\frac{Q_e}{C_e}\right) = \left(\frac{\Delta H°}{R}\right) - \left(\frac{\Delta S°}{R}\right)\frac{1}{T} \qquad \text{(Equation 6.1)}$$

$$\Delta G° = \Delta H° - T\Delta S° \qquad \text{(Equation 6.2)}$$

Where Q_e/C_e is the adsorption affinity; $\Delta G°$, $\Delta H°$ and $\Delta S°$ are the change in free energy, enthalpy, and entropy respectively. All experiments were performed in triplicates.

6.2.8. Fluoride removal from spiked drinking water by using Ce-Ti@Fe_3O_4 NPs

To determine the effect of the presence of other ions on the removal of fluoride, drinking tap water was spiked only with 10 mg/L of fluoride. Tap water samples were obtained from the Universitat Autònoma de Barcelona (Spain). Drinking tap water first was turned on a steady stream with flow 500 mL/min and run for 10 min to remove any stagnant in the plumbing network. The adsorption experiment was carried out at pH 7.0 in 250 mL flasks containing 0.10 g Ce-Ti@Fe_3O_4 adsorbents per 100 mL of spiked water, at 25 and 30°C, and shaking at 200 rpm for 60 min.

6.2.9. Statistical data analysis

Statistical analysis was performed using the Tukey's method based on one factor ANOVA at the 5% confidence level using SPSS 15.0.1 (SPSS Inc., USA). Statistically significant differences were reported when the probability of the results, assuming the null hypothesis (p) value is less than 0.05.

6.3. Results and discussion

6.3.1. Characterization of the synthesized nanomaterials

The metal content of the synthesized Ce-Ti oxides NPs was analyzed using ICP-OES. The results showed the presence of 84.99 ± 5.05 mg_{Ti}/g_{NP} (1.8 $mmol_{Ti}/g_{NP}$) and 106.93 ± 3.54 mg_{Ce}/g_{NP} (0.8 $mmol_{Ce}/g_{NP}$) at the synthesis conditions. This means that the synthesized nanomaterial contains the desired metals and that the molar ratio of Ce:Ti was 1:2. Comparing with the previous characterized Ce-Ti@Fe_3O_4 nanomaterial, Ce:Ti:Fe molar ratio was 1:2:1 [31]. Thus, the incorporation of Fe into the Ce-Ti oxide NPs did not affect the metals molar ratio in the final Ce-Ti@Fe_3O_4 adsorbent.

Further, morphological characterization of the Ce-Ti oxides was also studied. Figure 6.1 illustrates the TEM images coupled with EDS and SAED pattern for Ce-Ti oxide NPs. As shown in Figure 6.1a, Ce-Ti oxide NPs size is estimated to be about 1-2 nm, much smaller than the Ce-Ti@Fe_3O_4 NPs (10 – 15 nm) probably due to the addition of Fe_3O_4 core in the structure that induces an increase of the total NPs size. The SAED pattern for Ce-Ti oxides NPs (Figure 6.1b) exhibit no crystal orientation (as no bright dots or rings are observed) and hence, amorphous structure [36]. Conversely, the SAED pattern for Ce-Ti@Fe_3O_4 NPs sample (Figure 6.2 and 6.3), exhibited a poly-nanocrystalline structure which corresponds to magnetite NPs [37].

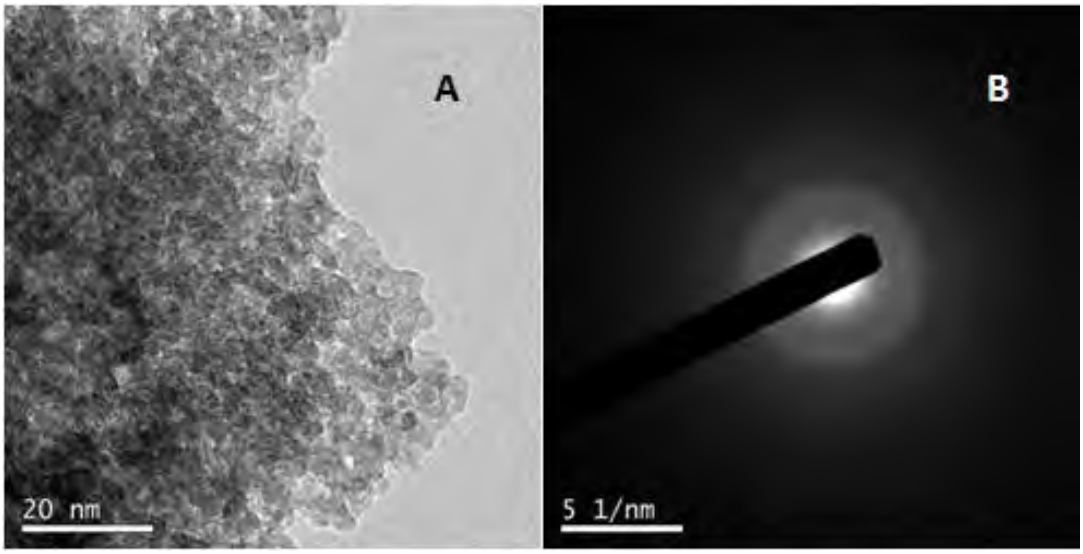

Figure 6.1. (A) HRTEM image and, (B) SAED pattern of Ce-Ti oxide NPs.

The morphological characterization of the Ce-Ti@Fe_3O_4 NPs is shown in Figure 6.2. Figure 6.2 (a) corresponds to a TEM image from which the size if the NPs is shown and quantified within the range of 10 – 15 nm. The SAED pattern for Ce-Ti@Fe_3O_4 NPs, Figure 6.2 (b), suggested that the core-shell NP is based on nanocrystals [38].

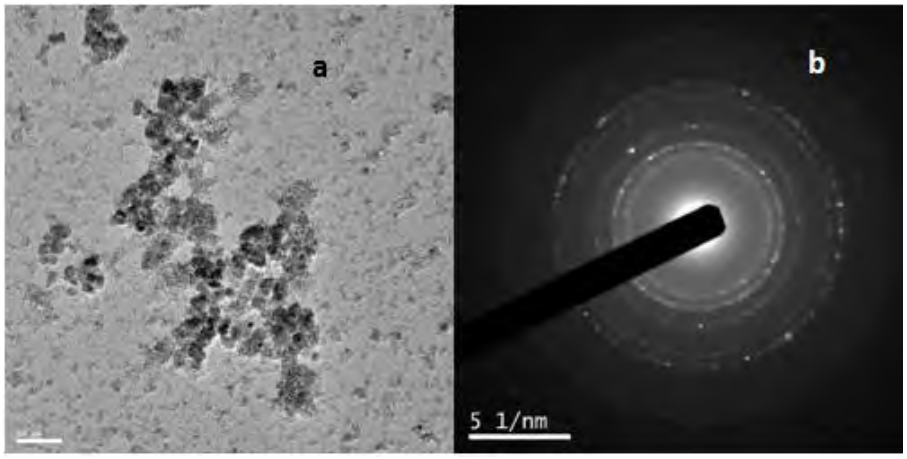

Figure 6.2. (a) TEM image and (b) SAED pattern, of Ce-Ti@Fe_3O_4 NPs.

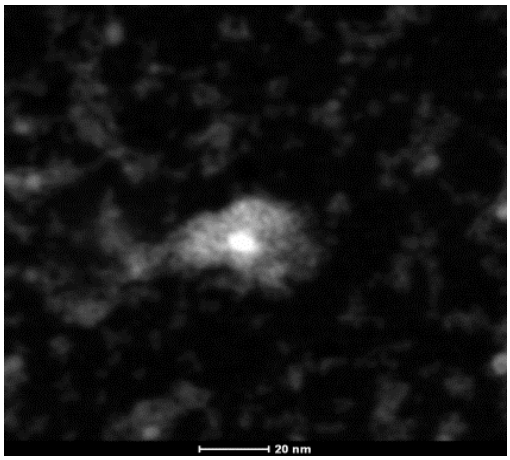

Figure 6.3. STEM-HAADF image of the core-shell Ce-Ti@Fe_3O_4.

6.3.2. Fluoride adsorption on Ce-Ti@Fe_3O_4 adsorbents

The time required to achieve the equilibrium for the fluoride adsorption was determined at 10 and 100 mg/L of fluoride and an adsorbent dose of 1 g/L of Ce-Ti@Fe_3O_4 NPs at pH 7 and 25°C. The equilibrium time was reached at 0.5 min for 10 mg/L and at 15 min for 100 mg/L of initial fluoride concentration. These results showed a high adsorption rate for the synthesized nanomaterial. Therefore, to assure the completed adsorption of the contaminant, the adsorption time was fixed to be 60 min for the rest of the batch experiments. The fast kinetics of this novel adsorbent could be attributed to a large number of available adsorption sites on the Ce-Ti@Fe_3O_4 adsorbent surface. Moreover, the presence of Ce in the Ce-Ti@Fe_3O_4 NPs enhanced the adsorption time compared with the reported one Fe-Ti@Fe_3O_4 [32] under the same conditions. Further explanation about the improved adsorption mechanism of the Ce-Ti@Fe_3O_4 NPs is following discussed.

6.3.3. Adsorption isotherms and modeling for the adsorption mechanism

Maximum adsorption capacity was estimated from the adsorption isotherm models by performing the experiments over the fluoride initial concentration range until saturation at pH 7. A broad range of initial fluoride concentration (1 to 500 mg/L) was selected to ensure saturation and allow isotherm fitting. Figure 6.4 corresponds to the adsorption isotherms for both, Ce-Ti oxides and Ce-Ti@Fe_3O_4 NPs. It is shown that the adsorption capacities of both nanomaterials increased with increasing fluoride concentrations, and maximum values were achieved at the equilibrium fluoride concentration above 100 mg/L.

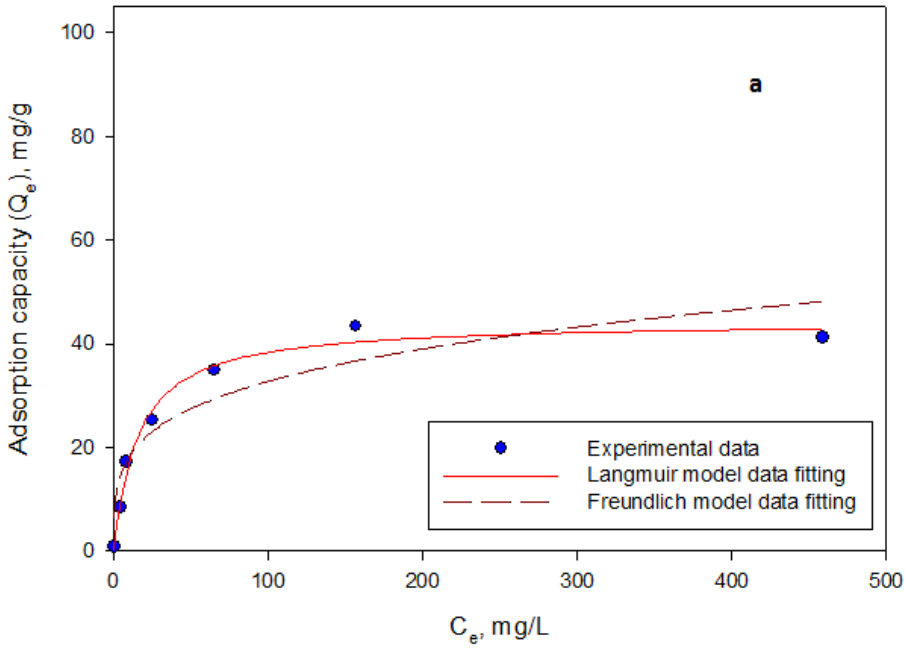

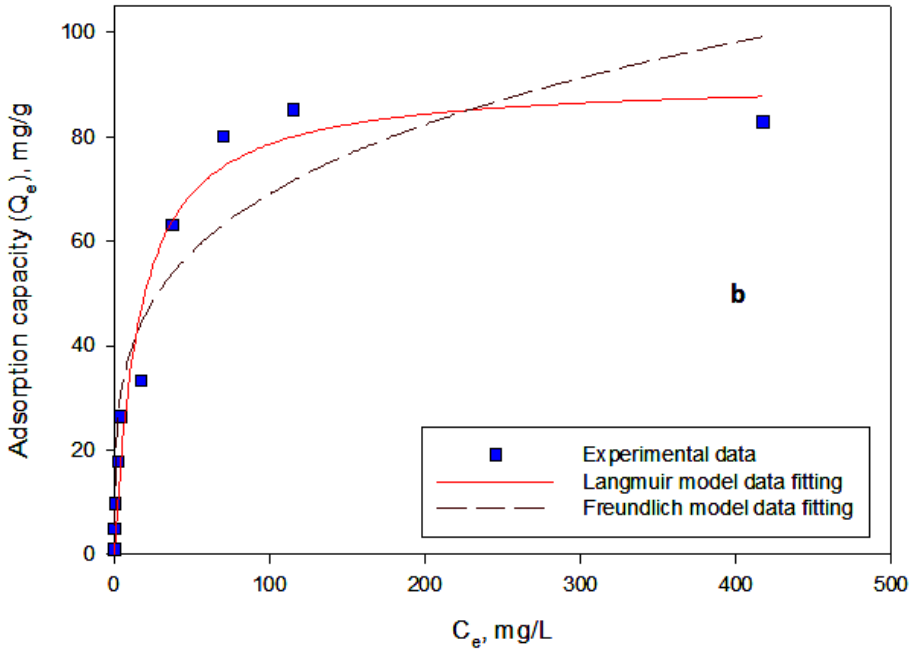

Figure 6.4. Adsorption isotherms and experimental data fitting using Langmuir and Freundlich models for fluoride removal using: (a) Ce-Ti oxide, and (b) Ce-Ti@Fe_3O_4 NPs [adsorbent dose 1 g/L, 60 min shaking at 200 rpm at room temperature].

Furthermore, data were fitted to both Langmuir and Freundlich models (Table 6.1). The Langmuir model seems to be more suitable for fluoride adsorption than the Freundlich one as Langmuir model regression coefficient (R^2) was higher than 0.95. However, it is possible to obtain mechanistic information on the adsorption process from both models. The maximum monolayer adsorption capacity (Q_m) obtained for Ce-Ti@Fe_3O_4 NPs was 91.04 mg/g, higher than for Ce-Ti oxide NPs (Q_m = 44.37 mg/g). The Freundlich adsorption intensity parameter (n values) were higher than 2, also supporting the favorable adsorption of fluoride and meaning that the sorption process is mainly physical rather than chemical.

Table 6.1. Langmuir, Freundlich, and Dubinin–Radushkevich isotherms for fluoride adsorption onto Ce-Ti oxides and Ce-Ti@Fe_3O_4 NPs

Isotherm models		**Nanomaterial**	
		Ce-Ti@Fe_3O_4	**Ce-Ti oxide**
Langmuir	**Q_m (mg/g)**	91.04	44.37
	K_L (L/mg)	0.063	0.064
	R^2	0.952	0.986
Freundlich	**K_F ($mg^{1-(1/n)}L^{1/n}g^{-1}$)**	21.543	10.214
	n	3.95	3.95
	R^2	0.895	0.877
D-R	**Q_m (mg/g)**	83.86	37.14
	K_{DR} (mol^2/kJ^2)	4.77e-5	8.05e-6
	R^2	0.887	0.895
	E (kJ/mol)	0.102	0.250

The calculated parameter of the energy, E, of the Dubinin–Radushkevich isotherm is indicated in Table 6.1. The E values were 0.10 and 0.25 kJ/mol for Ce-Ti@Fe_3O_4 and Ce-Ti oxides adsorbents, respectively, which proved that the interaction between the fluoride and the surface of the nanomaterials is physical [39, 40]. The lower E value for Ce-Ti@Fe_3O_4 means that it needs lower energy for adsorbing F^- than Ce-Ti oxides NPs. It confirms its higher adsorption capacity. Fluoride removal may suffer a surface ion-exchange process as physisorption based on the exchange of the hydroxyl ions (OH^-) from the surface of the adsorbent with F^- [31]. The OH^- on the surface of the NPs is present due to the nature of the media (e.g. pH) [41]. According to [27], the physical mechanism could be expressed by Equations 6.3 and 6.4:

$$M^{n+} + nH_2O \rightarrow M(OH)_n \quad \text{(Equation 6.3)}$$

$$M(OH)_n + xF^- \rightarrow M(OH)_{n-x}F_x + xOH^- \quad \text{(Equation 6.4)}$$

Where M, n, and x are the adsorbent's metal ion, the valence of the metal ion and, the number of moles of fluoride, respectively.

Further, it is worth to mention that the crystalline structure of the adsorbents plays an important role in the adsorption capacity. As shown, the crystalline Ce-Ti@Fe_3O_4 material showed higher adsorption capacity than the amorphous Ce-Ti oxide due to the higher developed crystalline faces of the NPs which could increase the ability of the surface to adsorb [42]. Fluoride adsorption capacity using the Ce-Ti oxides and Ce-Ti@Fe_3O_4 NPs is highly competitive in comparison with other adsorbents from literature (Table 6.2). The Q_{max} of the adsorbents in this study is similar to the best ones reported so far. However, those materials present some disadvantages in comparison with the Ce-Ti@Fe_3O_4 adsorbent. For instance, Mn–Ce oxide and the Fe_3O_4@$Al(OH)_3$ adsorbents reached the equilibrium after 3 h and 60 min, respectively [23, 35]. The new developed nanomaterial, Ce-Ti@Fe_3O_4, presents promising properties in terms of adsorption capacity, adsorption rate, as well as magnetic properties and, consequently, Ce-Ti@Fe_3O_4 nanomaterial was used for the rest of the experiments.

Table 6.2. Comparison of adsorption capacity of fluoride on different nanomaterials from this work and the literature. "Maximum adsorption capacity" indicates that the value of Adsorption capacity was obtained through an isotherm modelling.

Adsorbents	**Adsorption capacity (mg/g)**	**sorbent/ sorbate ratio**	**Adsorption conditions**	**Reference**
Fe_3O_4@ZrO_2	158.60	Maximum adsorption capacity	deionized water, 25 °C, adsorption time 1 h, pH 2.5, adsorbent dose 1 g/L	[43]
Ce-Ti@Fe_3O_4 powder	91.04	Maximum adsorption capacity	deionized water, 25 °C, adsorption time 1 h, pH 7.0, adsorbent dose 1.0 g/L	This work
Fe_3O_4@$Al(OH)_3$	88.48	Maximum adsorption capacity	deionized water, 25 °C, adsorption time 1 h, pH 6.5, adsorbent dose 1 g/L	[35]
Powder Mn-Ce oxide	79.50	Maximum adsorption capacity	deionized water, 25 °C, adsorption time 24 h, pH 6.0, adsorbent dose 0.01 g/L	[23]
Ce-Fe bimetal oxides	60.97	Maximum adsorption capacity	deionized water, 20 °C, adsorption time 1 h, pH 5.5, adsorbent dose 0.5 g/L	[44]
Fe-Ti@Fe_3O_4	57.22	Maximum adsorption capacity	deionized water, 25 °C, adsorption time 12 h, adsorbent dose 1 g/L	[32]
Iron-doped titanium oxide	53.22	Maximum adsorptio	deionized water, 25 °C, adsorption	[30]

		n capacity	time 12 h, pH 5.0, adsorbent dose 0.5 g/L	
Fe-Ti bimetallic oxide	47.00	Maximum adsorption capacity	deionized water, 25 °C, adsorption time 12 h, pH 5.0, adsorbent dose 0.5 g/L	[30]
Ti-La hybrid	46.60	Maximum adsorption capacity	deionized water, 25 °C, adsorption time 12 h, pH 6.0, adsorbent dose 0.01 g/L	[29]
Granular Mn-Ce oxide	45.50	Maximum adsorption capacity	deionized water, 25 °C, adsorption time 24 h, pH 6.0, adsorbent dose 0.01 g/L	[23]
Ce-Ti oxide powder	44.37	Maximum adsorption capacity	deionized water, 25 °C, adsorption time 1 h, pH 7.0, adsorbent dose 1.0 g/L	This work
Fe-Ti/Fe_3O_4	41.80	Maximum adsorption capacity	deionized water, 25 °C, adsorption time 12 h, pH 7.0, adsorbent dose 1.0 g/L	[45]
Ti-Ce hybrid	30.60	Maximum adsorption capacity	deionized water, 25 °C, adsorption time 12 h, pH 6.0, adsorbent dose 0.01 g/L	[29]
$TiOH_4$	30.40	Maximum adsorption capacity	deionized water, 25 °C, adsorption time 12 h, pH 5.0, adsorbent dose 2.0 g/L	[46]

CeO_2-TiO_2/SiO_2	21.40	Maximum adsorption capacity	deionized water, 35 °C, adsorption time 1 h, pH 4.0, adsorbent dose 5.0 g/L	[47]
Fe-Al	17.70	Maximum adsorption capacity	deionized water, 30 °C, adsorption time 12 h, pH 6.8, adsorbent dose 0.1 g/L	[48]
Fe-Cr	16.34	Maximum adsorption capacity	deionized water, 25 °C, adsorption time 1.5 h, pH 6.5, adsorbent dose 0.1 g/L	[49]
Fe-Sn	10.50	Maximum adsorption capacity	deionized water, 30 °C, adsorption time 2 h, pH 6.4, adsorbent dose 0.1 g/L	[50]
Fe-Zr	8.20	Maximum adsorption capacity	deionized water, 30 °C, adsorption time 12 h, pH 6.8, adsorbent dose 0.1 g/L	[48]
Aluminium modified zeolite tuff	3.24	Maximum adsorption capacity	deionized water, 30 °C, flow rate 1 mL/min, bed height 4 cm, pH 6.2, adsorbent dose 1 g/L	[51]
Fe_3O_4	0.30	20.00	deionized water, 25 °C, adsorption time 12 h, adsorbent dose 1 g/L	[32]

6.3.4. Evaluation of the fluoride recovery and the reusability of the Ce-Ti@Fe_3O_4 NPs

The efficiency of the adsorbent is demonstrated by performing adsorption-desorption cycles of 10mg/L of F^- for evaluating the reuse and regeneration of the adsorbent. Ce-Ti@Fe_3O_4 was separated from the treated solution by a magnet [31]. In this work, it was shown that the recovery percentage of fluoride was affected by desorption time (ANOVA analysis, $p < 0.05$). As shown in Figure 6.5, by using 5 mL of 0.1 M NaOH, it was obtained the highest recovery percentage of 98.51 % at 12 hours of desorption time (Figure 6.5b) which were the chosen desorption conditions for each regeneration step due to low concentration and volume of NaOH. However, the little decrease of the recovery percentage of fluoride at 8 h desorption using 0.5 M NaOH could be attributed to a saturation of the fluoride recovery after 6 h desorption time.

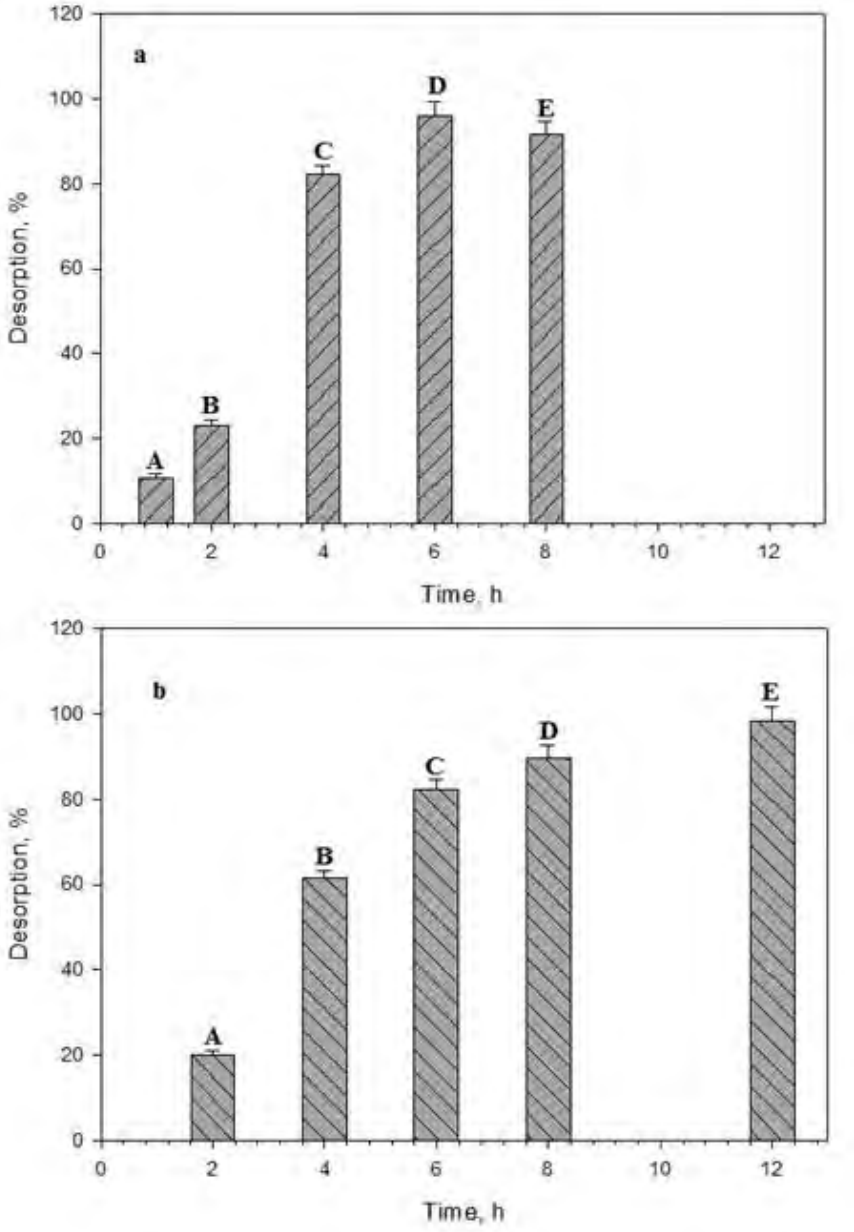

Figure 6.5. The effect of the desorption time for the efficient fluoride desorption (%); (a) 25 mL of 0.5M NaOH and, (b) 5 mL of 0.1M NaOH, using 1 g/L of Ce-Ti@Fe_3O_4 nanomaterial, and shaking at 200 rpm. Statistical data analysis using ANOVA was illustrated by letters A, B, C, D, and E.

The reusability of the Ce-Ti@Fe_3O_4 adsorbent was carried out by performing five consecutive adsorption-desorption cycles under both optimal experimental conditions were obtained for both processes. Thus, Figure 6.6 illustrates the adsorption capacities values of

the Ce-Ti@Fe_3O_4 adsorbent and the fluoride recovery versus the cycle's number. It is shown that the fluoride recovery % is high (> 90%) for all the cycles tested and also in comparison with other reported works, where the maximum fluoride recovery has been up to 86.35 % [27]. Also, a very little decrease in the recovery exists from the first to the fifth cycle to be from 98.51 to 92.97% that could be attributed to the change of the morphology of the NPs or because of the metal release from the adsorbent during the regeneration process, as it is following discussed. However, the high removal % in all the cycles was demonstrated.

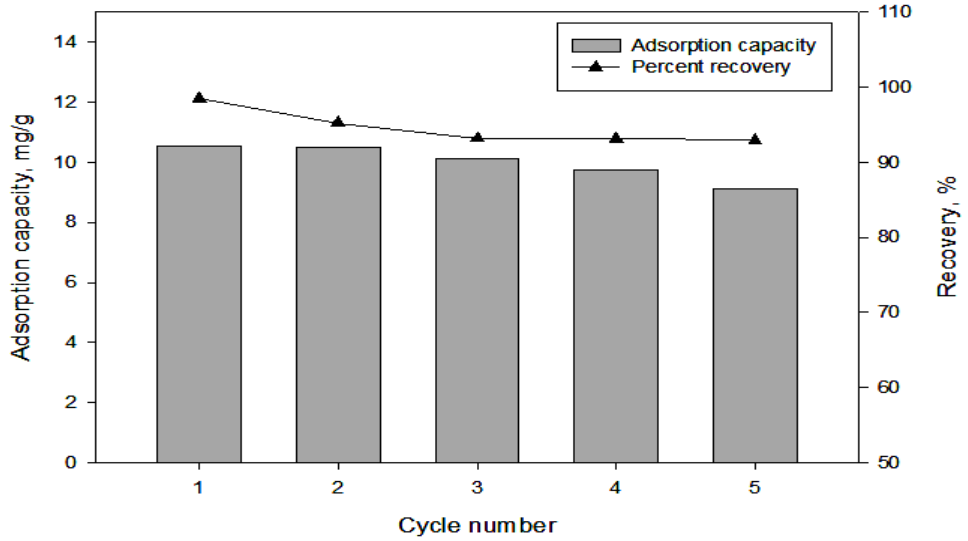

Figure 6.6. Fluoride adsorption capacities (mg/g) and fluoride recovery (%) for the use of Ce-Ti@Fe_3O_4 NPs at different adsorption-desorption cycles (up to 5).

6.3.5. Characterization of the Ce-Ti@Fe_3O_4 NPs as adsorbent after reuse

Figure 6.7a illustrates the TEM image of the corresponding Ce-Ti@Fe_3O_4 adsorbent after its use for five cycles of the adsorption-desorption process. It is shown an aggregation of the NPs in comparison with the size of the original NPs, leading to an increase of the size and hence, a decrease on the adsorption capacity. In this sense, Figure 6.7b showed the SAED pattern of the adsorbent and it showed a decrease in the crystalline phases in

comparison with the original adsorbent (Figure 6.2). As discussed in section 6.3.1, the loss of the crystalline structure may affect the adsorption efficiency of the nanomaterial.

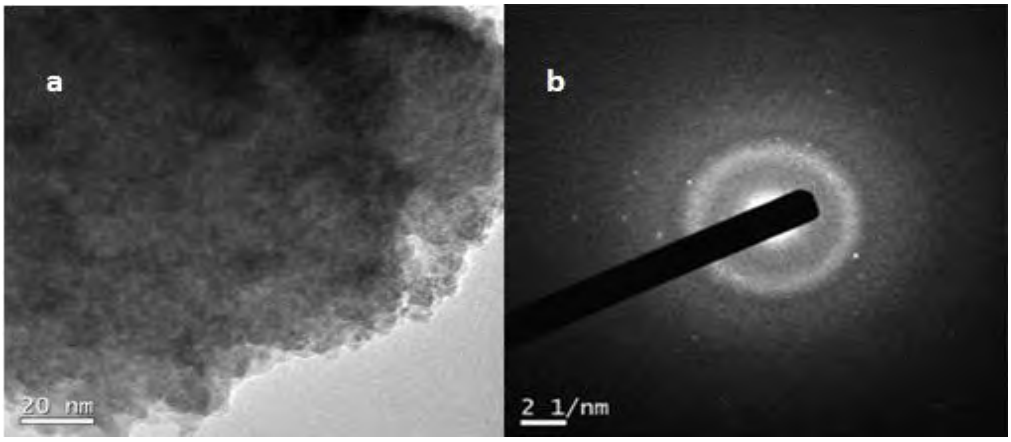

Figure 6.7. TEM image (a) and, ED pattern (b) of the Ce-Ti@Fe_3O_4 nanomaterial after five adsorption-desorption cycles under the optimal experimental conditions used for each process.

Furthermore, the core-shell structure of the original Ce-Ti@Fe_3O_4 nanomaterial is shown in Figure 6.3. Here, the STEM-EELS technique was used to characterize the NPs structure after it is used and a slight modification of the core-shell structure, due to its aggregation, is shown (HAADF image, Figure 6.8a). Moreover, the elemental analysis of the three metals was proved using STEM-based EDS (Figure 6.8b and 6.8c) and thus, the metal composition remains stable in the NPs' structure. Anyway, the nanomaterial still presents magnetic properties and high adsorption activity after its reuse.

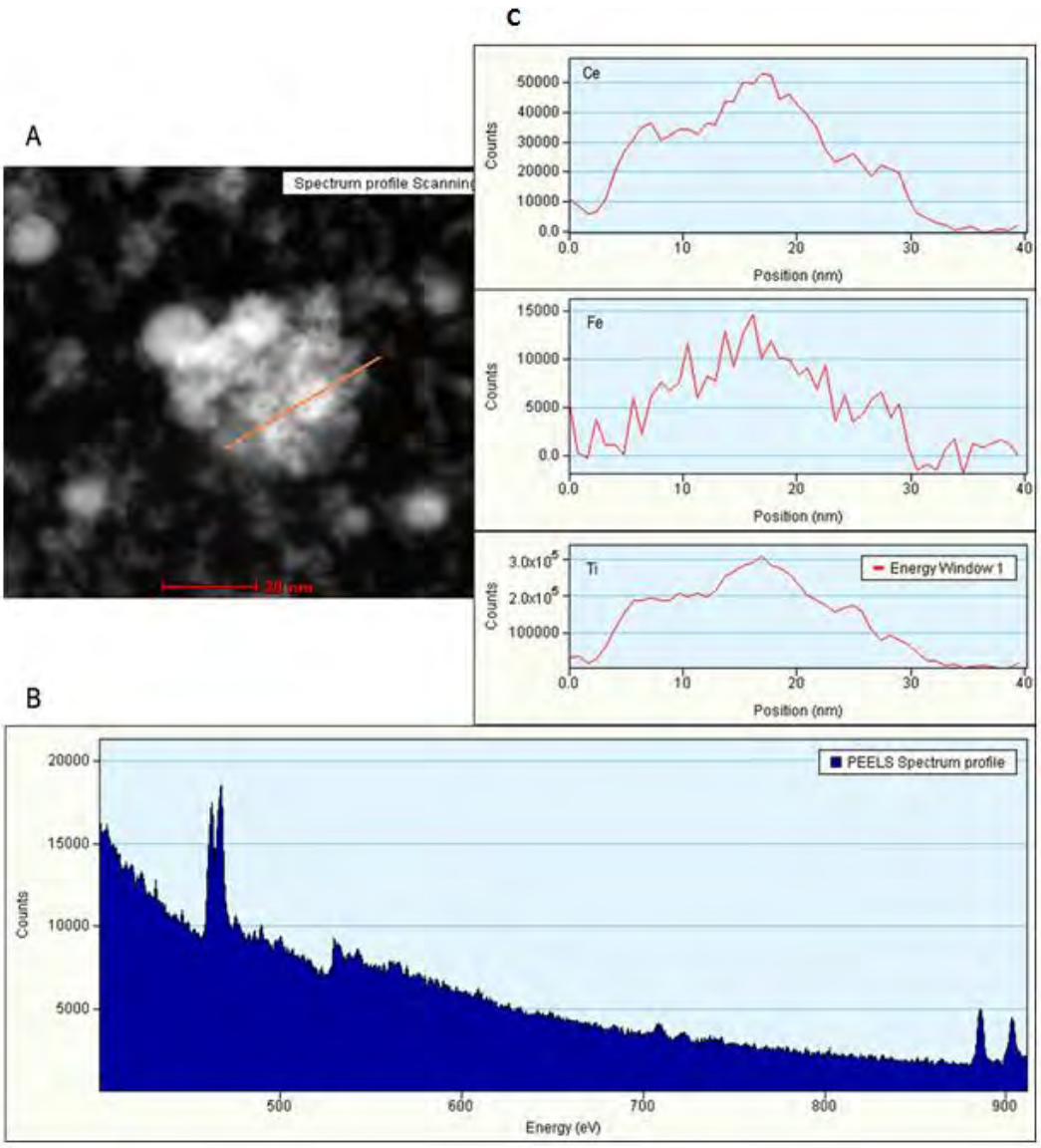

Figure 6.8. EELS line scan of the core-shell Ce-Ti@Fe_3O_4 NPs after the 5 cycles of adsorption-desorption. (A) STEM HAADF image of the Ce-Ti@Fe_3O_4 and position of the line scan; (B) PEELS spectrum of the nanomaterial; and (C) Ions profile spectra along the line scanning.

The observed modification of the morphology for the nanomaterial may be attributed to the release of metal. As a result, the analysis of the metal content in the Ce-Ti@Fe_3O_4 nanomaterial after the 5 cycles showed a metal concentration of 113.68 ± 1.75 mg_{Ti}/g_{NP}, 173.82 ± 15.73 mg_{Ce}/g_{NP} and 77.41 ± 8.04 mg_{Fe}/g_{NP}. Comparing with the original metal values of the Ce-Ti@Fe_3O_4 NPs, (121.01±7.70 mg Ti/g, 199.29±10.47 mg Ce/g

and 81.07±4.49 mg Fe/g), a leakage of Ti, Ce, and Fe of 6.06, 12.78, and 4.51%, respectively, is observed, being the loss of Ce the most important one. Then, ICP-MS was used to analyze the Ce amount in both, the water treated and the desorbing solutions, after each adsorption-desorption cycle. The Ce concentration in the final treated aqueous solution after 5 cycles was not detected (Table 6.3), indicating that there is no release of Ce in the treated aqueous solution. However, the Ce concentration in the desorbing NaOH solution increases with the number of desorbing cycles, being the maximum value at the 5th cycle and corresponding to a total Ce release of 0.70 mg, which agrees with the estimated Ce lose from the NPs (12.78 %). This result may be due to the low stability of the NPs at basic pH [52].

Table 6.3. ICP-MS analysis for Ce-Ti@Fe_3O_4 after 5 adsorption-desorption cycles of fluoride

Desorption cycles, solution analyzed	**Cerium, mg/L**
Cycle 1, H_2O	N.D
Cycle 1, NaOH	N.D
Cycle 2, NaOH	N.D
Cycle 3, NaOH	0.36
Cycle 4, NaOH	10.20
Cycle 5, NaOH	20.00
Cycle 5, H_2O	N.D

N.D: Not detected

Therefore, we can conclude that the Ce-Ti@Fe_3O_4 nanomaterial is suitable for its use and reuse for at least five cycles of adsorption-desorption of fluoride with high removal and recovery. Also, it was demonstrated its adsorption capacity for five cycles. Although, there is a low metal leakage from the nanomaterial, there is no effect in the treated water or the environment, due to this leakage remains in the desorbing reagent.

6.3.6. Effect of the pH value for the fluoride adsorption

The optimum pH for drinking water is in the range of 6.5–9.5 [53] and it is known that pH can significantly affect the adsorption of fluoride [54]. Figure 6.9 shows the removal percentage and adsorption capacity (Q_e) at pH from 5 to 11 for the Ce-Ti@Fe_3O_4 adsorbent. The fluoride removal percentage and Q_e decrease by increasing the pH when applying 10 mg/L initial fluoride concentration and 1 g/L of Ce-Ti@Fe_3O_4 NPs. Even though, at pH 11, the removal percentage was still more than 80 %. The decrease of the removal percentage could be attributed to the changes in the surface of the NPs, which became more negatively charged. Therefore, a competition for the adsorption sites of more OH^- ions with fluoride ions occurs in the aqueous solution as well as modifications of the nanomaterial in this pH range [55]. At 10 mg/L F^- initial concentration, the highest fluoride removal percentage and Q_e values were at pH 5 and 7 to be 99.85, 98.33 % and 10.31, 10.32 mg/g, respectively.

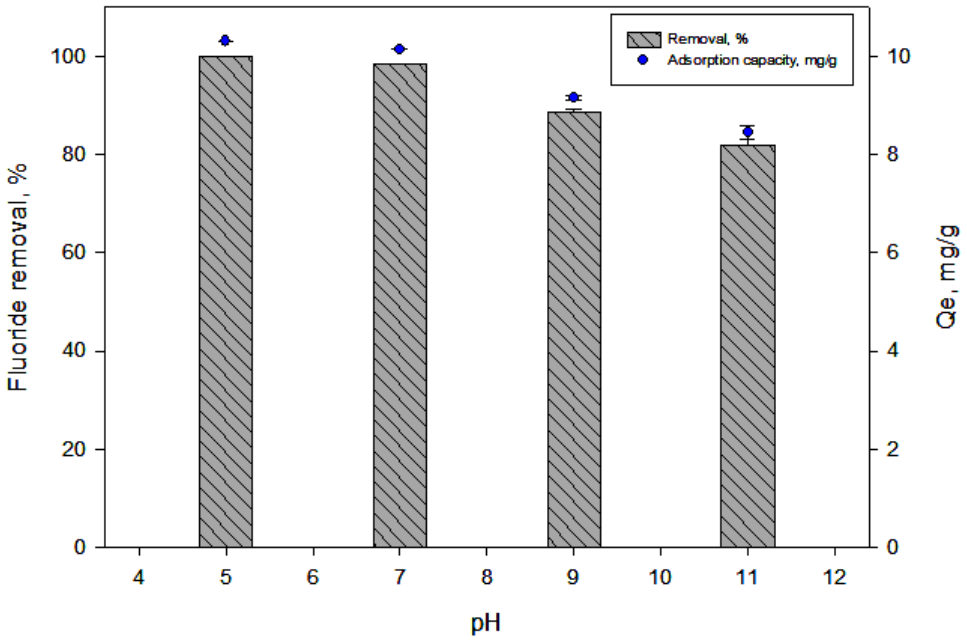

Figure 6.9. Effect of pH on fluoride removal percentage (%) and adsorption capacity (Qe) for initial fluoride concentration of 10 mg/L, 1 g/L of Ce-Ti-Fe oxides NP at 200 rpm and room temperature.

6.3.7. Temperature effect and thermodynamic parameters

The temperature affects the adsorption of the pollutants and provides information about the spontaneity of the fluoride removal process [56]. The adsorption capacity values using Ce-Ti@Fe_3O_4 NPs and fluoride removal percentage are illustrated in Figure 6.10 versus temperature in the range of 20 – 40 °C. The highest adsorption capacity is reached at 30 °C. Next, the values showed a stable removal percentage until 40 °C that indicates that the optimum temperature for fluoride adsorption is at 30 °C when using 30 mg/L initial fluoride concentration.

Table 6.4 shows the thermodynamic parameters for the fluoride removal at different temperatures. The positive value of the enthalpy, $\Delta H°$, verifies the endothermic nature of the process. The positive entropy, ΔS^o, values confirmed the increased randomness at the solid–solute interface during adsorption, but its low value indicated that no remarkable change in entropy occurs. Moreover, the negative free Gibbs energy, ΔG^o, values attributed to the adsorption processes, were spontaneous in all cases. The spontaneity adsorption process of fluoride was enhanced by increasing the temperature. The statistical analysis also showed that the temperature has a significant effect on the removal percentage of fluoride when applying the one-way ANOVA (p-value was less than 0.05) as illustrated in Figure 6.10.

Table 6.4. Thermodynamic parameters for fluoride adsorption using Ce-Ti@Fe_3O_4 nanomaterial.

Temperature (°C)	- ΔG (kJ mol^{-1})	ΔH° (kJ mol^{-1})	ΔS° (J $mol^{-1}K^{-1}$)	R^2
20	13.84 ± 0.02	2.52	55.79	0.996
25	14.12 ± 0.02			
30	14.40 ± 0.01			
35	14.67 ± 0.04			
40	14.95 ± 0.02			

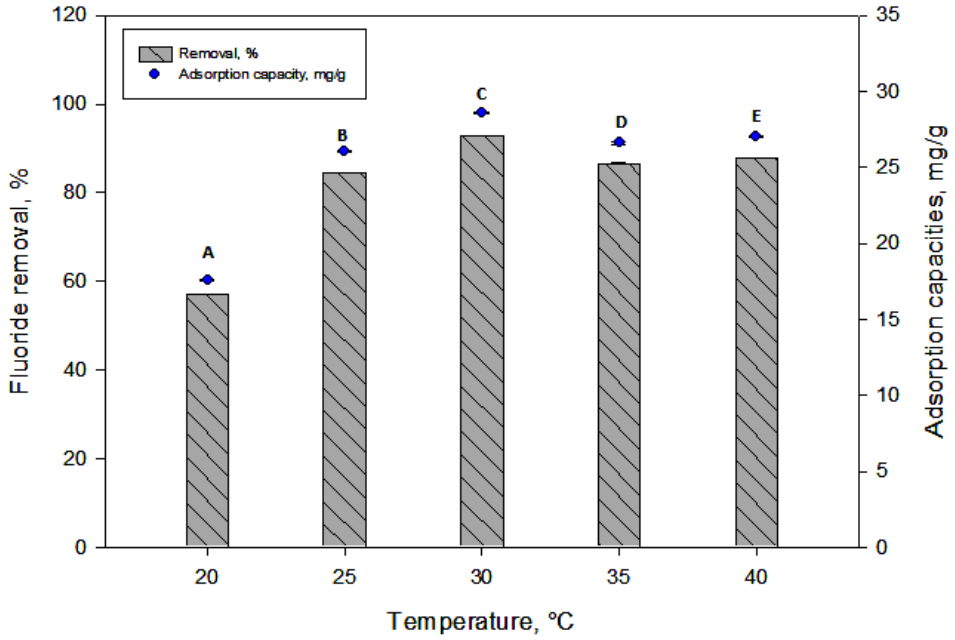

Figure 6.10. Effect of temperature on fluoride removal percentage (%) and adsorption capacity (Q_e) using; 30 mg/L initial fluoride concentration, 1 g/L of Ce-Ti-Fe oxide nanomaterials and shaking at 200 rpm for 60 min. Statistical data analysis using ANOVA was illustrated by letters A, B, C, D, and E.

6.3.8. Application of Ce-Ti@Fe_3O_4 nano adsorbent for fluoride removal from real water sample

The efficiency of the magnetic Ce-Ti@Fe_3O_4 NPs for fluoride removal from drinking water sample spiked with 10 mg/L of fluoride was studied. The results (Table 6.5) proved that the Ce-Ti@Fe_3O_4 adsorbent had a strong affinity for fluoride removal in the presence of other anions. The removal percentage of fluoride decreased from about 99 to 73 % (0.11 to 2.94 mg/L) at ambient temperature due to the presence of other co-existing anions. In addition, the adsorbent posed affinity towards other anions, under the tested conditions, with removal percentage of 15, 36, 11, and 99 % for chloride (Cl^-), nitrite (NO_2^-), sulphate (SO_4^{2-}), and nitrate (NO_3^-) respectively. This could be attributed to some anions competition and others enhanced columbic repulsion forces with fluoride for the active sites [57].

Moreover, increasing the temperature from 25 to 30 °C increased the removal percentage of fluoride from 73 to 87 % (2.94 to 1.44 mg/L) being the residual concentration of fluoride 1.44 mg/L, which is below the maximum acceptable level, 1.50 mg/L. Furthermore, the removal percentage increased to be 18 and 100 % for the chloride and nitrate anions, respectively while it decreased to be 35 and 10 % for the nitrite and sulphate anions, respectively. Subsequently, the novel magnetic Ce-Ti@Fe_3O_4 nanomaterial is a promising and efficient material for anions removal from water not only fluoride, but also for nitrate, nitrite, chloride, and sulphate.

Table 6.5. Efficiency of the Ce-Ti@Fe_3O_4 adsorbents on the fluoride removal from drinking water

Anions	**Anions concentration, mg/L**		
	Spiked tap water	**After adsorption[a]**	**After adsorption[b]**
Fluoride	10.93 ± 0.13 (< 0.010[c])	2.94 ± 0.23	1.44 ± 0.04
Chloride	32.71 ± 0.05	27.86 ± 0.02	26.78 ± 0.04
Nitrite as NO_2^-	1.51 ± 0.01	0.97 ± 0.02	0.98 ± 0.03
Sulphate	16.14 ± 0.02	14.33 ± 0.10	14.47 ± 0.04
Nitrate as NO_3^-	3.16 ± 0.01	0.01 ± 0.00	N.D[d]

a: Adsorption at 25 °C, 1.0 g/L Ce-Ti-Fe oxide, 60 min adsorption time, and 200 rpm.

b: Adsorption at 30 °C, 1.0 g/L Ce-Ti-Fe oxide, 60 min adsorption time, and 200 rpm.

c: Fluoride concentration in drinking water before spiking.

d: N.D: Not detected

6.4. Conclusions

The synthesized magnetic core-shell Ce-Ti@Fe_3O_4 NPs showed high efficiency for fluoride removal and high sorption capacity. The maximum adsorption capacity was 91.04 mg/g at pH 7, which outperformed many reported adsorbents and the synthesized Ce-Ti oxides NPs (44.37mg/L). Ce-Ti@Fe_3O_4 nanomaterial as adsorbent is applicable over a wide pH range (from 5 to 11) and shows a fast adsorption rate. Moreover, it is easy to recover from the reaction mixture for further reuse and it has been used for 5 cycles. The reusability of the NPs under those conditions was evaluated, showing a little modification in its

structure after the cycles and no Ce release is presented in the treated water. In addition to the spontaneous adsorption process, it was shown an increasing of the adsorption capacities by increasing the temperature. Furthermore, the physical sorption mechanism was estimated according to the Dubbinin-Radushkevich isotherm model: anion exchange between the hydroxyl group on the surface of the adsorbents and fluoride ions was involved. Besides, the efficacy of the Ce-Ti@Fe_3O_4 NPs as adsorbent was demonstrated for a real water matrix by spiking 10 mg/L of fluoride in drinking water, as it showed a residual fluoride concentration of 1.44 mg/L. Therefore, magnetic Ce-Ti@Fe_3O_4 nanomaterial was arbitrated to be a suitable adsorbent to treat fluoride contaminated water to achieve the quality standard of drinking water.

6.5. References

1. N. Gandhi, et al., *Adsorption studies of fluoride on multani matti and red soil.* Res. J. Chem. Sci., 2012. **2**: p. 32-37.
2. Rafique, A., et al., *Removal of Fluoride from Drinking Water Using Modified Immobilized Activated Alumina.* Journal of Chemistry, 2013. **2013**: p. 7.
3. Shen, F., et al., *Electrochemical removal of fluoride ions from industrial wastewater.* Chemical Engineering Science, 2003. **58**(3–6): p. 987-993.
4. Teng, S.-X., et al., *Removal of fluoride by hydrous manganese oxide-coated alumina: Performance and mechanism.* Journal of Hazardous Materials, 2009. **168**(2–3): p. 1004-1011.
5. WHO, *Chemical fact sheets: fluoride. In: Guidelines for drinking-water quality (electronic resource): incorporation first addendum.* 2006. **1 third edition, Geneva**: p. 375-377.
6. Singh, K., et al., *Removal of fluoride from aqueous solution: Status and techniques.* Desalination and Water Treatment, 2013. **51**(16-18): p. 3233-3247.
7. Karthikeyan, M., K.K.S. Kumar, and K.P. Elango, *Batch sorption studies on the removal of fluoride ions from water using eco-friendly conducting polymer/bio-polymer composites.* Desalination, 2011. **267**(1): p. 49-56.

8. Liu, R., et al., *Defluoridation by freshly prepared aluminum hydroxides.* Chemical Engineering Journal, 2011. **175**: p. 144-149.
9. Vinati, A., B. Mahanty, and S.K. Behera, *Clay and clay minerals for fluoride removal from water: A state-of-the-art review.* Applied Clay Science, 2015. **114**: p. 340-348.
10. Bhatnagar, A., E. Kumar, and M. Sillanpää, *Fluoride removal from water by adsorption—A review.* Chemical Engineering Journal, 2011. **171**(3): p. 811-840.
11. Shiklomanov, I.A., *Appraisal and assessment of world water resources.* Water International, 2000. **25**(1): p. 11-32.
12. Viswanathan, G., et al., *Mapping of fluoride endemic areas and assessment of fluoride exposure.* Science of The Total Environment, 2009. **407**(5): p. 1579-1587.
13. Martínez-Acuña, M.I., et al., *Preliminary human health risk assessment of arsenic and fluoride in tap water from Zacatecas, México.* Environmental Monitoring and Assessment, 2016. **188**(8): p. 476.
14. Gupta, P. and A. Kumar, *Fluoride levels of bottled and tap water sources in Agra City, India.* Fluoride, 2012. **45**(3): p. 307-310.
15. Dai, S., D. Ren, and S. Ma, *The cause of endemic fluorosis in western Guizhou Province, Southwest China.* Fuel, 2004. **83**(14–15): p. 2095-2098.
16. Mohapatra, M., et al., *Review of fluoride removal from drinking water.* Journal of Environmental Management, 2009. **91**(1): p. 67-77.
17. Kumar, E., et al., *Defluoridation from aqueous solutions by nano-alumina: Characterization and sorption studies.* Journal of Hazardous Materials, 2011. **186**(2–3): p. 1042-1049.
18. Lee, G., et al., *Enhanced adsorptive removal of fluoride using mesoporous alumina.* Microporous and Mesoporous Materials, 2010. **127**(1–2): p. 152-156.
19. Minju, N., et al., *Removal of fluoride from aqueous media by magnesium oxide-coated nanoparticles.* Desalination and Water Treatment, 2013. **53**(11): p. 2905-2914.
20. Sivasankar, V., T. Ramachandramoorthy, and A. Darchen, *Manganese dioxide improves the efficiency of earthenware in fluoride removal from drinking water.* Desalination, 2011. **272**(1–3): p. 179-186.

21. Meenakshi and R.C. Maheshwari, *Fluoride in drinking water and its removal.* Journal of Hazardous Materials, 2006. **137**(1): p. 456-463.
22. Tomar, V., S. Prasad, and D. Kumar, *Adsorptive removal of fluoride from water samples using Zr–Mn composite material.* Microchemical Journal, 2013. **111**: p. 116-124.
23. Deng, S., et al., *Mn–Ce oxide as a high-capacity adsorbent for fluoride removal from water.* Journal of Hazardous Materials, 2011. **186**(2–3): p. 1360-1366.
24. Chen, L., et al., *Optimization of a Fe–Al–Ce nano-adsorbent granulation process that used spray coating in a fluidized bed for fluoride removal from drinking water.* Powder Technology, 2011. **206**(3): p. 291-296.
25. Sujana, M.G. and S. Anand, *Iron and aluminium based mixed hydroxides: A novel sorbent for fluoride removal from aqueous solutions.* Applied Surface Science, 2010. **256**(23): p. 6956-6962.
26. Liu, H., et al., *Preparation of Al–Ce hybrid adsorbent and its application for defluoridation of drinking water.* Journal of Hazardous Materials, 2010. **179**(1–3): p. 424-430.
27. Zhang, K., et al., *Wide pH range for fluoride removal from water by MHS-MgO/MgCO3 adsorbent: Kinetic, thermodynamic and mechanism studies.* Journal of Colloid and Interface Science, 2015. **446**: p. 194-202.
28. Taylor, N.S., et al., *Molecular toxicity of cerium oxide nanoparticles to the freshwater alga Chlamydomonas reinhardtii is associated with supra-environmental exposure concentrations.* Nanotoxicology, 2016. **10**(1): p. 32-41.
29. Li, Z., et al., *Removal of fluoride from water using titanium-based adsorbents.* Frontiers of Environmental Science & Engineering in China, 2010. **4**(4): p. 414-420.
30. Chen, L., et al., *Fe—Ti oxide nano-adsorbent synthesized by co-precipitation for fluoride removal from drinking water and its adsorption mechanism.* Powder Technology, 2012. **227**: p. 3-8.
31. Abo Makeb, A., et al., *Novel magnetic core-shell Ce-Ti@Fe3O4 nanoparticles as adsorbent for water contaminants removal.* RSC Advances, 2016.

32. Zhang, C., et al., *Synthesis and properties of a magnetic core–shell composite nano-adsorbent for fluoride removal from drinking water*. Applied Surface Science, 2014. **317**(0): p. 552-559.
33. Zhang, Y., et al., *Arsenate adsorption on an Fe-Ce bimetal oxide adsorbent: Role of surface properties.* Environmental Science and Technology, 2005. **39**(18): p. 7246-7253.
34. Mahramanlioglu, M., I. Kizilcikli, and I.O. Bicer, *Adsorption of fluoride from aqueous solution by acid treated spent bleaching earth.* Journal of Fluorine Chemistry, 2002. **115**(1): p. 41-47.
35. Zhao, X., et al., *Removal of fluoride from aqueous media by Fe3O4@Al(OH)3 magnetic nanoparticles.* Journal of Hazardous Materials, 2010. **173**(1–3): p. 102-109.
36. Martos, M., et al., *Sol–Gel Synthesis of Tunable Cerium Titanate Materials.* European Journal of Inorganic Chemistry, 2008. **2008**(20): p. 3163-3171.
37. Wang, B., Q. Wei, and S. Qu, *Synthesis and Characterization of Uniform and Crystalline Magnetite Nanoparticles via Oxidation-precipitation and Modified co-precipitation Methods.* Int. J. Electrochem. Sci., 2013. **8**: p. 3786 -3793.
38. Markeb, A.A., et al., *Novel magnetic core-shell Ce-Ti@Fe3O4 nanoparticles as an adsorbent for water contaminants removal.* RSC Advances, 2016. **6**(62): p. 56913-56917.
39. Babaeivelni, K. and A.P. Khodadoust, *Adsorption of fluoride onto crystalline titanium dioxide: Effect of pH, ionic strength, and co-existing ions.* Journal of Colloid and Interface Science, 2013. **394**: p. 419-427.
40. Dorado, A.D., et al., *The role of water in the performance of biofilters: Parameterization of pressure drop and sorption capacities for common packing materials.* Journal of Hazardous Materials, 2010. **180**(1–3): p. 693-702.
41. Pattanaik, M. and S.K. Bhaumik, *Adsorption behaviour of polyvinyl pyrrolidone on oxide surfaces.* Materials Letters, 2000. **44**(6): p. 352-360.
42. Giammar, D.E., C.J. Maus, and L. Xie, *Effects of Particle Size and Crystalline Phase on Lead Adsorption to Titanium Dioxide Nanoparticles.* Environmental Engineering Science, 2006. **24**(1): p. 85-95.

43. Riahi, F., M. Bagherzadeh, and Z. Hadizadeh, *Modification of Fe3O4 superparamagnetic nanoparticles with zirconium oxide; preparation, characterization and its application toward fluoride removal.* RSC Advances, 2015. **5**(88): p. 72058-72068.
44. Tang, D. and G. Zhang, *Efficient removal of fluoride by hierarchical Ce–Fe bimetal oxides adsorbent: Thermodynamics, kinetics and mechanism.* Chemical Engineering Journal, 2016. **283**: p. 721-729.
45. Zhang, C., et al., *Adsorption of drinking water fluoride on a micron-sized magnetic Fe3O4@Fe-Ti composite adsorbent.* Applied Surface Science, 2016. **363**: p. 507-515.
46. Ishihara, T., et al., *Titanium Hydroxide as a New Inorganic Fluoride Ion Exchanger.* Journal of the Ceramic Society of Japan, 2002. **110**(1285): p. 801-803.
47. Y. Xiuru, et al., *Preparation of CeO2-TiO2/SiO2 and its removal properties for fluoride ion.* Journal of Rare Earths 1998. **16**(4): p. 279-280.
48. Biswas, K., D. Bandhoyapadhyay, and U.C. Ghosh, *Adsorption kinetics of fluoride on iron(III)-zirconium(IV) hybrid oxide.* Adsorption, 2007. **13**(1): p. 83-94.
49. Biswas, K., S. Debnath, and U.C. Ghosh, *Physicochemical Aspects on Fluoride Adsorption for Removal from Water by Synthetic Hydrous Iron(III) – Chromium(III) Mixed Oxide.* Separation Science and Technology, 2010. **45**(4): p. 472-485.
50. Biswas, K., K. Gupta, and U.C. Ghosh, *Adsorption of fluoride by hydrous iron(III)–tin(IV) bimetal mixed oxide from the aqueous solutions.* Chemical Engineering Journal, 2009. **149**(1–3): p. 196-206.
51. Teutli-Sequeira, A., et al., *Behavior of Fluoride Removal by Aluminum Modified Zeolitic Tuff and Hematite in Column Systems and the Thermodynamic Parameters of the Process.* Water, Air, & Soil Pollution, 2015. **226**(8): p. 1-15.
52. CP, T., et al., *Stability of metal oxide nanoparticles in aqueous solutions.* Water Sci Technol., 2010. **61**(1): p. 127-33.
53. Drinking-water, p.i., *Background document for development of WHO Guidelines for Drinking-water Quality.* WHO, 2004.
54. Habuda-Stanić, M., M. Ravančić, and A. Flanagan, *A Review on Adsorption of Fluoride from Aqueous Solution.* Materials, 2014. **7**(9): p. 6317.

55. Raichur, A.M. and M. Jyoti Basu, *Adsorption of fluoride onto mixed rare earth oxides.* Separation and Purification Technology, 2001. **24**(1–2): p. 121-127.
56. Deniz, F., *Adsorption Properties of Low-Cost Biomaterial Derived from Prunus amygdalus L. for Dye Removal from Water.* The Scientific World Journal, 2013. **2013**: p. 961671.
57. Onyango, M.S., et al., *Adsorption equilibrium modeling and solution chemistry dependence of fluoride removal from water by trivalent-cation-exchanged zeolite F-9.* Journal of Colloid and Interface Science, 2004. **279**(2): p. 341-350.

Chapter 7

Phosphate removal and recovery from water using nanocomposite of immobilized magnetite nanoparticles on cationic polymer

This chapter was performed in collaboration with: Universitat Politècnica de Catalunya, Manresa, Barcelona.

The results presented in this chapter has been published in Environmental Technology journal:

"Ahmad Abo Markeb, Amanda Alonso, Antonio David Dorado, Antoni Sánchez, Xavier Font. Phosphate removal and recovery from water using nanocomposite of immobilized magnetite nanoparticles on cationic polymer. Environmental Technology, 2017, 37:16 p. 2099-2112".

7.1. Introduction

High amount of phosphorus in water promotes algae growth, regulated by microorganisms, which in its turn decreases oxygen concentration and leads to eutrophication on rivers, lakes, and seas worldwide [1, 2]. Due to phosphorus is a non-renewable element and huge amount of phosphorus is lost annually for lack of phosphorus recovery, its recycling is of great interest especially with increasing demands, such as in the agriculture [3] as a fertilizer [4, 5] or industrial usages as ingredients for human food, pharmaceuticals, detergents, and food additive in the animal feed [6, 7]. Therefore, phosphorus is a critical element in water, where it was found frequently contained in groundwater, domestic and industrial wastewaters.

The common forms of phosphorus found in wastewater include phosphates ($H_2PO_4^-$, HPO_4^{2-}, and PO_4^{3-}), polyphosphates and organic phosphates [8]. Phosphorus concentrations in water matrices can be very different. For instance, municipal wastewater may contain 4-15 mg/L phosphorus as PO_4^{3-}, domestic wastewater contains about 10–30 mg/L of PO_4^{3-}, and treated sewage contains lower concentration, 1–5 mg/L of PO_4^{3-}. However, industrial wastewater (such as detergent manufacturing and metal coating processes) may contain phosphate levels of more than 10 mg/L [9]. Due to the potential interest of phosphate removal from water, various techniques have been employed, including constructed wetlands [10], physicochemical treatment method based on the precipitation of slightly soluble phosphorous [11], and biological nutrient removal (BNR) methods [5, 12-18]. Sludge used in BNR methods had disadvantages especially with a high phosphorous content due to there is a risk of phosphate release and flowing back to water treatment system if the aeration is not sufficient [19]. Thus, precipitation and activated-sludge process were studied for removing high concentration (hundreds to thousands of mg/L) [20] of phosphate in wastewaters. However, in the case of low concentration (several mg/L) of phosphates, precipitation or activated-sludge method are not much effective [21]. For instance, the precipitation and crystallization methodologies require pH higher than 9 to complete precipitation which is disadvantageous, especially in the presence of carbonate/bicarbonate anions due to the competitive interaction, difficulty of regeneration and reusability which led to high cost for treatment. Other purification process, as high recovery reverse osmosis [5, 22], suffers problems associated with phosphate ions and in combination with calcium ions as

precipitating agent for phosphate salts which lead to membrane blockage what limits water recovery [23].

Many challenges of the previous described water treatments were faced by the use of the nanotechnology that provides also cost effective treatment capabilities [24]. Nanomaterials have a number of key physicochemical properties that make them particularly attractive for water purification such as separation media or reusability. On a mass basis, they have much large surface areas than bulk particles. Nanomaterials can also be functionalized with various chemical groups to increase their affinity toward a given compound. They can also serve as high capacity - selectivity and recyclable ligands for toxic metal ions, radionuclides, organic and inorganic solutes [25]. Water treatment based on the adsorption of contaminants using metal oxide nanoparticles (NPs), such as cerium oxide, titanium oxide and iron oxide NPs as well as the core/shell NPs, is relatively useful for water contaminants removal such as phosphate, nitrate, and fluoride as shown in Chapters 4 and 5.

In general, adsorption technology has been a well-established technology for phosphate removal and recovery from water and wastewater, though more selective and cost-effective sorbents developed. Compared with chemical precipitation, adsorption does not produce large volumes of chemical sludge. Various types of phosphorus adsorbents made from zeolites [26], lanthanum and yttrium compounds [27, 28], aluminum compounds [29-33], zero-valent iron [34], amine-functionalize, $Pr(OH)_3$ [35], magnesium amorphous calcium carbonate [36], zirconium compounds [37, 38], and iron(III) oxide compounds [8, 31, 39-45] were studied. In addition to all of these nanoadsorbents, studies were also focused on the iron based adsorbents, with magnetic properties, due to their low cost [46] and their magnetic separation methodology which offers great advantages, such as high speed, simplicity, accuracy and effectiveness to operate as compared to the conventional separation methods [47]. Thus, magnetic nanoparticles (NPs) have a high potential to be applied in adsorption systems because they can easily be separated in a magnetic field. However, there are just a few studies of phosphate removal from water by using magnetite (Fe_3O_4) NPs [48, 49].

On the other hand, the modification of polymers with surface functional groups, such as acrylamide [50], N-vinylpyrrolidone [51] and also the modification of surfaces with magnetic properties have been reported. In this sense, polymeric ligand exchangers exhibit high phosphate selectivity over competing sulfate and chloride ions [12, 15] and efficient regeneration and reuse.

However, they are relatively expensive, which is the most important parameter for the industrial applications. In this regard, the modifications of polymers or other supports with NPs have been used recently [52, 53] to enhance the adsorption capacity of the materials. For instance, Hydrated Ferric Oxide (HFO) was doped in various support materials such as zeolites, alginates, activated carbon and cation exchange resins [54-57] as well as in polymeric anionic exchanger [58, 59]. Anionic resins impregnated with HFO were studied for phosphorus removal [60-63]. In general, polymeric anion exchange resins have low phosphate exchange capacity and poor selectivity factors against common ions present in wastewater (chloride, sulfate, bicarbonate, nitrate and dissolved organic matter) [15]. In this sense, other polymeric materials, such as the cation exchange resin, from Purolite (C100), is a simple, fast and economic polymeric matrix for the removal of metals such as Ce^{4+}, Fe^{3+}, and Pb^{2+} from aqueous systems [64]. Furthermore, taking into account some works reported about the use of iron-based nanoadsorbents for phosphorus removal in waters, it has been shown that the adsorption capacities at room temperature were: 0.3 mg/g for α-Fe_2O_3 [8], 0.9 mg/g for Goethite + Maghemite ($FeO(OH)$ + γ-Fe_2O_3) [65], 1.1 mg/g Hematite (Fe_2O_3) [66], and 2.6 mg/g for hydrothermally synthesized Fe_3O_4 [48]. However, higher adsorption capacities are required and no studies were conducted on the removal of phosphate based on cationic polymers. Thus, iron based nanoadsorbents based on polymeric supports could be a promoting solution. And due to the exhibition of its efficiency for phosphate removal as described in Chapter 4.

Therefore, this work aims to develop and use an optimal nanocomposite (NC) as adsorbent based on immobilized Fe_3O_4 NPs on the polymeric cationic resin, C100, for phosphate removal by adsorption and its recovery from water in a continuous fixed bed column. More precisely, the main objectives of this study are: 1) the optimization of the NC based on the immobilization of different Fe_3O_4 NPs concentrations on the surface of the C100 material to obtain the highest adsorption capacity for phosphate, and 2) the adsorption- desorption optimization process to regenerate the adsorbent for the reusability of the NC and phosphate recovery during several cycles of usage.

7.2. Material and methods

7.2.1. Materials

Iron (II) chloride; $FeCl_2$, Iron (III) chloride hexahydrate; $FeCl_3.6H_2O$, sodium phosphate monobasic; NaH_2PO_4, citric acid and ammonium hydroxide, NH_4OH, were purchased from Sigma-Aldrich, Spain. Sodium hydroxide pellets, NaOH, was purchased from Merck. Hydrochloric acid, HCl, was purchased from Panreac, SA. All the chemicals were of analytical grade or higher, and all solutions were prepared with Milli-Q water and filtered using 0.45 µm Nylon membrane filter. The cationic exchange polymer (C100) supplied by Purolite S.A, Spain.

7.2.2. Synthesis of the nanocomposite based on magnetite NPs

The cationic exchange polymer (C100) consists of strong acidic group ($R\text{-}SO_3^-$) as a functional group. Pre-treatment of the C100, based on the reported method [67, 68], was carried out as described in Chapter 4 (Section 4.2.3.2).

Immobilization of the Fe_3O_4 NPs on the polymeric matrix, C100, was carried out using a variation of the Intermatrix Synthesis (IMS) protocol coupled to a co-precipitation method already reported [67]. The experimental procedure for the preparation of iron oxide based ferrites in this work involves the precipitation of Fe^{2+} and Fe^{3+} salts in a strict ratio of 1:2 in deoxygenated water by the addition of a strong basic solution. Specifically, 125 mL of deoxygenated aqueous solution of NaOH (0.5M) was added slowly with continuous stirring into 100 mL mixture of deoxygenated iron salts suspension, with Fe^{2+}/Fe^{3+} molar ratio of 1:2, which contained 0.4 g of C100 polymer under N_2 atmosphere and at 40 °C. To optimize the concentration of NPs on the surface of polymeric cationic resin, we have used four different concentrations of $FeCl_2/FeCl_3$. These are: protocol A: 26/52 mM, protocol B: 13/26 mM, protocol C: 6.5/13 mM and protocol D: 3.25/6.50 mM. Then, the suspension was incubated for 1h at 40 ºC. During the incubation, the polymer became black in color due to the formation of Fe_3O_4-NPs on the polymeric material. The IMS of Fe_3O_4-NPs in sulfonated polymers can be described by Equations 7.1 and 7.2 [69].

$8(R\text{-}SO_3^-Na^+) + Fe^{2+} + 2Fe^{3+} \rightarrow (R\text{-}SO_3^-)_2(Fe^{2+}) + 2[(R\text{-}SO_3^-)_3(Fe^{3+})] + 8Na^+$ (Equation 7.1)

$(R\text{-}SO_3^-)_2(Fe^{2+}) + 2[(R\text{-}SO_3^-)_3(Fe^{3+})] + 8NaOH \rightarrow 8(R\text{-}SO_3^-Na^+) + Fe_3O_4 + 4H_2O$ (Equation 7.2)

7.2.3. Characterization of the nanocomposites

The metal content of the NC samples was analyzed by using Inductively coupled plasma optical emission spectrometry, ICP-OES. The identification of magnetite was based on the characteristic peaks in the diffractograms and comparing with the database using X-Ray Diffraction, XRD. Scanning Electron Microscopy (SEM) and the Energy Dispersive Spectroscopy (EDS) were used to study the cross-sectioned NCs samples. Particle size and morphology of the magnetite NCs were determined using Transmission Electron Microscopy (TEM). Surface area of the dry polymer and the NCs samples were determined from conventional nitrogen sorption isotherms using Brunauer-Emmett-Teller method (BET). Samples preparation are explained in Chapter 3.

7.2.4. Ionic chromatography for phosphate analysis

The determination of phosphate, as phosphorous (PO_4^{3-}-P), was performed utilizing Ionic Chromatography (IC) as previously explained in Chapter 3 (Section 3.2.1).

7.2.5. Adsorption-desorption tests

7.2.5.1. Phosphate solutions

Phosphate solutions were prepared using a Na_2HPO_4 stock solution of 10000 mg/L in milli-Q water. Then, series of dilutions with a range of concentration from 0.1 to 100 mg/L of phosphate in milli-Q water were prepared for calibration. Each solution was filtered using 0.45 µm nylon membrane filter prior to analysis. When necessary, different pH was adjusted using 0.1 M citric acid or 0.1M sodium hydroxide.

7.2.5.2. Adsorption studies in a fixed bed column

The fixed bed column experiments were performed using polyamide column of 1 cm inner diameter and 16 cm length. The column was packed with the synthesized NC. A glass wool plug was placed at the bottom of the column to avoid the adsorbent washing out. Prior to start the experiment, the NC was fully wetted by pumping the column upwards for 4 h with milli-Q water with flow rate 1mL/min. The flow rate was maintained in each experiment using a peristaltic pump (Watson Marlow, 403U).

The continuous adsorption process is usually characterized by the so-called breakthrough curves, i.e., a representation of the pollutant effluent concentration versus time profile in a fixed bed column. In addition, breakthrough curves prediction through mathematical models is a useful tool for scale-up and design purposes [70].

Breakthrough curve determination experiments were performed for all the experiments at 1 mL/min and 1.0 g of adsorbent (NCs). The breakthrough curves show the loading behavior of phosphate to be removed from solution in a fixed-bed column and are usually expressed in terms of adsorbed phosphate as PO_4^{3-}-P concentration (C_{ad}) as a function of time. Equilibrium uptake q_{eq} ($mg_{PO4\text{-}P}/g_{NC}$) is defined as the adsorption capacity of phosphate per mass of NC at a certain initial phosphate concentration [71]. In all experiments, the initial concentration for phosphate was 10mg/L. Different pHs of the phosphate media were also evaluated of the pH range from 4 to 7 to evaluate the effect of the pH on the adsorption capacity as well as to evaluate the NC stability after the adsorption experiments.

7.2.5.3. Phosphate adsorption isotherm and modeling

To estimate the maximum adsorption capacity of the adsorbent, isotherm modeling is an important aspect for establishing adsorption system which provides information on the amount required for removing unit mass of pollutant. In this study, isotherms were performed continuously with phosphate interval concentrations (1, 2.5, 5, 10, 20, 30, 50, 80 and 100 mg/L), 1 g/L of nanoadsorbent, 1 mL/min at room temperature and two pH values; 5 and 7.

The experimental quantities of the phosphate adsorbed have been fitted to adsorption isotherms models available in the literature, including two-parameter isotherms (Langmuir,

Freundlich, Dubinin–Radushkevich, DR), three-parameter isotherms (Brunauer–Emmett–Tellerand, BET) and a combination of them. Isotherms were determined from the breakthrough curves of step changes in the feed concentration by non-linear regression according to the value of the objective function defined as the norm of the difference between experimental data and model predictions. The sorption capacity of the material was evaluated at different pHs by frontal analysis following the stair case method [72]. Moreover, a confidence interval has been determined in the estimation of model parameters according to the Fisher information matrix method as function of the quantity and quality of experimental data [73].

Columns experiments started with 1 mg/L phosphate as initial concentration until equilibrium was reached. At that point, inlet phosphate concentration was increased corresponding to the interval of phosphate concentration. For each initial phosphate concentration, q_{eq} was calculated.

7.2.6. Desorption of phosphate and reusability of the nanocomposite

The desorption process for the phosphate previously adsorb on the NC, as previously described, was optimized to be able to reuse the nanomaterial as adsorbent for further adsorption process and to recover the phosphate. To determine the optimal process for the adsorbent regeneration, different desorbing solutions, specifically NH_4OH, NaOH with different concentrations (0.01 – 1.0 M) and milli-Q water, were used. After 90 min adsorption of 10 mg/L phosphate solution at pH 7, 1mL/min and 1.0 g of the nanoadsorbent, aliquots of the NC (0.5 g of wetted adsorbent) were treated using the desorbing solutions. Once the optimal desorption system was defined, the adsorption-desorption processes were performed seven times at the optimal adsorption and desorption experimental conditions for evaluating the reusability of the synthesized NC for phosphate removal and its recovery.

7.3. Results and discussion

7.3.1. Synthesis and characterization of the nanocomposites

7.3.1.1. Metal ions content in the nanocomposites

The NCs, synthesized by using the four A, B, C and D, were analyzed by ICP-OES. Table 7.1 shows the mean of iron (Fe) concentration (mg_{Fe}/g_{NC}) for the three replicates of the four samples. It is shown that increasing the Fe salts concentration in the synthesis lead to increase the Fe content in the final NC. Furthermore, data show that the Fe concentration on the polymer is saturated at around 80 mg_{Fe}/g_{NC} (samples A and B), being the maximum level of metal concentration during the synthesis of 13/26 mM of $FeCl_2/FeCl_3$ (for Protocol B).

Table 7.1. Iron synthesis ratio, iron content (mg_{Fe}/g_{NC}) and adsorption capacities ($mg_{PO4\text{-}P}/g_{NC}$) at pH 5 of 10 mg/L of phosphate using different protocols; A, B, C and D.

	$FeCl_2/FeCl_3$ synthesis ratio	**Iron concentration, mg_{Fe}/g_{NC}**	**Adsorption capacities, $mg_{PO4\text{-}P}/g_{NC}$**
C100 polymer	0	0	< 0.01
Protocol A	26/52	77.0 ± 1.21	2.88
Protocol B	13/26	81.2 ± 1.56	2.30
Protocol C	6.5/13	23.6 ± 1.34	3.60
Protocol D	3.25/6.5	5.59 ± 0.28	< 0.01

7.3.1.2. SEM-EDS, XRD and TEM analysis of the nanocomposites

The SEM images coupled with EDS of the cross-sections for each synthetic protocol (A, B and C) of the NCs are shown in Figure 7.1. This data shows the success of the immobilization of the Fe_3O_4 NPs on the surface of the NC. As it is clearly seen in Figure 7.1a, 7.1b, and 7.1c, the major part of the Fe_3O_4 NPs is located near the polymer surface (shown by the light white zone)

with different thickness corresponding to each synthetic protocol showing a deeper layer when the loading concentration of iron during the synthesis is higher. Figure 7.1d shows cross section for polymer without NPs.

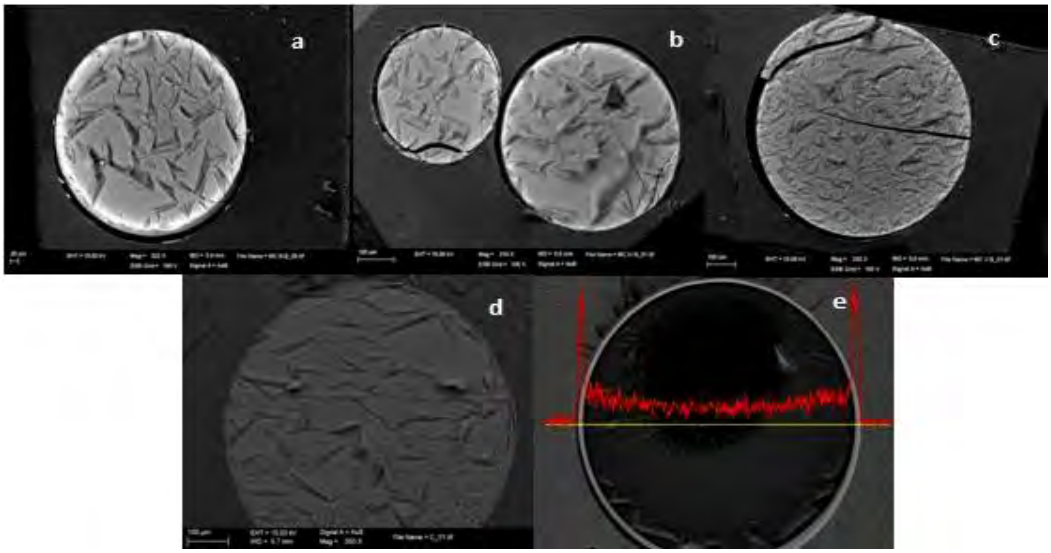

Figure 7.1. SEM image of the magnetite nanocomposites cross-sectioned: (a) protocol A, (b) protocol B, (c) protocol C. (d) SEM image of the polymeric matrix without magnetite NPs. (e) EDS spectra for the profile distribution of the Fe on the cross-section of nanocomposite (protocol C).

Further confirmation about the immobilization of magnetite NPs on the surface of the polymer was illustrated in Figure 7.1e, where the line spectrum shows the iron content profile obtained by SEM coupled with EDS, on the cross-sectioned of protocol C. It can be seen that the profile distribution of Fe presents a peak at the surface of the polymer meaning that the distribution of the Fe_3O_4 NPs is concentrated on the surface of the polymer which makes the material more suitable for its application as a nanoadsorbent. Furthermore, TEM images of the cross-sectioned nanomaterials for protocol C is illustrated in Figure 7.2a. As it is observed, the NPs on the polymer show a size of 15 - 20 nm as it was also shown at [67]. Crystalline structure of Fe_3O_4-NPs was confirmed by electron diffraction pattern as shown in Figure 7.2b.

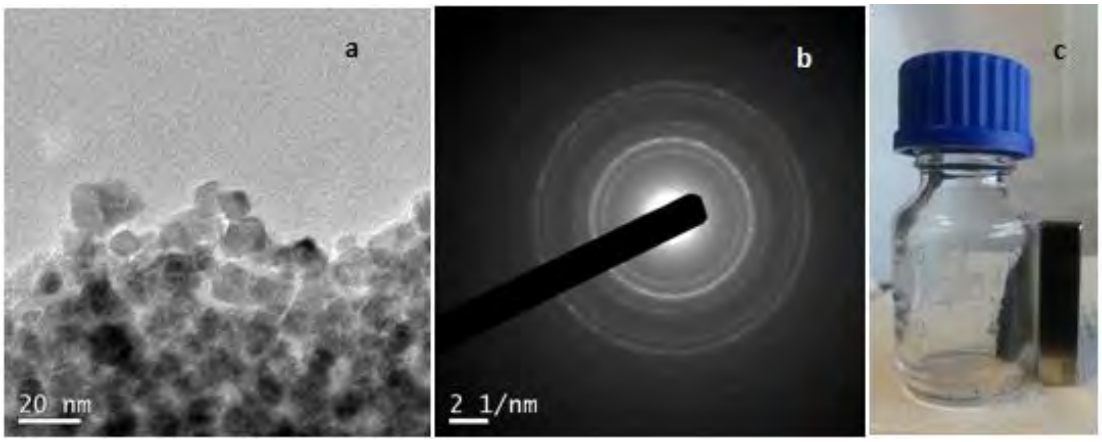

Figure 7.2. TEM image of magnetite NPs in the nanocomposite (protocol C) (a), Electron diffraction of magnetite NPs in the nanocomposite (protocol C) (b), and magnetic properties test of the nanocomposite (Protocol C) using a magnet (c).

In addition, the X-ray diffractogram shows the crystalline structure of the pattern Fe_3O_4-NPs (Figure 7.3a), and the Fe_3O_4-NPs immobilized on the polymer before adsorption (Figure 7.3b). The typical peaks can be found at 35.5°, 43.0°, 57.1° and 62.7°, which preferably correspond to the Fe_3O_4 according to the JCPDS database [74]. The Miller indices of these peaks are 311, 400, 511 and 440, respectively. The broad peak in the XRD pattern could be attributed to the ultrafine nature and small crystallite size of magnetite nanocomposites, in addition to the formation of thin layer of magnetite nanoparticles immobilized on the surface of the cationic polymer. Moreover, the decrease of the intensity of the peaks could be attributed to the low concentration of iron contents [75, 76].

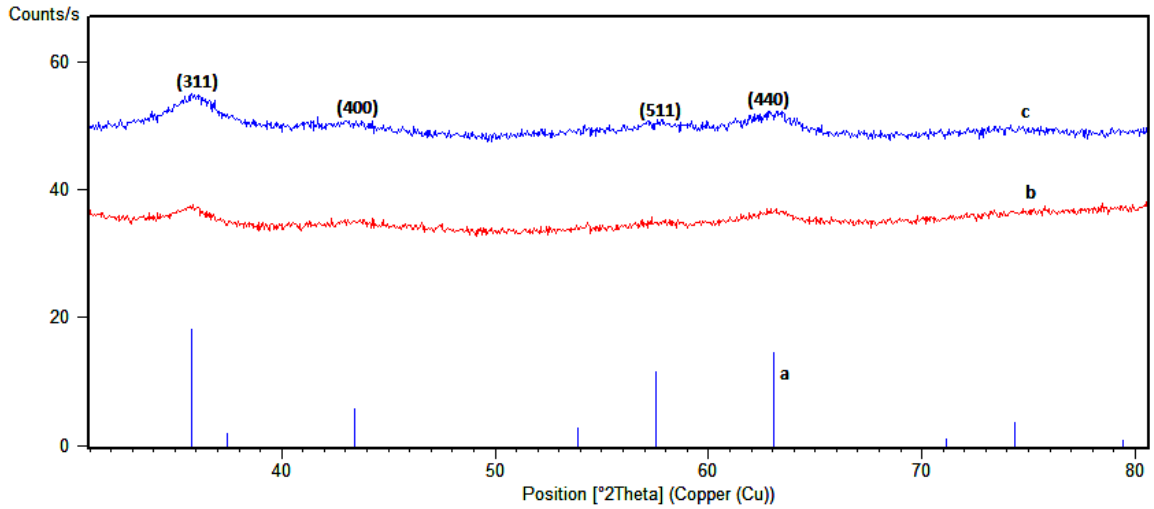

Figure 7.3. XRD spectra of: (a) magnetite reference pattern and; magnetite nanocomposite (protocol C) (b) before, and (c) after the adsorption process at 10mg/L of phosphates.

7.3.1.3. Magnetic characterization and surface area measurements of the nanocomposites

Figure 7.2c shows a photograph of the qualitative test of the magnetic properties of NC by using a permanent magnet, where one can clearly see the NC beads stuck to the magnet. This means that the NC material can be easily recovered from the medium for further reuse which is an advantage for the separation process in this application.

On the other hand, BET analysis reports that surface area for all protocols was lower than 2 m^2/g (N_2 sorption, BET). These results agree with the gel-type resins in the dry state that are characterized by very low porosity and a far lower surface area, which usually does not exceed 5 m^2/g (N_2 sorption, BET) [77].

7.3.2. Adsorption studies in fixed-bed column

7.3.2.1 Determination of the adsorption capacities for the NCs with different Fe_3O_4 NPs content (Protocol A, B, C and D)

The influence of Fe_3O_4 NPs concentration in the NC on the adsorption capacities of 10 mg/L phosphate at pH 5 is shown in Table 7.1. The highest adsorption capacity was 3.62 mg_{PO4-}

$_{P}/g_{NC}$ obtained by using the material corresponding to Protocol C (23.59 ± 1.34 mg_{Fe}/g_{NC}) indicating that a higher concentration of NPs leads to a decrease of the adsorption capacity of the NC (as shown for Protocol A and B adsorption capacities, corresponding to 2.88 and 2.30 $mg_{PO4-P}/g_{NC,}$ respectively). This can be explained because an excess of NPs leads to decrease the surface/volume ratio of the NPs by the presence of aggregates or higher NPs size. On the other hand, protocol D did show an adsorption capacity lower than 0.01 mg_{PO4-P}/g_{NC} (corresponding to the limit detection of the Ionic Chromatograph), which indicates that approximately less than 6.0 mg_{Fe}/g_{NC} had no significant effect on the NC for the adsorption process of phosphates like it is observed the adsorption capacity for C100 without NP. Thus, it was considered that protocol C (23.59 mg_{Fe}/g_{NC}) is the optimal iron content as well as NPs size and distribution in this NC for the adsorption of phosphates in water. Thus, the following experiments in this work and the majority of the characterization techniques used were carried out for sample C.

7.3.2.2. Effect of the pH on the adsorption capacities and on the nanocomposite stability

pH, as a critical water chemistry parameter, can significantly affect the adsorption of phosphate by any material. Figure 7.4 shows the adsorption capacities of 10 mg/L phosphate, as initial concentration, using Protocol C NC at a pH range from 4 – 7. Generally, phosphate has three pK_a values, 2.2, 7.2, and 12.3 which correspond to $pK_{a1,}$ $pK_{a2,}$ and pK_{a3} respectively, according to the presence of three species. HPO_4^{2-} and $H_2PO_4^-$ are the predominant species in the pH solution region between 4 and 10. HPO_4^{2-} is being more widespread in slightly alkaline conditions while $H_2PO_4^-$ in slightly acidic conditions [78]. As shown in Figure 4, in this study, the highest adsorption capacities value was at pH 7 indicating that the species involved in adsorption process are those which are related to the pK_{a2} value of 7.2. Thus, HPO_4^{2-} seems to have better affinity to form bidentate complexes with the magnetite NPs than $H_2PO_4^-$ forming $M\text{-}OH^+$ complex [79-81]. Moreover, when the $pH<pK_a$ (as pK_{a2} in this case), the surface of the adsorbent is more positively charged and more efficient for attracting negatively charged phosphate species through electrostatic interaction. It is also reported that phosphate adsorption on the surfaces of other iron-based species (e.g. oxyhydroxide polymorphs goethite) is based on the formation of inner-sphere complexes between the phosphate anion and the iron oxyhydroxide surface, indicating the presence of Fe–O–P

covalent bonds what it seems to be also contributing to the adsorption process in the system here reported [82].

Furthermore, the effect of pHs on the immobilized Fe_3O_4-NPs on the C100 after the adsorption processes described in Figure 7.4 was also determined by ICP-OES analysis to detect the stability of the NPs on the polymer for the adsorption mechanism. Thus, iron content after adsorption at different pHs showed the highest iron decrease at pH 4 of 43.4% while at pH 7 the decrease of iron content was 7% of the iron content. This decrease could be explained due to an oxidation of the iron present in the NPs that is finally released from the polymer. At the view of these results pH 7 is the optimum pH for phosphate adsorption, due to both the highest adsorption capacity and the NC stability. Even more, adsorption process of 10 mg/L phosphate on the NC (protocol C) at pH 7 did not affect the crystalline structure (Figure 7.3c) of the NPs.

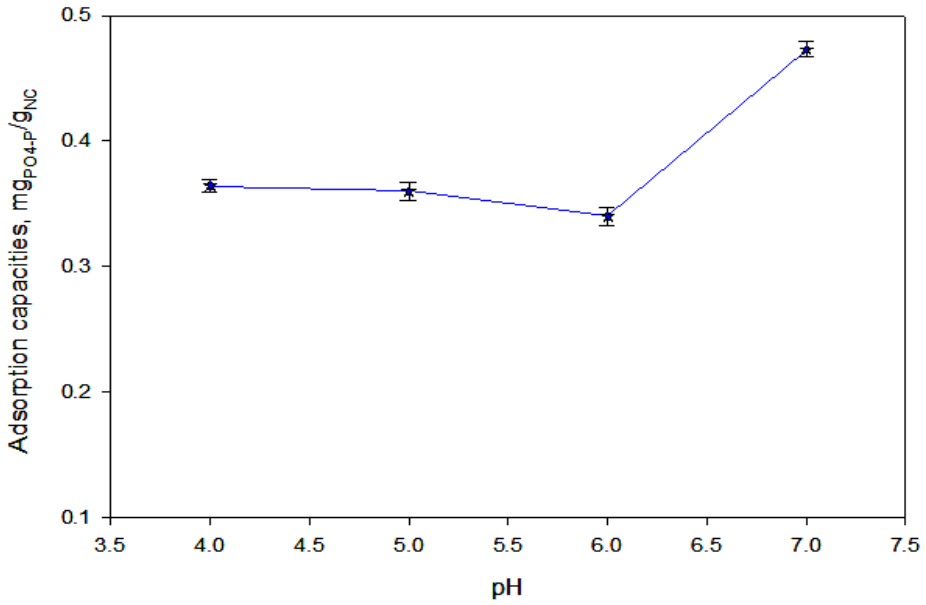

Figure 7.4. Variation of the phosphate adsorption capacities (mg_{PO4-P}/g_{NC}) for the nanocomposite (Protocol C) at different pHs of the medium.

7.3.3. Adsorption Isotherms and modeling

Isotherm fitting results for the five different models tested are shown in Figure 7.5 up to a concentration of 100 mg/L. While in Figure 7.5a is observed that saturation conditions are achieved at pH 5, maximum capacity is not reached when material is operated at pH 7 (Figure

7.5b). These isotherms make it possible to accurately predict the experimental data (low fval) (Table 7.2). Wider confidence intervals are obtained in three-parameter isotherms in particular showing that a large number of possible combinations of parameters are able to fit model predictions to the experimental phosphate adsorbed on the materials. Thus, estimated parameters show a low sensitivity to the final result of the isotherm expression as in the case of BET isotherm. Thus, the Freundlich, Langmuir and the isotherm that combines three parameter-isotherms are the most suitable for fitting the experimental data and for interpreting the influence of pH on the sorption.

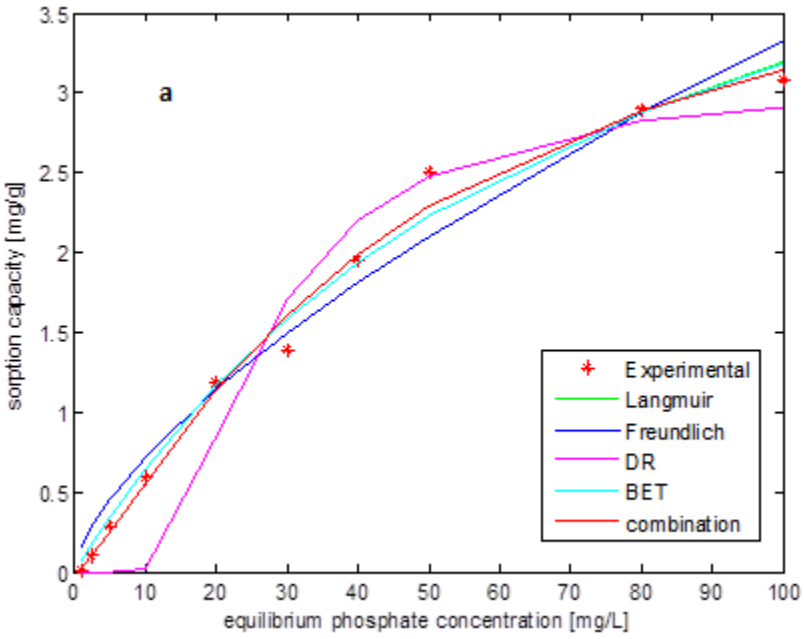

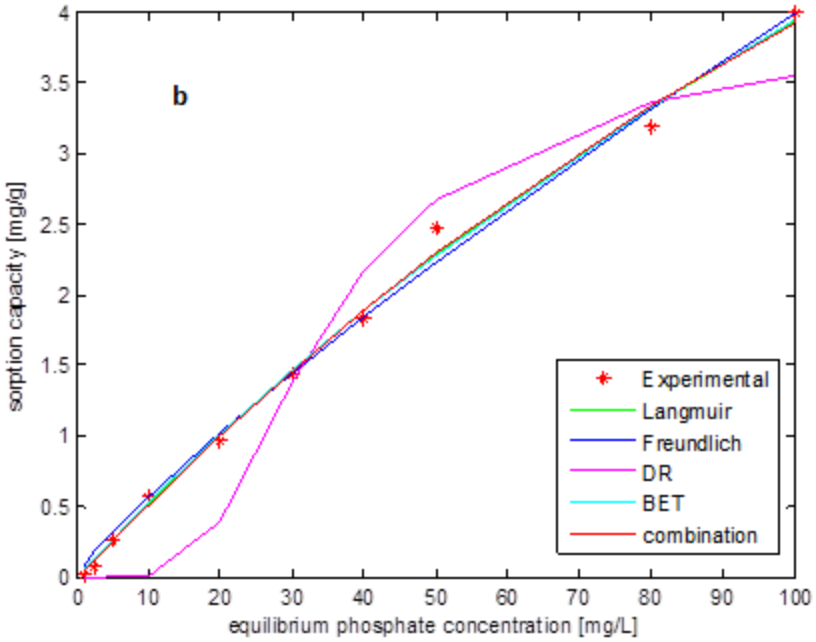

Figure 7.5 – Isotherm fitting results for the five different models tested up to a concentration of 100 mg/L at a) pH 5 and, b) pH 7.

Freundlich isotherm is commonly used for describing sorption on heterogeneous surfaces. The n value indicates the degree of non-linearity between solution concentration and adsorptive material. As n value is lower than 1, the sorption process is more chemical than physical for both pHs. The estimated values of n are lower at pH 5 indicating that the behavior deviates in this case further from the linear isotherm, so it approaches a rectangular isotherm or irreversible isotherm. That means that the concentration needs to go down to an extremely low value before adsorbate molecules desorb from the surface. A higher value of this parameter at pH 7 reveals a weaker affinity between contaminant and material comparing with pH 5 results.

The higher value of Langmuir parameter K1 obtained for the isotherm at pH 7 underlines a higher sorption capacity of the material at these conditions (as also shown in Figure 7.4). The Langmuir isotherm assumes monolayer adsorption onto a surface containing a finite number of adsorption sites of uniform strategies with no transmigration of adsorbate in the plane surface. Once a site is filled, no further sorption can take place at that site. This indicates that at pH 5 the surface reaches a saturation point where the maximum adsorption of the surface is achieved. Since experimental data at pH 7 is not strictly following a saturation model as Langmuir, the maximum capacity of the material is an extrapolation that it should be checked if higher

concentration than those tested in the present study are required. The higher value of k2 for pH 7 highlights again a lower affinity between material and contaminant compared to pH 5.

The Dubinin–Radushkevich isotherm equation, widely used for describing adsorption on microporous solids such as activated carbons, has a semi-empirical origin and is based on the assumptions of a change in the potential energy between the adsorbed phases and a characteristic energy of a given solid. Previous results are partially improved by means of the Redlich–Peterson isotherm. Unlike pH 5, sorption experiments conducted at pH 7 exhibits behavior similar to that of Henry's law, according to the parameter n, which is close to 0. In contrast, at the same range of phosphate concentrations, working a lower pH, the material reduces its capacity and reaches quickly saturation conditions.

From the modeling of the process, it is concluded that the kind of relationship set between contaminant and sorbent is described by a chemical interaction, as already mentioned in Section 7.3.2.2, through a Fe-OH complex system mechanism. While a pH 5, monolayer absorption reproduces more accurately the experimental behavior, saturation conditions are not achieved a pH 7. This means a stronger interaction at pH 5. Clearly, pH plays an important role in the affinity and capacities of materials when they are under adsorption conditions.

Table 7.2. Parameters for the isotherms models used for data fitting.

MODEL		pH = 5	pH = 7
Langmuir	k1	5.612 ± 0.180	14.378 ± 1.094
	k2	75.743 ± 2.679	265.089 ± 20.884
	fval	0.377	0.2702
Freundlich	kf	0.158 ± 0.001	0.081 ± 0.000
	n	0.663 ± 0.003	0.846 ± 0.003
	fval	0.592	0.3122
Dubinin	B	0.891 ± 0.031	1.577 ± 0.045
	qm	3.072 ± 0.055	3.902 ± 0.075
	fval	0.870	1.0504
BET	Cs	9.4E+09 ± 1E+11	1.4E+03 ± 3.0E+03
	B	1.2E+08 ± 2E+08	7.838 ± 12.252
	Q	5.606 ± 0.796	9.525 ± 6.636
	fval	0.377	0.2700
Combination	b	0.008 ± 3.1E-04	0.004 ± 0.001
	qm	4.257 ± 0.165	12.102 ± 1.554
	n	0.788 ± 0.008	0.961 ± 0.008
	fval	0.325	0.2685

The adsorption capacity of the magnetic nanocomposite for the removal of PO_4^{-3}-P has been compared with various iron-based adsorbents in Table 7.3. The adsorption capacities of magnetite immobilized on C100 developed and tested in this work are much higher than other iron based nanoadsorbents but the one based on zirconium. However, the NC used in this work has an advantage in a real application pH medium and it is easier to recover than the other ones. Therefore, the NC used in this study show highly competitive for phosphate removal.

Table 7.3. Comparison of PO_4^{3-}-P adsorption capacity of the NC (Fe_3O_4-C100) of this work with other iron-based adsorbents from the literature at the corresponding conditions of pH.

Adsorbent	pH	PO_4^{3-}-P adsorption capacity (mg/g)	References
Fe_3O_4@ZrO_2	3.0	39.1	[83]
Fe_3O_4-C100	**7.0**	**> 4**	**This work**
La-EDTA coated Fe_3O_4	6.0	4.2	[49]
Fe_3O_4-C100	**5.0**	**2.8**	**This work**
Fe_3O_4	2.8	2.6	[48]
Hematite	6.0	1.1	[66]
Geothite + Maghemite	4.0	0.9	[65]
α-Fe_2O_3	3.0	0.3	[8]

7.3.4. Evaluation of the phosphate recovery procedure and the reusability of the magnetite nanocomposite for several adsorption-desorption cycles.

It is known that at high alkaline pH, PO_4^{3-} species are the predominant in the solution medium and the magnetite is deprotonated and negatively charged, which is favorable for desorption of the adsorbed phosphate [58]. In this work, among the reagents used for the regeneration of magnetite based NC (protocol C), NaOH was found to be the most effective in desorbing the phosphate comparing to NH_4OH and Milli-Q water after one hour shaking at 200 rpm (31.5 and 12.6 % of phosphate recovered respectively). Further optimization procedure for desorbing process was performed using different concentration of NaOH. As shown in Figure 7.6 we can conclude that 0.5 M NaOH is the optimum concentration for desorption process. Under these conditions phosphates desorption was 52.9 %. Therefore, enhancement of desorbability percent was achieved by three washing cycles with 0.5 M NaOH to obtain 97.5 %

of the phosphate recovered. This result is clearly interesting if ones compares with the recovered phosphate % reported in the literature (i.e. 40 % for phosphate for initial concentrations less than 100 mg/L [60]).

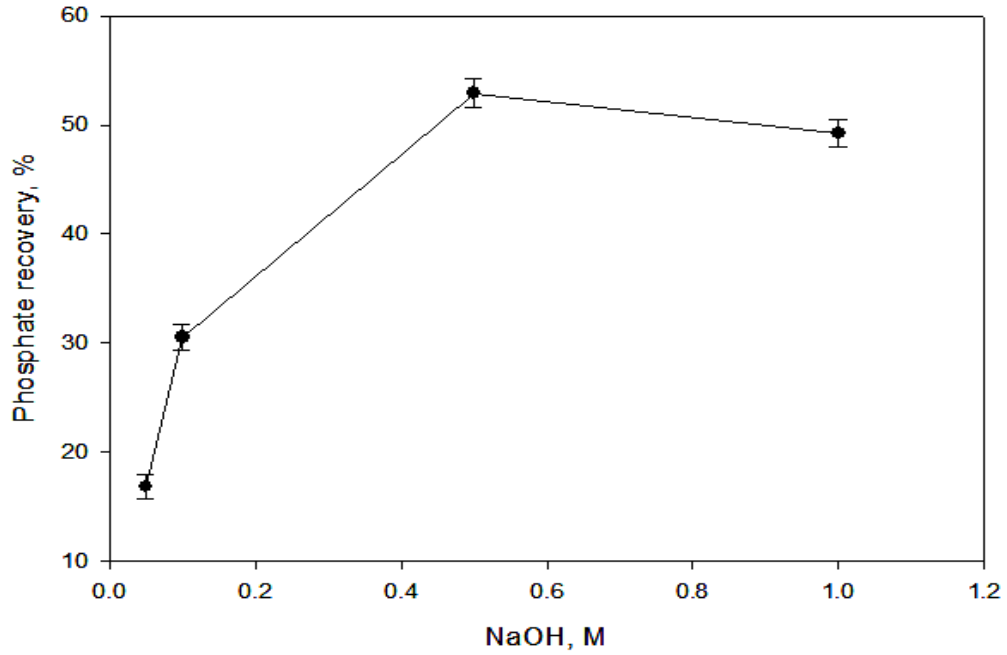

Figure 7.6 – Effect of NaOH concentration for the phosphate desorption (% of recovery).

Afterwards, the regenerated magnetite NC was tested for reusability. After every adsorption process, desorption by using 0.5 M NaOH and three washing steps was performed. The results (Figure 7.7) showed that there is only a drop in the adsorption capacity after the 1st cycle, while the efficiency of phosphate adsorption–desorption was nearly the same for the rest of six cycles. An explanation of the drop of the adsorption capacity after the first adsorption-desorption cycle could be explained by the loss of iron detected from ICP-OES analysis which was of 30% after the first cycle while remaining constant for the rest of cycles. The loss of the iron content from the NC could be due to the experimental conditions in which some of the iron ions dissolves in the media but the rest of the iron content remain stabilized in the polymeric matrix.

On the other hand, as mentioned, the recovery of phosphate was 97.5 % for the 1st cycle. A decrease on the recovery % was observed from the 1st to the 4th cycle of adsorption-desorption. After that, the recovery % removal remains constant at 45% approximately, as shown in Figure

7. In this sense, it could be confirmed the assumed adsorption mechanism (see section 7.3.2.2) in which a strong Fe-HPO_4 complex could be formed in each adsorption-desorption cycle and thus, avoiding the total recovery of the phosphate.

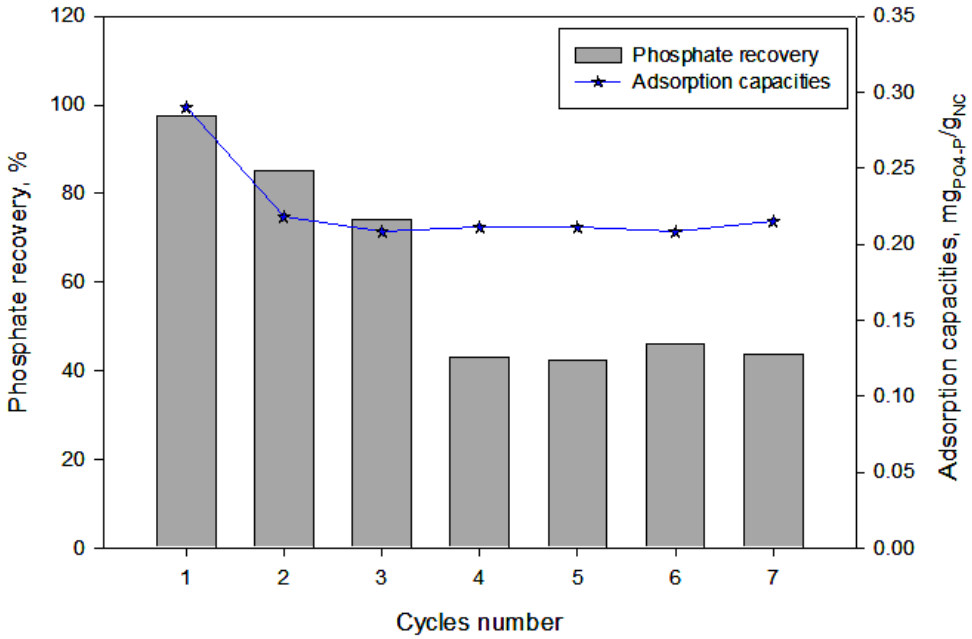

Figure 7.7. Adsorption capacities and % of phosphate recovery for the nanocomposite (protocol C) at different adsorption-desorption cycles (7).

7.4. Conclusions

The present study provides magnetite nanoparticles immobilized on the surface of cationic polymer (C100) which displayed successful application to remove phosphate ions from aqueous solutions. Adsorption experiments of phosphate in a fixed-bed column using different concentrations of magnetite nanoparticles immobilized on the polymer proves that the optimum concentration of iron in the nanocomposites is 23.59 mg_{Fe}/g_{NC}. The effect of pH on the adsorption capacity showed a higher adsorption capacity from the optimized material at pH 7 comparing to pH 4, 5, and 6. Afterwards, continuous adsorption isotherms were performed and it is shown a higher adsorption capacity (> 4.0 mg_{PO4-P}/g_{NC}) at pH 7 compared to pH 5 (2.8 mg_{PO4-P}/g_{NC}). Therefore, the magnetic nanocomposite used in this study is highly competitive for

phosphate removal comparing to other iron-based nanoparticles reported in the literature. Furthermore, regeneration of the nanocomposite was optimized to obtain 97.5 % recovery of phosphate using 0.5 M NaOH for three consecutive cycles desorption process. Then, reusability was demonstrated for 7 cycle's adsorption-desorption process. Therefore, we can conclude that the magnetite nanoparticles immobilized on the cationic polymer has great potential for adsorbing and recovering phosphate.

7.5. References

1. Lau, P.S., N.F.Y. Tam, and Y.S. Wong, *Wastewater Nutrients (N and P) Removal by Carrageenan and Alginate Immobilized Chlorella Vulgaris.* Environmental Technology, 1997. **18**(9): p. 945-951.
2. Trépanier, C., et al., *Phosphorus budget as a water quality management tool for closed aquatic mesocosms.* Water Research, 2002. **36**(4): p. 1007-1017.
3. Reijnders, L., *Phosphorus resources, their depletion and conservation, a review.* Resources, Conservation and Recycling, 2014. **93**(0): p. 32-49.
4. Sengupta, S. and A. Pandit, *Selective removal of phosphorus from wastewater combined with its recovery as a solid-phase fertilizer.* Water Research, 2011. **45**(11): p. 3318-3330.
5. de-Bashan, L.E. and Y. Bashan, *Recent advances in removing phosphorus from wastewater and its future use as fertilizer (1997–2003).* Water Research, 2004. **38**(19): p. 4222-4246.
6. Kebreab, E., A.V. Hansen, and A.B. Strathe, *Animal production for efficient phosphate utilization: from optimized feed to high efficiency livestock.* Current Opinion in Biotechnology, 2012. **23**(6): p. 872-877.
7. Vitti, D.M.S.S.k.E., *Phosphorus and Calcium Utilization and Requirements in Farm Animals.* Phosphorus and Calcium Utilization and Requirements in Farm Animals, 2010: p. 1-178.
8. Zhu, Z., et al., *Kinetics and thermodynamic study of phosphate adsorption on the porous biomorph-genetic composite of α-Fe2O3/Fe3O4/C with eucalyptus wood microstructure.* Separation and Purification Technology, 2013. **117**(0): p. 124-130.

9. Mezenner, N.Y. and A. Bensmaili, *Kinetics and thermodynamic study of phosphate adsorption on iron hydroxide-eggshell waste.* Chemical Engineering Journal, 2009. **147**(2–3): p. 87-96.
10. Prochaska, C.A. and A.I. Zouboulis, *Removal of phosphates by pilot vertical-flow constructed wetlands using a mixture of sand and dolomite as substrate.* Ecological Engineering, 2006. **26**(3): p. 293-303.
11. Ramadori, R., et al., *Chemical Precipation of Phosphate From Sewage At Low Lime Dosage*, in *Studies in Environmental Science*, E.M.W.J.L. L. Pawlowski and C. Sarzanini, Editors. 1988, Elsevier. p. 223-233.
12. SenGupta, A. and D. Zhao, *Using a chelating ion exchange resin saturated with lewis acid, i.e., copper, cations*. 2000, Google Patents.
13. Federation, W.E., *Biological Nutrient Removal (BNR) Operation in Wastewater Treatment Plants: WEF Manual of Practice*. 2005: McGraw-Hill Education.
14. Sedlak, R.I., *Phosphorus and Nitrogen Removal from Municipal Wastewater: Principles and Practice, Second Edition*. 1991: Taylor & Francis.
15. Zhao, D. and A.K. Sengupta, *Ultimate removal of phosphate from wastewater using a new class of polymeric ion exchangers.* Water Research, 1998. **32**(5): p. 1613-1625.
16. Isanta, E., et al., *A novel control strategy for enhancing biological N-removal in a granular sequencing batch reactor: A model-based study.* Chemical Engineering Journal, 2013. **232**(0): p. 468-477.
17. Carrera, J., T. Vicent, and J. Lafuente, *Effect of influent COD/N ratio on biological nitrogen removal (BNR) from high-strength ammonium industrial wastewater.* Process Biochemistry, 2004. **39**(12): p. 2035-2041.
18. Bai, L., et al., *Reuse of drinking water treatment residuals in a continuous stirred tank reactor for phosphate removal from urban wastewater.* Environmental Technology, 2014. **35**(21): p. 2752-2759.
19. EMIS. *Biological nutrient removal*, http://emis.vito.be/techniekfiche/biological-nutrient-removal?language=en. 2010 [cited 2015 March 3]; Available from: http://emis.vito.be/techniekfiche/biological-nutrient-removal.

20. Yilmaz, G., et al., *Simultaneous nitrification, denitrification, and phosphorus removal from nutrient-rich industrial wastewater using granular sludge.* Biotechnology and Bioengineering, 2008. **100**(3): p. 529-541.
21. Saha, B., S. Chakraborty, and G. Das, *A mechanistic insight into enhanced and selective phosphate adsorption on a coated carboxylated surface.* Journal of Colloid and Interface Science, 2009. **331**(1): p. 21-26.
22. de la Noue, J. and N. de Pauw, *The potential of microalgal biotechnology: A review of production and uses of microalgae.* Biotechnology Advances, 1988. **6**(4): p. 725-770.
23. Zelmanov, G. and R. Semiat, *The influence of competitive inorganic ions on phosphate removal from water by adsorption on iron (Fe+3) oxide/hydroxide nanoparticles-based agglomerates.* Journal of Water Process Engineering, 2014(0).
24. Qu, X., P.J.J. Alvarez, and Q. Li, *Applications of nanotechnology in water and wastewater treatment.* Water Research, 2013. **47**(12): p. 3931-3946.
25. Savage, N. and M. Diallo, *Nanomaterials and Water Purification: Opportunities and Challenges.* Journal of Nanoparticle Research, 2005. **7**(4-5): p. 331-342.
26. Geelhoed, J.S., T. Hiemstra, and W.H. Van Riemsdijk, *Phosphate and sulfate adsorption on goethite: Single anion and competitive adsorption.* Geochimica et Cosmochimica Acta, 1997. **61**(12): p. 2389-2396.
27. Wasay, S.A., S. Tokunaga, and S.-W. Park, *Removal of Hazardous Anions from Aqueous Solutions by La(lll)- and Y(lll)-lmpregnated Alumina.* Separation Science and Technology, 1996. **31**(10): p. 1501-1514.
28. Zhang, L., et al., *Expanded graphite loaded with lanthanum oxide used as a novel adsorbent for phosphate removal from water: performance and mechanism study.* Environmental Technology, 2015. **36**(8): p. 1016-1025.
29. Kabayama, M., et al., *Adsorption/Desorption Characteristics of Phosphate Ion onto Calcined Boehmite Surface.* e-Journal of Surface Science and Nanotechnology, 2005. **3**: p. 63-69.
30. Kabayama, M., et al., *Characteristics of Phosphate Ion Adsorption–Desorption onto Aluminum Oxide Hydroxide for Preventing Eutrophication.* JOURNAL OF CHEMICAL ENGINEERING OF JAPAN, 2003. **36**(4): p. 499-505.

31. Gao, S., C. Wang, and Y. Pei, *Comparison of different phosphate species adsorption by ferric and alum water treatment residuals.* Journal of Environmental Sciences, 2013. **25**(5): p. 986-992.
32. Guaya, D., et al., *Simultaneous phosphate and ammonium removal from aqueous solution by a hydrated aluminum oxide modified natural zeolite.* Chemical Engineering Journal, 2015. **271**: p. 204-213.
33. Oliveira, M., et al., *Removal of phosphorus from water using active barriers: Al2O3 immobilized on to polyolefins.* Environmental Technology, 2011. **32**(9): p. 989-995.
34. Wu, D., et al., *Phosphate removal from aqueous solutions by nanoscale zero-valent iron.* Environmental Technology, 2013. **34**(18): p. 2663-2669.
35. Tang, J., et al., *Porous Pr(OH)3 nanowires as novel high-performance adsorbents for phosphate removal.* Chemical Engineering Journal, 2014. **252**: p. 202-209.
36. Xu, N., et al., *Synthesis and application of magnesium amorphous calcium carbonate for removal of high concentration of phosphate.* Chemical Engineering Journal, 2014. **251**: p. 102-110.
37. Su, Y., et al., *Synthesis of mesoporous cerium–zirconium binary oxide nanoadsorbents by a solvothermal process and their effective adsorption of phosphate from water.* Chemical Engineering Journal, 2015. **268**: p. 270-279.
38. Zong, E., et al., *Adsorptive removal of phosphate ions from aqueous solution using zirconia-functionalized graphite oxide.* Chemical Engineering Journal, 2013. **221**: p. 193-203.
39. Zach-Maor, A., R. Semiat, and H. Shemer, *Synthesis, performance, and modeling of immobilized nano-sized magnetite layer for phosphate removal.* Journal of Colloid and Interface Science, 2011. **357**(2): p. 440-446.
40. Lin, Y.-F., et al., *Application of magnetite modified with polyacrylamide to adsorb phosphate in aqueous solution.* Journal of the Taiwan Institute of Chemical Engineers, 2013. **44**(1): p. 45-51.
41. Bastin, O., et al., *Phosphorus removal by a synthetic iron oxide–gypsum compound.* Ecological Engineering, 1999. **12**(3–4): p. 339-351.
42. Zeng, L., X. Li, and J. Liu, *Adsorptive removal of phosphate from aqueous solutions using iron oxide tailings.* Water Research, 2004. **38**(5): p. 1318-1326.

43. Chitrakar, R., et al., *Phosphate adsorption on synthetic goethite and akaganeite.* Journal of Colloid and Interface Science, 2006. **298**(2): p. 602-608.
44. Luengo, C., et al., *Kinetics of phosphate adsorption on goethite: Comparing batch adsorption and ATR-IR measurements.* Journal of Colloid and Interface Science, 2006. **300**(2): p. 511-518.
45. Lakshmanan, R., et al., *Microemulsion prepared magnetic nanoparticles for phosphate removal: Time efficient studies.* Journal of Environmental Chemical Engineering, 2014. **2**(1): p. 185-189.
46. Zhang, C., et al., *Synthesis and properties of a magnetic core–shell composite nano-adsorbent for fluoride removal from drinking water.* Applied Surface Science, 2014. **317**(0): p. 552-559.
47. Bhaumik, M., et al., *Removal of fluoride from aqueous solution by polypyrrole/Fe3O4 magnetic nanocomposite.* Journal of Hazardous Materials, 2011. **186**(1): p. 150-159.
48. Tu, Y.-J., et al., *Application of magnetic nano-particles for phosphorus removal/recovery in aqueous solution.* Journal of the Taiwan Institute of Chemical Engineers, 2015. **46**(0): p. 148-154.
49. Yang, J., et al., *La-EDTA coated Fe3O4 nanomaterial: Preparation and application in removal of phosphate from water.* Journal of Environmental Sciences, 2013. **25**(2): p. 413-418.
50. Zou, C., et al., *Experimental Study of Cucurbit[7]uril Derivatives Modified Acrylamide Polymer for Enhanced Oil Recovery.* Industrial & Engineering Chemistry Research, 2014. **53**(18): p. 7570-7578.
51. Roy, S., et al., *Fabrication of smart COC chips: Advantages of N-vinylpyrrolidone (NVP) monomer over other hydrophilic monomers.* Sensors and Actuators B: Chemical, 2013. **178**(0): p. 86-95.
52. Shin, Y., et al., *Surface properties of silica nanoparticles modified with polymers for polymer nanocomposite applications.* Journal of Industrial and Engineering Chemistry, 2008. **14**(4): p. 515-519.
53. Xiong, H.-M., *Photoluminescent ZnO nanoparticles modified by polymers.* Journal of Materials Chemistry, 2010. **20**(21): p. 4251-4262.

54. DeMarco, M.J., A.K. SenGupta, and J.E. Greenleaf, *Arsenic removal using a polymeric/inorganic hybrid sorbent.* Water Research, 2003. **37**(1): p. 164-176.
55. Cumbal, L., et al., *Polymer supported inorganic nanoparticles: characterization and environmental applications.* Reactive and Functional Polymers, 2003. **54**(1–3): p. 167-180.
56. Onyango, M.S., et al., *Adsorption Kinetics of Arsenic Removal from Groundwater by Iron-Modified Zeolite.* JOURNAL OF CHEMICAL ENGINEERING OF JAPAN, 2003. **36**(12): p. 1516-1522.
57. Katsoyiannis, I.A. and A.I. Zouboulis, *Removal of arsenic from contaminated water sources by sorption onto iron-oxide-coated polymeric materials.* Water Research, 2002. **36**(20): p. 5141-5155.
58. Cumbal, L. and A.K. SenGupta, *Arsenic Removal Using Polymer-Supported Hydrated Iron(III) Oxide Nanoparticles: Role of Donnan Membrane Effect†.* Environmental Science & Technology, 2005. **39**(17): p. 6508-6515.
59. Zhang, Y. and B. Pan, *Modeling batch and column phosphate removal by hydrated ferric oxide-based nanocomposite using response surface methodology and artificial neural network.* Chemical Engineering Journal, 2014. **249**: p. 111-120.
60. You, X., et al., *Phosphate removal from aqueous solution using a hybrid impregnated polymeric sorbent containing hydrated ferric oxide (HFO).* Journal of Chemical Technology & Biotechnology, 2015: p. n/a-n/a.
61. Pan, B., et al., *Development of polymer-based nanosized hydrated ferric oxides (HFOs) for enhanced phosphate removal from waste effluents.* Water Research, 2009. **43**(17): p. 4421-4429.
62. Blaney, L.M., S. Cinar, and A.K. SenGupta, *Hybrid anion exchanger for trace phosphate removal from water and wastewater.* Water Research, 2007. **41**(7): p. 1603-1613.
63. Yang, W., et al., *Simultaneous organic/inorganic removal from water using a new nanocomposite adsorbent: A case study of p-nitrophenol and phosphate.* Chemical Engineering Journal, 2015. **268**: p. 399-407.
64. Abo-Farha, S.A., et al., *Removal of some heavy metal cations by synthetic resin purolite C100.* Journal of Hazardous Materials, 2009. **169**(1–3): p. 190-194.
65. Liu, C. and P.M. Huang, *Kinetics of phosphate adsorption on iron oxides formed under the influence of citrate.* Canadian Journal of Soil Science, 2000. **80**(3): p. 445-454.

66. Colombo, C., V. Barrón, and J. Torrent, *Phosphate adsorption and desorption in relation to morphology and crystal properties of synthetic hematites.* Geochimica et Cosmochimica Acta, 1994. **58**(4): p. 1261-1269.
67. Alonso, A., et al., *Environmentally-safe bimetallic Ag@Co magnetic nanocomposites with antimicrobial activity.* Chemical Communications, 2011. **47**(37): p. 10464-10466.
68. Alonso, A., *Development of polymeric nanocomposites with enhanced distribution of catalytically active or bactericide nanoparticles*, in *Departament d'Enginyeria Química, Escola d'Enginyeria* 2012, Universitat Autònoma de Barcelona (UAB).
69. Alonso, A., et al., *Recyclable polymer-stabilized nanocatalysts with enhanced accessibility for reactants.* Catalysis Today, 2012. **193**(1): p. 200-206.
70. Dorado, A.D., et al., *Cr(III) removal from aqueous solutions: A straightforward model approaching of the adsorption in a fixed-bed column.* Journal of Environmental Science and Health, Part A, 2013. **49**(2): p. 179-186.
71. Nur, T., et al., *Phosphate removal from water using an iron oxide impregnated strong base anion exchange resin.* Journal of Industrial and Engineering Chemistry, 2014. **20**(4): p. 1301-1307.
72. Vente, J.A., et al., *Evaluation of sugar sorption isotherm measurement by frontal analysis under industrial processing conditions.* Journal of Chromatography A, 2005. **1066**(1–2): p. 71-79.
73. Dorado, A.D., et al., *The role of water in the performance of biofilters: Parameterization of pressure drop and sorption capacities for common packing materials.* Journal of Hazardous Materials, 2010. **180**(1–3): p. 693-702.
74. Lemine, O.M., et al., *Sol–gel synthesis of 8 nm magnetite (Fe3O4) nanoparticles and their magnetic properties.* Superlattices and Microstructures, 2012. **52**(4): p. 793-799.
75. Neyaz, N., M.S.S. Zarger, and W.A. Siddiqui, *Synthesis and characterisation of modified magnetite super paramagnetic nano composite for removal of toxic metals from ground water.* International Journal of Environmental Sciences, 2014. **5**(2): p. 260-269.
76. Farghali, M.A., et al., *Graphene/ Magnetite Nanocomposite for Potential Environmental Application.* Int. J. Electrochem. Sci., 2015. **10**: p. 529 - 537.

77. Ahn, J.-H., et al., *Rapid Generation and Control of Microporosity, Bimodal Pore Size Distribution, and Surface Area in Davankov-Type Hyper-Cross-Linked Resins.* Macromolecules, 2006. **39**(2): p. 627-632.
78. Rodrigues, L. and M. da Silva, *Adsorption kinetic, thermodynamic and desorption studies of phosphate onto hydrous niobium oxide prepared by reverse microemulsion method.* Adsorption, 2010. **16**(3): p. 173-181.
79. Zeng, H., B. Fisher, and D.E. Giammar, *Individual and competitive adsorption of arsenate and phosphate to a high-surface-area iron oxide-based sorbent.* Environmental Science and Technology, 2008. **42**(1): p. 147-152.
80. Krishnan, K.A. and A. Haridas, *Removal of phosphate from aqueous solutions and sewage using natural and surface modified coir pith.* Journal of Hazardous Materials, 2008. **152**(2): p. 527-535.
81. Das, J., et al., *Adsorption of phosphate by layered double hydroxides in aqueous solutions.* Applied Clay Science, 2006. **32**(3–4): p. 252-260.
82. Kim, J., et al., *Phosphate adsorption on the iron oxyhydroxides goethite ([small alpha]-FeOOH), akaganeite ([small beta]-FeOOH), and lepidocrocite ([gamma]-FeOOH): a 31P NMR Study.* Energy & Environmental Science, 2011. **4**(10): p. 4298-4305.
83. Sarkar, A., S.K. Biswas, and P. Pramanik, *Design of a new nanostructure comprising mesoporous ZrO2 shell and magnetite core (Fe3O4@mZrO2) and study of its phosphate ion separation efficiency.* Journal of Materials Chemistry, 2010. **20**(21): p. 4417-4424.

Chapter 8

Optimization of high efficiency *Scenedesmus sp.* microalgae harvesting using low-cost magnetic iron oxide based nanoparticles

This chapter was performed in collaboration with: GEMMA – Group of Environmental Engineering and Microbiology, Department of Civil and Environmental Engineering, Universitat Politècnica de Catalunya· Barcelona Tech, Barcelona, Spain.

The results presented in this chapter are in preparation for submission at an international SCI journal:

"Ahmad Abo Markeb, Ivet Ferrer, Paqui Blanquez, Amanda Alonso, Antoni Sánchez, Xavier Font. Optimization of high efficiency Scenedesmus sp. microalgae harvesting using low-cost magnetic iron oxide based nanoparticles".

8.1. Introduction

Microalgae are nowadays cultured to produce high value-added compounds like nutraceuticals and pharmaceuticals. During the last decade, attention has been paid to the production of non-food bioproducts like biofuels or biopolymers. Regarding biofuels, the main advantages of microalgae over terrestrial crops are: i) their high photosynthetic efficiency, which leads to a high growth rate and biomass production; ii) not competition with food crops for arable land and; iii) their accumulation of certain compounds under stress conditions, e.g. lipids or carbohydrates. On the other hand, the main disadvantages are: i) the requirement of high amounts of water and nutrients and; ii) microalgal biomass harvesting. The first barrier can be overcome by using wastewater, which already has a high concentration of nutrients and thus must be treated. Indeed, this alternative provides a public service along with a valuable biomass feedstock. High Rate Algal Ponds (HRAP) are typically used for secondary wastewater treatment, while open or closed photobioreactors can be used for the tertiary treatment. However, the microalgae harvesting is still a challenge. Moreover, in recent years, algae pollution has become a global issue [1]. The occurrence of harmful algal bloom in water source has posed a serious water safety problem to local water supply systems. Several problems could occur using the conventional water treatment such as bad taste and odors, formation of disinfection by-products such as trihalomethanes (THMs) and chloroacetic acids, and clogging of filter beds due to the algal bloom in water reservoir [2]. Therefore, the algal bloom is directly endangering human and biological health [3]. In addition, the blue–green algae contain toxins and secrete mucus, resulting in the emergence of flocculation in the distribution pipeline network. THM parent could be formed by conversion those secretions. Unfortunately, this THM could make the removal process of algae from water very difficult, also it causes the growth of algae in the eutrophic water. So, the blue-green algae, and other freshwater algae are among diverse types microbiological contaminants in drinking water [4]. Besides, a lot of researches in the recent years are performed to remove the algae and the algae toxins due to the quick propagation of algae and the great damage that cause to water quality [5].

When microalgae are harvested to produce high value-added compounds, the cost of biomass harvesting is not a limitation. Indeed, energy intensive processes, as centrifugation, that achieve relatively high solids concentration (e.g. 10%) are generally used. However, in the

context of biofuels or biopolymers, these processes are hardly affordable. When wastewater is used to produce microalgae, the presence of bacteria in the culture enhances floc formation and eases biomass separation by gravity settling, which can reach a biomass recovery of 70-80% or even higher through biomass recycling [6]. Gravity settling and dissolved air flotation can be further enhanced by coagulation-flocculation with chemicals, which has low energetic requirements as compared to centrifugation. Certainly, natural products like starch and tannin–based flocculants have shown promising results [7, 8]. The main drawback is that the addition of chemicals has an economic cost and can affect downstream processing of harvested biomass. However, when pure microalgae cultures are used, gravity settling only achieves a biomass recovery of 50-60%.

Although flocculation method is the most commonly used for harvesting microalgae [9], its sedimentation process needs a long time as well as a low harvesting efficiency [10, 11]. There is an increasing attention for the harvesting of microalgae in the recent years by using the magnetophoretic separation due to the time-saving technology and the low cost of the process [12, 13]. Specifically, magnetic NPs have been reported for the harvesting due to its high specific surface area, biocompatibility and that they could adhere to the algae cells and then easily be separated from the medium by applying an external magnetic field [14, 15]. Moreover, by surface coating or modification of the magnetic nanoparticles (NPs), with diverse materials such as polymers and surfactants, the stability of the NPs suspension can be enhanced, jointly with the harvesting efficiency [11, 16, 17]. Different types of magnetic NPs (Fe_3O_4 NPs), with or without surface coating, have been used for the harvesting of different microalgae such as the oleaginous *Chlorella sp*. [11], *Scenedesmus Dimorphus* [16] and *Chlorella Vulgaris* [13]. The aims of this work are; i) screening the harvesting efficiency of the algae using different synthesized NPs and estimation of the effect of coating on the separation process, ii) optimization of the algae separation process in terms of efficiency and separation time, and iii) estimation of the maximum adsorption capacity and evaluation of the reusability of the NPs.

8.2.Materials and Methods

8.2.1 Materials

Iron (II) chloride ($FeCl_2$), Iron (III) chloride hexahydrate ($FeCl_3.6H_2O$), polyethylene imine (PEI), 3-Aminopropyl triethoxysilane (APTES), and cetyltrimethyl ammonium bromide (CTAB), were purchased from Sigma-Aldrich (Barcelona, Spain). Sodium hydroxide pellet (NaOH) was purchased from Merck. All the chemicals were of analytical grade or higher.

8.2.2 Microalgae production

Microalgae was produced in a pilot plant that treats real wastewater from the municipal sewer system in Barcelona (Spain). In this plant, wastewater undergoes a screening pretreatment, primary treatment in gravity settlers and secondary treatment in high rate algal ponds (HRAPs) with a nominal volume of 0.5 m^3 and a surface area of 1.5 m^2, operating with a hydraulic retention time (HRT) of 4 days at the time the experiments were conducted. Following, a clarifier is used to separate microalgal biomass from the secondary effluent. This wastewater treatment system is located outdoors, as previously reported [6].

Harvested microalgal biomass thickened and digested in 3 lab-scale anaerobic reactors (1.5 L) with an HRT of 20 days under mesophilic conditions, as described in a previous paper [18]. The digestate is then diluted with the secondary effluent from the clarifier (1:50 v:v) and treated in an airlift-photobioreactor (30 L) with an HRT of 10 days. This photobioreactor is located indoors and has light-dark cycles of 12h. Light intensity is XX. The microalgae culture (mainly *Scenedesmus* sp) from the closed photobioreactor was used to assess the harvesting capacity of the magnetite-based NPs.

8.2.3 Synthesis of magnetite based NPs

8.2.3.1 Magnetite (Fe_3O_4) NPs

Two different concentrations of $FeCl_2$ and $FeCl_3 \cdot 6H_2O$, by keeping the Fe^{2+}/Fe^{3+} molar ratio of 1:2 were used to produce Fe_3O_4 NPs and coded as Fe_3O_4 NPs-I (25 and 50 mM) and Fe_3O_4 NPs-II (100 and 200 mM). Detailed information is described in Chapter 4.

8.2.3.2 CTAB coated Fe_3O_4 NPs

CTAB coated Fe_3O_4 NPs were prepared as explained in Chapter 4 (Section 4.2.2.2.3) to produce Fe_3O_4@CTAB NPs.

8.2.3.3 PEI-modified Fe_3O_4 NPs

Fe_3O_4@PEI NPs were prepared by coating of Fe_3O_4 NPs with PEI as described in Chapter 4 (Section 4.2.2.2.2).

8.2.3.4 Amine functionalized Fe_3O_4 NPs

Production of the NPs containing amine groups, Fe_3O_4@$SiONH_2$ NPs, was carried out by functionalization the Fe_3O_4 NPs with APTES as described in Chapter 4 (Section 4.2.2.2.1).

8.2.4 Characterization of nanoparticles and microalgae

8.2.4.1 Inductively coupled plasma optical emission spectrometry

Inductively Coupled Plasma Optical Emission Spectrometry (ICP-OES) was used for metal content determination of the NPs. Samples preparation were described in Chapter 3 (Section 3.1.1).

8.2.4.2 Scanning Electron Microscopy and Transmission Electron Microscopy

The morphology and size of the NPs were characterized, by one side, using a Zeiss Merlin Scanning Electron Microscopy (SEM). On the other side a JEM-2011/JEOL, High-Resolution Transmission Electron Microscopy (HR-TEM) equipped with Energy-Dispersive Spectroscopy (EDS) was also used. Measurements were acquired with an Oxford INCA X-MAX detector at the *Servei de Microscopia* at UAB, Spain. Microalgae harvesting using the magnetite-based NPs was characterized by using the cross-sectioned analysis of the prepared samples as reported in a previous study [23]. Briefly, the pellets were firstly obtained by centrifugation the

samples for 10 min at 3000 rpm. Next, the cells were fixed with 2.5% glutaraldehyde in 0.1 M phosphate buffer (pH 7.0) at 4 °C overnight, rinsed twice with the phosphate buffer (pH 7.0), then post-fixed with 1% OsO_4 in a 0.1 M phosphate buffer (pH 7.0) at 4 °C for 4 h and again rinsed twice with the phosphate buffer (pH 7.0). After fixation, dehydration of the sample cells was performed by a washing series of ethanol (50%, 70% and 90%), 1:1 mixture of ethanol (90%) and acetone (90%), acetone (90%) and acetone (100%) at 4°C for15 min at each step. Following this, the samples were immersed in1:1 and 1:2mixtures of acetone and ethoxyline resin for 1 h and 4 h, respectively, transferred to ethoxyline resin at room temperature overnight, placed in baking box and heated at 60°C for 48 h. Finally, the cross sections were obtained by embedding the ultra-thin sections of the samples in epoxy resin after cutting using a 35° diamond knife from Diatome and a Leica UC7 ultra microtome. Finally, staining the cross-sectioning part with uranyl acetate and lead citrate was performed, followed by the characterization using JEM-2011/ JEOL HR-TEM microscope.

8.2.5 Microalgae analysis

The microalgae culture was characterized by the concentration of total suspended solids (TSS) as dry cell weight (DCW), volatile suspended solids (VSS) and soluble chemical oxygen demand (SCOD), following the Standard Methods [24]. Microalgae identification was carried out by optic microscope examination (Axioskop 40 Zeiss, Germany), using a photo camera and the Motic Image Plus 2.0 software and identified from literature. Turbidity was determined as explained in Chapter 3 (Section 3.2.5) and it was used to calculate algae removal efficiency during magnetic decantation.

8.2.6 Zeta potential measurements

The zeta potential of the *Scenedesmus* sp. (0.63 g/L) and Fe_3O_4 NPs (0.38 g/L) at pH 7.38 were determined as explained in Chapter 3 (Section 3.1.10).

8.2.7 Algae separation experiments

8.2.7.1 Procedure of the algae harvesting using the nanoparticles

The removal of the microalgae was carried out by mixing 10 mL of algae suspension with 0.25 g/L of NPs in a capped glass vial at 25 °C on an orbital shaker at 200 rpm to improve the interaction between the NPs and microalgae.

8.2.7.2 Screening of the algae separation using magnetite-based nanoparticles

The efficiency of the microalgae removal was compared by testing different types of magnetite-based NPs: Fe_3O_4 (I), Fe_3O_4 (II), Fe_3O_4@SiO-NH_2, Fe_3O_4@CTAB and Fe_3O_4@PEI NPs to estimate the significant effect of the positively coated NPs regarding the non-coated one on the microalgae separation. The removal percentage (%) was calculated based on the measurements of the turbidity of the microalgae before and after interaction with the NPs. Initially, microalgae and the NPs were mixed in a weight ratio of 2:1 for 20 min on a shaker at 200 rpm, and 25°C as described in section 2.5.1. Then the magnetic decantation for 20 min was performed prior to the measurements of the turbidity of the supernatant. All the tests were performed in triplicate.

8.2.7.3 Effect of the shaking type for the algae removal using the Fe_3O_4 NPs

Optimization of interactions between the NPs and the algae cells was carried out by studying the effect of shaking before the magnetophoretic separation of the algae. The harvesting efficiency of the microalgae was obtained by testing different types of shaker as a orbital and roller and comparing with the non-shaking as a control. Briefly, 0.25 g/L of Fe_3O_4 NPs was added into three vials containing 10 mL of the microalgae suspension, followed by exposure two of the mixture suspension vials to the orbital and roller shakers, and keeping the third one without shaking. Then, the turbidity was measured for each one after 5 min of magnetic separation and the removal efficiency was calculated. All the experiments were performed in triplicates. The effect of shaking type was statistically evaluated using one way ANOVA.

8.2.8 Optimization of the microalgae harvesting efficiency using the response surface method

Optimum conditions for the removal of microalgae by Fe_3O_4 NPs were determined by means of central composite design (CCD) under response surface methodology (RSM). In this study, two experimental designs with two variables were carried out. The first experimental design (CCD 1) with two variables; concentration of Fe_3O_4 NPs (0.13, 0.25 and 0.38 g/L), and magnetic decantation time (1, 5 and 20 min) was performed. Then, further optimization was conducted by performing the experimental design (CCD 2) with two variables; the amount of Fe_3O_4 NPs (0.05, 0.08 and 0.13 g/L), and magnetic decantation time (1, 5 and 20 min) to see the efficiency of the Fe_3O_4 NPs in the lowest dose of the NPs on the separation of microalgae. Detailed information of the experimental design and its evaluation by the analysis of variance (ANOVA) of the data fitting to the quadratic model were explained in Chapter 3 (Sections 3.5 and 3.6).

8.2.9 Adsorption isotherms and zeta potential measurements

Adsorption isotherm experiments were carried out in a range of concentration from 0.1 to 1.25 g/L of *Scenedesmus* sp. microalgae by dilution or concentration using centrifugation. Fe_3O_4 NPs was used at a dose of 0.38 g/L at pH 7.38 (pH of the wastewater). Different isotherm models, Langmuir, Freundlich, and Dubinin–Radushkevich were used for fitting the experimental data and could be expressed in a nonlinear form as illustrated in Chapter 3 (Section 3.4).

8.2.10 Reusability of the nanoparticles

The reduction of the harvesting costs could be achieved by the recuperation of NPs, first by the separation from the microalgae and followed by the regeneration of the NPs. The regeneration and reusability of the Fe_3O_4 NPs-I were accomplished with a slight change of the reported method [11]. Typically, the NPs and the algae cells obtained after the magnetic separation were suspended in 5 mL of NaOH (0.5 M), by shaking at 200 rpm for 10 min. Then,

the suspension was subjected to ultrasonication for 10 min. Followed by the addition of 2 mL methanol and 2 mL of chloroform into the mixture and after mixing well, the mixture solution was exposed to ultrasonication for 15 min. Finally, the NPs were gathered by using a permanent magnet and washed twice using ultra-pure water. Then, the regenerated NPs were tested five times by repeating the same process to evaluate the harvesting efficiency of the microalgae after each cycle under the same conditions of algae and NPs concentrations.

8.3. Results and Discussion

8.3.1. Microalgal biomass characterization

The microalgae culture composition is summarized in Table 8.1. The average biomass concentration was 0.629 g TSS/L, with an organic content of 0.357 g VSS/L. The turbidity of the culture was 327 NTU and pH around 7.38. It consisted of a mixed culture clearly dominated by *Scenedesmus* sp (99.8%).

Table 8.1. Characterization of the microalgae culture in the closed photobioreactor.

Parameter	Value	Unit
pH	7.38	
Turbidity	327	NTU
TSS	0.629	g/L
VSS	0.357	g/L
SCOD	115.76	mg/L
Dissolved oxygen	7.82	mg/L
Alkalinity	205	mg/L
Ammonium	0.041	mg/L
Nitrite	2.899	mg/L
Nitrate	1.058	mg/L
Sulphate	105.544	mg/L
Scenedesmus sp.	42620000	*Scenedesmus* sp./mL

8.3.2. Characterization of the nanoparticles

8.3.2.1. Metals ion concentration in the nanoparticles

The synthesized NPs were analyzed by ICP-OES and the mean of the duplicates of the iron (Fe) metal contents of the five samples was presented in Table 8.2 and expressed as mg_{Fe}/g_{NPs}. Because of the increase of the iron salts during the synthesis protocol, the iron content increases as shown in Table 8.2 for Fe_3O_4NPs-I, and Fe_3O_4NPs-II. In addition, 95.64 % of the Fe_3O_4 NPs successfully coated to the CTAB, while 91.74 % of Fe_3O_4 NPs coated to the PEI. This could be attributed to the high affinity of the cationic surfactant rather than the cationic polymer to the Fe_3O_4 NPs.

Table 8.2. Iron contents of the five synthesized nanoparticles

Nanoparticles	Iron concentration, (mg_{Fe}/g_{NPs})
Fe_3O_4 (I)	579.1 ± 11.3
Fe_3O_4 (II)	699.0 ± 4.9
Fe_3O_4@CTAB	668.6 ± 4.6
Fe_3O_4@PEI	641.3 ± 3.0
Fe_3O_4@SiO-NH_2	541.7 ± 6.1

8.3.2.2. TEM-EDS analysis of the nanoparticles

The TEM images of the NPs before the harvesting of the microalgae are shown in Figure 8.1. The average sizes of the NPs were determined by using ImageJ software to be 11.15 ± 1.57 nm for Fe_3O_4 NPs-I, 11.73 ± 1.61 nm for Fe_3O_4 NPs-II, 11.49 ± 1.83 nm for Fe_3O_4 with 1.65 nm shell thickness of CTAB, and 12.57 ± 1.86 nm for Fe_3O_4 with 0.86 nm shell thickness of PEI. As shown in Figure 8.1a-f, there is a decrease of the aggregation and increase of the dispersibility of the Fe_3O_4 NPs by using the surfactant or the polymer. Besides, all the Fe_3O_4 NPs for the naked NPs or the modified ones have the crystalline structure as shown in the electron diffraction patterns as illustrated in Figure 8.1g-j which means that the modification of the surface did not affect the crystallinity of the Fe_3O_4 NPs. These results are in agreement with the reported one [22].

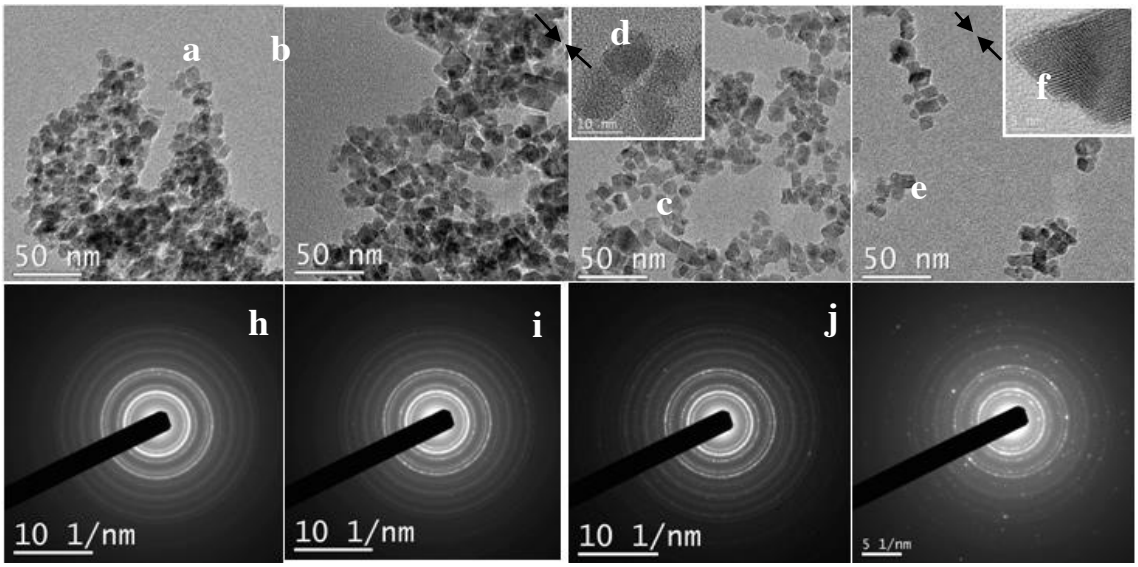

Figure 8.1. TEM images of: (a) Fe_3O_4 NPs-I, (b) Fe_3O_4 NPs-II, (c, and d) Fe_3O_4@CTAB NPs, and (e, and f) Fe_3O_4@PEI NPs; and ED patterns of: (g) Fe_3O_4 NPs-I, (h) Fe_3O_4 NPs-II, (i) Fe_3O_4@CTAB NPs, and (j) Fe_3O_4@PEI NPs.

8.3.3 Optimization procedure of the microalgae harvesting efficiency

8.3.3.1 Screening of the nanoparticles for the removal of microalgae

Screening of the harvesting efficiency (in terms of turbidity reduction) of *Scenedesmus* sp. microalgae using the Fe_3O_4based NPs is shown in Figure 8.2. As illustrated, the highest harvesting efficiency of the *Scenedesmus* sp. was higher than 82 % for Fe_3O_4@SiO-NH_2 followed by Fe_3O_4@PEI > Fe_3O_4@CTAB > Fe_3O_4 (I) > Fe_3O_4 (II). The highest values of the harvesting efficiency were observed in the cases of the functionalized Fe_3O_4 NPs due to the positive functional groups which enhance the interactions between the NPs and the microalgae. Moreover, significant differences were found between the NPs used for the algae harvesting efficiency due to the p value was less than 0.05 ($P =< 0.001$) by applying one way ANOVA test. In addition, multi-comparison procedures using Tukey test showed that the only significant differences were observed when comparing the Fe_3O_4 NPs-I versus Fe_3O_4 NPs-II due to the p value was found to be less than 0.05, while no significant differences were observed when comparing the Fe_3O_4 NPs-I versus Fe_3O_4@SiO-NH_2, Fe_3O_4@PEI, and Fe_3O_4@CTABNPs. Therefore, in terms of cost-effectives process, the naked Fe_3O_4 NPs, with the lowest

concentration of iron salts during the synthesis protocol of magnetite NPs (Fe_3O_4 NPs-I) were selected in the following studies of the optimization procedures.

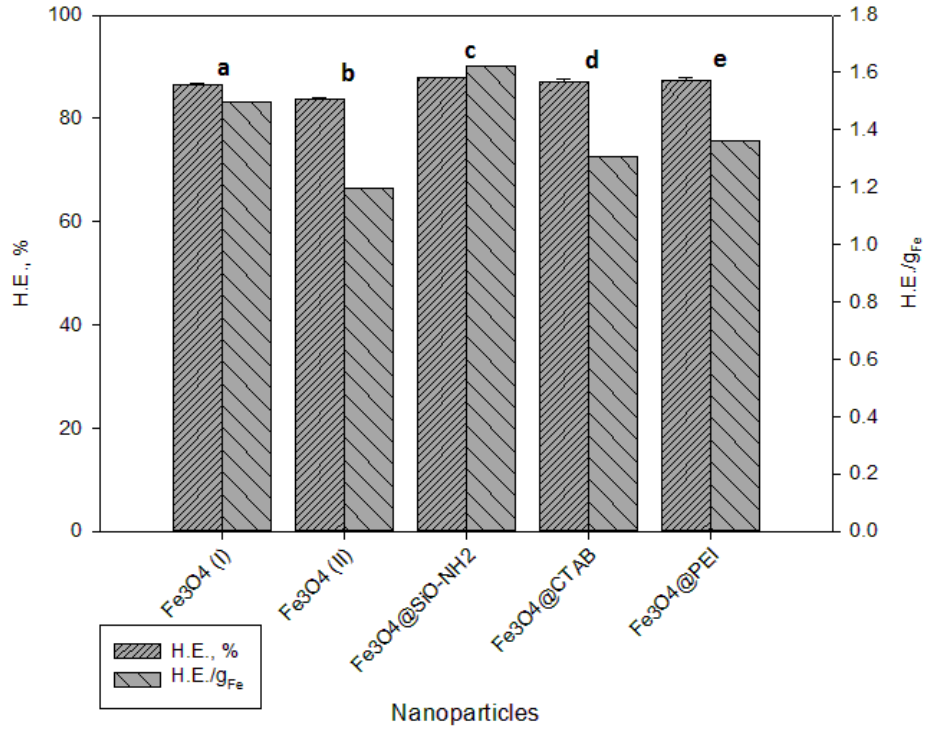

Figure 8.2. Screening of the harvesting efficiency (H.E.), and H.E./g_{Fe} of *Scenedesmus* sp. using Fe_3O_4 based NPs (Statistical data analysis using ANOVA was illustrated by the letters a, b, c, d, and e).

The magnetic separation of the microalgae can be qualitatively evaluated as shown in Figure 8.3. High harvesting efficiency was observed by the change in the green water color.

Figure 8.3. Magnetic separation of microalgae; (A) Without NPs, and (B) With Fe_3O_4 NPs-I (0.25 g/L of the NPs, and 20 min magnetic decantation time).

8.3.4 Characterization of algae with nanoparticles using TEM and SEM

The interaction of the microalgae with the NPs was proved by the characterization of the *Scenedesmus* sp. algae before and after the NPs interaction using TEM and SEM. In addition, the size and morphology of the NPs after the interaction are illustrated in Figures 8.4 and 8.5. Average size (Figure 8.4) of the Fe_3O_4 NPs after the interactions with the *Scenedesmus* sp. microalgae was determined by using ImageJ software and were found to be 14.58 ± 1.38 nm for Fe_3O_4 NPs-I, 13.77 ± 3.05 nm for Fe_3O_4 NPs-II, 15.08 ± 2.04 nm for Fe_3O_4@CTAB, 15.52 ± 2.07 nm for Fe_3O_4@PEI, and 18.31 ± 3.16 nm for Fe_3O_4@SiO-NH_2 NPs. Obviously, the interaction of microalgae with the NPs was shown by the increase in the size of the NPs. Moreover, the crystalline structure of the Fe_3O_4 NPs was not affected by the interaction with the algae cells that it is a crucial aspect in the viability to reuse the Fe_3O_4 NPs. In addition, the crystalline structure of the Fe_3O_4@CTAB could not be observed due to the insufficient scattering of the electrons from the NPs.

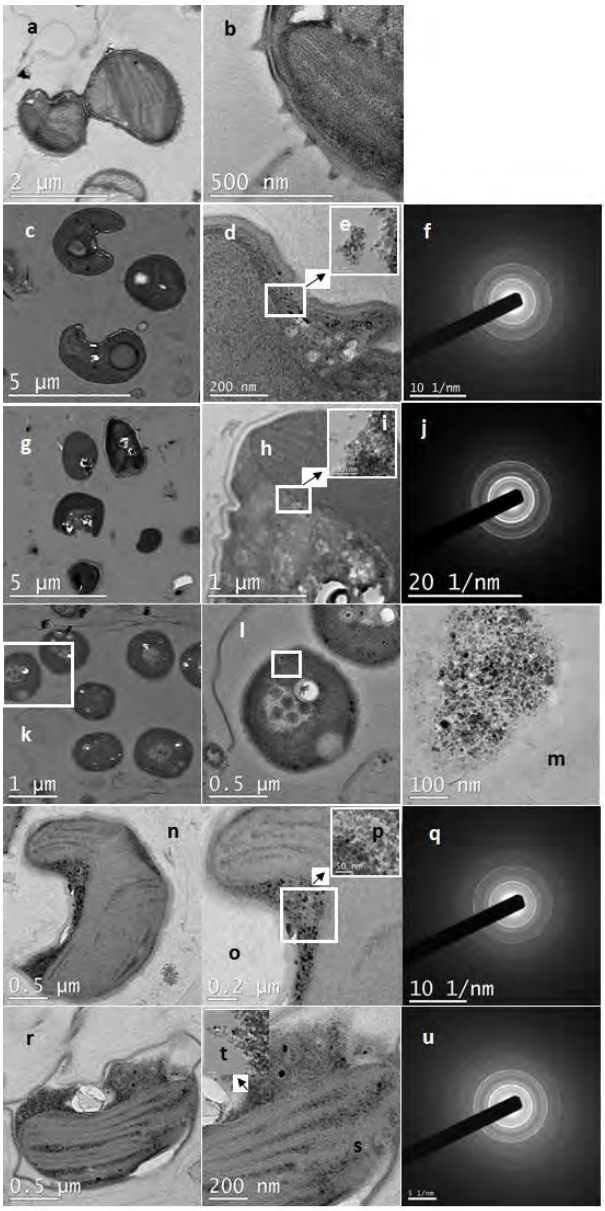

Figure 8.4. HETEM images of; (a, b) *Scenedesmus* sp. microalgae, and *Scenedesmus* sp. with; (c, and d) Fe_3O_4 NPs-I, (g, and h) Fe_3O_4 NPs-II, (k, and l) Fe_3O_4@CTAB, (n, and o) Fe_3O_4@PEI, (r, and s) Fe_3O_4@SiO-NH_2 NPs; (e) Fe_3O_4 NPs-I, (i) Fe_3O_4 NPs-II, (m) Fe_3O_4@CTAB, (p) Fe_3O_4@PEI, (t) Fe_3O_4@SiO-NH_2inside the *Scenedesmus* sp. and the ED patterns of; (f, j, q, and u) Fe_3O_4 NPs-I, Fe_3O_4 NPs-II, Fe_3O_4@PEI and Fe_3O_4@SiO-NH_2 NPs.

Moreover, the confirmation of the interaction between the algae and the NPs was confirmed by the analysis of SEM. As shown in Figure 8.5b-f, there is a coverage layer of NPs over the surface of *Scenedesmus* sp. microalgae.

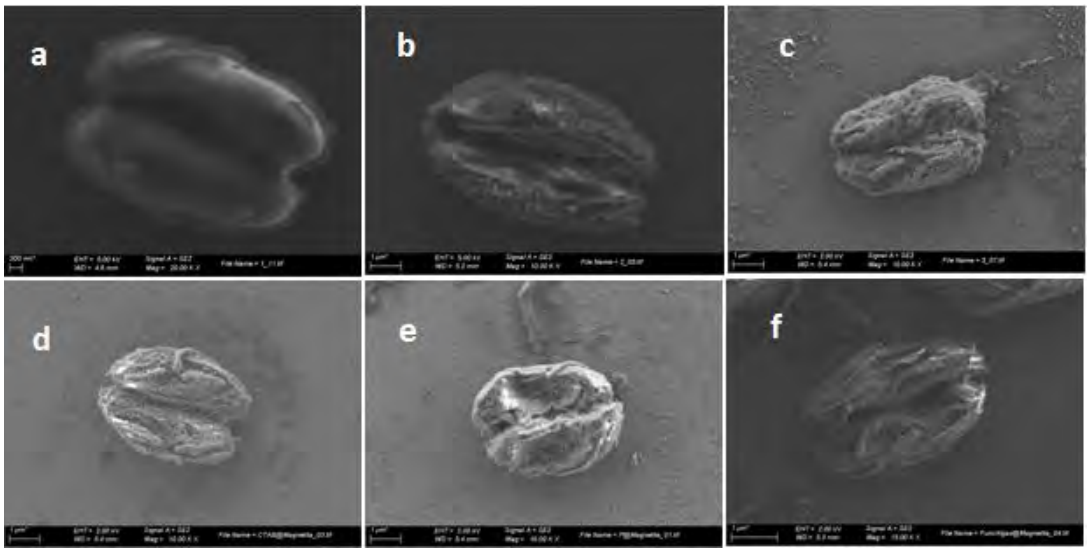

Figure 8.5. SEM images of; (a) naked *Scenedesmus* sp. microalgae, and NPs inside the *Scenedesmus* sp.; (b) Fe_3O_4 NPs-I, (c) Fe_3O_4 NPs-II, (d) Fe_3O_4@CTAB, (e) Fe_3O_4@PEI, (f) Fe_3O_4@SiO-NH_2.

8.3.5 Effect of shaking type

Enhancement of the removal efficiency of the microalgae using Fe_3O_4 NPs-I was carried out by testing the effect of the shaking type between the NPs and the microalgae before the magnetic decantation of the NPs. As illustrated in Figure 8.6, the average values of the harvesting efficiency of the microalgae were found to be 82, 80.7, and 75.5 % by using the orbital shaker, roller, and without agitation respectively. Significant difference between the type of shaking were found due to the p value is lower than 0.05 ($p = 0.017$). In addition, by applying Tukey test for all pairwise multiple comparison procedures, only statistically significant differences were found in the cases of using orbital and roller shakers versus without use of shaker, however, no difference statistically between the orbital versus the roller. This could be attributed to a better mixing in the case of orbital shaker, increasing the exposure of the NPs to the algae, which led to a high interaction between the algae and NPs and hence high harvesting efficiency of the *Scenedesmus* sp. Moreover, a Therefore, the orbital shaker was selected for the following optimization procedures of the algae removal.

8.3.6 Central composite design with a response surface method to optimize the harvesting efficiency

Optimization and modelling the maximum harvesting efficiency of the microalgae were performed in batch experiments by using the central composite design (CCD) under the response surface methodology (RSM). The range and level of the experimental variables used in this work were shown in Tables 8.3 and 8.4.

Table 8.3. Experimental design used for Algae removal using Fe_3O_4 NPs

Exp	Normalized values		Real values			Predicted values
	NPs concentration (g/L)	Time (min)	NPs concentration (g/L)	Time (min)	Removal (%)	Removal (%)
1	-1	-1	0.13	1	82.81	82.49
2	-1	0	0.13	5	82.47	81.19
3	-1	1	0.13	20	84.36	83.07
4	0	-1	0.25	1	78.43	82.49
5	0	0	0.25	5	84.09	86.27
6	0	0	0.25	5	82.81	79.16
7	0	0	0.25	5	82.14	84.32
8	0	0	0.25	5	81.12	79.32
9	0	1	0.25	20	84.67	82.49
10	1	-1	0.38	1	78.43	82.49
11	1	0	0.38	5	84.56	84.12
12	1	1	0.38	20	85.67	84.14

Second order Equation 8.1, was obtained after estimations of the regression coefficients based on the calculation of the sum of squares of the effects of the factors when studying the two independent variables of the dose of Fe_3O_4 NPs-I and the decantation time (CCD 1). The R^2 value of this model was found to be 0.764.

Removal, % = 84.921 – 45.282 * NPs concentration + 0.861 * time + 72.529 * (NPs concentration)^2 – 0.038 * (time)^2 + 0.805 * (NPs concentration) * (time)

(Equation 8.1)

The maximum harvesting efficiency was obtained by solving the regression model at 0.38 g/L of Fe_3O_4 NPs-I and 15.2 min of the magnetic decantation time to obtain 88.12 % removal of the microalgae.

Table 8.4. Experimental design used for Algae removal using Fe_3O_4 NPs

Exp	Normalized values		Real values			Predicted values
	NPs concentration (g/L)	Time (min)	NPs concentration (g/L)	Time (min)	Removal (%)	Removal (%)
1	-1	-1	0.05	1	82.67	82.98
2	-1	0	0.05	5	83.43	82.20
3	-1	1	0.05	20	83.59	81.17
4	0	-1	0.08	1	81.67	82.98
5	0	0	0.08	5	82.42	84.90
6	0	0	0.08	5	82.67	80.67
7	0	0	0.08	5	83.33	83.42
8	0	0	0.08	5	82.33	78.13
9	0	1	0.08	20	84.16	82.98
10	1	-1	0.13	1	76.67	82.98
11	1	0	0.13	5	83.00	83.97
12	1	1	0.13	20	84.54	84.07

Furthermore, by performing the CCD 2 with a lower dose of Fe_3O_4 NPs-I, as presented in Table 4, to optimize the amount of the NPs, the data obtained were analyzed and the second order model equation is shown in Equation 8.2.

Removal, % = 84.325 – 54.661 * NPs concentration + 0.448 * time + 1.011 * (NPs concentration)^2 - 0.027 * (time)^2 + 3.650 * (NPs concentration) * (time) (Equation 8.2)

The quality of this model equation was determined by estimating the R^2 value which was found to be 0.815. The optimum levels for the real values of Fe_3O_4 NPs-I and the magnetic decantation time were estimated to be 0.13 g/L and 11.75 min, respectively to obtain 86.28 % microalgae removal after solving the regression model.

The larger observed values of the linear coefficients for Fe_3O_4 NPs amount in equations 8.7 and 8.8 of both CCD 1 and CCD 2 imply the significant effect of the NPs amount on the harvesting efficiency of microalgae, which means by increasing the amount of the NPs enhance the separation efficiency of the algae. In addition, the negative values of the quadratic coefficients of the magnetic decantation time and the linear coefficient values of Fe_3O_4 NPs amount indicate the existence of optimum values for the harvesting efficiencies of microalgae. Moreover, as shown in Tables 8.4, and 8.5, there is a well observed correlation between the found and predicted values of the removal percentage of algae, which implies that the mathematical models were suitable for predicting harvesting efficiency of the microalgae in both cases of CCD 1 and CCD 2.

A combination of the two previously mentioned experimental designs was analyzed and a second order model equation was obtained (Equation 8.3). As with the previous models, the larger and positive value of the quadratic coefficient of the Fe_3O_4 NPs-I amount indicates that increasing the amount of the NPs, increase the harvesting efficiency of the microalgae.

Removal, % = 81.262 – 20.165 * NPs concentration + 0.791 * time + 33.885 * (NPs concentration)^2 – 0.0318 * (time)^2 + 0.6314 * (NPs concentration) * (time) (Equation 8.3)

The optimum values of the NPs dose and magnetic decantation time were found to be 0.38 g/L and 12.85 min reporting 89.30 % of harvesting efficiency of the microalgae.

Response surfaces and contour plots as a function of two variables is helpful to understand the main and the interaction effect of these two factors. Figure 8.6 shows the interaction effect of Fe_3O_4 NPs-I dose and magnetic decantation time on the harvesting efficiency of the microalgae. It is clear from the 3D response surface plot, Figure 8.6, that the harvesting efficiency of the microalgae increased by increasing the amount of NPs. This could be attributed to by increasing the dose of Fe_3O_4 NPs, increase the active sites for the interaction between the NPs and microalgae. Moreover, the 3D plots showed a slight change on the removal of the microalgae, until approximately 5 min, which suggests that the time had no effect up to 5 min. In addition, a high harvesting efficiency of the microalgae was observed in the range of 9 to 15 min of the magnetic decantation time and beyond this interval, a decrease of the microalgae removal was observed as shown in Figure 8.6. Therefore, 0.38 g/L of the NPs and 13 min of the magnetic separation time were selected as the optimum conditions for the following studies.

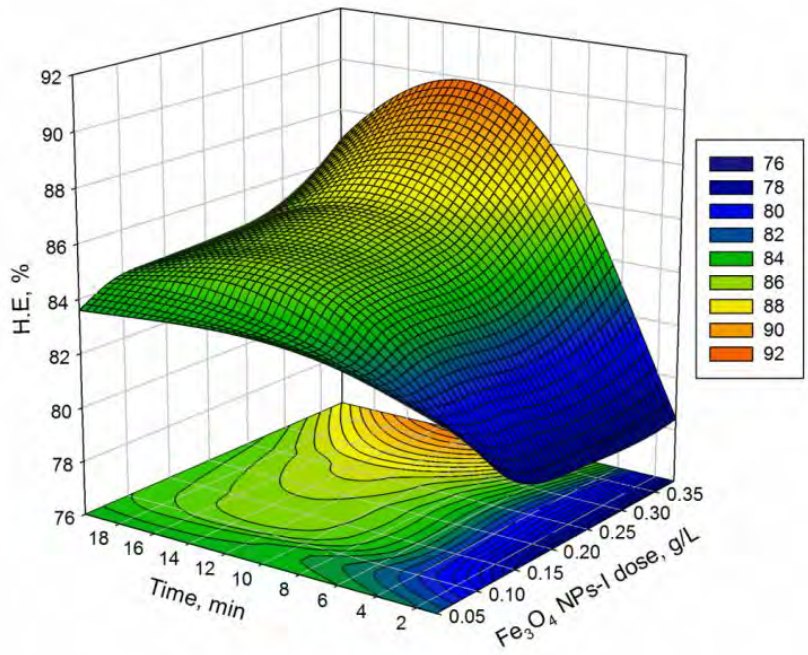

Figure 8.6. Response surface and contour plots of microalgae harvesting efficiency using (0.05-0.38 g/L) Fe_3O_4 NPs, and decantation time (1 – 20 min).

8.3.7 Statistical analysis

The fitness and validity of the model were evaluated by the analysis of variance (ANOVA) for the combined experimental design used. The significant of the factors was statistically significant when the probability > F value is less than 0.05 ($P < 0.05$) at 95% confidence limit. As shown in Table 8.5, the model F value of 7.04 implies the model is significant. There is only a 0.08% chance that a "Model F-Value" this large could occur due to noise.Values of $p < 0.05$ indicate model terms are significant. In this case (time) and $(time)^2$ are significant model terms. The Lack of Fit F value of 0.46 implies that the Lack of Fit is not significant due to the P value was higher than 0.05, hence the quadratic model was valid for prediction of experimental data [26]. Regarding the "Adeq Precision" parameter, it indicates that the experimental signal to noise ratio was adequate as it was greater than 4 [27, 28].

Table 8.5. Analysis of variance (ANOVA) for the fitted quadratic model of algae removal as a function of NPs concentration and time of magnetic decantation

Source	Sum of squares	Degree of freedom	Mean square	F value	P < 0.05	
Model	69.45	5	13.89	7.04	0.0008	S
NPs dose	0.26	1	0.26	0.13	0.7198	NS
Time	63.97	1	63.97	32.43	< 0.0001	S
$(NPs\ dose)^2$	2.66	1	2.66	1.35	0.2608	NS
$(time)^2$	18.43	1	18.43	9.34	0.0068	
(NPs dose*Time)	6.26	1	6.26	3.17	0.0918	NS
Residual	35.51	18	1.97			
Lack of fit	11.24	9	1.25	0.46	0.8665	NS
Pure Error	24.27	9	2.70			
Adeq precision						10.174

S: Significant
NS: Not significant

8.3.8 Adsorption isotherms and possible mechanism of interactions

Description of the equilibrium relationship between the amount of *Scenedesmus sp.* per unit of Fe_3O_4 NPs was determined by the adsorption isotherms to evaluate the affinity of the NPs for the algae. In this study, Langmuir, Freundlich, and Dubinin–Radushkevich isotherm models were used due to its relative simplicity, and reasonable accuracy [29]. The Langmuir model assumes that the harvesting of algae occurs on a homogenous surface by monolayer, while, Freundlich model assumes that occurs on heterogenous surface of the NPs. Moreover, the Dubinin-Radushkevich (D-R) isotherm model was used to estimate the possible mechanism of interaction as physisorption or chemisorption process. Data fitting of the experimental data using Langmuir and Freundlich isotherms are shown in Figure 8.7. Estimated parameters for all models were calculated using non-linear regression, and its values with the corresponding correlation coefficients (R^2) were presented in Table 8.6. The Langmuir model showed the higher R^2 value (0.99) in comparison to the other models used and this could indicate that the harvesting of microalgae could be monolayer coverage on Fe_3O_4 NPs. Thus, the maximum monolayer adsorption capacity, Q_m, obtained was 3.49 mg/g. Moreover, the higher value of K_L indicates that the *Scenedesmus sp*. microalgae cells were bonded strongly by the Fe_3O_4 NPs [30]. In addition, the type of the isotherm was found to be highly favorable due to the low separation factor constant (R_L 0.36) which is in the range between 0 and 1 [21]. Moreover, for the Freundlich isotherm model, the Fe_3O_4 NPs were favorable for the separation of the *Scenedesmus sp*. microalgae due to the 1/n value is 0.51 which is the range between 0 and 1[31].

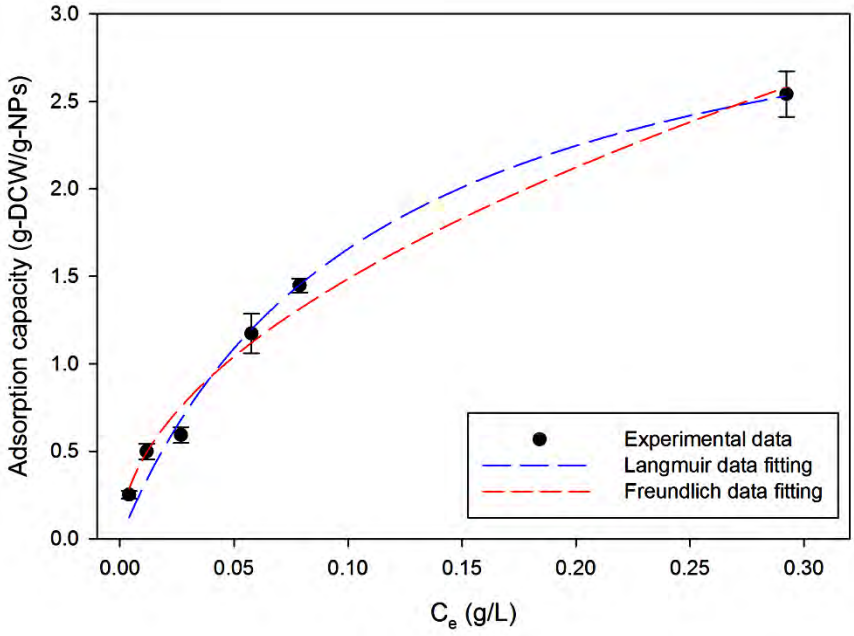

Figure 8.7. Adsorption isotherm of *Scenedesmus sp*. microalgae using Fe_3O_4 NPs.

Table 8.6. Langmuir, Freundlich, and Dubinin–Radushkevich (D-R) isotherm parameters for *Scenedesmus sp*. microalgae on Fe_3O_4 NPs.

Langmuir	**$Q_m(g_{DCW}/g_{NPs})$**	3.49
	K_L (L/mg)	9.06
	R^2	0.99
	R_L	0.36
Freundlich	**K_F ($mg^{1-(1/n)}L^{1/n}g^{-1}$)**	4.86
	1/n	0.51
	R^2	0.98
D-R	**Q_m(g/g)**	2.93
	K_{DR} (mol^2/kJ^2)	1.66E-8
	R^2	0.91
	E (kJ/mol)	8.73

As indicated in Table 8.6, the calculated parameter of the apparent energy, E, of the Dubinin–Radushkevich isotherm was found to be 8.73 kJ/mol. Therefore, the harvesting of

Scenedesmus sp. microalgae by Fe_3O_4 NPs could be attributed to chemisorption due to the magnitude of E-value was higher than 8.00 kJ/mol [31].

Further investigation of the possible mechanism of interaction between the Fe_3O_4 NPs and microalgae was performed by measuring their zeta potential values. Figure 8.8, shows the zeta potential values of the *Scenedesmus sp*. microalgae, the Fe_3O_4 NPs, and the *Scenedesmus sp*. algae with NPs at pH 7.38. A strong electrostatic attraction was observed between the *Scenedesmus sp*. algae and the Fe_3O_4 NPs. This possible mechanism of interaction was in agreement with using Fe_3O_4 NPs for the harvesting efficiency of *B. Braunii* and *C. ellipsoidea* cells [30].

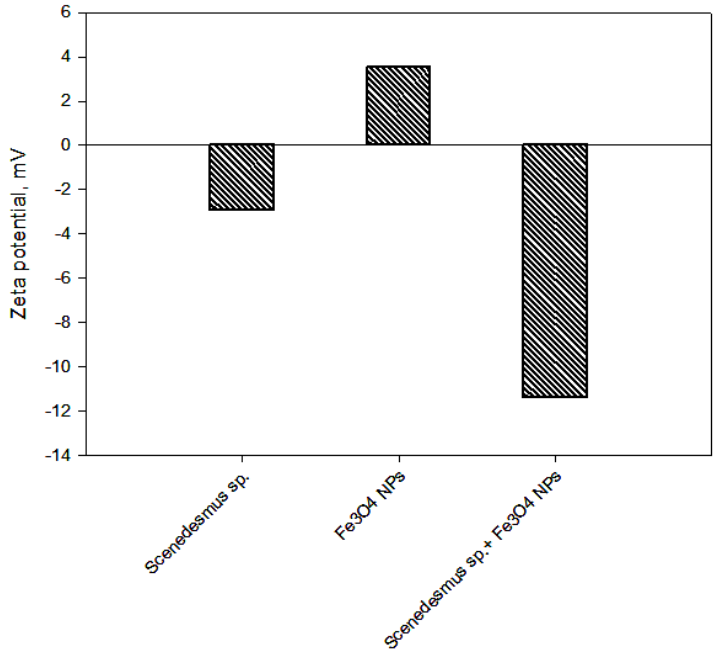

Figure 8.8. Zeta potential of *Scenedesmus sp*. microalgae, Fe_3O_4 NPs, and *Scenedesmus sp*. microalgae with Fe_3O_4 NPs

8.3.9 Regeneration and reusability studies of the Fe_3O_4 NPs

Regeneration of NPs was assayed to test the viability of the NPs after microalgae harvesting. The combination of the strongest alkaline treatments, with ultrasonication detachment method, showed the high detachment potential of the magnetite NPs compared to the alkaline or the ultrasonication methods [11]. As shown in Figure 8.9, the Fe_3O_4 NPs-I could be

used 5 times successfully for the harvesting of the *Scenedesmus sp*. microalgae with a slight decrease in the removal efficiency. The break-up of the Fe_3O_4 NPs from the algae at high pH value could be attributed to the weak electrostatic attraction between the algae and the NPs due to the increase of the negative charge of the NPs, and the algae cells in a strongly alkaline medium [32]. In addition, the use of a mixture of methanol and chloroform combined with the ultrasonic treatment could enhance the disintegration between the algae cells and the NPs [17]. Therefore, the combination of strong alkaline medium and ultrasonication treatments is not efficient only for the separation of NPs from the algae, but also for the lipid extraction of microalgae cells. Moreover, this study showed that the modified combination method had a lower decrease in the harvesting efficiency after 5 cycles by 5.90 %, in comparison with the same method of regeneration reported in the previous study that had a decrease by 22.16 % [11]. This could be attributed to the use of a lower concentration of NaOH in the detachment method and longer time of ultrasonication. Therefore, the proposed modified regeneration method, by using a combination of strong alkaline medium with a lower concentration and prolonged time of ultrasonic treatment, enhances the potential efficiency of the NPs compared to the previous used methods [11, 17, 33].

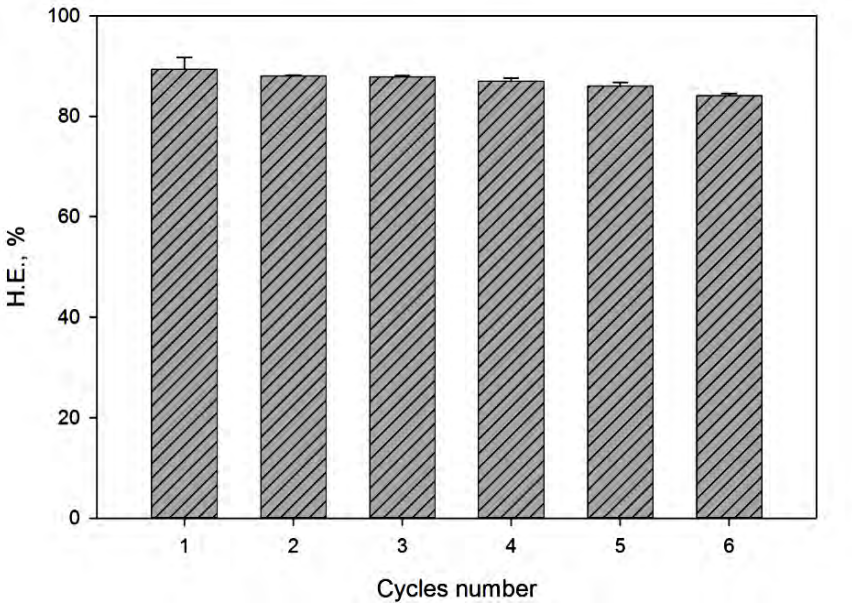

Figure 8.9. Harvesting efficiency % of *Scenedesmus sp*. microalgae using Fe_3O_4 NPs after 5 cycles using 0.38 g/L of the NPs, and 13 min magnetic decantation time.

8.4 Conclusions

In this work, the harvesting efficiency of the *Scenedesmus sp*. microalgae has been evaluated by using different Fe_3O_4 based nanoparticles as adsorbents. Naked, coated and functionalized Fe_3O_4 nanoparticles were used. All the synthesized magnetite-based NPs showed a high potential efficiency for the microalgae separation from water. Response surface method indicates that the optimum value for the harvesting was 0.38 g/L of naked Fe_3O_4 NPs and 13 min magnetic separation time. Monolayer adsorption was found in the separation of the algae due to the high correlation coefficient of the Langmuir isotherm model, and yielding a maximum adsorption capacity, 3.49 g_{DCW}/g_{NPs}, for *Scenedesmus sp.* using Fe_3O_4 NPs. The electrostatic interaction mechanism is proposed to describe the interaction between the algae cells and the NPs. Reactivation of the Fe_3O_4 NPs was successfully conducted using a low concentration of the alkaline medium combined with an ultrasonication treatment method for 5 cycles of the microalgae separation from wastewater.

8.5 References

1. Shen, Q., et al., *Enhanced algae removal by drinking water treatment of chlorination coupled with coagulation.* Desalination, 2011. **271**(1–3): p. 236-240.
2. Hung, M.T. and J.C. Liu, *Microfiltration for separation of green algae from water.* Colloids and Surfaces B: Biointerfaces, 2006. **51**(2): p. 157-164.
3. Henriksen, P., *Estimating nodularin content of cyanobacterial blooms from abundance of Nodularia spumigena and its characteristic pigments—a case study from the Baltic entrance area.* Harmful Algae, 2005. **4**(1): p. 167-178.
4. EPA, *Drinking water standards and health advisories table*. 2007, United states environmental protection agency. p. 1-30.
5. Gao, S., et al., *Electro-coagulation–flotation process for algae removal.* Journal of Hazardous Materials, 2010. **177**(1–3): p. 336-343.
6. Gutiérrez, R., et al., *Microalgae recycling improves biomass recovery from wastewater treatment high rate algal ponds.* Water Research, 2016. **106**: p. 539-549.

7. Gutiérrez, R., et al., *Influence of starch on microalgal biomass recovery, settleability and biogas production.* Bioresource Technology, 2015. **185**: p. 341-345.
8. Gutiérrez, R., et al., *Harvesting microalgae from wastewater treatment systems with natural flocculants: Effect on biomass settling and biogas production.* Algal Research, 2015. **9**: p. 204-211.
9. Vandamme, D., I. Foubert, and K. Muylaert, *Flocculation as a low-cost method for harvesting microalgae for bulk biomass production.* Trends in Biotechnology, 2013. **31**(4): p. 233-239.
10. Wang, S.-K., et al., *Magnetic Flocculant for High Efficiency Harvesting of Microalgal Cells.* ACS Applied Materials & Interfaces, 2014. **6**(1): p. 109-115.
11. Wang, T., et al., *Magnetic nanoparticles grafted with amino-riched dendrimer as magnetic flocculant for efficient harvesting of oleaginous microalgae.* Chemical Engineering Journal, 2016. **297**: p. 304-314.
12. Hu, Y.-R., et al., *Efficient harvesting of marine microalgae Nannochloropsis maritima using magnetic nanoparticles.* Bioresource Technology, 2013. **138**: p. 387-390.
13. Prochazkova, G., I. Safarik, and T. Branyik, *Harvesting microalgae with microwave synthesized magnetic microparticles.* Bioresource Technology, 2013. **130**: p. 472-477.
14. Schwertmann, U. and R.M. Cornell, *Magnetite*, in *Iron Oxides in the Laboratory*. 2007, Wiley-VCH Verlag GmbH. p. 135-140.
15. Procházková, G., I. Šafařík, and T. Brányik, *Surface Modification of Chlorella Vulgaris Cells Using Magnetite Particles.* Procedia Engineering, 2012. **42**: p. 1778-1787.
16. Ge, S., et al., *Influences of Surface Coating, UV Irradiation and Magnetic Field on the Algae Removal Using Magnetite Nanoparticles.* Environmental Science & Technology, 2015. **49**(2): p. 1190-1196.
17. Lin, Z., et al., *Application and reactivation of magnetic nanoparticles in Microcystis aeruginosa harvesting.* Bioresource Technology, 2015. **190**: p. 82-88.
18. Passos, F., et al., *Microalgae production in wastewater treatment systems, anaerobic digestion and modelling using ADM1.* Algal Research, 2015. **10**: p. 55-63.
19. Abo Markeb, A., et al., *Phosphate removal and recovery from water using nanocomposite of immobilized magnetite nanoparticles on cationic polymer.* Environmental Technology, 2016. **37**(16): p. 2099-2112.

20. Khoshnevisan, K., et al., *Preparation and Characterization of CTAB-Coated Fe_3O_4 Nanoparticles.* Synthesis and Reactivity in Inorganic, Metal-Organic, and Nano-Metal Chemistry, 2012. **42**(5): p. 644-648.
21. Hasanzadeh, R., et al., *Effective removal of toxic metal ions from aqueous solutions: 2-Bifunctional magnetic nanocomposite base on novel reactive PGMA-MAn copolymer@Fe3O4 nanoparticles.* Journal of Colloid and Interface Science, 2017. **490**: p. 727-746.
22. Yazid, N.A., R. Barrena, and A. Sánchez, *The immobilisation of proteases produced by SSF onto functionalized magnetic nanoparticles: Application in the hydrolysis of different protein sources.* Journal of Molecular Catalysis B: Enzymatic, 2017.
23. Zhang, L., et al., *Uptake and effect of highly fluorescent silver nanoclusters on Scenedesmus obliquus.* Chemosphere, 2016. **153**: p. 322-331.
24. APHA, AWWA, and WPCF, *Standard Methods for examination of water and wastewater*. 1999, Washington: American Public Health Association. 1325.
25. Babaeivelni, K. and A.P. Khodadoust, *Adsorption of fluoride onto crystalline titanium dioxide: Effect of pH, ionic strength, and co-existing ions.* Journal of Colloid and Interface Science, 2013. **394**: p. 419-427.
26. Subbalaxmi, S. and V.R. Murty, *Process optimization for tannase production by Bacillus gottheilii M2S2 on inert polyurethane foam support.* Biocatalysis and Agricultural Biotechnology, 2016. **7**: p. 48-55.
27. Asfaram, A., et al., *Experimental design and modeling of ultrasound assisted simultaneous adsorption of cationic dyes onto ZnS: Mn-NPs-AC from binary mixture.* Ultrasonics Sonochemistry, 2016. **33**: p. 77-89.
28. Kumar Gupta, V., et al., *Application of response surface methodology to optimize the adsorption performance of a magnetic graphene oxide nanocomposite adsorbent for removal of methadone from the environment.* Journal of Colloid and Interface Science, 2017. **497**: p. 193-200.
29. Nassar, N.N., *Rapid removal and recovery of Pb(II) from wastewater by magnetic nanoadsorbents.* Journal of Hazardous Materials, 2010. **184**(1–3): p. 538-546.
30. Xu, L., et al., *A simple and rapid harvesting method for microalgae by in situ magnetic separation.* Bioresource Technology, 2011. **102**(21): p. 10047-10051.

31. Chaudhry, S.A., Z. Zaidi, and S.I. Siddiqui, *Isotherm, kinetic and thermodynamics of arsenic adsorption onto Iron-Zirconium Binary Oxide-Coated Sand (IZBOCS): Modelling and process optimization.* Journal of Molecular Liquids, 2017. **229**: p. 230-240.
32. Seo, J.Y., et al., *Effect of barium ferrite particle size on detachment efficiency in magnetophoretic harvesting of oleaginous Chlorella sp.* Bioresource Technology, 2014. **152**: p. 562-566.
33. Prochazkova, G., et al., *Physicochemical approach to freshwater microalgae harvesting with magnetic particles.* Colloids and Surfaces B: Biointerfaces, 2013. **112**: p. 213-218.

Part B:

Gases treatment

Chapter 9

Catalytic oxidation of CO using Au/CeO_2 core-shell nanoparticles supported in UiO-66 beads

This chapter was performed in collaboration with Institut Català de Nanociència i Nanotecnologia (ICN2).

The results presented in this chapter has been accepted in Journal of Material Chemistry A:

"A. Yazdi, A. Abo Markeb, L. Garzon-Tovar, J. Patarroyo, J. Moral-Vico, A. Alonso, A. Sánchez, N. G. Bastús, I. Imaz, X. Font, V. Puntes and D. Maspoch. Core-shell Au/CeO2 nanoparticles supported in UiO-66 beads exhibiting full CO conversion at 100 ˚C".

9.1. Introduction

Long-term exposure to carbon monoxide gas is a cause of lethal damage to humans and animals [1]. Only in 2014, 6381 kilotons of CO were emitted in the world, mainly from transportation, power plants and industrial activities [2]. To date, one of the most efficient solutions for mitigating CO emissions to atmosphere is its catalytic oxidation to CO_2 [3, 4].

Good-performance catalysts for CO oxidation are metal nanoparticles (NPs) such as Au, Pd, Pt and Ru NPs [5-8]. These NPs are usually supported on/in zeolites [9], activated carbon [10], and metal oxides, including alumina [11], mesoporous silica [12], ceria [13-17], zirconia [18], titania [19], and iron oxides [3]. These supports avoid NP aggregation and, eventually, enhance the catalytic activity of NPs. A remarkable case is the use of nanocrystalline CeO_2 to support Au NPs [20, 21].

In this particular composite, CeO_2 acts as an active support that enhances the catalytic performance of Au NPs for CO oxidation. Indeed, because CeO_2 has a high oxygen storage and release capacity [22] and facile oxygen vacancy formation, its surface can be easily enriched with oxygen vacancies so that Au NPs can strongly bind to these vacancies [23, 24]. Also, the oxygen vacancies in CeO_2 can create Ce^{3+} ions, opening a new CO oxidation pathway by O_2 adsorbed on Au-Ce^{3+} bridge site [23]. Moreover, the interaction between the ceria and the metal NPs can prevent reorganization of the metallic atoms under operating conditions [22].

Inspired by these latter results, herein we show a fast method that enables integrating pre-designed core-shell Au/CeO_2 NPs [25-27] in metal-organic frameworks (MOFs). Because, recently, MOFs have attracted much attention as new porous supports for catalytic NPs due to their exceptionally high surface areas, structural diversity and tailorable pore chemical functionalities [28]. Due to the enhancement of the properties of the nanocomposites (NCs) when the inorganic NPs incorporated into organic support (Chapter 1), this work aims to (1) evaluate the catalytic activity of the hybrid Au/CeO_2 (Core/shell) NPs encapsulated into UiO-66 (porous organic frame work) for CO oxidation, and (2) estimate the stability and reusability of the NCs.

9.2. Materials and methods

9.2.1. Materials

All reagents were purchased from Sigma-Aldrich and used without further purification. All gases were purchased from Carburos Metálicos. Deionized water, obtained with a Milli-Q system (18.2 MQ cm), was used in all reactions.

9.2.2. Synthesis of PVP-Stabilized Au/CeO_2 Nanoparticles

Au/CeO_2 (Ce:Au = 1:1) NPs were synthesized in water following the simultaneous reduction/oxidation of Au and Ce precursors. More specifically, 400 mL of an aqueous solution containing sodium citrate (10 mM) was prepared and heated with a heating mantle in a three-neck round-bottomed flask for 15 min under vigorous stirring. A condenser was used to prevent the evaporation of the solvent. After boiling had commenced, $HAuCl_4$ (25 mM) and cerium (III) nitrate hexahydrate (25 mM) were sequentially injected to this solution. After cooling down to room temperature, 4 g of poly (vinylpyrrolidone) (PVP, M.W 10,000) in 200 mL of water was added dropwise to the NP solution while stirring and left overnight at room temperature. Then, 800 mL of acetone was added to the NP solution and left 24 h at room temperature without stirring for precipitation of the NPs. After removing the supernatant, NPs were washed three times with DMF and finally, redispersed in DMF to give a colloidal solution of Au/CeO_2 NPs with a concentration of 1 mg/mL.

9.2.3. Synthesis of UiO-66@Au/CeO_2

100 mg of terephthalic acid (BDC), 3 mL of acetic acid, a volume of Au/CeO_2 NPs (concentration = 1 mg/mL; 4 mL for UiO-66@Au/CeO_2-2.8; 8.5 mL for UiO-66@Au/CeO_2-5.5; and 12.5 mL for UiO-66@Au/CeO_2-7) and 280 µL of $Zr(OPr^n)_4$ were sequentially mixed in 40 mL DMF. These solutions were injected into a coil flow reactor (inner diameter: 3 mm) at a feed rate of 2.4 $mL.min^{-1}$ at 115 ˚C. The resulting pre-heated solution was then spray dried at 180 ˚C and a flow rate of 336 $mL.min^{-1}$ using a B-290 Mini Spray Dryer (BUCHI Labortechnik) using a spray cap with a 0.5 mm diameter hole. Then, the resulting solid was dispersed in DMF and

washed twice with DMF and ethanol. The final product was calcined in the presence of air at 250 ˚C for 12 h. Encapsulation efficiency was calculated based on the initial amount of NPs in the precursors solution (4, 8.5 and 12 mg for UiO-66@Au/CeO_2-2.8, UiO-66@Au/CeO_2-5.5 and UiO-66@Au/CeO_2-7, respectively), the final mass of the product after washing (144, 140 and 125 mg for UiO-66@Au/CeO_2-2.8, UiO-66@Au/CeO_2-5.5 and UiO-66@Au/CeO_2-7, respectively) and the Au/CeO_2 content determined by ICP-OES.

9.2.4. Synthesis of PVP-Stabilized Pd Nanoparticles

$NaPdCl_2$ (44 mg) was dissolved in 20 mL of ethylene glycol in the presence of 222 mg of PVP (MW = 55,000) in a three-neck round-bottomed flask. This solution was heated up to 180 °C for 10 min and, after cooling down to room temperature, 150 mL of acetone was added into it. Precipitated Pd NPs were then dispersed in DMF and washed twice with DMF by centrifugation. Finally, they were redispersed in 5 mL of DMF to give a colloidal solution of Pd NPs with a concentration of 0.8 mg/mL.

9.2.5. Synthesis of UiO-66@Pd

127 mg of $ZrCl_4$, 89 mg of BDC and 2 mL of PVP-stabilized Pd NPs solution with a concentration of 0.8 mg/mL were added to mixture of DMF (5 mL) and H_2O (0.4 mL). The resulting mixture was injected into a coil flow reactor (inner diameter: 3 mm) at a feed rate of 2.4 $mL.min^{-1}$ at 115 ˚C. The resulting pre-heated solution was then spray dried at 180 ˚C and a flow rate of 336 $mL.min^{-1}$ using a B-290 Mini Spray Dryer (BUCHI Labortechnik) using a spray cap with a 0.5 mm diameter hole. The resulting solid was dispersed in DMF and washed twice times with DMF and ethanol [29]. Then, it was dispersed in ethanol and stirred at room temperature overnight and precipitated by centrifugation. The process was repeated one more time with ethanol. The final product was dried for 12 h at 160˚ C under vacuum. A final step involved its calcination at 250˚C overnight in the presence of air. This calcination process facilitates the removal of PVP from the surface of Au/CeO_2 NPs. It also enhances the interfacial interaction of Au and

CeO_2 and increases the crystallinity of CeO_2, which leads to an enhancement of oxygen generation/storage capacity of ceria [30-32].

9.2.6. Catalytic CO Oxidation Study

The catalytic oxidation of CO was carried out in a fixed bed column reactor with dimensions of 9.0 cm in length and 0.5 cm in inner diameter set in a controlled temperature oven. 50 mg of the catalyst was packed into the column, and a mixture of gases consisting of 1 % CO, 21 % O_2 and 78 % N_2 was passed through the column reactor at a fixed flow rate of 100 mL/min. After that, the catalyst was heated up to the desired temperature and maintained until a steady state was achieved. Within this interval of time, set of samples of the outlet gas were withdrawn and analyzed to determine the CO_2 produced. A Hewlett-Packard, GC-5890, gas chromatograph equipped with TCD detector using an Agilent J&W GC column, HP-Plot Q, was used to determine the CO_2. The produced CO_2 gas was determined based on the integration area of the CO_2 peak using the relevant calibration curve. The process of the effluent gas measurements was continued until 100 % conversion of CO. Activation energy was calculated using the rate method [33].

9.2.7. Characterization

Field-Emission Scanning Electron Microscopy (FE-SEM) images were collected on a FEI Magellan 400L scanning electron microscope at an acceleration voltage of 1.0–2.0 kV, using aluminum as support. High-angle annular dark-field scanning transmitted electron microscopy (HAADF-STEM) images were obtained with a FEI Tecnai G2 F20 at 200 kV. Inductively Coupled Plasma – Optical Emission Spectroscopy (ICP-OES) measurements were performed using an ICP-OES Perkin-Elmer, model Optima 4300DV. X-ray powder diffraction (XRPD) patterns were collected on an X'Pert PRO MPDP analytical diffractometer (Panalytical) at 45 kV, 40 mA using CuKa radiation (1.5419°A). Nitrogen adsorption and desorption measurements were done at 77˚ K using an Autosorb-IQ-AG analyser (Quantachrome Instruments). A Hewlett-Packard, GC-5890, gas chromatograph equipped with TCD detector using an Agilent J&W GC column, HP-Plot Q, was used to determine CO_2.

9.3. Results and discussion

9.3.1. Characterization of the nanomaterials

The method used in this work started with the synthesis of core-shell Au/CeO_2 (Ce:Au = 1:1) NPs in water following the simultaneous reduction/oxidation of Au and Ce precursors. Synthesized NPs had an average particle size of 9.6 ± 2 nm and Au core size of 4.2 ± 1.2 nm (Figure 9.1). Then, they were functionalized with PVP, allowing them to be transferred from water to dimethylformamide (DMF). This step enables the dispersion of Au/CeO_2 NPs in the solvent needed for synthesizing the UiO-66 beads.

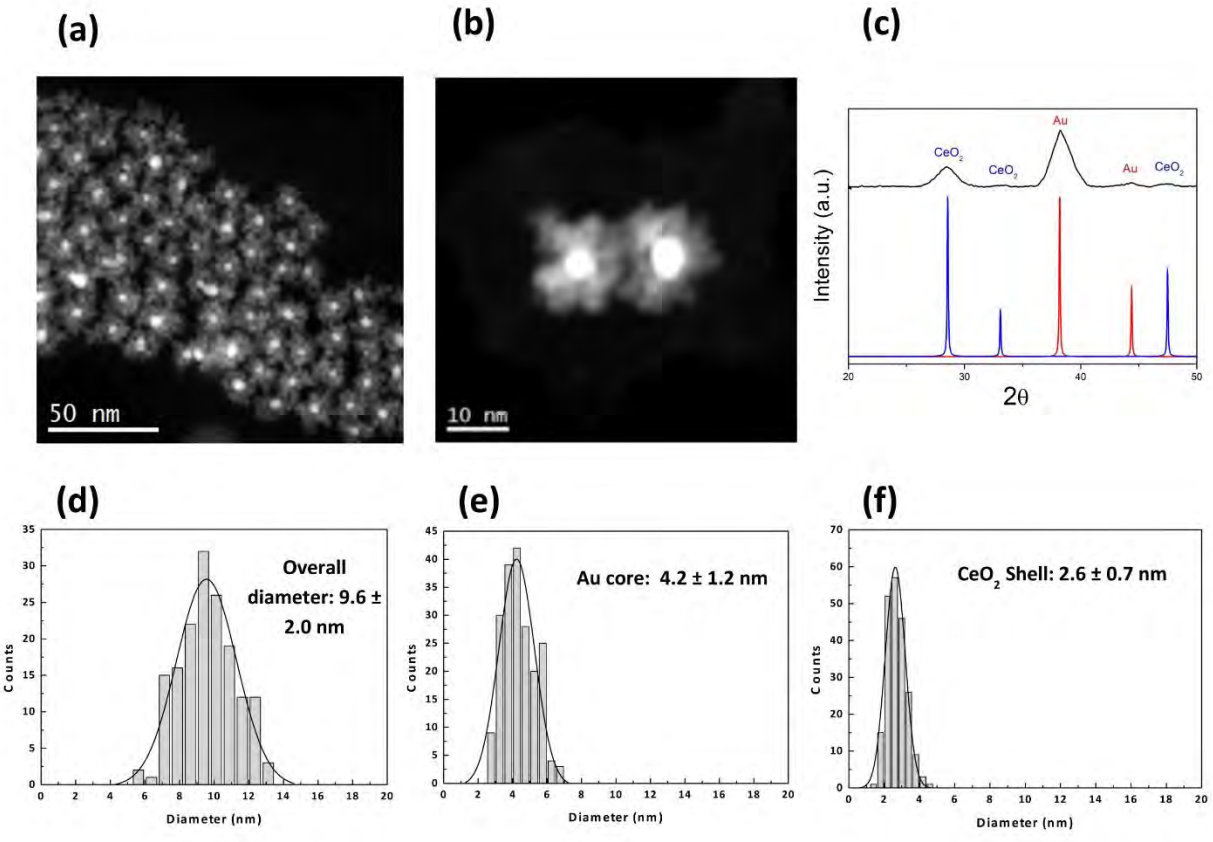

Figure 9.1 (a,b) HAADF-STEM and (c) XRPD pattern of core-shell Au/CeO_2 NPs (black) in comparison to simulate patterns of Au (red) and CeO_2 (blue). Histogram of the (d) overall diameter of Au/CeO_2, (e) Au core and (f) CeO_2 shell.

When $ZrCl_4$ was used as the metal salt to synthesize UiO-66@Au/CeO_2, the resulting acidic precursors solution (pH~1) at high temperature caused dissolution of

CeO_2 in the process. $ZrCl_4$, which is the common salt used to synthesize UiO-66, was replaced by $Zr(OPr^n)_4$ because of the dissolution of CeO_2 in the acidic precursor solution (Figure 9.2) [34]. As a result, a composite made of large Au NPs encapsulated into UiO-66 beads was produced. This phenomenon was confirmed by ICP-OES from which a Au content of 2.6 w.t. % and a Ce content of 0.02 w.t. % were found.

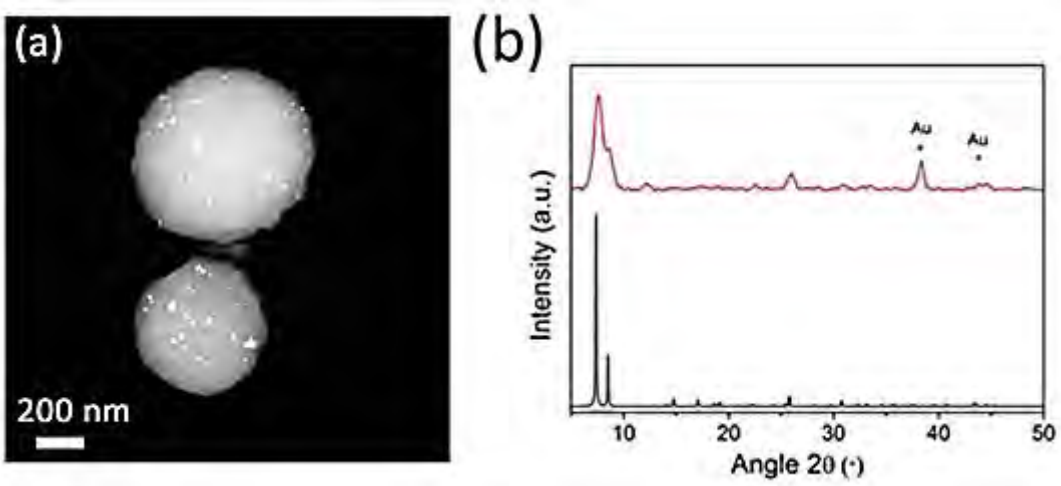

Figure 9.2. (a) HAADF-STEM and (b) XRPD pattern of UiO-66@Au (red) in comparison to simulated pattern of UiO-66 (black).

Field-emission scanning electron microscopy (FE-SEM) of the calcinated powder revealed the formation of spherical beads (average size = 3.4 ± 1.8 μm) formed by the assembly of nanocrystals of UiO-66 (Figure 9.3a). Figures 9.3 b, and c show high angle annular dark field scanning transmission electron microscopy (HAADF-STEM) of these beads, confirming the encapsulation of well-dispersed Au/CeO_2 NPs inside them.

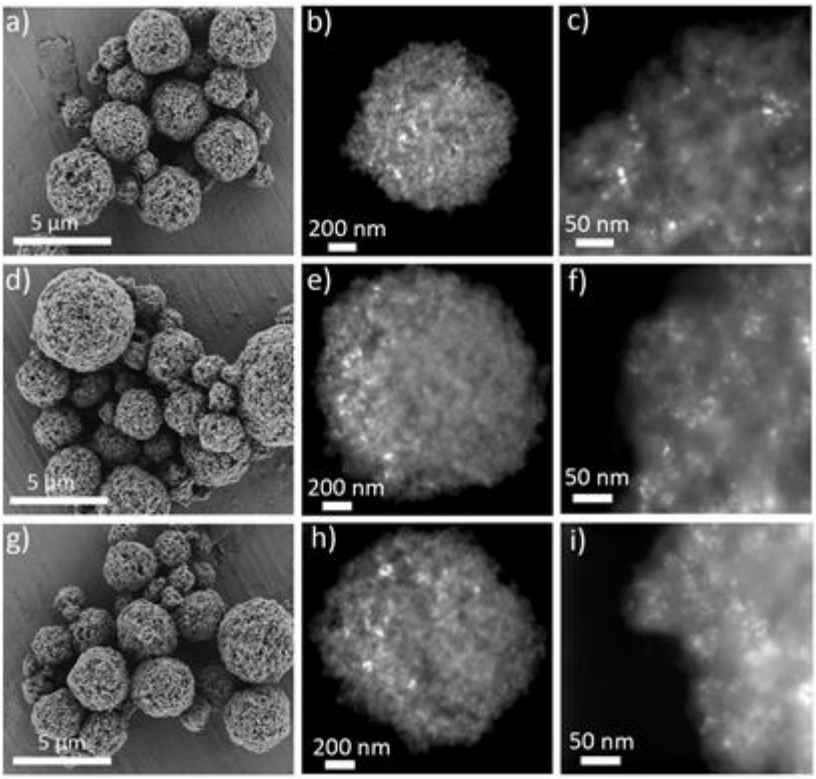

Figure 9.3 (a-i) Representative FE-SEM and HAADF-STEM images of UiO-66@Au/CeO_2-2.8 (a-c), UiO-66@Au/CeO_2-5.5 (d-f) and UiO-66@Au/CeO_2-7 (g-i). (j) XRPD patterns of UiO-66@Au/CeO_2-2.8 (green), UiO-66@Au/CeO_2-5.5 (red) and UiO-66@Au/CeO_2-7 (blue) in comparison to the simulated pattern for UiO-66 (black).

It is known that, if no aggregation occurs, higher loading of NPs tends to increase the catalytic activity of this class of supported composites. To this end, we systematically synthesized a series of composites in which we increased the added amount of Au/CeO_2 NPs dispersion (1 mg/mL) in the precursor solution to 8.5 mL, 12 mL and 16 mL. Again, FESEM and HAADF-STEM images revealed the formation of beads containing Au/CeO_2 NPs for all samples (Figures 9.3d-i). However, the latter sample was discarded because it showed the presence of a high amount of non-encapsulated Au/CeO_2 NPs together with the beads as well as lower crystallinity of UiO-66 (Figure 9.4).

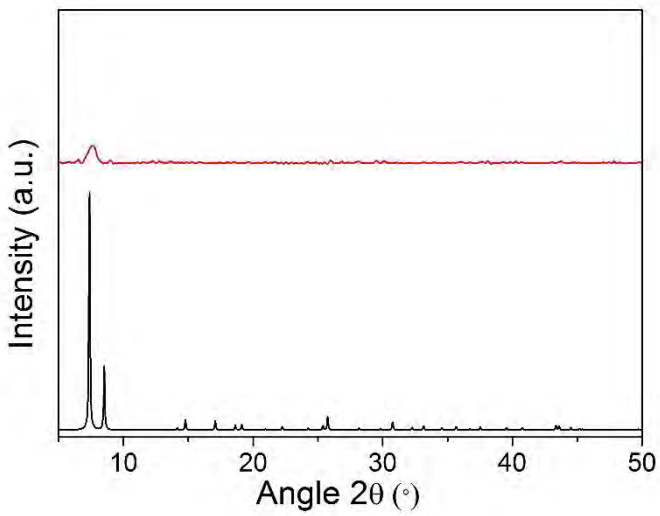

Figure 9.4. XRPD pattern of UiO-66@Au/CeO_2 synthesized with 16 ml of Au/CeO_2 NPs solution (red) in comparison to simulated pattern of UiO-66 (black).

In addition, energy dispersive X-ray spectroscopy (EDX) mapping of the beads showed the homogeneous distribution of Au and Ce inside the beads (Figure 9.5).

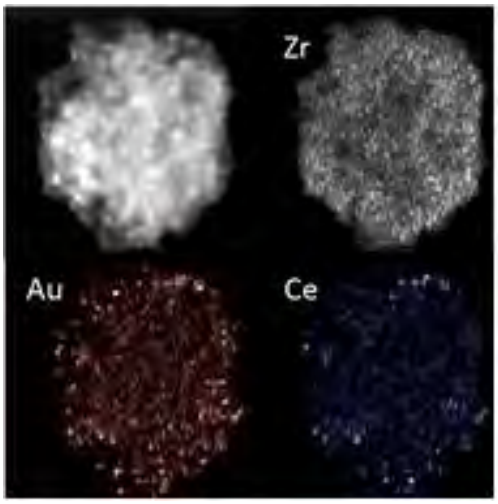

Figure 9.5. Elemental mapping (Zr, Ce and Au) of the composite UiO-66@Au/CeO_2-2.8.

X-ray powder diffraction (XRPD) indicated that the beads were pure crystalline UiO-66 (Figure 9.6).

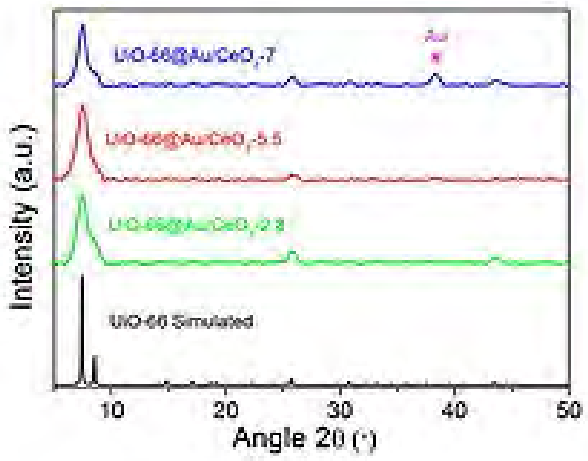

Figure 9.6 XRPD patterns of UiO-66@Au/CeO_2-2.8 (green), UiO-66@Au/CeO_2-5.5 (red) and UiO-66@Au/CeO_2-7 (blue) in comparison to the simulated pattern for UiO-66 (black).

For the first two compositions, XRPD patterns confirmed the formation of UiO-66 (Fig. 1j), from which Au/CeO_2 contents of 5.5 % (Ce: 2.48 %, Au: 2.50 %) and 7 % (Ce: 3.22 %, Au: 3.18 %) in the composites (hereafter, UiO-66@Au/CeO_2-5.5 and UiO-66@Au/CeO_2-7) were determined. These amounts correspond to 91 % and 74 % of encapsulation efficiency for UiO-66@Au/CeO_2-5.5 and UiO-66@Au/CeO_2-7, respectively.

The content of Au/CeO_2 in this composite was estimated by digesting the powder in a mixture of concentrated HCl and HNO_3 and analysed by inductively coupled plasma optical emission spectrometry (ICP-OES), from which a Au/CeO_2 content of 2.8 % (Ce: 1.28 %, Au: 1.31 %) in the composite (hereafter, UiO-66@Au/CeO_2-2.8) was determined. The comparison of this value to the initial percentage of Au/CeO_2 NPs added into the UiO-66 precursor solution leads to an encapsulation yield of 92 %, confirming the efficiency of the spray drying method for incorporating Au/CeO_2 NPs into the UiO-66 beads. Finally, the adsorption capacity of UiO-66@Au/CeO_2-2.8 was determined.

N_2 physical adsorption measurements of UiO-66@Au/CeO2-2.8 showed a measured Brunauer Emmet Teller (BET) surface area (A_{BET}) of 1095 m^2/g (Figure 9.7a),

very close to that of pristine UiO-66 superstructures [34]. Also N_2 physical adsorption measurements confirmed that both composites of UiO-66@Au/CeO2-5.5 and UiO-66@Au/CeO2-7 are porous, showing measured BET surface areas of 1070 and 870 m^2/g, respectively (Figures 9.7b, and c).

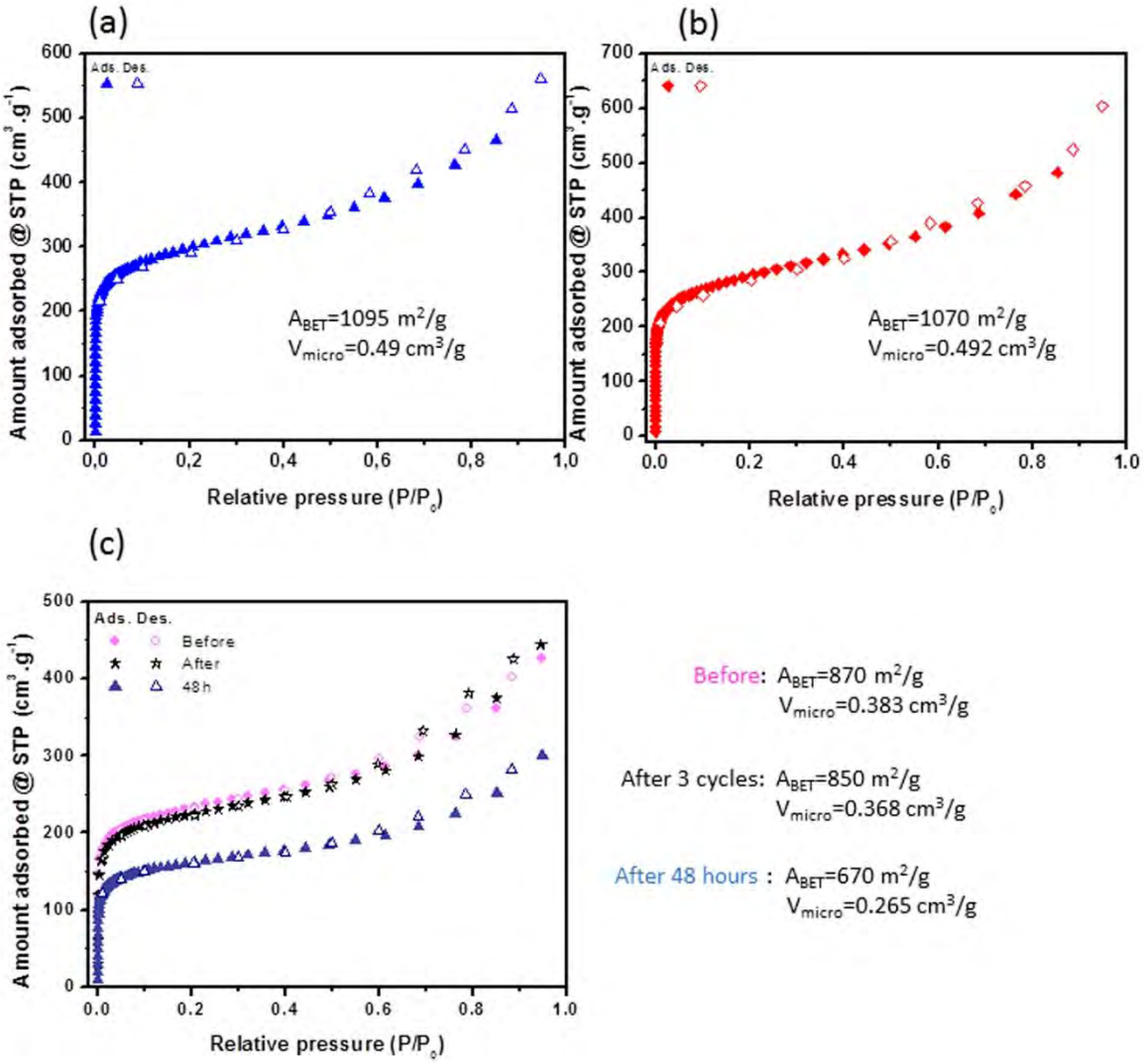

Figure 9.7. N_2 sorption isotherms collected at 77 K for (a) UiO-66@Au/CeO_2-2.8, (b) UiO-66@Au/CeO_2-5.5 and (c) UiO-66@Au/CeO_2-7. In this latter case, it is shown the isotherms collected before and after three temperature-programed cycles and 50 hours of continuous CO conversion.

9.3.2. Catalytic oxidation of CO

In an initial step, the catalytic activity of UiO-66 beads without Au/CeO_2 NPs was measured as a control reaction. As expected, UiO-66 beads showed no conversion of CO to CO_2 up to 200 ˚C, and full conversion took place at 440 ˚C (Figure 9.8).

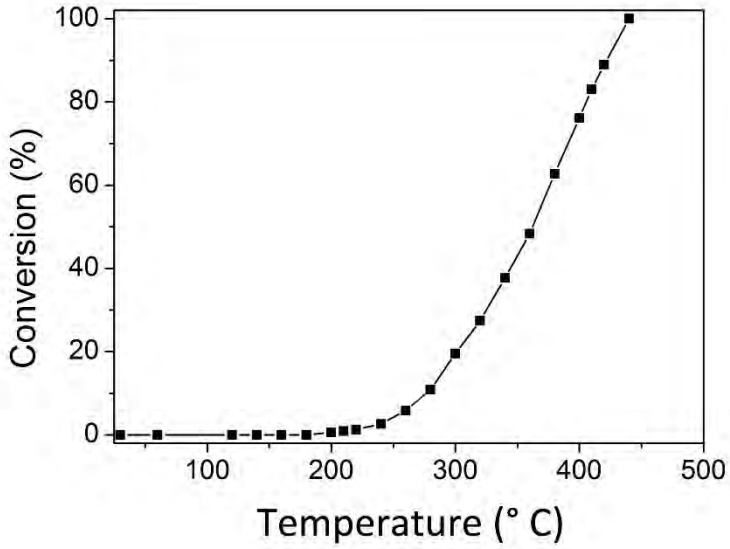

Figure 9.8 CO conversion rate as a function of reaction temperature for pristine UiO-66 beads.

On the contrary, the catalytic activity of UiO-66@Au/CeO_2-2.8 was remarkably enhanced. As is shown in Figure 9.9, this composite showed a CO conversion starting at room temperature and exhibited a 50 % (T_{50}) and 100 % (T_{100}) CO conversion at temperatures of 98 ˚C and 180˚C, respectively.

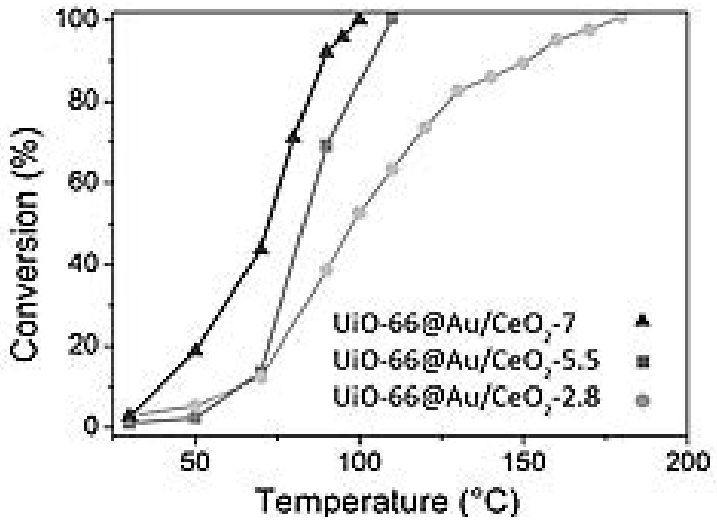

Figure 9.9 CO conversion rate as a function of reaction temperature for UiO-66@Au/CeO_2-2.8, UiO-66@Au/CeO_2-5.5 and UiO-66@Au/CeO_2-7.

The recyclability of these composites was evaluated using the composite UiO-66@Au/CeO_2-7 that shows the lower T_{100}. Initially, we performed three cycles of catalysis without detecting any loss of activity (Figure 9.10).

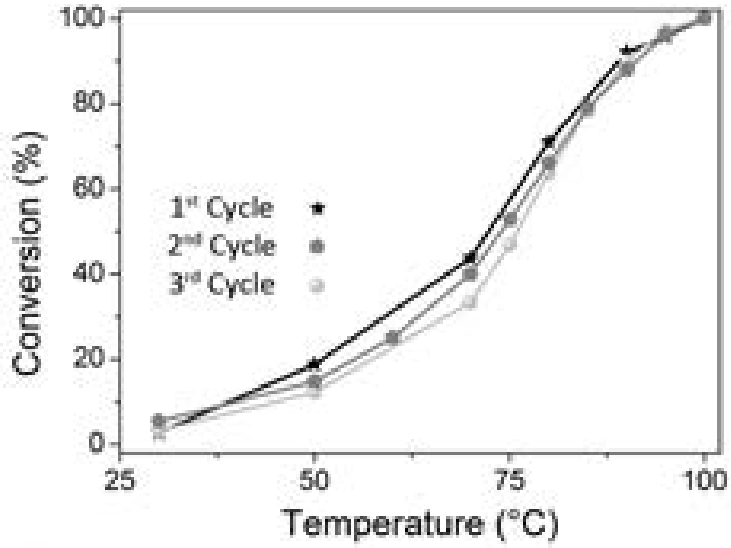

Figure 9.10 CO conversion rate as a function of reaction temperature for three consecutive cycles over the UiO-66@Au/CeO_2-7 composite.

After these cycles, the stability of UiO-66@Au/CeO_2-7 was analyzed by XRPD that showed a complete retention of the crystallinity of UiO-66 (Figure 9.11), as also confirmed by its unaffected surface area (A_{BET} = 850 m^2/g).

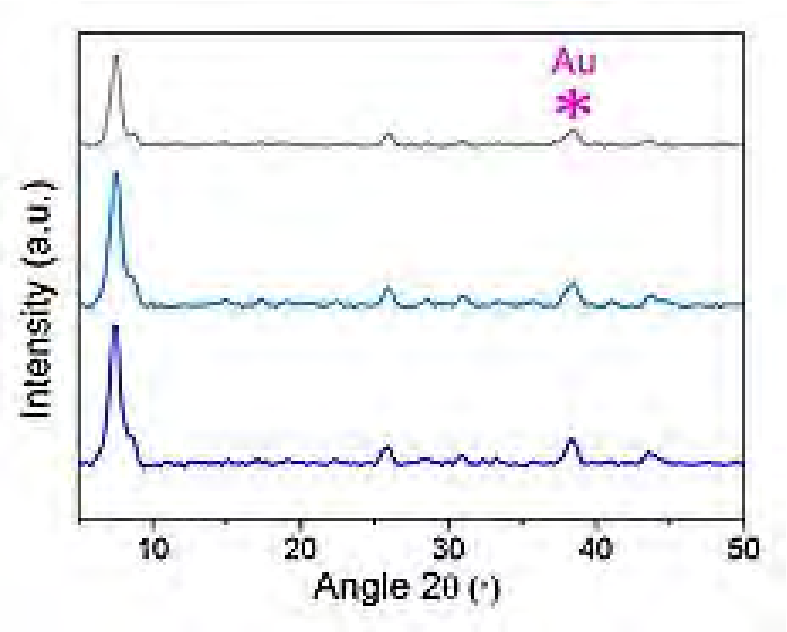

Figure 9.11 XRPD patterns of as-synthesized UiO-66@Au/CeO_2-7 (blue) and after three temperature-programed cycles (light blue) and 50 hours of continuous CO conversion (grey).

Similarly, no sign of NP sintering or aggregation and alteration of the morphology of the beads were observed by STEM and FE-SEM (Figure 9.12).

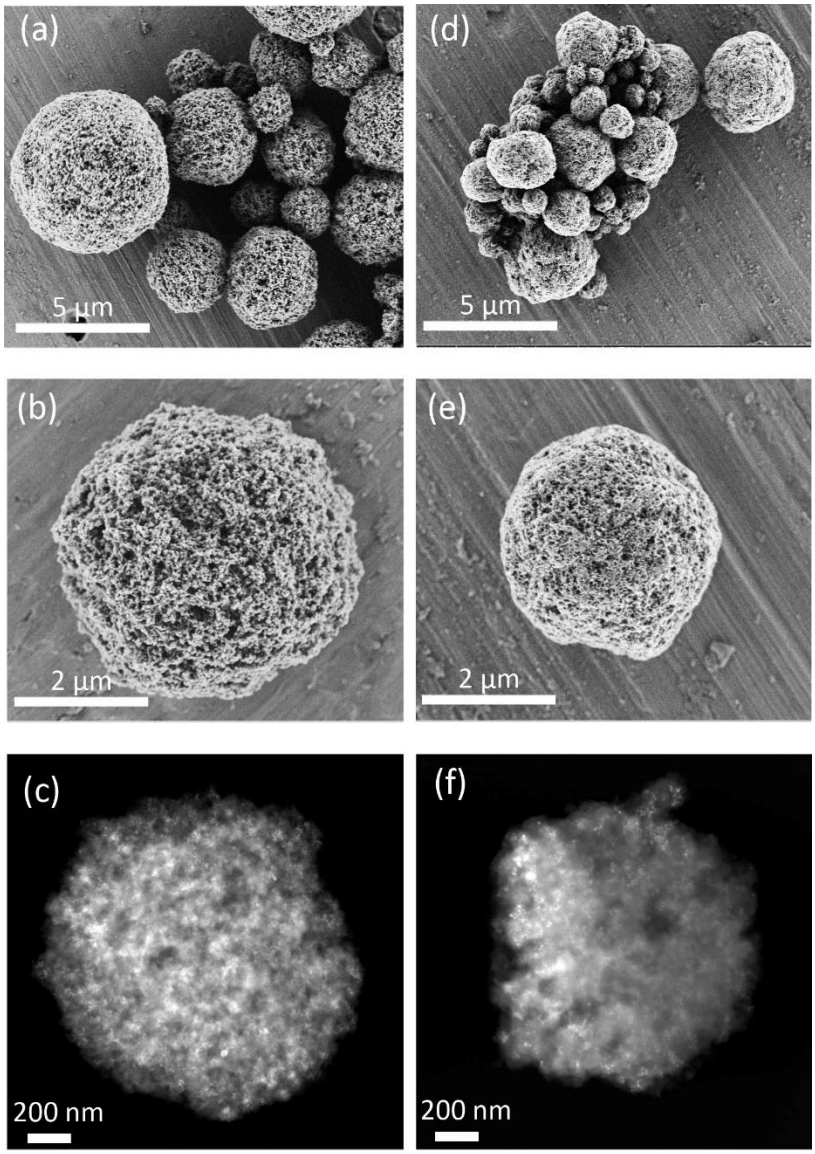

Figure 9.12. Stability test. (a,b) FE-SEM and (c) HAADF-STEM of UiO-66@Au/CeO_2-7 after three temperature-programed cycles. (d,e) FE-SEM and (f) HAADF-STEM of UiO-66@Au/CeO_2-7 after 50 hours of continuous CO conversion.

Then, the catalytic activity of UiO-66@Au/CeO_2-7 sample was also studied during a longer period of time. For this, the conversion of CO was followed in continue at 100 ℃ during 50 h, from which it was not observed any loss of activity during the first 37 hours and a slight decrease of activity (5 %) after 50 hours (Figure 9.13). We attributed this decrease in catalytic activity to a loss of crystallinity of UiO-66 (Figure 9.11) and its porosity capabilities (A_{BET} = 670 m^2/g).

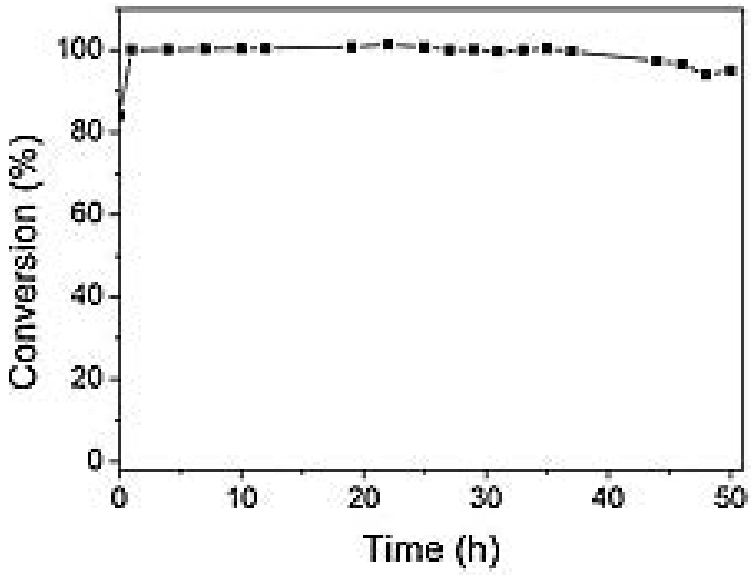

Figure 9.13. CO conversion rate at 100 ºC for 50 h over the UiO-66@Au/CeO_2-7 composite.

Ensuing temperature-programed oxidation measurements confirmed a clear improvement of CO conversion for both new composites, achieving lower T_{50} and T_{100} values by increasing the percentage of Au/CeO_2 NPs (Figure 9.9). In the case of UiO-66@Au/CeO_2-5.5, T_{50} and T_{100} were found to be 82 ℃ and 110 ℃, respectively. For UiO-66@Au/CeO_2-7, these temperatures decreased down to 72 ℃ and 100 ℃. Remarkably, in this latter case, a CO conversion of 3.8 % was achieved at room temperature.

Moreover, for this latter reaction, the activation energy was found to be 40.2 kJ/mol, whereas the TOF values at temperatures of 30, 50, 75 and 100 ºC were 10, 39, 106 and 204 h^{-1}, respectively (for comparison purposes, TOF values of other reported catalysts based on Au NPs are given in Table 9.1).

Table 9.1. Summary of catalysts based on Au NPs and their corresponding TOF values.

Material	T(ºC)	Au NP size (nm)	TOF (h^{-1})	Ref.
UiO-66@Au/CeO_2	30	5	10	This work
	50	5	39	
	75	5	106	
	100	5	204	
2.32Au/ZnOx/CeO_2-Al_2O_3	25	5	1188	[35]
1.9Au/0.5ZnO/CeAl	25	5	1584	
1.82Au/1ZnO/Al	25	5	396	
1.7Au/1ZnO/CeAl	25	5	1836	
1.99Au/1.5ZnO/CeAl	25	5	1548	
1.57Au/0.5Fe_2O_3/CeAl	25	5.7	1152	
1.91 Au/1 Fe_2O_3/Al	25	5	72	
1.26 Au/1 Fe_2O_3/CeAl	25	18	4356	
Au/1.5 Fe_2O_3/CeAl	25	21	1368	
Pt/SiO_2	177	10	36	[36]
Al_2O_3-supported Pt	250	10	720	[37]
Al_2O_3-supported Pd	250	10	14400	
Al_2O_3-supported Rh	250	10	21600	
Au/TiO_2/Mo (100)	27	2.4	720*	[38]

* at a reaction time of 100 min

In addition, Pd NPs dispersed into UiO-66 beads were also fabricated and tested for CO oxidation as demonstrated in Figure 9.14. The average size of synthesized Pd NPs was 3.3 ± 1.1 nm. ICP-OES showed a Pd content of 2.3 w.t. %. As shown in Figure 9.14, the T_{50} = 164 ºC and T_{100} = 180 ºC were obtained for CO conversion using UiO-66@Pd.

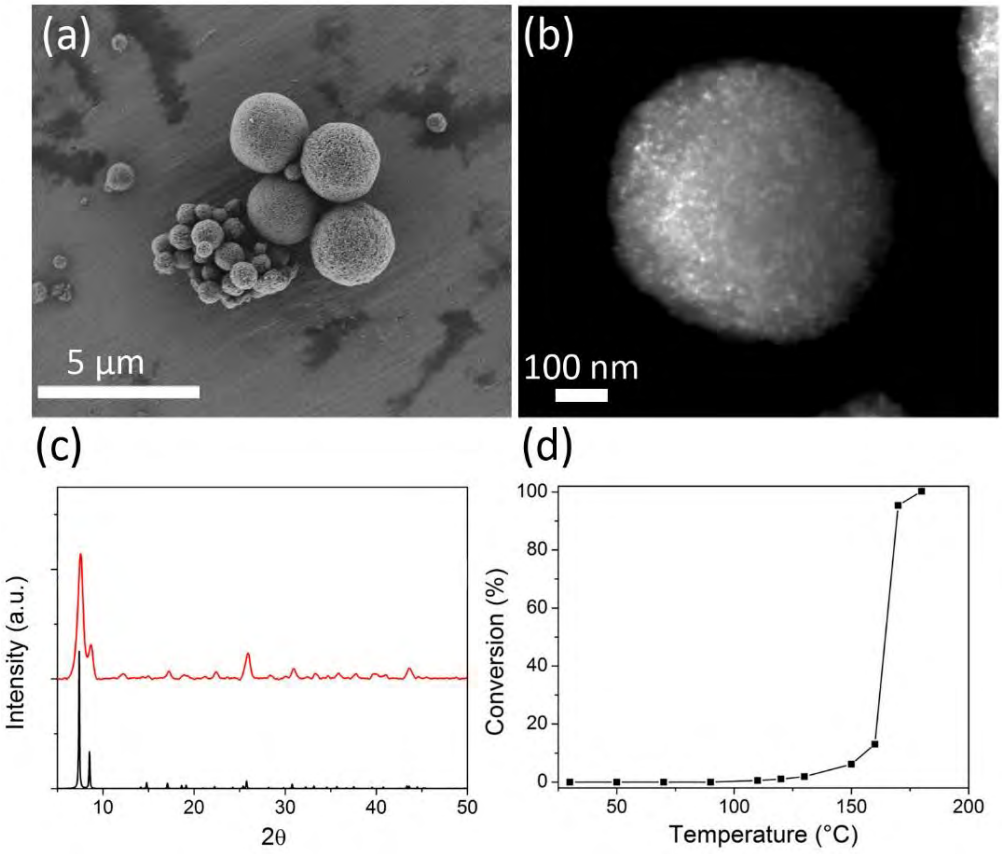

Figure 9.14. (a) HAADF-STEM, (b) FE-SEM and (c) XPDR pattern of UiO-66@Pd (red) in comparison to simulated pattern of UiO-66(black). (d) CO conversion rate as a function of reaction temperature for UiO-66@Pd, T_{50} = 164 ºC and T_{100} = 180 ºC.

For CO oxidation, Xu *et al.* have shown that ZIF-8 MOF can support Au NPs to fully oxidize CO at a temperature of 225 ˚C [39]. Similarly, Pd and Pt NPs and hybrid Pd/Pt NPs supported on MIL-101, ZIF-8, UiO-67 and UiO-66 MOFs showed full CO conversion at temperatures ranging from 120 ℃ to 200 ℃ (Table 9.2) [40-43]. In this work, we combine the catalytic properties for CO oxidation of both nanocrystalline CeO_2 and Au counterparts in a single particle entity, which is supported in UiO-66 beads using the spray-drying continuous-flow method. This method allows the simultaneously synthesis and shaping of MOF beads while encapsulating the pre-synthesized NPs in a fast, continuous one-step process [29, 44, 45].

Table 9.2 Inorganic nanoparticles supported on MOFs for CO oxidation.

Catalyst	NPs w.t.%	T_{50} (˚C)	T_{100} (˚C)	ref.
UiO-66@Au/CeO_2	7	72	100	this work
UiO-66@Au/CeO_2	5.5	82	110	this work
UiO-67@Pt	5	100	120	[27]
MIL-101@Pt/Pd		160	175	[24]
MIL-101@Pt		160	175	[24]
UiO-66@Au/CeO_2	2.8	98	180	this work
UiO-66@Pt	2	160	180	[26]
MIL-101@Pd		185	200	[24]
ZIF-8@Pt	2	170	200	[25]
ZIF-8@Au	5	170	225	[23]
UiO-66		369	440	this work

9.4. Conclusions

The formation of a new composite was described based on the entrapment and dispersion of core-shell Au/CeO_2 NPs into microsized spherical, porous UiO-66 beads using the spray-drying continuous-flow method. The combination of nanocrystalline CeO_2 and Au allows accessing to CO conversion T_{50} and T_{100} as low as 72 ˚C and 100 ˚C. These values are to our knowledge one of the lowest CO conversion temperatures achieved using catalysts based on NPs supported on MOFs. In addition, UiO-66 provides enough protection to avoid NP sintering/aggregation. We consider this method as a general approach for making composites consisting of functional NPs dispersed in MOFs already shaped into spherical beads

9.5. References

1. Jones, R.A., et al., *Effects on experimental animals of long-term inhalation exposure to carbon monoxide.* Toxicology and Applied Pharmacology, 1971. **19**(1): p. 46-53.
2. Environment and Climate Change Canada Canadian Environmental Sustainability Indicators: Air Pollutant Emissions. Available at: http://www.ec.gc.ca/indicateurs-indicators/default.asp?lang=en&n=E79F4C12-1. , 2016.
3. Liu, L., et al., *Low-temperature CO oxidation over supported Pt, Pd catalysts: Particular role of FeOx support for oxygen supply during reactions.* Journal of Catalysis, 2010. **274**(1): p. 1-10.
4. Qiao, B., et al., *Single-atom catalysis of CO oxidation using Pt1/FeOx.* Nat Chem, 2011. **3**(8): p. 634-641.
5. Chen, M.S., et al., *Highly active surfaces for CO oxidation on Rh, Pd, and Pt.* Surface Science, 2007. **601**(23): p. 5326-5331.
6. Wang, J., Z. Wang, and C.-J. Liu, *Enhanced Activity for CO Oxidation over WO3 Nanolamella Supported Pt Catalyst.* ACS Applied Materials & Interfaces, 2014. **6**(15): p. 12860-12867.
7. Berlowitz, P.J., C.H.F. Peden, and D.W. Goodman, *Kinetics of carbon monoxide oxidation on single-crystal palladium, platinum, and iridium.* The Journal of Physical Chemistry, 1988. **92**(18): p. 5213-5221.
8. Alayon, E.M.C., et al., *On highly active partially oxidized platinum in carbon monoxide oxidation over supported platinum catalysts.* Journal of Catalysis, 2009. **263**(2): p. 228-238.
9. Han, W., et al., *Low temperature CO oxidation over Pd–Ce catalysts supported on ZSM-5 zeolites.* Process Safety and Environmental Protection, 2014. **92**(6): p. 822-827.
10. Wang, L., et al., *Pd catalyst supported on activated carbon honeycomb monolith for CO oxidation and the application in air purification of vehicular tunnel.* Fuel Processing Technology, 2014. **122**: p. 23-29.
11. Ivanova, A.S., et al., *Metal–support interactions in Pt/Al2O3 and Pd/Al2O3 catalysts for CO oxidation.* Applied Catalysis B: Environmental, 2010. **97**(1–2): p. 57-71.
12. Wang, H. and C.-j. Liu, *Preparation and characterization of SBA-15 supported Pd catalyst for CO oxidation.* Applied Catalysis B: Environmental, 2011. **106**(3–4): p. 672-680.

13. Khder, A.E.R.S., et al., *CO oxidation over Au and Pd nanoparticles supported on ceria–hafnia mixed oxides.* Reaction Kinetics, Mechanisms and Catalysis, 2014. **112**(1): p. 61-75.
14. Zhang, D., et al., *Shape-controlled synthesis and catalytic application of ceria nanomaterials.* Dalton Transactions, 2012. **41**(48): p. 14455-14475.
15. Liu, W., et al., *The synthesis of CeO(2) nanospheres with different hollowness and size induced by copper doping.* Nanoscale, 2014. **6**(18): p. 10693-700.
16. Zhang, D., et al., *Cu-doped CeO2 spheres: Synthesis, characterization, and catalytic activity.* Catalysis Communications, 2012. **26**: p. 164-168.
17. Liu, W., et al., *Designed synthesis and formation mechanism of CeO2 hollow nanospheres and their facile functionalization with Au nanoparticles.* CrystEngComm, 2015. **17**(26): p. 4850-4858.
18. Olmos, C.M., et al., *CO Oxidation over Bimetallic Au–Pd Supported on Ceria–Zirconia Catalysts: Effects of Oxidation Temperature and Au:Pd Molar Ratio.* Catalysis Letters, 2015. **146**(1): p. 144-156.
19. Wang, J., et al., *Au–Pd Nanoparticles Dispersed on Composite Titania/Graphene Oxide-Supports as a Highly Active Oxidation Catalyst.* ACS Catalysis, 2015. **5**(6): p. 3575-3587.
20. Carrettin, S., et al., *Nanocrystalline CeO2 increases the activity of Au for CO oxidation by two orders of magnitude.* Angew Chem Int Ed Engl, 2004. **43**(19): p. 2538-40.
21. Centeno, M., et al., *Au/CeO2 Catalysts: Structure and CO Oxidation Activity.* Catalysts, 2016. **6**(10): p. 158.
22. Divins, N.J., et al., *Nanomaterials. Influence of the support on surface rearrangements of bimetallic nanoparticles in real catalysts.* Science, 2014. **346**(6209): p. 620-3.
23. Kim, H.Y., H.M. Lee, and G. Henkelman, *CO oxidation mechanism on CeO(2)-supported Au nanoparticles.* J Am Chem Soc, 2012. **134**(3): p. 1560-70.
24. Zhang, C., A. Michaelides, and S.J. Jenkins, *Theory of gold on ceria.* Physical Chemistry Chemical Physics, 2011. **13**(1): p. 22-33.
25. Mitsudome, T., et al., *One-step Synthesis of Core-Gold/Shell-Ceria Nanomaterial and Its Catalysis for Highly Selective Semihydrogenation of Alkynes.* Journal of the American Chemical Society, 2015. **137**(42): p. 13452-13455.
26. Zhu, F., et al., *In situ growth of Au@CeO2 core-shell nanoparticles and CeO2 nanotubes from Ce(OH)CO3 nanorods.* Journal of Materials Chemistry A, 2013. **1**(2): p. 288-294.

27. Qu, Y.H., et al., *Forming ceria shell on Au-core by LSPR photothermal induced interface reaction.* Applied Surface Science, 2015. **343**: p. 207-211.
28. Falcaro, P., et al., *Application of metal and metal oxide nanoparticles@MOFs.* Coordination Chemistry Reviews, 2016. **307, Part 2**: p. 237-254.
29. Garzon-Tovar, L., et al., *A spray-drying continuous-flow method for simultaneous synthesis and shaping of microspherical high nuclearity MOF beads.* Reaction Chemistry & Engineering, 2016. **1**(5): p. 533-539.
30. He, B., et al., *Effect of hydrothermal reaction time and calcination temperature on properties of Au@CeO2 core–shell catalyst for CO oxidation at low temperature.* Journal of Materials Science, 2015. **50**(19): p. 6339-6348.
31. Zhou, L., et al., *Transition-Metal Doped Ceria Microspheres with Nanoporous Structures for CO Oxidation.* Sci Rep, 2016. **6**: p. 23900.
32. Liu, Y., et al., *Morphology adjustment of one dimensional CeO2nanostructures via calcination and their composite with Au nanoparticles towards enhanced catalysis.* RSC Adv., 2015. **5**(47): p. 37585-37591.
33. Shalabi, M.A., B.H. Harji, and C.N. Kenney, *Kinetic modeling of CO oxidation on Pt/CeO2 in a gradientless reactor.* Journal of Chemical Technology & Biotechnology, 1996. **65**(4): p. 317-324.
34. Rungtaweevoranit, B., et al., *Copper Nanocrystals Encapsulated in Zr-based Metal-Organic Frameworks for Highly Selective CO2 Hydrogenation to Methanol.* Nano Lett, 2016. **16**(12): p. 7645-7649.
35. Reina, T.R., et al., *Sub-ambient CO oxidation over Au/MOx/CeO2-Al2O3 (M = Zn or Fe).* Applied Catalysis A: General, 2012. **419–420**: p. 58-66.
36. Cant, N.W., *Metal crystallite size effects and low-temperature deactivation in carbon monoxide oxidation over platinum.* Journal of Catalysis, 1980. **62**(1): p. 173-175.
37. Yao, Y.-F.Y., *The oxidation of CO and hydrocarbons over noble metal catalysts.* Journal of Catalysis, 1984. **87**(1): p. 152-162.
38. Santra, A.K. and D.W. Goodman, *Catalytic oxidation of CO by platinum group metals: from ultrahigh vacuum to elevated pressures.* Electrochimica Acta, 2002. **47**(22): p. 3595-3609.

39. Jiang, H.-L., et al., *Au@ZIF-8: CO Oxidation over Gold Nanoparticles Deposited to Metal−Organic Framework.* Journal of the American Chemical Society, 2009. **131**(32): p. 11302-11303.
40. Aijaz, A., et al., *Metal-organic framework-immobilized polyhedral metal nanocrystals: reduction at solid-gas interface, metal segregation, core-shell structure, and high catalytic activity.* J Am Chem Soc, 2013. **135**(44): p. 16356-9.
41. Lu, G., et al., *Imparting functionality to a metal-organic framework material by controlled nanoparticle encapsulation.* Nat Chem, 2012. **4**(4): p. 310-6.
42. Zhang, W., et al., *A Family of Metal-Organic Frameworks Exhibiting Size-Selective Catalysis with Encapsulated Noble-Metal Nanoparticles.* Advanced Materials, 2014. **26**(24): p. 4056-4060.
43. Zhuang, G.-l., et al., *The Effect of N-Containing Supports on Catalytic CO Oxidation Activity over Highly Dispersed Pt/UiO-67.* European Journal of Inorganic Chemistry, 2017. **2017**(1): p. 172-178.
44. Carné-Sánchez, A., et al., *A spray-drying strategy for synthesis of nanoscale metal–organic frameworks and their assembly into hollow superstructures.* Nat Chem, 2013. **5**(3): p. 203-211.
45. L. Garzon-Trovar, J.P.-C., I. Imaz, D. Maspoch, *Composite salt in porous metal-organic frameworks for adsorption heat transfer transformation.* Adv. Funct. Mater., 2017.

Chapter 10

Methane adsorption with modified polyurethane sponges with magnetite nanoparticles synthesized by chemical co-precipitation method

This chapter was performed in collaboration with: Universitat Politècnica de Catalunya· Terrassa, Barcelona, Spain.

The results presented in this chapter are in preparation for submission at an international SCI journal:

"Methane adsorption with modified polyurethane sponges with magnetite nanoparticles synthesized by chemical co-precipitation method".

10.1. Introduction

Today, one of the biggest environmental challenges is global climate change due to Global Warming. The Global Warming is a result of increased concentrations of greenhouse gases (GHGs) such as carbon dioxide (CO_2), methane (CH_4), nitrous oxide (N_2O), hydrofluorocarbons (HFCs), perfluorocarbons (PFCs), and hexafluorocarbono sulfur (SF_6). These gases trap an increasing proportion of terrestrial infrared radiation so that it is expected that the global temperature increases between 1.4 and 5.8 ° C in 2100 in the absence of policies on climate change [1, 2]. The variation on the temperature causes widespread and devastating effects in different parts of the globe such as: possible variations in sea levels, changes in ecosystems, loss of biodiversity, reduction in crop yields and changes in global precipitation patterns, among other [3]. The GHG capture and storage could play a significant role in reducing their emissions. The aforementioned technologies based on adsorption processes, have limitations in terms of retention capabilities of GHG per adsorbent mass. In this sense, there is a widespread interest in the development of advanced adsorbent materials having better characteristics than conventional materials and incorporate appropriate features for each specific contaminant.

For instance, CH_4 is an alkane hydrocarbon gas being the major component of the natural gas (80- 90%). There are various sources of production and release of CH_4 including, decontaminating wastewater, landfills, natural gas extraction, among others. Although it is a gas that produces adverse effects on climate change, it has a high energy value and prized as a source of energy, being sued for nearly a quarter of the energy required by homes, vehicles, industries, power plants, etc [4]. Besides, the use of adsorbent materials, such as activated carbons and zeolites, among others, for the purification of biogas and the storage of natural gas at low pressures [5-7] stills need to be developed. Also, it was concluded that none of those conventional adsorbents showed sufficient CH_4 storage capacity to meet that required for commercial viability [8]. Nanomaterials have a number of physicochemical properties [9] that make them particularly attractive as separation media for gas purification and gas capture, such as higher surface area per unit volume or mass, hundreds of functional square meters cleaning the air that weight less than

a gram, or the ability to be functionalized with a number of surfactants to enhance their affinity towards target molecules [10]. Advanced materials have been investigated as potential CH_4 adsorbents including modified activated carbons, metal-organic frameworks (MOFs) and other porous polymers [11]. In this context, the high adsorption capacity of nanomaterials has been demonstrated in many cases. Besides, their solid inorganic nature confers them an extra stability and robustness intended for many uses and easiness of use. MOFs are getting attention due to their application in separation, catalysis, nonlinear optics, and gas storage [12]. In particular, MOFs were the ones that exhibited the highest adsorption for CO_2 and CH_4 [8]. For example, Mason *et al.* studied different MOFs and compared the effects of the volumetric and gravimetric adsorption on CH_4 uptake [13]. Among the various MOFs, the recorded CH_4 adsorption capacities are 283.4 mg/g for Ni_2(dhtp) and 363 mg/g for Mg_2(dhtp) [14]. Although, MOFs adsorbents exihibits efficiency for CH_4 adsorption, they are expensive in production [15].

As result of the widely applications of the metal oxide NPs and the low cost of iron oxide NPs, as previously mentioned (Chapter 1), the objectives of this Chapter are: (1) to immobilize iron oxide NPs into polyurethane foam (PUF) as support due to the use of PUFs could be a good approach since these materials exhibit high stability against chemical degradation, high mechanical durability, good swelling behaviour, ease of separation, and they are also one of the most cost-effective available polymers [16], (2) to evaluate its efficiency for CH_4 adsorption, (3) to estimate the maximum adsorption capacity of CH_4 by applying different isotherm models, and (4) to evaluate its efficiency for reusability study.

10.2. Materials and methods

10.2.1. Materials

Iron (II) chloride; $FeCl_2$, Iron (III) chloride hexahydrate and; $FeCl_3.6H_2O$ were purchased from Sigma-Aldrich, Spain. Sodium hydroxide pellets, NaOH, was purchased from Merck. Acetone from Panreac Company (Spain) was used as received. All the chemicals were of analytical grade or higher, and all solutions were prepared with Milli-Q

water and filtered using 0.45 µm Nylon membrane filter. CH_4 was obtained from Carburos metálicos (Spain) with a purity of 99.999 %. Commercial polyurethane foam (PUF) was obtained from Comercial del Caucho (Daplasca, Spain) (Figure 10.1).

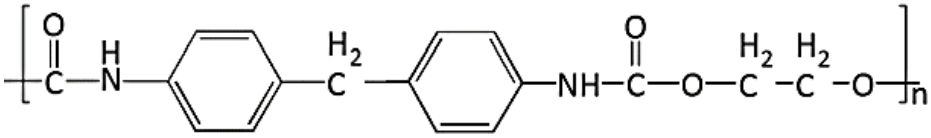

Figure 10.1. Structural unit of the PUF matrix.

10.2.2. Synthesis of the Fe_3O_4 NPs stabilized in the PUF matrix

First, PUF supports, after cutting into 0.6 cm diameter and 1.0 cm height, were washed with acetone for 24 h and then with distilled water for 24 h to eliminate the possible commercial treatments applied to the material. Next, immobilization of the Fe_3O_4-NPs on the polymeric PUF matrix was carried out using a variation of the Intermatrix Synthesis (IMS) protocol coupled to a co-precipitation method already reported [17] and described in Chapter 7 (Section 7.2.2). Typically, 125 mL of deoxygenated aqueous solution of NaOH 0.5 M was added slowly with continuous stirring into 100 mL mixture of deoxygenated iron salts suspension, with Fe^{2+}/Fe^{3+} molar ratio of 1:2, which contained 0.5 g of pre-treated PUF under N_2 atmosphere and at 40°C. To optimize the concentration of NPs on the surface of the PUF matrix, we have used two different concentrations of the $FeCl_2/FeCl_3$ ratio: Protocol A: 33/66 mM and, Protocol B: 66/132 mM. The corresponding samples are defined as Fe_3O_4-PUF(A) and Fe_3O_4-PUF(B) NCs, respectively. After the synthesis, the PUF containing Fe_3O_4-NPs were washed with Milli-Q water three times, to remove the excess of NPs not stabilized in the matrix, and then dried at 80 ^oC for 24 h.

10.2.3. Characterization of the NC

The metal contents present in the NCs, both Fe_3O_4-PUF(A) and (B), were analyzed by using Inductively coupled plasma optical emission spectrometry (ICP-OES). Transmission Electron Microscopy (TEM) coupled with Energy-Dispersive Spectroscopy (EDS) was used to characterize the particle size, morphology, electron diffraction (ED) pattern and composition of Fe_3O_4 NPs on the PUF matrices. Samples preparation is explained in Chapter 3 (Section 3.1).

10.2.4. CH_4 analysis

The determination of CH_4 was performed utilizing gas chromatography (GC) coupled with flame ionization detector (FID) system. The GC analysis method for CH_4 was previously set by the research team using HP-plot/Q column of 30 m length, 530 µm diameter and 40 µm of film. The method consisted on 250 °C for the detector, 240°C for the injector, 60°C for the oven and an injection volume of 20 µL with a split ratio mode. Error in the measurements is < 1.2%.

10.2.5. Adsorption-desorption tests

10.2.5.1. Adsorption studies in a fixed bed column

The fixed bed column experiments, by using Fe_3O_4-NPs stabilized in PUF as adsorbents, were performed using polyamide column of 0.6 cm inner diameter and 16 cm length. The column was packed with the synthesized NC. Nylon filters were placed at both bottom and top ends. At the lower end of the column, the peristaltic pump (Watson Marlow, 403U) was connected to a bag of pure methane. While, at the upper end, a "T" connector is placed with sampling port connected to the methane gas collections as shown in Figure 10.2.

The continuous adsorption process is usually characterized by the so-called breakthrough curves, i.e., a representation of the pollutant effluent concentration versus time

profile in a fixed bed column [18]. Breakthrough curve experiments were performed at 0.5, 1.0 or 2.0 mL/min of CH_4 flow, 2000 ppmv initial concentration of CH_4, and 100 mg of the adsorbent for all the cases. The initial concentration of CH_4 was prepared by diluting the stock of pure CH_4 in 1.0 L bag contains pure N_2. Samples were taken from the fixed bed column system at different times from 0 to 70 min when the bed reached the saturation.

The breakthrough curves show the loading behavior of CH_4 to be removed in a fixed-bed column and are usually expressed in terms of adsorbed CH_4 (C_{ad}) as a function of time. Equilibrium uptake q_{eq} (mg_{CH4}/g_{NC}) is defined as the amount of CH_4 adsorbed per mass of NC, the NPs stabilized in the PUF, at certain initial CH_4 concentration [19]. Adsorption capacity was calculated as previously mentioned in Chapter 3 (Equation 3.2).

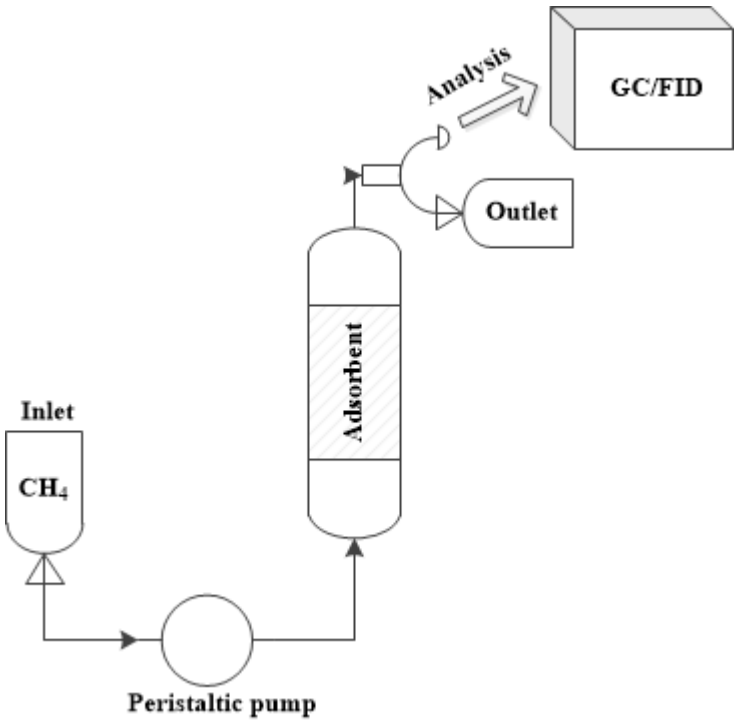

Figure 10.2. Experimental set-up for CH_4 adsorption.

10.2.5.2. Methane adsorption Isotherm

To estimate the maximum adsorption capacity of the CH_4 using the NCs, adsorption isotherms were performed. In this study, isotherms were carried out continuously with CH_4 initial concentrations (100, 250, 500, 1000, 1500, 2000, 3000, 5000 y 7000 ppmv), 100 mg of NCs and, of raw PUF as a control, at 0.5 mL/min of CH_4 flow and at room temperature.

10.2.5.3. Isotherm models for CH_4 adsorption

The most appropriate method in designing and assessing the performance of the sorption systems is to have an idea on the sorption isotherms. Therefore, in order to optimize the design of a specific adsorbate/adsorbent system, it is important to establish the most appropriate correlation for the experimental equilibrium data [20]. Linear regression has been the frequently used method to determine the most fitted isotherm. However, previously, researchers showed that depending on the way the isotherm equations are fitted, the error distribution changes either the worse or the better. Thus, non-linear method would be a better way to obtain the equilibrium isotherm parameters [21].

In the present study, experimental data were fitted to the adsorption isotherm models [21, 22] including three of two parameters, namely; Freundlich, Langmuir, and Dubinin–Radushkevich, three of three parameters, namely; Redlich–Peterson, Radke–Prausnitz, Brunauer–Emmett–Teller (BET), and a combination isotherm model. Non-linear expression of these models and detailed information are explained in Chapter 3 (Section 3.4).

10.2.5.4. Desorption of methane and reusability of the nanocomposite

The desorption process for the CH_4 previously adsorb on the NC was conducted to be able to recover CH_4 and to reuse the adsorbent for further adsorption process. Regeneration process was carried out by passing N_2 through the fixed bed column for 40

min. The reusability experiment was performed under ambient conditions and at a flow rate of 0.5 ml/min for five cycles of adsorption/ desorption.

10.3. Results and discussion

10.3.1. Synthesis and characterization of the NCs

10.3.1.1. Metal ions content in the NCs

Both NCs were analyzed by ICP-OES. The mean of iron (Fe) concentration (mg_{Fe}/g_{NC}) for the three replicates of the two samples were: 4.03 ± 0.16 and 8.12 ± 0.44 mgFe/gNC for Fe_3O_4-PUF(A) and (B), respectively. It is shown that increasing twice the Fe salts concentration in the synthesis lead to increase twice the Fe content in the final NC. After applying the synthetic methodology, a darkening of the sponges was observed, indicative of the metal loading. The darker color due to the iron load in PUF is shown in Figure 10.3. The loading of the ionic Fe can be attributed to coordination with lone electron pairs of nitrogen atoms. The generation of coordination bonds between species may also result in the immobilization of the ionic species in the polymeric matrix. In addition, the entry of metal ions into the matrix could be significantly affected by the synthetic conditions which can affect the structural organization of the polymer matrices thus making the matrix temporarily accessible to the metal ions by opening their structure. After the synthesis, the fibres of the sponges revert back to their closely packed state thus trapping the NPs within the polymer structure [23].

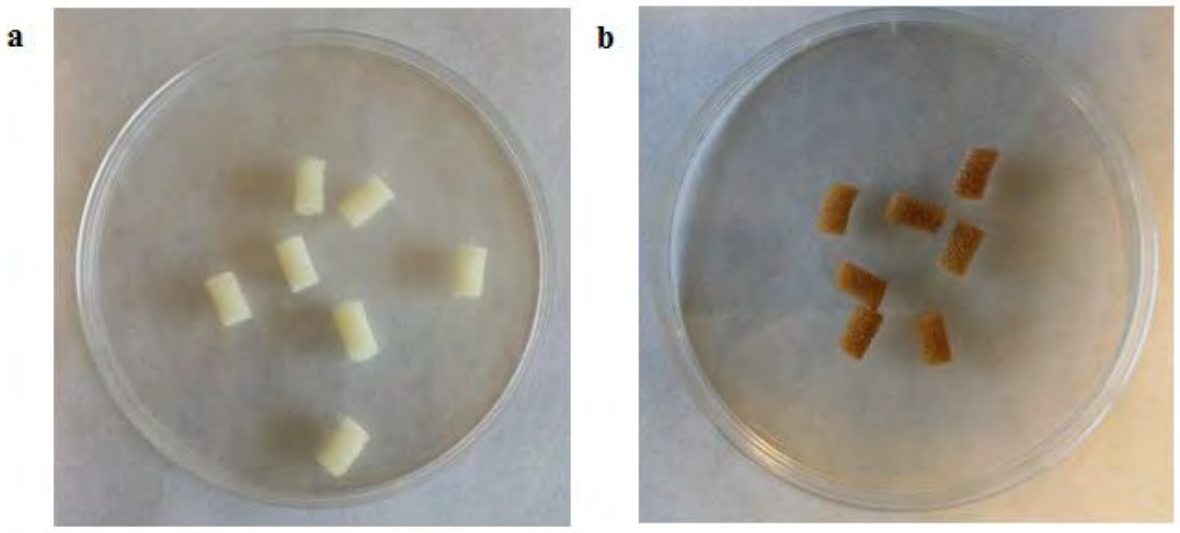

Figure 10.3. Image of the raw PUF material (a), and Fe_3O_4-PUF(B) (b).

10.3.1.2. TEM/EDX/EDS analysis of the NCs

TEM images coupled with EDS of the cross-section for the synthetic nanomaterial (Fe_3O_4-PUF(B)) of the NCs are shown in Figure 10.4. As it is observed, the Fe_3O_4 NPs on the PUF show a size of 87 - 108 nm for Fe_3O_4-PUF(A). This data also shows the success of the immobilization of the Fe_3O_4-NPs on the surface of the PUF (Figure 10.4a) which makes the material more suitable for its application as adsorbent. Further confirmation about the immobilization of magnetite NPs on the surface of the PUF was illustrated in Figure 10.4b, where the line spectrum shows the iron content profile obtained by TEM coupled with EDS, on the cross-sectioned of protocol B. Furthermore, crystalline structure of Fe_3O_4-NPs was confirmed by ED pattern as shown in Figure 10.4c. Characteristics of Fe_3O_4-PUF(A) NCs are not shown due to Fe_3O_4-PUF(B) NCs was selected for the rest of experiments for a better result in the adsorption capacity as it will be discussed later.

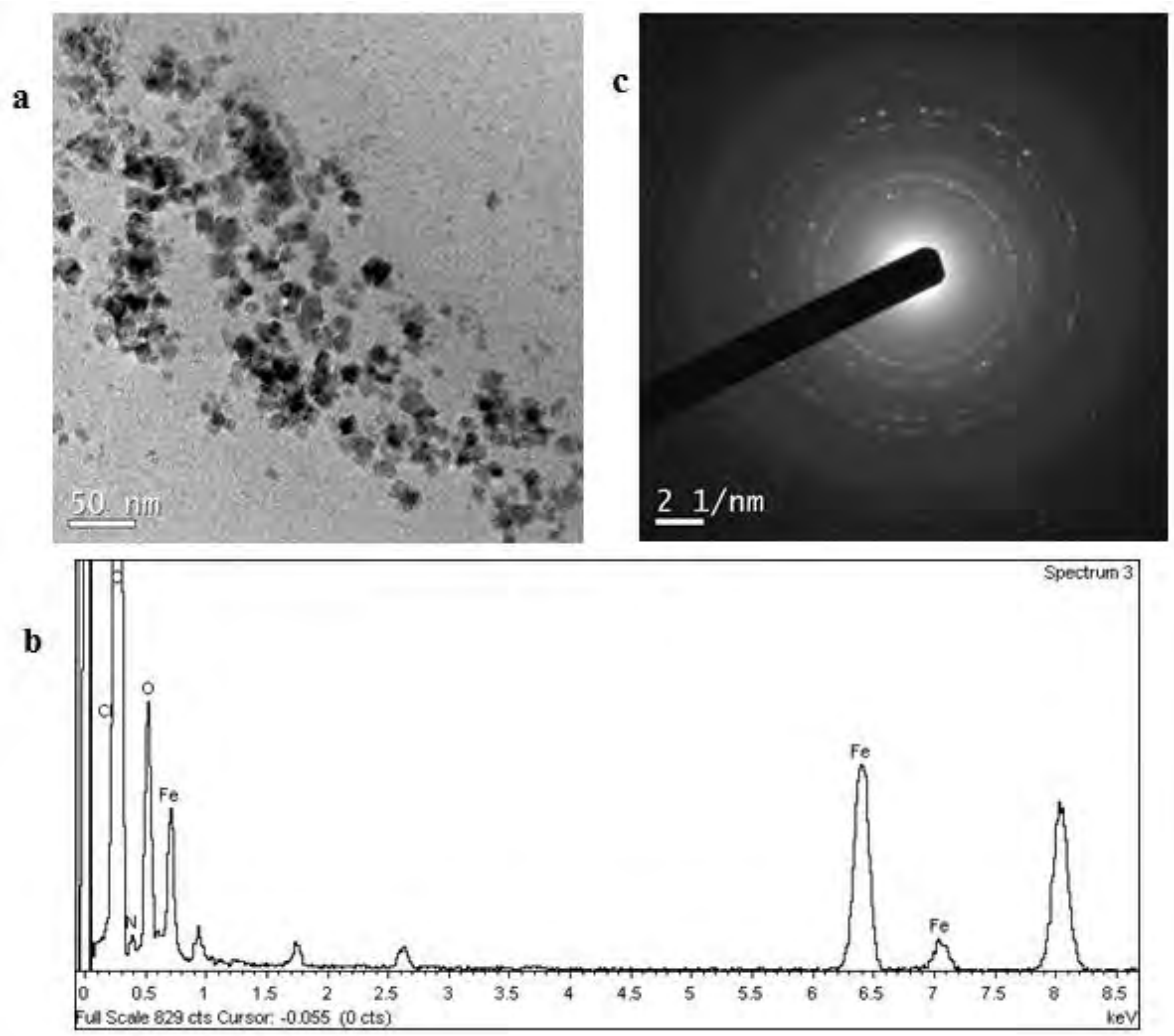

Figure 10.4. (a) TEM image, b) EDS spectra and, c) ED pattern of the cross-sectioned sample (Fe_3O_4-PUFs(B)).

10.3.2. Adsorption studies in fixed-bed column

10.3.2.1. Effect of flow effect on the adsorption capacity of CH_4

The effect of flow rate on CH_4 adsorption using Fe_3O_4-PUF(B) NCs was illustrated in Figure 10.5. As shown, better results of CH_4 adsorption were obtained when working with flow rate of 0.5 mL/min. The higher the flow rate was lower material efficiency. This is because the internal porosity of the material at higher flow prevents NPs CH_4 molecules

adsorbed by the fluid velocity while the smaller the flow time of contact between gas and increases NPs. Significant differences were found between the flow rate used for CH_4 adsorption due to the p value was less than 0.05 (P =<0.001) by applying one way ANOVA test.

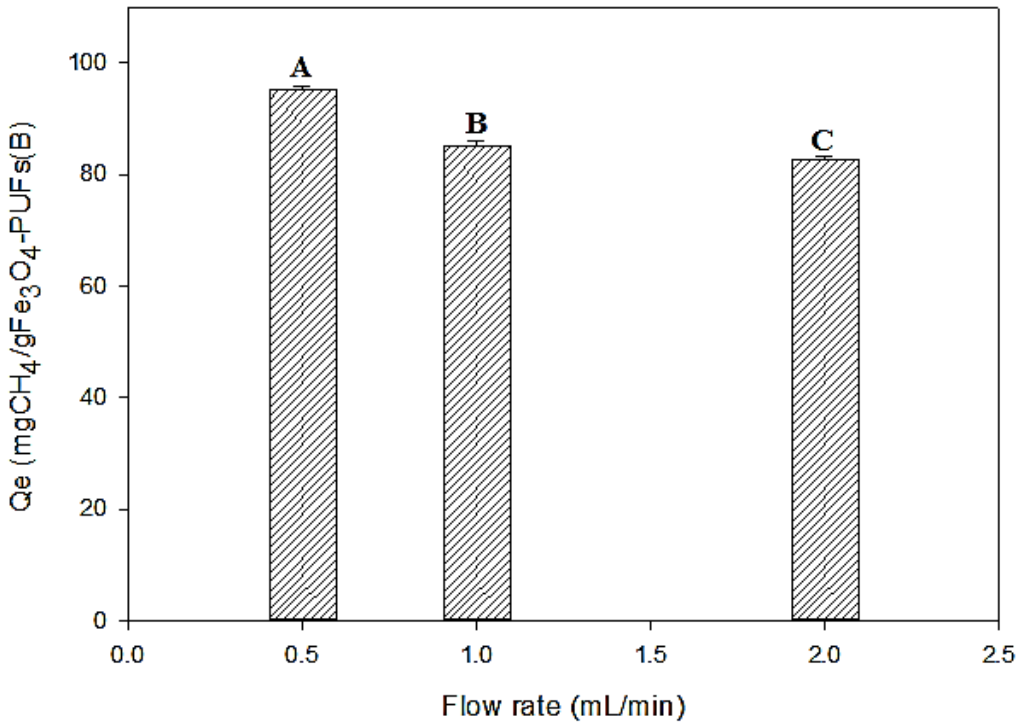

Figure 10.5. Effect of flow rate on CH_4 adsorption using Fe_3O_4-PUFs(B) NCs (2000 ppmv intial CH_4 concentration, 100 mg of the NCs, and room temperature [Statistical data analysis using ANOVA was illustrated by the letters A, B, and C].

10.3.2.2. Determination of the adsorption capacities for the Fe_3O_4-PUF (A) and (B) NCs

Because of the favorable results obtained with a flow rate of 0.5 ml/min and with an initial concentration of methane of 2000 ppmv at room temperature, effect of the iron oxide NPs loading into PUF on the adsorption capacity of CH_4 using the two NCs at the same conditions was performed. Raw PUF sponges were used as control. The mean values of the

triplicate measurements of the adsorption capacity for CH_4 using Fe_3O_4-PUF(A) was found to be 86.8 ± 0.5 mgCH_4/gNC while for Fe_3O_4-PUF(B) was 95.4 ± 0.62 mgCH_4/gNC. However, the adsorption capacity of the PUF matrix without NPs was 52.9 ± 0.19 mg/gPUF. It is noteworthy that NPs formed in the sponge structures are responsible for improving the adsorption of the raw sponges. Thus, the following experiments in this work and the majority of the characterization techniques used were carried out for the Fe_3O_4-PUF(B) NC and 0.5 mL/min flow rate.

10.3.2.3. Adsorption isotherms and modellings

Figure 10.6 represents the adsorption isotherms of both the NCs and the raw PUF material as a control at the different concentrations tested at 0.5 mL/min of Flow. It is shown from the experimental data that the NCs of Protocol A and Protocol B reach the maximum adsorption capacity of 690.20, and 726.70 mg/gNC, respectively, while the raw PUF shows an adsorption capacity of 501.83 mg/gPUF.

Also, the experimental data are fitted to two-parameter, three-parameter, and to a combined isotherm model for the methane adsorption using PUF, Fe_3O_4-PUF(A), and Fe_3O_4-PUF(B) NCs, respectively as illustrated in Figure 10.6.

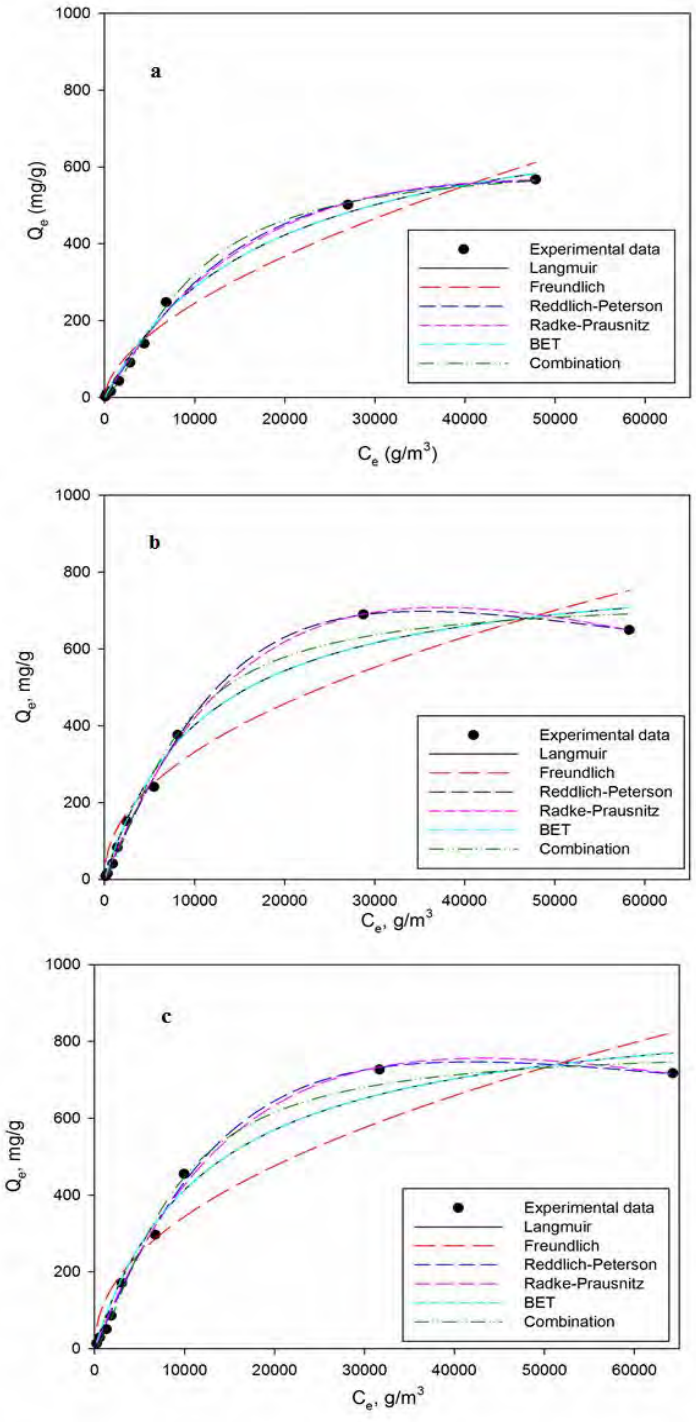

Figure 10.6. Adsortpion isotherm of CH_4 using (a) PUF, (b) Fe_3O_4-PUFs(A) NCs, (b) Fe_3O_4-PUFs(B) NCs (100 mg of the adsorbent, 0.5 mL/min flow, and room temperature).

The best fitted models of the two and three parameter isotherms were demonstrated according to the higher value of the correlation coefficient (R^2). The calculated isotherm parameters and their corresponding coefficient of determination, R^2, values were shown in Table 10.1. It was observed that the higher R^2 values for the three-parameter; Redlich–Peterson, Radke-Prausnitz, and BET, the two-parameter; Langmuir, and the combined isotherms suggest the applicability of these models to represent the equilibrium adsorption of methane utilizing PUF adsorbent. In addition to the lower values of R^2 for Fruendlich and Dubinin isotherm models show that it is not appropriate to use these models to represent the uptake of methane by PUF adsorbent at equilibrium. Moreover, as presented in Figure 10.6a, the BET isotherm overlapped the Langmuir isotherm due to the same correlation coefficient (R^2). This means that the adsorption of methane could be applied to each layer which mean an extension of monolayer (Langmuir) to multilayer adsorption (BET isotherm). Furthermore, as indicated in Table 10.1, the maximum adsorption capacity (Q_{max}) of methane was estimated to be about 800 mg/g which is approximately the same using the Langmuir and BET isotherm models utilizing PUF adsorbent. While in the case of the use of Fe_3O_4-PUF(A) and (B) NCs, the highest correlation coefficients (R^2) were observed using the three parameter isotherm models; Radke-Prausnitz, Redlich-Peterson, and the combined one as presented in Table 10.1. In addition, Langmuir and BET isotherm models were overlapped as shown in Figures 10.6b and c due to the same correlation coefficients. Therefore, as shown in Table 10.1, the estimated Q_{max} were found to be 840.1 mg/g and 915.5 mg/g using Fe_3O_4-PUF(A) and (B) NCs, respectively. Moreover, as it is clear from Table 10.1, the estimated n value is less than 1 in all cases of adsorbents using Freundlich isotherm model which indicates that the mechanism of adsorption of methane is more physically than chemically and the lower value of this parameter indicate that the behavior of the isotherm in this case tends to be a rectangular or irreversible and deviates from the linear [22]. Furthermore, as indicated in Table 10.1, the calculated parameter of the energy, E, using the Dubinin–Radushkevich isotherm was found to be less than 90 kJ/g for all cases of adsorbents. Thus, a physical adsorption of methane was confirmed using all the adsorbents under investigation. Also, impregnation of Fe_3O_4 NPs into PUF adsorbent led to a decrease of the energy of adsorption as observed in Table 10.1 according to the E

value. Also, the increase of Fe_3O_4 NPs decreases the energy of adsorption of methane using Fe_3O_4-PUF NCs and hence increase the adsorption capacity as indicated in Table 10.1 for (A) and (B) respectively. Therefore, the mechanism of interaction between the PUF and Fe_3O_4 NPs could be described as physical adsorption. Also, based on the combination isotherm moel, the maximum adsorption capacities of CH_4 are 639.55, 726.52, and 796.02 mg/g utilizing PUF, Fe_3O_4-PUF(A), and Fe_3O_4-PUF(B) NCs, respectively.

Table 10.1 Estimated parameters for the adsorption isotherm of CH_4

Model		**PUF**	**Fe_3O_4-PUF(A)**	**Fe_3O_4-PUF(B)**
Langmuir	Qm	801.001	840.098	915.53
	k2	5.593E-5	9.17E-5	8.24E-5
	R^2	0.993	0.978	0.981
Freundlich	kf	1.128	4.57	4.56
	n	1.71	2.15	2.13
	R^2	0.966	0.912	0.909
Dubinin-Radushkevich	B	4.76	5.40	6.541
	Q_m	540.92	678.13	729.21
	R^2	0.969	0.939	0.941
	E	0.32	0.30	0.28
Radke-Prausnitz	α_{RP}	3217.74	8511.51	5074.75
	K_{RP}	1.24E-5	6.84E-6	1.17E-5
	m_{RP}	2.61	4.93	2.98
	R^2	0.996	0.998	0.996
Redlich–Peterson	A	0.038	0.052	0.054
	B	8.09E-7	7.74E-8	2.23E-7
	g	1.374	1.611	1.504
	R^2	0.997	0.998	0.997
BET	Cs	9.49E10	9.56E10	1.50E11
	B	5.31E6	8.76E6	12.4E6

	Q_m	800.612	839.924	915.663
	R^2	0.993	0.978	0.981
Combination	b	1.56E-6	3.85E-6	2.01E-6
	Q_m	639.55	726.52	796.02
	n	0.685	0.718	0.68
	R^2	0.999	0.986	0.993

The adsorption capacity of the magnetic NC for the adsorption of CH_4 has been compared with various adsorbents in Table 10.2. The adsorption capacities of magnetite immobilized on PUF developed and tested in this work are much higher than other adsorbents under research or currently in use. In addition, the NC used in this work is easier to recover than the others ones what is an added value. Therefore, the NC used in this study show highly competitive for CH_4 adsorption. For instance, the difference between the adsorption using Fe_3O_4-PUF(B) regarding MOF-177 is of 260.02 mg/gNC (32.67% higher) and 156.47 mg/gNC (19.65 % higher) compared to raw PUF. This indicates that the Fe-based NC is functioning and has a considerable higher adsorption capacity than the comparative PUF or other novel materials such as MOF-177. The promising results on CH_4 adsorption can be discussed as the high stability of the NPs on the matrix and the crystalline forms of the molecules as well as the magnetism feature. In addition, the Fe_3O_4-NCs is a cheaper product regarding commercial MOF-177 or others [15, 24].

Table 10.2. Comparison of the maximum adsorption capcity (Q_m) of CH_4 with other adsorbents in the literature

Adsorbents	Temperature, K	Q_m, mg/g	Reference
Fe_3O_4-PUF(B)	298.15	796.02	This work
Fe_3O_4-PUF(A)	298.15	726.52	This work
PUF	298.15	639.55	This work
MOF-177	298.15	536.00	[25]
Zeolite 13X	298.15	157.44	[4]
Activated carbon	293.15	82.46	[26]
DAY	303.15	46.77	[27]
HSZ-320	303.15	25.07	[27]
MWCNT	303.15	16.90	[27]

10.3.2.4. Reusability of the magnetite NC for several adsorption-desorption cycles for methane

The regenerated magnetite NC was tested for reusability after five cycles of adsorption-desorption. After every adsorption process, desorption by using N_2 was performed. The results (Figure 10.7) showed that the efficiency of CH_4 adsorption–desorption was nearly the same for the cycles. Therefore, the Fe_3O_4-PUFs(B) NCs could be used 5 cycles successfully for the CH_4 adsorption.

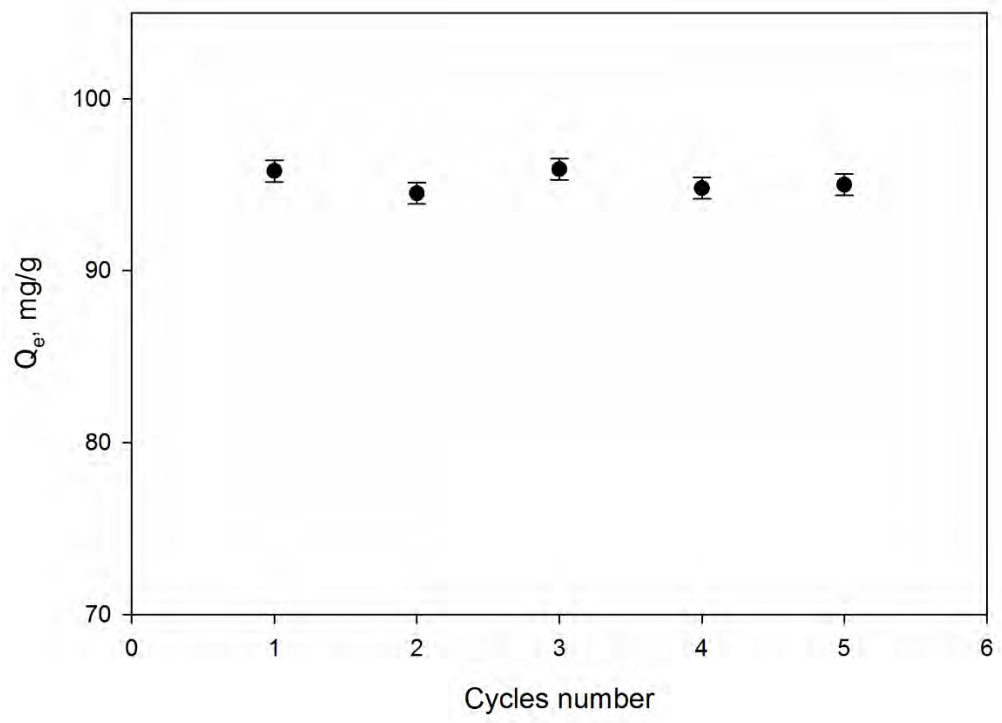

Figure 10.7. Reusability study of Fe_3O_4-PUFs(B) NCs for CH_4 adsorption (100 mg of the adsorbent, 0.5 mL/min flow, and room temperature).

10.4. Conclusion

The Fe_3O_4 NPs were synthesized by chemical co-precipitation in polyurethane foams (PUF) to give particles of 87-108 nm in size. Impregnation of iron oxide NPs enhances the adsorption capacity of methane at room temperature in comparison to PUF as control at the conditions of (0.5 mL/min of flow, 298.15 K of temperature, and 100 mg of adsorbent and 2000 ppmv of methane) Additionally, the higher iron concentration in PUF mantrix the higher adsorption capacity of methane. . The maximum adsorption capacities, Q_m were found to be 796.02 mgCH_4/gNCs for Fe_3O_4-PUF(B), 726.52 mgCH_4/gNCs for Fe_3O_4-PUF(A), and 639.55 mgCH_4/gPUF for PUF. The structures of NPs are extremely stable, achieving similar adsorption for five cycles. Fe_3O_4-PUF NC is highly competitive in comparison with other adsorbents from the literature.

10.5. References

1. Smithson, P.A., *IPCC, 2001: climate change 2001: the scientific basis. Contribution of Working Group 1 to the Third Assessment Report of the Intergovernmental Panel on Climate Change, edited by J. T. Houghton, Y. Ding, D. J. Griggs, M. Noguer, P. J. van der Linden, X. Dai, K. Maskell and C. A. Johnson (eds). Cambridge University Press, Cambridge, UK, and New York, USA, 2001. No. of pages: 881. Price £34.95, US$ 49.95, ISBN 0-521-01495-6 (paperback). £90.00, US$ 130.00, ISBN 0-521-80767-0 (hardback).* International Journal of Climatology, 2002. **22**(9): p. 1144-1144.
2. Meinshausen, M., et al., *Greenhouse-gas emission targets for limiting global warming to 2 C.* Nature, 2009. **458**(7242): p. 1158-1162.
3. McCarthy, J.J., *Climate Change 2001: Impacts, Adaptation, and Vulnerability: Contribution of Working Group II to the Third Assessment Report of the Intergovernmental Panel on Climate Change*. 2001: Cambridge University Press.
4. Cavenati, S., C.A. Grande, and A.E. Rodrigues, *Adsorption Equilibrium of Methane, Carbon Dioxide, and Nitrogen on Zeolite 13X at High Pressures.* Journal of Chemical & Engineering Data, 2004. **49**(4): p. 1095-1101.
5. Feroldi, M., et al., *Adsorption technology for the storage of natural gas and biomethane from biogas.* International Journal of Energy Research, 2016. **40**(14): p. 1890-1900.
6. Esteves, I.A.A.C., et al., *Adsorption of natural gas and biogas components on activated carbon.* Separation and Purification Technology, 2008. **62**(2): p. 281-296.
7. Kennedy, D.A., et al., *Pure and Binary Adsorption Equilibria of Methane and Nitrogen on Activated Carbons, Desiccants, and Zeolites at Different Pressures.* Journal of Chemical & Engineering Data, 2016. **61**(9): p. 3163-3176.
8. Saha, D., et al., *Adsorption of CO2, CH4, N2O, and N2 on MOF-5, MOF-177, and Zeolite 5A.* Environmental Science & Technology, 2010. **44**(5): p. 1820-1826.
9. Buzea, C., I.I. Pacheco, and K. Robbie, *Nanomaterials and nanoparticles: Sources and toxicity.* Biointerphases, 2007. **2**(4): p. MR17-MR71.

10. Alonso, A., et al., *Critical review of existing nanomaterial adsorbents to capture carbon dioxide and methane.* Science of The Total Environment, 2017. **595**: p. 51-62.
11. Austin, C.K., et al., *Enhanced Methane Sorption in Densified Forms of a Porous Polymer Network.* Materials Sciences and Applications, 2014. **5**: p. 387-394.
12. Hafizovic, J., et al., *The Inconsistency in Adsorption Properties and Powder XRD Data of MOF-5 Is Rationalized by Framework Interpenetration and the Presence of Organic and Inorganic Species in the Nanocavities.* Journal of the American Chemical Society, 2007. **129**(12): p. 3612-3620.
13. Mason, J.A., M. Veenstra, and J.R. Long, *Evaluating metal-organic frameworks for natural gas storage.* Chemical Science, 2014. **5**(1): p. 32-51.
14. Wu, H., W. Zhou, and T. Yildirim, *High-Capacity Methane Storage in Metal−Organic Frameworks M2(dhtp): The Important Role of Open Metal Sites.* Journal of the American Chemical Society, 2009. **131**(13): p. 4995-5000.
15. Sigma-Aldrich. *MOF-177*. Available from: http://www.sigmaaldrich.com/technical-documents/articles/materials-science/metal-organic-frameworks/mof-177.html (Access date 10/06/2017).
16. Domenech, B., et al., *Polyurethane foams doped with stable silver nanoparticles as bactericidal and catalytic materials for the effective treatment of water.* New Journal of Chemistry, 2016. **40**(4): p. 3716-3725.
17. Alonso, A., et al., *Environmentally-safe bimetallic Ag@Co magnetic nanocomposites with antimicrobial activity.* Chemical Communications, 2011. **47**(37): p. 10464-10466.
18. Dorado, A.D., et al., *Cr(III) removal from aqueous solutions: A straightforward model approaching of the adsorption in a fixed-bed column.* Journal of Environmental Science and Health, Part A, 2013. **49**(2): p. 179-186.
19. Nur, T., et al., *Phosphate removal from water using an iron oxide impregnated strong base anion exchange resin.* Journal of Industrial and Engineering Chemistry, 2014. **20**(4): p. 1301-1307.
20. Ncibi, M.C., *Applicability of some statistical tools to predict optimum adsorption isotherm after linear and non-linear regression analysis.* Journal of Hazardous Materials, 2008. **153**(1–2): p. 207-212.

21. Kumar, K.V. and K. Porkodi, *Relation between some two- and three-parameter isotherm models for the sorption of methylene blue onto lemon peel.* Journal of Hazardous Materials, 2006. **138**(3): p. 633-635.
22. Abo Markeb, A., et al., *Phosphate removal and recovery from water using nanocomposite of immobilized magnetite nanoparticles on cationic polymer.* Environmental Technology, 2016. **37**(16): p. 2099-2112.
23. Domènech, B., et al., *Development of novel catalytically active polymer-metal-nanocomposites based on activated foams and textile fibers.* Nanoscale Research Letters, 2013. **8**(1): p. 238.
24. Chae, H.K., et al., *A route to high surface area, porosity and inclusion of large molecules in crystals.* Nature, 2004. **427**(6974): p. 523-527.
25. Llewellyn, P.L., et al., *High Uptakes of CO2 and CH4 in Mesoporous Metal—Organic Frameworks MIL-100 and MIL-101.* Langmuir, 2008. **24**(14): p. 7245-7250.
26. Choi, B.-U., et al., *Adsorption Equilibria of Methane, Ethane, Ethylene, Nitrogen, and Hydrogen onto Activated Carbon.* Journal of Chemical & Engineering Data, 2003. **48**(3): p. 603-607.
27. Lee, J.-W., et al., *Methane Adsorption on Multi-Walled Carbon Nanotube at (303.15, 313.15, and 323.15) K.* Journal of Chemical & Engineering Data, 2006. **51**(3): p. 963-967.

Chapter 11

General conclusions and future work

11.1. General conclusions

Through the research study, the main conclusions that can be drawn from the current investigation could be divided into two groups as mentioned below;

Part A: Water remediation

Synthesis, characterization and initial screening of nanomaterials

- High resolution transmission electron microscopy showed average sizes of 13.00 ± 1.77 nm, 3.75 ± 0.65 nm, and 9.86 ± 1.40 nm and cubic, tetrahedral, and cubic structure for the synthesized Fe_3O_4, TiO_2, and CeO_2 nanoparticles, respectively.
- Approximately same particle sizes of Fe_3O_4 and CeO_2 NPs were obtained when they are impregnated into the reduced graphene oxide nanomaterials.
- CeO_2 nanoparticles demonstrated the highest efficiency for phosphate (33.71 %) and fluoride (81.87 %) removal at pH 5.0.
- TiO_2 nanoparticles showed the highest removal of nitrate (21.0 %).
- Fe_3O_4 nanoparticles exhibited removal efficiency of cadmium and nickel to be 25 %, and 47.83 %, respectively.
- Cationic exchange polymer, C100, presented a potential efficiency for the removal of cadmium (70.16 %) as well as nickel (100 %).
- Fe_3O_4/r-G.O nanocomposites showed 96.23 % removal of cadmium.
- High removal of percentage of atrazine (96.60 %) was obtained by using Fe_3O_4/r-G.O nanocomposites.
- Novel magnetic core/shell, Ce-Ti@Fe_3O_4, nanoparticles was successfully synthesized via one pot synthetic method.
- The removal efficiency for nitrate, phosphate, and fluoride was ranged from 85 % to 100 % using Ce-Ti@Fe_3O_4 nanoparticles, that is corresponding to equilibrium adsorption capacity of 42.50, 11.10, and 10.31 mg/gNPs for nitrate, phosphate, and fluoride, respectively.
- Low removal efficiency for heavy metal such as cadmium (45.28 %) was observed using Ce-Ti@Fe_3O_4 nanoparticles.

Fluoride removal:

- Fast removal of fluoride from aqueous solution was demonstrated using Ce-Ti@Fe_3O_4 nanoparticles (less than 5 min).
- Ce-Ti@Fe_3O_4 nanomaterial as adsorbent is applicable over a wide pH range (from 5 to 11).
- The maximum adsorption capacity for fluoride using Ce-Ti@Fe_3O_4 nanoparticles was found to be 91.04 mg F^- /g nanomaterial at pH 7, which outperformed many reported adsorbents.
- Ce-Ti@Fe_3O_4 nanomaterial was demonstrated to be easily removed from the aqueous medium by magnetic separation.
- Reusability of the core/shell nanoparticles was evaluated for 5 adsorption-desorption cycles for fluoride removal with no cerium release in the treated water.
- The adsorption capacity of fluoride was increased by increasing the temperature.
- Anion exchanged mechanism, between the hydroxyl group on the surface of the adsorbents and fluoride ions, was estimated according to the Dubbinin-Radushkevich isotherm model.
- The efficacy of the Ce-Ti@Fe_3O_4 nanoparticles as adsorbent was demonstrated for a real water matrix by spiking 10 mg/L of fluoride in drinking water, as it showed a residual fluoride concentration less than the maximum contaminant level.

Phosphate removal:

- Potential application of magnetite nanoparticles immobilized on cationic polymer (C100/Fe_3O_4 nanocomposite) was proved for phosphate removal.
- The optimum concentration of iron in the C100/Fe_3O_4 NCs is 23.59 mg_{Fe}/g_{NC} for phosphate adsorption.
- The maximum adsorption capacity of phosphate was found to be higher than 4.0 mg/gNCs at pH 7.0 using C100/Fe_3O_4 nanocomposites.
- Regeneration of the C100/Fe_3O_4 NCs was optimized to obtain 97.5 % recovery of phosphate using 0.5 M NaOH for three consecutive cycles desorption process.
- Reusability of the C100/Fe_3O_4 nanocomposites was demonstrated for 7 adsorption-desorption cycles.

Microalgae separation from water

- Naked, coated and functionalized Fe_3O_4 nanoparticles were used for the harvesting efficiency of the *Scenedesmus sp*. Microalgae from water.
- Optimum value for the microalgae harvesting was estimated to be 0.38 g/L of naked Fe_3O_4 NPs and 13 min magnetic separation time using response surface method obtaining a removal efficiency of 89.30 %.
- Langmuir isotherm model was the best model for fitting the experimental date for microalgae harvesting, and showed maximum adsorption capacity of 3.49 gDCW/gNPs, for *Scenedesmus sp.* using Fe_3O_4 NPs.
- Electrostatic interaction mechanism is proposed to describe the interaction between the algae cells and the NPs according to zeta potential measurements.
- Low concentration of the alkaline medium combined with an ultrasonication treatment method was used to regenerate Fe_3O_4 NPs before testing for reusability study.
- Fe_3O_4 NPs was successfully used for 5 cycles of the microalgae separation from wastewater.

Part B: Gases treatment

Metal Organic Frameworks

- Encapsulation of the core-shell Au/CeO_2 nanoparticles into microsized spherical, porous UiO-66 beads to produce metal organic frameworks (MOFs, MN-245) showed catalytic activity for CO oxidation.
- The temperatures required for 100 %, and 50 % conversion of CO into CO_2 were found to be 100 ℃, and 72 ℃, respectively.
- Better catalytic activity of MN-245 for the CO oxidation in comparison to other adsorbents in the literature.
- MN-245 showed high stability for CO conversion up to 50 h.

Methane removal from gas stream

- Impregnation of Fe_3O_4 NPs into polyurethane foam (PUF) to produce Fe_3O_4-PUF NCs was successfully synthesized using co-precipitation method.
- Fe_3O_4-PUF NCs showed better CH_4 adsorption in comparison to PUF.
- Higher CH_4 adsorption was observed at 0.5 mL/min.
- The maximum adsorption capacities were found to be 796.02 mg CH_4/gNCs for Fe_3O_4-PUF(B), and 639.55 mgCH_4/gPUF for PUF.
- Five adsorptions–desorption cycles could be conducted for CH_4 adsorption with stable adsorption capacity.

11.2. Future work

At the end of the present study, different nanomaterials could be applied for water remediation and gases treatment. However, the following recommendations are proposed for future work that could be undertaken before implementing into industrial applications:

- Full study of the effect of co-existing ions for contaminant removal from water for each adsorbent as mimic step for real water matrix.
- Detailed information for the kinetic study.
- Evaluate the efficiency of the core-shell nanoparticles for water purification using fixed-bed column.
- Enhancement the properties of the core/sell nanoparticles to obtain high removal of anions as well as heavy metals.
- Scale-up system is needed to investigate the efficiency of the adsorbents.
- Study the life cycle assessment of the nanomaterials.
- More information on the toxicity of the nanomaterials on the environment is needed.

Annexes

A-1

RSC Advances

COMMUNICATION

View Article Online
View Journal | View Issue

Cite this: RSC Adv., 2016, 6, 56913

Received 10th May 2016
Accepted 2nd June 2016

DOI: 10.1039/c6ra12144f

www.rsc.org/advances

Novel magnetic core–shell Ce–Ti@Fe_3O_4 nanoparticles as an adsorbent for water contaminants removal†

Ahmad A. Markeb, Laura A. Ordosgoitia, Amanda Alonso,* Antoni Sánchez and Xavier Font

Magnetic core–shell Ce–Ti@Fe_3O_4 nanoparticles were synthesized by coating cerium titanate on magnetite under mild experimental conditions. Combining magnetism, crystallinity, stability and adsorption capacity, it can be a promising nanomaterial as an adsorbent for anionic water contaminants, exhibiting high removal capacity, from 85% to 100%, for nitrates, phosphates and fluoride.

Contamination of water is a widespread problem throughout the world as a result of pollution and a wide range of pollutants can be considered for remediation.[1] Thus, the development of new technologies is fundamental. Among all the current decontamination methods, adsorption is considered the most effective, environmentally friendly, and economical method for contaminant removal.[2] In addition, nanotechnology can offer new products and process alternatives for water purification.[3] Some examples are based on nanoparticles (NPs), nanomembranes, carbon nanotubes (CNTs) and nanofibers, among others.[4] Thus, the use of adsorbents nanomaterials has become an interesting way for the removal of various contaminants from drinking water[5] such as of heavy metals[6] and, in a minor extent, nutrients.[7] For instance, the use of CeO_2, Fe_3O_4 and TiO_2 NPs and magnetic nanocomposite[7] for the adsorption of cadmium[8] and phosphate[7,9] has been reported by our group. Finally, other metal oxides and metal hydroxides had also been reported[10] for fluoride removal from water as well as bimetallic or mixed oxides.[11] Further, it is worthy to consider the reusability and the regeneration of the adsorbents as well as the trapping of the NPs to prevent its environmental and health safety risks.[12] Thus, the use of magnetic NPs for pollutants removal provides efficient, easy separation, and reusability. The magnetic NPs can be either used directly or as the core material in a core–shell NPs structure.[13] For instance, cerium titanates nanomaterials ($Ce_{2/3}TiO_3$) have many applications as photocatalytic and ferroelectric materials.[14] However, its properties exhibits canted-antiferromagnetic order[15] and few studies for improving its properties have been reported.[16] In this work, a novel nanomaterial was synthesized by coating cerium titanate on magnetite NPs using a simple and easy method as one step synthesis under room temperature to obtain magnetic core–shell Ce–Ti@Fe_3O_4 NPs (shell@core). Moreover, its efficiency was demonstrated for water remediation as a versatile nanoadsorbent for typical inorganic contaminants.

Briefly, the synthesis of the nanoadsorbent here reported was based in the following procedure: previously of the synthesis of the core–shell Ce–Ti@Fe_3O_4 NPs, magnetite nanoparticles (Fe_3O_4-NPs) were prepared by the co-precipitation method as reported elsewhere[7,17] by using cetyl trimethyl ammonium bromide, CTAB, as dispersant. During the synthesis, the mixture's colour turned from light yellow to red brown and then eventually to black which confirmed the formation of Fe_3O_4-NPs. Once the Fe_3O_4-NPs were washed and dried, Ce–Ti@Fe_3O_4 NPs were synthetized. $TiCl_4$ and $Ce(NO_3)_3 \cdot 6H_2O$ were mixed with 100 mL of Milli-Q water containing the previous formed Fe_3O_4-NPs, with a Ti^{4+} : Ce^{3+} molar ratio of 1 : 1 and to reach a total molar concentration of 50 mM. Mixing was under agitation at room temperature for 30 min. Next, a slowly dropwise titration with 12.5% v/v NH_3 solution until pH 7.0 was reached. Then, the Ce–Ti@Fe_3O_4 NPs produced were washed with ultrapure water and magnetic decantation and finally dried at 80 °C for 24 h. The synthetic procedure was adapted from similar works about core–shell magnetic Ti-NPs synthesis.[13a] Further details about the materials used and the synthetic protocols are found in ESI 1.† The Ce–Ti@Fe_3O_4 nanomaterial obtained was fully characterized for a deep understanding of its structure and properties. Thus, the metal content of the Ce–Ti@Fe_3O_4 NPs was determined by Inductively Coupled Plasma Optical Emission Spectrometry, ICP-OES (ESI 2.1†). The metal content (Ce, Ti and Fe) is detailed in terms of $mg_M\ g^{-1}$ and $mmol_M\ g^{-1}$ of the nanomaterial, where M corresponds to Ti, Ce and Fe, respectively. The results showed a metal content of 121.01 ± 7.70 $mg_{Ti}\ g^{-1}$, 199.29 ±

Department of Chemical, Biological and Environmental Engineering, Universitat Autònoma de Barcelona, 08193-Bellaterra, Spain. E-mail: amanda.alonso@uab.cat

† Electronic supplementary information (ESI) available. See DOI: 10.1039/c6ra12144f

10.47 $mg_{Ce}\ g^{-1}$ and 81.07 ± 4.49 $mg_{Fe}\ g^{-1}$, meaning 2.50 ± 0.16 $mmol_{Ti}\ g^{-1}$, 1.40 ± 0.07 $mmol_{Ce}\ g^{-1}$ and 1.50 ± 0.08 $mmol_{Fe}\ g^{-1}$. Thus, the synthesized nanoadsorbent contents the molar ratio of Ce : Ti : Fe of 1 : 2 : 1, which is in accordance with the experimental synthetic protocol. High resolution transmission electron microscopy (HRTEM) coupled with energy-dispersive spectroscopy (EDS), and electron diffraction (ED) pattern were used to characterize the morphology, size and crystalline structure of the Ce–Ti@Fe_3O_4 NPs (ESI 2.2†). Fig. 1 illustrates the TEM images coupled with EDS and ED pattern for Ce–Ti@Fe_3O_4 NPs. As shown in Fig. 1A, Ce–Ti@Fe_3O_4 NPs present a particle size within the range of 10–15 nm. Electron diffraction pattern allows studying the crystal structure of the NPs. Thus, the ED pattern for Ce–Ti@Fe_3O_4 NPs (Fig. 1B), taken from randomly selected area of the nanomaterial (SAED), exhibits multiple rings consisting of discrete spots, which suggested that the core–shell NP is based on nanocrystals.

In addition, EDS provided the metal composition of the samples and Fig. 1C proved the presence of the three components Ce, Ti, and Fe in the material. Moreover, magnetic properties of the Ce–Ti@Fe_3O_4 nanomaterial were qualitatively tested using a square magnet, showing the strong magnetism of the material (Fig. 1D). This result demonstrates an enhancement on its properties comparing to the literature where $Ce_{2/3}TiO_3$ exhibits antiferromagnetic properties.[15] This also demonstrates that the NPs could be easily recovered from the reaction mixture for further reuse in its application. Further, as shown in Table S1 (ESI 2.2†), the calculated interplanar distance (d) from the SAED pattern of the Ce–Ti@Fe_3O_4 NPs and the corresponding Miller indices (*h k l* diffraction plan) were compared to the standard values.[18] The values concluded that the crystal pattern presented similarity to both cerium titanate

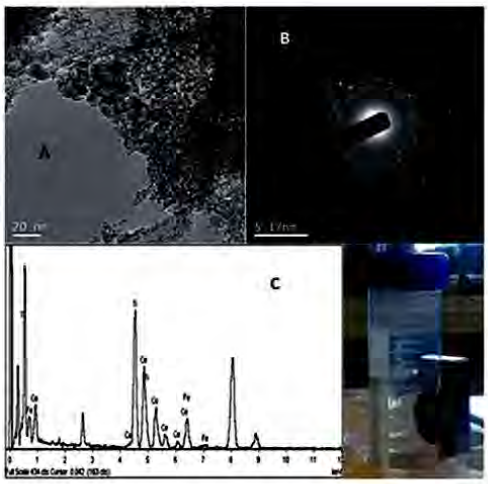

Fig. 1 (A) HRTEM image, (B) SAED pattern; (C) EDS spectra and; (D) qualitative magnetic properties test for Ce–Ti@Fe_3O_4 NPs.

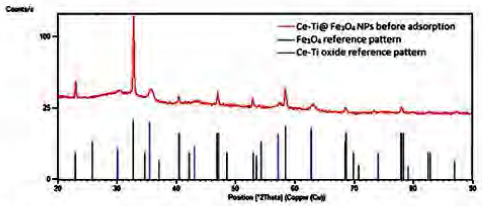

Fig. 2 XRD pattern of the Ce–Ti@Fe_3O_4 material and matching comparison with both Fe_3O_4 and Ce–Ti oxide reference pattern from database.

and Fe_3O_4 patterns, which was in agreement with the XRD data further reported.

XRD technique was used to obtain the crystalline structure of the Ce–Ti@Fe_3O_4 NPs. In a diffraction pattern, the location of the peaks on the Bragg angles (2θ scale) can be compared to the reference peaks (ESI 2.3†). Fig. 2 shows the XRD pattern of the original Ce–Ti@Fe_3O_4 nanomaterial, which consists of two phases: magnetite and cerium titanate reference patterns that were proved by matching from database (Table S2, ESI 2.3†). Additionally, Table S3 (ESI 2.3†) shows the experimental 2θ positions from the XRD pattern and its comparison with the standard 2θ values[18] and their respective diffracting plan index (*h k l*) in Fe_3O_4 and Ce–Ti oxide NPs. These results could suggest that the diffracted peaks can be indexed to be face centre cubic structure of the Fe_3O_4 NPs according to the JCPDS 00-001-111118b. From the XRD patterns shown in Fig. 2, one can notice the characteristic diffraction peaks belonging to cubic Fe_3O_4. They correspond to (220), (311), (400), (511) and (440) family planes (PDF 89-4319). After cerium titanium oxide coating, the characteristic peaks of cerium titanate were appeared and its Bragg angles were found to be close to that of $Ce_{2/3}TiO_{2.98}$. Two peaks were observed corresponding to rutile/anatase in the magnetic cerium titanate NPs: (110) peak of anatase and (101) peak of rutile closely positioned at each other, namely at around $2\theta = 25.3$ and $2\theta = 27.4$, respectively.

The morphology of the core–shell structure of the Ce–Ti@Fe_3O_4 nanomaterial was demonstrated by Scanning Transmission Electron Microscopy (STEM) coupled with Electron Energy Loss Spectra (EELS), (ESI 2.4†). Thus, the images obtained from a HAADF detector provide density-based contrast, the core appeared bright due to their higher scattering probability.[19] As illustrated in Fig. 3, the HAADF image of Ce–Ti@Fe_3O_4 shows that the Fe_3O_4 NPs was coated with Ce–Ti oxide layer (Fig. 3A) as it can be seen a brightest core covered by a shell. STEM based EDS was used to confirm the elemental distribution of the Ti, Fe and Ce, respectively, as shown in Fig. 3B. In addition, the scanning line profile appears as a strong peak corresponding to the position of the bright Fe particle core, whilst the spectra on each side of the core are dominated by Ce and Ti edges (in the shell) as illustrated in Fig. 3C.

UV/vis absorption and luminescence spectra of Ce–Ti@Fe_3O_4 NPs were performed to estimate the valence of the

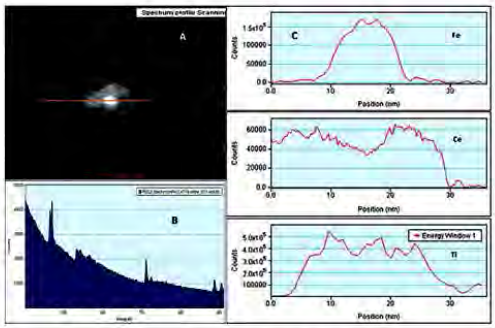

Fig. 3 EELS line scan of the core–shell Ce–Ti@Fe_3O_4 nanocomposite. (A) STEM HAADF image of the Ce–Ti@Fe_3O_4 and position of line scan; (B) PEELS spectrum of the nanocomposite; and (C) ions profile spectra along the line scanning.

cerium in the NP and confirm its speciation (ESI 2.5†). As reported, the cerium ion in the cerium titanate, $Ce_{2/3}TiO_3$, is mainly Ce(III).[16] Fig. S1 (ESI 2.5†) shows the absorption UV-vis spectra of the Ce–Ti@Fe_3O_4 nanomaterial. As shown, two peaks were observed at 250 and 310 nm respectively, which could be attributed to the presence of either Ce(III) or both Ce(III) and Ce(IV) in the nanomaterial.[20] Therefore, because of the overlapping of both bands, it is difficult to determine the species responsible of colour with the colorimetric technique. Thus, luminescence spectroscopy is necessary to obtain information about the valence of the cerium. Ce(III) ions presents a characteristic intense blue emission upon UV excitation.[21] Therefore, Fig. S2 (ESI 2.5†) represents the excitation and emission spectra of the Ce–Ti@Fe_3O_4 nanomaterial. The excitation spectrum for $\lambda_{em} = 363$ nm shows a band at 258 nm and the emission spectrum recorded upon $\lambda_{exc} = 266$ nm shows the characteristic emission band at 325 nm, which corresponds to the transition to ground state to excited state as compared to literature.[20,22,23] The slightly shift of the wavelength comparing to the literature could be attributed to the lower temperature of the synthesis of the materials and to the presence of magnetite NPs in the core.

In this work, we also investigated the adsorption capacity and removal efficiency of the nanomaterials for different water contaminants: fluoride, nitrate, phosphates and cadmium. The adsorption experiments procedures are based on batch adsorption tests to determine the adsorption efficiency by the synthesized NPs (ESI 4†). Residual contaminant concentration in the solution after 24 h of adsorption (Ce) was determined by the corresponding analytical method detailed in ESI 3† and the equilibrium adsorption capacity (Q_e) of the adsorbent was calculated as eqn (S1) (ESI 4†). Adsorption experiments were performed using different initial concentrations for each contaminant that are based either on the reported typical concentration in water or on the maximum contaminated level (MCL). For instance, phosphate initial concentration tested was 10 mg L^{-1} due to municipal wastewater may contain 4–15 mg L^{-1}, and domestic wastewater may contains 10–30 mg L^{-7}. Furthermore, 10 mg L^{-1} was selected as initial fluoride concentration because the maximum contaminated level in water is 1.5 mg L^{-1}.[24] In the case of fluoride, it has been reported that its concentration in groundwater ranges from under 1.0 mg L^{-1} to more than 35.0 mg L^{-1} in several regions.[25] In addition, the initial nitrate concentration tested is 50 mg L^{-1} according to the WHO guidelines, where the MCL is 50 mg L.[24b] Also, 10 mg L^{-1} of initial cadmium concentration was selected as wastewater contains 10–100 mg L^{-1} of cadmium contaminant.[26] All the experiments were performed at pH 7 as a typical value in real media. Table 1 shows the equilibrium adsorption capacities after 24 h, the percentage of removal of each contaminant using a concentration of 1g L^{-1} of the adsorbent for all the cases.

It is shown that the Ce–Ti@Fe_3O_4 NPs have a potential effect for removal anionic contaminants (*i.e.* fluoride, nitrate and phosphates) from 85% removal for nitrate to 100% for phosphates and fluoride. However, it presents low removal for cationic contaminants such as cadmium (45% removal). The differences obtained on the adsorption process for the different contaminants tested may be discussed in terms of the physicochemical properties of the material and thus, the adsorption mechanism of the Ce–Ti@Fe_3O_4 material could be hypothesized. On the one hand, the metal oxides NPs present a relatively negative charge (hydroxyl groups, OH^-) on the oxide surface due to its hydrolysis in aqueous media. On the other hand, as discussed in this study, Ce–Ti@Fe_3O_4 NPs consist of Ce(III) ions and also it has a potential of +165 mV at pH 7. Thus, different sorption processes could take place for these contaminants tested. The adsorption mechanism for the anions could be attributed to two explanations: (i) electrostatic attraction (*i.e.* chemisorption)[27] and (ii) surface ion-exchange process (*i.e.* physisorption).[28] Phosphate removal could be explained in terms of the formation of cerium phosphate, as reported.[29] In this sense, we may consider that the presence of Ce(III) should be the driven force and thus, the adsorption takes place throughout electrostatic attraction. On the contrary, the OH^- groups on the adsorbent surface played a dominant role. Therefore, fluoride or nitrate removal may suffer a surface ion-exchange process based on the exchange of the OH^- group with the contaminant anion as already reported.[28] The OH^- on the surface of the NPs are present due to the nature of the media (*e.g.* pH, which is further evaluated). Thus, the physical mechanism could be expressed by eqn (1) and (2):[28]

$$M^{n+} + nH_2O \rightarrow M(OH)_n \quad (1)$$

Table 1 Adsorption capacities and removal efficiencies values for contaminants removal

Pollutant	Initial concentration, mg L^{-1}	Dose, g L^{-1}	Q_e, mg g^{-1}	Removal, %
PO_4–P	10	0.90	11.10	99.90
F	10	0.97	10.31	100.0
NO_3–N	50	1.0	42.50	85.00
Cd^{2+}	10	1.0	4.53	45.28

$$M(OH)_n + xA^- \rightarrow M(OH)_{n-x}A_x + xOH^- \quad (2)$$

where M, n, x are the adsorbent's metal ion, valency of the metal ion and, number of mole of anion (A), respectively. Further studies are under investigation by our group.

On the other hand, it has been reported that heavy metal adsorption onto NPs is an emerging technique for the removal of these pollutants due to its suitable electric charge given by an adequate Z-potential.[30] However, Ce–Ti@Fe_3O_4 material shows a low removal for cadmium due to the positive charge of the NPs surface (positive potential) that contributes to a weak electrostatic interaction between cadmium and the OH^- from the oxide surface of the NPs. Further, the efficiency of this material was demonstrated by comparing the equilibrium adsorption capacities with those reported in literature (Table SI 2, ESI 4†). As indicated, Ce–Ti@Fe_3O_4 NPs show high efficiency for anions comparing to cations. Thus, further studies on the promising properties of this new material in terms of adsorption capacity should be focused on anionic pollutants dissolved in water.

Conclusions

Magnetic core–shell Ce–Ti@Fe_3O_4 nanoparticles were designed and synthesized by incorporating magnetite into Ce–Ti oxide nanoparticles by mild experimental conditions. The resulting magnetic and core–shell nanomaterial exhibited a suitable composition, crystallinity and magnetic properties to be functional as adsorbent for the removal of inorganic pollutants from aqueous media. Remarkably, the adsorption capacity and removal efficiency at pH 7 for anionic contaminants such as nitrates, phosphates and fluoride was from 85 to 100% under the experimental conditions. In comparison with other materials reported in literature, this nanomaterial as adsorbent is highly competitive, as it has high adsorption capacity and promising features and magnetic properties for recovering. Further studies regarding to adsorption mechanism and effect of other parameters will be focusing in our future work.

Acknowledgements

The author, Ahmad Abo Markeb, appreciated and would like to thank the Ministry of Higher Education of Egypt for the PhD external mission grant. Special thanks are given to Servei de Microscopia from Universitat Autònoma de Barcelona and from the Institut Català de Nanociencia i Nanotecnologia.

Notes and references

1 P. B. Tchounwou, C. G. Yedjou, A. K. Patlolla and D. J. Sutton, in *Molecular, Clinical and Environmental Toxicology: Environmental Toxicology*, ed. A. Luch, Springer Basel, Basel, 2012, vol. 3, p. 133.
2 A. Bhatnagar, E. Kumar and M. Sillanpää, *Chem. Eng. J.*, 2011, **171**, 811.
3 I. Gehrke, A. Geiser and A. Somborn-Schulz, *Nanotechnol., Sci. Appl.*, 2015, **8**, 1.
4 S. Recillas, J. Colón, E. Casals, E. González, V. Puntes, A. Sánchez and X. Font, *J. Hazard. Mater.*, 2010, **184**, 425.
5 X. Qu, P. J. J. Alvarez and Q. Li, *Water Res.*, 2013, **47**, 3931.
6 A. Sánchez, S. Recillas, X. Font, E. Casals, E. González and V. Puntes, *TrAC, Trends Anal. Chem.*, 2011, **30**, 507.
7 A. Abo Markeb, A. Alonso, A. D. Dorado, A. Sánchez and X. Font, *Environ. Technol.*, 2016, 1.
8 A. R. Contreras, A. García, E. González, E. Casals, V. Puntes, A. Sánchez, X. Font and S. Recillas, *Desalin. Water Treat.*, 2012, **41**, 296.
9 S. Recillas, A. García, E. González, E. Casals, V. Puntes, A. Sánchez and X. Font, *Water Sci. Technol.*, 2012, **66**, 503.
10 (*a*) E. Kumar, A. Bhatnagar, U. Kumar and M. Sillanpää, *J. Hazard. Mater.*, 2011, **186**, 1042; (*b*) G. Lee, C. Chen, S.-T. Yang and W.-S. Ahn, *Microporous Mesoporous Mater.*, 2010, **127**, 152; (*c*) S.-X. Teng, S.-G. Wang, W.-X. Gong, X.-W. Liu and B.-Y. Gao, *J. Hazard. Mater.*, 2009, **168**, 1004; (*d*) S. M. Maliyekkal, A. K. Sharma and L. Philip, *Water Res.*, 2006, **40**, 3497; (*e*) S. S. Tripathy, J.-L. Bersillon and K. Gopal, *Sep. Purif. Technol.*, 2006, **50**, 310; (*f*) S. Ghorai and K. K. Pant, *Sep. Purif. Technol.*, 2005, **42**, 265; (*g*) K. Biswas, D. Bandhoyapadhyay and U. C. Ghosh, *Adsorption*, 2007, **13**, 83; (*h*) K. Biswas, K. Gupta and U. C. Ghosh, *Chem. Eng. J.*, 2009, **149**, 196; (*i*) D. Thakre, S. Rayalu, R. Kawade, S. Meshram, J. Subrt and N. Labhsetwar, *J. Hazard. Mater.*, 2010, **180**, 122; (*j*) N. Minju, K. Venkat Swaroop, K. Haribabu, V. Sivasubramanian and P. Senthil Kumar, *Desalin. Water Treat.*, 2013, **53**, 2905; (*k*) V. Sivasankar, T. Ramachandramoorthy and A. Darchen, *Desalination*, 2011, **272**, 179.
11 (*a*) V. Tomar, S. Prasad and D. Kumar, *Microchem. J.*, 2013, **111**, 116; (*b*) S. Deng, H. Liu, W. Zhou, J. Huang and G. Yu, *J. Hazard. Mater.*, 2011, **186**, 1360; (*c*) L. Chen, T.-J. Wang, H.-X. Wu, Y. Jin, Y. Zhang and X.-M. Dou, *Powder Technol.*, 2011, **206**, 291; (*d*) H.-X. Wu, T.-J. Wang, L. Chen, Y. Jin, Y. Zhang and X.-M. Dou, *Powder Technol.*, 2011, **209**, 92; (*e*) M. G. Sujana and S. Anand, *Appl. Surf. Sci.*, 2010, **256**, 6956; (*f*) X. Wu, Y. Zhang, X. Dou and M. Yang, *Chemosphere*, 2007, **69**, 1758; (*g*) N. Chen, Z. Zhang, C. Feng, M. Li, D. Zhu and N. Sugiura, *Mater. Chem. Phys.*, 2011, **125**, 293; (*h*) N. Chen, Z. Zhang, C. Feng, N. Sugiura, M. Li and R. Chen, *J. Colloid Interface Sci.*, 2010, **348**, 579; (*i*) H. Liu, S. Deng, Z. Li, G. Yu and J. Huang, *J. Hazard. Mater.*, 2010, **179**, 424.
12 A. Alonso, *Development of polymeric nanocomposites with enhanced distribution of catalytically active or bactericide nanoparticles*, Chemistry Departament, Universitat Autònoma de Barcelona, Spain, 2012.
13 (*a*) C. Zhang, L. Chen, T.-J. Wang, C.-L. Su and Y. Jin, *Appl. Surf. Sci.*, 2014, **317**, 552; (*b*) L. Chen, B.-Y. He, S. He, T.-J. Wang, C.-L. Su and Y. Jin, *Powder Technol.*, 2012, **227**, 3.
14 L. Kong, D. J. Gregg, I. Karatchevtseva, Z. Zhang, M. G. Blackford, S. C. Middleburgh, G. R. Lumpkin and G. Triani, *Inorg. Chem.*, 2014, **53**, 6761.
15 K. Yoshii and H. Abe, *J. Alloys Compd.*, 2002, **343**, 199.
16 W. H. Jung, *J. Phys.: Condens. Matter*, 1998, **10**, 8553.

17 S. Laurent, D. Forge, M. Port, A. Roch, C. Robic, L. Vander Elst and R. N. Muller, *Chem. Rev.*, 2008, **108**, 2064.
18 (*a*) L. G. Berry and R. M. Thompson, *X-ray diffraction data for minerals*, Waverly Press, New York, 1962, p. 194; (*b*) J. L. Zhang, R. S. Srivastava and R. D. K. Misra, *Langmuir*, 2007, **23**, 6342.
19 B. R. Knappett, P. Abdulkin, E. Ringe, D. A. Jefferson, S. Lozano-Perez, T. C. Rojas, A. Fernandez and A. E. H. Wheatley, *Nanoscale*, 2013, **5**, 5765.
20 M. Martos, B. Julián-López, J. V. Folgado, E. Cordoncillo and P. Escribano, *Eur. J. Inorg. Chem.*, 2008, **2008**, 3163.
21 L. Huang, X. Wang, H. Lin and X. Liu, *J. Alloys Compd.*, 2001, **316**, 256.
22 G. Q. Xu, Z. X. Zheng, W. M. Tang and Y. C. Wu, *J. Lumin.*, 2007, **124**, 151.
23 E. Cordoncillo, F. J. Guaita, P. Escribano, C. Philippe, B. Viana and C. Sanchez, *Opt. Mater.*, 2001, **18**, 309.
24 (*a*) WHO, Chemical fact sheets: fluoride, in *Guidelines for drinking-water quality (electronic resource): incorporation first addendum*, Geneva, 3rd edn, 2006, vol. 1, p. 375; (*b*) P. I. Drinking-water, WHO, 2004.
25 S. Meenakshi and R. C. Maheshwari, *J. Hazard. Mater.*, 2006, **137**, 456.
26 Y. Yurekli, *J. Hazard. Mater.*, 2016, **309**, 53.
27 M. Pattanaik and S. K. Bhaumik, *Mater. Lett.*, 2000, **44**, 352.
28 K. Zhang, S. Wu, X. Wang, J. He, B. Sun, Y. Jia, T. Luo, F. Meng, Z. Jin, D. Lin, W. Shen, L. Kong and J. Liu, *J. Colloid Interface Sci.*, 2015, **446**, 194.
29 Y. G. Ko, T. Do, Y. Chun, C. H. Kim, U. S. Choi and J.-Y. Kim, *J. Hazard. Mater.*, 2016, **307**, 91.
30 A. R. C. Rodríguez, in *Departament d'Enginyeria Química Universitat Autònoma de Barcelona (UAB)*, Escola d'Enginyeria, 2015.

A-2

Science of the Total Environment 598 (2017) 949–958

Contents lists available at ScienceDirect

Science of the Total Environment

journal homepage: www.elsevier.com/locate/scitotenv

Adsorption process of fluoride from drinking water with magnetic core-shell Ce-Ti@Fe_3O_4 and Ce-Ti oxide nanoparticles

Ahmad Abo Markeb, Amanda Alonso *, Antoni Sánchez, Xavier Font

Department of Chemical, Biological and Environmental Engineering, Universitat Autònoma de Barcelona, 08193 Bellaterra, Spain

HIGHLIGHTS

- Synthesized Ce-Ti oxides and Ce-Ti@Fe_3O_4 NPs were tested as adsorbents for fluoride removal from drinking water.
- Langmuir, Freundlich, and Dubinin–Radushkevich isotherm models and mechanism estimation were evaluated.
- Ce-Ti@Fe_3O_4 NPs maximum adsorption capacity was 91 mg F/g NP.
- Regeneration and reusability of the magnetic Ce-Ti@Fe_3O_4 NPs as adsorbent were performed.
- Thermodynamic parameters for the adsorption process were calculated.

GRAPHICAL ABSTRACT

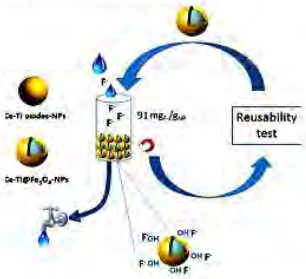

ARTICLE INFO

Article history:
Received 10 November 2016
Received in revised form 22 April 2017
Accepted 25 April 2017
Available online xxxx

Keywords:
Magnetic core-shell nanoparticles
Fluoride removal
Drinking water
Adsorption
Reusability

ABSTRACT

Synthesized magnetic core-shell Ce-Ti@Fe_3O_4 nanoparticles were tested, as an adsorbent, for fluoride removal and the adsorption studies were optimized. Adsorption capacity was compared with the synthesized Ce-Ti oxide nanoparticles. The adsorption equilibrium for the Ce-Ti@Fe_3O_4 adsorbent was found to occur in < 15 min and it was demonstrated to be stable and efficient in a wide pH range of 5–11 with high fluoride removal efficiency over 80% of all cases. Furthermore, isotherm data were fitted using Langmuir and Freundlich models, and the adsorption capacities resulted in 44.37 and 91.04 mg/g, at pH 7, for Ce-Ti oxides and Ce-Ti@Fe_3O_4 nanoparticles, respectively. The physical sorption mechanism was estimated using the Dubinin-Radushkevich model. An anionic exchange process between the OH^- group on the surface of the Ce-Ti@Fe_3O_4 nanomaterial and the F^- was involved in the adsorption. Moreover, thermodynamic parameters proved the spontaneous process for the adsorption of fluoride on Ce-Ti@Fe_3O_4 nanoparticles. The reusability of the material through magnetic recovery was demonstrated for five cycles of adsorption-desorption. Although the nanoparticles suffer slight structure modifications after their reusability, they keep their adsorption capacity. Likewise, the efficiency of the Ce-Ti@Fe_3O_4 was demonstrated when applied to real water to obtain a residual concentration of F^- below the maximum contaminated level, 1.5 mg/L (WHO, 2006).

1. Introduction

Fluoride contamination could be found in ground and surface water (N. Gandhi et al., 2012; Rafique et al., 2013) as well as in wastewater from fluoride chemical industries (Shen et al., 2003; Teng et al., 2009). Fluoride presents hazardous effects if it exceeds 1.5 mg/L in water (Karthikeyan et al., 2011; Singh et al., 2013; WHO, 2006) leading to various diseases (Bhatnagar et al., 2011; Liu et al., 2011; Vinati et al., 2015). The main source of these effects is from fluoride contaminated drinking water, which leads to 65% of endemic fluorosis diseases over the world (Shiklomanov, 2000; Viswanathan et al., 2009). For example, contents in drinking water of 4.8 and 1.7 mg/L in Greece and India, respectively,

* Corresponding author at: Departament d'Enginyeria Química, Biològica i Ambiental, Escola d'Enginyeria. Universitat Autònoma de Barcelona, 08193 Bellaterra, Spain.
E-mail address: amanda.alonso@uab.cat (A. Alonso).

http://dx.doi.org/10.1016/j.scitotenv.2017.04.191
0048-9697/

have been reported (Dai et al., 2004; Gupta and Kumar, 2012; Martínez-Acuña et al., 2016). Therefore, drinking water defluoridation is necessary to prevent human illness (Mohapatra et al., 2009). Defluoridation of drinking water using several technologies, including precipitation-coagulation, membrane separation process, ion exchange, electrodialysis, adsorption and reverse osmosis, had been developed (Amor et al., 2001; Chang and Liu, 2007; Meenakshi and Viswanathan, 2007; Sehn, 2008; Solangi et al., 2009; Velizarov et al., 2004). Among these methods, adsorption is the most effective, environmentally friendly, and economic method due to the simplicity of design, relatively low cost, high efficiency, and ease of operation (Bhatnagar et al., 2011). For instance, the use of biochar (Mohan et al., 2014) and biomass (Sinha et al., 2003) as adsorbent materials, were reported for fluoride removal. Furthermore, the removal of various contaminants from drinking water were performed by using nanomaterial adsorbents due to their unique properties such as large surface area, high reactivity, high specificity, and self-assembly (Qu et al., 2013). Various metal oxides and hydroxides of aluminium, iron, zirconium, magnesium, chromium and manganese ions based nanoparticles (NPs) had been reported (Kumar et al., 2011; Lee et al., 2010; Minju et al., 2013; Sivasankar et al., 2011) for fluoride removal from water (Meenakshi and Maheshwari, 2006). Although bimetallic or mixed oxides such as Mn-Ce, Al-Ce, Zr-Mn and ceramic adsorbents were also studied for fluoride removal, some of these materials present disadvantages in terms of pH range, high cost and low adsorption capacity. (Chen et al., 2011; Deng et al., 2011; Liu et al., 2010; Sujana and Anand, 2010; Tomar et al., 2013). Thus, Zhang et al. (2015), used magnesium oxide nanomaterial for fluoride removal and it showed high adsorption capacity (about 300 mg/g) but regeneration was reported not to be favoured. V. Sivasankar et al. (2011), reported low adsorption capacity (9.02 mg/g) for fluoride removal from drinking water utilizing manganese dioxide based nanomaterial compared to previously reported results. Using an Al-Ce hybrid nanomaterial, Liu et al. (2010) found high adsorption capacity of fluoride (91.4 mg/g), but slow kinetics to reach the equilibrium. However, to our knowledge, no studies about the reusability of the adsorbents have been reported for the reported materials (Deng et al., 2011; Liu et al., 2010). In this sense, the use of magnetic NPs for pollutants removal may provide efficient, rapid and easy separation, and especially reusability. The magnetic NPs can be either used directly as an adsorbent or as the core material in a core-shell NPs (Chai et al., 2013; Chen et al., 2012; Zhang et al., 2014). On the other hand, the hydrous Ce oxide, as rare earth metal, is reported to be more effective material for fluoride removal (46.84 mg/g) compared to other metals, although it is not useful for drinking water treatment due to its toxicity (Taylor et al., 2016). Furthermore, titanium based nanomaterials have also a great interest for fluoride removal with adsorption capacities that ranged from 15 to 47 mg/g (Chen et al., 2012; Li et al., 2010). Therefore, mixing rare earth metals (i.e. Ce) with low-cost metals (i.e. Fe) could be advantageous for high adsorption capacities at neutral pH medium, improving the separation of the adsorbent by magnetism as well as avoiding Ce-toxicity.

Our research group was succeeded in synthesizing a new adsorbent based on magnetic core-shell Ce-Ti@Fe_3O_4 NPs (shell@core) which presented promising properties in terms of magnetism, crystalline structure and adsorption for some inorganic water contaminants (Abo Markeb et al., 2016).

In the present work, two novel nanomaterials based on Ce-Ti oxide and Ce-Ti@Fe_3O_4 NPs were synthesized and compared as adsorbents for fluoride ion removal from aqueous solution. Adsorption kinetics, isotherms and the effect of different parameters (i.e. pH and temperature) in the adsorption capacity of the materials were studied. Also, the use of the Ce-Ti@Fe_3O_4 NPs for the treatment of real drinking water was performed. Further, the reuse of the Ce-Ti@Fe_3O_4 adsorbent was evaluated.

2. Materials and methods

2.1. Materials

Iron (II) chloride ($FeCl_2$, 98%), iron (III) chloride hexahydrate ($FeCl_3 \cdot 6H_2O$, ≥99%), sodium fluoride (NaF, ≥99%), titanium chloride ($TiCl_4$, ≥99.98%), cerium nitrate hexahydrate ($Ce(NO_3)_3.6H_2O$, ≥99%), and ammonia solution were purchased from Sigma-Aldrich, Spain. Sodium hydroxide pellets (NaOH), was purchased from Merk. Hydrochloric acid (HCl), and cetyltrimethylammonium bromide (CTAB) were purchased from Panreac, SA. All the chemicals were of analytical grade or higher, and all solutions were prepared with Milli-Q water and filtered using 0.45 μm Nylon membrane filter.

2.2. Preparation of the Ce-Ti oxide nanoparticles and Ce-Ti@Fe_3O_4 nanoparticles

This synthetic procedure for Ce-Ti oxide NPs was adapted from similar works about core-shell magnetic Ti-NPs synthesis (Zhang et al., 2014). Briefly, in this work, $TiCl_4$ and $Ce(NO_3)_3 \cdot 6H_2O$ were dissolved in Milli-Q water and mixed at 25 °C. Then 12.5% NH_3 solution was slowly added dropwise until pH 7.0 was reached. Then, the Ce-Ti NPs produced were washed, centrifuged and dried. Detailed information about the methodology is reported in the Supporting Information (SI.1).

The Ce-Ti@Fe_3O_4 NPs were prepared by the co-precipitation method reported by our research group (Abo Markeb et al., 2016) (detailed information is provided in SI.1).

2.3. Characterization of the nanomaterials

Inductively Coupled Plasma Optical Emission Spectrometry (ICP-OES) was used for the metal concentration analysis of both synthesized nanomaterials. The detailed sample preparation for ICP-OES analysis is in SI.2.1. Also, High-Resolution Transmission Electron Microscopy (HRTEM) coupled with Energy-Dispersive Spectroscopy (EDS), and Electron Diffraction (ED) Pattern were acquired using a JEM-2011/JEOL microscope operated at 200 kV and equipped with an INCA X-MAX detector. HRTEM was used to characterize the morphology and sizes of both Ce-Ti@Fe_3O_4 and Ce-Ti oxide NPs and, EDS and ED were used to analyze the composition and the crystalline structure (SI.3). The morphology of the NPs was determined by Scanning Transmission Electron Microscopy (STEM) coupled with high-angle annular dark field (HAADF) detector and Electron Energy Loss Spectra (EELS).

2.4. Adsorption and desorption experiments procedure

For all the experiments, batch adsorption tests were used to determine the fluoride adsorption efficiency of both synthesized NPs. A dose of adsorbent (W) (g/L) was added into a conical flask containing fluoride solution with an initial fluoride concentration (C_0). Typically, 25 mg of the adsorbent was added into the conical flask, which contains 25 mL of the fluoride ion solution, C_0. Depending on the experiment, pH of the solution was adjusted using NaOH or HCl, both at 0.1 M. The flask was shaken (200 rpm) at 25 °C using a thermostatic shaker. Residual fluoride concentration in the solution, C_e, was determined by ionic chromatography by using ICS-2000 (Dionex) system (SI.4). Equilibrium adsorption capacity, Q_e, of the adsorbent was calculated as Eq. (1):

$$Q_e = (C_0 - C_e)/W \quad (1)$$

2.4.1. Adsorption isotherms

Adsorption isotherm experiments of both synthesized Ce-Ti oxides and Ce-Ti@Fe_3O_4 NPs were performed at different concentrations of fluoride from 1 to 500 mg/L at pH 7 with an adsorbent amount of 1 g/L and treated, as described in Section 2.4.1, for 60 min, to assure to

reach the equilibrium. Then, residual fluoride concentrations were measured after filtration using 0.45 μm Nylon membrane filter. All experiments were performed in triplicate. Detailed information of the adsorption isotherm models is provided in SI.5.

2.4.2. Fluoride desorption procedure

Different studies proved that the most effective desorbing reagent for regeneration of the adsorbent is the NaOH solution (Mahramanlioglu et al., 2002; Zhang et al., 2005). The desorption experiments were performed after adsorption of 10 mg/L of fluoride using 1.0 g/L of Ce-Ti@Fe_3O_4 NPs for 60 min at pH 7.0, by shaking the adsorbent at 200 rpm using two different concentrations and volumes of NaOH desorbing solution: 25 mL of 0.5 M NaOH, and 5 mL of 0.1 M NaOH, at intervals of time of 2, 4, 6, 8, and 12 h. Then, the fluoride concentrations of the desorbing solutions were analyzed as previously mentioned.

2.4.3. Reusability of the Ce-Ti@Fe_3O_4 NPs as adsorbent and characterization

Under the optimized conditions for desorption, five cycles of the adsorption-desorption processes were performed for evaluating the reusability of the synthesized NPs for fluoride removal and its recovery. The composition, morphology, and size of the Ce-Ti@Fe_3O_4 NPs were analyzed after its use for five adsorption-desorption cycles and compared to the original material (SI2 and SI6). TEM images were obtained to analyze the size and NPs distribution and EELS spectra (SI.6) were obtained after the use of Ce-Ti@Fe_3O_4 NPs for 5 cycles of adsorption-desorption of fluoride.

Moreover, the possibility of Ce releases from the Ce-Ti@Fe_3O_4 NPs after its use was determined by Inductively Coupled Plasma Mass Spectrometry (ICP-MS) either in the treated water or in the regenerating solution, after each adsorption-desorption cycle. The detailed sample preparation and analysis for ICP-MS analysis is explained in SI.2.2.

2.4.4. pH effect on the adsorption capacity

The effect of the pH value in the media for fluoride adsorption was conducted using 10 mg/L initial fluoride concentration with 1 g/L of Ce-Ti@Fe_3O_4 adsorbent. Then, each conical flask at fixed pH of 5, 7, 9 and 11 was shaken and the adsorption capacity was calculated. All experiments were performed in triplicates.

2.4.5. Effect of temperature on the fluoride adsorption and estimation of the thermodynamic parameters

The effect of the temperature on the fluoride adsorption onto Ce-Ti@Fe_3O_4 adsorbent was studied at 20, 25, 30, 35, and 40 °C using 30 mg/L of fluoride initial concentration at pH 7 with 1 g/L adsorbent dose, 60 min contact time, and 200 rpm shaking. The adsorption capacity was calculated in all the cases. To estimate the effect of temperature on the adsorption of fluoride onto Ce-Ti@Fe_3O_4 NPs, the free energy Gibbs change (ΔG°), enthalpy change (ΔH°), and entropy change (ΔS°) were determined as previously reported (Zhao et al., 2010). In this method, the thermodynamic parameters were obtained directly from the plot of $\log(Q_e/C_e)$ versus 1/T as presented in Eqs. (2) and (3).

$$\ln\left(\frac{Q_e}{C_e}\right) = \left(\frac{\Delta H^\circ}{R}\right) - \left(\frac{\Delta S^\circ}{R}\right)\frac{1}{T} \quad (2)$$

$$\Delta G^\circ = \Delta H^\circ - T\Delta S^\circ \quad (3)$$

where Q_e/C_e is the adsorption affinity; ΔG°, ΔH° and ΔS° are the change in free energy, enthalpy, and entropy respectively. All experiments were performed in triplicates.

2.4.6. Fluoride removal from spiked drinking water by using Ce-Ti@Fe_3O_4 NPs

To determine the effect of the presence of other ions on the removal of fluoride, drinking tap water was spiked only with 10 mg/L of fluoride. Tap water samples were obtained from the Universitat Autònoma de Barcelona (Spain). Drinking tap water first was turned on a steady stream with flow 500 mL/min and run for 10 min to remove any stagnant in the plumbing network. The adsorption experiment was carried out at pH 7.0 in 250 mL flasks containing 0.10 g Ce-Ti@Fe_3O_4 adsorbents per 100 mL of spiked water, at 25 and 30 °C, and shaking at 200 rpm for 60 min.

2.4.7. Statistical data analysis

Statistical analysis was performed using the Tukey's method based on one factor ANOVA at the 5% confidence level using SPSS 15.0.1 (SPSS Inc., USA). Statistically significant differences were reported when the probability of the results, assuming the null hypothesis (p) value is <0.05.

3. Results and discussion

3.1. Characterization of the synthesized nanomaterials

The metal content of the synthesized Ce-Ti oxides NPs was analyzed using ICP-OES. The results showed the presence of 84.99 ± 5.05 mg_{Ti}/g_{NP} (1.8 $mmol_{Ti}/g_{NP}$) and 106.93 ± 3.54 mg_{Ce}/g_{NP} (0.8 $mmol_{Ce}/g_{NP}$) at the synthesis conditions. This means that the synthesized nanomaterial contains the desired metals and that the molar ratio of Ce:Ti was 1:2. Comparing with the previous characterized Ce-Ti@Fe_3O_4 nanomaterial, Ce:Ti:Fe molar ratio was 1:2:1 (Abo Markeb et al., 2016). Thus, the incorporation of Fe into the Ce-Ti oxide NPs did not affect the metals molar ratio in the final Ce-Ti@Fe_3O_4 adsorbent.

Further, morphological characterization of the Ce-Ti oxides was also studied. Fig. 1 illustrates the TEM images coupled with EDS and SAED pattern for Ce—Ti oxide NPs. As shown in Fig. 1A, Ce-Ti oxide NPs size is estimated to be about 1–2 nm, much smaller than the Ce-Ti@Fe_3O_4 NPs (10–15 nm) probably due to the addition of Fe_3O_4 core in the structure that induces an increase of the total NPs size.

The SAED pattern for Ce-Ti oxides NPs (Fig. 1B) exhibit no crystal orientation (as no bright dots or rings are observed) and hence, amorphous structure (Martos et al., 2008). Conversely, the SAED pattern for Ce-Ti@Fe_3O_4 NPs sample (Fig. S1, S2), exhibited a poly-nanocrystalline structure which corresponds to magnetite NPs (Wang et al., 2013).

3.2. Fluoride adsorption on Ce-Ti@Fe_3O_4 adsorbents

The time required to achieve the equilibrium for the fluoride adsorption was determined at 10 and 100 mg/L of fluoride and an adsorbent dose of 1 g/L of Ce-Ti@Fe_3O_4 NPs at pH 7 and 25 °C. The equilibrium time was reached at 0.5 min for 10 mg/L and at 15 min for 100 mg/L of initial fluoride concentration. These results showed a high adsorption rate for the synthesized nanomaterial. Therefore, to assure the completed adsorption of the contaminant, the adsorption time was fixed to be 60 min for the rest of the batch experiments. The fast kinetics of this novel adsorbent could be attributed to a large number of available adsorption sites on the Ce-Ti@Fe_3O_4 adsorbent surface. Moreover, the presence of Ce in the Ce-Ti@Fe_3O_4 NPs enhanced the adsorption time compared with the reported one Fe-Ti@Fe_3O_4 (Zhang et al., 2014) under the same conditions. Further explanation about the improved adsorption mechanism of the Ce-Ti@Fe_3O_4 NPs is following discussed.

3.2.1. Adsorption isotherms and modeling for the adsorption mechanism

Maximum adsorption capacity was estimated from the adsorption isotherm models by performing the experiments over the fluoride initial concentration range until saturation at pH 7. A broad range of initial fluoride concentration (1 to 500 mg/L) was selected to ensure

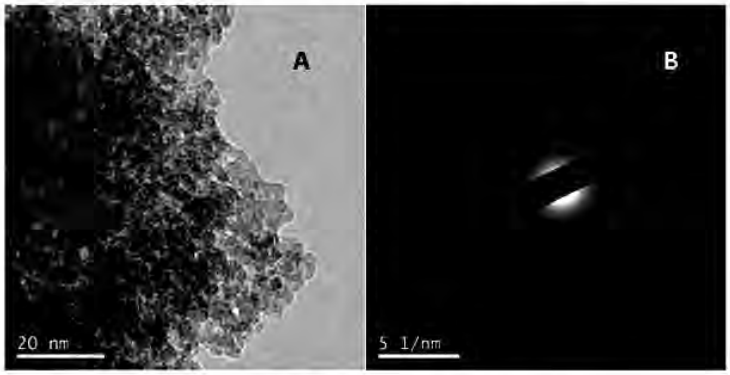

Fig. 1. (A) HRTEM image and, (B) SAED pattern of Ce-Ti oxide NPs.

saturation and allow isotherm fitting. Fig. 2 corresponds to the adsorption isotherms for both, Ce-Ti oxides and Ce-Ti@Fe_3O_4 NPs. It is shown that the adsorption capacities of both nanomaterials increased with increasing fluoride concentrations, and maximum values were achieved at the equilibrium fluoride concentration above 100 mg/L.

Furthermore, data were fitted to both Langmuir and Freundlich models (Table 1). The Langmuir model seems to be more suitable for fluoride adsorption than the Freundlich one as Langmuir model regression coefficient (R^2) was higher than 0.95. However, it is possible to obtain mechanistic information on the adsorption process from both models. The maximum monolayer adsorption capacity (Q_m) obtained for Ce-Ti@Fe_3O_4 NPs was 91.04 mg/g, higher than for Ce-Ti oxide NPs (Q_m = 44.37 mg/g). The Freundlich adsorption intensity parameter (n values) were higher than 2, also supporting the favorable adsorption of fluoride and meaning that the sorption process is mainly physical rather than chemical.

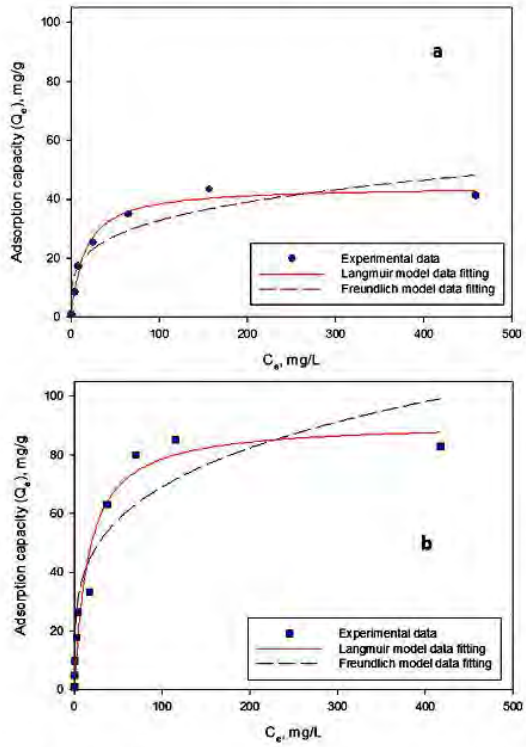

Fig. 2. Adsorption isotherms and experimental data fitting using Langmuir and Freundlich models for fluoride removal using: (a) Ce-Ti oxide, and (b) Ce-Ti@Fe_3O_4 NPs [adsorbent dose 1 g/L, 60 min shaking at 200 rpm at room temperature].

The calculated parameter of the energy, E, of the Dubinin-Radushkevich isotherm (SI.6) is indicated in Table 1. The E values were 0.10 and 0.25 kJ/mol for Ce-Ti@Fe_3O_4 and Ce-Ti oxides adsorbents, respectively, which proved that the interaction between the fluoride and the surface of the nanomaterials is physical (Babaeivelni and Khodadoust, 2013; Dorado et al., 2010). The lower E value for Ce-Ti@Fe_3O_4 means that it needs lower energy for adsorbing F^- than Ce-Ti oxides NPs. It confirms its higher adsorption capacity. Fluoride removal may suffer a surface ion-exchange process as physisorption based on the exchange of the hydroxyl ions (OH^-) from the surface of the adsorbent with F^- (Abo Markeb et al., 2016). The OH^- on the surface of the NPs is present due to the nature of the media (e.g. pH) (Pattanaik and Bhaumik, 2000). According to Zhang et al. (2015), the physical mechanism could be expressed by Eqs. (4) and (5):

$$M^{n+} + nH_2O \rightarrow M(OH)_n \quad (4)$$

$$M(OH)_n + xF^- \rightarrow M(OH)_{n-x}F_x + xOH^- \quad (5)$$

where M, n, and x are the adsorbent's metal ion, the valence of the metal ion and, the number of moles of fluoride, respectively.

Table 1
Langmuir, Freundlich, and Dubinin-Radushkevich isotherms for fluoride adsorption onto Ce-Ti oxides and Ce-Ti@Fe_3O_4 NPs.

Isotherm models		Nanomaterial	
		Ce-Ti@Fe_3O_4	Ce-Ti oxide
Langmuir	Q_m (mg/g)	91.04	44.37
	K_L (L/mg)	0.063	0.064
	R^2	0.952	0.986
Freundlich	K_F ($mg^{1-(1/n)}$ $L^{1/n}g^{-1}$)	21.543	10.214
	n	3.95	3.95
	R^2	0.895	0.877
D-R	Q_m (mg/g)	83.86	37.14
	K_{DR} (mol^2/kj^2)	4.77e-5	8.05e-6
	R^2	0.887	0.895
	E (kJ/mol)	0.102	0.250

Further, it is worth to mention that the crystalline structure of the adsorbents plays an important role in the adsorption capacity. As shown, the crystalline Ce-Ti@Fe_3O_4 material showed higher adsorption capacity than the amorphous Ce-Ti oxide due to the higher developed crystalline faces of the NPs which could increase the ability of the surface to adsorb (Giammar et al., 2006).

Fluoride adsorption capacity using the novel Ce-Ti oxides and Ce-Ti@Fe_3O_4 NPs is highly competitive in comparison with other adsorbents from literature (Table 2). The Q_{max} of the adsorbents in this study is similar to the best ones reported so far. However, those materials present some disadvantages in comparison with the Ce-Ti@Fe_3O_4 adsorbent. For instance, Mn–Ce oxide and the Fe_3O_4@$Al(OH)_3$ adsorbents reached the equilibrium after 3 h and 60 min, respectively (Deng et al., 2011; Zhao et al., 2010). The new developed nanomaterial, Ce-Ti@Fe_3O_4, presents promising properties in terms of adsorption capacity, adsorption rate, as well as magnetic properties and, consequently, Ce-Ti@Fe_3O_4 nanomaterial was used for the rest of the experiments.

3.3. Evaluation of the fluoride recovery and the reusability of the Ce-Ti@Fe_3O_4 NPs

The efficiency of the adsorbent is demonstrated by performing adsorption-desorption cycles of 10 mg/L of F^- for evaluating the reuse and regeneration of the adsorbent. Ce-Ti@Fe_3O_4 was separated from the treated solution by a magnet (Abo Markeb et al., 2016).

In this work, it was shown that the recovery percentage of fluoride was affected by desorption time (ANOVA analysis, $p < 0.05$). As shown in Fig. 3, by using 5 mL of 0.1 M NaOH, it was obtained the highest recovery percentage of 98.51% at 12 h of desorption time (Fig. 3b) which were the chosen desorption conditions for each regeneration step due to low concentration and volume of NaOH. However, the little decrease of the recovery percentage of fluoride at 8 h desorption using 0.5 M NaOH could be attributed to a saturation of the fluoride recovery after 6 h desorption time.

The reusability of the Ce-Ti@Fe_3O_4 adsorbent was carried out by performing five consecutive adsorption-desorption cycles under both optimal experimental conditions were obtained for both processes. Thus, Fig. 4 illustrates the adsorption capacities values of the Ce-Ti@Fe_3O_4 adsorbent and the fluoride recovery versus the cycle's number. It is shown that the fluoride recovery % is high (>90%) for all the cycles tested and also in comparison with other reported works, where the maximum fluoride recovery has been up to 86.35% (Zhang et al., 2015). Also, a very little decrease in the recovery exists from the first to the fifth cycle to be from 98.51 to 92.97% that could be attributed to the change of the morphology of the NPs or because of the metal release from the adsorbent during the regeneration process, as it is following discussed. However, the high removal % in all the cycles was demonstrated.

Table 2
Comparison of adsorption capacity of fluoride on different nanomaterials from this work and the literature. "Maximum adsorption capacity" indicates that the value of adsorption capacity was obtained through an isotherm modeling.

Adsorbents	Adsorption capacity (mg/g)	Sorbent/sorbate ratio	Adsorption conditions	Reference
Fe_3O_4@ZrO_2	158.60	Maximum adsorption capacity	Deionized water, 25 °C, adsorption time 1 h, pH 2.5, adsorbent dose 1 g/L	Riahi et al., 2015
Ce-Ti@Fe_3O_4 powder	91.04	Maximum adsorption capacity	Deionized water, 25 °C, adsorption time 1 h, pH 7.0, adsorbent dose 1.0 g/L	This work
Fe_3O_4@$Al(OH)_3$	88.48	Maximum adsorption capacity	Deionized water, 25 °C, adsorption time 1 h, pH 6.5, adsorbent dose 1 g/L	Zhao et al., 2010
Powder Mn-Ce oxide	79.50	Maximum adsorption capacity	Deionized water, 25 °C, adsorption time 24 h, pH 6.0, adsorbent dose 0.01 g/L	Deng et al., 2011
Ce-Fe bimetal oxides	60.97	Maximum adsorption capacity	Deionized water, 20 °C, adsorption time 1 h, pH 5.5, adsorbent dose 0.5 g/L	Tang and Zhang, 2016
Fe-Ti@Fe_3O_4	57.22	Maximum adsorption capacity	Deionized water, 25 °C, adsorption time 12 h, adsorbent dose 1 g/L	Zhang et al., 2014
Iron-doped titanium oxide	53.22	Maximum adsorption capacity	Deionized water, 25 °C, adsorption time 12 h, pH 5.0, adsorbent dose 0.5 g/L	Chen et al., 2012
Fe-Ti bimetallic oxide	47.00	Maximum adsorption capacity	Deionized water, 25 °C, adsorption time 12 h, pH 5.0, adsorbent dose 0.5 g/L	Chen et al., 2012
Ti-La hybrid	46.60	Maximum adsorption capacity	Deionized water, 25 °C, adsorption time 12 h, pH 6.0, adsorbent dose 0.01 g/L	Li et al., 2010
Granular Mn-Ce oxide	45.50	Maximum adsorption capacity	Deionized water, 25 °C, adsorption time 24 h, pH 6.0, adsorbent dose 0.01 g/L	Deng et al., 2011
Ce-Ti oxide powder	44.37	Maximum adsorption capacity	Deionized water, 25 °C, adsorption time 1 h, pH 7.0, adsorbent dose 1.0 g/L	This work
Fe-Ti/Fe_3O_4	41.80	Maximum adsorption capacity	Deionized water, 25 °C, adsorption time 12 h, pH 7.0, adsorbent dose 1.0 g/L	Zhang et al., 2016
Ti-Ce hybrid	30.60	Maximum adsorption capacity	Deionized water, 25 °C, adsorption time 12 h, pH 6.0, adsorbent dose 0.01 g/L	Li et al., 2010
$TiOH_4$	30.40	Maximum adsorption capacity	Deionized water, 25 °C, adsorption time 12 h, pH 5.0, adsorbent dose 2.0 g/L	Ishihara et al., 2002
CeO_2-TiO_2/SiO_2	21.40	Maximum adsorption capacity	Deionized water, 35 °C, adsorption time 1 h, pH 4.0, adsorbent dose 5.0 g/L	Y. Xiuru et al., 1998
Fe-Al	17.70	Maximum adsorption capacity	Deionized water, 30 °C, adsorption time 12 h, pH 6.8, adsorbent dose 0.1 g/L	Biswas et al., 2007
Fe-Cr	16.34	Maximum adsorption capacity	Deionized water, 25 °C, adsorption time 1.5 h, pH 6.5, adsorbent dose 0.1 g/L	Biswas et al., 2010
Fe-Sn	10.50	Maximum adsorption capacity	Deionized water, 30 °C, adsorption time 2 h, pH 6.4, adsorbent dose 0.1 g/L	Biswas et al., 2009
Fe-Zr	8.20	Maximum adsorption capacity	Deionized water, 30 °C, adsorption time 12 h, pH 6.8, adsorbent dose 0.1 g/L	Biswas et al., 2007
Aluminium modified zeolite tuff	3.24	Maximum adsorption capacity	Deionized water, 30 °C, flow rate 1 mL/min, bed height 4 cm, pH 6.2, adsorbent dose 1 g/L	Teutli-Sequeira et al., 2015
Fe_3O_4	0.30	20.00	Deionized water, 25 °C, adsorption time 12 h, adsorbent dose 1 g/L	Zhang et al., 2014

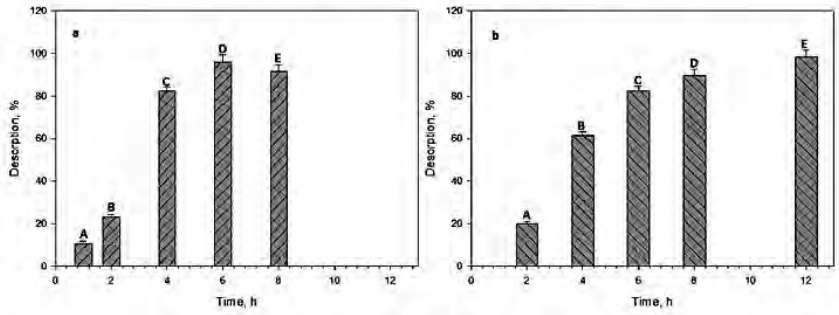

Fig. 3. The effect of the desorption time for the efficient fluoride desorption (%); (a) 25 mL of 0.5 M NaOH and, (b) 5 mL of 0.1 M NaOH, using 1 g/L of Ce-Ti@Fe_3O_4 nanomaterial, and shaking at 200 rpm. Statistical data analysis using ANOVA was illustrated by letters A, B, C, D, and E.

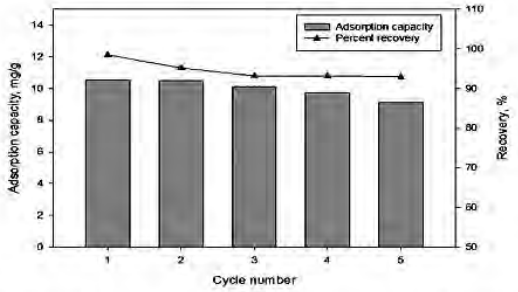

Fig. 4. Fluoride adsorption capacities (mg/g) and fluoride recovery (%) for the use of Ce-Ti@Fe_3O_4 NPs at different adsorption-desorption cycles (up to 5).

3.4. Characterization of the Ce-Ti@Fe_3O_4 NPs as adsorbent after reuse

Fig. 5a illustrates the TEM image of the corresponding Ce-Ti@Fe_3O_4 adsorbent after its use for five cycles of the adsorption-desorption process. It is shown an aggregation of the NPs in comparison with the size of the original NPs, leading to an increase of the size and hence, a decrease on the adsorption capacity. In this sense, Fig. 5b showed the SAED pattern of the adsorbent and it showed a decrease in the crystalline phases in comparison with the original adsorbent (SI.2). As discussed in Section 3.1, the loss of the crystalline structure may affect the adsorption efficiency of the nanomaterial.

Furthermore, the core-shell structure of the original Ce-Ti@Fe_3O_4 nanomaterial is shown in SI.2 and SI.6. Here, the STEM-EELS technique was used to characterize the NPs structure after it is used and a slight modification of the core-shell structure, due to its aggregation, is shown (HAADF image, Fig. 6A). Moreover, the elemental analysis of the three metals was proved using STEM-based EDS (Fig. 6B and C) and thus, the metal composition remains stable in the NPs' structure. Anyway, the nanomaterial still presents magnetic properties and high adsorption activity after its reuse.

The observed modification of the morphology for the nanomaterial may be attributed to the release of metal. As a result, the analysis of the metal content in the Ce-Ti@Fe_3O_4 nanomaterial after the 5 cycles showed a metal concentration of 113.68 ± 1.75 mg_{Ti}/g_{NP}, 173.82 ± 15.73 mg_{Ce}/g_{NP} and 77.41 ± 8.04 mg_{Fe}/g_{NP}. Comparing with the original metal values of the Ce-Ti@Fe_3O_4 NPs, (121.01 ± 7.70 mg Ti/g, 199.29 ± 10.47 mg Ce/g and 81.07 ± 4.49 mg Fe/g), a leakage of Ti, Ce, and Fe of 6.06, 12.78, and 4.51%, respectively, is observed, being the loss of Ce the most important one. Then, ICP-MS was used to analyze the Ce amount in both, the water treated and the desorbing solutions, after each adsorption-desorption cycle. The Ce concentration in the final treated aqueous solution after 5 cycles was not detected (Table 3), indicating that there is no release of Ce in the treated aqueous solution. However, the Ce concentration in the desorbing NaOH solution increases with the number of desorbing cycles, being the maximum value at the 5th cycle and corresponding to a total Ce release of 0.70 mg, which agrees with the estimated Ce lose from the NPs (12.78%). This result may be due to the low stability of the NPs at basic pH (Tso et al., 2010).

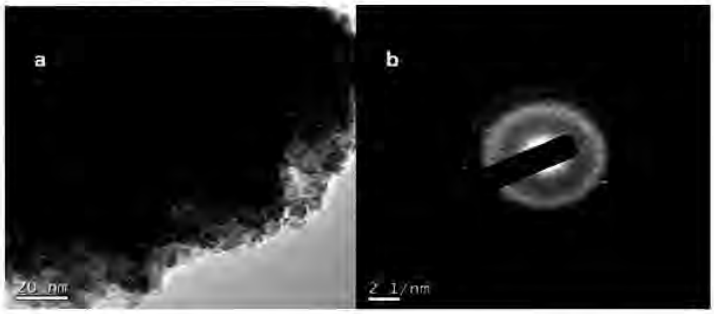

Fig. 5. TEM image (a) and, ED pattern (b) of the Ce-Ti@Fe_3O_4 nanomaterial after five adsorption-desorption cycles under the optimal experimental conditions used for each process.

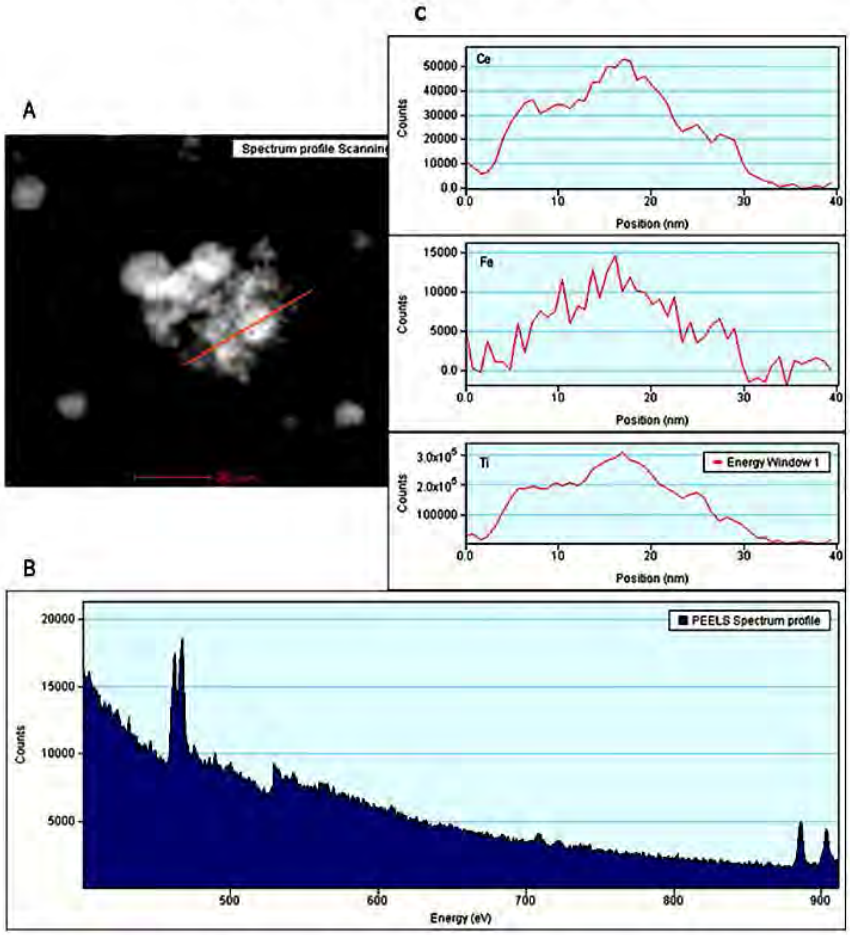

Fig. 6. EELS line scan of the core-shell Ce-Ti@Fe_3O_4 NPs after the 5 cycles of adsorption-desorption. (A) STEM HAADF image of the Ce-Ti@Fe_3O_4 and position of the line scan; (B) PEELS spectrum of the nanomaterial; and (C) Ions profile spectra along the line scanning.

Therefore, we can conclude that the Ce-Ti@Fe_3O_4 nanomaterial is suitable for its use and reuse for at least five cycles of adsorption-desorption of fluoride with high removal and recovery. Also, it was demonstrated its adsorption capacity for five cycles. Although, there is a low metal leakage from the nanomaterial, there is no effect in the treated water or the environment, due to this leakage remains in the desorbing reagent.

Table 3
ICP-MS analysis for Ce-Ti@Fe_3O_4 after 5 adsorption-desorption cycles of fluoride.

Desorption cycles, solution analyzed	Cerium, mg/L
Cycle 1, H_2O	N.D
Cycle 1, NaOH	N.D
Cycle 2, NaOH	N.D
Cycle 3, NaOH	0.36
Cycle 4, NaOH	10.20
Cycle 5, NaOH	20.00
Cycle 5, H_2O	N.D

N.D: not detected.

3.5. Effect of the pH value for the fluoride adsorption

The optimum pH for drinking water is in the range of 6.5–9.5 (Drinking-water, 2004) and it is known that pH can significantly affect the adsorption of fluoride (Habuda-Stanić et al., 2014). Fig. 7 shows the removal percentage and adsorption capacity (Q_e) at pH from 5 to 11 for the Ce-Ti@Fe_3O_4 adsorbent. The fluoride removal percentage and Q_e decrease by increasing the pH when applying 10 mg/L initial fluoride concentration and 1 g/L of Ce-Ti@Fe_3O_4 NPs. Even though, at pH 11, the removal percentage was still >80%. The decrease of the removal percentage could be attributed to the changes in the surface of the NPs, which became more negatively charged. Therefore, a competition for the adsorption sites of more OH^- ions with fluoride ions occurs in the aqueous solution as well as modifications of the nanomaterial in this pH range (Raichur and Jyoti, 2001). At 10 mg/L F^- initial concentration, the highest fluoride removal percentage and Q_e values were at pH 5 and 7 to be 99.85, 98.33% and 10.31, 10.32 mg/g, respectively.

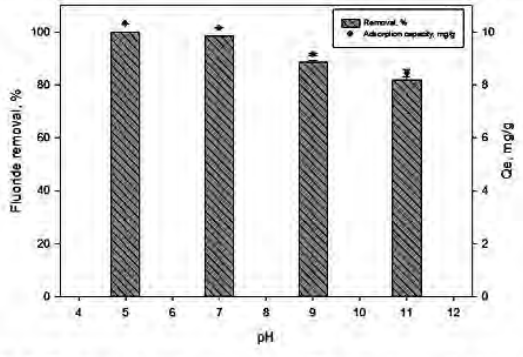

Fig. 7. Effect of pH on fluoride removal percentage (%) and adsorption capacity (Qe) for initial fluoride concentration of 10 mg/L, 1 g/L of Ce-Ti-Fe oxides NP at 200 rpm and room temperature.

3.6. Temperature effect and thermodynamic parameters

The temperature affects the adsorption of the pollutants and provides information about the spontaneity of the fluoride removal process (Deniz, 2013). The adsorption capacity values using Ce-Ti@Fe_3O_4 NPs and fluoride removal percentage are illustrated in Fig. 8 versus temperature in the range of 20–40 °C. The highest adsorption capacity is reached at 30 °C. Next, the values showed a stable removal percentage until 40 °C that indicates that the optimum temperature for fluoride adsorption is at 30 °C when using 30 mg/L initial fluoride concentration.

Table 4 shows the thermodynamic parameters for the fluoride removal at different temperatures. The positive value of the enthalpy, ΔH°, verifies the endothermic nature of the process. The positive entropy, ΔS°, values confirmed the increased randomness at the solid–solute interface during adsorption, but its low value indicated that no remarkable change in entropy occurs. Moreover, the negative free Gibbs energy, ΔG°, values attributed to the adsorption processes, were spontaneous in all cases. The spontaneity adsorption process of fluoride was enhanced by increasing the temperature. The statistical analysis also showed that the temperature has a significant effect on the removal percentage of fluoride when applying the one-way ANOVA (p-value was <0.05) as illustrated in Fig. 8.

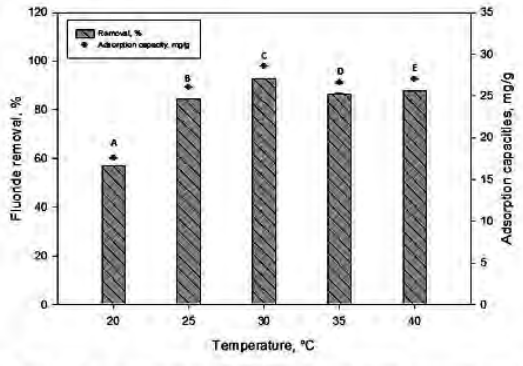

Fig. 8. Effect of temperature on fluoride removal percentage (%) and adsorption capacity (Q_e) using; 30 mg/L initial fluoride concentration, 1 g/L of Ce-Ti-Fe oxide nanomaterials and shaking at 200 rpm for 60 min. Statistical data analysis using ANOVA was illustrated by letters A, B, C, D, and E.

Table 4
Thermodynamic parameters for fluoride adsorption using Ce-Ti@Fe_3O_4 nanomaterial.

Temperature (°C)	$-\Delta G$ (kJ/mol)	ΔH° (kJ/mol)	ΔS° (J mol^{-1} K^{-1})	R^2
20	13.84 ± 0.02	2.52	55.79	0.996
25	14.12 ± 0.02			
30	14.40 ± 0.01			
35	14.67 ± 0.04			
40	14.95 ± 0.02			

3.7. Application of Ce-Ti@Fe_3O_4 nano-adsorbent for fluoride removal from real water sample

The efficiency of the magnetic Ce-Ti@Fe_3O_4 NPs for fluoride removal from drinking water sample spiked with 10 mg/L of fluoride was studied. The results (Table 5) proved that the Ce-Ti@Fe_3O_4 adsorbent had a strong affinity for fluoride removal in the presence of other anions. The removal percentage of fluoride decreased from about 99 to 73% (0.11 to 2.94 mg/L) at ambient temperature due to the presence of other co-existing anions. In addition, the adsorbent posed affinity towards other anions, under the tested conditions, with removal percentage of 15, 36, 11, and 99% for chloride (Cl^-), nitrite (NO_2^-), sulphate (SO_4^{2-}), and nitrate (NO_3^-) respectively. This could be attributed to some anions competition and others enhanced columbic repulsion forces with fluoride for the active sites (Onyango et al., 2004). Moreover, increasing the temperature from 25 to 30 °C increased the removal percentage of fluoride from 73 to 87% (2.94 to 1.44 mg/L) being the residual concentration of fluoride 1.44 mg/L, which is below the maximum acceptable level, 1.50 mg/L. Furthermore, the removal percentage increased to be 18 and 100% for the chloride and nitrate anions, respectively while it decreased to be 35 and 10% for the nitrite and sulphate anions, respectively. Subsequently, the novel magnetic Ce-Ti@Fe_3O_4 nanomaterial is a promising and efficient material for anions removal from water not only fluoride, but also for nitrate, nitrite, chloride, and sulphate.

4. Conclusions

The synthesized magnetic core-shell Ce-Ti@Fe_3O_4 NPs showed high efficiency for fluoride removal and high sorption capacity. The maximum adsorption capacity was 91.04 mg/g at pH 7, which outperformed many reported adsorbents and the synthesized Ce-Ti oxides NPs (44.37 mg/L). Ce-Ti@Fe_3O_4 nanomaterial as adsorbent is applicable over a wide pH range (from 5 to 11) and shows a fast adsorption rate. Moreover, it is easy to recover from the reaction mixture for further reuse and it has been used for 5 cycles. The reusability of the NPs under those conditions was evaluated, showing a little modification in its structure after the cycles and no Ce release is presented in the treated water. In addition to the spontaneous adsorption process, it was shown an increasing of the adsorption capacities by increasing the

Table 5
Efficiency of the Ce-Ti@Fe_3O_4 adsorbents on the fluoride removal from drinking water.

Anions	Anions concentration, mg/L		
	Spiked tap water	After adsorption[a]	After adsorption[b]
Fluoride	10.93 ± 0.13 (<0.010[c])	2.94 ± 0.23	1.44 ± 0.04
Chloride	32.71 ± 0.05	27.86 ± 0.02	26.78 ± 0.04
Nitrite as NO_2^-	1.51 ± 0.01	0.97 ± 0.02	0.98 ± 0.03
Sulphate	16.14 ± 0.02	14.33 ± 0.10	14.47 ± 0.04
Nitrate as NO_3^-	3.16 ± 0.01	0.01 ± 0.00	N.D[d]

[a] Adsorption at 25 °C, 1.0 g/L Ce-Ti-Fe oxide, 60 min adsorption time, and 200 rpm.
[b] Adsorption at 30 °C, 1.0 g/L Ce-Ti-Fe oxide, 60 min adsorption time, and 200 rpm.
[c] Fluoride concentration in drinking water before spiking.
[d] N.D: not detected.

temperature. Furthermore, the physical sorption mechanism was estimated according to the Dubinin-Radushkevich isotherm model: anion exchange between the hydroxyl group on the surface of the adsorbents and fluoride ions was involved. Besides, the efficacy of the Ce-Ti@Fe_3O_4 NPs as adsorbent was demonstrated for a real water matrix by spiking 10 mg/L of fluoride in drinking water, as it showed a residual fluoride concentration of 1.44 mg/L. Therefore, magnetic Ce-Ti@Fe_3O_4 nanomaterial was arbitrated to be a suitable adsorbent to treat fluoride contaminated water to achieve the quality standard of drinking water.

Acknowledgement

The author, Ahmad Abo Markeb, appreciated and would like to thank the Ministry of Higher Education (CAM-751-FM-06-01) of Egypt for the Ph.D. external mission grant.

Appendix A. Supplementary data

Supplementary data to this article can be found online at http://dx.doi.org/10.1016/j.scitotenv.2017.04.191.

References

Abo Markeb, A., Ordosgoitia, L., Alonso, A., Sanchez, A., Font, X., 2016. Novel magnetic core-shell Ce-Ti@Fe_3O_4 nanoparticles as adsorbent for water contaminants removal. RSC Adv.

Amor, Z., Bariou, B., Mameri, N., Taky, M., Nicolas, S., Elmidaoui, A., 2001. Fluoride removal from brackish water by electrodialysis. Desalination 133, 215–223.

Babaeivelni, K., Khodadoust, A.P., 2013. Adsorption of fluoride onto crystalline titanium dioxide: effect of pH, ionic strength, and co-existing ions. J. Colloid Interf. Sci. 394, 419–427.

Bhatnagar, A., Kumar, E., Sillanpää, M., 2011. Fluoride removal from water by adsorption—a review. Chem. Eng. J. 171, 811–840.

Biswas, K., Bandhoyapadhyay, D., Ghosh, U.C., 2007. Adsorption kinetics of fluoride on iron(III)–zirconium(IV) hybrid oxide. Adsorption 13, 83–94.

Biswas, K., Gupta, K., Ghosh, U.C., 2009. Adsorption of fluoride by hydrous iron(III)–tin(IV) bimetal mixed oxide from the aqueous solutions. Chem. Eng. J. 149, 196–206.

Biswas, K., Debnath, S., Ghosh, U.C., 2010. Physicochemical aspects on fluoride adsorption for removal from water by synthetic hydrous iron(III)–chromium(III) mixed oxide. Sep. Sci. Technol. 45, 472–485.

Chai, L., Wang, Y., Zhao, N., Yang, W., You, X., 2013. Sulfate-doped Fe_3O_4/Al_2O_3 nanoparticles as a novel adsorbent for fluoride removal from drinking water. Water Res. 47, 4040–4049.

Chang, M.F., Liu, J.C., 2007. Precipitation removal of fluoride from semiconductor wastewater. J. Environ. Eng. 133, 419–425.

Chen, L., Wang, T.-J., Wu, H.-X., Jin, Y., Zhang, Y., Dou, X.-M., 2011. Optimization of a Fe–Al–Ce nano-adsorbent granulation process that used spray coating in a fluidized bed for fluoride removal from drinking water. Powder Technol. 206, 291–296.

Chen, L., He, B.-Y., He, S., Wang, T.-J., Su, C.-L., Jin, Y., 2012. Fe–Ti oxide nano-adsorbent synthesized by co-precipitation for fluoride removal from drinking water and its adsorption mechanism. Powder Technol. 227, 3–8.

Dai, S., Ren, D., Ma, S., 2004. The cause of endemic fluorosis in western Guizhou Province, Southwest China. Fuel 83, 2095–2098.

Deng, S., Liu, H., Zhou, W., Huang, J., Yu, G., 2011. Mn–Ce oxide as a high-capacity adsorbent for fluoride removal from water. J. Hazard. Mater. 186, 1360–1366.

Deniz, F., 2013. Adsorption properties of low-cost biomaterial derived from *Prunus amygdalus* L. for dye removal from water. Scientific World J. 2013, 961671.

Dorado, A.D., Lafuente, J., Gabriel, D., Gamisans, X., 2010. The role of water in the performance of biofilters: parameterization of pressure drop and sorption capacities for common packing materials. J. Hazard. Mater. 180, 693–702.

Drinking-water pi, 2004. Background Document for Development of WHO Guidelines for Drinking-water Quality. WHO.

Gandhi, N., Sirisha, D., Asthana, S., Manjusha, A., 2012. Adsorption studies of fluoride on multani matti and red soil. Res. J. Chem. Sci. 2, 32–37.

Giammar, D.E., Maus, C.J., Xie, L., 2006. Effects of particle size and crystalline phase on lead adsorption to titanium dioxide nanoparticles. Environ. Eng. Sci. 24, 85–95.

Gupta, P., Kumar, A., 2012. Fluoride levels of bottled and tap water sources in Agra City, India. Fluoride 45, 307–310.

Habuda-Stanić, M., Ravančić, M., Flanagan, A., 2014. A review on adsorption of fluoride from aqueous solution. Materials 7, 6317.

Ishihara, T., Shuto, Y., Ueshima, S., Ngee, H.L., Nishiguchi, H., Takita, Y., 2002. Titanium hydroxide as a new inorganic fluoride ion exchanger. J. Ceram. Soc. Jpn. 110, 801–803.

Karthikeyan, M., Kumar, K.K.S., Elango, K.P., 2011. Batch sorption studies on the removal of fluoride ions from water using eco-friendly conducting polymer/bio-polymer composites. Desalination 267, 49–56.

Kumar, E., Bhatnagar, A., Kumar, U., Sillanpää, M., 2011. Defluoridation from aqueous solutions by nano-alumina: characterization and sorption studies. J. Hazard. Mater. 186, 1042–1049.

Lee, G., Chen, C., Yang, S.-T., Ahn, W.-S., 2010. Enhanced adsorptive removal of fluoride using mesoporous alumina. Micropor. Mesopor. Mater. 127, 152–156.

Li, Z., Deng, S., Zhang, X., Zhou, W., Huang, J., Yu, G., 2010. Removal of fluoride from water using titanium-based adsorbents. Front. Environ. Sci. Eng. China 4, 414–420.

Liu, H., Deng, S., Li, Z., Yu, G., Huang, J., 2010. Preparation of Al–Ce hybrid adsorbent and its application for defluoridation of drinking water. J. Hazard. Mater. 179, 424–430.

Liu, R., Gong, W., Lan, H., Gao, Y., Liu, H., Qu, J., 2011. Defluoridation by freshly prepared aluminum hydroxides. Chem. Eng. J. 175, 144–149.

Mahramanlioglu, M., Kizilcikli, I., Bicer, I.O., 2002. Adsorption of fluoride from aqueous solution by acid treated spent bleaching earth. J. Fluor. Chem. 115, 41–47.

Martínez-Acuña, M.I., Mercado-Reyes, M., Alegría-Torres, J.A., Mejía-Saavedra, J.J., 2016. Preliminary human health risk assessment of arsenic and fluoride in tap water from Zacatecas, México. Environ. Monit. Assess. 188, 476.

Martos, M., Julián-López, B., Folgado, J.V., Cordoncillo, E., Escribano, P., 2008. Sol–gel synthesis of tunable cerium titanate materials. Eur. J. Inorg. Chem. 2008, 3163–3171.

Meenakshi, Maheshwari, R.C., 2006. Fluoride in drinking water and its removal. J. Hazard. Mater. 137, 456–463.

Meenakshi, S., Viswanathan, N., 2007. Identification of selective ion-exchange resin for fluoride sorption. J. Colloid Interf. Sci. 308, 438–450.

Minju, N., Venkat Swaroop, K., Haribabu, K., Sivasubramanian, V., Senthil, Kumar P., 2013. Removal of fluoride from aqueous media by magnesium oxide-coated nanoparticles. Desalin. Water Treat. 53, 2905–2914.

Mohan, D., Kumar, S., Srivastava, A., 2014. Fluoride removal from ground water using magnetic and nonmagnetic corn stover biochars. Ecol. Eng. 73, 798–808.

Mohapatra, M., Anand, S., Mishra, B.K., Giles, D.E., Singh, P., 2009. Review of fluoride removal from drinking water. J. Environ. Manag. 91, 67–77.

Onyango, M.S., Kojima, Y., Aoyi, O., Bernardo, E.C., Matsuda, H., 2004. Adsorption equilibrium modeling and solution chemistry dependence of fluoride removal from water by trivalent-cation-exchanged zeolite F-9. J. Colloid Interf. Sci. 279, 341–350.

Pattanaik, M., Bhaumik, S.K., 2000. Adsorption behaviour of polyvinyl pyrrolidone on oxide surfaces. Mater. Lett. 44, 352–360.

Qu, X., Alvarez, P.J.J., Li, Q., 2013. Applications of nanotechnology in water and wastewater treatment. Water Res. 47, 3931–3946.

Rafique, A., Awan, M.A., Wasti, A., Qazi, I.A., Arshad, M., 2013. Removal of fluoride from drinking water using modified immobilized activated alumina. J. Chem. 2013, 7.

Raichur, A.M., Jyoti, Basu M., 2001. Adsorption of fluoride onto mixed rare earth oxides. Sep. Purif. Technol. 24, 121–127.

Riahi, F., Bagherzadeh, M., Hadizadeh, Z., 2015. Modification of Fe_3O_4 superparamagnetic nanoparticles with zirconium oxide; preparation, characterization and its application toward fluoride removal. RSC Adv. 5, 72058–72068.

Sehn, P., 2008. Fluoride removal with extra low energy reverse osmosis membranes: three years of large scale field experience in Finland. Desalination 223, 73–84.

Shen, F., Chen, X., Gao, P., Chen, G., 2003. Electrochemical removal of fluoride ions from industrial wastewater. Chem. Eng. Sci. 58, 987–993.

Shiklomanov, I.A., 2000. Appraisal and assessment of world water resources. Water Int. 25, 11–32.

Singh, K., Lataye, D.H., Wasewar, K.L., Yoo, C.K., 2013. Removal of fluoride from aqueous solution: status and techniques. Desalin. Water Treat. 51, 3233–3247.

Sinha, S., Pandey, K., Mohan, D., Singh, K.P., 2003. Removal of fluoride from aqueous solutions by *Eichhornia crassipes* biomass and its carbonized form. Ind. Eng. Chem. Res. 42, 6911–6918.

Sivasankar, V., Ramachandramoorthy, T., Darchen, A., 2011. Manganese dioxide improves the efficiency of earthenware in fluoride removal from drinking water. Desalination 272, 179–186.

Solangi, I.B., Memon, S., Bhanger, M.I., 2009. Removal of fluoride from aqueous environment by modified amberlite resin. J. Hazard. Mater. 171, 815–819.

Sujana, M.G., Anand, S., 2010. Iron and aluminium based mixed hydroxides: a novel sorbent for fluoride removal from aqueous solutions. Appl. Surf. Sci. 256, 6956–6962.

Tang, D., Zhang, G., 2016. Efficient removal of fluoride by hierarchical Ce–Fe bimetal oxides adsorbent: thermodynamics, kinetics and mechanism. Chem. Eng. J. 283, 721–729.

Taylor, N.S., Merrifield, R., Williams, T.D., Chipman, J.K., Lead, J.R., Viant, M.R., 2016. Molecular toxicity of cerium oxide nanoparticles to the freshwater alga *Chlamydomonas reinhardtii* is associated with supra-environmental exposure concentrations. Nanotoxicology 10, 32–41.

Teng, S.-X., Wang, S.-G., Gong, W.-X., Liu, X.-W., Gao, B.-Y., 2009. Removal of fluoride by hydrous manganese oxide-coated alumina: performance and mechanism. J. Hazard. Mater. 168, 1004–1011.

Teutli-Sequeira, A., Solache-Ríos, M., Martínez-Miranda, V., Linares-Hernández, I., 2015. Behavior of fluoride removal by aluminum modified zeolitic tuff and hematite in column systems and the thermodynamic parameters of the process. Water Air Soil Pollut. 226, 1–15.

Tomar, V., Prasad, S., Kumar, D., 2013. Adsorptive removal of fluoride from water samples using Zr–Mn composite material. Microchem. J. 111, 116–124.

Tso, C.P., Zhung, C.M., Shih, Y.H., Tseng, Y.M., Wu, S.C., Doong, R.A., 2010. Stability of metal oxide nanoparticles in aqueous solutions. Water Sci. Technol. 61, 127–133.

Velizarov, S., Crespo, J.G., Reis, M.A., 2004. Removal of inorganic anions from drinking water supplies by membrane bio/processes. Rev. Environ. Sci. Biotechnol. 3, 361–380.

Vinati, A., Mahanty, B., Behera, S.K., 2015. Clay and clay minerals for fluoride removal from water: a state-of-the-art review. Appl. Clay Sci. 114, 340–348.

Viswanathan, G., Jaswanth, A., Gopalakrishnan, S., Siva ilango, S., 2009. Mapping of fluoride endemic areas and assessment of fluoride exposure. Sci. Total Environ. 407, 1579–1587.

Wang, B., Wei, Q., Qu, S., 2013. Synthesis and characterization of uniform and crystalline magnetite nanoparticles via oxidation-precipitation and modified co-precipitation methods. Int. J. Electrochem. Sci. 8, 3786–3793.

WHO, 2006. Chemical fact sheets: fluoride. Guidelines for Drinking-water Quality (Electronic Resource): Incorporation First Addendum, 1 third ed., pp. 375–377 Geneva.
Xiuru, Y., Kuanxiu, S., Jianping, W., Zhaohui, Y., 1998. Preparation of CeO_2–TiO_2/SiO_2 and its removal properties for fluoride ion. J. Rare Earths 16, 279–280.
Zhang, Y., Yang, M., Dou, X.M., He, H., Wang, D.S., 2005. Arsenate adsorption on an Fe–Ce bimetal oxide adsorbent: role of surface properties. Environ. Sci. Technol. 39, 7246–7253.
Zhang, C., Chen, L., Wang, T.-J., Su, C.-L., Jin, Y., 2014. Synthesis and properties of a magnetic core–shell composite nano-adsorbent for fluoride removal from drinking water. Appl. Surf. Sci. 317, 552–559.
Zhang, K., Wu, S., Wang, X., He, J., Sun, B., Jia, Y., et al., 2015. Wide pH range for fluoride removal from water by MHS-MgO/$MgCO_3$ adsorbent: kinetic, thermodynamic and mechanism studies. J. Colloid Interf. Sci. 446, 194–202.
Zhang, C., Li, Y., Wang, T.-J., Jiang, Y., Wang, H., 2016. Adsorption of drinking water fluoride on a micron-sized magnetic Fe_3O_4@Fe–Ti composite adsorbent. Appl. Surf. Sci. 363, 507–515.
Zhao, X., Wang, J., Wu, F., Wang, T., Cai, Y., Shi, Y., et al., 2010. Removal of fluoride from aqueous media by Fe_3O_4@$Al(OH)_3$ magnetic nanoparticles. J. Hazard. Mater. 173, 102–109.

A-3

Environmental Technology

ISSN: 0959-3330 (Print) 1479-487X (Online) Journal homepage: http://www.tandfonline.com/loi/tent20

Phosphate removal and recovery from water using nanocomposite of immobilized magnetite nanoparticles on cationic polymer

Ahmad Abo Markeb, Amanda Alonso, Antonio David Dorado, Antoni Sánchez & Xavier Font

To cite this article: Ahmad Abo Markeb, Amanda Alonso, Antonio David Dorado, Antoni Sánchez & Xavier Font (2016) Phosphate removal and recovery from water using nanocomposite of immobilized magnetite nanoparticles on cationic polymer, Environmental Technology, 37:16, 2099-2112, DOI: 10.1080/09593330.2016.1141999

To link to this article: http://dx.doi.org/10.1080/09593330.2016.1141999

Accepted author version posted online: 05 Feb 2016.
Published online: 19 Feb 2016.

ENVIRONMENTAL TECHNOLOGY, 2016
VOL. 37, NO. 16, 2099–2112
http://dx.doi.org/10.1080/09593330.2016.1141999

Taylor & Francis
Taylor & Francis Group

Phosphate removal and recovery from water using nanocomposite of immobilized magnetite nanoparticles on cationic polymer

Ahmad Abo Markeb[a], Amanda Alonso[a], Antonio David Dorado[b], Antoni Sánchez[a] and Xavier Font[a]

[a]Department of Chemical, Biological and Environmental Engineering, Escola d'Enginyeria, Universitat Autònoma de Barcelona, Bellaterra, Spain; [b]Department of Mining Engineering and Natural Resources, Universitat Politècnica de Catalunya, Barcelona, Spain

ABSTRACT

A novel nanocomposite (NC) based on magnetite nanoparticles (Fe_3O_4-NPs) immobilized on the surface of a cationic exchange polymer, C100, using a modification of the co-precipitation method was developed to obtain magnetic NCs for phosphate removal and recovery from water. High-resolution transmission electron microscopy-energy-dispersive spectroscopy, scanning electron microscopy , X-ray diffraction, and inductively coupled plasma optical emission spectrometry were used to characterize the NCs. Continuous adsorption process by the so-called breakthrough curves was used to determine the adsorption capacity of the Fe_3O_4-based NC. The adsorption capacity conditions were studied under different conditions (pH, phosphate concentration, and concentration of nanoparticles). The optimum concentration of iron in the NC for phosphate removal was 23.59 mg_{Fe}/g_{NC}. The sorption isotherms of this material were performed at pH 5 and 7. Taking into account the real application of this novel material in real water, the experiments were performed at pH 7, achieving an adsorption capacity higher than 4.9 mg_{PO4-P}/g_{NC}. Moreover, Freundlich, Langmuir, and a combination of them fit the experimental data and were used for interpreting the influence of pH on the sorption and the adsorption mechanism for this novel material. Furthermore, regeneration and reusability of the NC were tested, obtaining 97.5% recovery of phosphate for the first cycle, and at least seven cycles of adsorption–desorption were carried out with more than 40% of recovery. Thus, this work described a novel magnetic nanoadsorbent with properties for phosphate recovery in wastewater.

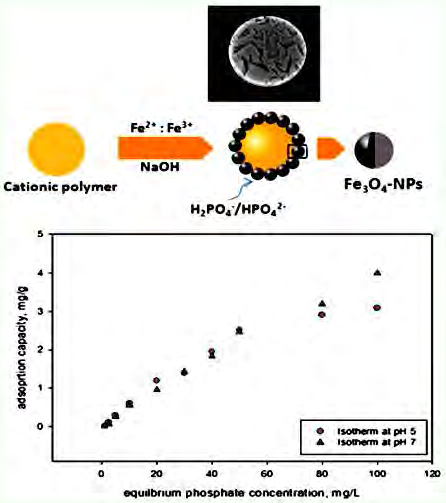

ARTICLE HISTORY
Received 14 October 2015
Accepted 8 January 2016

KEYWORDS
Magnetite nanoparticles; polymeric nanocomposite; adsorption; phosphate removal; wastewater

CONTACT Amanda Alonso amanda.alonso@uab.cat

Highlights

- Immobilization of magnetite nanoparticles on cationic polymer was carried out.
- Phosphate removal using magnetite-based nanocomposites was tested.
- Adsorption isotherms of phosphate at two pH, 5 and 7, were performed.
- Different isotherm models were applied for experimental data fitting.
- Regeneration and reusability of the magnetite-based nanocomposites were carried out.

1. Introduction

Contamination of water is a widespread problem throughout the world as a result of pollution. Hence, a wide range of pollutants, from organic pollutants such as pesticides,[1] to metals such as hexavalent chromium [2,3] and cadmium, [4] in the aqueous environment can be considered for remediation. Also, one of the most important pollutants in water is the excess of nutrients (nitrogen and phosphorus) that threatens human health and the environment. In particular, high amount of phosphorus promotes algal growth in water, since it is usually regulated by microorganisms, which in turn decreases oxygen concentration and leads to eutrophication (extraordinary growth of algae as a result of excess nutrients in water bodies) in rivers, lakes, and seas worldwide.[5,6] As phosphorus is a non-renewable element and a huge amount of phosphorus is lost annually for lack of phosphorus recovery, its recycling is of great interest especially with increasing demands, such as in the agriculture [7] as a fertilizer [8,9] or in industrial usages as ingredients for human food, pharmaceuticals, detergents, and food additive in animal feed.[10,11] Therefore, phosphorus is a critical element in water, and is found frequently in groundwater and domestic and industrial wastewaters.

The common forms of phosphorus found in wastewater include phosphates (H_2PO_4, HPO_4^{2-}, and PO_4^{3-}), polyphosphates, and organic phosphates.[12] Phosphorus concentrations in water matrices can be very different. For instance, municipal wastewater may contain 4–15 mg/L phosphorus as PO_4^{3-}, domestic wastewater contains about 10–30 mg/L of PO_4^{3-}, and treated sewage contains lower concentration, 1–5 mg/L of PO_4^{3-}. However, industrial wastewater (such as detergent manufacturing and metal coating processes) may contain phosphate levels of more than 10 mg/L.[13] Due to the potential interest in phosphate removal from water, various techniques have been employed, including constructed wetlands,[14] physicochemical treatment methods based on the precipitation of slightly soluble phosphorous,[15] and biological nutrient removal (BNR) methods.[9,16–22] The sludge used in BNR methods had disadvantages, especially with a high phosphorous content due to the risk of phosphate release and flowing back into the water treatment system if aeration is not sufficient.[23] Thus, precipitation and activated-sludge process were studied for removing high concentrations (hundreds to thousands of mg/L) [24] of phosphate in wastewaters. However, in the case of low concentration (several mg/L) of phosphates, precipitation or activated-sludge method is not much effective.[25] For instance, precipitation and crystallization methodologies present some disadvantages such as the requirement of a pH higher than 9, which leads to competitive interaction, difficulty to regeneration and reuse, and thus, high cost. Other purification processes performed on polluted water bodies, such as high recovery reverse osmosis,[9,26] suffer problems associated with phosphate ions and in combination with calcium ions as precipitating agents for phosphate salts, which lead to membrane blockage limiting water recovery.[27]

Many challenges of the previously described water treatments were faced by using nanotechnology, which is also a cost-effective treatment.[28] Nanomaterials have a number of key physicochemical properties that make them particularly attractive for water purification such as separation media or reusability. On a mass basis, they have much large surface areas than bulk particles. Nanomaterials can also be functionalized with various chemical groups to increase their affinity towards a given compound. They can also serve as high capacity/selectivity and recyclable ligands for toxic metal ions, radionuclides, and organic and inorganic solutes.[29] Therefore, water treatment based on the adsorption of contaminants using nanomaterials, such as cerium oxide- or iron oxide-based nanoparticles (NPs), is a relatively useful and cost-effective method for removing water contaminants [30–43] and also for phosphate removal.[30–36,38–41,43] Adsorption is generally used to remove organic [44] and inorganic contaminants such as heavy metals [45] during water and wastewater treatment. Nanoadsorbents offer significant improvement with their extremely high specific surface area and associated sorption sites, short intra-particle diffusion distance, and tuneable pore size and surface chemistry. In general, adsorption technology has been a well-established technology for phosphate removal and recovery from water and wastewater, though more selective and cost-effective sorbents have to be

developed. Compared with chemical precipitation, adsorption does not produce large volumes of chemical sludge. Various types of phosphorus adsorbents made from zeolites,[46] lanthanum and yttrium compounds, [47,48] aluminium compounds,[49–53] zero-valent iron, [54] amine-functionalized NPs, $Pr(OH)_3$,[55] magnesium amorphous calcium carbonate,[56] zirconium compounds,[57,58] and iron(III) oxide compounds [12,30,31,38,40,51,59,60,61] were studied.

In addition to all these nanoadsorbents, studies also focused on iron-based adsorbents with magnetic properties due to their low cost [62] and their magnetic separation methodology which offers great advantages, such as high speed, simplicity, accuracy, and effectiveness to operate as compared to the conventional separation methods.[63] Thus, magnetic NPs have a high potential to be applied in adsorption systems because they can be easily separated in a magnetic field. However, there are just a few studies on phosphate removal from water by using magnetite (Fe_3O_4) NPs.[64,65]

On the other hand, the modification of polymers with surface functional groups, such as acrylamide[66] and N-vinylpyrrolidone,[67] and also the modification of surfaces with magnetic properties have been reported. In this sense, polymeric ligand exchangers exhibit high phosphate selectivity over competing sulphate and chloride ions [16,19] and efficient regeneration and reuse. However, they are relatively expensive, which is the most important parameter for industrial applications. In this regard, modifications of polymers or other supports with NPs have been used recently [68,69] to enhance the adsorption capacity of materials. For instance, hydrated ferric oxide (HFO) was doped in various support materials such as zeolites, alginates, activated carbon, and cation exchange resins [70–73] as well as in polymeric anionic exchanger.[74,75] Anionic resins impregnated with HFO were studied for phosphorus removal.[76–79] In general, polymeric anion exchange resins have low phosphate exchange capacity and poor selectivity factors against common ions present in wastewater (such as chloride, sulphate, bicarbonate, nitrate, and dissolved organic matter).[19] In this sense, other polymeric materials, such as the cation exchange resin, from Purolite (C100), form a simple, fast, and economic polymeric matrix for the removal of metals such as Ce^{4+}, Fe^{3+}, and Pb^{2+} from aqueous systems.[80] Furthermore, taking into account some works reported about the use of iron-based nanoadsorbents for phosphorus removal in waters, it has been shown that the adsorption capacities at room temperature were 0.3 mg/g for α-Fe_2O_3,[12] 0.9 mg/g for goethite + maghemite (FeO(OH) + γ-Fe_2O_3),[81] 1.1 mg/g for Hematite (Fe_2O_3),[82] and 2.6 mg/g for hydrothermally synthesized Fe_3O_4.[64] However, higher adsorption capacities are required and no studies have been conducted on the removal of phosphate based on cationic polymers so far. Thus, iron-based nanoadsorbents based on polymeric supports could be a promoting solution.

Therefore, this work aims to develop and use an optimal nanoadsorbent based on Fe_3O_4-NPs immobilized on the polymeric cationic resin, C100, for phosphate removal by adsorption and its recovery from water in a continuous fixed-bed column. More precisely, the main objectives of this study are to carry out (1) the optimization of the nanocomposite (NC) based on the immobilization of different Fe_3O_4–NP concentrations on the surface of the C100 material to obtain the highest adsorption capacity for phosphate and (2) the adsorption–desorption optimization process to regenerate the adsorbent for the reusability of the NC and for phosphate recovery during several cycles of usage.

2. Material and methods

2.1. Materials

Iron (II) chloride; $FeCl_2$, Iron (III) chloride hexahydrate; $FeCl_3{\cdot}6H_2O$, sodium phosphate monobasic; NaH_2PO_4, citric acid, and ammonium hydroxide, NH_4OH, were purchased from Sigma-Aldrich, Spain. Sodium hydroxide pellets, NaOH, were purchased from Merck. Hydrochloric acid, HCl, was purchased from Panreac, SA. All the chemicals were of analytical grade or higher, and all solutions were prepared with Milli-Q water and filtered using 0.45 µm Nylon membrane filter.

The cationic exchange polymer (C100) consists of polystyrene cross-linked with divenyl benzene functionalized with gel type sulphonated group and was kindly supplied by Purolite S.A, Spain. The ion-exchange capacity of the polymer was 2.0 mequiv/g.

2.2. Synthesis of the NC based on magnetite NPs

Pre-treatment of the C100 was carried out by following the procedure already described elsewhere.[83,84] First, the raw material was treated with 1.0 M NaCl for 2 h and washed with deionized water (three times) so as to convert all the functional groups into Na^+ form. Afterwards, the resins were dried at 80°C for 24 h.

Immobilization of the Fe_3O_4–NPs on the polymeric matrix, C100, was carried out using a variation of the Intermatrix Synthesis (IMS) protocol coupled to a co-precipitation method already reported.[83]

The experimental procedure for the preparation of iron oxide-based ferrites involves the precipitation of Fe^{2+} and Fe^{3+} salts in a strict ratio of 1:2 in deoxygenated

water by the addition of a strong basic solution, in this work NaOH, at 40°C under N_2 as an inert atmosphere (Equation (1)).

$$Fe^{2+} + 2Fe^{3+} + 8OH^- \rightarrow Fe_3O_4 + 4H_2O. \quad (1)$$

Specifically, 125 mL of deoxygenated aqueous solution of NaOH 0.5M was added slowly with continuous stirring into a 100 mL mixture of deoxygenated iron salts suspension, at Fe^{2+}/Fe^{3+} molar ratio of 1:2, which contained 0.4 g of C100 polymer under N_2 atmosphere and at 40°C. To optimize the concentration of NPs on the surface of the polymeric cationic resin, we have used four different concentrations of $FeCl_2/FeCl_3$. These are as follows: Protocol A: 26/52 mM, Protocol B: 13/26 mM, Protocol C: 6.5/13 mM, and Protocol D: 3.25/6.50 mM. Then, the suspension was incubated for 1 h at 40° C. During the incubation, the polymer became black in colour due to the formation of Fe_3O_4–NPs on the polymeric material. The IMS of Fe_3O_4–NPs in sulphonated polymers can be described by Equations (2) and (3).[85]

$$8(R - SO_3^-Na^+) + Fe^{2+} + 2Fe^{3+} \rightarrow (R - SO_3^-)_2(Fe^{2+}) + 2[(R - SO_3^-)_3(Fe^{3+})] + 8Na^+, \quad (2)$$

$$(R - SO_3^-)_2(Fe^{2+}) + 2[((R - SO_3^-)_3(Fe^{3+}))] + 8NaOH \rightarrow 8(R - SO_3^-Na^+) + Fe_3O_4 + 4H_2O. \quad (3)$$

2.3. Characterization of the NCs

2.3.1. Inductively coupled plasma optical emission spectrometry

The metal content of the NC samples was analysed by using inductively coupled plasma optical emission spectrometry (ICP-OES), Perkin Elmer model Optima 4300DV. Pretreatment of the samples consists of acid digestion, dilution, and filtration using 0.45 µm Nylon filters. The metal amount was reported in terms of mg_{Fe}/g_{NC} (where g_{NC} refers to the mass of the NCs). The analyses were performed at Servei d'Anàlisi Química, Universitat Autònoma de Barcelona (UAB), Spain.

2.3.2. X-ray diffraction

X-ray diffraction (XRD) technique was used to obtain the crystalline structure of the particles. In a diffraction pattern, the location of the peaks on the 2θ scale can be compared to reference peaks. Diffraction patterns were collected on Panalytical X'Pert PRO MPD (Multipurpose Diffractometer). The analyses were performed at Institut Català de Nanociència i Nanotecnologia (ICN2), Spain. The identification of magnetite was based on the characteristic peaks in the diffractograms and comparing with the database.

2.3.3. Scanning electron microscopy and energy-dispersive spectroscopy

Zeiss Merlin with a Field Emission microscope from Servei de Microscopia at UAB was used to study the cross-sectioned NC samples. Cross sections were obtained by embedding the NC in epoxy resin and then cross-sectioning with a Leica UC7 ultramicrotome (using a 35° diamond knife from Diatome) to obtain the metal concentration profiles along the materials. Energy-dispersive spectroscopy (EDS) measurements were acquired using an Oxford INCA X-MAX detector.[85]

2.3.4. Transmission electron microscopy

JEM-2011/ JEOL microscope from Servei de Microscopia at UAB was used to characterize the cross section of Fe_3O_4–NPs on the NC. The samples were embedded in epoxy resin for cross-sectional analysis as described in the scanning electron microscopy (SEM) section (Section 2.3.3).

2.3.5. Surface area measurements by Brunauer–Emmett–Teller method

Surface area of dry resin and the NCs was determined from conventional nitrogen sorption isotherms at Institut Català de Materials Avançats de Barcelona (ICMAB), Spain, by utilizing the Brunauer–Emmett–Teller (BET) theory. The instrument employed was a Micromeritics ASAP2000 with dedicated software.

2.4. Ionic chromatography for phosphate analysis

The determination of phosphate, as phosphorous (PO_4–P), was performed utilizing an ion chromatography system (ICS-2000, Dionex), with an UltiMate 3000 autosampler. An ion-exchange column specifically designed for rapid analysis of inorganic anion (Dionex IonPac AS18, 4 × 250 mm) equipped with an IonPac guard column (Dionex IonPac AG18, 4 × 50 mm) was used. Chromeleon® software was used to acquire data and control the instrumentation. Calibration standards and samples were filtered using 0.45 µm Nylon membrane filter before injection. Error in the measurements is <1.2%.

2.5. Adsorption–desorption tests

2.5.1. Phosphate solutions

Phosphate solutions were prepared using a Na_2HPO_4 stock solution of 10,000 mg/L in milli-Q water. Then, a series of dilutions with a range of concentration from

0.1 to 100 mg/L of phosphate in milli-Q water were prepared for calibration. Each solution was filtered using a 0.45 µm nylon membrane filter prior to analysis. When necessary, pH was adjusted using 0.1 M citric acid or 0.1 M sodium hydroxide.

2.5.2. Adsorption studies in a fixed-bed column

The fixed-bed column experiments were performed using a polyamide column of 1 cm inner diameter and 16 cm length. The column was packed with the synthesized NC. A glass wool plug was placed at the bottom of the column to avoid the adsorbent washing out. Prior to the start of the experiment, the NC was fully wetted by pumping the column upwards for 4 hours with milli-Q water at a flow rate of 1 mL/min. The flow rate was maintained in each experiment using a peristaltic pump (Watson Marlow, 403U).

The continuous adsorption process is usually characterized by the so-called breakthrough curves, that is, a representation of the pollutant effluent concentration versus time profile in a fixed-bed column. In addition, breakthrough curves prediction through mathematical models is a useful tool for scale-up and design purposes.[86]

Breakthrough curve determination experiments were performed for all the experiments at 1 mL/min and 1.0 g of adsorbent (NCs).

The breakthrough curves show the loading behaviour of phosphate to be removed from the solution in a fixed-bed column and are usually expressed in terms of adsorbed phosphate as PO_4–P concentration (C_{ad}) as a function of time. Equilibrium uptake q_{eq} (mg_{PO4-P}/g_{NC}) is defined as the adsorption capacity of phosphate per mass of NC at a certain initial phosphate concentration. [87] In all experiments, the initial concentration of phosphate was 10 mg/L. Different pHs of the phosphate media were also evaluated of the pH range from 4 to 7 to determine the effect of pH on the adsorption capacity as well as to evaluate the NC stability after the adsorption experiments.

2.5.3. Phosphate adsorption isotherm and modelling

To estimate the maximum adsorption capacity of the adsorbent, isotherm modelling is an important aspect for establishing the adsorption system which provides information on the amount required for removing a unit mass of pollutant. In this study, isotherms were performed continuously with phosphate interval concentrations (1, 2.5, 5, 10, 20, 30, 50, 80, and 100 mg/L), 1 g/L of nanoadsorbent, 1 mL/min at room temperature and two pH values; 5 and 7.

The experimental quantities of the phosphate adsorbed were fitted to adsorption isotherm models available in the literature, including two-parameter isotherms (Langmuir, Freundlich, Dubinin–Radushkevich (DR)), three-parameter isotherms (BET), and a combination of them. The isotherms were determined from the breakthrough curves of step changes in the feed concentration by non-linear regression according to the value of the objective function defined as the norm of the difference between experimental data and model predictions. The sorption capacity of the material was evaluated at different pHs by frontal analysis following the stair case method.[88] Moreover, a confidence interval was determined in the estimation of model parameters according to the Fisher information matrix method as a function of the quantity and quality of experimental data.[89]

Column experiments were carried out with 1 mg/L phosphate as the initial concentration until equilibrium was reached. At that point, inlet phosphate concentration was increased corresponding to the interval of phosphate concentration. For each initial phosphate concentration, q_{eq} was calculated.

2.5.4. Desorption of phosphate and reusability of the NC

The desorption process for the phosphate previously adsorbed on the NC, as previously described, was optimized to be able to reuse the nanoadsorbent for further adsorption process and to recover the phosphate. To determine the optimal process for the adsorbent regeneration, different desorbing solutions, specifically NH_4OH, NaOH with different concentrations (0.01–1.0 M), and milli-Q water, were used. After 90 min adsorption of 10 mg/L phosphate solution at pH 7, 1 mL/min and 1.0 g of the nanoadsorbent, aliquots of the NC (0.5 g of wetted adsorbent) were treated using the desorbing solutions. Once the optimal desorption system was defined, the adsorption–desorption processes were performed seven times at the optimal adsorption and desorption experimental conditions for evaluating the reusability of the synthesized NC for phosphate removal and recovery.

3. Results and discussion

3.1. Synthesis and characterization of the NCs

3.1.1. Metal ions content in the NCs

The NCs, synthesized by using the four (A, B, C, and D) samples, were analysed by ICP-OES. Table 1 shows the

mean of iron (Fe) concentration (mg_{Fe}/g_{NC}) for the three replicates of the four samples. It is shown that increasing the Fe salts concentration in the synthesis leads to an increase in the Fe content in the final NC. Furthermore, data show that the Fe concentration on the polymer is saturated at around 80 mg_{Fe}/g_{NC} (samples A and B), being the maximum level of metal concentration during the synthesis of 13/26 mM of $FeCl_2/FeCl_3$ (for Protocol B).

3.1.2. SEM-EDS, XRD, and TEM analysis of the NCs

The SEM images coupled with EDS of the cross sections for each synthetic protocol (A, B, and C) of the NCs are shown in Figure 1. These data show the success of the immobilization of the Fe_3O_4–NPs on the surface of the NC. As it is clearly seen in Figure 1(a)–(c), the major part of the Fe_3O_4–NPs is located near the polymer surface (shown by the light white zone) with different thicknesses corresponding to each synthetic protocol showing a deeper layer when the loading concentration of iron during the synthesis is higher. Figure 1(d) shows the cross section of the polymer without NPs.

Table 1. Iron synthesis ratio, iron content (mg_{Fe}/g_{NC}), and adsorption capacities (mg_{PO4-P}/g_{NC}) at pH 5 of 10 mg/L of phosphate using different protocols; A, B, C, and D.

	$FeCl_2/FeCl_3$ synthesis ratio	Iron concentration, mg_{Fe}/g_{NC}	Adsorption capacities, mg_{PO4-P}/g_{NC}
C100 polymer	0	0	<0.01
Protocol A	26/52	77.0 ± 1.21	2.88
Protocol B	13/26	81.2 ± 1.56	2.30
Protocol C	6.5/13	23.6 ± 1.34	3.60
Protocol D	3.25/6.5	5.59 ± 0.28	< 0.01

Further confirmation about the immobilization of magnetite NPs on the surface of the polymer is illustrated in Figure 1(e), where the line spectrum shows the iron content profile obtained by SEM coupled with EDS, on the cross section of Protocol C. It can be seen that the profile distribution of Fe presents a peak at the surface of the polymer, meaning that the distribution of Fe_3O_4–NPs is concentrated on the surface of the polymer, which makes the material more suitable for its application as a nanoadsorbent. Furthermore, TEM images of the cross-sectioned nanomaterials for Protocol C are illustrated in Figure 2(a). As it is observed, the NPs on the polymer show a size of 15–20 nm as it was also shown in [83]. The crystalline structure of Fe_3O_4–NPs was confirmed by the electron diffraction pattern as shown in Figure 2(b).

In addition, the X-ray diffractogram shows the crystalline structure of the Fe_3O_4–NPs (Figure 3(a)), and the Fe_3O_4–NPs immobilized on the polymer before adsorption (Figure 3(b)). The typical peaks can be found at 35.5°, 43.0°, 57.1°, and 62.7°, which preferably correspond to Fe_3O_4 according to the joint committee on powder diffraction standards database.[90] The Miller indices of these peaks are 311, 400, 511, and 440, respectively. The broad peak in the XRD pattern could be attributed to the ultra-fine nature and small crystallite size of

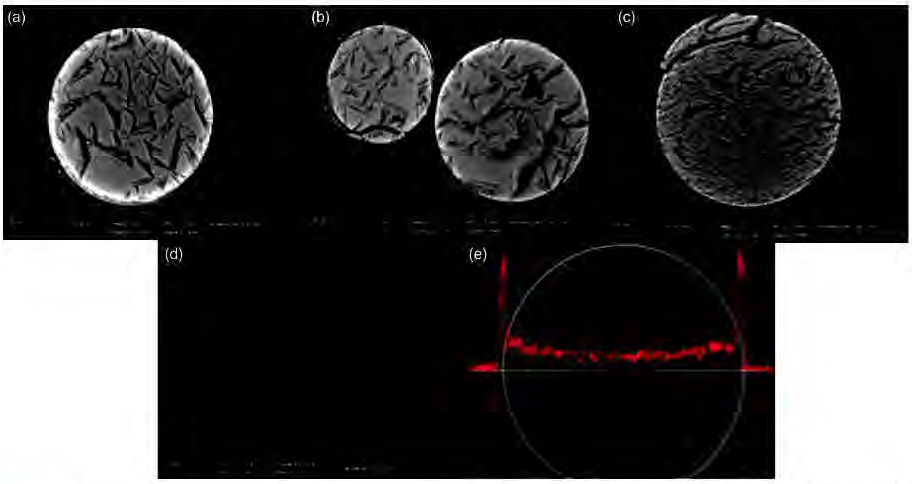

Figure. 1. SEM image of the cross section of the magnetite-based NCs for the samples synthesized by: (a) Protocol A, (b) Protocol B, (c) Protocol C, and (d) any protocol (raw polymeric matrix without Fe_3O_4–NPs). (e) SEM image and EDS spectra for the profile distribution of the Fe on the cross section of NC (Protocol C).

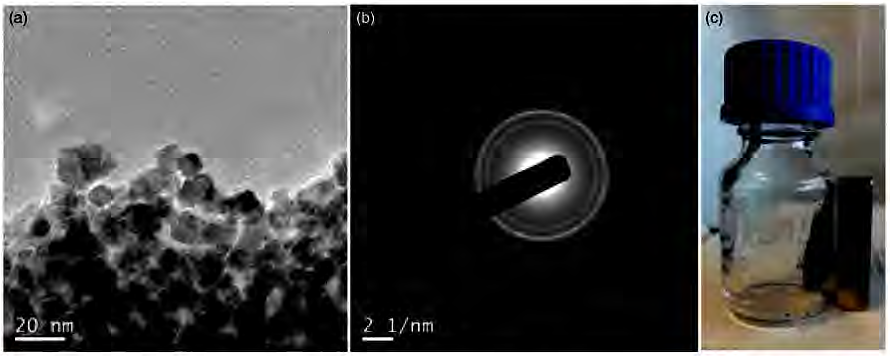

Figure 2. TEM image of magnetite NPs in the NC (Protocol C) (a), electron diffraction of magnetite NPs in the NC (Protocol C) (b), and magnetic properties test of the NC (Protocol C) using a magnet (c).

magnetite NCs, in addition to the formation of a thin layer of magnetite NPs immobilized on the surface of the cationic polymer. Moreover, the decrease in the intensity of the peaks could be attributed to the low concentration of iron contents.[91,92]

3.1.3. Magnetic characterization and surface area measurements of the NCs

Figure 2(c) shows a photograph of the qualitative test of the magnetic properties of NC by using a permanent magnet, where one can clearly see the NC beads stuck to the magnet. This means that the NC material can be easily recovered from the medium for further reuse, which is an advantage of the separation process in this application.

On the other hand, BET analysis reports that the surface area for all protocols was lower than 2 m^2/g (N_2 sorption, BET). These results agree with that of the gel-type resins in the dry state that are characterized by very low porosity and a far lower surface area, which usually does not exceed 5 m^2/g (N_2 sorption, BET).[93]

3.2. Adsorption studies in fixed-bed column

3.2.1. Determination of the adsorption capacities for the NCs with different Fe_3O_4–NPs contents (Protocols A, B, C, and D)

The influence of Fe_3O_4–NPs concentration in the NC on the adsorption capacities of 10 mg/L phosphate at pH 5 is shown in Table 1. The highest adsorption capacity was 3.62 mg_{PO4-P}/g_{NC} obtained by using the material corresponding to Protocol C (23.59 ± 1.34 mg_{Fe}/g_{NC}), indicating that a higher concentration of NPs leads to a decrease in the adsorption capacity of the NC (as shown for Protocol A and B adsorption capacities, corresponding to 2.88 and 2.30 mg_{PO4-P}/g_{NC}, respectively). This can be explained because an excess of NPs leads to a decrease in the surface/volume ratio of the NPs by the presence of aggregates or higher NPs size. On the other hand, Protocol D showed an adsorption capacity lower than 0.01 mg_{PO4-P}/g_{NC} (corresponding to the limit detection of the IC), which indicates that approximately less than 6.0 mg_{Fe}/g_{NC} had no significant effect on the NC for the adsorption process of phosphates similar to that observed for the adsorption capacity for C100 without NP. Thus, it was considered that Protocol C (23.59 mg_{Fe}/g_{NC}) is the optimal iron content as well as NPs size and distribution in this NC for the adsorption of phosphates in water. Thus, the following experiments in this work and the majority of the characterization techniques used were carried out for sample C.

3.2.2. Effect of pH on the adsorption capacities and on the NC stability

pH, as a critical water chemistry parameter, can significantly affect the adsorption of phosphate by any material. Figure 4 shows the adsorption capacities of 10 mg/L phosphate, as initial concentration, using Protocol C NC at a pH range from 4 to 7. Generally, phosphate has three pi_{ke} values, 2.2, 7.2, and 12.3, which correspond to pK_{a1}, pK_{a2}, and pK_{a3}, respectively, according to the presence of three species. HPO_4^{2-} and $H_2PO_4^-$ are the predominant species in the solution at pH between 4 and 10. HPO_4^{2-} is more widespread in slightly alkaline conditions, while $H_2PO_4^-$ is more widespread in slightly acidic conditions.[94] As shown in Figure 4, in this study, the highest adsorption capacity values were obtained at pH 7, indicating that the species involved in the adsorption process are those which are related

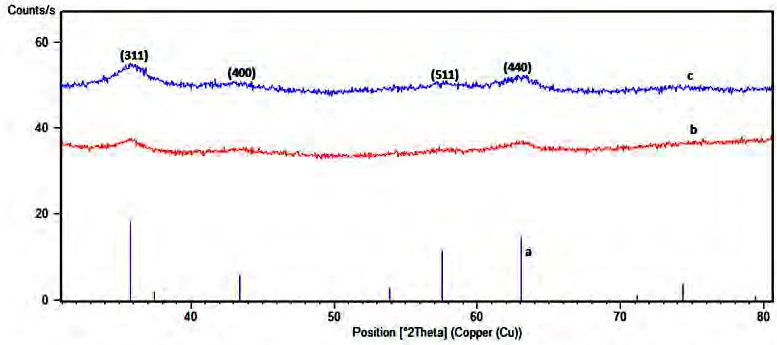

Figure 3. XRD pattern of (a) magnetite reference pattern and magnetite NC (Protocol C), (b) before, and (c) after the adsorption process with 10 mg/L of phosphates.

to the pK_{a2} value of 7.2. Thus, HPO_4^{2-} seems to have better affinity to form bidentate complexes with the magnetite NPs than $H_2PO_4^-$ forming an $M\text{–}OH^+$ complex.[95–97] Moreover, when $pH < pK_a$ (as pK_{a2} in this case), the surface of the adsorbent is more positively charged and more efficient for attracting negatively charged phosphate species through electrostatic interaction. It is also reported that phosphate adsorption on the surfaces of other iron-based species (e.g. oxyhydroxide polymorphs goethite) is based on the formation of inner-sphere complexes between the phosphate anion and the iron oxyhydroxide surface, indicating the presence of Fe–O–P covalent bonds, which seems to be also contributing to the adsorption process in the system here reported.[98]

Furthermore, the effect of pH on the immobilized Fe_3O_4–NPs on C100 after the adsorption processes described in Figure 4 was also determined by ICP-OES analysis to detect the stability of the NPs on the polymer for the adsorption mechanism. Thus, iron content after adsorption at different pHs showed the highest iron decrease at pH 4 of 43.4%, while at pH 7 the decrease in iron content was 7%. This decrease could be explained due to an oxidation of the iron present in the NPs that is finally released from the polymer. In view of these results, pH 7 is the optimum pH for phosphate adsorption, due to both the highest adsorption capacity and the NC stability. Even more, the adsorption of 10 mg/L phosphate on the NC (Protocol C) at pH 7 did not affect the crystalline structure (Figure 3(c)) of the NPs.

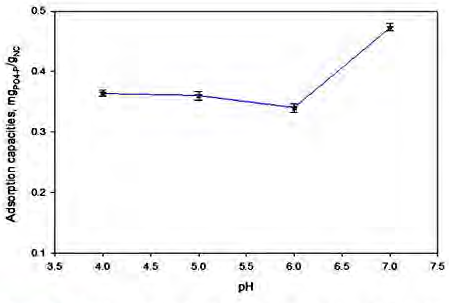

Figure 4. Variation in the phosphate adsorption capacities (mg_{PO4-P}/g_{NC}) for the NC (Protocol C) at different pHs of the medium.

3.3. Adsorption Isotherms and modelling

Isotherm fitting results for the five different models tested are shown in Figure 5 up to a concentration of 100 mg/L. While in Figure 5(a) it is observed that the saturation conditions are achieved at pH 5, maximum capacity is not reached when the material is operated at pH 7 (Figure 5(b)). These isotherms make it possible to accurately predict the experimental data (low fval) (Table 2). Wider confidence intervals are obtained in three-parameter isotherms in particular, showing that a large number of possible combinations of parameters are able to fit the model predictions to the experimental phosphate adsorbed on the materials. Thus, the estimated parameters show a low sensitivity to the final result of the isotherm expression as in the case of BET isotherm. Thus, the Freundlich, the Langmuir, and the isotherm that combines the three-parameter isotherms are the most suitable for fitting the experimental data and for interpreting the influence of pH on the sorption.

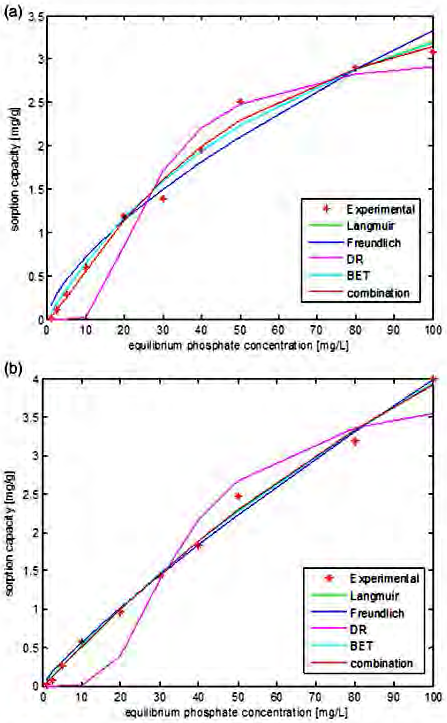

Figure 5. Isotherm fitting results for the five different models tested up to a concentration of 100 mg/L at (a) pH 5 and (b) pH 7.

Table 2. Parameters for the isotherm models used for data fitting.

Model		pH = 5	pH = 7
Langmuir	k1	5.612 ± 0.180	14.378 ± 1.094
	k2	75.743 ± 2.679	265.089 ± 20.884
	fval	0.377	0.2702
Freundlich	kf	0.158 ± 0.001	0.081 ± 0.000
	n	0.663 ± 0.003	0.846 ± 0.003
	fval	0.592	0.3122
Dubinin	B	0.891 ± 0.031	1.577 ± 0.045
	qm	3.072 ± 0.055	3.902 ± 0.075
	fval	0.870	1.0504
BET	Cs	9.4E + 09 ± 1E + 11	1.4E + 03 ± 3.0E + 03
	B	1.2E + 08 ± 2E + 08	7.838 ± 12.252
	Q	5.606 ± 0.796	9.525 ± 6.636
	fval	0.377	0.2700
Combination	b	0.008 ± 3.1E − 04	0.004 ± 0.001
	qm	4.257 ± 0.165	12.102 ± 1.554
	n	0.788 ± 0.008	0.961 ± 0.008
	fval	0.325	0.2685

Freundlich isotherm is commonly used for describing sorption on heterogeneous surfaces. The *n* value indicates the degree of non-linearity between solution concentration and adsorptive material. As *n* value is lower than 1, the sorption process is more chemical than physical for both pHs. The estimated values of n are lower at pH 5, indicating that the behaviour deviates in this case further from the linear isotherm, so it approaches a rectangular isotherm or an irreversible isotherm. This means that the concentration needs to go down to an extremely low value before the adsorbate molecules desorb from the surface. A higher value of this parameter at pH 7 reveals a weaker affinity between the contaminant and material compared to pH 5 results.

The higher value of Langmuir parameter k1 obtained for the isotherm at pH 7 underlines a higher sorption capacity of the material at these conditions (as also shown in Figure 4). The Langmuir isotherm assumes monolayer adsorption onto a surface containing a finite number of adsorption sites of uniform strategies with no transmigration of adsorbate in the plane surface. Once a site is filled, no further sorption can take place at that site. This indicates that at pH 5, the surface reaches a saturation point where the maximum adsorption of the surface is achieved. Since the experimental data at pH 7 are not strictly following a saturation model as Langmuir, the maximum capacity of the material is an extrapolation that it should be checked if a higher concentration than those tested in the present study is required. The higher value of k2 for pH 7 highlights again a lower affinity between the material and the contaminant compared to that at pH 5.

The DR isotherm equation, widely used for describing adsorption on microporous solids such as activated carbons, has a semi-empirical origin and is based on the assumptions of a change in the potential energy between the adsorbed phases and a characteristic energy of a given solid. Previous results are partially improved by means of the Redlich–Peterson isotherm. Unlike pH 5, sorption experiments conducted at pH 7 exhibit a behaviour similar to that of Henry's law, according to the parameter *n*, which is close to 0. In contrast, at the same range of phosphate concentrations, working a lower pH, the material reduces its capacity and reaches quickly saturation conditions.

From the modelling of the process, it is concluded that the kind of relationship set between a contaminant and a sorbent is described by a chemical interaction, as already mentioned in Section 3.2.2, through a Fe–OH complex system mechanism. While at pH 5 monolayer absorption reproduces more accurately the experimental behaviour, saturation conditions are not achieved at pH 7. This means a stronger interaction is observed at pH 5. Clearly, pH plays an important role in the affinity

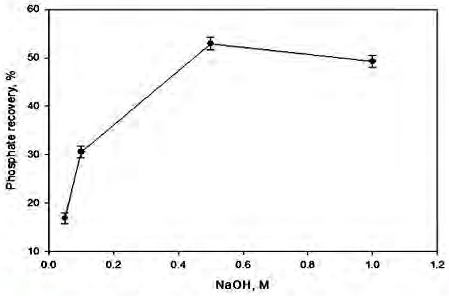

Figure 6. Effect of NaOH concentration on phosphate desorption (% of recovery)

Table 3. Comparison of PO4–P adsorption capacity of the NC (Fe_3O_4–C100) of this work with other iron-based adsorbents from the literature at the corresponding conditions of pH.

Adsorbent	pH	PO_4–P adsorption capacity (mg/g)	References
Fe_3O_4@ZrO_2	3.0	39.1	[92]
Fe_3O_4–C100	7.0	>4	This work
La-EDTA-coated Fe_3O_4	6.0	4.2	[61]
Fe_3O_4–C100	5.0	2.8	This work
Fe_3O_4	2.8	2.6	[60]
Hematite	6.0	1.1	[78]
Geothite + maghemite	4.0	0.9	[77]
α-Fe_2O_3	3.0	0.3	[12]

and capacities of materials when they are under adsorption conditions.

The adsorption capacity of the magnetic NC for the removal of PO_4–P has been compared with that of various iron-based adsorbents in Table 3. The adsorption capacities of magnetite immobilized on C100 developed and tested in this work are much higher than that of other iron-based nanoadsorbents but the one based on zirconium. However, the NC used in this work has an advantage in a real application pH medium and it is easier to recover than the others. Therefore, the NC used in this study is highly competitive for phosphate removal.

3.4. Evaluation of the phosphate recovery procedure and the reusability of the magnetite NC for several adsorption–desorption cycles

It is known that at high alkaline pH, PO_4^{3-} species are the predominant in the solution medium and the magnetite is deprotonated and negatively charged, which is favourable for the desorption of the adsorbed phosphate.[74] In this work, among the reagents used for the regeneration of magnetite-based NC (Protocol C), NaOH was found to be the most effective in desorbing phosphate compared to NH_4OH and Milli-Q water after 1 h of shaking at 200 rpm (31.5% and 12.6% of phosphate recovered, respectively). A further optimization procedure for the desorbing process was performed using different concentrations of NaOH. As shown in Figure 6, we can conclude that 0.5 M NaOH is the optimum concentration for the desorption process. Under these conditions, phosphates desorption was 52.9%. Therefore, enhancement of desorbability per cent was achieved by three washing cycles with 0.5 M NaOH to recover 97.5% of the phosphate. This result is clearly interesting if ones compares it with the recovered phosphate % reported in the literature (i.e. 40% for phosphate for initial concentrations less than 100 mg/L).[76]

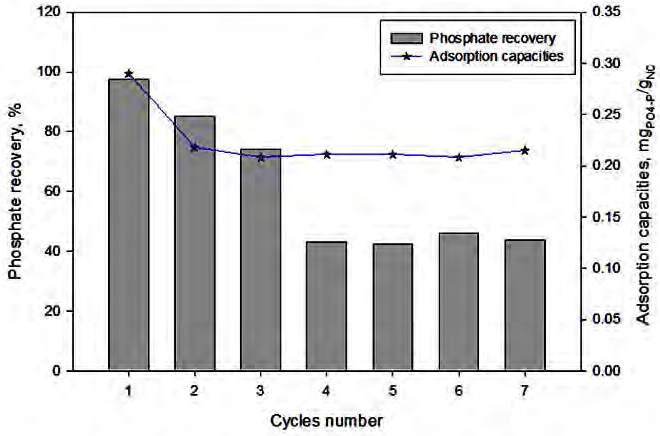

Figure 7. Adsorption capacities and % of phosphate recovery for the NC (Protocol C) at different adsorption–desorption cycles (7).

Afterwards, the regenerated magnetite NC was tested for reusability. After every adsorption process, desorption by using 0.5 M NaOH and three washing steps was performed. The results (Figure 7) showed that there is only a drop in the adsorption capacity after the first cycle, while the efficiency of phosphate adsorption–desorption was nearly the same for the rest of the six cycles. The drop in the adsorption capacity after the first adsorption–desorption cycle could be explained by the loss of iron detected from the ICP-OES analysis, which was 30% after the first cycle and remained constant for the rest of cycles. The loss of the iron content from the NC could be due to the experimental conditions in which some of the iron ions dissolves in the media but the rest of the iron content remains stabilized in the polymeric matrix.

On the other hand, as mentioned, the recovery of phosphate was 97.5% for the first cycle. A decrease in the recovery per cent was observed from the first to the fourth cycle of adsorption–desorption. After that, the recovery per cent removal remained constant at 45% approximately, as shown in Figure 7. In this sense, it could be confirmed the assumed adsorption mechanism (see Section 3.2.2) in which a strong Fe–HPO_4 complex could be formed in each adsorption–desorption cycle and thus, avoiding the total recovery of the phosphate.

4. Conclusions

The present study provides magnetite NPs immobilized on the surface of a cationic polymer (C100) which proved to be a successful application to remove phosphate ions from aqueous solutions. Adsorption experiments of phosphate in a fixed-bed column using different concentrations of magnetite NPs immobilized on the polymer prove that the optimum concentration of iron in the NCs is 23.59 mg_{Fe}/g_{NC}. The effect of pH on the adsorption capacity showed a higher adsorption capacity of the optimized material at pH 7 compared to that at pH 4, 5, and 6. Afterwards, continuous adsorption isotherms were performed and it is shown a higher adsorption capacity (>4.0 mg_{PO4-P}/g_{NC}) at pH 7 compared to that at pH 5 (2.8 mg_{PO4-P}/g_{NC}). Therefore, the magnetic NC used in this study is highly competitive for phosphate removal compared to other iron-based NPs reported in the literature. Furthermore, regeneration of the NC was optimized to obtain 97.5% recovery of phosphate using 0.5 M NaOH for three consecutive cycles of the desorption process. Then, reusability was demonstrated for seven cycles of the adsorption–desorption process. Therefore, we can conclude that the magnetite NPs immobilized on the cationic polymer has a great potential for adsorbing and recovering phosphate.

Acknowledgements

One of the authors, Ahmad Abo Markeb is grateful to the Ministry of Higher Education of Egypt for the PhD external mission. The authors would like to extend their gratitude to Purolite for kindly supply the cationic polymer.

Disclosure statement

No potential conflict of interest was reported by the authors.

References

[1] Foo KY, Hameed BH. Detoxification of pesticide waste via activated carbon adsorption process. J Hazard Mater. 2010;175:1–11.
[2] Mohan D, Pittman CU, Jr. Activated carbons and low cost adsorbents for remediation of tri- and hexavalent chromium from water. J Hazard Mater. 2006;137:762–811.
[3] Recillas S, Colón J, Casals E, et al. Chromium VI adsorption on cerium oxide nanoparticles and morphology changes during the process. J Hazard Mater. 2010;184:425–431.
[4] Contreras AR, García A, González E, et al. Potential use of CeO2, TiO2 and Fe3O4 nanoparticles for the removal of cadmium from water. Desalin Water Treat. 2012;41:296–300.
[5] Lau PS, Tam NFY, Wong YS. Wastewater nutrients (N and P) removal by carrageenan and alginate immobilized Chlorella vulgaris. Environ Technol. 1997;18:945–951.
[6] Trépanier C, Parent S, Comeau Y, Bouvrette J. Phosphorus budget as a water quality management tool for closed aquatic mesocosms. Water Res. 2002;36:1007–1017.
[7] Reijnders L. Phosphorus resources, their depletion and conservation, a review. Resour Conserv Recycl. 2014;93:32–49.
[8] Sengupta S, Pandit A. Selective removal of phosphorus from wastewater combined with its recovery as a solid-phase fertilizer. Water Res. 2011;45:3318–3330.
[9] de-Bashan LE, Bashan Y. Recent advances in removing phosphorus from wastewater and its future use as fertilizer (1997–2003). Water Res. 2004;38:4222–4246.
[10] Kebreab E, Hansen AV, Strathe AB. Animal production for efficient phosphate utilization: from optimized feed to high efficiency livestock. Curr Opin Biotechnol. 2012;23:872–877.
[11] Vitti DMSSkE. General introduction. In: Vitti DMSS, Kebreab E, editors. Phosphorus and calcium utilization and requirements in farm animals. London: CAB International; 2010; p. 1–178.
[12] Zhu Z, Zeng H, Zhu Y, et al. Kinetics and thermodynamic study of phosphate adsorption on the porous biomorph-genetic composite of α-Fe2O3/Fe3O4/C with eucalyptus wood microstructure. Sep Purif Technol. 2013;117:124–130.
[13] Mezenner NY, Bensmaili A. Kinetics and thermodynamic study of phosphate adsorption on iron hydroxide-eggshell waste. Biochem Eng J. 2009;147:87–96.

[14] Prochaska CA, Zouboulis AI. Removal of phosphates by pilot vertical-flow constructed wetlands using a mixture of sand and dolomite as substrate. Ecol Eng. 2006;26:293–303.
[15] Ramadori R, di Pinto AC, Tandoi V, Sasso C. Chemical precipation of phosphate from sewage at low lime dosage. In: Pawlowski EMWJL, Sarzanini C, editors. Studies in environmental science. Vol. 34. Rome: Elsevier; 1988. p. 223–233.
[16] SenGupta A, Zhao D. Using a chelating ion exchange resin saturated with lewis acid, i.e., copper, cations. Google Patents; 2000.
[17] Federation WE. Biological nutrient removal (BNR) operation in wastewater treatment plants: WEF manual of practice. Alexandria: McGraw-Hill Education; 2005.
[18] Sedlak RI. Phosphorus and nitrogen removal from municipal wastewater: principles and practice, 2nd ed. Abingdon: Taylor & Francis; 1991.
[19] Zhao D, Sengupta AK. Ultimate removal of phosphate from wastewater using a new class of polymeric ion exchangers. Water Res. 1998;32:1613–1625.
[20] Isanta E, Figueroa M, Mosquera-Corral A, Campos L, Carrera J, Pérez J. A novel control strategy for enhancing biological N-removal in a granular sequencing batch reactor: a model-based study. Chem Eng J. 2013;232:468–477.
[21] Carrera J, Vicent T, Lafuente J. Effect of influent COD/N ratio on biological nitrogen removal (BNR) from high-strength ammonium industrial wastewater. Process Biochem. 2004;39:2035–2041.
[22] Bai L, Wang C, Pei Y, Zhao J. Reuse of drinking water treatment residuals in a continuous stirred tank reactor for phosphate removal from urban wastewater. Environ Technol. 2014;35:2752–2759.
[23] EMIS. Biological nutrient removal, http://emis.vito.be/techniekfiche/biological-nutrient-removal?language=en 2010 [cited 2015 March 3]. Available from: http://emis.vito.be/techniekfiche/biological-nutrient-removal
[24] Yilmaz G, Lemaire R, Keller J, Yuan Z. Simultaneous nitrification, denitrification, and phosphorus removal from nutrient-rich industrial wastewater using granular sludge. Biotechnol Bioeng. 2008;100:529–541.
[25] Saha B, Chakraborty S, Das G. A mechanistic insight into enhanced and selective phosphate adsorption on a coated carboxylated surface. J Colloid Interface Sci. 2009;331:21–26.
[26] de la Noue J, de Pauw N. The potential of microalgal biotechnology: a review of production and uses of microalgae. Biotechnol Adv. 1988;6:725–770.
[27] Zelmanov G, Semiat R. The influence of competitive inorganic ions on phosphate removal from water by adsorption on iron (Fe+3) oxide/hydroxide nanoparticles-based agglomerates. J Water Process Eng. 2015;5:143–152.
[28] Qu X, Alvarez PJJ, Li Q. Applications of nanotechnology in water and wastewater treatment. Water Res. 2013;47:3931–3946.
[29] Savage N, Diallo M. Nanomaterials and water purification: opportunities and challenges. J Nanopart Res. 2005;7:331–342.
[30] Zeng L, Li X, Liu J. Adsorptive removal of phosphate from aqueous solutions using iron oxide tailings. Water Res. 2004;38:1318–1326.
[31] Zach-Maor A, Semiat R, Shemer H. Synthesis, performance, and modeling of immobilized nano-sized magnetite layer for phosphate removal. J Colloid Interface Sci. 2011;357:440–446.
[32] Strauss R, BrÜMmer GW, Barrow NJ. Effects of crystallinity of goethite: II. Rates of sorption and desorption of phosphate. Eur J Soil Sci. 1997;48:101–114.
[33] Streat M, Hellgardt K, Newton NLR. Hydrous ferric oxide as an adsorbent in water treatment: part 3: batch and mini-column adsorption of arsenic, phosphorus, fluorine and cadmium ions. Process Saf Environ. 2008;86:21–30.
[34] Oguz E. Removal of phosphate from aqueous solution with blast furnace slag. J Hazard Mater. 2004;114:131–137.
[35] Nowack B, Stone AT. Competitive adsorption of phosphate and phosphonates onto goethite. Water Res. 2006;40:2201–2209.
[36] Ma J, Zhu L. Simultaneous sorption of phosphate and phenanthrene to inorgano–organo-bentonite from water. J Hazard Mater. 2006;136:982–988.
[37] Luengo C, Brigante M, Avena M. Adsorption kinetics of phosphate and arsenate on goethite. a comparative study. J Colloid Interface Sci. 2007;311:354–360.
[38] Luengo C, Brigante M, Antelo J, Avena M. Kinetics of phosphate adsorption on goethite: comparing batch adsorption and ATR-IR measurements. J Colloid Interface Sci. 2006;300:511–518.
[39] Genz A, Kornmüller A, Jekel M. Advanced phosphorus removal from membrane filtrates by adsorption on activated aluminium oxide and granulated ferric hydroxide. Water Res. 2004;38:3523–3530.
[40] Chitrakar R, Tezuka S, Sonoda A, Sakane K, Ooi K, Hirotsu T. Phosphate adsorption on synthetic goethite and akaganeite. J Colloid Interface Sci. 2006;298:602–608.
[41] Ernst M, Sperlich A, Zheng X, et al. An integrated wastewater treatment and reuse concept for the Olympic Park 2008, Beijing. Desalin. 2007;202:293–301.
[42] Sánchez A, Recillas S, Font X, Casals E, González E, Puntes V. Ecotoxicity of, and remediation with, engineered inorganic nanoparticles in the environment. Trends Anal Chem. 2011;30:507–516.
[43] Recillas S, García A, González E, et al. Preliminary study of phosphate adsorption onto cerium oxide nanoparticles for use in water purification; nanoparticles synthesis and characterization. Water Sci Technol. 2012;66:503–509.
[44] Gupta VK, Ali I. Chapter 3 – water treatment for organic pollutants by adsorption technology. In: Ali VKG, editor. Environmental water. Roorkee: Elsevier; 2013. p. 93–116.
[45] Ungureanu G, Santos S, Boaventura R, Botelho C. Arsenic and antimony in water and wastewater: overview of removal techniques with special reference to latest advances in adsorption. J Environ Manage. 2015;151:326–342.
[46] Geelhoed JS, Hiemstra T, Van Riemsdijk WH. Phosphate and sulfate adsorption on goethite: single anion and competitive adsorption. Geochim Cosmochim Acta. 1997;61:2389–2396.
[47] Wasay SA, Tokunaga S, Park S-W. Removal of hazardous anions from aqueous solutions by La(III)- and Y(III)-Impregnated alumina. Sep Sci Technol. 1996;31:1501–1514.
[48] Zhang L, Gao Y, Li M, Liu J. Expanded graphite loaded with lanthanum oxide used as a novel adsorbent for phosphate removal from water: performance and mechanism study. Environ Technol. 2015;36:1016–1025.

[49] Kabayama M, Kawasaki N, Nakamura T, Tanada S. Adsorption/desorption characteristics of phosphate ion onto calcined boehmite surface. J Sur Sci Nanotechnol. 2005;3:63–69.
[50] Kabayama M, Sakiyama T, Kawasaki N, Nakamura T, Araki M, Tanada S. Characteristics of phosphate ion adsorption–desorption onto aluminum oxide hydroxide for preventing eutrophication. J Chem Eng Jpn. 2003;36:499–505.
[51] Gao S, Wang C, Pei Y. Comparison of different phosphate species adsorption by ferric and alum water treatment residuals. J Environ Sci. 2013;25:986–992.
[52] Guaya D, Valderrama C, Farran A, Armijos C, Cortina JL. Simultaneous phosphate and ammonium removal from aqueous solution by a hydrated aluminum oxide modified natural zeolite. Chem Eng J. 2015;271:204–213.
[53] Oliveira M, Ribeiro D, Nobrega JM, Machado AV, Brito AG, Nogueira R. Removal of phosphorus from water using active barriers: Al2O3 immobilized on to polyolefins. Environ Technol. 2011;32:989–995.
[54] Wu D, Shen Y, Ding A, Qiu M, Yang Q, Zheng S. Phosphate removal from aqueous solutions by nanoscale zero-valent iron. Environ Technol. 2013;34:2663–2669.
[55] Tang J, Chen J, Huang W, et al. Porous Pr(OH)3 nanowires as novel high-performance adsorbents for phosphate removal. Chem Eng J. 2014;252:202–209.
[56] Xu N, Li Y, Zheng L, et al. Synthesis and application of magnesium amorphous calcium carbonate for removal of high concentration of phosphate. Chem Eng J. 2014;251:102–110.
[57] Su Y, Yang W, Sun W, Li Q, Shang JK. Synthesis of mesoporous cerium–zirconium binary oxide nanoadsorbents by a solvothermal process and their effective adsorption of phosphate from water. Chem Eng J. 2015;268:270–279.
[58] Zong E, Wei D, Wan H, Zheng S, Xu Z, Zhu D. Adsorptive removal of phosphate ions from aqueous solution using zirconia-functionalized graphite oxide. Chem Eng J. 2013;221:193–203.
[59] Lin Y-F, Chen H-W, Chen Y-C, Chiou C-S. Application of magnetite modified with polyacrylamide to adsorb phosphate in aqueous solution. Taiwan Inst Chem E. 2013;44:45–51.
[60] Bastin O, Janssens F, Dufey J, Peeters A. Phosphorus removal by a synthetic iron oxide–gypsum compound. Ecol Eng. 1999;12:339–351.
[61] Lakshmanan R, Okoli C, Boutonnet M, Järås S, Rajarao GK. Microemulsion prepared magnetic nanoparticles for phosphate removal: time efficient studies. J Environ Chem Eng. 2014;2:185–189.
[62] Zhang C, Chen L, Wang T-J, Su C-L, Jin Y. Synthesis and properties of a magnetic core–shell composite nanoadsorbent for fluoride removal from drinking water. Appl Surf Sci. 2014;317:552–559.
[63] Bhaumik M, Leswifi TY, Maity A, Srinivasu VV, Onyango MS. Removal of fluoride from aqueous solution by polypyrrole/Fe3O4 magnetic nanocomposite. J Hazard Mater. 2011;186:150–159.
[64] Tu Y-J, You C-F, Chang C-K, Chen M-H. Application of magnetic nano-particles for phosphorus removal/recovery in aqueous solution. Taiwan Inst Chem E. 2015;46:148–154.
[65] Yang J, Zeng Q, Peng L, et al. La-EDTA coated Fe3O4 nanomaterial: preparation and application in removal of phosphate from water. J Environ Sci. 2013;25:413–418.
[66] Zou C, Gu T, Xiao P, Ge T, Wang M, Wang K. Experimental study of Cucurbit[7]uril derivatives modified acrylamide polymer for enhanced oil recovery. Ind Eng Chem Res. 2014;53:7570–7578.
[67] Roy S, Yue CY, Venkatraman SS, Ma LL. Fabrication of smart COC chips: advantages of N-vinylpyrrolidone (NVP) monomer over other hydrophilic monomers. Sens Actuators, B. 2013;178:86–95.
[68] Shin Y, Lee D, Lee K, Ahn KH, Kim B. Surface properties of silica nanoparticles modified with polymers for polymer nanocomposite applications. J Ind Eng Chem. 2008;14:515–519.
[69] Xiong H-M. Photoluminescent ZnO nanoparticles modified by polymers. J Mater Chem. 2010;20:4251–4262.
[70] DeMarco MJ, SenGupta AK, Greenleaf JE. Arsenic removal using a polymeric/inorganic hybrid sorbent. Water Res. 2003;37:164–176.
[71] Cumbal L, Greenleaf J, Leun D, SenGupta AK. Polymer supported inorganic nanoparticles: characterization and environmental applications. React Funct Polym. 2003;54:167–180.
[72] Onyango MS, Kojima Y, Matsuda H, Ochieng A. Adsorption kinetics of arsenic removal from groundwater by Iron-Modified Zeolite. J Chem Eng Jpn. 2003;36:1516–1522.
[73] Katsoyiannis IA, Zouboulis AI. Removal of arsenic from contaminated water sources by sorption onto iron-oxide-coated polymeric materials. Water Res. 2002;36:5141–5155.
[74] Cumbal L, SenGupta AK. Arsenic removal using polymer-supported hydrated iron(III) oxide nanoparticles: role of donnan membrane effect. Environ Sci Technol. 2005;39:6508–6515.
[75] Zhang Y, Pan B. Modeling batch and column phosphate removal by hydrated ferric oxide-based nanocomposite using response surface methodology and artificial neural network. Chem Eng J. 2014;249:111–120.
[76] You X, Guaya D, Farran A, Valderrama C, Cortina JL. Phosphate removal from aqueous solution using a hybrid impregnated polymeric sorbent containing hydrated ferric oxide (HFO). J Chem Technol Biotechnol. 2016;91(3):693–704.
[77] Pan B, Wu J, Pan B, et al. Development of polymer-based nanosized hydrated ferric oxides (HFOs) for enhanced phosphate removal from waste effluents. Water Res. 2009;43:4421–4429.
[78] Blaney LM, Cinar S, SenGupta AK. Hybrid anion exchanger for trace phosphate removal from water and wastewater. Water Res. 2007;41:1603–1613.
[79] Yang W, Yu Z, Pan B, Lv L, Zhang W. Simultaneous organic/inorganic removal from water using a new nanocomposite adsorbent: a case study of p-nitrophenol and phosphate. Chem Eng J. 2015;268:399–407.
[80] Abo-Farha SA, Abdel-Aal AY, Ashour IA, Garamon SE. Removal of some heavy metal cations by synthetic resin purolite C100. J Hazard Mater. 2009;169:190–194.
[81] Liu C, Huang PM. Kinetics of phosphate adsorption on iron oxides formed under the influence of citrate. Canadian J Soil Sci. 2000;80:445–454.
[82] Colombo C, Barrón V, Torrent J. Phosphate adsorption and desorption in relation to morphology and crystal properties of synthetic hematites. Geochim Cosmochim Acta. 1994;58:1261–1269.

[83] Alonso A, Vigues N, Munoz-Berbel X, et al. Environmentally-safe bimetallic Ag@Co magnetic nanocomposites with antimicrobial activity. Chem Commun. 2011;47:10464–10466.
[84] Alonso A. Development of polymeric nanocomposites with enhanced distribution of catalytically active or bactericide nanoparticles. 2012.
[85] Alonso A, Shafir A, Macanás J, et al. Recyclable polymer-stabilized nanocatalysts with enhanced accessibility for reactants. Catal Today. 2012;193:200–206.
[86] Dorado AD, Gamisans X, Valderrama C, Solé M, Lao C. Cr (III) removal from aqueous solutions: a straightforward model approaching of the adsorption in a fixed-bed column. J Environ Sci Health Part A. 2013;49:179–186.
[87] Nur T, Johir MAH, Loganathan P, Nguyen T, Vigneswaran S, Kandasamy J. Phosphate removal from water using an iron oxide impregnated strong base anion exchange resin. J Ind Eng Chem. 2014;20:1301–1307.
[88] Vente JA, Bosch H, de Haan AB, Bussmann PJT. Evaluation of sugar sorption isotherm measurement by frontal analysis under industrial processing conditions. J Chromatogr A. 2005;1066:71–79.
[89] Dorado AD, Lafuente J, Gabriel D, Gamisans X. The role of water in the performance of biofilters: parameterization of pressure drop and sorption capacities for common packing materials. J Hazard Mater. 2010;180:693–702.
[90] Lemine OM, Omri K, Zhang B, et al. Sol–gel synthesis of 8 nm magnetite (Fe3O4) nanoparticles and their magnetic properties. Superlattices Microstruct. 2012;52:793–799.
[91] Neyaz N, Zarger MSS, Siddiqui WA. Synthesis and characterisation of modified magnetite super paramagnetic nano composite for removal of toxic metals from ground water. Int J Environ Sci. 2014;5:260–269.
[92] Farghali MA, El-Din TAS, Al-Enizi AM, Bahnasawy RME. Graphene/ magnetite nanocomposite for potential environmental application. Int J Electrochem Sci. 2015;10:529–537.
[93] Ahn J-H, Jang J-E, Oh C-G, Ihm S-K, Cortez J, Sherrington DC. Rapid generation and control of microporosity, bimodal pore size distribution, and surface area in davankov-type hyper-cross-linked resins. Macromolecules. 2006;39:627–632.
[94] Rodrigues L, da Silva M. Adsorption kinetic, thermodynamic and desorption studies of phosphate onto hydrous niobium oxide prepared by reverse microemulsion method. Adsorption. 2010;16:173–181.
[95] Zeng H, Fisher B, Giammar DE. Individual and competitive adsorption of arsenate and phosphate to a high-surface-area iron oxide-based sorbent. Environ Sci Technol. 2008;42:147–152.
[96] Krishnan KA, Haridas A. Removal of phosphate from aqueous solutions and sewage using natural and surface modified coir pith. J Hazard Mater. 2008;152:527–535.
[97] Das J, Patra BS, Baliarsingh N, Parida KM. Adsorption of phosphate by layered double hydroxides in aqueous solutions. Appl Clay Sci. 2006;32:252–260.
[98] Kim J, Li W, Philips BL, Grey CP. Phosphate adsorption on the iron oxyhydroxides goethite ([small alpha]-FeOOH), akaganeite ([small beta]-FeOOH), and lepidocrocite ([gamma]-FeOOH): a 31P NMR Study. Energy Environ Sci. 2011;4:4298–4305.

A-4

Science of the Total Environment 595 (2017) 51–62

Contents lists available at ScienceDirect

Science of the Total Environment

journal homepage: www.elsevier.com/locate/scitotenv

Review

Critical review of existing nanomaterial adsorbents to capture carbon dioxide and methane

Amanda Alonso [a,*], J. Moral-Vico [a], Ahmad Abo Markeb [a], Martí Busquets-Fité [b], Dimitrios Komilis [a,c], Victor Puntes [d,e], Antoni Sánchez [a], Xavier Font [a]

[a] Department of Chemical, Biological and Environmental Engineering, Escola d'Enginyeria, Universitat Autònoma de Barcelona, 08193 Bellaterra, Spain
[b] Applied Nanoparticles S.L, Carrer Còrcega 516, 08025 Barcelona, Spain
[c] Department of Environmental Engineering, Democritus University of Thrace, Xanthi 67132, Greece
[d] Institut Català de Nanotecnologia (ICN), Campus de la UAB, 08193 Bellaterra, Spain
[e] Institució Catalana de Recerca i EstudisAvançats (ICREA), Passeig Lluís Companys, 23, 08010 Barcelona, Spain

HIGHLIGHTS

- Novel materials and nanomaterials for CO_2 and CH_4 sorption are presented and compared.
- These materials have high selectivity for both gases, are easy to regenerate and cheap.
- Fe_3O_4-graphene and MOF-117 based NPs have reported the highest CO_2 sorption capacities.
- IRMOF-6, MOF-177 and MOF-5 showed the highest adsorption capacities for CH_4.
- Further studies are needed to prove their long term efficacy in real applications.

GRAPHICAL ABSTRACT

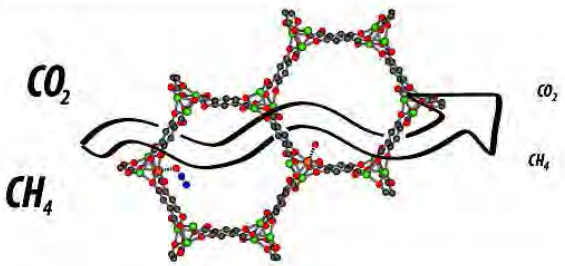

ARTICLE INFO

Article history:
Received 20 January 2017
Received in revised form 24 March 2017
Accepted 25 March 2017
Available online xxxx

Editor: D. Barcelo

Keywords:
Adsorption
Nanomaterials
Methane
Carbon dioxide
Metal organic framework
Zeolite

ABSTRACT

Innovative gas capture technologies with the objective to mitigate CO_2 and CH_4 emissions are discussed in this review. Emphasis is given on the use of nanoparticles (NP) as sorbents of CO_2 and CH_4, which are the two most important global warming gases. The existing NP sorption processes must overcome certain challenges before their implementation to the industrial scale. These are: i) the utilization of the concentrated gas stream generated by the capture and gas purification technologies, ii) the reduction of the effects of impurities on the operating system, iii) the scale up of the relevant materials, and iv) the retrofitting of technologies in existing facilities. Thus, an innovative design of adsorbents could possibly address those issues. Biogas purification and CH_4 storage would become a new motivation for the development of new sorbent materials, such as nanomaterials. This review discusses the current state of the art on the use of novel nanomaterials as adsorbents for CO_2 and CH_4. The review shows that materials based on porous supports that are modified with amine or metals are currently providing the most promising results. The Fe_3O_4-graphene and the MOF-117 based NPs show the greatest CO_2 sorption capacities, due to their high thermal stability and high porosity. Conclusively, one of the main challenges would be to decrease the cost of capture and to scale-up the technologies to minimize large-scale power plant CO_2 emissions.

* Corresponding author at: Departament d'Enginyeria Química, Biològica i Ambiental, Escola d'Enginyeria, Universitat Autònoma de Barcelona, Carrer de les Sitges, Edifici Q Campus UAB, Spain.
E-mail address: amanda.alonso@uab.cat (A. Alonso).

http://dx.doi.org/10.1016/j.scitotenv.2017.03.229
0048-9697/

Contents

1. Introduction . . . 52
   1.1. Greenhouse gases – problem statement . . . 52
   1.2. Capture of GHGs via sorption . . . 52
   1.3. Gaps in knowledge and objectives . . . 53
2. Conventional and novel adsorbents for CO_2 and CH_4 capture . . . 53
   2.1. Conventional adsorbents . . . 53
   2.2. Novel adsorbents . . . 53
      2.2.1. Ionic liquids for CO_2 removal . . . 53
      2.2.2. Modified porous supports . . . 53
3. Nanomaterial based CO_2 and CH_4 capture systems . . . 54
   3.1. Nanosized zeolites versus conventional zeolites . . . 55
   3.2. Mesoporous silica nanoparticles . . . 56
   3.3. Metal organic frameworks (MOFs) with embedded nanoparticles . . . 56
   3.4. Metal and metal oxide nanoparticles (MNPs and MONPs) versus alkali-metal based absorbents . . . 56
   3.5. Carbonaceous nano-sorbents versus conventional carbonaceous sorbents . . . 57
      3.5.1. Nanoporous carbon-based materials . . . 57
      3.5.2. Carbon nanotubes (CNT) . . . 57
      3.5.3. Graphene . . . 58
4. Techno-economic views on nanomaterials as CO_2 and CH_4 sorbents . . . 58
5. Conclusions . . . 60

Acknowledgements . . . 60

References . . . 60

1. Introduction

1.1. Greenhouse gases – problem statement

Global Warming (GW) is the result of the increased concentration of Green House Gases (GHGs), primarily carbon dioxide (CO_2) and methane (CH_4), but also of nitrous oxide (N_2O), hydrofluorocarbons (HFCs), perfluorocarbons (PFCs) and sulfur hexafluorocarbon (F_6C). The GHGs that are most abundantly emitted today are CO_2 (56%) and CH_4 (18%) (Houghton et al., 2001; McCarthy, 2001). As CO_2 is the most important gas in terms of amounts emitted, it has been widely studied (Pacala and Socolow, 2004).

CO_2 is produced in many industrial processes (i.e. fossil fuel power plants) including new prospective areas, such as the purification of hydrogen from biomass. Fossil fuel power plants are the largest point sources of CO_2 emissions (40% of total CO_2 emissions) (D'Alessandro et al., 2010); thus, they are the main targets for imminent CO_2 reduction (Doman et al., 2010; Metz et al., 2005).

Atmospheric concentrations of CH_4 (~1800 ppb) are currently much higher than those in preindustrial levels (~680–715 ppb) (Butler and Montzka, 2012). Anthropogenic CH_4 emissions account for 50–65% of the global CH_4 budget of ~395–427 TgC y^{-1} (526–569 Tg CH_4) (Kirschke et al., 2013). It is estimated that the principal CH_4 anthropogenic sources are (i) livestock (enteric fermentation and manure management), (ii) natural gas production and distribution, (iii) landfills, and (iv) coal mining (EPA, 2016). Also, it is reported that a rise in natural wetland emissions and fossil fuel emissions probably accounts for the renewed increase in global methane levels after 2006, although the relative contribution of these two sources remains uncertain (Kirschke et al., 2013).

The most convenient path towards lower CO_2 concentrations in the atmosphere would be to strongly reduce CO_2 emissions through cleaner and more environmentally friendly industrial processes. However, it is not expected that this can be achieved in the imminent future (Ciferno et al., 2009). Several options exist to reduce CO_2 emissions, such as demand-side conservation, supply-side efficiency improvement, increasing dependence on nuclear and renewable energy, and implementation of Carbon Capture and Storage (CCS) systems (D'Alessandro et al., 2010; Ciferno et al., 2009; Spigarelli and Kawatra, 2013; Yang et al., 2008).

The CO_2 capture is preferred to be applied directly on-site, since the capture materials and technologies have demonstrated better performances at high CO_2 concentrations rather than at atmospheric levels (400 ppm in 2014, Mauna Loa Observatory) (Baltrėnaitė et al., 2016).

1.2. Capture of GHGs via sorption

The storage of CH_4 on adsorbents has been pursued actively as an alternative to high pressure compressed gas storage. Thus, the use of adsorbent materials, such as activated carbons and zeolites for the storage of natural gas at low pressures, has also been reported (Solar et al., 2010). However, it was concluded that none of those conventional adsorbents showed sufficient CH_4 storage capacity to meet that required for commercial viability (Saha et al., 2010). Advanced materials have been investigated as potential CH_4 adsorbents including modified activated carbons, metal-organic frameworks (MOFs) and other porous polymers (Kizzie et al., 2014).

The technologies based on adsorption processes, such as activated carbon, zeolites and mesoporous silica, present limitations on the CO_2 retention capabilities per adsorbent mass (Cinke et al., 2003; Lu et al., 2008; Smart et al., 2006). In this sense, there is a widespread interest in the development of advanced adsorbent materials with better characteristics than conventional materials and with a specialized functionality for each pollutant.

Since CH_4 often co-exists with CO_2 in gaseous mixtures, such as natural gas, biogas and landfill gas, selective removal of CO_2 is an important process to upgrade the energy content of those mixtures (Li et al., 2013).

Nanotechnology can be defined as the engineering of functional systems "designed to measure" molecular scale. One of the benefits of these nanomaterials is the high surface to volume ratio and the ability to be synthesized with specific physicochemical properties. Nanotechnology has been applied in various areas of environmental sciences, such as catalysis, sensors and water treatment (Birgisson et al., 2012).

Several articles on water purification processes using NPs have been published focusing on the removal of metals (Contreras et al., 2015; Recillas et al., 2010; Sánchez et al., 2011; Xu and Zhao, 2007) or nutrients (Abo Markeb et al., 2016a; Abo Markeb et al., 2016b; Choe et al., 2000; Sá et al., 2009). This shows the potential of nanotechnology to remove contaminants. Only recently, certain nanomaterials, namely the metal-organic frameworks (MOFs), have achieved satisfactory CO_2

removal capacities at low concentrations (Bhatt et al., 2016; Shekhah et al., 2014).

1.3. Gaps in knowledge and objectives

Recently, there have been studies on the use of nanomaterials (i.e. carbon nanotubes (CNTs) and amine functionalized nanotubes) to remove CO_2. The comparison of those materials with traditional commercial adsorbents, such as active carbon and zeolite, suggests that these nanomaterials are good candidates to capture CO_2 (Li et al., 2011; Lu et al., 2009). In addition, there is limited work on the use of inorganic NPs to remove and recycle CO_2. There are even scarcer reports on the removal of other GHGs such as N_2O, CH_4 or fluorinated compounds. For these reasons, it is necessary to systematize the studies on different types of NPs and nanomaterials under the same operating conditions, and to investigate their ability to adsorb at different reaction conditions and their potential for reuse to reduce processing costs.

The use of nanoparticles as sorbent materials for GHG capture has only recently attracted the interest of researchers. Therefore, this review aims to discuss the current research status on the use of such nanomaterials for the sorption of CO_2 and CH_4 and to make a comparison with conventional sorption materials.

2. Conventional and novel adsorbents for CO_2 and CH_4 capture

2.1. Conventional adsorbents

Adsorption of a gas onto a solid surface (adsorbent) can be defined as the gain of one or more constituents of the gas (adsorbate) in the gas-solid interface (Solar et al., 2010). CO_2 capture using solid adsorbents is considered one of the most promising technologies for CCS (Figueroa et al., 2008). Adsorption can reduce energy and cost of the capture or separation of CO_2 in post-combustion capture technologies (Solar et al., 2010). However, the success of this approach depends on the development of easily recoverable and durable adsorbents with high CO_2 selectivity and adsorption capacities (Songolzadeh et al., 2012).

The most common conventional CO_2 adsorbents are natural zeolites, activated carbon and alkali-based metal materials. Table 1 shows the main characteristics, key strengths and main drawbacks of the aforementioned three groups.

2.2. Novel adsorbents

There is a huge interest in the development of advanced adsorbent materials that present better features than the conventional materials and have specialized functionalities for each pollutant (Li et al., 2013). These novel sorbents are i) ionic liquids, and ii) modified porous supports.

2.2.1. Ionic liquids for CO_2 removal

Ionic liquids (IL) are solvent sorbents that are based on a stable liquid composed by a combination of inorganic or organic anions and large organic bulky asymmetric cations (Han et al., 2012). Due to their thermal stability, negligible vapor pressure, tunable physico-chemical characteristics and high CO_2 solubility, IL are utilized in CO_2 removal applications (Park et al., 2015). Furthermore, modification of IL with functional groups (Bates et al., 2002) to better adsorb and solubilize CO_2 has been developed. For instance, Galán Sánchez et al. (2007) functionalized ILs with an amine group or a hydroxyl functional group and successfully enhanced their performance for CO_2 capture at room temperature and pressures up to 1 MPa compared to the non-functionalized ionic liquids (Lee et al., 2012).

The high CO_2 solubility in ionic liquids, when compared to CH_4, gives them the potential to be utilized in the separation of CO_2 from natural gas (Ramdin et al., 2015). Some other studies have demonstrated the potential of different ionic liquids to remove CO_2 from natural gas based on the CO_2/CH_4 solubility and selectivity. However, those studies had been based on Monte Carlo simulations (Ramdin et al., 2015).

2.2.2. Modified porous supports

Zeolite-templated N-doped carbons exhibit a high CO_2 uptake capacity in comparison to carbonaceous or inorganic and organic porous materials. Their sorption capacity can reach up to 304.5 mg/g at 273 K and ambient pressure, or up to 192.7 mg/g at 298 K and ambient pressure. Considering their excellent recyclability and regeneration stability, as well as their high selectivity for CO_2, the N-doped zeolite-templated carbons are among the most promising solid-state adsorbents for CO_2 capture and storage (Xia et al., 2011). Fig. 1 shows the effect of the N-

Table 1
Summary of characteristics of conventional adsorbents for CO_2 and CH_4.

Sorbent	CO_2 adsorption capacity (mg CO_2/g sorbent)	CH_4 adsorption capacity (mg CH_4/g sorbent)	Experimental conditions	Process scale	Key strengths	Main drawbacks
NaXzeolite (Li et al., 2013)	263	50.7	0.1 MPa, 303 K	Lab scale	• Good adsorption kinetics	• Impurities
Zeolite 5A (Saha et al., 2010)	222.7	143.1	1.4 MPa for CO_2, 10 MPa for CH_4, 298 K	Lab scale	• Good performance at mild conditions	• Elevated temperatures for regeneration
Zeolite 13X (Cavenati et al., 2004)	324.37	91.50	3.2 MPa for CO_2, 4.7 MPa for CH_4, 298 K	Lab scale		
Activated carbon (MAXSORB) (Cheng-Hsiu et al., 2012; Himeno et al., 2005)	1408	224	3.2 MPa for CO_2, 4.6 MPa for CH_4,273 K	Lab scale	• High thermal stability. • Good adsorption kinetics. • Cheap raw material • Large adsorption capacity at elevated pressures. • Easy regeneration	• Low capacity at mild conditions • Low selectivity • Impacted by NOx, SOx.
K_2CO_3/TiO_2 (Lee et al., 2006)	119	–	0.1 MPa, 333 K	Lab scale	•Enhancement of regeneration capacity compared to other oxide based sorbents	• Lower capture capacity than other oxide based sorbents
Alkali based Li_2ZrO_3 (Ochoa-Fernández et al., 2005)	220	–	Patm, 873 K	Lab scale & simulation	• Unique thermal stability • 20 absorption/regeneration cycles • Small volume change during cycles	• Slow absorption kinetics

Patm: atmospheric pressure.

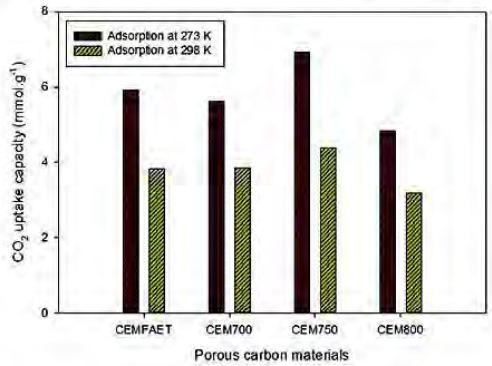

Fig. 1. CO_2 uptake capacity using porous carbon materials templated from zeolite [where CEMFAET is the free N-sample, and CEM700, CEM750, and CEM800 are the N-doped samples prepared at chemical vapor deposition temperatures of 700, 750, and 800 °C, respectively] (Xia et al., 2011).

doping samples on the CO_2 uptake capacity at 273 K, and 298 K and at 0.1 MPa (adapted from Xia et al., 2011).

HZSM-5 zeolites modified with Zn^{2+} ions (1.9 wt%), (i.e. ZnZSM-5), were tested for methane adsorption at room temperature at different equilibrium pressures (Kazansky et al., 2004). Methane adsorption by ZnZSM-5 did occur at the distantly separated zinc ions.

On the other hand, the use of waste for the synthesis of materials as adsorbents is a recent research area. For instance, the CO_2 capture process by zeolites synthesized from paper sludge and scrap glass has been recently reported (Espejel-Ayala et al., 2014). Zeolite analcime showed higher CO_2 sorption capacity (74.71 mg/g) at 320 K than the commercial zeolite ZSM-5 at the same conditions (Espejel-Ayala et al., 2014).

There have been many attempts to add amine-based functional groups on different original supports to improve CO_2 capture capacities. It is reported that CO_2 capture capacities of the modified sorbent have been successfully increased. For instance, Przepiorski et al. (Przepiórski et al., 2004) used NH_3-treated CWZ-35 activated carbon to adsorb CO_2 and obtained a sorption capacity of 76 mg/g. Kim et al. measured a CH_4 adsorption capacity of 85 mg/g on a multi-walled carbon nanotube (MW-CNT) preloaded with water at 10 MPa and at 275 K (Kim et al., 2008). Son et al. impregnated KIT-6 silica adsorbent with polyethylamine (PEI) and measured a CO_2 capacity of 135 mg/g (Son et al., 2008).

Regarding CH_4, Lee et al. tested phenol-based activated carbon for its adsorption and measured a sorption capacity of 128.9 mg/g at 3.5 MPa and at 193.15 K (Lee et al., 2007). Zhou et al. obtained a CH_4 adsorption capacity of 85 mg/g on an MW-CNT preloaded with water at 10 MPa and 275 K (Zhou et al., 2005).

Table 2 shows the main characteristics, key strengths and main drawbacks of the aforementioned novel materials for CO_2 and CH_4 sorption.

In summary, although new materials and techniques are being developed, several challenges are still to be overcome, in particular with regard to methane sorption. Therefore, CO_2 and CH_4 storage becomes a new motivation to develop novel materials. In fact, advances in nanoscale science and engineering are providing unprecedented opportunities to develop more cost effective and environmentally acceptable gas purification systems, since it is preferable to have a low-cost, widely available raw material and a simple synthesis process to develop a gas removal system (Songolzadeh et al., 2012).

3. Nanomaterial based CO_2 and CH_4 capture systems

Many of the sorbent materials presented here have a natural origin and their uses and properties are known for centuries. It has been during the last 50 years, however, that researchers focused their efforts on

Table 2
Summary of characteristics of novel adsorbents for CO_2 and CH_4.

Sorbent	Maximum CO_2 capacity (mg CO_2/g sorbent)	Maximum CH_4 capacity (mg CH_4/g sorbent)	Experimental conditions	Process scale	Key strengths	Main drawbacks
Zeolites N-doped C (Xia et al., 2011)	304.5	–	0.1 MPa, 273 K	Lab scale	• High selectivity for CO_2 • Excellent recyclability and regeneration stability • Ease of preparation	• Low content of N could not determine the interaction of CO_2 and carbon material
	192.7	–	0.1 MPa, 298 K	Lab scale		
Zeolite (analcime) (Espejel-Ayala et al., 2014)	74.71	–	0.101 MPa, 323.1 K	Lab scale	• Can be used in the purification of gas. • Production of energy without increasing atm. CO_2 concentrations	• Leaching of calcium in the treatment of PSA. • Costly using synthesized zeolite. • Emission of GHGs
Phenol based activated carbon (Lee et al., 2007)	–	128.90	3.7 MPa, 293.1 K	Lab scale & simulation	• Production of monolith using RP-20 • Increase the adsorption capability of methane on a volume basis	• Low surface area and high packing density using monolith on a mass basis
MW-CNT preloaded with H_2O (Zhou et al., 2005)	–	85	10 MPa, 275 K	Lab scale	• Five times higher sorption capacity than dry CNT	• Limited surface area and pore volume to use CNT as energy carriers
NH_3-CWZ-35 activated carbon (Przepiórski et al., 2004	76.0	–	0.1 MPa, 309.1 K	Lab scale	• High stability of N-containing groups used for CO2 adsorption.	• High temperatures of ammonia treatment (200 °C–1000 °C). • Formation of cyanide groups.
NH_2 functionalized mesoporous silica (PEI50%-KIT-6) (Kim et al., 2008)	78.8	–	298 K	Lab scale	• Strong and simple introduction of amine groups using anionic surfactants. • Success for 10 adsorption-desorption cycles	• High temperatures of ammonia treatment (200 °C–1000 °C). • Formation of cyanide groups.
KIT-6-PEI 50 mesoporous silica (Son et al., 2008)	135	–	348 K	Lab scale	• Fastest response time • Success for 3 adsorption-desorption cycles	• Information of the meaningful textural properties cannot be obtained from the N_2 adsorption–desorption isotherms for PEI loadings.

the development of novel materials with engineered features in the nano-range (Fox-Rabinovich and Totten, 2006). Due to their small size and high surface area per unit volume or mass, nanomaterials show unique electric, magnetic, optical, structural, mechanical, and chemical characteristics that are already exploited in a large number of industrial and consumer products (Royal Society and Royal Academy of Engineering, 2004). In this context, the high adsorption capacity of nanomaterials has been demonstrated in several cases.

Nanomaterials have a number of physicochemical properties that make them particularly attractive as separation supports for gas purification and gas capture. One is the ability to be functionalized with different compounds (such as surfactants) so that to enhance their affinity towards target molecules (Buzea et al., 2007). In addition, their size makes their surface especially reactive and their nature provides them with an extra stability and robustness intended for many uses and an easiness of use (Buzea et al., 2007). Gas treatment with nanoparticles (NPs) can be considered an attractive field. Hence, the occurrence of this phenomenon in gas-solid interactions is a major focus of nanotechnology research today (Fernández-García et al., 2006).

Novel nanomaterials, like advanced nanoporous materials, MOFs and porous organic polymers, have received considerable attention in adsorption storage applications due to their exceptionally high surface areas and their chemically-tunable structures (Gadipelli and Guo, 2015). Some of these materials have been tested for CH_4 and CO_2 adsorption and have gained increased interest recently. In fact, several research papers have reported improved CO_2 sorption and, more interestingly, improved CH_4 adsorption capacity compared to conventional sorbents. In particular, MOFs were the ones that exhibited the highest adsorption (Saha et al., 2010). Fig. 2 shows different MOFs used to capture CO_2 and CH_4.

In Fig. 3, Mason et al. studied different MOFs and compared the effects of the volumetric and gravimetric adsorption on CH_4 uptake (Mason et al., 2014).

A bibliography search (Web of Knowledge) using the keywords "nanomaterials" and "CO_2 capture" detected 20 publications from 2007 to 2016; 8 of them were related to this study and are discussed later on. A similar search for "CH_4 capture" detected 8 publications. The majority of those studies were based on simulations, rather than on experimental work, demonstrating a promising research opportunity using experimental work.

Among all the nanomaterials used for CO_2 or CH_4 capture, this review focuses on the most significant ones, namely: 1) Nanosized Zeolites; 2) Mesoporous Silica NPs; 3) MOFs and derived MOFs with embedded NPs; 4) Metal and Metal Oxide NPs (MNPs and MONPs), and 5) Carbonaceous nanoadsorbents.

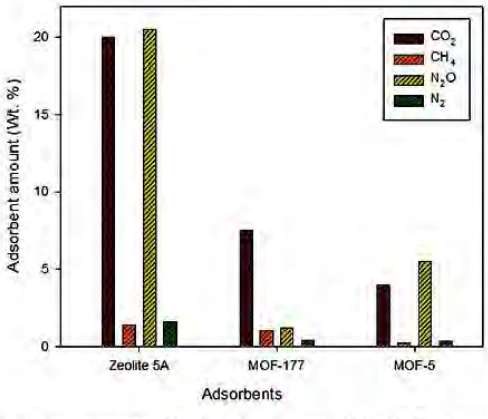

Fig. 2. Adsorption capacities of CO_2, CH_4, N_2O, and N_2 using MOF-5, MOF-177, and zeolite 5A at 298 K and 0.1 MPa (Saha et al., 2010).

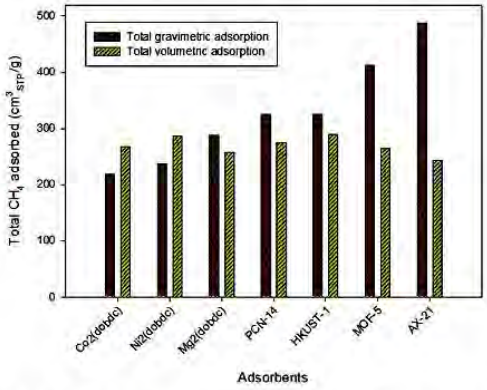

Fig. 3. Comparison of the total gravimetric and total volumetric adsorption capacities of CH_4 at 10 MPa and at 298 K.
(Adapted from Mason et al., 2014).

3.1. Nanosized zeolites versus conventional zeolites

Zeolites are 3-dimensional highly ordered porous crystalline aluminosilicates that contain alkali and alkaline earth elements (usually, Na^+, K^+ and Ca^{2+}). Zeolites have been used in the petroleum refining industries for many decades as ion exchangers, adsorbents and selective catalysts (Yang and Xu, 1997). The key characteristics of zeolites that are of interest for adsorption processes, such as the separation of CO_2 from air, include molecular pore size distribution, polarity, reversibility, selectivity and adsorption capacity. Their high adsorption capacity at ambient temperatures and pressures, and their uniform molecular-sized pores (3–8 Å) (Flanigen, 1991) give zeolites their high molecular sieving property. Zeolites have a high affinity towards polar molecules such as H_2O and CO_2 (Flanigen, 1991). Zeolites favour CO_2 adsorption, but they show significant decreases in sorption capacity at elevated temperatures and humid conditions. Adsorption capacities at mild operating conditions range from 4 to 300 mg CO_2/g zeolite. Although zeolites adsorb gases physically, it has been found that part of the CO_2 does irreversibly chemisorb on the zeolite surface in the form of carbonates and carboxylates, which complicates desorption. Despite that, complete regeneration of zeolites can be accomplished using a temperature swing system at temperatures around 620 K (D'Alessandro et al., 2010; Lee et al., 2008).

Further development needs to be done on the modification of zeolites in the nanoscale range to improve CO_2 adsorption. Unfortunately, few studies of nanocrystalline zeolites for CH_4 adsorption exist. The T-type zeolite is an intergrowth-type zeolite with an effective pore size of 0.36 nm × 0.51 nm. This is smaller than the molecular size of N_2 (0.364 nm) and CH_4 (0.38 nm) and larger than the molecular size of CO_2 (0.33 nm) (Jiang et al., 2013). T-type zeolite NPs were synthesized and resulted in an 176 mg CO_2/g adsorption capacity, which was 30% higher than that of the micro-level T-type zeolite at 288 K and 0.1 MPa (Jiang et al., 2013).

Zeolite NaA nanocrystals with a size of 100 nm presented a high CO_2 uptake capacity (220 mg/g at 293 K at 0.1 MPa) (Shakarova et al., 2014).

All-silica zeolite deca-dodecasil 3R (DD3R) is a silica based-membrane composed by dodecasil 3R (clathrasil with zeolite properties) (Gies et al., 1982) and a pore size of 0.36 × 0.44 nm (Auerbach

et al., 2003). The reported adsorption isotherms of all-silica DD3R for CO_2 and CH_4 were 27 mg CH_4/g and 123 mg CO_2/g at 298 K, respectively (Himeno et al., 2007).

3.2. Mesoporous silica nanoparticles

Mesoporous silica nanoparticles (MSNs) is a recent development in material science. They were synthesized in 1990 by researchers in Japan and were later produced at Mobil Corporation laboratories (Kresge et al., 1992). Later on, Kruk et al. developed silica NPs with a hexagonal array of pores up to 30 nm, named SBA-15 (Kruk et al., 2000). An ordered mesoporous carbon, synthesized with the SBA-15 as a template, showed a high adsorption capacity of 412 mg CH_4/gC at 275 K and at pressures < 7 MPa at the presence of water. This sorption capacity is 31% higher than the largest sorption capacity measured in activated carbon at the presence of water (Liu et al., 2006).

A novel high efficiency solid nanocomposite sorbent for CO_2 capture has been developed based on oligomeric amine (PEI) functionalized mesoporous silica capsules, which exhibit high capture capacities of up to 347 mg CO_2/g under simulated flue gas conditions (Qi et al., 2011). This material is inexpensive, easy to recover and useful in high concentration streams (Meth et al., 2012).

Atriamine-grafted pore-expanded mesoporous silica (MCM-41; TRI-PE-MCM-41) was recently investigated. It exhibited a CO_2 capacity twice higher than that of Zeolite 13X (i.e. 112.6 mg/g at 298 K). However, the methane adsorption capacity for this material was low (Belmabkhout et al., 2009).

These findings indicate that acidic gases (CO_2) can be successfully separated from CH_4-containing mixtures (i.e. natural gas and biogas).

3.3. Metal organic frameworks (MOFs) with embedded nanoparticles

MOFs are an emerging class of nanoporous crystalline structures composed of central cation molecules linked together by organic linkers to form a 3D structure. MOFs are getting attention due to their application in separation, catalysis, nonlinear optics, and gas storage (Hafizovic et al., 2007). They have a broad flexibility and variety in shapes, geometries and functionalities, and present a high selectivity and capacity in the adsorption of gases, due to the tunable size of their particle pores (Huang et al., 2003). However, they have poor adsorption capacities at low CO_2 partial pressures (Bloch et al., 2013).

Several modifications have been performed on MOFs to enhance their adsorption capacity. Some strategies are based on functionalizing the pore-surface with amines, creating accessible metal sites (Xiang et al., 2011), exposing Lewis base sites and exchanging counter ions included in the charged framework (Hong and Suh, 2012). All these tunable properties open a promising field of research in the study of MOFs to store gases. For instance, Millward and Yaghi measured CO_2 adsorption on various Zn-based MOFs and found that MOF-177, a framework consisting of a Zn_4O_6 cluster and 1,3,5-benzenetribenzoate (BTB) ligands, can adsorb 1452 mg/g of CO_2 at 4.5 MPa and at room temperature. This is higher than that of MOF-5 ($Zn_4O(BDC)_3$, 1,4-benzenedicarboxylate, BDC), which was 479.8 mg/g and of those of other porous materials (Millward and Yaghi, 2005). The same trend was reported with regard to the adsorption of CH_4 by the two MOFs; the CH_4 adsorption capacity of MOF-5 was 171.5 mg/g and 220.3 mg/g for MOF-177 (Saha et al., 2010).

Other examples are the isostructural M_2(dhtp) MOFs [M: open metal; dhtp: $C_8H_2O_6$)], which have high densities of open metal sites in their crystal structures providing an exceptionally high adsorption capacity. Among the various MOFs, the recorded CH_4 adsorption capacities are 283.4 mg/g for Ni_2(dhtp) and 363 mg/g for Mg_2(dhtp) (Wu et al., 2009a).

On the other hand, zeolite imidazolate frameworks (ZIFs), a subclass of MOFs, have emerged as a novel type of crystalline porous materials, which combines highly desirable properties from both zeolites and MOFs, such as microporosity, high surface areas, and exceptional thermal and chemical stability. In particular, ZIF-8 (1,6,7 zeoliticimidazolate framework-8) has been investigated as a potential gas storage medium (CO_2, H_2, and acetylene). At 0.1 MPa and room temperature, the ZIF-8 crystals adsorbed 14 times more CO_2 than CH_4 (Venna and Carreon, 2010). In addition, amino-functionalized Zr-MOF (amino-Zr-MOF) showed good CO_2 and CH_4 absorption behavior. The CO_2 adsorption capacity on amino-Zr-MOF was 396 mg/g at 0.988 MPa and at 273 K, while CH_4 adsorption capacity was 59.2 mg/g at 0.900 MPa and 273 K (Abid et al., 2013).

In the specific case of the CH_4 adsorption, Eddaoudi et al. reported that a new material, namely IRMOF-6, which is based on isoreticular metal-organic frameworks, presented the advantage of higher crystallinity over activated carbon. IRMOF-6 exhibited a high CH_4 uptake equal to 409 mg/g at 3.5 MPa, based on physical adsorption (Düren et al., 2004), as measured experimentally.

It is worth mentioning that some researchers determined the CH_4 locations and orientations in MOFs. Upon methane loading, the MOFs first attracted the gas adsorbents onto the strongest and primary binding sites (i.e. the organic linkers or metal clusters in, for instance ZIF-8 and MOF-5, respectively) and this molecular interaction fully defined the methane molecular orientation. Hence, these sites are essential for an ideal MOF to store methane (Wu et al., 2009b).

Other strategies have been investigated to construct the targeted MOFs, such as the employment of highly aromatic pillars that can enhance the stability of the material and increase CH_4 uptake through favorable $\pi\cdots CH_4$ electronic interactions. These interactions could be further enhanced by functionalizing the aromatic rings with methyl groups in the presence of Co^{2+}, Cu^{2+}, and Zn^{2+}. The inducement of the CH_4-framework interaction enhancement can lead to the increase of the total CH_4 storage capacity. The Cu-tbo-MOF-5 showed excellent structural stability and methane sorption capabilities compared to HKUST-1. CH_4 adsorption measurements revealed that Cu-tbo-MOF-5 exhibits high volumetric storage capacities (Spanopoulos et al., 2016).

Overall, it seems that MOF-177 has been the material with the highest adsorption capacity for CO_2 and CH_4. That is, MOF-177 can be the adsorbent of choice for removing CH_4 from air with an adsorption capacity at 220 mg/g at 298 K and at 10 MPa (Llewellyn et al., 2008; Saha et al., 2010). Also, the comparison of the volumetric capacity of MOF-177 with that of the current benchmark materials, namely Zeolite 13X and MAXSORB (Table 1), showed that MOFs represent a new direction for removing CO_2 and CH_4 in exhaust gases (Millward and Yaghi, 2005). However, it is not easy to compare all those nanomaterials for their efficiency to capture both CO_2 and CH_4 given that the pressure and temperature experimental conditions were different in all cases.

Furthermore, one of the problems of the application of MOFs in packed bed columns is that their crystals are difficult to compress into larger pellets which is usually required to limit the pressure drop over the adsorption column or the catalytic reactor (Finsy et al., 2009). Although most MOF materials show relatively good CO_2 and CH_4 uptakes, their CO_2 and CH_4 adsorption capacities can be enhanced by using nanomaterial-modified MOFs; for instance, through the incorporation of carbon nanotubes (CNTs) (Khdary and Ghanem, 2012; Xiang et al., 2011).

3.4. Metal and metal oxide nanoparticles (MNPs and MONPs) versus alkali-metal based absorbents

Alkali-metal based adsorbents are alkali metal carbonates immobilized onto inorganic supports, such as solid silica, zirconia, ceramics and alumina (Duan et al., 2011). Chemically, CO_2 adsorption is achieved by reaction with moisture (carbonation), and desorption is performed through decarbonation (Lu et al., 2006). Two alkaline-earth metal oxides (CaO and MgO) have attracted special attention because of their accessibility and favorable thermodynamics. This is particularly true for CaO because it has a high CO_2 adsorption capacity (Feng et al.,

2006) and a high raw material availability (e.g. limestone) at a rather low cost. However, in general, the long-term stability and performance of alkali metal-based sorbents under actual flue gas conditions remains to be established (Songolzadeh et al., 2012). Recently, Li-, Na- and K-based silicates or zirconates also gained interest due to their high CO_2 absorption capacities (Kumar and Saxena, 2014). Two examples of the materials used in this technique with a high CO_2 capture potential are the Li-based zirconate (Li_2ZrO_3) and the Li-based silicate (Li_4SiO_4). Li_2ZrO_3 showed an excellent CO_2 sorption capacity (220 mg/g, Table 1) (Ochoa-Fernández et al., 2005). On the contrary, they present problems with long term stabilities (Pfeiffer, 2010). No literature has been found so far on the use of this technology on methane adsorption.

Another important issue is the study of post-combustion treatment from the point of view of Life Cycle Assessment (LCA). To our knowledge, there is limited work on this topic. Several studies have proved that CO_2 sorption in liquid materials presents up to a 10-fold increase in the toxic impact to freshwater ecosystems and a minor increase in the toxic impact to terrestrial ecosystems when compared to solid based adsorption technologies (Veltman et al., 2010). In a more generic work, Nie et al. presented a comparative life cycle assessment of alternative CO_2 capture technologies after a combustion process. In most cases, the capture of CO_2 resulted in a reduction of the Global Warming Potential by 78.8% and 80.0%, respectively, compared to conventional plants without CO_2 capture (Nie et al., 2011). Other environmental impacts, such as Ecotoxicity, Human toxicity and Acidification, varied significantly with the different CO_2 capture routes employed.

In the case of methane, several technologies were analyzed through LCA. However, the works published were at a lab scale and have mostly used costly adsorbents and to a limited extent natural low-cost materials. For instance, Azevedo et al. presented the environmental benefits of using microporous activated carbon samples prepared from coconut shells, although no Life Cycle Assessment was specifically performed (Azevedo et al., 2007). Other studies on adsorption of CH_4 in biogas have been presented, but in this case the simultaneous adsorption of CO_2 and CH_4 hampered the interpretations of the Life Cycle Assessment results (Starr et al., 2012).

Both metal and metal oxides have been also produced in nanoporous form. Bhagiyalakshmi et al. produced mesoporous MgO using mesoporous carbon obtained from SBA-15 as a template, and obtained a CO_2 adsorption capacity of 80 mg/g at 298 K (Bhagiyalakshmi et al., 2010). However, in general, the adsorption capacities of MgO-based systems are usually small (<15 wt%), and, therefore, strategies to improve those capacities are desirable (Wang et al., 2011).

CaO is another material that was developed in nano-hollow structured. Absorption capacity of CaO nanopods (770 mg CO_2/g) was apparently higher than commercial CaO (532 mg CO_2/g) (Lee et al., 2012; Yang et al., 2009).

Other nanomaterials reported, i.e. hydroxylated Fe_2O_3, y-$Al_2O_3$and TiO_2NPs, have been tested for CO_2 adsorption at 296 K. In addition, the different species of CO_2 formed on the oxide surface of the different nanomaterials were analyzed. Bicarbonate was the most abundant species adsorbed on Fe_2O_3 and γ-Al_2O_3 NPs, whilst bidentate carbonate was adsorbed on TiO_2 NPs (Baltrusaitis et al., 2011; Lee et al., 2012). Moreover, activated carbon was used to enhance the surface area of metal oxides, which are mainly responsible for physical adsorption. Fe_2O_3 supported on activated carbon was used for CO_2 adsorption at 298 K and exhibited an adsorption capacity of 115.2 mg/g. The CO_2 adsorption mechanism is based on the initial adsorption of CO_2 molecules by the empty pores of activated carbon followed by the adsorption using the activated carbon pores filled with Fe_2O_3. Thus, the mechanism is based on physisorption in addition to the chemical interaction on the Fe_2O_3 surface as carbonate complexes (Hakim et al., 2015).

γ-Al_2O_3 does not show any affinity for CO_2 below 673 K, whereas K_2CO_3-promoted γ-Al_2O_3 has a CO_2 adsorption capacity of 12 mg/g at 22 wt% K_2CO_3 loadings (Walspurger et al., 2008).

3.5. Carbonaceous nano-sorbents versus conventional carbonaceous sorbents

Carbonaceous adsorbents have been widely used for CO_2 capture or storage due to their wide availability, low cost, electrical and heat conductivity, high thermal and chemical stability and low sensitivity to moisture (Cheng-Hsiu et al., 2012). However, the weak CO_2 adsorption of carbonaceous materials in a range of 323–393 K leads to high sensitivity in temperature and relatively low selectivity in operation. Carbonaceous materials have a limited application in high pressure gases as well (Sevilla et al., 2011).

Activated carbon adsorption capacity depends on the textural properties and surface groups of the carbon-based adsorbents. Generally, adsorption capacities for activated carbon at mild operating conditions (0.01–0.1 MPa CO_2 and 295–345 K) range between 3 and 154 mg CO_2/g activated carbon (D'Alessandro et al., 2010; Lee et al., 2008). This is slightly lower than that of zeolites under similar operating conditions (Table 1). Himeno et al. reported a systematic study of the adsorption of CO_2 on several Activated Carbons at temperatures ranging from 273 to 333 K and at pressures up to 6 MPa. They concluded that activated carbon MAXSORB had the highest adsorption capacity (1408 mg CO_2/g) at 3.2 MPa and 273 K) (Himeno et al., 2005). There are few reports on CH_4 adsorption on activated carbons. Again, Himeno et al. (2005) performed CH_4 adsorption on various kinds of commercially available Activated Carbons and reported adsorption capacities up to 224 mg/g at 4.6 MPa and 273 K.

Other modifications of activated carbon to improve their surface area and pore structure, and thus their adsorption capacity, are under research. The physical adsorbents can be modified after increasing alkalinity by chemical modification on the surface by adding basic groups, such as amino groups and metal oxides (Cheng-Hsiu et al., 2012).

Current research focuses on how to improve the CO_2 and CH_4 adsorption capacity and selectivity by using carbonaceous materials. These are the most common sorbents to adsorb CH_4 adsorption nowadays via the following mechanisms:

i) Improvement of the surface area and the pore structure of the carbonaceous adsorbents by either using different precursors or by fabricating different structures such as ordered mesoporous carbon, single-wall carbon nanotubes, multi-walled CNT (MW-CNTs), graphene, etc.

ii) Modification of the activated carbons with Metal Oxide NPs or other nano-compounds.

CNTs, carbon nanofibers, carbon nanospheres, nanodiamond and fullerene have been progressively used due to their excellent physical, chemical and electronic properties. More specifically, graphene, as a new member of carbon-based materials, has emerged as a promising nano-platform with enormous potential for research in various fields (Wang et al., 2013).

Regarding carbonaceous materials, this review focuses on: nanoporous carbon materials, carbon nanotubes and graphene-based nanomaterials.

3.5.1. Nanoporous carbon-based materials

Since promising adsorption results for CO_2 capture by mesoporous carbon materials have been reported, a series of nanoporous carbon materials of tunable mesopore size have been synthesized (i.e. CMK-1, CMK-3 and CMK-5). These are quite promising materials for the storage of natural gas due to: large pore volume, high specific surface area, high thermal stability, high chemical stability, high mechanical stability, and ordered pore structure. The sorption isotherms of CH_4 in the synthesized CMK-3-1.25 sample at 275 K of both the dry and wet samples showed that the highest sorptive capacity at 112.3 mg/g was reached at 9.03 MPa on dry samples (Liu et al., 2006).

3.5.2. Carbon nanotubes (CNT)

Carbon nanotubes (CNT) are the most famous among nano-hollow structured materials with dimensions ranging from 0.8 to 2 nm in

diameter and from <100 nm to several cm in length (De Volder et al., 2013). The enrichment of CH_4 using different types of CNTs in a mixture of gases that initially contained CH_4, CO_2 and H_2S has been reported. In general, CO_2 is preferentially adsorbed onto CNTs more than either CH_4 or H_2S (Esteves et al., 2008). However, Zhou et al. investigated the adsorption of CH_4 on dry and water-loaded MW-CNT with good results, and reported a CH_4 uptake of 80 mg/g at 10 MPa and at 275 °K (Zhou et al., 2005).

Furthermore, CNTs have been investigated and used as composite fillers for various applications (Zhu et al., 2013). In particular, CNTs can be an effective additive to improve the kinetics of gas storage materials (Yoo et al., 2014). For instance, MW-CNTs@JUC32 nanocomposites (i.e. MOFs NPs synthesized in situ on MW-CNTs) showed enhanced adsorption for CO_2 and CH_4. The CO_2 and CH_4 uptake for MW-CNTs@JUC32 is 67.8 and 12 mg/g, respectively, at room temperature. This is 70% and 90% higher for CO_2 and CH_4, respectively, than the single MW-CNTs tested at the same conditions (Kang et al., 2015). Also, CNTs modified with 3-aminopropyl-triethoxysilane ($H_2NCH_2CH_2CH_2$-$Si(OCH_2CH_3)_3$, APTS) presented a CO_2 adsorption capacity equal to 96.3 mg/g, which is 40% higher than non-modified CNT adsorbents (Lu et al., 2008).

However, in most of the cases, the few reports regarding CH_4 adsorption on CNTs-based materials, although promising, are still based on conceptual models (Tanaka et al., 2002; Zhang and Wang, 2002) and mathematical simulations. CNTs are ideal templates onto which NPs can be immobilized, allowing the construction of designed nano architectures that are extremely attractive as supports for heterogeneous catalysts (Nhut et al., 2002).

3.5.3. Graphene

Graphene is an ideal two-dimensional material and single-atom layer of graphite, and has attracted increasing interests in multidisciplinary research because of its unique structure and exceptional physicochemical properties (Wang et al., 2013). Therefore, there have been multiple reports on the structure, chemistry and the use of graphene, but very few on environmental concerns (Kemp et al., 2013). It is known that graphene-based materials can offer a large potential for environmental remediation and energy applications. This is due to their tremendous adsorption capacity and the excellent catalytic performances, especially during removal of pollutants from water, during gas upgrading and purification, and during hydrogen generation and storage (Wang et al., 2013). Graphene, like other carbon-based materials, is lighter and cheaper to produce than other solid-state gas adsorbent materials (D'Alessandro et al., 2010; Schlapbach and Zuttel, 2001). For instance, nanoporous graphene materials have been applied as sorbents for CO_2 sequestration, biogas upgrading, SO_2 pollution control, and air dehumidification. In those processes, the physisorption of gas on the surface depended on the electrostatic and dispersion interactions with adsorbates (Gadipelli and Guo, 2015).

Graphene has been modified with different compounds to enhance its properties. Ning et al. produced nanomesh graphene (NMG) with porous MgO layers which present great storage capacities for CH_4 and CO_2 (Ning et al., 2012). Also, the preparation of Mg–Al Layered double hydroxides (LDHs) onto negatively charged graphene oxide (GO) has been reported (Garcia-Gallastegui et al., 2012). The inclusion of GO (7 wt%) led to an enhancement in adsorption capacity, which was 2.5 times higher than that of the pure LDH (62% at 573 K and $P(CO_2) = 0.02$ MPa). In addition, it led to stability upon recycling and increased the active/effective LDH surface area (Kemp et al., 2013).

Although it has been shown that graphene-based materials can be utilized as adsorbents for gas storage, the majority of the studies are based on conceptual models. Among them, it is worth to mention the study reported by Liu et al., which has shown that graphite defect sites can react with CH_4 (Liu et al., 2012). This study showed that a CH_4 molecule is activated at certain mono-vacancy sites on the graphite surface. This activation can lead to chemisorption that occurs as the CH_4 ruptures into CH_2 and 2H which then chemisorb at the vacancy sites. Furthermore, graphene materials could also be non-covalently decorated with MNPs (e.g., Au, Ag, Pt, Ni, Ru) through different synthetic procedures such as in situ reduction, electro-deposition, or thermal evaporation (Wang et al., 2016). However, they have not been yet widely used for CO_2 or CH_4 adsorption but for hydrogen storage and catalysis (Huang et al., 2011; Wang et al., 2012).

The sorption of gas-phase molecules on the surface of graphene-based materials strongly depends on the electrostatic attraction, dispersion interactions, van der Waals interactions or charge transfer (Du et al., 2011; Leenaerts et al., 2008; Leenaerts et al., 2009; Wang et al., 2013).

Overall, Table 3 shows a summary of the most representative nanomaterials for CO_2 and CH_4 sorption.

In summary, the Fe_3O_4-graphene and the MOF-117 based NPs have the greatest CO_2 sorption capacities among all materials tackled in this review. Among all adsorbents for CH_4 capture, IRMOF-6, ordered mesoporous carbon, MOF-177 and MOF-5 have shown the highest adsorption capacities compared to the graphene-based NPs. This was due to their high thermal stability and the presence of high porosity in those materials.

4. Techno-economic views on nanomaterials as CO_2 and CH_4 sorbents

Apart from achieving high CO_2 and CH_4 capture efficiencies in the laboratory, the economic viability of the sorption processes at field scale is important. The cost of a complete CO_2 removal process includes cost of sorbents, cost of process installation and commissioning, operation and maintenance costs, additional fuel resources, and CO_2 compression, and the cost of transport and storage. To develop a sustainable CO_2 removal system, many factors should be considered such as high CO_2 capture capacity, sustainability of the sorbent throughout multiple sorption/desorption cycles and the low production cost. Thus, it is preferred to have a low-cost, widely available raw material and a simple synthesis process. For instance, lithium salts have been reported to be good sorbents for CO_2 removal. However, the high price of the pertinent raw materials makes them unattractive compared to other metal salts. According to Abanades et al. (2004), the cost of lithium carbonate (Li_2CO_3) was $4.47 per kg, whereas the cost of $CaCO_3$ (raw material for CaO), at the same time, was only $0.005 per kg.

Another example are the carbonaceous adsorbents. For instance, CNTs with a specialized structure are only available at extremely high prices (i.e. $5/g) compared to granular activated carbon (GActivated Carbon), which typically costs around $1/kg. Also, reusability of the captured CO_2 would also be an added advantage in order to make the CO_2 removal process economically feasible (Lee et al., 2012). Moreover, a CO_2 removal system that operates close to flue gas emission temperatures would be ideal as no extra energy would be needed.

Based on the above, the challenges are to decrease the cost of capture and to scale-up the technologies to the size required so that to minimize large-scale power generation emissions. For example, a large coal plant of 1000 MW will typically generate about 8000 tons of CO_2 per day or about 3 million tons of CO_2 per year, provided that it runs at base load. This is more than one order of magnitude larger than the capacities of existing separation technologies. From the point of view of cost, the current technologies, if applied, would cost between €20 and €50 per ton of CO_2 separated, which would increase the cost of the electricity produced by 30% for a large coal plant. Fossil fuel based power generation with CO_2 capture and storage technologies would be competitive if these costs are properly addressed and reduced (CO_2 capture, https://ec.europa.eu/research/energy/pdf/synopses_co2_en.pdf).

Nanomaterials are promising sorbents to overcome many limitations of the CO_2 capture processes. They have relatively high CO_2 capture capacities, they are reusable throughout multiple sorption/desorption cycles, and some of them have relatively low energy requirements. However, to tailor and control their sizes and dimensions,

Table 3
Summary of characteristics of nanomaterial based sorbents for CO_2 and CH_4.

Sorbent	Maximum CO_2 capacity (mg CO_2/g sorbent)	Maximum CH_4 capacity (mg CH_4/g sorbent)	Experimental conditions (P,T)	Process scale	Key strengths	Main drawbacks
DD3R nano zeolite (Himeno et al., 2007)	123	26.6	3 MPa, 273–348 K	Lab scale	• High selectivity for CO_2. • Used for biogas separation.	• At pressures higher than 2000 kPa, high-pressure data points deviate from the MSL model-fit lines.
T-type Zeolite NPs (Jiang et al., 2013)	176.4	–	0.1 MPa, 288 K	Lab scale	• Potential application in the natural gas purification process. • Recyclability • Applicability for post-combustion CO_2 separation.	• >100 h to synthesize the T-type zeolite. • Decrease of the adsorption capacities with increasing temperature from 288 to 313 K.
Zeolite NaA nanocrystals (Shakarova et al., 2014)	215.6	–	0.1 MPa, 293 K	Lab scale	• Use of a cost-effective method for the synthesis of highly active nanosized zeolites. • High adsorption capacity for CO_2.	• No expected dependence of the diffusion time constant on the square of the radius of the crystals for the CO_2 uptake.
Ordered mesoporous carbon, SBA-15 template (Liu et al., 2006)	–	412	<7 MPa, 275 K	Lab scale	• Wet material has adsorption capacity 31% higher than AC	• Long time to reach the equilibrium if the water content is higher than the critical value
PEI-mesoporous silica (Qi et al., 2011)	347.6	–	P_{atm}, 348 K	Lab scale	• Inexpensive material • Can be regenerated • Easy to operate • Fast CO_2 adsorption kinetics	• Lack of the selectivity factor for both CO_2 and H_2S
TRI-PE-MCM-41 (Belmabkhout et al., 2009)	112.6	–	0.1 MPa, 298 K	Lab scale	• Potential application in purification of biogas • Separation of biogas	• Low CH_4 adsorption
MOF-177	a) 1452 (Millward and Yaghi, 2005) b) 396.9 (Saha et al., 2010)	c) 220.3 (Saha et al., 2010)	a) 4.5 MPa, RT b) 1.4 MPa, 298 K c) 10 MPa, 298 K	Lab scale	• High thermal stability • Extra high porosity • High adsorption capacity at elevated pressures	• Negatively impacted by NOx, SOx, and H_2O. • Low selectivity in CO_2/N_2 gas streams.
MOF-5 (Saha et al., 2010)	480	171.5	1.4 MPa for CO_2, 10 MPa for CH_4; 298 K	Lab scale	• Easily tunable pore and chemical characteristics.	• Lack of experimental data on performance after multiple cycles.
Ni_2(dhtp) MOF (Wu et al., 2009a)	–	283.4	3.5 MPa, 298 K	Lab scale		• Desorption approaches have not been adequately researched. • Chemical instability upon time. • High pressures
Mg_2(dhtp) MOF (Wu et al., 2009a)	–	363	3.5 MPa, 298 K	Lab scale		
IRMOF-6 (Düren et al., 2004)	–	409	3.500 MPa, 298 K	Lab scale & simulation		
MgO/SBA-15 (Bhagiyalakshmi et al., 2010)	80	–	Patm, 298 K	Lab scale	• Thermally stable NPs. • Can be regenerated. • High selectivity to CO_2 • Can be used in different technologies applications for CO_2 separation.	• Slight decrease of surface area and pore volume.
CaO nanopods (Yang et al., 2009)	770	–	Patm, 873 K	Lab scale	• Can be regenerated during 50 cycles • Better than commercial CaO	• High temperatures
Fe_2O_3 on AC (Hakim et al., 2015)	103.7	–	Patm, 298 K	Lab scale	• Enhancement the surface area of Fe_2O_3/AC	• Decrease the adsorption capacity of CO_2 comparing to AC
MW-CNTs@JUC32 (Kang et al., 2015)	67.8	12	Patm, 273 K	Lab scale	• 70% and 90% higher than non-modified MW-CNTs • Increase the CO_2 adsorption enthalpy	
APTS-CNTs (Lu et al., 2008)	96.3	–	Patm, 298 K	Lab scale	• 40% higher than non-modified CNTs	• Lack of information on the reusability, maximum adsorption capacity, and kinetics
Fe_3O_4-Graphene (Mishra and Ramaprabhu, 2014)	2640	–	1.1 MPa, 298 K	Lab scale	• Easy synthesis • Can be reused	• High pressures
Graphene (Mishra and Ramaprabhu, 2011)	950.4	–	1.1 MPa, 298 K	Lab scale	• High adsorption capacity compared to other carbon nanostructures. • Possible use for industrial applications	• High pressures

Patm: atmospheric pressure.

synthesis of nanomaterials usually needs costly materials, while the application methods are complicated. Besides screening and identifying an ideal nanomaterial sorbent, future research should focus on designing simple and low-cost production routes for those nanomaterials. This should be followed by a scale-up and process study for the sorbent.

Regarding CH_4, the storage capacity and the adsorption/desorption cycle durability of existing adsorbents should be improved. The study

of superior adsorbents for CH_4 storage requires the implementation of techno-economical systems. So far, it is significant that a large amount of data has been collected using adsorption reactors and gas storage systems. In addition, because of the progress of nanoporous adsorbents for CH_4 storage, it is expected that improved techno-economical systems will enhance the adsorption performance of CH_4 gas. Consequently, it is expected that nanoporous carbonaceous materials for CH_4 storage will be extensively developed and used in the future (Pil-Seon et al., 2016).

In summary, although some discrete adsorption capacity values can be found for CO_2, there is a lack of rigorous technical and economical data for CH_4. This clearly hampers the implementation of such capture systems for methane at field scale.

5. Conclusions

The conclusions drawn from this review are:

- The introduction of nanomaterials for the capture of CO_2 and CH_4 is expected to be efficient due to their exceptional and unmatchable properties. Adsorbents based on porous supports, modified with amine or metals, are currently providing the most promising results in terms of sorption capacity for the aforementioned GHGs.
- The Fe_3O_4-graphene and the MOF-117 based NPs showed the greatest CO_2 sorption capacities, due to their high thermal stability and the presence of high porosity.
- Although IRMOF-6, ordered mesoporous carbon, MOF-177 and MOF-5 have shown the highest adsorption capacities for CH_4, their adsorption capacities values were low in real scale applications compared to graphene or graphene-based NPs.
- One of the main challenges is to decrease the cost of capture and to scale-up the technologies to the size required in order to address large-scale power generation emission issues and to render them CO_2/CH_4 emission free.
- Further research is needed to prove the long-term efficacy of the nanomaterials as sorbents in real scale applications. In addition, the precise mechanisms of adsorption of the GHG onto the nanoparticles need to be further elucidated and researched in future studies.

Acknowledgements

Authors wish to thank the financial support of Fundación Areces, (project Nano-GEI). Dimitrios Komilis is grateful to the TECNIOspring fellowship programme (TECSPR13-1-0006) which was co-financed by the European Union through the Marie Curie Actions and ACCIÓ (Generalitat de Catalunya). Ahmad Abo Markeb acknowledges the financial support provided by the Ministry of Higher Education of Egypt (CAM-751-FM-06-01) for his Ph.D. external mission grant.

References

Abanades, J.C., Anthony, E.J., Lu, D.Y., Salvador, C., Alvarez, D., 2004. Capture of CO_2 from combustion gases in a fluidized bed of CaO. AIChE J. 50, 1614–1622.
Abid, H.R., Shang, J., Ang, H.-M., Wang, S., 2013. Amino-functionalized Zr-MOF nanoparticles for adsorption of CO_2 and CH_4. Int. J. Smart Nano Mater. 4, 72–82.
Abo Markeb, A., Ordosgoitia, L., Alonso, A., Sanchez, A., Font, X., 2016a. Novel magnetic core-shell Ce-Ti@Fe_3O_4 nanoparticles as adsorbent for water contaminants removal. RSC Adv. 6, 56913–56917.
Abo Markeb, A., Alonso, A., Dorado, A.D., Sánchez, A., Font, X., 2016b. Phosphate removal and recovery from water using nanocomposite of immobilized magnetite nanoparticles on cationic polymer. Environ. Technol. 37, 2099–2112.
Auerbach, S.M., Carrado, K.A., Dutta, P.K., 2003. Handbook of Zeolite Science and Technology. CRC Press, Boca Raton.
Azevedo, D.C.S., Araújo, J.C.S., Bastos-Neto, M., Torres, A.E.B., Jaguaribe, E.F., Cavalcante, C.L., 2007. Microporous activated carbon prepared from coconut shells using chemical activation with zinc chloride. Microporous Mesoporous Mater. 100, 361–364.
Baltrėnaitė, E., Baltrėnas, P., Lietuvninkas, A., 2016. The Sustainable Role of the Tree in Environmental Protection Technologies. Springer International Publishing, Switzerland.
Baltrusaitis, J., Schuttlefield, J., Zeitler, E., Grassian, V.H., 2011. Carbon dioxide adsorption on oxide nanoparticle surfaces. Chem. Eng. J. 170, 471–481.
Bates, E.D., Mayton, R.D., Ntai, I., Davis, J.H., 2002. CO_2 capture by a task-specific ionic liquid. J. Am. Chem. Soc. 124, 926–927.
Belmabkhout, Y., De Weireld, G., Sayari, A., 2009. Amine-bearing mesoporous silica for CO_2 and H_2S removal from natural gas and biogas. Langmuir 25, 13275–13278.
Bhagiyalakshmi, M., Lee, J.Y., Jang, H.T., 2010. Synthesis of mesoporous magnesium oxide: its application to CO_2 chemisorption. Int. J. Greenhouse Gas Control 4, 51–56.
Bhatt, P.M., Belmabkhout, Y., Cadiau, A., Adil, K., Shekhah, O., Shkurenko, A., Barbour, L.J., Eddaoudi, M., 2016. A fine-tuned fluorinated MOF addresses the needs for trace CO_2 removal and air capture using physisorption. J. Am. Chem. Soc. 138, 9301–9307.
Birgisson, B., Mukhopadhyay, A.K., Geary, G., Khan, M., Sobolev, K., 2012. Transportation Research Circular E-C170: Nanotechnology in Concrete Materials: A Synopsis. Transportation Research Board, Washington.
Bloch, W.M., Babarao, R., Hill, M.R., Doonan, C.J., Sumby, C.J., 2013. Post-synthetic structural processing in a metal–organic framework material as a mechanism for exceptional CO_2/N_2 selectivity. J. Am. Chem. Soc. 135, 10441–10448.
Butler J.H., Montzka S.A., 2012. The NOAA annual greenhouse gas index (AGGI). NOAA Earth System Research Laboratory, R/GMD, 325 Broadway, Boulder, CO 80305-3328.
Buzea, C., Pacheco, I.I., Robbie, K., 2007. Nanomaterials and nanoparticles: sources and toxicity. Biointerphases 2, MR17–MR71.
Cavenati, S., Grande, C.A., Rodrigues, A.E., 2004. Adsorption equilibrium of methane, carbon dioxide, and nitrogen on zeolite 13x at high pressures. J. Chem. Eng. Data 49, 1095–1101.
Cheng-Hsiu, Y., Chih-Hung, H., Tan, C.S., 2012. A review of CO_2 capture by absorption and adsorption. Aerosol Air Qual. Res. 12, 745–769.
Choe, S., Chang, Y.Y., Hwang, K.Y., Khim, J., 2000. Kinetics of reductive denitrification by nanoscale zero-valent iron. Chemosphere 41, 1307–1311.
Ciferno, J.P., Fout, T.E., Jones, A.P., Murphy, J.T., 2009. Capturing carbon existing coal-fired power plants. Chem. Eng. Prog. 105, 33–41.
Cinke, M., Li, J., Bauschlicher Jr., C.W., Ricca, A., Meyyappan, M., 2003. CO_2 adsorption in single-walled carbon nanotubes. Chem. Phys. Lett. 376, 761–766.
Contreras, A.R., Casals, E., Puntes, V., Komilis, D., Sánchez, A., Font, X., 2015. Use of cerium oxide (CeO2) nanoparticles for the adsorption of dissolved cadmium (II), lead (II) and chromium (VI) at two different pHs in single and multi-component systems. Global Nest Journal 17, 536–543.
D'Alessandro, D.M., Smit, B., Long, J.R., 2010. Carbon dioxide capture: prospects for new materials. Angew. Chem. Int. Ed. 49, 6058–6082.
De Volder, M.F.L., Tawfick, S.H., Baughman, R.H., Hart, A.J., 2013. Carbon nanotubes: present and future commercial applications. Science 339, 535–539.
Doman, L.E., Smith, K.A., Mayne, L.D., Yucel, E.M., Barden, J.L., Fawzi, A.M., Martin, P.D., Zaretskaya, D.B., Mellish, M.L., Kearney, D.R., Murphy, B.T., Vincent, K.R., Lindstrom, P.M., 2010. Energy-related Carbon Dioxide Emissions: International Energy Outlook International Energy Outlook. US Energy Information Administration, Washington DC.
Du, H., Li, J., Zhang, J., Su, G., Li, X., Zhao, Y., 2011. Separation of hydrogen and nitrogen gases with porous graphene membrane. J. Phys. Chem. C 115, 23261–23266.
Duan, Y., Zhang, B., Sorescu, D.C., Johnson, J.K., 2011. CO_2 capture properties of M–C–O–H (M = Li, Na, K) systems: a combined density functional theory and lattice phonon dynamics study. J. Solid State Chem. 184, 304–311.
Düren, T., Sarkisov, L., Yaghi, O.M., Snurr, R.Q., 2004. Design of new materials for methane storage. Langmuir 20, 2683–2689.
EPA, 2016. Inventory of U.S. Greenhouse Gas Emissions and Sinks: 1990–2014. EPA 430-R-16-002. U.S. Environmental Protection Agency, Washington, DC 20460, USA.
Espejel-Ayala, F., Corella, R.C., Pérez, A.M., Pérez-Hernández, R., Ramírez-Zamora, R., 2014. Carbon dioxide capture utilizing zeolites synthesized with paper sludge and scrap-glass. Waste Manag. Res. 32, 1219–1226.
Esteves, I.A.A.C., Lopes, M.S.S., Nunes, P.M.C., Mota, J.P.B., 2008. Adsorption of natural gas and biogas components on activated carbon. Sep. Purif. Technol. 62, 281–296.
Feng, B., Liu, W., Li, X., An, H., 2006. Overcoming the problem of loss-in-capacity of calcium oxide in CO_2 capture. Energy Fuel 20, 2417–2420.
Fernández-García, M., Rodríguez, J.A., Scott, R.A. (Eds.), 2006. Metal Oxide Nanoparticles. Encyclopedia of Inorganic Chemistry. John Wiley & Sons, Ltd., USA.
Figueroa, J.D., Fout, T., Plasynski, S., McIlvried, H., Srivastava, R.D., 2008. Advances in CO_2 capture technology—the U.S. Department of Energy's Carbon Sequestration Program. International Journal of Greenhouse Gas Control 2, 9–20.
Finsy, V., Ma, L., Alaerts, L., De Vos, D.E., Baron, G.V., Denayer, J.F.M., 2009. Separation of CO_2/CH_4 mixtures with the MIL-53(Al) metal–organic framework. Microporous Mesoporous Mater. 120, 221–227.
Flanigen, E.M., 1991. Chapter 2: zeolites and molecular sieves an historical perspective. In: van Bekkum, H., Flanigen, E.M., Jansen, J.C. (Eds.), Studies in Surface Science and Catalysis. Vol. 58. Elsevier, Amsterdam, pp. 13–34.
Fox-Rabinovich, G., Totten, G.E., 2006. Self-organization During Friction: Advanced Surface-engineered Materials and Systems Design. CRC Press, Boca Raton.
Gadipelli, S., Guo, Z.X., 2015. Graphene-based materials: synthesis and gas sorption, storage and separation. Prog. Mater. Sci. 69, 1–60.
Galán Sánchez, L.M., Meindersma, G.W., de Haan, A.B., 2007. Solvent properties of functionalized ionic liquids for CO_2 absorption. Chem. Eng. Res. Des. 85, 31–39.
Garcia-Gallastegui, A., Iruretagoyena, D., Gouvea, V., Mokhtar, M., Asiri, A.M., Basahel, S.N., Al-Thabaiti, S.A., Alyoubi, A.O., Chadwick, D., Shaffer, M.S.P., 2012. Graphene oxide as support for layered double hydroxides: enhancing the CO_2 adsorption capacity. Chem. Mater. 24, 4531–4539.
Gies, H.P.F., Gibson, S.T., Blake, A.J., McCoy, D.G., 1982. The Schumann-Runge continuum of oxygen at wavelengths greater than 175 NM. J. Geophys. Res.: Space Physics 87, 8307–8310.
Hafizovic, J., Bjørgen, M., Olsbye, U., Dietzel, P.D.C., Bordiga, S., Prestipino, C., Lamberti, C., Lillerud, K.P., 2007. The inconsistency in adsorption properties and powder xrd data of MOF-5 is rationalized by framework interpenetration and the presence of organic and inorganic species in the nanocavities. J. Am. Chem. Soc. 129, 3612–3620.

Hakim, A., Abu Tahari, M.N., Marliza, T.S., Wan Isahak, W.N.R., Yusop, M.R., Mohamed Hisham, M.W., Yarmoa, M.O., 2015. Study of CO_2 adsorption and desorption on activated carbon supported iron oxide by temperature programmed desorption. Jurnal Teknologi 77, 75–84.

Han, D., Tang, B., Ri Lee, Y., Ho Row, K., 2012. Application of ionic liquid in liquid phase microextraction technology. J.Sep. Sci. 35, 2949–2961.

Himeno, S., Komatsu, T., Fujita, S., 2005. High-pressure adsorption equilibria of methane and carbon dioxide on several activated carbons. J. Chem. Eng. Data 50, 369–376.

Himeno, S., Tomita, T., Suzuki, K., Yoshida, S., 2007. Characterization and selectivity for methane and carbon dioxide adsorption on the all-silica DD3R zeolite. Microporous Mesoporous Mater. 98, 62–69.

Hong, D.H., Suh, M.P., 2012. Selective CO_2 adsorption in a metal-organic framework constructed from an organic ligand with flexible joints. Chem. Commun. 48, 9168–9170.

Houghton, J.T., Ding, Y., Griggs, D.J., Noguer, M., van der Linden, P.J., Dai, K.X., Maskell, Johnson C.A., 2001. IPCC: Climate Change 2001: The Scientific Basis. Contribution of Working Group I to the Third Assessment Report of the Intergovernmental Panel on Climate Change. Vol. 881. Cambridge University Press, Cambridge & New York, pp. 1–83.

Huang, L., Wang, H., Chen, J., Wang, Z., Sun, J., Zhao, D., Yan, Y., 2003. Synthesis, morphology control, and properties of porous metal–organic coordination polymers. Microporous Mesoporous Mater. 58, 105–114.

Huang, C.-C., Pu, N.-W., Wang, C.-A., Huang, J.-C., Sung, Y., Ger, M.-D., 2011. Hydrogen storage in graphene decorated with Pd and Pt nano-particles using an electroless deposition technique. Sep. Purif. Technol. 82, 210–215.

Jiang, Q., Rentschler, J., Sethia, G., Weinman, S., Perrone, R., Liu, K., 2013. Synthesis of T-type zeolite nanoparticles for the separation of CO_2/N_2 and CO_2/CH_4 by adsorption process. Chem. Eng. J. 230, 380–388.

Kang, Z., Xue, M., Zhang, D., Fan, L., Pan, Y., Qiu, S., 2015. Hybrid metal-organic framework nanomaterials with enhanced carbon dioxide and methane adsorption enthalpy by incorporation of carbon nanotubes. Inorg. Chem. Commun. 58, 79–83.

Kazansky, V.B., Serykh, A.I., Pidko, E.A., 2004. DRIFT study of molecular and dissociative adsorption of light paraffins by HZSM-5 zeolite modified with zinc ions: methane adsorption. J. Catal. 225, 369–373.

Kemp, K.C., Seema, H., Saleh, M., Le, N.H., Mahesh, K., Chandra, V., Kim, K.S., 2013. Environmental applications using graphene composites: water remediation and gas adsorption. Nano 5, 3149–3171.

Khdary, N.H., Ghanem, M.A., 2012. Metal-organic-silica nanocomposites: copper, silver nanoparticles-ethylenediamine-silica gel and their CO_2 adsorption behaviour. J. Mater. Chem. 22, 12032–12038.

Kim, S.-N., Son, W.-J., Choi, J.-S., Ahn, W.-S., 2008. CO_2 adsorption using amine-functionalized mesoporous silica prepared via anionic surfactant-mediated synthesis. Microporous Mesoporous Mater. 115, 497–503.

Kirschke, S., Bousquet, P., Ciais, P., Saunois, M., Canadell, J.G., Dlugokencky, E.J., et al., 2013. Three decades of global methane sources and sinks. Nat. Geosci. 6, 813–823.

Kizzie, A.C., Dailly, A., Perry, L., Lail, M.A., Lu, W., Nelson, T.O., Mei, C., Hong-Cai, Z., 2014. Enhanced methane sorption in densified forms of a porous polymer network. Mater. Sci. Appl. 5, 387–394.

Kresge, C.T., Leonowicz, M.E., Roth, W.J., Vartuli, J.C., Beck, J.S., 1992. Ordered mesoporous molecular sieves synthesized by a liquid-crystal template mechanism. Nature 359, 710–712.

Kruk, M., Jaroniec, M., Ko, C.H., Ryoo, R., 2000. Characterization of the porous structure of SBA-15. Chem. Mater. 12, 1961–1968.

Kumar, S., Saxena, S.K., 2014. A comparative study of CO_2 sorption properties for different oxides. Mater. Renew. Sustain. Energy 3, 1–15.

Lee, S.C., Choi, B.Y., Lee, T.J., Ryu, C.K., Ahn, Y.S., Kim, J.C., 2006. CO_2 absorption and regeneration of alkali metal-based solid sorbents. Catal. Today 111, 385–390.

Lee, J.-W., Balathanigaimani, M.S., Kang, H.-C., Shim, W.-G., Kim, C., Moon, H., 2007. Methane storage on phenol-based activated carbons at (293.15, 303.15, and 313.15) K. J. Chem. Eng. Data 52, 66–70.

Lee, K.B., Beaver, M.G., Caram, H.S., Sircar, S., 2008. Reversible chemisorbents for carbon dioxide and their potential applications. Ind. Eng. Chem. Res. 47, 8048–8062.

Lee, Z.H., Lee, K.T., Bhatia, S., Mohamed, A.R., 2012. Post-combustion carbon dioxide capture: evolution towards utilization of nanomaterials. Renew. Sust. Energ. Rev. 16, 2599–2609.

Leenaerts, O., Partoens, B., Peeters, F.M., 2008. Adsorption of H_2O, NH_3, CO, NO_2, and NO on graphene: a first-principles study. Phys. Rev. B 77, 125416.

Leenaerts, O., Partoens, B., Peeters, F.M., 2009. Adsorption of small molecules on graphene. Microelectron. J. 40, 860–862.

Li, J.-R., Ma, Y., McCarthy, M.C., Sculley, J., Yu, J., Jeong, H.-K., Balbuena, P.B., Zhou, H.C., 2011. Carbon dioxide capture-related gas adsorption and separation in metal-organic frameworks. Coord. Chem. Rev. 255, 1791–1823.

Li, Y., Yi, H., Tang, X., Li, F., Yuan, Q., 2013. Adsorption separation of CO_2/CH_4 gas mixture on the commercial zeolites at atmospheric pressure. Chem. Eng. J. 229, 50–56.

Liu, X., Zhou, L., Li, J., Sun, Y., Su, W., Zhou, Y., 2006. Methane sorption on ordered mesoporous carbon in the presence of water. Carbon 44, 1386–1392.

Liu, F., Chu, W., Sun, W., Xue, Y., Jiang, Q., 2012. A DFT study of methane activation on graphite surfaces with vacancy defects. J. Nat. Gas Chem. 21, 708–712.

Llewellyn, P.L., Bourrelly, S., Serre, C., Vimont, A., Daturi, M., Hamon, L., De Weireld, G., Chang, J.-S., Hong, D.-Y., Kyu, Hwang Y., Hwa, Jhung S., Férey, G., 2008. High uptakes of CO_2 and CH_4 in mesoporous metal–organic frameworks MIL-100 and MIL-101. Langmuir 24, 7245–7250.

Lu, H., Reddy, E.P., Smirniotis, P.G., 2006. Calcium oxide based sorbents for capture of carbon dioxide at high temperatures. Ind. Eng. Chem. Res. 45, 3944–3949.

Lu, C., Bai, H., Wu, B., Su, F., Hwang, J.F., 2008. Comparative study of CO_2 capture by carbon nanotubes, activated carbons, and zeolites. Energy Fuel 22, 3050–3056.

Lu, C., Su, F., Hsu, S.-C., Chen, W., Bai, H., Hwang, J.F., Lee, H.-H., 2009. Thermodynamics and regeneration of CO_2 adsorption on mesoporous spherical-silica particles. Fuel Process. Technol. 90, 1543–1549.

Mason, J.A., Veenstra, M., Long, J.R., 2014. Evaluating metal-organic frameworks for natural gas storage. Chem. Sci. 5, 32–51.

McCarthy, J.J., 2001. Climate Change 2001: Impacts, Adaptation, and Vulnerability: Contribution of Working Group II to the Third Assessment Report of the Intergovernmental Panel on Climate Change. Cambridge University Press, Cambridge, pp. 1–1005.

Meth, S., Goeppert, A., Prakash, G.K.S., Olah, G.A., 2012. Silica nanoparticles as supports for regenerable CO_2 sorbents. Energy Fuel 26, 3082–3090.

Metz, B., Davidson, O., de Coninck, H.C., Loos, M. (Eds.), 2005. IPCC Special Report on Carbon Dioxide Capture and Storage. Prepared by Working Group III of the Intergovernmental Panel on Climate Change. Vol. 442. Cambridge University Press, Cambridge, pp. 1–406.

Millward, A.R., Yaghi, O.M., 2005. Metal–organic frameworks with exceptionally high capacity for storage of carbon dioxide at room temperature. J. Am. Chem. Soc. 127, 17998–17999.

Mishra, A.K., Ramaprabhu, S., 2011. Carbon dioxide adsorption in graphene sheets. AIP Adv. 1, 032152.

Mishra, A.K., Ramaprabhu, S., 2014. Enhanced CO_2 capture in Fe_3O_4-graphene nanocomposite by physicochemical adsorption. J. Appl. Phys. 116, 064306.

Nhut, J.-M., Vieira, R., Pesant, L., Tessonnier, J.-P., Keller, N., Ehret, G., Pham-Huu, C., Ledoux, M.J., 2002. Synthesis and catalytic uses of carbon and silicon carbide nanostructures. Catal. Today 76, 11–32.

Nie, Z., Korre, A., Durucan, S., 2011. Life cycle modelling and comparative assessment of the environmental impacts of oxy-fuel and post-combustion CO_2 capture, transport and injection processes. Energy Procedia 4, 2510–2517.

Ning, G., Xu, C., Mu, L., Chen, G., Wang, G., Gao, J., Fan, Z., Qian, W., Wei, F., 2012. High capacity gas storage in corrugated porous graphene with a specific surface area-lossless tightly stacking manner. Chem. Commun. 48, 6815–6817.

Ochoa-Fernández, E., Rusten, H.K., Jakobsen, H.A., Rønning, M., Holmen, A., Chen, D., 2005. Sorption enhanced hydrogen production by steam methane reforming using Li_2ZrO_3 as sorbent: sorption kinetics and reactor simulation. Catal. Today 106, 41–46.

Pacala, S., Socolow, R., 2004. Stabilization wedges: solving the climate problem for the next 50 years with current technologies. Science 305, 968–972.

Park, Y., Lin, K.Y., Park, A.H., Petit, C., 2015. Recent advances in anhydrous solvents for CO_2 capture: ionic liquids, switchable solvents, and nanoparticle organic hybrid materials. Frontiers in Energy Research 3 (article 42), 1–14.

Pfeiffer, H., 2010. Advances on alkaline ceramics as possible CO_2 captors. Advances in CO_2 conversion and utilization. 1056. ACS Symp. Ser. 1056, 233–253.

Pil-Seon, C., Ji-Moon, J., Yong-Ki, C., Myung-Seok, K., Gi-Joo, S., Park, S.-J., 2016. A review: methane capture by nanoporous carbon materials for automobiles. Carbon Lett. 17, 18–28.

Przepiórski, J., Skrodzewicz, M., Morawski, A.W., 2004. High temperature ammonia treatment of activated carbon for enhancement of CO_2 adsorption. Appl. Surf. Sci. 225, 235–242.

Qi, G., Wang, Y., Estevez, L., Duan, X., Anako, N., Park, A.-H.A., Li, W., Jones, C.W., Giannelis, E.P., 2011. High efficiency nanocomposite sorbents for CO_2 capture based on amine-functionalized mesoporous capsules. Energy Environ. Sci. 4, 444–452.

Ramdin, M., Balaji, S.P., Torres-Knoop, A., Dubbeldam, D., de Loos, T.W., Vlugt, T.J.H., 2015. Solubility of natural gas species in ionic liquids and commercial solvents: experiments and monte carlo simulations. J. Chem. Eng. Data 60, 3039–3045.

Recillas, S., Colón, J., Casals, E., González, E., Puntes, V., Sánchez, A., Font, X., 2010. Chromium VI adsorption on cerium oxide nanoparticles and morphology changes during the process. J. Hazard. Mater. 184, 425–431.

Sá, J., Agüera, C.A., Gross, S., Anderson, J.A., 2009. Photocatalytic nitrate reduction over metal modified TiO_2. Appl. Catal. B Environ. 85, 192–200.

Saha, D., Bao, Z., Jia, F., Deng, S., 2010. Adsorption of CO_2, CH_4, N_2O, and N_2 on MOF-5, MOF-177, and Zeolite 5A. Environ. Sci. Technol. 44, 1820–1826.

Sánchez, A., Recillas, S., Font, X., Casals, E., González, E., Puntes, V., 2011. Ecotoxicity of, and remediation with, engineered inorganic nanoparticles in the environment. Trends Anal. Chem. 30, 507–516.

Schlapbach, L., Zuttel, A., 2001. Hydrogen-storage materials for mobile applications. Nature 414, 353–358.

Sevilla, M., Valle-Vigón, P., Fuertes, A.B., 2011. N-doped polypyrrole-based porous carbons for CO_2 capture. Adv. Funct. Mater. 21, 2781–2787.

Shakarova, D., Ojuva, A., Bergström, L., Akhtar, F., 2014. Methylcellulose-directed synthesis of nanocrystalline zeolite naa with high CO_2 uptake. Materials 7, 5507.

Shekhah, O., Belmabkhout, Y., Chen, Z., Guillerm, V., Cairns, A., Adil, K., Eddaoudi, M., 2014. Made-to-order metal-organic frameworks for trace carbon dioxide removal and air capture. Nat. Commun. 5 (article number 4228), 1–7.

Smart, S.K., Cassady, A.I., Lu, G.Q., Martin, D.J., 2006. The biocompatibility of carbon nanotubes. Carbon 44, 1034–1047.

Society, Royal, Royal Academy of Engineering, 2004. Nanoscience and nanotechnologies: opportunities and uncertainties. London. pp 1–116.

Solar, C., García Blanco, A., Vallone, A., Sapag, K., 2010. In: Potocnik, P. (Ed.), Adsorption of methane in porous materials as the basis for the storage of natural gas. Intech, Rijeka, pp. 205–244.

Son, W.-J., Choi, J.-S., Ahn, W.-S., 2008. Adsorptive removal of carbon dioxide using polyethyleneimine-loaded mesoporous silica materials. Microporous Mesoporous Mater. 113, 31–40.

Songolzadeh, M., Takht Ravanchi, M., Soleimani, M., 2012. Carbon dioxide capture and storage: a general review on adsorbents. Int. J. Chem. Mol. Nucl. Mater. Metall. Eng. 6, 900–907.

Spanopoulos, I., Tsangarakis, C., Klontzas, E., Tylianakis, E., Froudakis, G., Adil, K., Belmabkhout, Eddaoudi M., Trikalitis, P.N., 2016. Reticular synthesis of HKUST-like tbo-MOFs with enhanced CH_4 storage. J. Am. Chem. Soc. 138, 1568–1574.

Spigarelli, B.P., Kawatra, S.K., 2013. Opportunities and challenges in carbon dioxide capture. J. CO_2 Utilization 1, 69–87.

Starr, K., Gabarrell, X., Villalba, G., Talens, L., Lombardi, L., 2012. Life cycle assessment of biogas upgrading technologies. Waste Manag. 32, 991–999.

Tanaka, H., El-Merraoui, M., Steele, W.A., Kaneko, K., 2002. Methane adsorption on single-walled carbon nanotube: a density functional theory model. Chem. Phys. Lett. 352, 334–341.

Veltman, K., Singh, B., Hertwich, E.G., 2010. Human and environmental impact assessment of postcombustion CO_2 capture focusing on emissions from amine-based scrubbing solvents to air. Environ. Sci. Technol. 44, 1496–1502.

Venna, S.R., Carreon, M.A., 2010. Highly permeable zeolite Imidazolate framework-8 membranes for CO_2/CH_4 separation. J. Am. Chem. Soc. 132, 76–78.

Walspurger, S., Boels, L., Cobden, P.D., Elzinga, G.D., Haije, W.G., van den Brink, R.W., 2008. The crucial role of the K^+-aluminium oxide interaction in K^+-promoted alumina and hydrotalcite-based materials for CO_2 sorption at high temperatures. ChemSusChem 1, 643–650.

Wang, S., Yan, S., Ma, X., Gong, J., 2011. Recent advances in capture of carbon dioxide using alkali-metal-based oxides. Energy Environ. Sci. 4, 3805–3819.

Wang, Y., Zhao, Y., Bao, T., Li, X., Su, Y., Duan, Y., 2012. Preparation of Ni-reduced graphene oxide nanocomposites by Pd-activated electroless deposition and their magnetic properties. App. Surf. Sci. 258, 8603–8608.

Wang, H., Yuan, X., Wu, Y., Huang, H., Peng, X., Zeng, G., Zhong, H., Liang, J., Ren, M., 2013. Graphene-based materials: fabrication, characterization and application for the decontamination of wastewater and wastegas and hydrogen storage/generation. Adv. Colloid Interf. Sci. 195–196, 19–40.

Wang, X., Ou, G., Wang, N., Wu, H., 2016. Graphene-based recyclable photo-absorbers for high-efficiency seawater desalination. ACS Appl. Mater. Interfaces 8, 9194–9199.

Wu, H., Zhou, W., Yildirim, T., 2009a. High-capacity methane storage in metal–organic frameworks M_2(dhtp): the important role of open metal sites. J. Am. Chem. Soc. 131, 4995–5000.

Wu, H., Zhou, W., Yildirim, T., 2009b. Methane sorption in nanoporous metal–organic frameworks and first-order phase transition of confined methane. J. Phys. Chem. C 113, 3029–3035.

Xia, Y., Mokaya, R., Walker, G.S., Zhu, Y., 2011. Superior CO_2 adsorption capacity on n-doped, high-surface-area, microporous carbons templated from zeolite. Adv. Energy Mater. 1, 678–683.

Xiang, Z., Hu, Z., Cao, D., Yang, W., Lu, J., Han, B., WAng, W., 2011. Metal–organic frameworks with incorporated carbon nanotubes: improving carbon dioxide and methane storage capacities by lithium doping. Angew. Chem. Int. Ed. 50, 491–494.

Xu, Y., Zhao, D., 2007. Reductive immobilization of chromate in water and soil using stabilized iron nanoparticles. Water Res. 41, 2101–2108.

Yang, C., Xu, Q., 1997. Aluminated zeolites β and their properties part 1.-Alumination of zeolites β. J. Chem. Soc. Faraday Trans. 93, 1675–1680.

Yang, H., Xu, Z., Fan, M., Gupta, R., Slimane, R.B., Bland, A.E., Wright, I., 2008. Progress in carbon dioxide separation and capture: a review. J. Environ. Sci. 20, 14–27.

Yang, Z., Zhao, M., Florin, N.H., Harris, A.T., 2009. Synthesis and characterization of CaO nanopods for high temperature CO_2 capture. Ind. Eng. Chem. Res. 48, 10765–10770.

Yoo, J., Lee, S., Lee, C.K., Kim, C., Fujigaya, T., Park, H.J., Nakashima, N., Shim, J.K., 2014. Homogeneous decoration of zeolitic imidazolate framework-8 (ZIF-8) with core-shell structures on carbon nanotubes. RSC Adv. 4, 49614–49619.

Zhang, X., Wang, W., 2002. Methane adsorption in single-walled carbon nanotubes arrays by molecular simulation and density functional theory. Fluid Phase Equilib. 194–197, 289–295.

Zhou, L., Sun, Y., Yang, Z., Zhou, Y., 2005. Hydrogen and methane sorption in dry and water-loaded multiwall carbon nanotubes. J. Colloid Interface Sci. 289, 347–351.

Zhu, X.-D., Tian, J., Le, S.-R., Chen, J.-R., Sun, K.-N., 2013. Enhanced electrochemical performances of $CuCrO_2$–CNTs nanocomposites anodes by in-situ hydrothermal synthesis for lithium ion batteries. Mater. Lett. 107, 147–149.

A-5

Journal of Materials Chemistry A

Accepted Manuscript

This article can be cited before page numbers have been issued, to do this please use: A. Yazdi, A. Abo Makeb, L. Garzón-Tovar, J. Patarroyo, J. Moral-Vico, A. Alonso, A. Sanchez, N. G. Bastús, I. Imaz, X. Font, V. puntes and D. Maspoch, *J. Mater. Chem. A*, 2017, DOI: 10.1039/C7TA03006A.

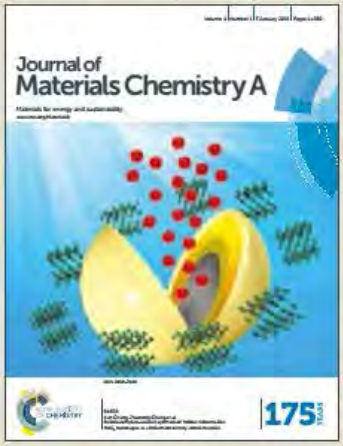

ROYAL SOCIETY OF CHEMISTRY

rsc.li/materials-a

View Article Online
DOI: 10.1039/C7TA03006A

Journal of Materials Chemistry A

PAPER

Core-shell Au/CeO_2 nanoparticles supported in UiO-66 beads exhibiting full CO conversion at 100 ˚C

Received 00th January 20xx,
Accepted 00th January 20xx

DOI: 10.1039/x0xx00000x

www.rsc.org/

A. Yazdi,[a] A. Abo Markeb,[b] L. Garzón-Tovar,[a] J. Patarroyo,[a] J. Moral-Vico,[b] A. Alonso,[*,b] A. Sánchez,[b] N. Bastus,[a] I. Imaz,[a] X. Font,[b] V. Puntes,[*,a,c,d] and D. Maspoch[*,a,d]

Hybrid core-shell Au/CeO_2 nanoparticles (NPs) dispersed in UiO-66 shaped into microspherical beads are created using the spray-drying continuous-flow method. The combined catalytic properties of nanocrystalline CeO_2 and Au in a single particle and the support and protective function of porous UiO-66 beads make the resulting composites showing good performances as catalysts for CO oxidation (T_{50} = 72 ˚C; T_{100} = 100 ˚C) and recyclability.

Long-term exposure to carbon monoxide gas is a cause of lethal damage to humans and animals.[1] Only in 2014, 6381 kilotons of CO were emitted in the world, mainly from transportation, power plants and industrial activities[2]. To date, one of the most efficient solutions for mitigating CO emissions to atmosphere is its catalytic oxidation to CO_2.[3, 4] Good-performance catalysts for CO oxidation are metal nanoparticles (NPs) such as Au, Pd, Pt and Ru NPs.[5-8] These NPs are usually supported on/in zeolites,[9] activated carbon,[10] and metal oxides, including alumina,[11] mesoporous silica,[12] ceria,[13-17] zirconia,[18] titania,[19] and iron oxides.[3] These supports avoid NP aggregation and, eventually, enhance the catalytic activity of NPs. A remarkable case is the use of nanocrystalline CeO_2 to support Au NPs.[20, 21] In this particular composite, CeO_2 acts as an active support that enhances the catalytic performance of Au NPs for CO oxidation. Indeed, because CeO_2 has a high oxygen storage and release capacity[22] and facile oxygen vacancy formation, its surface can be easily enriched with oxygen vacancies so that Au NPs can strongly bind to these vacancies.[23,24] Also, the oxygen vacancies in CeO_2 can create Ce^{3+} ions, opening a new CO oxidation pathway by O_2 adsorbed on Au-Ce^{3+} bridge site.[23] Moreover, the interaction between the ceria and the metal NPs can prevent reorganization of the metallic atoms under operating conditions.[22]

Inspired by these latter results, herein we show a fast method that enables integrating pre-designed core-shell Au/CeO_2 NPs[25-27] in metal-organic frameworks (MOFs). Recently, MOFs have attracted much attention as new porous supports for catalytic NPs due to their exceptionally high surface areas, structural diversity and tailorable pore chemical functionalities.[28] For CO oxidation, Xu *et al.* have shown that ZIF-8 MOF can support Au NPs to fully oxidize CO at a temperature of 225 ˚C.[29] Similarly, Pd and Pt NPs and hybrid Pd/Pt NPs supported on MIL-101, ZIF-8, UiO-67 and UiO-66 MOFs showed full CO conversion at temperatures ranging from 120 ˚C to 200 ˚C (Table 1).[30-33] In this work, we combine the catalytic properties for CO oxidation of both nanocrystalline CeO_2 and Au counterparts in a single particle entity, which is supported in UiO-66 beads using the spray-drying continuous-flow method. This method allows the simultaneously synthesis and shaping of MOF beads while encapsulating the pre-synthesized NPs in a fast, continuous

Table 1 Inorganic nanoparticles supported on MOFs for CO oxidation.

Catalyst	*NPs w.t.%*	T_{50} (˚C)	T_{100} (˚C)	*ref.*
UiO-66@Au/CeO_2	7	72	100	this work
UiO-66@Au/CeO_2	5.5	82	110	this work
UiO-67@Pt	5	100	120	33
MIL-101@Pt/Pd		150	175	30
MIL-101@Pt		160	175	30
UiO-66@Au/CeO_2	2.8	98	180	this work
UiO-66@Pt	2	160	180	32
MIL-101@Pd		185	200	30
ZIF-8@Pt	2	170	200	31
ZIF-8@Au	5	170	225	29
UiO-66		369	440	this work

[a] Catalan Institute of Nanoscience and Nanotechnology (ICN2), CSIC and The Barcelona Institute of Science and Technology, Campus UAB, Bellaterra, 08193 Barcelona, Spain. E-mail: victor.puntes@icn2.cat; daniel.maspoch@icn2.cat
[b] Department of Chemical, Biological and Environmental Engineering, Escola d'Enginyeria, Universitat Autònoma de Barcelona, 08193 Bellaterra, Spain. E-mail: Amanda.Alonso@uab.cat
[c] Vall, d'Hebron Institut de Recerca (VHIR), 08035, Barcelona, Spain.
[d] ICREA, Pg. Lluis Companys 23, 08010 Barcelona, Spain

† Footnotes relating to the title and/or authors should appear here.
Electronic Supplementary Information (ESI) available. See DOI: 10.1039/x0xx00000x

DOI: 10.1039/C7TA03006A
ARTICLE Journal Name

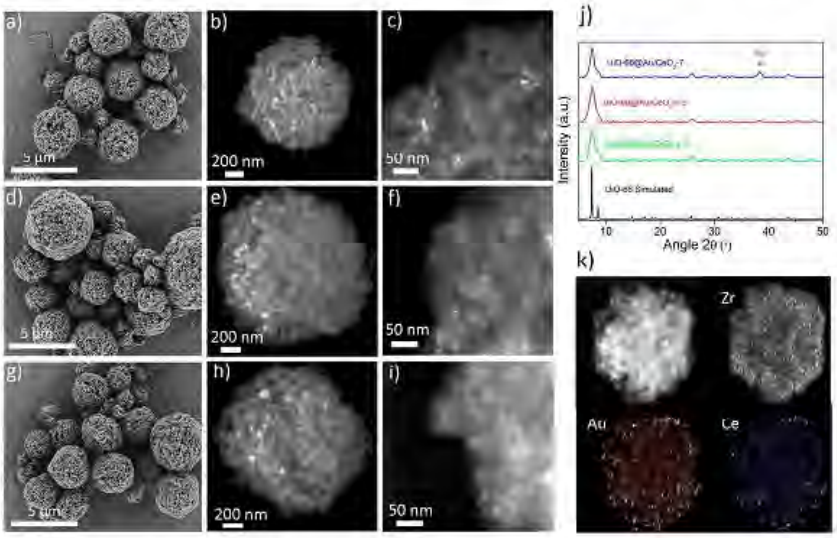

Fig. 1 (a-i) Representative FE-SEM and HAADF-STEM images of UiO-66@Au/CeO_2-2.8 (a-c), UiO-66@Au/CeO_2-5.5 (d-f) and UiO-66@Au/CeO_2-7 (g-i). (j) XRPD patterns of UiO-66@Au/CeO_2-2.8 (green), UiO-66@Au/CeO_2-5.5 (red) and UiO-66@Au/CeO_2-7 (blue) in comparison to the simulated pattern for UiO-66 (black). (k) Elemental mapping (Zr, Ce and Au) of the composite UiO-66@Au/CeO_2-2.8.

one-step process.[34-36]

Our method started with the synthesis of core-shell Au/CeO_2 (Ce:Au = 1:1) NPs in water following the simultaneous reduction/oxidation of Au and Ce precursors (ESI†). Synthesized NPs had an average particle size of 9.6 ± 2.0 nm and Au core size of 4.2 ± 1.2 nm (Fig. S1, ESI†). Then, they were functionalized with PVP, allowing them to be transferred from water to dimethylformamide (DMF). This step enables the dispersion of Au/CeO_2 NPs in the solvent needed for synthesizing the UiO-66 beads. Afterwards, 100 mg of terephthalic acid, 3 mL of acetic acid, 4 ml of Au/CeO_2 NPs (concentration = 1 mg/mL) and 280 µL of $Zr(OPr^n)_4$ were sequentially mixed in 40 ml DMF. Note here that $ZrCl_4$, which is the common salt used to synthesize UiO-66, was replaced by $Zr(OPr^n)_4$ because of the dissolution of CeO_2 in the acidic precursor solution when $ZrCl_4$ is utilized (Fig. S2, ESI†).[37] This mixture was injected into a coil flow reactor at a feed rate of 2.4 $ml.min^{-1}$ at 115 °C. The resulting pre-heated solution was then spray dried at 180 °C and a flow rate of 336 ml/min using a spray cap with a 0.5 mm diameter hole. The collected solid was dispersed in DMF and washed twice with DMF and ethanol.[34]

A final step involved its calcination at 250°C overnight in the presence of air. This calcination process facilitates the removal of PVP from the surface of Au/CeO_2 NPs. It also enhances the interfacial interaction of Au and CeO_2 and increases the crystallinity of CeO_2, which leads to an enhancement of oxygen generation/storage capacity of ceria.[38-40]

Field-emission scanning electron microscopy (FE-SEM) of the calcinated powder revealed the formation of spherical beads (average size = 3.4 ± 1.8 µm) formed by the assembly of nanocrystals of UiO-66 (Fig. 1a). X-ray powder diffraction (XRPD) indicated that the beads were pure crystalline UiO-66 (Fig. 1j). Fig. 1b,c shows high angle annular dark field scanning transmission electron microscopy (HAADF-STEM) of these beads, confirming the encapsulation of well-dispersed Au/CeO_2 NPs inside them. In addition, energy dispersive X-ray spectroscopy (EDX) mapping of the beads showed the homogeneous distribution of Au and Ce inside the beads (Fig. 1k). The content of Au/CeO_2 in this composite was estimated by digesting the powder in a mixture of concentrated HCl and HNO_3 and analysed by inductively coupled plasma optical emission spectrometry (ICP-OES), from which a Au/CeO_2 content of 2.8 % (Ce: 1.28 %, Au: 1.31 %) in the composite (hereafter, UiO-66@Au/CeO_2-2.8) was determined. The comparison of this value to the initial percentage of Au/CeO_2 NPs added into the UiO-66 precursor solution leads to an encapsulation yield of 92 %, confirming the efficiency of the spray drying method for incorporating Au/CeO_2 NPs into the UiO-66 beads. Finally, the adsorption capacity of UiO-66@Au/CeO_2-2.8 was determined. N_2 physical adsorption measurements showed a measured Brunauer Emmet Teller

DOI: 10.1039/C7TA03006A

(BET) surface area (A_{BET}) of 1095 m^2/g (Fig. S3a, ESI†), very close to that of pristine UiO-66 superstructures.[37]

The catalytic activity of the UiO-66@Au/CeO_2-2.8 in CO oxidation was evaluated by the temperature-programed oxidation method. The catalytic oxidation of CO was carried out in a fixed bed column reactor with dimensions of 9.0 cm in length and 0.5 cm in inner diameter set in a controlled temperature oven. 50 mg of the catalyst was packed into the column, and a mixture of gases consisting of 1 % CO, 21 % O_2 and 78 % N_2 was allowed to pass through the column reactor at a constant flow rate of 100 ml/min. After that, the catalyst was heated up to the desired temperature and maintained until a steady state was achieved. Within this interval of time, set of samples of the outlet gas were withdrawn and analyzed to determine the CO converted.

In an initial step, the catalytic activity of UiO-66 beads without Au/CeO_2 NPs was measured as a control reaction. As expected, UiO-66 beads showed no conversion of CO to CO_2 up to 200 °C, and full conversion took place at 440 °C (Fig. S4, ESI†). On the contrary, the catalytic activity of UiO-66@Au/CeO_2-2.8 was remarkably enhanced. As is shown in Fig. 2a, this composite showed a CO conversion starting at room temperature and exhibited a 50 % (T_{50}) and 100 % (T_{100}) CO conversion at temperatures of 98 °C and 180°C, respectively (Table 1).

It is known that, if no aggregation occurs, higher loading of NPs tends to increase the catalytic activity of this class of supported composites. To this end, we systematically synthesized a series of composites in which we increased the added amount of Au/CeO_2 NPs dispersion (1 mg/mL) in the precursor solution to 8.5 mL, 12 mL and 16 mL. Again, FESEM and HAADF-STEM images revealed the formation of beads containing Au/CeO_2 NPs for all samples (Fig. 1d-i). However, the latter sample was discarded because it showed the presence of a high amount of non-encapsulated Au/CeO_2 NPs together with the beads as well as lower crystallinity of UiO-66 (Fig. S5, ESI†). For the first two compositions, XRPD patterns confirmed the formation of UiO-66 (Fig. 1j), from which Au/CeO_2 contents of 5.5 % (Ce: 2.48 %, Au: 2.50 %) and 7 % (Ce: 3.22 %, Au: 3.18 %) in the composites (hereafter, UiO-66@Au/CeO_2-5.5 and UiO-66@Au/CeO_2-7) were determined. These amounts correspond to 91 % and 74 % of encapsulation efficiency for UiO-66@Au/CeO_2-5.5 and UiO-66@Au/CeO_2-7, respectively. Finally, N_2 physical adsorption measurements confirmed that both composites are porous, showing measured BET surface areas of 1070 and 870 m^2/g (Fig. S3b,c, ESI†).

Ensuing temperature-programed oxidation measurements confirmed a clear improvement of CO conversion for both new composites, achieving lower T_{50} and T_{100} values by increasing the percentage of Au/CeO_2 NPs (Fig 2a). In the case of UiO-66@Au/CeO_2-5.5, T_{50} and T_{100} were found to be 82 °C and 110 °C, respectively. For UiO-66@Au/CeO_2-7, these temperatures decreased down to 72 °C and 100 °C. Remarkably, in this latter case, a CO conversion of 3.8 % was achieved at room temperature. Moreover, for this latter reaction, the activation energy was found to be 40.2 kJ/mol, whereas the turnover

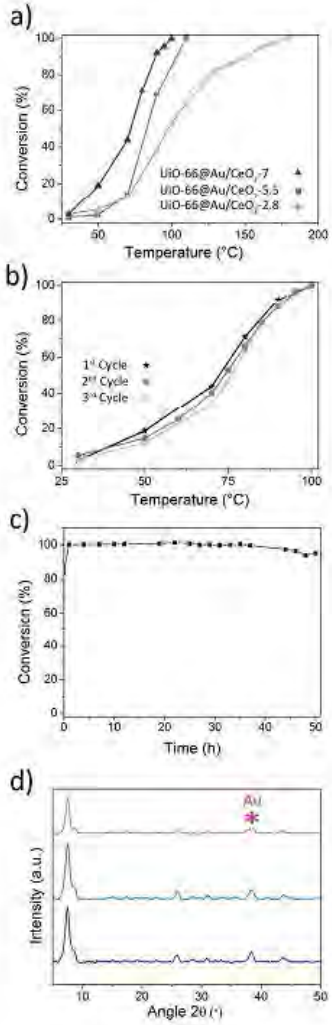

Fig. 2 (a) CO conversion rate as a function of reaction temperature for UiO-66@Au/CeO_2-2.8, UiO-66@Au/CeO_2-5.5 and UiO-66@Au/CeO_2-7. (b) CO conversion rate as a function of reaction temperature for three consecutive cycles over the UiO-66@Au/CeO_2-7 composite. (c) CO conversion rate at 100 °C for 12 hours over the UiO-66@Au/CeO_2-7 composite. (d) XRPD patterns of as-synthesized UiO-66@Au/CeO_2-7 (blue) and after after three temperature-programed cycles (light blue) and 50 hours of continuous CO conversion (grey).

DOI: 10.1039/C7TA03006A
ARTICLE Journal Name

frequencies (TOF) values at temperatures of 30, 50, 75 and 100 ºC were 10, 39, 106 and 204 h^{-1}, respectively (for comparison purposes, TOF values of other reported catalysts based on Au NPs are given in Table S1, ESI†).

Finally, the recyclability of these composites was evaluated using the composite UiO-66@Au/CeO_2-7 that shows the lower T_{100}. Initially, we performed three cycles of catalysis without detecting any loss of activity (Fig. 2b). After these cycles, the stability of UiO-66@Au/CeO_2-7 was analyzed by XRPD that showed a complete retention of the crystallinity of UiO-66 (Fig. 2d), as also confirmed by its unaffected surface area (A_{BET} = 850 m^2/g). Similarly, no sign of NP sintering or aggregation and alteration of the morphology of the beads was observed by STEM and FE-SEM (Fig. S6, ESI†). Then, the catalytic activity of UiO-66@Au/CeO_2-7 sample was also studied during a longer period of time. For this, the conversion of CO was followed in continue at 100 ºC during 50 hours, from which it was not observed any loss of activity during the first 37 hours and a slight decrease of activity (5 %) after 50 hours (Fig. 2c). We attributed this decrease in catalytic activity to a loss of crystallinity of UiO-66 (Fig. 2d) and its porosity capabilities (A_{BET} = 670 m^2/g).

In conclusion, we have described the formation of a new composite based on the entrapment and dispersion of core-shell Au/CeO_2 NPs into microsized spherical, porous UiO-66 beads using the spray-drying continuous-flow method. The combination of nanocrystalline CeO_2 and Au allows accessing to CO conversion T_{50} and T_{100} as low as 72 ºC and 100 ºC. These values are to our knowledge one of the lowest CO conversion temperatures achieved using catalysts based on NPs supported on MOFs. In addition, UiO-66 provides enough protection to avoid NP sintering/aggregation. We consider this method as a general approach for making composites consisting of functional NPs dispersed in MOFs already shaped into spherical beads, as demonstrated by the fact that other composites made of Pd NPs dispersed into UiO-66 beads (Fig. S7, ESI†) were also fabricated and tested for CO oxidation.

Acknowledgements

This work was supported by the Spanish MINECO (projects PN MAT2015-65354-C2-1-R and MAT2015-70725-R), the Catalan AGAUR (projects 2014-SGR-80 and 2014-SGR-612), and the ERC under the EU FP7 (ERC-Co 615954). N.G.B. thanks the MINECO for her RyC grant RYC-2012- 10991 and the financial support by the European Commission Seventh Framework Program (FP7) through the Marie Curie Career Integration Grant (322153-MINE). ICN2 acknowledges the support of the Spanish MINECO through the Severo Ochoa Centres of Excellence Programme, under Grant SEV-2013-0295.

Notes and references

1. R. A. Jones, J. A. Strickland, J. A. Stunkard and J. Siegel, *Toxicol. Appl. Pharmacol.*, 1971, **19**, 46-53.
2. *Environment and Climate Change Canada Canadian Environmental Sustainability Indicators: Air Pollutant Emissions. Available at:* http://www.ec.gc.ca/indicateurs-indicators/default.asp?lang=en&n=E79F4C12-1 , 2016.
3. L. Liu, F. Zhou, L. Wang, X. Qi, F. Shi and Y. Deng, *J. Catal.*, 2010, **274**, 1-10.
4. B. Qiao, A. Wang, X. Yang, L. F. Allard, Z. Jiang, Y. Cui, J. Liu, J. Li and T. Zhang, *Nat. Chem.*, 2011, **3**, 634-641.
5. M. S. Chen, Y. Cai, Z. Yan, K. K. Gath, S. Axnanda and D. W. Goodman, *Surf. Sci.*, 2007, **601**, 5326-5331.
6. J. Wang, Z. Wang and C.-J. Liu, *Appl. Mater. Interfaces*, 2014, **6**, 12860-12867.
7. P. J. Berlowitz, C. H. F. Peden and D. W. Goodman, *J. Phys. Chem.*, 1988, **92**, 5213-5221.
8. E. M. C. Alayon, J. Singh, M. Nachtegaal, M. Harfouche and J. A. van Bokhoven, *J. Catal.*, 2009, **263**, 228-238.
9. W. Han, P. Zhang, Z. Tang and G. Lu, *Process Saf. Environ. Prot.*, 2014, **92**, 822-827.
10. L. Wang, Y. Zhang, Y. Lou, Y. Guo, G. Lu and Y. Guo, *Fuel Process. Technol.*, 2014, **122**, 23-29.
11. A. S. Ivanova, E. M. Slavinskaya, R. V. Gulyaev, V. I. Zaikovskii, O. A. Stonkus, I. G. Danilova, L. M. Plyasova, I. A. Polukhina and A. I. Boronin, *Appl. Catal., B*, 2010, **97**, 57-71.
12. H. Wang and C.-j. Liu, *Appl. Catal., B*, 2011, **106**, 672-680.
13. A. E. R. S. Khder, H. M. A. Hassan, M. A. Betiha, K. S. Khairou and A. A. Ibrahim, *Reac. Kinet. Mech. Cat.*, 2014, **112**, 61-75.
14. D. Zhang, X. Du, L. Shi and R. Gao, *Dalton Trans.*, 2012, **41**, 14455-14475.
15. W. Liu, X. Liu, L. Feng, J. Guo, A. Xie, S. Wang, J. Zhang and Y. Yang, *Nanoscale*, 2014, **6**, 10693-10700.
16. D. Zhang, Y. Qian, L. Shi, H. Mai, R. Gao, J. Zhang, W. Yu and W. Cao, *Catal. Commun.*, 2012, **26**, 164-168.
17. W. Liu, T. Deng, L. Feng, A. Xie, J. Zhang, S. Wang, X. Liu, Y. Yang and J. Guo, *CrystEngComm*, 2015, **17**, 4850-4858.
18. C. M. Olmos, L. E. Chinchilla, J. J. Delgado, A. B. Hungria, G. Blanco, J. J. Calvino and X. Chen, *Catal. Lett.*, 2015, **146**, 144-156.
19. J. Wang, S. A. Kondrat, Y. Wang, G. L. Brett, C. Giles, J. K. Bartley, L. Lu, Q. Liu, C. J. Kiely and G. J. Hutchings, *ACS Catalysis*, 2015, **5**, 3575-3587.
20. S. Carrettin, P. Concepcion, A. Corma, J. M. Lopez Nieto and V. F. Puntes, *Angew. Chem. Int. Ed.*, 2004, **43**, 2538-2540.
21. M. Centeno, T. Ramírez Reina, S. Ivanova, O. Laguna and J. Odriozola, *Catalysts*, 2016, **6**, 158.
22. N. J. Divins, I. Angurell, C. Escudero, V. Perez-Dieste and J. Llorca, *Science*, 2014, **346**, 620-623.
23. H. Y. Kim, H. M. Lee and G. Henkelman, *J. Am. Chem. Soc.*, 2012, **134**, 1560-1570.
24. C. Zhang, A. Michaelides and S. J. Jenkins, *PCCP*, 2011, **13**, 22-33.
25. T. Mitsudome, M. Yamamoto, Z. Maeno, T. Mizugaki, K. Jitsukawa and K. Kaneda, *J. Am. Chem. Soc.*, 2015, **137**, 13452-13455.
26. F. Zhu, G. Chen, S. Sun and X. Sun, *J. Mater. Chem. A*, 2013, **1**, 288-294.
27. Y. H. Qu, F. Liu, Y. Wei, C. L. Gu, L. H. Zhang and Y. Liu, *Appl. Surf. Sci.*, 2015, **343**, 207-211.

DOI: 10.1039/C7TA03006A

28. P. Falcaro, R. Ricco, A. Yazdi, I. Imaz, S. Furukawa, D. Maspoch, R. Ameloot, J. D. Evans and C. J. Doonan, *Coord. Chem. Rev.*, 2016, **307, Part 2**, 237-254.
29. H.-L. Jiang, B. Liu, T. Akita, M. Haruta, H. Sakurai and Q. Xu, *J. Am. Chem. Soc.*, 2009, **131**, 11302-11303.
30. A. Aijaz, T. Akita, N. Tsumori and Q. Xu, *J. Am. Chem. Soc.*, 2013, **135**, 16356-16359.
31. G. Lu, S. Li, Z. Guo, O. K. Farha, B. G. Hauser, X. Qi, Y. Wang, X. Wang, S. Han, X. Liu, J. S. DuChene, H. Zhang, Q. Zhang, X. Chen, J. Ma, S. C. Loo, W. D. Wei, Y. Yang, J. T. Hupp and F. Huo, *Nat. Chem.*, 2012, **4**, 310-316.
32. W. Zhang, G. Lu, C. Cui, Y. Liu, S. Li, W. Yan, C. Xing, Y. R. Chi, Y. Yang and F. Huo, *Adv. Mater.*, 2014, **26**, 4056-4060.
33. G.-l. Zhuang, J.-q. Bai, X. Zhou, Y.-f. Gao, H.-l. Huang, H.-q. Cui, X. Zhong, C.-L. Zhong and J.-g. Wang, *Eur. J. Inorg. Chem.*, 2017, **2017**, 172-178.
34. L. Garzon-Tovar, M. Cano-Sarabia, A. Carne-Sanchez, C. Carbonell, I. Imaz and D. Maspoch, *React. Chem. Eng.*, 2016, **1**, 533-539.
35. A. Carné-Sánchez, I. Imaz, M. Cano-Sarabia and D. Maspoch, *Nat. Chem.*, 2013, **5**, 203-211.
36. J. P.-C. L. Garzon-Tovar, I. Imaz, D. Maspoch, *Adv. Funct. Mater.*, 2017, DOI: 10.1002/adfm.201606424.
37. B. Rungtaweevoranit, J. Baek, J. R. Araujo, B. S. Archanjo, K. M. Choi, O. M. Yaghi and G. A. Somorjai, *Nano Lett.*, 2016, **16**, 7645-7649.
38. B. He, Q. Zhao, Z. Zeng, X. Wang and S. Han, *J. Mater. Sci.*, 2015, **50**, 6339-6348.
39. L. Zhou, X. Li, Z. Yao, Z. Chen, M. Hong, R. Zhu, Y. Liang and J. Zhao, *Sci. Rep.*, 2016, **6**, 23900.
40. Y. Liu, H.-S. Chen, J. Li and P. Yang, *RSC Adv.*, 2015, **5**, 37585-37591.

View Article Online
DOI: 10.1039/C7TA03006A